JSST2022

The 41st JSST Annual International Conference on Simulation Technology

Conference Proceedings

Kyushu Institute of Technology, Iizuka, Fukuoka, JAPAN

Online Conference, Aug. 31—Sep. 2, 2022

Kyutech
Kyushu Institute of Technology

Supporting Companies

CYBERNET

HPC TECH

最先端をカスタマイズ・CAEソフトウェアMeshman

株式会社インサイト

PROMETECH.

HOLDINGS SOFT CREATE

Cooperating Societies

The Institute of Electrical Engineers of Japan

The Institute of Electrical Engineers of Japan, Kyushu Branch

The Japan Society for Industrial and Applied Mathematics

The Japan Society of Plasma Science and Nuclear Fusion Research

The Japan Society of Mechanical Engineers

The Visualization Society of Japan

The Robotics Society of Japan

Session Schedule

Day 1: Wednesday, 31st August, 2022					
Time	**Hall A**	**Hall B**	**Hall C**	**Hall D**	**Hall E**
09:45 – 10:00	**Opening Ceremony (Hall A)**				
10:00 – 10:30	**Plenary Talk 1 (Hall A)**				
10:30 – 11:00					
11:00 – 11:15	**Group Photo**				
11:15 – 11:30	**Invited Talk 1** **Tutorial Talk 1** **Session 1 (2)**		**OS 6 ①** **Session 6 (4)**	**OS 7 ①** **Session 9 (3)**	
11:30 – 11:45					
11:45 – 12:00					
12:00 – 12:15					
12:15 – 12:30					
12:30 – 13:30	**Lunch Time**				
13:30 – 13:45	**Corporate Seminar 1A**	**Corporate Seminar 1B**			
13:45 – 14:00					
14:00 – 14:15					
14:15 – 14:30					
14:30 – 15:00	**Plenary Talk 3 (Hall A)**				
15:00 – 15:30					
15:30 – 15:45					
15:45 – 16:00	**Symposium 1 ①** **Session 2 (3)**	**OS 8 ①** **Session 4 (3)**	**OS 2 ①** **Session 7 (3)**	**OS 7 ②** **Session 10 (3)**	**OS 4 ①** **Session 12 (3)**
16:00 – 16:15					
16:15 – 16:30					
16:30 – 16:45					
16:45 – 17:00					
17:00 – 17:15	**Symposium 1 ②** **Session 3 (2)**	**OS 8 ②** **Session 5 (2)**	**OS 2 ②** **Session 8 (2)**	**OS 7 ③** **Session 11 (3)**	**OS 4 ②** **Session 13 (3)**
17:15 – 17:30					
17:30 – 17:45					
17:45 – 18:00					

Day 2: Thursday, 1st September, 2022					
Time	**Hall A**	**Hall B**	**Hall C**	**Hall D**	**Hall E**
09:00 – 09:15	Symposium 1 ③ Session 14 (3)	Symposium 2 ① Session 17 (3)	Invited Talk 3 Tutorial Talk 3 Session 20 (2)	OS 7 ④ Session 23 (3)	OS 4 ③ Session 26 (3)
09:15 – 09:30					
09:30 – 09:45					
09:45 – 10:00					
10:00 – 10:15					
10:15 – 10:30	Symposium 1 ④ Session 15 (3)	Symposium 2 ② Session 18 (2)	Symposium 3 ① Session 21 (3)	OS 5 ① Session 24 (3)	OS 4 ④ Session 27 (2)
10:30 – 10:45					
10:45 – 11:00					
11:00 – 11:15					
11:15 – 11:30					
11:30 – 11:45	Symposium 1 ⑤ Session 16 (2)	Symposium 2 ③ Session 19 (3)	Symposium 3 ② Session 22 (2)	OS 5 ② Session 25 (2)	OS 7 ⑤ Session 28 (3)
11:45 – 12:00					
12:00 – 12:15					
12:15 – 12:30					
12:30 – 13:30	Lunch Time				
13:30 – 13:45	Corporate Seminar 2A	Corporate Seminar 2B			
13:45 – 14:00					
14:00 – 14:15					
14:15 – 14:30					
14:30 – 14:35	Announcement about JSST2023 (Hall C)				
14:35 – 15:15	Shotgun Session (Hall C)				
15:15 – 15:30					
15:30 – 16:30	Student Session + Corporate Exhibition (Remo)				
16:30 – 18:00					

<table>
<tr><th colspan="6">Day 3: Friday, 2nd September, 2022</th></tr>
<tr><th>Time</th><th>Hall A</th><th>Hall B</th><th>Hall C</th><th>Hall D</th><th>Hall E</th></tr>
<tr><td>09:00 – 09:30</td><td colspan="5" rowspan="2">Plenary Talk 2 (Hall B)</td></tr>
<tr><td>09:30 – 10:00</td></tr>
<tr><td>10:00 – 10:15</td><td colspan="5"></td></tr>
<tr><td>10:15 – 10:30</td><td rowspan="4">OS 3 ①
Session 29 (3)</td><td rowspan="4">Invited Talk 2
Tutorial Talk 2
Session 32 (2)</td><td rowspan="4">Symposium 3 ③
Session 35 (3)</td><td rowspan="4">OS 1 ①
Session 38 (3)</td><td rowspan="4">OS 9 + OS 10 ①
Session 41 (3)</td></tr>
<tr><td>10:30 – 10:45</td></tr>
<tr><td>10:45 – 11:00</td></tr>
<tr><td>11:00 – 11:15</td></tr>
<tr><td>11:15 – 11:30</td><td colspan="5"></td></tr>
<tr><td>11:30 – 11:45</td><td rowspan="4">OS 3 ②
Session 30 (3)</td><td rowspan="2">Symposium 2 ④
Session 33 (2)</td><td rowspan="2">Symposium 3 ④
Session 36 (2)</td><td rowspan="4">OS 1 ②
Session 39 (3)</td><td rowspan="4">OS 9 + OS 10 ②
Session 42 (3)</td></tr>
<tr><td>11:45 – 12:00</td></tr>
<tr><td>12:00 – 12:15</td><td rowspan="2"></td></tr>
<tr><td>12:15 – 12:30</td></tr>
<tr><td>12:30 – 13:30</td><td colspan="5">Lunch Time</td></tr>
<tr><td>13:30 – 13:45</td><td rowspan="3">OS 3 ③
Session 31 (2)</td><td rowspan="3">Symposium 2 ⑤
Session 34 (2)</td><td rowspan="3">Symposium 3 ⑤
Session 37 (2)</td><td rowspan="3">OS 1 ③
Session 40 (2)</td><td rowspan="3"></td></tr>
<tr><td>13:45 – 14:00</td></tr>
<tr><td>14:00 – 14:15</td></tr>
<tr><td>14:15 – 14:30</td><td colspan="5"></td></tr>
<tr><td>14:30 – 15:00</td><td colspan="5">Closing Ceremony (Hall A)</td></tr>
</table>

Symposium1

Plenary Talk

Presenter:

Prof. Toshihiro Hanawa

Information Technology Center, The University of Tokyo

Title:

Smart Supercomputing by Integration of Simulation, Data, and Learning

Abstract:

Traditionally, supercomputers have been used for Computational Science and Engineering (CSE) simulations. For future supercomputing, we should consider integrating data analysis and machine learning to leverage knowledge in a smarter way than just traditional simulation.
This talk will introduce our activities toward “smart supercomputing,” including Wisteria/BDEC-01 in the Information Technology Center, the University of Tokyo, and the “mdx” data platform under the joint operation with nine national universities and two national research institutes in Japan.

Biography:

Toshihiro Hanawa received his M.E. degree and his Ph.D. degree in computer science from Keio University in 1995 and 1998. He was an assistant professor at Tokyo University of Technology, Japan, from 1998 to 2007, a research fellow at Center for Computational Sciences (CCS), University of Tsukuba, from 2007 to 2008, and an associate professor of CCS from 2008 to 2013. He was a project associate professor at Information Technology Center, The University of Tokyo, from 2013 to 2015 and an associate professor from 2015 to 2020. Since Dec. 2020, he has been a professor at the Information Technology Center, The University of Tokyo.
He is also the division leader of the Operations Support Division in JCAHPC (Joint Center for Advanced High-Performance Computing), a joint organization by the University of Tsukuba and the University of Tokyo to operate the Oakforest-PACS supercomputer system. He leads the design of

the next Oakforest-PACS II system.
His research interests include computer architecture, interconnection networks, and acceleration using GPU and FPGA.

Invited Talk

Presenter:

Prof. Mitsuteru Asai

Department of Civil and Structural Engineering,
Faculty of Engineering, Kyushu University

Title:

Multi-scale and -physics particle simulations for natural hazard

Abstract:

Particle methods such as the SPH and MPS methods can compute more efficiently problems involving large deformation, splitting, and coupling of the object of interest than mesh-based methods such as the finite element methods. For example, when applied to the design of disaster prevention and countermeasures, free-surface flow problems in complex geometries, such as tsunami runup and flooding in heavy rain disaster, can be easily solved, and even multi-scale and -physics phenomena involving the failure of solids, such as seepage collapse and scouring of breakwaters and seawalls. This talk will share the recent progress on the multi-physics particle simulation related to natural disaster issues.

Biography:

Mitsuteru Asai received the M.E. and Dr. Eng. degrees from Tohoku University in 2000 and 2003. After working at the Ohio State University as a postdoctoral fellow, he became an Asistant Professor at Ritsumeikan University in 2005. Since 2007, he has been an Associate Professor in the Department of Civil Engineering, Kyushu University. His research area is computational mechanics, computational science, and VR/AR related to natural disaster issues.

Tutorial Talk

Presenter:

Dr. Shintaro Kawahara

Research Institute for Value-Added-Information Generation (VAiG), Japan Agency for Marine-Earth Science and Technology (JAMSTEC)

Title:

VisAssets: A Visualization Framework for Unity

Abstract:

This tutorial introduces the procedure for developing visualization applications using VisAssets, a framework that runs on the Unity game engine. VisAssets provides the elements that constitute a general visualization flow as module icons and visualization applications with GUI can be built by simply connecting them appropriately on Unity Editor. This tutorial will show you examples of building applications to visualize scalar and vector field data using VisAssets.

VisAssets can download from the following URL.
https://github.com/kawaharas/VisAssets

Biography:

Shintaro Kawahara received Dr. Eng. from Ibaraki University in 2001. After working as a flexible researcher at the Ibaraki Prefectural Industrial Technology Center and as an assistant at the Information Processing Center of Ibaraki University, he joined the Japan Agency for Marine-Earth Science and Technology (JAMSTEC) in 2003. He belonged to the Earth Simulator Center and was engaged in research on visualization of large-scale simulation data and observation data. He is also involved in the dissemination of visualization software that he has developed.

Symposium2

Plenary Talk

Presenter:

Prof. Kensei Kobayashi

Department of Chemistry Presentation,
Yokohama National University

Title:

Origins of Bioorganic Compounds and Their Homochirality: Approaches from Simulation Experiments

Abstract:

How life was generated on the Earth? Are there any extraterrestrial bodies that foster life on them? The novel scientific field to challenge such questions is astrobiology. Laboratory simulation is one of the most useful approaches to study prebiotic chemical evolution. In this talk, I will present simulation experiments to synthesize bioorganic molecules like amino acids in early Earth or extraterrestrial environments. It was proved that high-energy particles irradiation was quite effective to produce them. Amino acids are chiral molecules and we utilize mostly L-isomers in our biosystem. Simulation experiments to prove the origin of the homochirality of biomolecules will also be introduced, where such quantum beams as circularly polarized light and spin-polarized leptons were used.

Biography:

Kensei Kobayashi is currently a professor emeritus of Yokohama National University. He received his D. Sc. In Department of Chemistry, University of Tokyo in 1982. In 1982-86, he studied in Laboratory of Chemical Evolution, University of Maryland, U.S.A. He has been working in Yokohama National University (YNU) since 1987, and was a professor at YNU in 2003-2020. He has been studying astrobiology, especially focused on prebiotic chemistry toward generation of life and detection of life in extreme terrestrial and extraterrestrial environments.

Invited Talk

Presenter:

Mr. Ryuta Kawanami

Graduate School of Science and Technology,
Kyoto Institute of Technology

Title:

Molecular dynamics study of microscopic mechanism of OH radical-induced DNA damage

Abstract:

DNA sugar-phosphate backbone has sugars joined by phosphodiester bonds. Highly reactive hydroxyl radicals are produced by ionizing radiation in a cell, which can abstract any hydrogen atoms from DNA. Carbon centered sugar radicals produced by the hydrogen abstraction triggers a common lesion, single-strand break (SSB) which induces disease such as carcinogenesis. However, the abstraction mechanisms at the molecular level remain unsolved. Thus, we employed molecular dynamics (MD) simulations on hydroxyl radicals around DNA to evaluate their spatial distribution and accessibility to DNA. In particular, we introduced restraining potentials on the hydroxyl radicals, which enabled us to sufficiently sample the hydroxyl radicals around the sugar moiety of DNA. The result showed that the accessibility of hydroxyl radicals to each hydrogen atom on DNA was very different from the evaluations reported previously. This indicates that the previous evaluations based on the solvent-accessible surface area, or the water accessibility are needed to be modified.

Biography:

Ryuta Kawanami is a doctoral student in soft materials chemistry at Kyoto Institute of Technology. He is interested in physical mechanisms of soft matter in life.

Invited Talk

Presenter:

Prof. Naohisa Yahagi

Graduate School of Media and Governance,
Keio University

Title:

The Secret to Successful medical-industrial Collaboration

Abstract:

The field of medicine is often described as a complex system. However, it is not difficult for physicians to make diagnostic and therapeutic decisions based on their perception of a patient's condition and its changes to find the data representing the pathology accurately.

In other words, the key to successful medical-engineering collaboration begins with the engineers accurately understanding the tacit knowledge of the physician who knows the patient well, while the physicians accurately understand the advanced technology and theory. This interrelationship enables the development of high-precision technology.

In this lecture, I would like to talk about a case in which such an overly complicated event was derived from simple medical common sense, dreaming of the day when the solid results of medical engineering collaboration with you will surpass the world.

Biography:

Born in Palo Alto, the USA, in 1974. I graduated from Keio University School of Medicine and completed the doctoral program at Keio University Graduate School. Pediatrician. Completed (summa cum laude) in the medical business and management course at the University of Tokyo. Invited to and completed the Harvard Business School "Managing healthcare delivery" as a Scholarship. Designed and launched the world's first Clinical Data Management Network, enabling centralized management of medical information throughout Japan. Engaged in research and development of automated diagnosis and treatment support technology based on disease state change prediction. Head of Digital Health, Digital Agency.

Symposium3

Plenary Talk

Presenter:

Prof. Shinobu Yoshimura

Department of Systems Innovation,
School of Engineering, The University of Tokyo

Title:

Super-simulations of Offshore Wind Farm on Fugaku

Abstract:

An offshore wind farm consists of tens of large-scale wind turbines. To promote such offshore wind farms in Japan, we need to consider severe weather conditions caused due to typhoons and narrower sites. To do so, we are developing multiscale and multiphysics integrated simulations for an entire offshore wind farm. The simulations consist of the following four components, (a) Large-scale LES simulator of a whole wind farm considering weather and terrain, RC HPC, (b) Large-scale LES simulator of two tandem wind turbines to evaluate an effect of wake into power generation, FFR, (c) flow-induced vibration of wind turbine, ADVENTURE_Solid and ADVENTURE_Fatigue, and (d) a parallel coupling tool to deal with Fluid-Structure Interaction, REVOCAP_Coupler. In this presentation, we describe Fugaku-based super-simulations of an actual German offshore wind warm in the North see, Alpha Ventus, consisting of twelve 5MW wind turbines.

Biography:

Prof. S. Yoshimura is currently Vice President and Professor, The University of Tokyo (UTokyo). In 1987, he completed his studies in UTokyo (specialized in nuclear engineering) as Doctor of Engineering. He became Lecturer, Associate Professor in UTokyo, then Professor since 1999. His specialties are High-performance and Intelligent Computational Mechanics with Real World's Applications. He serves as a Vice President of IACM and the President of APACM, and has received numerous awards, including IACM Fellow Award (2014) and APACM Computational Mechanics Award (2013).

Invited Talk

Presenter:

Dr. Prakasha Chigahalli Ramegowda

Institute of Microelectronics (IME)/
Sensors, Actuators & Microsystems (SAM),
Agency for Science, Technology and Research
(A*STAR), Singapore

Title:

Coupled multiphysics simulation model for analyzing piezoelectric sensors and actuators

Abstract:

The key to the design of advanced micro electro–mechanical (MEMS) piezoelectric devices for actuator and sensor applications surrounded by fluid media is an accurate evaluation of the electromechanical, fluid and circuit interaction leads to a general formulation as a fluid-structure–piezoelectric–circuit interaction. These four-field coupled problems can be decomposed into the fluid-structure, structure–piezoelectric, and piezoelectric–circuit interactions using hierarchical decomposition and exchange of the variables using partitioned approach. In this talk, we present computational methods [1,2,3,4,5] to solve structure–piezoelectric interaction, piezoelectric–circuit interaction, and fluid-structure-piezoelectric interactions in piezoelectric bimorph actuators and energy harvester.

References

[1] P. C. Ramegowda, D. Ishihara et al., *International Journal of Computational Methods*, Vol.16, 1850106, 2019.
[2] P. C. Ramegowda, D. Ishihara et al., *Finite Elements in Analysis and Design*, Vol.159, pp. 33-49, 2019.
[3] P. C. Ramegowda, D. Ishihara et al., *Computer Methods in Applied Mechanics and Engineering*, Vol. 365, 113006, 2020.
[4] P. C. Ramegowda, D. Ishihara et al., *Composite Structures*, Vol. 245, 112284, 2020.
[5] D. Ishihara et al., *Computers & Structures,* Vol. 253, 106572, 2021

Biography:

Dr. Prakasha Chigahalli Ramegowda received a BE in Mechanical engineering from the National Institute of Engineering in Mysore, India, in 2010. He was with the MEMS design group at Society for Integrated Circuit technology and Applied Research, India, as an Engineer, from 2011- 2015. In 2019 he completed his PhD in Mechanical Engineering from Kyushu Institute of technology, Japan. He is a recipient of the prestigious JSPS Postdoctoral Fellowship (Standard FY2019-22) from the Japan Society for Promotion of Science. He is currently Scientist at Institute of Microelectronics (IME), Agency for Science, Technology and Research (A*STAR), Singapore.

Tutorial Talk

Presenter:

Dr. Hiroshi Watanabe

DEP Systems Business Unit,
Technical Product & Support Promotion, Hexagon

Title:

Fusion of CAE and 3D Metrology

Abstract:

Recently, we often hear the term digital twin, but it is used in a wide range concept. It can be said that the common term is to reconstruct the event in the cyber physical space based on the digital data obtained by observing the event in the real world, and to predict the future by simulation. Some people claim that the traditional CAE is a digital twin. This is based on the fact that a product is built based on CAD, which is a blueprint, and the product is manufactured according to it. However, as is well known, it is difficult to process a product according to a blueprint. The accuracy of the simulation can be said “dizygotic twins” (similar because they are born from the same parent). In this paper, we will consider the points for constructing a digital twin suitable for “identical twins” in the field of computational engineering.

Biography:

Manufacturing Intelligence division, Hexagon
Vice President, JSCES

Committee

General Chair:
Hiroaki Nakamura (National Institute for Fusion Science)
Susumu Fujiwara (Kyoto Institute of Technology)

Conference Chair:
Daisuke Ishihara (Kyushu Institute of Technology)

Conference Co-Chair:
Katsuhiko Yamaguchi (Fukushima University)
Amane Takei (University of Miyazaki)

Program Chair:
Seiki Saito (Yamagata University)
Hiroshi Tamura (Chuo University)

Program Co-Chair:
Ryosuke Ueda (Tohoku University)
Yoshihide Shibata (National Institute of Technology, Gifu College)
Yoshihisa Fujita (Ritsumeikan University)
Kazuhiro Fujita (Saitama Institute of Technology)

Post-Conference Chair:
Hiroaki Ohtani (National Institute for Fusion Science)

Post-Conference Co-Chair:
Tomoko Mizuguchi (Kyoto Institute of Technology)
Susumu Fujiwara (Kyoto Institute of Technology)
Keisuke Nakano (Niigata University)

Publication Chair:
Taku Itoh (Nihon University)

Publication Co-Chair:
Soichiro Ikuno (Tokyo University of Technology)
Hiroto Tadano (University of Tsukuba)

Finance Chair:
Tomoya Niho (Kyushu Institute of Technology)

Publicity Chair:
Nobuaki Ohno (University of Hyogo)

Exhibition Chair:
Amane Takei (University of Miyazaki)

Conference Adviser:
Takuo Yasunaga (Kyushu Institute of Technology)
Takahiro Kenmotsu (Doshisha University)

Committee Member:
Takashi Hara (National Institute of Technology, Kagoshima College)
Masafumi Yoshida (National Institute of Technology, Ube College)
Yuki Uchida (National Institute of Technology, Nagaoka College)
Makoto Nakamura (National Institute of Technology, Kushiro College)

Table of Contents

Day 1: Wednesday, 31st August, 2022

Plenary Talk 1 (Numerical Simulation and Visual Analytics of Nonlinear Problems)
Time: 10:00 – 11:00
Room: Hall A
Chair: ***Soichiro Ikuno (Tokyo University of Technology)***

Symposium 1 on Numerical Simulation and Visual Analytics of Nonlinear Problems (Session 01, Invited and Tutorial Talks)
Time: 11:15 – 12:15
Room: Hall A
Chair: ***Satoshi Tanaka (Ritsumeikan University)***

OS6: Design and Simulations for System Integration (Session 06)
Time: 11:15 – 12:35
Room: Hall C
Chair: ***Shunsuke Nansai (Tokyo Denki University)***

OS7: Plasma, Materials, Fusion Science, and their AI applications (Session 09)
Time: 11:15 – 12:15
Room: Hall D
Chair: ***Seiki Saito (Yamagata University)***

Plenary Talk 3 (Advanced Numerical Analysis and Software in Multiphysics and Coupled Problems)
Time: 14:30 – 15:30
Room: Hall A
Chair: ***Daisuke Ishihara (Kyushu Institute of Technology)***

Symposium 1 on Numerical Simulation and Visual Analytics of Nonlinear Problems (Session 02)
Time: 15:45 – 16:45
Room: Hall A
Chair: ***Ran Dong (Tokyo University of Technology)***

OS8: Numerical Harmonic Analysis and Signal Processing (Session 04)
Time: 15:45 – 16:45
Room: Hall B
Chair: *Kensuke Fujinoki (Kanagawa University)*

OS2: Verified Numerical Computations (Session 07)
Time: 15:45 – 16:45
Room: Hall C
Chair: *Katsuhisa Ozaki (Shibaura Institute of Technology) and Kazuaki Tanaka (Waseda University)*

OS7: Plasma, Materials, Fusion Science, and their AI applications (Session 10)
Time: 15:45 – 16:45
Room: Hall D
Chair: *Ryosuke Ueda (Tohoku University)*

OS4: Computational Electromagnetics and Its Applications (Session 12)
Time: 15:45 – 16:45
Room: Hall E
Chair: *Hideki Kawaguchi (Muroran Institute of Technology)*

Symposium 1 on Numerical Simulation and Visual Analytics of Nonlinear Problems (Session 03)
Time: 17:00 – 17:40
Room: Hall A
Chair: *Teruou Takayama (Yamagata University)*

OS8: Numerical Harmonic Analysis and Signal Processing (Session 05)
Time: 17:00 – 17:40
Room: Hall B
Chair: ***Toshio Suzuki (Tokyo University of Science)***

OS2: Verified Numerical Computations (Session 08)
Time: 17:00 – 17:40
Room: Hall C
Chair: ***Kazuaki Tanaka (Waseda University)***

OS7: Plasma, Materials, Fusion Science, and their AI applications (Session 11)
Time: 17:00 – 18:00
Room: Hall D
Chair: ***Makoto Nakamura (National Institute of Technoology, Kushiro College)***

OS04: Computational Electromagnetics and Its Applications (Session 13)
Time: 17:00 – 18:00
Room: Hall E
Chair: ***Yoshihisa Fujita (Ritsumeikan University)***

Day 2: Thursday, 1st September, 2022

Symposium 1 on Numerical Simulation and Visual Analytics of Nonlinear Problems (Session 14)
Time: 9:00 – 10:00
Room: Hall A
Chair: ***Soichiro Ikuno (Tokyo University of Technology)***

Symposium 2 on Advanced Concept and Methodology in Bioscience (Session 17)
Time: 9:00 – 10:00
Room: Hall B
Chair: ***Susumu Fujiwara (Kyoto Institute of Technology)***

Symposium 3 on Advanced Numerical Analysis and Software in Multiphysics and Coupled Problems (Session 20, Invited and Tutorial Talks)
Time: 9:00 – 10:00
Room: Hall C
Chair: ***Amane Takei (University of Miyazaki)***

OS7: Plasma, Materials, Fusion Science, and their AI applications (Session 23)
Time: 9:00 – 10:00
Room: Hall D
Chair: ***Shunsuke Usami (National Institute for Fusion Science)***

OS4: Computational Electromagnetics and Its Applications (Session 26)
Time: 9:00 – 10:00
Room: Hall E
Chair: ***Hajime Igarashi (Hokkaido University)***

Symposium 1 on Numerical Simulation and Visual Analytics of Nonlinear Problems (Session 15)
Time: 10:15 – 11:15
Room: Hall A
Chair: *Taku Itoh (Nihon University)*

Symposium 2 on Advanced Concept and Methodology in Bioscience (Session 18)
Time: 10:15–10:55
Room: Hall B
Chair: *Takahiro Kenmotsu (Doshisha University)*

Symposium 3 on Advanced Numerical Analysis and Software in Multiphysics and Coupled Problems (Session 21)
Time: 10:15 – 11:15
Room: Hall C
Chair: ***Tomohiro Sawada (National Institute of Advanced Industrial Science and Technology)***

OS5: Multi Dimensional Communication Networks (Session 24)
Time: 10:15 – 11:15
Room: Hall D
Chair: ***Kenichi Ito (Niigata Institute of Technology)***

OS4: Computational Electromagnetics and Its Applications (Session 27)
Time: 10:15 – 10:55
Room: Hall E
Chair: ***Kota Watanabe (Muroran Institute of Technology)***

Symposium 1 on Numerical Simulation and Visual Analytics of Nonlinear Problems (Session 16)
Time: 11:30 – 12:10
Room: Hall A
Chair: ***Ayumu Saitoh (Yamagata University)***

Symposium 2 on Advanced Concept and Methodology in Bioscience (Session 19)
Time: 11:30 – 12:30
Room: Hall B
Chair: ***Susumu Fujiwara (Kyoto Institute of Technology)***

Symposium 3 on Advanced Numerical Analysis and Software in Multiphysics and Coupled Problems (Session 22)
Time: 11:30 – 12:10
Room: Hall C
Chair: ***Akihiro Kudo (National Institute of Technology, Tomakomai College)***

OS5: Multi Dimensional Communication Networks (Session 25)
Time: 11:30 – 12:10
Room: Hall D
Chair: ***Naoyuki Karasawa (Kaishi Professional University)***

OS7: Plasma, Materials, Fusion Science, and their AI applications (Session 28)
Time: 11:30 – 12:30
Room: Hall E
Chair: ***Satoshi Togo (Tsukuba University)***

Day 3: Friday, 2 September, 2022

Plenary Talk 2 (Advanced Concept and Methodology in Bioscience)
Time: 9:00 – 10:00
Room: Hall B
Chair: ***Hiroaki Nakamura (National Institute for Fusion Science)***

(Plenary) Origins of Bioorganic Compounds and Their Homochirality: Approaches from Simulation Experiments
Kensei Kobayashi

OS3: XR (VR, AR and MR) and Its Application (Session 29)
Time: 10:15 – 11:15
Room: Hall A
Chair: ***Yuichi Tamura (Konan University)***

Symposium 2 on Advanced Concept and Methodology in Bioscience (Session 32, Invited and Tutorial Talks)
Time: 10:15 – 11:15
Room: Hall B
Chair: ***Yoshihide Shibata (National Institute of Technology, Gifu College)***

(Invited) The Secret to Successful medical-industrial Collaboration
Naohisa Yahagi

Symposium 3 on Advanced Numerical Analysis and Software in Multiphysics and Coupled Problems (Session 35)
Time: 10:15 – 11:15
Room: Hall C
Chair: ***Amane Takei (University of Miyazaki)***

OS1: Simulation Technology in Origami (Session 38)
Time: 10:15 – 11:15
Room: Hall D
Chair: ***Sachiko Ishida (Meiji University)***

OS9 + OS10: Complex Networks and Complex Systems (OS9), Complex and Ultimate Systems (OS10) (Session 41)
Time: 10:15 – 11:15
Room: Hall E
Chair: ***Atsushi Tanaka (Yamagata University)***

OS3: XR (VR, AR and MR) and Its Application (Session 30)
Time: 11:30 – 12:30
Room: Hall A
Chair: *Hiroaki Ohtani (National Institute for Fusion Science)*

Symposium 2 on Advanced Concept and Methodology in Bioscience (Session 33)
Time: 11:30 – 12:10
Room: Hall B
Chair: *Yoshihide Shibata (National Institute of Technology, Gifu College)*

Symposium 3 on Advanced Numerical Analysis and Software in Multiphysics and Coupled Problems (Session 36)
Time: 11:30 – 12:10
Room: Hall C
Chair: *Koji Nishiguchi (Nagoya University)*

OS1: Simulation Technology in Origami (Session 39)
Time: 11:30 – 12:30
Room: Hall D
Chair: *Kazuya Saito (Kyushu University)*

OS9 + OS10: Complex Networks and Complex Systems (OS9), Complex and Ultimate Systems (OS10) (Session 42)
Time: 11:30 – 12:30
Room: Hall E
Chair: *Ken Naitoh (Waseda University) and Toru Ohira (Nagoya University)*

OS3: XR (VR, AR and MR) and Its Application (Session 31)
Time: 13:30 – 14:10
Room: Hall A
Chair: *Nobuaki Ohno (University of Hyogo)*

Symposium 2 on Advanced Concept and Methodology in Bioscience (Session 34)
Time: 13:30 – 14:10
Room: Hall B
Chair: *Hiroaki Nakamura (National Institute for Fusion Science)*

Symposium 3 on Advanced Numerical Analysis and Software in Multiphysics and Coupled Problems (Session 37)
Time: 13:30 – 14:10
Room: Hall C
Chair: *Kawai Hiroshi (Toyo University)*

OS1: Simulation Technology in Origami (Session 40)
Time: 13:30 – 14:10
Room: Hall D
Chair: *Luis Diago (Meiji University/Interlocus Inc.)*

Control of a contractible and bendable wire-pulling mechanism for a robotic tongue

Amane Sakota[1*], Nobutsuna Endo[1**], Norihiro Kamamichi[1***]

[1] Department of Robotics and Mechatronics, Graduate School of Science and Technology for Future Life, Tokyo Denki University

*21fmr20@ms.dendai.ac.jp

** noble@ruri.waseda.jp

***nkama@mail.dendai.ac.jp

Abstract. Several artificial tongue mechanisms have been developed as a way to clarify the mechanisms of human speech. These artificial tongue mechanisms were insufficient to realize the same level of motion as the human tongue due to the lack of the range of deformation and controllability. Therefore, this study aims to develop a tongue mechanism that is flexible, deformable, and capable of controlling the shape of the tongue within the size of the human tongue. In this paper, we constructed a wire-pulling mechanism that can be applied to a tongue mechanism and designed a control system for simultaneous control of contraction and bending.

Keywords: Wire-driven mechanism, Soft mechanism, Robotic tongue

1. Introduction

Several speech robots have been studied as a way to clarify the mechanisms of human speech. The human tongue plays an important role in speech because of contribution to a large part of the vocal tract deformation [1]. However, evaluating the deformation is difficult since the tongue is driven by a complex combination of muscle arrangements. Also, direct measurement of the shape of the tongue in the oral cavity is difficult. In order to clarify the deformation of the vocal tract and tongue movement in speech, robotic tongue mechanisms have been studied.

Robotic tongue mechanisms that do not have rigid links include AnTon [2] and ZETS [3]. Both are made of silicone resin. In AnTon, meshes are embedded in a tongue part made of silicone resin, and wires are attached to the meshes. AnTon is driven by pulling the wires using an electrical motors. However, AnTon has a disadvantage that the deformation is smaller than the human tongue. ZETS is driven by flexible pneumatic actuators, but it is difficult to construct a mechanical model and has not been realized continuous control of tongue shape during speech. Therefore, we aimed to create a tongue mechanism that has a wide range of motion within the size of a human tongue and can control the shape of the tongue. In the previous study[4], a flexible pneumatic bending actuator with thin pneumatic artificial muscles was constructed, to realize a flexible tongue mechanism. However, the response was slow as a settling time is less

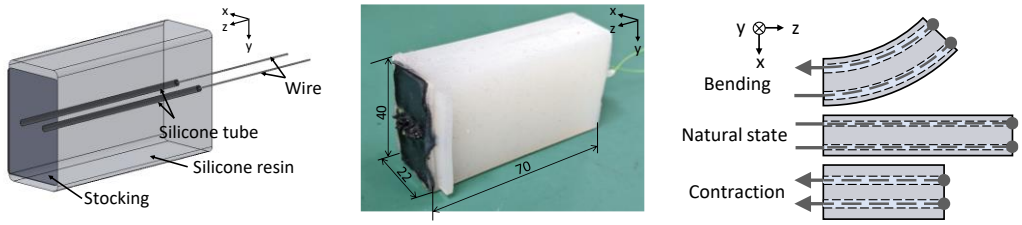

(a) Structure (b) Appearance (c) Example of movement

Fig. 1 Contractible and bendable wire-pulling mechanism

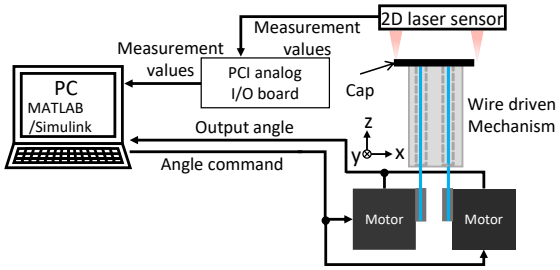

Fig. 2 Experimental system

than 500 ms for contraction and 1-2 s for bending [4]. Therefore, this paper aims to improve the response by using a wire-driven mechanism instead of pneumatic control.

2. Contractible and bendable wire-pulling mechanism

To realize a flexible tongue mechanism, we employed a contractible and bendable wire-pulling mechanism [5, 6]. The mechanism shown in Fig. 1(a) consists of a pair of wires (Super BRAID No. 2, SUNLINE) surrounded by a soft body made of silicone resin. The mixing ratio of the plasticizer (Silicone Thinner, Smooth-On) to the silicone resin (Dragon Skin FX-Pro, Smooth-On) is 50 wt% (see previous literature [7, 4] for durometer hardness and elasticity/compliance of silicone resins mixed with plasticizers). The end of the wire is attached to a polyurethane mesh fabric which is commacialed stocking. The wire and the mesh fabric are tied together, and the mesh fabric and silicone resin are entangled and stuck when the silicone resin is molded. A silicone tube (MGJG-1.0, Monotaro) is used to prevent the wire from tearing the silicone resin. In this paper, the size of this mechanism is D22×W40×H70 mm, and the distance between the wires is 10 mm.

As shown in Fig. 1(c), this mechanism bends when one wire is pulled, and contracts when both are pulled by the same amount. This feature is used to realize the tongue mechanism.

3. Control experiment

3.1. Experimental System

Figure 2 shows the configuration of the experimental system used for the control experiment. MATLAB/Simulink and Simulink Desktop Real-Time are used for the measurement and control environment. The wires are pulled by position-controlled servo motors (Dynamixcel XH540-W150-R, ROBOTIS). The target angles of the motors are transmitted from the PC via serial communication. The displacements at both ends of the caps attached to the top surface

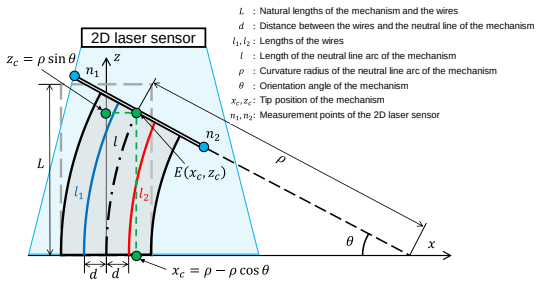

Fig. 3 Two-dimensional model

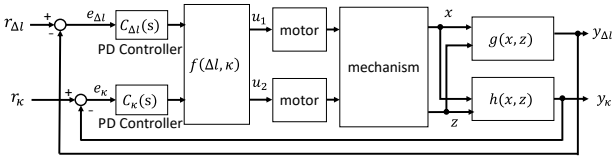

Fig. 4 Block diagram

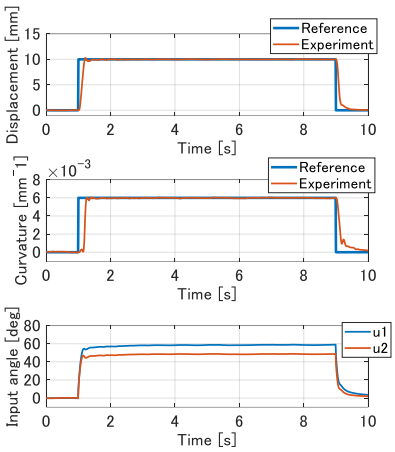

Fig. 5 Experimental results

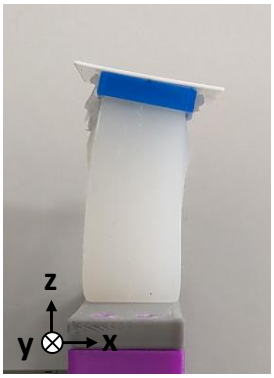

Fig. 6 Movement

of the mechanism are measured using a two-dimensional laser sensor (LJ-V7200, KEYENCE). The measured values are processed by a PC using a PCI analog input/output board (PCI-6251, National Instruments).

3.2. Modeling and control system design

The same mathematical model and two-dimensional model, shown in Fig. 3, as in the previous study are used [4]. This model shows that the length of the mechanism's neutral line arc l is determined by the sum of the lengths of the right and left wires l_1, l_2, and the curvature $\kappa = 1/\rho$ is determined by the difference between the lengths of the pair of wires.

Figure 3 shows the block diagram used in this experiment. Both the displacement Δl and curvature κ control systems are applied using a PD controller. The control gains were determined by trial and error.

The input angle to the motor u_1, u_2 is such that the reference displacement $r_{\Delta l}$ and reference curvature r_κ are obtained from

$$f(\Delta l, \kappa) = \begin{bmatrix} u_1 \\ u_2 \end{bmatrix} = \begin{bmatrix} \frac{D_p}{2} & \frac{Ld}{2D_p} \\ \frac{D_p}{2} & -\frac{Ld}{2D_p} \end{bmatrix} \begin{bmatrix} r_{\Delta l} \\ r_\kappa \end{bmatrix} \quad (1)$$

where D_p is the pulley diameter, L is the initial length of the mechanism, and d is the distance between the wires and the neutral line of the mechanism.

3.3. Result

Figure 5,6 shows the results of control experiment with reference displacement of 10 mm and reference curvature of 0.006 mm^{-1} (approximately 24°). Both displacement and curvature are followed, therefore the effectiveness of the control system was confirmed. The settling time was 190 ms for contraction and 240 ms for bending. This is an improvement over the flexible pneumatic bending actuator which takes 500 ms for contraction and 1-2 s for bending [4].

4. Conclusion

To realize a flexible tongue mechanism, we constructed a contractible and bendable wire pulling mechanism consisting of pair of wires covered with silicone resin. Furthermore, we designed a control system that simultaneously performs contraction and bending. The contraction and bending control was performed using a PD controller, and the settling time was confirmed to be 190 ms and 240 ms, respectively. In the future, as a preliminary step to control the tongue shape, we plan to control a mechanism consisting of two of these mechanisms in series.S

Acknowledgments

This work was supported by JSPS KAKENHI Grant Numbers JP18K13717 and JP22K03988.

References

[1] N. Endo, " Mechanical Utterance Robot Using Soft Material," *Journal of the Society of Instrument and Control Engineers*, 59:11 (2020), pp.835-840 (in Japanese).

[2] R. Hofe and R.K.Moore, "Towards an Investigation of Speech Energetics using 'AnTon': an Animatronic Model of a Human Tongue and Vocal Tract," *Connection Science,* 20:4 (2008), pp.319-336.

[3] M. Kataoka, T. Yoshida, T. Kojima, N. Endo, and M. Asada, "Development of a Flexible Tounge Mechanism ZETS by using Flexible Pneumatic Actuators," *Proceedings of the 17th SICE System Integration Division Annual Conference*, (2016), pp.741-745 (in Japanese).

[4] N. Endo, Y. Kizaki, and N. Kamamichi, "Flexible Pneumatic Bending Actuator for a Robotic Tongue," *Journal of Robotics and Mechatronics*, 32:5 (2020), pp. 894-902.

[5] N. Endo, "Wire-Pulling Mechanism with Embedded Soft Tubes for Robot Tongue," *Proceedings of the 23rd CISM IFToMM Symposium on Robot Design, Dynamics and Control,* (2020), pp.313-320.

[6] N. Endo, "Deformation model and experimental evaluation of a contractable and bendable wire-pulling mechanism with embedded soft tubes for a robotic tongue," *ROBOMECH Journal*, 8:6, (2021), 13 pages.

[7] N. Endo, T. Kojima, H. Ishihara, T. Horii, M. Asada, "Design and Preliminary Evaluation of the Vocal Cords and Articulator of an Infant-like Vocal Robot “Lingua”," *Proceedings of the 2014 IEEE-RAS International Conference on Humanoid Robots*, (2014), pp.1063-1068.

Toolpath Planning for Simultaneous Fabrication with Multi-Nozzle in Material Extrusion-based Additive Manufacturing

Koki Jimbo[1*]

[1]Department of Advanced Machinery Engineering, School of Engineering,
Tokyo Denki University

[*]**kjimbo@mail.dendai.ac.jp**

Abstract. Material Extrusion-based Additive Manufacturing (MEAM) is able to fabricate complex structures using multiple materials simultaneously. Conventionally in this fabrication method, multiple nozzles extruding materials are run one by one in order to avoid interference of tool heads. It is inefficient for production. The purpose of this study is to propose a toolpath planning method to reduce fabrication time in MEAM fabrication using robotic arms. The planning methods that change toolpaths to avoid tool head collisions by calculating nozzle positions in the fabrication process and that activate multiple nozzles simultaneously are proposed. After that, a case study was performed. From that result, it was confirmed that the proposed methods are able to reduce the fabrication time.

Keywords: Additive manufacturing, Material extrusion, Toolpath planning

1. Introduction

Material Extrusion-based Additive Manufacturing (MEAM), which is known as Fused Deposition Modeling (FDM) type of 3D printing, is able to fabricate objects using multiple materials. In recent years, MEAM using a robotic arm has been researched for more complex fabrication [1]. Figure 1 shows the image of MEAM using multiple robotic arms equipped with material extrusion nozzles. By fabricating complex structures with multiple materials of different properties, realizing machine parts with a wide range of properties or functions is expected.

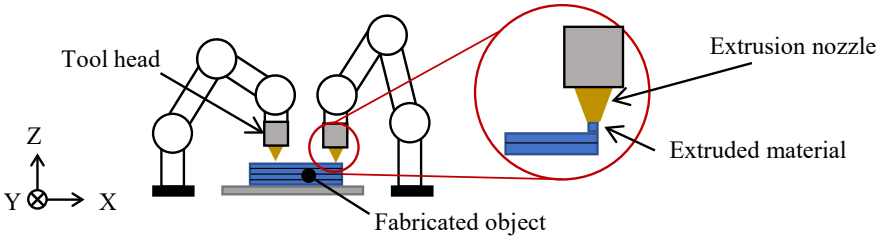

Figure 1: Image of MEAM fabrication with multiple extrusion nozzle using robotic arms.

However, even when multiple materials are used in one fabrication, the material extruder are usually run one by one, which leads to a long fabrication time. By activating extrusion nozzles simultaneously, fabrication time is expected to be reduced [2].

The purpose of this study is to propose and evaluate the toolpath planning method for simultaneous fabrication with multiple extrusion nozzles using robotic arms to reduce fabrication time.

2. Proposed toolpath planning method

Even when a single nozzle is used to fabricate a single layer, there are numerous patterns of toolpaths. For multiple nozzles, where collisions must be considered, it is difficult to generate a toolpaths with an overall optimization. For this reason, a toolpath planning method is proposed based on conventional software for a single nozzle in this study, which allows simultaneous fabrication of multiple nozzles by locally avoiding collisions.

In this study, toolpaths of two nozzles in a plane are assumed for a path planning target. Figure 2 shows the flow chart of the proposed method and the process is described below.

First, toolpaths obtained by a conventional slicer software, which generates toolpaths for a single nozzle running, are input. Next, the coordinates of the extrusion nozzle positions in the fabrication process are calculated at certain time intervals. If the distance between nozzles is less than a certain value, toolpaths are changed in order to avoid toolheads collision. In this study, the following two methods to change toolpaths are proposed.

(A) Stop one nozzle before traveling the path where interference would occur (Fig. 3 (a)). The nozzle stands by until there is no possibility of collision.

(B) Move one nozzle to other paths before traveling the path where interference would occur (Fig. 3 (b)). The nozzle is moved to the endpoint of the remaining path and travels it in the opposite direction.

To reduce the overall fabrication time, the nozzle that has the shorter remaining path than another, which needs less run time, is chosen to stand by or move away.

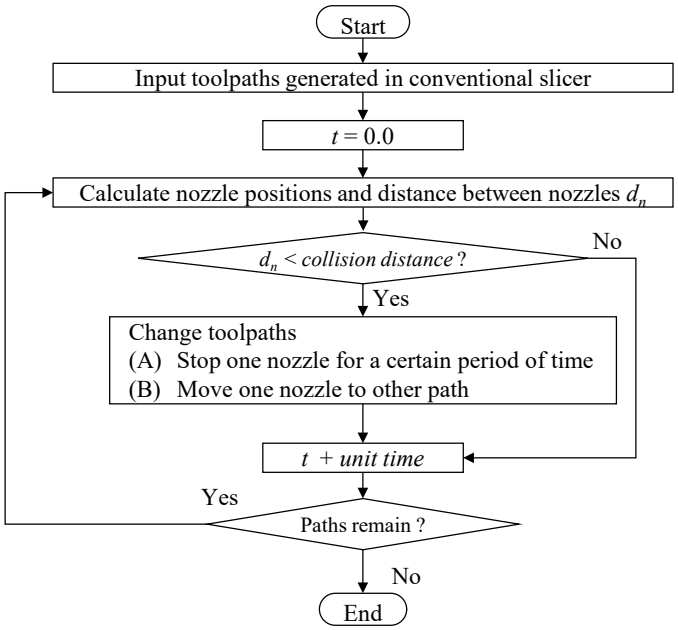

Figure 2: Flow chart of proposed toolpath planning method.

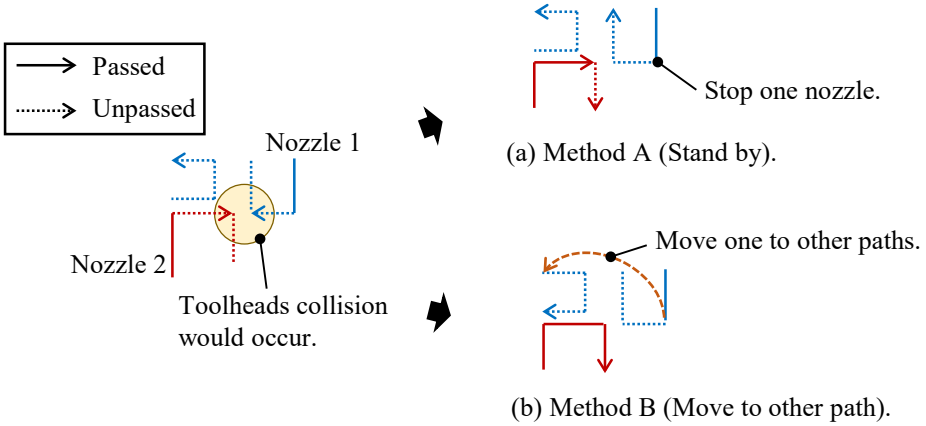

Figure 3: Images of proposed toolpath changing method.

3. Case study

A simple case study that assumes fabrication of a single layer was conducted to evaluate the time reductions by the proposed method.

3.1. Conditions

The use of two nozzles with a tool head size of 30 mm was assumed. Figure 4 shows the target model to be fabricated: (a) the size of a fabricated object and fabricated area for each nozzle and (b) the toolpaths for two extrusion nozzles generated by a slicer software.

When two nozzles are run simultaneously in this toolpath, the distance between the nozzles would be less than 30 mm at a certain time, and tool heads would collide.

Then, the proposed methods were applied to toolpath planning. Fabrication times were simulated under conditions listed in Table 1.

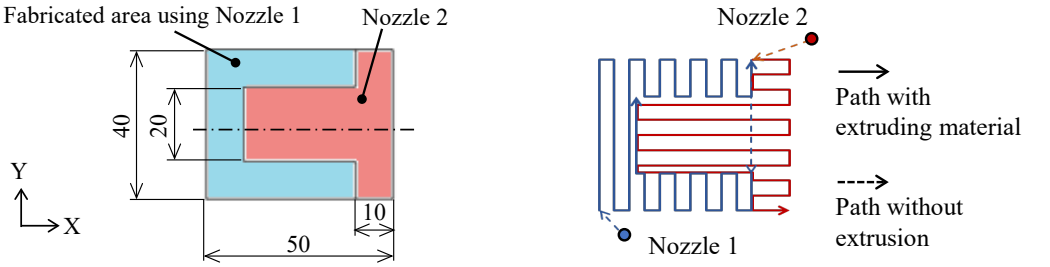

(a) Size of target model and fabrication area. (b) Original toolpath generated in slicer software.

Figure 4: Size of target model and original toolpath.

Table 1: Fabrication conditons in toolpath simulation and toolpath planning settings.

Nozzle travel speed with extrusion (G0)	600 [mm/min]
Nozzle travel speed without extrusion (G1)	2000 [mm/min]
Time to stand by in method B	1.0 [s]
Unit time to determine collision	0.5 [s]

3.2. Results and discussions

The toolpaths obtained in the two proposed methods are shown in Fig. 5 : (a) method A, in which one nozzle stands by, and (b) method B, in which one nozzle moves to other paths.

From Fig. 5 (a), it can be seen that, in method A, standby of nozzle running occurs at both nozzles. On the other hand, Fig. 5 (b) shows that, in method B, nozzle 2 changes its path many times later in the toolpath process.

Table 2 shows the simulated time to fabricate the single layer in these two methods and the conventional toolpath planning, in which nozzles are run one by one. From Table 2, it was confirmed that the run of two nozzles at the same time with both proposed methods reduces the fabrication time by about 40%. Here, in Method B, the toolpath becomes discontinuous in many places, which may reduce the accuracy of the fabrication and its strength. Actual fabrication and evaluation of modeling accuracy and strength are future work.

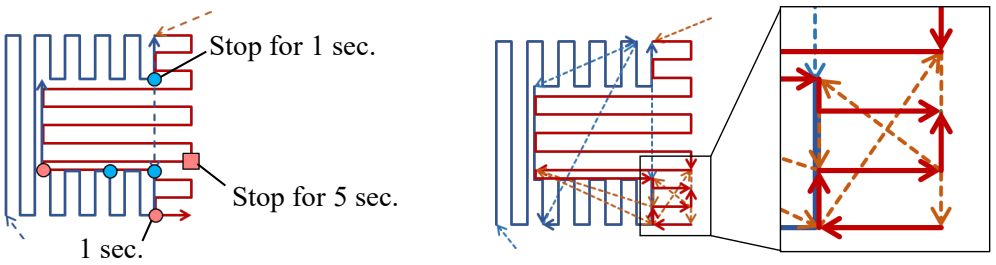

(a) Method A (Stand by). (b) Method B (Move to other path).

Figure 5: Resulted toolpaths obtained by proposed method.

Table 2: Results of fabrication time in toolpath simulation.

	Method A (Stand by)	Method B (Move to other path)	Conventional method (Run nozzles one by one)
Simulated fabrication time [s]	42.7	41.2	72.4

4. Conclusion

(1) In MEAM using robotic arms, two toolpath planning methods for simultaneous fabrication with multiple extrusion nozzles were proposed.
(2) A simple case study was conducted to evaluate the proposed method.
(3) It was confirmed that the proposed methods are able to reduce the fabrication time.

References

[1] C. Wu, C. Dai, G. Fang, Y. J. Liu, C. C. L. Wang: RoboFDM: A robotic system for support-free fabrication using FDM, *Proceedings - IEEE International Conference on Robotics and Automation*, (2017), pp. 1175–1180.

[2] Y. Cai, S. H. Choi: Deposition group-based toolpath planning for additive manufacturing with multiple robotic actuators, *Procedia Manufucturing*, volume: 34 (2019), pp. 584–593.

JSST 2022

An Elbow Joint Angle prediction method using a NN considering EMD with FE processed sEMG as inputs

Naoki Ikeda[1,*] and Teruyoshi Sadahiro[1]

[1]Graduate School of Engineering, Oita University

[*]v21e1001@oita-u.ac.jp

The full paper of this paper has been published in Journal of Advanced Simulation in Science and Engineering (JASSE).

DOI: https://doi.org/10.15748/jasse.10.102

Intelligent Snake-like Robot for Cable Laying Work

S. Takarabe, Y. Sadasue, H. Nagae, Y. Satoh, M. Iwase

Department of Robotics and Mechatronics, Tokyo Denki University

{sadasue,nagae,iwase}@ctrl.fr.dendai.ac.jp

Abstract. An intelligent snake-like robot for cable laying work is developed in this paper. A propulsion method of the snake-like robot is designed to move on cable racks and to achieve the cable laying task. The snake-like robot is equipped with a camera to incorporate image recognition technology to provide environment recoginition for moving on cable racks. A depth map is also created using the camera images from the snake-like robot to recognize the environment.

Keywords: Motion control, Depth map, Snake-like robot

1. Introduction

The purpose of this research is to develop a snake-like robot for cable laying work. Cable laying is one of the essential electrical work, in which cables are laid on cable racks and under ceilings. In general, cables are laid on the racks manually by workers on stepladders or elevating vehicles. Therefore this involves hazards. According to a survey conducted by METI in 2016, the number of workers in the occupation has decreased by approximately 22% from the peak period. Therefore, robots are expected to work for cable laying toward automation saving labor.

Against this background, robots to replace cable laying work have been developed. As a previous study, a cable extension rope laying device was developed to lay cables on a cable rack [1]. This device runs by itself on the side rail of the cable rack pulling a cable extension rope. In addition, a spoke-wheel type cable laying and wiring work robot has been developed for laying cables under the ceiling [2]. However, these robots are designed for specific environments. So, Its cannot work both on the cable rack and under the ceiling. It is desirable to use the same robot in both environments in order to save labor for the construction workers.

Based on the above, this study proposes the use of a snake-like robot. The snake-like robot can move even in inaccessible places by using its long and slender trunk [3,4]. To lay cables, a snake-like robot must be propelled through a narrow space and on cable racks. The investigation is required on the shape, propulsion, and traction capabilities of cables of the snake-like robot.

Authors have realized propulsion on cable racks whose small girders are arranged at even intervals. However, the racks are often spliced or cut according to the space available. So the spacing of the small girders is not same. Therefore, it is essential for a snake-like robot to be

This work is partially supported by Toko Electrical Construction Co.,Ltd.

intelligent enough to recognize the space interval and to change the shape in accordance with it. In this research, a camera is mounted at the head of the snake-like robot. Analyzing the camera images, we aim to realize propulsion on the rack in accordance with the interval. This is expected to make it possible for the robot to lay cables in real works.

2. Experimental device: Snake-like robot

The snake-like robot used in this study (Figure 1) has 16 links and 15 joints. Each link consists of two passive wheels and two servo motors. The servo motors of each link rotates in the pitch and yaw axes, with a range of motion of ± 90 degrees. The head has a built-in camera. In the experiment, the robot body is wrapped in a braided tube to reduce friction with the cable rack girders.The parameters and variables of the robot are shown in Table 1.

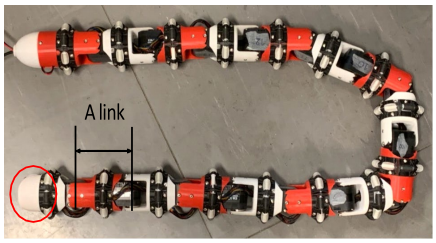

Figure 1: snake-like robot

Table 1: parameters and variables

Link number	i
Link length	l_i
Motor number	j
Yaw angle	ψ_j
Pitch angle	θ_j
Applitude of motion form	A
Phase of motion form	ϕ

3. Motion and attitude control

In order to make a snake-like robot move on a ladder-like cable rack, we propose an up-and-down meandering motion inspired by serpentoid propulsion on a horizontal plane. $\theta_i(t)$ is the reference angle of motor in the pitch axis at time t, and is given (1) with odd number i indicating the pitch angle joint, ω be the angular velocity, and ϕ be the phase.

$$\theta_i(t) = A \sin\left(\omega t - \phi\left(\frac{i}{2} + \frac{1}{2}\right)\right) \tag{1}$$

For the experimental robot, the amplitude, angular velocity, and phase in (1) were adjusted, and the amplitude, angular velocity, and phase were set to 90 deg, 1.0 rad/s, and 2.2 rad, respectively, for movement on the cable rack. Generally speaking, the angular velocity is related to the propulsion speed. The amplitude and phase are chosen to fit to the cable rack shape, that is the spacing between the small girders. In addition, the amplitude adjustment should be performed to be kept within the maximum range angle of joint in terms of the hardware limitation. After basic choice of these parameters, numerical simulations developed in MATLAB Simscape (Fig. 2) and experimental tests are performed to obtain better parameters.

Furthermore, to stabilize the camera image, the robot motion was designed to keep the head link level with the ground. The up-and-down meandering motion was divided into eight patterns, and the first joint that keeps the head horizontal was finded for in each posture. The eight patterns were obtained by dividing the one cycle of the snake-like robot propulsion movement. In each pattern, we adjusted the head angle to be parallel to the rack. The Fourier series expansion was applied to the head joint angle obtained from the eight patterns, and an interpolation formula for keeping the head joint angle horizontal was derived with a finite

term of the Fourier series expansion. By combining this leveling of the head joint angle with the vertical meandering motion, the snake-shaped robot was propelled while keeping its head horizontal in Figure 3.

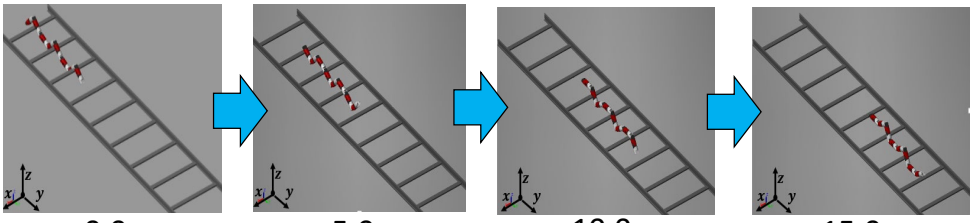

Figure 2: Simulation of snake-like roboto propulsion on cable rack

Common cable racks of the SR series of Negurosu Denko Co., Ltd. were selected for the experimental environment [5]. Figure 4 shows the specifications of a cable rack. The cable rack consists of small girders and parent girders. The width of the small girder is 40 mm, and the distance between the small girders is 300 mm, and the length of the parent girder is 3000 mm. The width of the cable rack ranges from 200 to 1000 mm. In this study, the 600 mm width is treated as the nominal model.

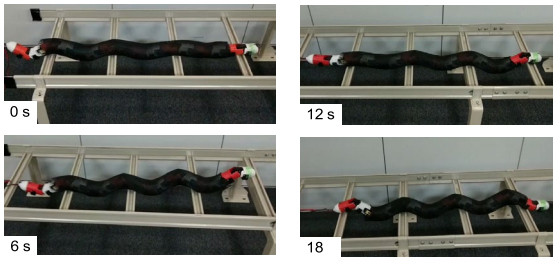

Figure 3: snake-like robot moving on rack

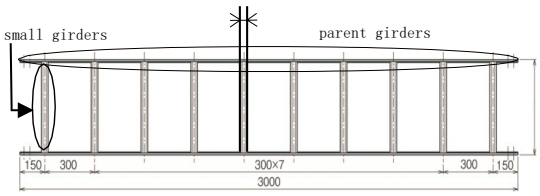

Figure 4: Cable rack SR series

4. Camera vision and environment recognition

Depth estimation from the acquired monocular camera images is used as an environment recognition to estimate the distance between small girders and between the girders and the support columns. A deep learning system that can provide depth maps from monocular camera images is constructed using MannequinChallenge (MC). Li et al. use MC to design a deep neural network that outputs a depth map including both the environment and the person [6]. Figure 5 shows the depth map created using the camera image in Figure 4. From Figure 5, the depth could be represented in grayscale with an accuracy of 3 to 5 cm in error.

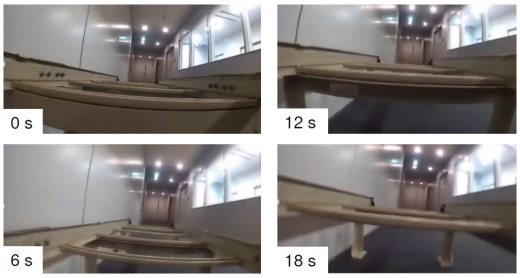

Figure 4: camera image from the robot

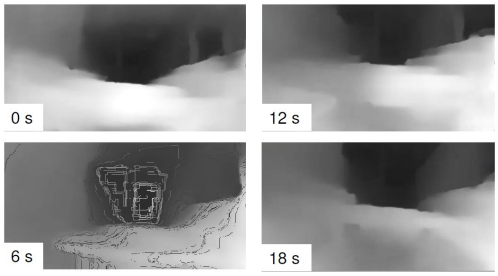

Figure 5: depth map generated by DNN

From this depth map, the distance between the girders of the cable rack can be recognized. The automatic tuning of the amplitude and phase parameters of the snake-like robot to match the recognized spacing between the girders will be considered in the future. This will allow the snake-like robot to automatically tune its motion to match the girder spacing.

5. Concluding remarks

In this study, a locomotion of the snake-like robot on a cable rack was investigated for cable laying work. The robot was propelled in an up-and-down meandering motion, and ran over the rack with its head horizontal in order to always acquire stable camera images. A depth map was created using the acquired camera images by DNN. As future works, we will design methods that can be used for propulsion of cable racks that are not equally spaced between the small girders and curved cable racks.

References

[1] Kinden, Wire drawing rope laying device for cable wiring, https://www.kinden.co.jp/pdf/dev_002.pdf (2018)

[2] M. Yamamoto, P. Gao, T. Ikeda, Traverse Ability of Flexible Spoke Wheel for the Wiring Task Mobile Robot, Tras. of the Japan Society of Mech. Eng. Series C, Volume 77, Issue 778, pp. 2343-2350 (2011)

[3] K. Ito, R. Murai, K. Nakamichi, Development of Snake-Like Rescue Robot Designed for Ease of Use, Journal of the Robotics Society of Japan, Volume 27, Issue 4, pp. 419-426 (2009)

[4] F. Kasahara, T. Yanagida, K. Onodera, M. Iwase, Modeling and Locomotion Control Using SDRE of Snake-like Robot Considering Side-slip, Tras. of the JSST, Vol. 10, Issue 1, pp. 35-45(2018)

[5] Melamine resin baking finish SR type straight line rack, Neguros Denko, https://products.negurosu.co.jp/

[6] LI, Zhengqi et. Al, Learning the depths of moving people by watching frozen people Proc. of the IEEE/CVF Conference on Computer Vision and Pattern Recognition, pp.4521-4530 (2019)

Development of hydrogen recycling model by machine learning based on molecular dynamics simulation

Masato Iida [1], Seiki Saito [1*], Hiroaki Nakamura [2, 3], Keiji Sawada [4], Kazuo Hoshino[5], Masahiro Kobayashi [2, 6], Masahiro Hasuo [7]

[1] Department of Information and Electronics, Graduate school of Science and Engineering, Yamagata University

[2] Department of Helical Plasma Research, National Institude for Fusion Science

[3] Department of Electrical Engineering, Graduate School of Engineering, Nagoya University

[4] Department of Material System Engineering, Faculty of Engineering, Shinsyu University

[5] Department of Applied Physics and Physico-Informatics, Fuculty of Science and Technology, Keio University

[6] Department of Fusion Science, Physical Sciences Research Section, The Graduate University for Adcanced Studies

[7] Department of Mechanical Engineering and Science, Graduate School of Engineering, Kyoto University

*saitos@yz.yamagata-u.ac.jp

Abstract. In fusion power generation, impurities in the plasma must be removed by the divertor. The hydrogen ions that contact with a divertor are neutralized and return to the plasma as hydrogen atoms and molecules by process called recycling. This study uses molecular dynamics (MD) simulation to compute the energy distribution of recycling hydrogen. The obtained energy distribution is used for the training of a machine learning model, and develop a model to calculate the energy distribution of recycling hydrogen atoms and molecules under given conditions.

Keywords: Molecular dynamics simulation, Machine learning, Carbon divertor

1. Introduction

In fusion power generation, the helium produced by the nuclear fusion is removed by the divertor. Plasma is transported by magnetic line and contacts the divertor. The hydrogen in the plasma that contact with a divertor are neutralized and return to the plasma as hydrogen atoms and molecules. This process is called recycling. The purpose is to understand the motion of recycling hydrogen. Firstly, MD simulation [1-4] of a hydrogen atom incident to the carbon

wall calculate the energy distribution of recycling hydrogen. Secondly, the distributions from the simulation is used as training data, and develop machine learning model that predicts the energy distribution of the recycling hydrogen.

2. Simulation Model

A carbon amorphous structure consisting of carbon atoms and hydrogen aroms is prepared for the target material. The size of target is 40Å ×40Å ×20Å. The temperature of the target is 300K. Brenner's potential [5] is used for interatomic potential between carbon and hydrogen atoms. One hydrogen atom is injected to the target. The incident angle is set to parallel to *z*-axis. Our previous research revealed that hydrogen atoms with high energy due to non-equilibrium processes caused by the direct collision by incident atoms are emitted within 1 ps after the injection. Figure 1 shows the distribution of vibrational state *v* and rotational state *J* of emitted hydrogen molecules. Therefore, emitted atoms and molecules can be divided into two groups: they emitted within 1 ps, they emitted after 1 ps. The two parameters of the simulation are incident energy and number of hydrogen atoms divided by carbon atoms (H/C). The simulation of emitted atoms within 1 ps has ten different incident energies (5, 10, 15, 20, 25, 30, 35, 40, 45, 50eV), and ten different H/C (0.05, 0.10, 0.15, 0.20, 0.25, 0.30, 0.35, 0.40, 0.45, 0.50). The number of simulations is 500 for each pattern. The simulation of emitted atoms after 1 ps has three different incident energies (10, 20, 50eV), and four different H/C (0.20, 0.30, 0.40, 0.50). The number of simulations is 1500 for each pattern.

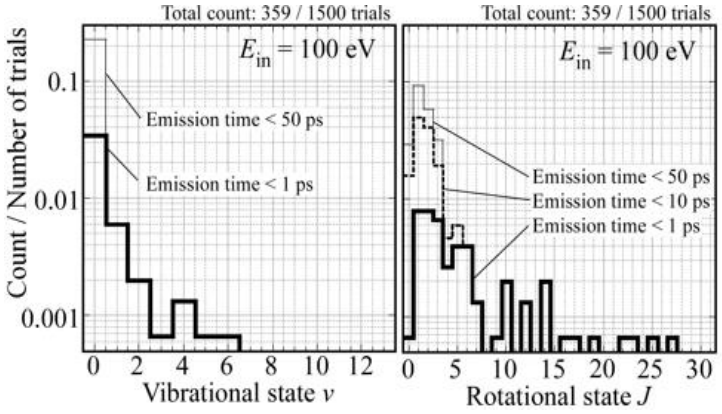

Fig. 1: Distribution of vibrational state *v* and rotational state *J*. [1]

3. Machine Learning Model

The predictions of the energy distribution of emitted atoms and molecules are obtained by machine learning the MD simulation results. The reason for using machine learning is MD simulation take too long to compute. For this machine learning, Fully coupled neural network and Convolutional neural network (CNN) are used for prediction. CNN consists of the convolution

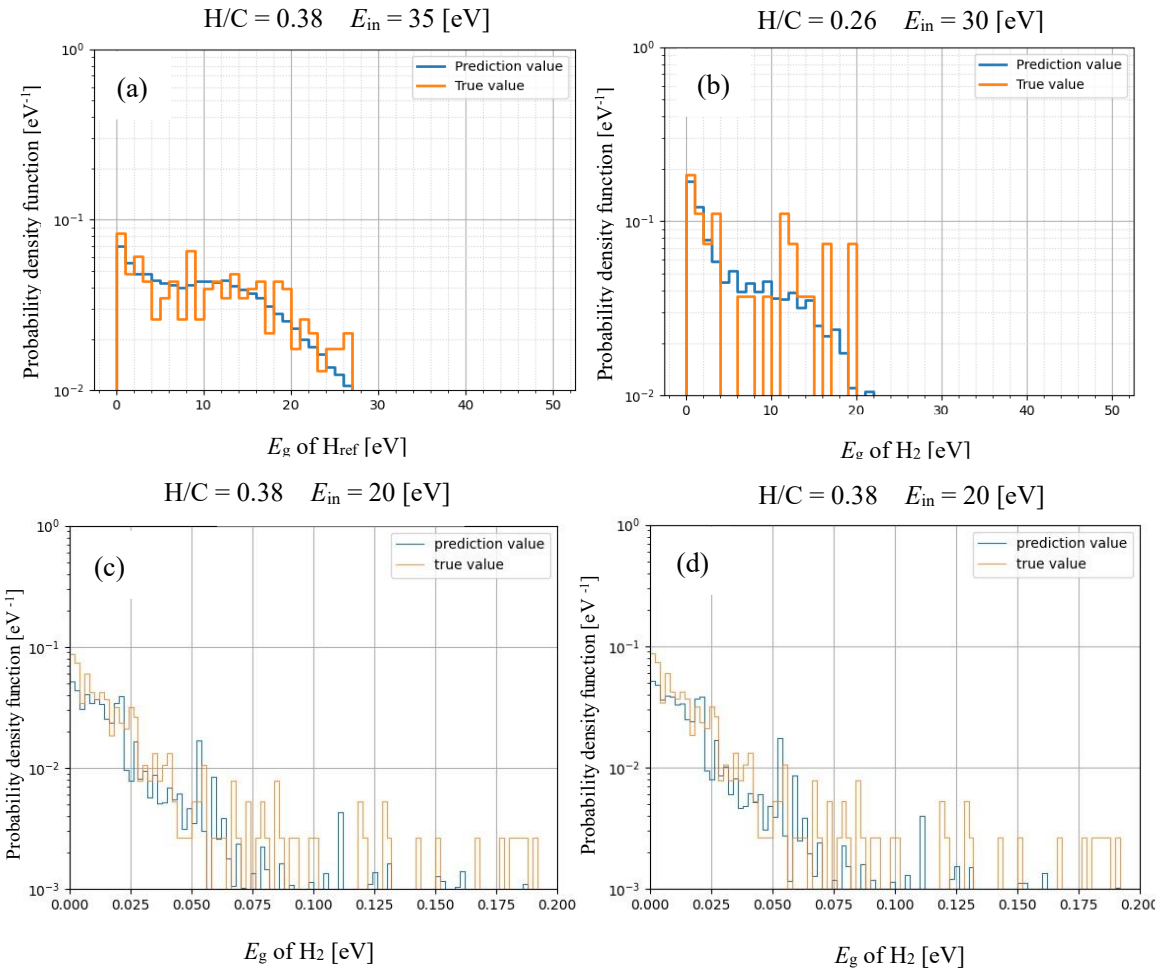

Fig. 2: (a) Prediction of reflection atoms within 1 ps
(b) Prediction of emitted molecules within 1 ps
(c) Prediction of vibrational energy after 1 ps
(d) Prediction of vibrational energy after 1 ps without incident energy

layer, the pooling layer and the fully coupled layer. The convolution layer convolves the data. The pooling layer extracts data features. The fully coupled layer make prediction based on the extracted features. CNN is used to input distribution data.

4. Results

Figure (a) and (b) are predictions of the translational energy distribution of reflection atoms and emitted molecules within 1 ps. The inputs are incident energy, H/C and depth distribution of hydrogen molecules. The orange line is the distribution obtained from the simulation and the blue line is the predicted distribution. The distribution of reflected atoms could be predicted with high accuracy. However, the distribution of emitted molecules could not be predicted with high accuracy. Figure (c) and (d) are predictions of the vibrational energy distribution of the

emitted molecules after 1ps. The inputs of Figure (c) are incident energy, H/C and depth distribution. The inputs of Figure (d) are H/C and depth distribution. A comparison of these two distributions shows that they are both similar. . This suggests that it can be seen that the conditions of incidence have no effect on the emitted molecules after 1 ps.

Acknowledgment

The research was partially supported by Grant-in-Aid for Scientific Research, No.22K03572 from the Japan Society for the Promotion of Science, and by the NIFS Collaborative Research Program NIFS20KUTR158, NIFS22KISS021 and NIFS22KIGS002. The computations were performed using the JFRS-1 supercomputer system at Computational Simulation Centre of International Fusion Energy Research Centre (IFERC-CSC) in Rokkasho Fusion Institute of QST (Aomori, Japan), Research Center for Computational Science (Okazaki, Aichi, Japan) and Plasma Simulator of NIFS (Toki, Gifu, Japan) .

References

[1] S. Saito, H. Nakamura, K. Sawada, G. Kawamura, M. Kobayashi, M. Hasuo. Molecular dynamics simulation model of hydrogen recycling on carbon divertor for neutral transport analysis in large helical device. Contributions to Plasma Physics. 2020; e201900152.

[2] K. Sawada, H. Nakamura, S. Saito, G. Kawamura, M. Kobayashi, K. Haga, T. Sawada, and M. Hasuo, Contrib. Plasma Phys. e201900153 (2020).

[3] S. Saito, H. Nakamura, K. Sawada, G. Kawamura, M. Kobayashi, and M. Hasuo, Plasma Fusion Res. **15**, 2403073 (2020).

[4] S. Saito, H. Nakamura, K. Sawada, M. Kobayashi, G. Kawamura, T. Sawada, and H. Masahiro: *Molecular dynamics simulation for hydrogen recycling on tungsten divertor for neutral transport analysis,* Jpn. J. Appl. Phys. **60** SAAB08 (2021).

[5] D. W. Brenner, O. A. Shenderova, J. A. Harrison, S. J. Stuart, B. Ni and S. B. Sinnott: J. Phys. Condens. Matter **14** (2002) 783.

A computational fluid simulation study of the free-surface flow of the liquid lithium target of Advanced Fusion Neutron Source A-FNS

Makoto M. Nakamura[1,*], Masami Ikeda[1], Takashi Ebisawa[2], Kai Masuda[2], Makoto Oyaidzu[2], Satoshi Sato[2]

[1]National Institute of Technology (KOSEN), Kushiro College, Kushiro, Japan
[2]Rokkasho Fusion Institute, National Institutes for Quantum Science and Technology, Rokkasho, Japan

[*]m-nakamura@kushiro-ct.ac.jp

Abstract. Accelerator-driven fusion neutron source is an experimental device for neutron irradiation testing of fusion reactor materials by simulating the fusion-relevant neutron environment by the Li-D nuclear reactions. The lithium (Li) target, on which the deuteron beam is injected, is in the liquid state with the free surface in the high vacuum environment. In this paper an initial result of a computational fluid dynamics (CFD) study of the free-surface liquid Li under a high vacuum condition is reported. The shape, i.e. thickness distribution, of the liquid Li obtained by the simulation is found to be consistent with the previous experimental result.

Keywords: Computational fluid dynamics, Fusion neutron source, Liquid lithium, Free surface flow, Curvature effect

1. Introduction

Fusion reactor materials will be in a harsh neutron (radiation) environment, but the damage natures, caused by the fusion neutrons, of the material structures are still unclear. Accelerator-driven fusion neutron source is an experimental device for neutron irradiation testing of fusion reactor materials, by simulating the fusion-relevant neutron environment by the Li-D nuclear reactions. The principle of the fusion neutron source is that the deuteron beam is injected on the liquid lithium (Li) target, in which the large amount of the neutron is generated by the Li-D reactions and used for the materials irradiation tests. In Japan, a fusion neutron source, named A-FNS [1] (Fig. 1), is being designed.

The Li target has unique hydrodynamic conditions that have rarely been observed in other natural or laboratory systems, as follows;

- The target is in the liquid state because the deposited D beam power of 5 MW has to be rejected by forced convection.

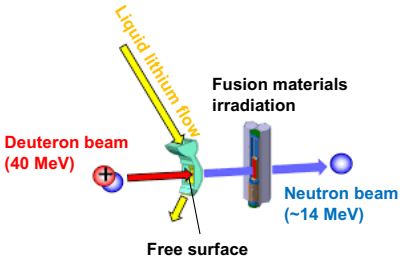

Figure 1: Principle of neutron generation in an accelerator-driven fusion neutron source.

- The liquid Li *cannot be contained by a container*, otherwise the D beam will damage the container and the liquid Li will be spilled out, so that the liquid Li should have the free surface of the D-beam injection side.
- The free surface contacts with the gas (vacuum) pressure of 10^{-3} Pa because the target section is connected directly to the D-beam accelerator that needs the ultra high vacuum.
- The target is concave to create the centrifugal force into the target, which leads to the effective pressure on the target and then increase the boiling point of the liquid Li in order to avoid the boiling by the D-beam heating in the high vacuum environment.

The liquid lithium target has been studied both computationally and experimentally. A computational fluid dynamics (CFD) study of the liquid Li target under such a high vacuum condition was previously reported [2]. The liquid Li target, without the D beam injection, in the vacuum condition of 10^{-3} Pa was experimentally demonstrated at the experimental campaigns of of the EVEDA Lithium Test Loop (ELTL) [3]. The shape of the free-surface of the ELTL liquid Li target was measured by means of an optical comb distance meter. It was found that the thickness of the free-surface target was increased in the order of mm, compared to the thickness at the nozzle exit part [4]. However, no comparison was made between the previous simulation and the experimental studies of the liquid Li target.

The purpose of the study is to develop a CFD model consistent with the experimental fact observed previously. Here we present an initial result of the CFD modeling and a comparison with the experimental fact.

2. Method

We have performed 3-dimensional (3D) CFD simulations of the liquid Li target in a simple slab geometry as shown in Fig. 2, while in the realistic configuration the Li target is concave. The centrifugal force $\vec{F_c}$ is modeled as a source term (external body force) in the Navier-Stokes (NS) equation. The curvature radius of $\vec{F_c}$ is given $R = 245$ mm, which is the design value of the A-FNS Li target [1]. The size of the simulation domain is 1,000 mm in height (H) $\times$ 50 mm in width (W) $\times$ 50 mm in depth (D). The depth of the liquid phase is 25

mm, and the rest domain is the gas (vacuum) phase. At the initial phase, the pressure of the gas phase is 10^{-3} Pa, and the liquid phase is at rest, i.e. $\vec{v} = 0$. As for the boundary conditions, the inlet liquid speed is a scan parameter ranging from $v_{in} = 10$ to 20 m/s. The outlet boundary is continuative.

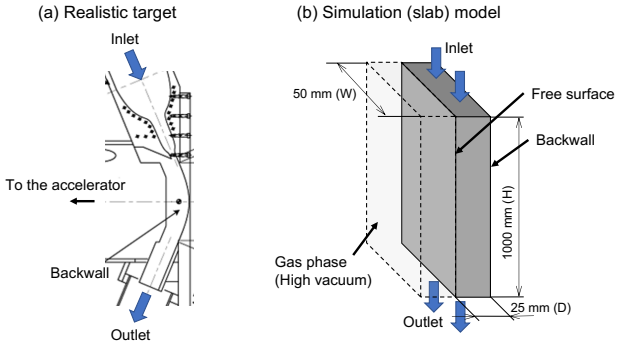

Figure 2: Free-surface liquid Li target of the fusion neutron source: (a) the realistic configuration and (b) the simulation model.

We used the InterFOAM solver of the open source CFD software package [5] to solve the Reynolds-Averaged Navier-Stokes (RANS) equation with the free surface. We used the standard $k - \epsilon$ model as the turbulence model. The VOF method is used for tracking the free surface. We define the liquid-gas surface as $\alpha = 0.5$, where α is the liquid fraction in a control volume.

3. Simulation results and discussion

We performed a scan in the inlet liquid velocity of the CFD simulation. The distribution of the surface height of the liquid Li in the streamwise direction from the inlet (nozzle exit) was constructed from the α-value distribution obtained by the CFD analysis.

The calculated thickness of the liquid Li target is shown in Fig. 3, in which, for comparison, the simulation case without the centrifugal force is also presented. The simulation result indicates that

1. the thickness of the free surface is increased in the streamwise direction in the case with the centrifugal force,
2. the larger the inlet liquid velocity, the larger the increase in the thickness, and
3. the increase in the thickness is not observed in the case without the centrifugal force.

The result suggests that the increase in the thickness is attributed to the centrifugal force.

The increase in the thickness of the liquid Li target was previously observed in the ELTL experimens [3,4]. It was also observed there that the thickness was increased with increasing the Li flow velocity. The mechanism of the increase in the thickness was also proposed

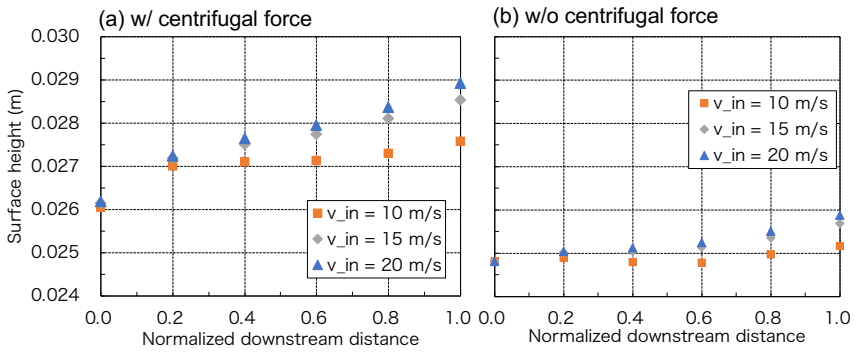

Figure 3: Spatial distribution of the thickness of the liquid Li target in the streamwise direction with (a) and without (b) the model centrifugal force. The downstream distance from the nozzle exit (horizontal axis) is normalized to 500 mm.

in [4]. Thus, the CFD simulation result of the present study agrees qualitatively with the previous experimental result. From a quantitative point of view, however, the present CFD simulation tends to overestimate the increase in the thickness compared to the previous experimental result. This may be due to the fact that in the realistic target configuration the curvature radius R of the target is inconstant [3] while in the present simulation R is assumed to be constant. CFD simulations in the realistic configuration and quantitative comparison with the experimental results are future work.

While the NS equation was *formally* solved for the gas region in the cases reported above, in general use of the NS equation is inappropriate for the rarefied gas (vacuum) region. It is noted, therefore, that the simulation results reported above are only valid in the liquid region. For more precise simulation, the Boltzmann equation for the (rarefied) gas region should be coupled with the NS equation for the free-surface liquid region.

Acknowledgments

This work was supported by QST Research Collaboration for Fusion DEMO, Nagaoka University of Technology (NUT) grant for collaborative research with National Institute of Technology (NIT), and JSPS KAKENHI Grant Number 22K03579.

References

[1] S. Sato, et al.: Conceptual design of Advanced Fusion Neutron Source (A-FNS) and irradiation test modules, *Nucl. Fusion*, 61:10 (2021), 106026 (12 pages).

[2] A. Peña, et al.: Hydraulics and heat transfer in the IFMIF liquid lithium target: CFD calculations, *Fusion Eng. Des.*, 84 (2009) 1489–1483.

[3] H. Kondo, et al.: Validation of liquid lithium target stability for an intense neutron source, *Nucl. Fusion*, 57:6 (2017) 066008 (10 pages).

[4] T. Kanemura, et al.: Measurement of Li target thickness in the EVEDA Li Test Loop, *Fusion Eng. Des.*, 98–99 (2015) 1991–1997.

[5] https://www.openfoam.com/

Estimation of Cs layer on plasma grid in ITER scale negative ion source

Masafumi Yoshida*, Shunsuke Hayashi, Yoichi Sato

Department of Electrical Engineering, National Institute of Technology, Ube College
*yoshida-m@ube-k.ac.jp

Abstract. A thickness of cesium (Cs) layer on a plasma grid (PG) like ITER scale negative ion source is estimated by using a physical model to control Cs distribution inside the negative ion source. It is suggested that over piling-up of Cs at the PG leads in the decrease of the negative ion beam current with increasing an initial Cs input, although the thickness of the Cs coverage is saturated.

Keywords: Cesium, Negative ion source, N-NBI

1. Introduction

In ITER, it is important to control a thickness of cesium (Cs) layer on a plasma grid (PG) of negative-ion-based neutral beam injector (N-NBI), because of maintaining higher production yield of negative ion [1]. In order to maintain stably the negative ion production, we have developed a model to control Cs distribution inside the negative ion source, based on the experimental data in JT-60SA negative ion source [2, 3]. Then, It was found that the desorption of Cs from the wall was successfully suppressed and the reasonable variation of Cs coverage during 100 s was obtained in JT-60SA negative ion source [4]. In this work, by using this model, time variation of thickness of Cs layer on the PG in ITER scale negative ion source.

2. Modeling and Results

The model is shown elsewhere in detail [2, 3]. Figure 2 shows the time variation of the Cs layer on the PG of ITER scale negative ion source in the case of maximum wall temperature ($T_{\mathrm{wall}}{}^{\mathrm{max}}$) of 60ºC at the overall chamber wall. Starting operation, the Cs layer is gradually increased until 200 s and saturated. The thickness saturated is increased with increasing initial input of Cs in the ion source. It is suggested that over piling-up of Cs at the PG leads in decrease of the negative ion beam current with increas-

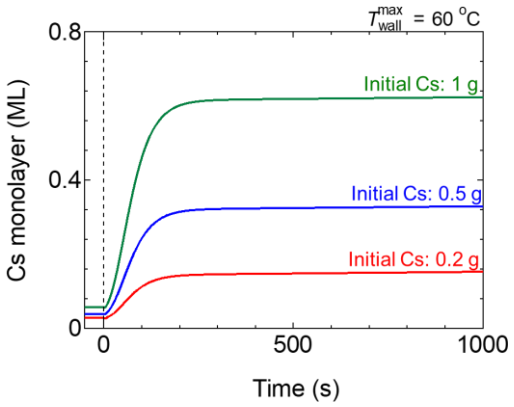

Fig. 1: Time variation of the Cs layer on the PG in ITER scale negative ion source.

ing an initial Cs input, although the thickness of the Cs layer is saturated. Therefore, lower Cs assumption negative ion source should be developed for steady long-pulse operation in the ITER scale negative ion source.

References

[1] Progress in the ITER physics basis, *Nucl. Fusion*, 47 (2007) S18.

[2] M. Yoshida, W. Oohara, M. Ichikawa, J. Hiratsuka, N. Umeda, A. Kojima, M. Kashiwagi: Evaluation of the Temperature Dependence of the Cesium Deposition on the Plasma Grid in the JT-60SA Negative Ion Source, *AIP Conference Proceedings*, vol:2052 (2018), 040008.

[3] M. Yoshida , W. Oohara, M. Ichikawa, J. Hiratsuka , G. Q. Saquilayan , N. Umeda, A. Kojima, and M. Kashiwag: Analysis of the cesium distribution in the JT-60SA negative ion sources for steady long-pulse operation, *Rev. Sci. Instrum.*, vol:91 (2020), 033313.

[4] M. Kashiwagi, J. Hiratsuka, M. Ichikawa, G. Q. Saquilayan, A. Kojima, H. Tobari, N. Umeda, K. Watanabe, M. Yoshida and L. Grisham: 100 s negative ion accelerations for the JT-60SA negative-ion-based neutral beam injector, *Nuclear Fusion*, vol:62 (2022), 026025.

JSST 2022

Application of Physics-informed Neural Network Surrogate Model on Linear Elasticity Problem

Jiarui OU[1,*] and Koji KOYAMADA[1]

[1]Kyoto University

[*]oujiarui@outlook.com

Abstract. This research is aimed at building one class of surrogate model utilizing physics-informed neural network (PINN) to solve elastic plane-strain problem. We first confirm the utility of PINN in constructing surrogate model on elasticity equation problems. In the experiment of elastic plane-strain problem, we take the coordinates of the point and all the parameters of interest as the input of the network, and take all the variables (physical quantities) in the equation as the output of the network. By participating in the optimization of the loss function representing the physical law, a surrogate model is finally obtained in which the user can easily obtain any relevant physical quantity in any condition and any position within the range. In addition, we also use PINN to build a class of solvers for this problem, and obtain the solution of the equation through physical equations and boundary conditions. This allows us to continue training the surrogate model even without the exact solution, making our model a data-free model.

Keywords: Physics-informed neural network, Surrogate model, Linear elasticity problem

1. Introduction

Linear elasticity is a problem that has a wide range of usage in the field of solid mechanics. The analysis of traditional numerical methods in such problems is a complex process, which also means that small changes in certain parameters often require recalculation of the entire system. In engineering, researchers usually need to build a corresponding surrogate model to deal with such parameters of interest. As a classic model of machine learning technology that has been widely developed in many fields recently, forward propagation artificial neural network (FNN) has also become a very popular surrogate model. Thanks to the simple and flexible structure of neural networks, based on general approximation theorem, it is expected to become a general model for such problems.

The optimization process of neural network is also the process of loss back propagation, in which the definition of loss function is the most important topic. Maziar Raissi et al.[1] calculated the PDE residuals through the automatic differentiation mechanism of the neural network itself, and added to the loss function. Known as PINN, this makes the neural network more in line with PDE, and further provides the possibility to solve the forward and

inverse problems related to PDE. LU LU et al.[2] developed library named DeepXDE based on the principle to solver wider range of problems. Ehsan Haghighat et al.[3] investigated construction of surrogate model based on the transfer learning of PINN.

Beyond these, in this study, we build a more comprehensive neural network for the linear elasticity problem, where all parameters and variables participate in network training independently. We also investigate the possibility of PINN solvers to obtain solutions from PDEs, which could replace exact solutions to serve the surrogate model into a totally data-free one.

2. Problem setup

The problem is defined on a unit square in two dimensions space ($0 \leq x \leq 1, 0 \leq y \leq 1$). Due to the momentum balance, the constitutive model and the kinematic relations, the equations should be:

$$\begin{aligned}
&\tfrac{\partial}{\partial x}\sigma_{xx} + \tfrac{\partial}{\partial y}\sigma_{xy} + f_x = 0 \\
&\tfrac{\partial}{\partial x}\sigma_{xy} + \tfrac{\partial}{\partial y}\sigma_{yy} + f_y = 0 \\
&\sigma_{xy} = 2\mu\varepsilon_{xy} \\
&\sigma_{xx} = \lambda\varepsilon_{xx} + \lambda\varepsilon_{yy} + 2\mu\varepsilon_{xx} \\
&\sigma_{yy} = \lambda\varepsilon_{xx} + \lambda\varepsilon_{yy} + 2\mu\varepsilon_{yy} \\
&\varepsilon_{xx} = \tfrac{\partial}{\partial x}u_x \\
&\varepsilon_{yy} = \tfrac{\partial}{\partial y}u_y \\
&\varepsilon_{xy} = \tfrac{1}{2}\left(\tfrac{\partial}{\partial y}u_x + \tfrac{\partial}{\partial x}u_y\right)
\end{aligned}$$

Specifically, the body forces here are set to:

$$\begin{aligned}
&f_x = \lambda\left[4\pi^2\cos(2\pi x)\sin(\pi y) - \pi\cos(\pi x)\,Qy^3\right] \\
&+\mu\left[9\pi^2\cos(2\pi x)\sin(\pi y) - \pi\cos(\pi x)\,Qy^3\right] \\
&f_y = \lambda\left[-3\sin(\pi x)\,Qy^2 + 2\pi^2\sin(2\pi x)\cos(\pi y)\right] \\
&+\mu\left[-6\sin(\pi x)\,Qy^2 + 2\pi^2\sin(2\pi x)\cos(\pi y) + \pi^2\sin(\pi x)\,Qy^4/4\right]
\end{aligned}$$

As definite conditions, the boundary are:

$$\begin{aligned}
&u_x = 0,\ y = 0\ or\ y = 1 \\
&u_y = 0,\ y = 0\ or\ x = 0\ or\ x = 1 \\
&\sigma_{xx} = 0,\ x = 0\ or\ x = 1 \\
&\sigma_{yy} = (\lambda + 2\mu)\,Q\sin(\pi x),\ y = 1
\end{aligned}$$

Then the exact solution could be:

$$\begin{aligned}
&u_x(x, y) = \cos(2\pi x)\sin(\pi y), \\
&u_y(x, y) = \sin(\pi x)\,Qy^4/4.
\end{aligned}$$

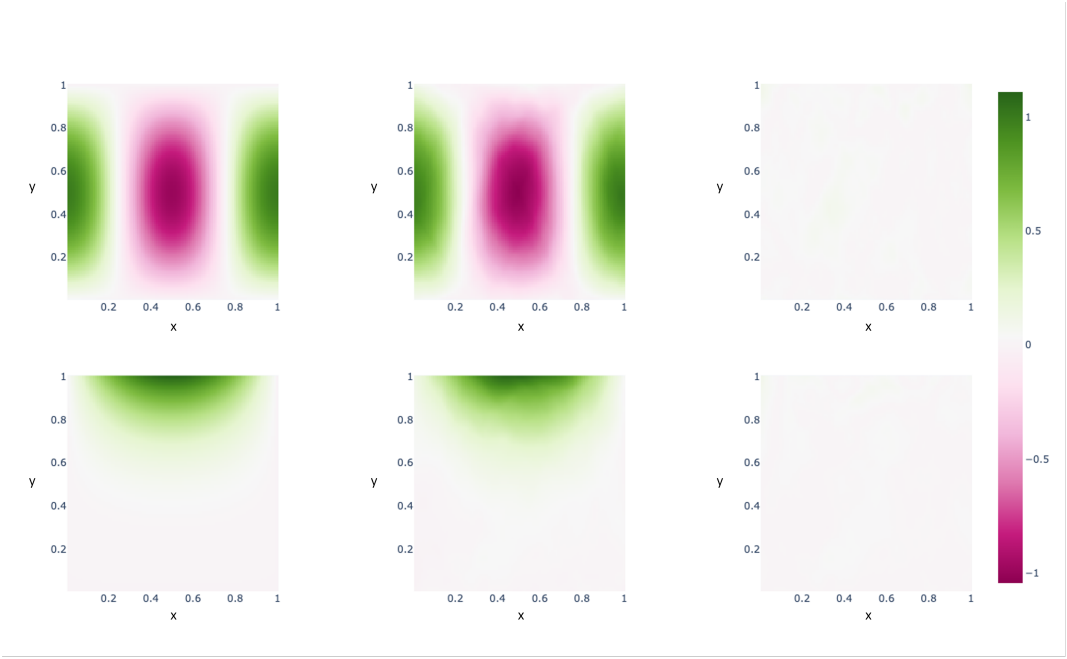

Figure 1: Exact solutions (the first column), Surrogate model results (the second column) and errors (the third column) of u_x (the first row) and u_y (the second row)

3. Method

To build the physics-informed surrogate model, the 5 inputs of the neural network are set as the 2 coordinates x, y and the three parameters of interest λ, μ and Q, while the 10 outputs are all physical quantities u_x, u_y, ε_{xx}, ε_{xy}, ε_{yy}, σ_{xx}, σ_{xy}, σ_{yy} and f_x, f_y. The physical residuals are calculated with 8 equations. The training data are from the exact solutions of 10000000 points with different conditions ($x, y = 0.01, 0.02, ..., 1.00; \lambda = 0.2, 0.4, ..., 2.0; \mu = 0.1, 0.2, ..., 1.0; Q = 1, 2, ..., 10$). Training epochs are set as 100.

4. Result

After training the network, we test the predictive ability of the model with a specific set of conditions ($\lambda = 1.11; \mu = 0.555; Q = 4.44$). The results of u_x and u_y are shown in Fig. 1. The mean error is 0.022, which could hardly be seen in the figures of error (column 3) of Fig. 1.

With DeepXDE, we also build a PINN solver to generate training data for surrogate model. The results from PINN solver in the condition with $\lambda = 1; \mu = 0.5; Q = 4$ could be as shown in Fig. 2.

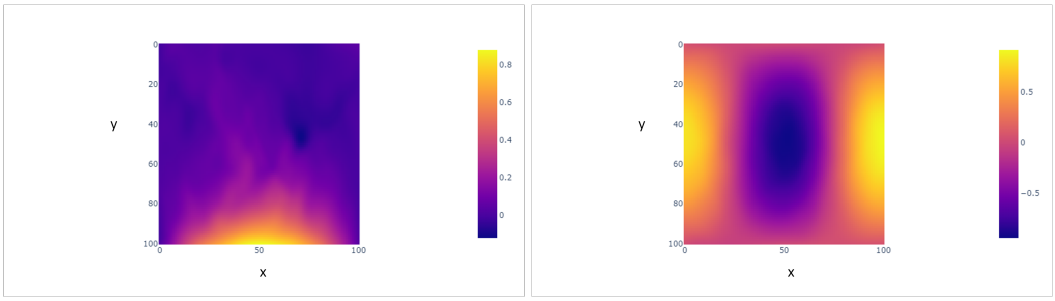

(a) (b)

Figure 2: Heat maps of results predicted by PINN solver about (a) u_x and (b) u_y

5. Conclusion

This study successfully proved that with PINN, we could build a high-precision model for Linear Elasticity Problem characterizes the corresponding PDE and effectively predicts physical quantities under more conditions. Additionally, we explored using the PINN solver to generate training data to support the surrogate model. The current prediction results have disadvantages such as less smoothness, but they can already reflect the correct data distribution characteristics to a large extent. In future research, we will further optimize the PINN solver so that its results are closer to and can replace the exact solution, making the entire model becomes an efficient and high-accuracy data-free model.

References

[1] Raissi Maziar, Paris Perdikaris, and George E. Karniadakis. Physics-informed neural networks: A deep learning framework for solving forward and inverse problems involving nonlinear partial differential equations. *Journal of Computational physics*, 378 (2019):686-707.

[2] Lu Lu and Meng Xuhui and Mao Zhiping and Karniadakis George Em. DeepXDE: A deep learning library for solving differential equations. *SIAM Review*, 63 (2021):208–228.

[3] Haghighat Ehsan and Raissi Maziar and Moure Adrian and Gomez Hector and Juanes Ruben. A physics-informed deep learning framework for inversion and surrogate modeling in solid mechanics. *Computer Methods in Applied Mechanics and Engineering*, 379 (2021):113741.

Improving the accuracy of Homography Matrix Estimation using Deep Learning for disturbed Images

Mikichika YOKONO[1*] and Hiroyuki KAMATA[2]

[1]Graduate School of Science and Technology, Meiji University, Japan
[2]School of Science and Technology, Meiji University, Japan
*ce211069@meiji.ac.jp

Abstract. The objective of this study is to improve the robustness of homography estimation using deep learning for images superimposed with various types of disturbances. In conventional homography matrix estimation using deep learning, the original image and the image with perturbations and disturbances are simultaneously input to the model for estimation. The disadvantages of this method are that the original image is affected by noise and the model itself is unclear. In this research, features are extracted separately for each of the two images, and a model is constructed based on ResNet using these features as input. In addition, when extracting the features of perturbed and disturbed images, the brightness tolerance property of principal component analysis is introduced into the filter of the CNN to add pinpoint tolerance to the disturbance. The estimation accuracy of the homography matrix in the proposed method in this study shows improved accuracy in various noises. These results suggest that the proposed method is effective in reducing the effects of disturbances by extracting features for each image.

Keywords: Homography Estimation, Image Processing, Deep Learning, PCA

1. Introduction

In this study, we aim to improve the accuracy of homography estimation using deep learning for various types of disturbances. Homography is a technique for mapping two images on a plane from different perspectives and plays an important role in computer vision [1]. Conventional deep learning methods [2] show a decrease in matching accuracy when disturbance is added to the image, compared to when high-definition images are used. This is thought to be due to the fact that the original image and the image with perturbation and disturbance are input simultaneously at the time of input to the model, and the original image is also affected by the noise. Another problem is that the behavior near the input layer is unclear.

In this study, in order to create robust deep learning even in various disturbances, we propose a model that estimates the homography matrix by extracting features separately from the original image and the image with disturbance and perturbation, and using them as inputs. This has three possible advantages: (1) By extracting features separately from the original image and the perturbed or noisy image, the effect of noise on the original image is suppressed. (2) By

forming a noise-resistant model during the feature extraction phase, the model can be tuned to be more robust to noise. (3) The role of each phase of the model is clarified to some extent.

2. Deep Homography Estimation

Deep homography estimation is a model that estimates the homography matrix between two images. In this case, the conventional 3 × 3 parameters have a large variance, so a 4-point homography parameterization is used, which is parameterized by taking the difference of the corresponding four points [3].

Assuming that $\boldsymbol{u_k^A} = (u_k^A, v_k^A, 1)$ and $\boldsymbol{u_k^B} = (u_k^B, v_k^B, 1)$ are four fixed points in images I_A and I_B, respectively, the four-point homography parameterization is as follows

$$H_{4pt} = \begin{pmatrix} u_k^B - u_k^A \\ v_k^B - v_k^A \end{pmatrix} = \begin{pmatrix} \Delta u_k \\ \Delta v_k \end{pmatrix} \quad (k = 1,2,3,4) \tag{1}$$

This reduces the variance of the homography matrix and the number of parameters to 2 x 4. Also, the original homography matrix and the 4-point parameterized homography have a one-to-one correspondence.

In the estimation flow, the original image I_A and the image I_B with perturbations and disturbances added to the original image are simultaneously input to the model to estimate the four-point parameterized homography matrix H_{4pt_pred} The model then takes the H_{4pt_truth} and L2 norm prepared as the correct answer labels and uses the following loss function.

$$Loss_{L2} = \frac{1}{2} \left\| H_{4pt\_pred} - H_{4pt\_truth} \right\|^2 \tag{2}$$

3. Expemiments

3.1 Technique

The models of the conventional and proposed methods are shown in Fig. 1(a) and (b), respectively. In the conventional method shown in Fig. 1(a), the original image and the image with perturbation and disturbance are input simultaneously and directly to the model to estimate the homography matrix. On the other hand, in the proposed method shown in Fig. 1(b), the phases of extracting the features of each image are first interspersed as the "original layer" and the "noise layer," and then the model is constructed to perform homography estimation using the extracted features as input. Two types of inputs to the features are being examined: (1) Input without any processing, (2) The input through the activation function by manipulating the number of channels by pointwise convolution for the combined features. In order to make the "noise layer" noise tolerant, the average of the filter weights, which is a condition of PCA (Principal Component Analysis), is set to 0. Assuming that this allows learning with less luminance tolerance, the following loss is defined [4].

$$Loss_{average\_\omega} = \sum_{num} \left| \frac{1}{|n|} \sum_{i=1}^{n} \omega_{i,num} \right| \tag{3}$$

where ω_i is the input layer weights of the "noise layer", num is the number of filters, and n is the number of weights per filter. We take the sum of $Loss_{L2}$ and $Loss_{average\_\omega}$ of the correct labels and predictions of the homography matrix, and use the following loss function for learning.

$$Loss = Loss_{L2} + Loss_{average\_\omega} \tag{4}$$

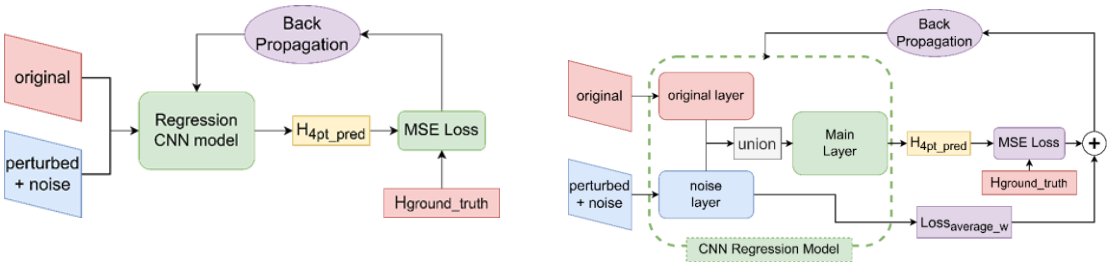

(a)Original Model (b)Proposal Model

Fig 1. Deep Homography Estimation Model

Table 1. Study Model

Model	Abstract
Normal	Conventional method with ResNet
Normal + PCA	Normal with PCA characteristics added
proposal_1	Proposed method (input without any processing)
proposal_2	Proposed method (input through Pointwise convolution and Activation function)

In addition, as a CNN model in this experiment, we will construct a model as shown in Table 4 based on ResNet, which is capable of deep layer model representation, for comparative study [5].

3.2 Datasets

The dataset is MS-COCO2014, a dataset of images provided by Microsoft, and brightness change, contrast, blur, Gaussian noise, and Radiation noise are added during training and validation. In the estimation, the results of 5000 validation images are evaluated as successful if they satisfy the following Mean Average corners Error equation.

$$L_{MACE} = \frac{1}{4}\sum_{i=4}\left\|(x_i, y_i)_{pred} - (x_i, y_i)_{truth}\right\|_2^2 \leq 3 \quad (5)$$

4. Results

Tables 2 and 3 show the ResNet34-based estimation accuracy [%] and estimation error [pixels] results, respectively. Comparing the conventional method with the proposed method, the accuracy and estimation error are improved in many noise cases. In particular, proposal_2 shows an improvement of 0.6% in accuracy and up to 20% in estimation error compared to the conventional method in the case of brightness change.

Table 2. Estimation Accuracy (ResNet34) [%]

	Normal	Bright	Contrast	Gaussian Blur	Gaussian Noise	Radiation Noise
Normal	99.56	98.02	97.52	99.52	97.72	97.68
Normal + PCA	99.68	98.14	97.14	99.42	97.84	97.74
proposal_1	99.8	98.42	97.92	99.52	97.98	96.66
proposal_2	99.84	98.64	98.18	99.54	98.1	96.32

Table 3. Estimation Error (Resnet34) [pixel]

	Normal	Bright	Contrast	Gaussian Blur	Gaussian Noise	Radiation Noise
Normal	0.737908669	0.915462175	0.979948377	0.786003457	0.957356938	0.93965536
Normal + PCA	0.676613099	0.855769602	0.975453756	0.765538186	0.921166107	0.929204516
proposal_1	0.549423116	0.730792289	0.78611619	0.629609871	0.797957745	0.991951737
proposal_2	0.55592289	0.727070196	0.783425539	0.634343756	0.815166971	1.037255014

5. Conclusion

In this study, experiments revealed that extracting features separately from the original image and the perturbed or noisy image is effective in reducing the effect of noise on the original image while making the operation in the input layer phase more clear. Two possible reasons for the higher accuracy of Proposal_2 than Proposal_1: (1) the improvement of nonlinearity by sandwiching the activation function, (2) the ability to maintain the original channel structure of ResNet by manipulating the number of channels in the Pointwise Convolution. We were also able to confirm that it is possible to tune the model to be more robust to noise by introducing PCA luminance tolerance during the feature extraction phase of the input image to form a noise-resistant model. In the future, we will consider noise-robust models for layers that perform feature extraction of noise images to improve accuracy even further. We will also continue to study more appropriate models for homography estimation and their structure.

References

[1] O. Chum, T. Pajdla, and P. Sturmb, “The geometric error for homographies”, Computer Vision and Image Understanding , Pages 86-102, 2005

[2] D. DeTone, T. Malisiewicz, and A. Rabinovich, “Deep image homography estimation”, arXiv:1606.03798, 2016.

[3] Ty Nguyen, Steven W. Chen, Shreyas and S. Shivakumar, Camillo J. Taylor, Vijay Kumar, “Unsupervised Deep Homography: A Fast and Robust Homography Estimation Model”, arXiv :1709.03966, 2017

[4] I. Nomura, T. Takino, J. Irie, K. Nagata, H. Kamata, K. Kariya, K. Takadama, T. Isida, S. Fukuda, S. Sawai, and S. Sakai, “Characterization and Performance of Crater Detection by Principal Component Analysis”, Aerospace Technology, 2014.

[5] K. He, X. Zhang, S. Ren, and J. Sun, “Deep Residual Learning for Image Recognition”, arXiv:1512.03385, 2015.

JSST 2022

Page extraction from sealed historical manuscripts by using physics-informed neural network

Zhongjiang Han[1,*] and Koji Koyamada[1]

[1]Kyoto University

[*]zhongjianghan@gmail.com

Abstract. X-ray-based computerized tomography scans are currently being used to analyze page information in noninvasively closed booklets. An important task is to extract the page information. We propose a page information extraction method using a physics-informed neural network. We extract pages from the data used in the existing research and compare the results to analyze the advantages and disadvantages of different methods.

Keywords: 3D CT, Page segmentation and extraction, deep learning, PINN

1. Introduction

Historical literature contains valuable descriptions of past events. Such documents are fundamental for historical research and have important implications for historians. However, owing to aging, external erosion, and the importance of documents, the text on some ancient literature cannot always be read. Certain letters cannot be opened, and documents are too charred to decipher. To read such documents, it is necessary to acquire and visualize the information that they contain using noninvasive measurement methods. In 1750, Karl Weber discovered more than 1,800 papyri carbonized by the eruption of Vesuvius in 79 AD near Herakraneum in Campania, Italy [1]. These papyri were wound into tubes and difficult to open without damage, making them impossible to decipher without a noninvasive technique. As another example, the 2004 fire at the Duchess Anna Amalia Library in Germany severely damaged more than 62,000 ancient documents through high temperatures and burning, as well as water used in firefighting [2].

X-ray computerized tomography (CT) imaging is the most widely used noninvasive literature browsing method. According to this method, an X-ray is irradiated onto an imaging target, and the transmitted X-ray is then measured to visualize the structure inside the measurement target. Daniel Stromer et al. [3] used home-made book data to study the effects of different inks and papers with a CT machine, and extracted page information using methods previously proposed.

Based on the universal approximation theorem, we believe that deep-learning models can be used to fit the spatial structure of booklets. We use a Laplace-equation-based physics-informed neural network (PINN) to approximate the page volume data. The difference of

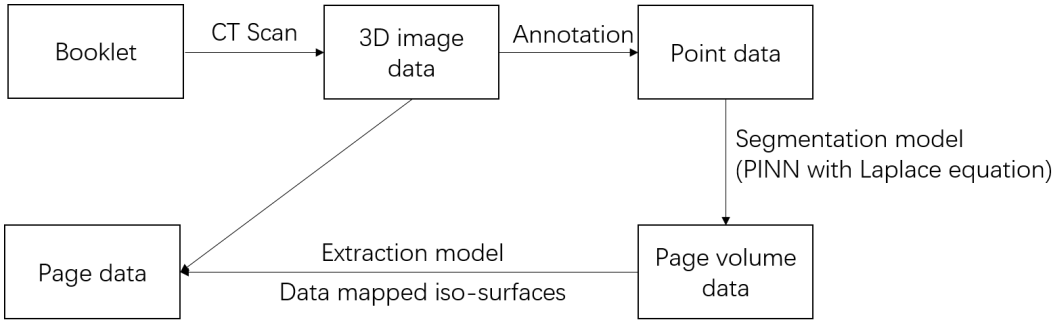

Figure 1: Overview of our proposed approach. Data is obtained from CT scans, annotated for deep learning, page volume data is obtained by learning, and finally page data is obtained by mapping.

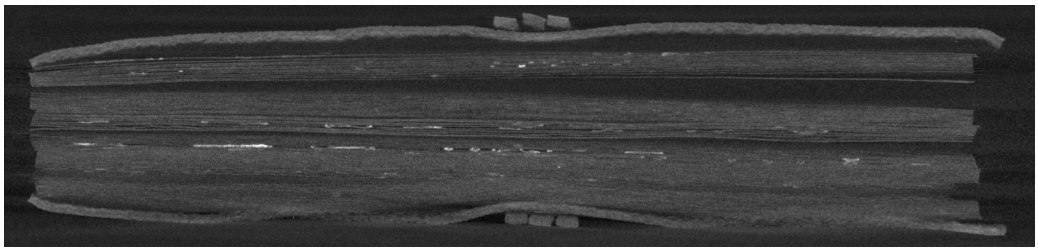

Figure 2: A slice of the data used in the experiment. The highlighted place is the position of the text, the gray is the paper position, and the black is the gap between the pages.

the proposed method is that our extraction method requires the user to manually annotate the region where the page is located, while the existing method can automatically calculate the region where the page is located. However, the annotated data in our method can be fitted into 3D volume data through deep learning, and the 3D shape of the page can be extracted more accurately.

2. Method

The specific process of our proposed method is as fig.2. The 3D image data were obtained by CT scanning, and the data were imported into the self-developed annotation tool to annotate the pages with page numbers. Thus, the 3D coordinates and the data corresponding to the page numbers were obtained. These data were trained by a deep-learning model to obtain the page volume data (where the scalar data value represents the page number), which can calculate all voxels where each page is located. Finally, the page data are obtained by mapping the corresponding iso-surfaces (i.e., the surface corresponding to the page).

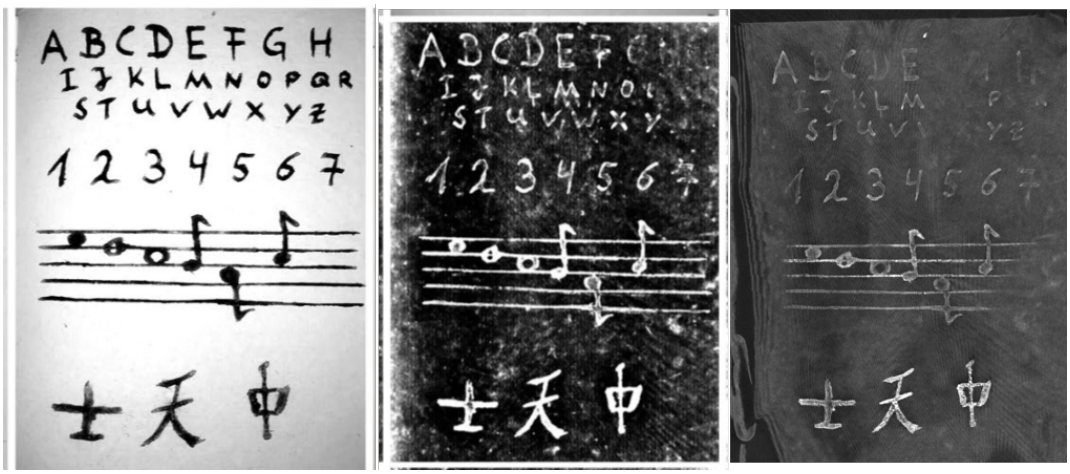

Figure 3: Comparison of page information extraction results, (left) ground truth, (middle) automatic page extraction method (right) deep learning extraction method based on manual annotation

3. Experiment

Our experimental part will use book data used in published studies [3] for page information extraction. Specifically, it is composed of 56 pages of three different types of paper and 5 different inks. Experiments have been carried out in the published study using the previously proposed automatic page extraction method, and the results of page information extraction by CT machines at voltages of 30 kV and 50 kV are shown. We will use our proposed method to conduct comparative experiments. Since there are no strict results evaluation criteria, we will directly compare the extracted result pages (2D images) and discuss the advantages and disadvantages of the research methods.

4. Result and Evaluation

At present, we have selected one of the pages to compare the results. The result is shown in the fig.3. Overall, our proposed method is longer in time than the automatic page extraction method. This is due to manual annotation and complex deep learning taking a lot of time. In the case of extracting the same data, the time consumed by the automatic method is 20 minutes, and the time consumed by ours is about 50 minutes. In terms of the accuracy of page information, both methods extract relatively complete information. In the results of the automatic extraction method, the letters ”H” and ”z” on the far right of the page are missing. This is because this part of the page has no space between the adjacent pages in the spatial distribution, and it is difficult to be identified by the algorithm, so there is a lack of information. We expect to address this issue with human annotation. The results show that the part of the letter ”z” can be extracted by annotation, and it is the part that is not annotated in detail, such as the letter ”F” and ”G”, the information is missing. This is where we need to improve.

References

[1] Diringer, David: The book before printing: ancient, medieval and oriental, *Courier Corporation*, 2013.

[2] Knoche, Michael: The Herzogin Anna Amalia library after the fire , *IFLA journal* 2005, 31.1: 90-92.

[3] Stromer, Daniel, et al. Browsing through sealed historical manuscripts by using 3-D computed tomography with low-brilliance X-ray sources. *Scientific reports* 2018, 8.1 : 1-10.

JSST 2022

Improvement of arrhythmias distinction accuracy using suitable combination of features of the Electrocardiograms

Md.Masudur Rahman[1,*], Sergio Albeverio[2], Toshinao Kagawa[3], Shuji Kawasaki[4], Takayuki Okai[5], Hidetoshi Oya[5], Yumi Yahagi[6], Minoru W.Yoshida[1]

[1]Graduate School of Engineering, Kanagawa University, Japan
[2]Inst. Angewandte Mathematik, and HCM, Univ. Bonn, Germany
[3]School of General Education and Management Studies, Suwa University of Science, Japan
[4]Faculty of Science and Engineering , Iwate University, Japan
[5]Faculty of Information Engineering, Tokyo City University, Japan
[6]Department of Information Systems, Tokyo City University, Japan

[*]masudur_2006@yahoo.com

Abstract. This paper presents a quantitative improvement of accuracy for the shockable and non-shockable arrhythmias discrimination by finding the suitable combination of features of the Electrocardiograms (ECG). By visualizing multivariate ECG classes on scatter plots, two-dimensional histogram plots for each combination of features in the different feature spaces, and numerical experiments, we select the best combination of features. Through the best combination, an improved discrimination performance in the decision stage is generated.

Keywords: Electrocardiograms (ECG), Wavelet transform, NSI, NTI, Numerical methods

1. Introduction

Arrhythmia is a heart disease when the heart does not beat in the systematic way. The arrhythmias are identified by analyzing electrocardiogram (ECG) signals. Among these arrhythmias, some are shockable and some are non-shockable arrhythmia. The shockable arrhythmias that lead to sudden death. Accurately and early diagnosis of arrhythmias by the Automatic external defibrillator (AED) increases the survival rate of the patients. The important challenge of AED is to distinguish shockable (ventricular fibrillation (VF), and ventricular tachycardia (VT)) and non-shockable (pulseless electrical activity (PEA)) arrhythmia in abnormal classes.

In order to increase the precision of AED, it is necessary to extract accurate information from the abnormal ECG signals. This issue is addressed by the novel method in Rahman et al. [1], where the wavelet transform with pseudo differential like operators was applied

to observe statistics on the scalogram of the ECG signal. In [1], the feature combination 'Mean of NSI' with the 'Variance of NSI' is used for the numerical experiments in the decision stage.

In the present paper, the sixteen statistical features are extracted from the scalogram by normalized spectrum index (NSI) and normalized time index (NTI) in order to investigate the possibility of increasing discrimination performance through a combination of these features. In this context, we first examine individual features with the help of a univariate histogram (see Figure 1), and then, look at the effect of all possible feature pairs using 16 individual features on the scatter plot matrix and the bivariate (two-dimensional) histogram plot (see Figures 1, and 2). Finally, the performance of the decision algorithm guarantees the best combination of features (see Table 1).

2. The data, fundamental formulas, and distinction procedure

In our work, we have collected 1079 samples from the Physio-bank, *https:physiobank.org* for evaluation. This database provides both shockable and non-shockable arrhythmia types. First, we separate original long ECG signals into pieces of five second signal segments and performed *detrending* to the segmented signals to remove the *linear trend*. Second, apply wavelet transform with pseudo differential like operators for accurately generate scalogram from the signal [1]. Third, as a basic statistics to quantize the different features over the abnormal class ECG signals, we take the NSI in the frequency direction [1] and NTI in the time direction. Fourth, In order to get the highest accuracy, we investigate the best combination of NSI and NTI features (see section 3.). Finally, histogram is used in the decision stage, and the separation of histograms of the scatter plot coordinates gives us the desired judgement of the distinction.

3. A suitable combination of the NSI and NTI features

The sixteen statistical features are derived from the scalograms through the NSI and NTI, and a matrix $(16 * 4 * 1079)$ of scatter plots with histograms is created (see Figure 1), where 1079 samples are grouped into four classes by the grouping variable. The Figure shows the pairwise scatter plot in the lower and upper triangular and represents the histogram diagonally from top left to right. From the figure, we see that the univariate histogram for 'Mean of NSI' shows the highest separable class. Also, the univariate histogram for 'Mean of NTI', and 'Variance of NSI' show almost the same level separable class. In addition, The scatter plots of the combination of 'Mean of NSI' with all features show the same level of distribution for the four types of arrhythmias. So, it is not clear which feature combination is effective for the discrimination of shockable and non-shockable arrhythmias.

Therefor, in order to find best feature combination we create a bivariate histogram plots for the mean of NSI along with each feature showing the separation of four different arrhythmias in figure 2. Now we observe each subplot histograms and select the suitable combination of features through numerical experiments, and by the following considerations.

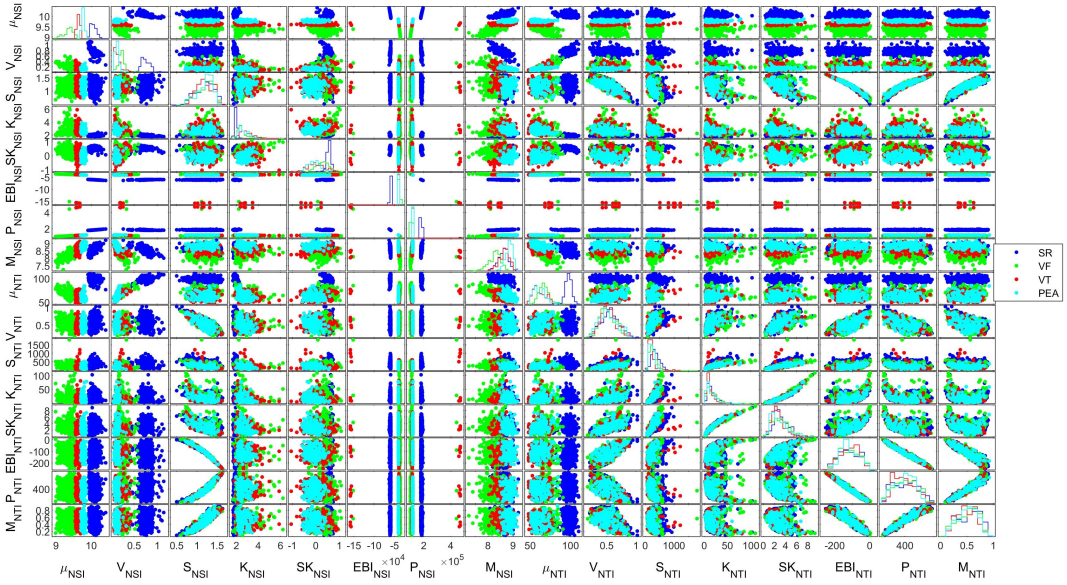

Figure 1: Multi-variable plot matrix with histogram

i) The first row in the figure 2, the combinations have low separation in both directions and the distribution is very much scattered.

ii) The second row in the figure 2, except the third subplot of 'M_{NSI}' with 'μ_{NSI}', the rest of the combinations are well distributed. The combination of 'μ_{NTI}' with 'μ_{NSI}' shown high separation in both directions, while ignoring the 'EBI_{NSI}' with 'μ_{NSI}', and 'P_{NSI}' with 'μ_{NSI}' combinations owing to their high inter-dependence in the 'EBI_{NSI}' and 'P_{NSI}' direction.

iii) The combinations have low separation in both direction and the distribution is very much scattered in the third and fourth rows in the figure 2.

From the experimental results (see Table 1, and Figure 1, and 2), and above instructive analysis, the combination of 'Mean of NSI' with 'Mean of NTI' is the best among all.

4. Results and discussion

For the evaluation, we performed 4-fold cross validation for stabilizing the performance, and consider three measurement metrics: sensitivity (Sen%), specificity (Sp%), and accuracy (Acc%) [1]. The discrimination performance for proposed and existing combination of features between different schemes of arrhythmias is demonstrated in Table 1. From the table we see that the proposed combination guarantees 100% accuracy for four groups comprising the normal group (SR), and the abnormal groups (PEA, VF, and VT), while accuracy increase from 91.58% to 93.32% for the distinction of shockable (VF, VT) versus non-shockable (PEA) arrhythmias.

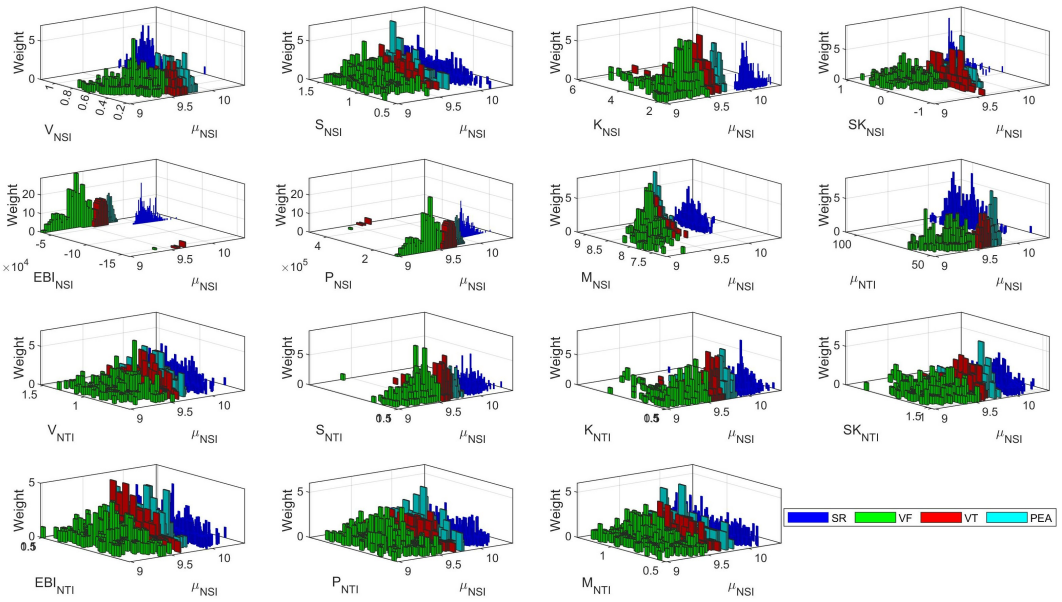

Figure 2: Bivariate histogram of Mean of NSI with all features for SR, VF, VT, and PEA

Table 1: Comparison between proposed and existing method

Feature combination	Group	Sen(%)	Sp(%)	Acc(%)
Mean of NSI with Mean of NTI (Proposed)	Normal (SR) vs Abnormal (PEA, VF and VT)	100.00	100.00	100.00
	Shockable (VF, VT) vs non-shockable (PEA)	92.89	94.30	93.32
Mean of NSI with Variance of NSI [1]	Normal (SR) vs Abnormal (PEA, VF and VT)	100.00	100.00	100.00
	Shockable (VF, VT) vs non-shockable (PEA)	91.90	91.38	91.58

References

[1] M.M. Rahman, T. Kagawa, S. Kawasaki, S. Nagai, T. Okai, H. Oya, Y. Yahagi, M.W. Yoshida: Various scalographic representation of electrocardiograms through wavelet transform with pseudo-differential operator like operators, *Journal of Advanced Simulation in Science and Engineering*, 2022, 9:1, 96-112.

JSST 2022

Asymptotic analysis for solutions to the generalized Fornberg–Whitham equation with dissipation

Ikki Fukuda[1,*]

[1]Division of Mathematics and Physics, Faculty of Engineering, Shinshu University

[*]i_fukuda@shinshu-u.ac.jp

Abstract. We consider the initial value problem for the generalized Fornberg–Whitham equation with dissipation. This is one of the nonlinear, nonlocal and dispersive-dissipative equations. The main topic of this paper is an asymptotic analysis for the solutions to this problem. Especially, we investigate the effects of the dispersion, dissipation and nonlinear terms on its asymptotic profile of the solutions. Actually, we prove that the solution to this problem converges to the Gaussian function. Also, we show that the effects of the dispersion term and the nonlinear term appear from the second asymptotic profile of the solution.

Keywords: Fornberg–Whitham equation, Initial value problem, Asymptotic analysis.

1. Introduction

We consider the initial value problem for the following integro-differential equation:

$$\begin{aligned} &u_t + u^p u_x + \int_{\mathbb{R}} Be^{-b|x-y|} u_y(y,t)dy = \mu u_{xx}, \quad x \in \mathbb{R},\ t > 0, \\ &u(x,0) = u_0(x), \quad x \in \mathbb{R}, \end{aligned} \tag{1}$$

where $p > 2$ is an integer and $B, b, \mu > 0$. The subscripts t and x denote the partial derivatives with respect to t and x, respectively. First of all, let us explain about the original equation of (1). If we take $\mu = 0$ and $p = 1$ in (1), we obtain the Fornberg–Whitham equation:

$$u_t + uu_x + \int_{\mathbb{R}} Be^{-b|x-y|} u_y(y,t)dy = 0, \quad x \in \mathbb{R},\ t > 0. \tag{2}$$

The above equation (2) was derived by Whitham and Fornberg [10, 2] in the late 1900s, as a mathematical model for so-called "breaking waves". Here, roughly speaking, wave-breaking means blow-up of the derivative of the solution, i.e. $\limsup_{t \uparrow T_0} \|u_x(\cdot,t)\|_{L^\infty} = \infty$ for some T_0. Mathematical analysis for the wave-breaking phenomena for equations with the nonlocal dispersion term like that of (2) was first done by Constantin and Escher [1]. After that, many researchers study this problem and proposed several blow-up conditions for (2). For these related results about blow-up conditions, we can refer to e.g. [8, 4, 6].

Next, let us introduce some results related to numerical analysis. Tanaka [9] and Hörmann and Okamoto [5] studied (2) numerically. They suggested that (2) has blow-up solutions and global solutions depending on the initial data and the parameters (B, b). As we mentioned in the above, mathematically rigorous blow-up conditions for (2) has been studied by many researchers. On the other hand, we have not had any mathematical result of the existence of global solutions for (2) yet. As a well known fact, the KdV equation always has global solutions. This is because the nonlinear effect and the dispersive effect balance each other, and then the energy is conserved. From this perspective, to show the global existence of solutions to (2), it would be effective to investigate some relationship between the nonlinear effect and the dispersive effect in (2) and compare the dispersion term with other type ones.

On the other hand, (1) is one of the generalized Fornberg–Whitham equation with dissipation. By virtue of the dissipation, we can easily see that the solutions to (1) exist globally in time. Therefore, it can be said that (1) is easier than (2) to investigate the structure of the nonlocal dispersion term and its interaction with the nonlinear term. Thus, we can expect to get some hints for analyzing (2) by looking at (1) instead of (2). From this point of view, the author and Itasaka [3] studied (1) with $p = 1$, and obtained the asymptotic profile of the solutions. However, compared with the case of $p = 1$, in the case of $p > 2$, the nonlinearity seems to be weak because if the solution decays, then $u^p u_x$ decays fast. For this reason, we can expect that the asymptotic profile of the solutions to (1) is different from its given in [3].

2. Main Result

Now, let us state our main result in this paper.

Theorem 1. *Assume that $u_0 \in H^1(\mathbb{R}) \cap L^1(\mathbb{R})$ and $E_0 := \|u_0\|_{H^1} + \|u_0\|_{L^1}$ is sufficiently small. Then,* (1) *has a unique global mild solution $u \in C([0,\infty); H^1(\mathbb{R}))$. Moreover, the solution satisfies the following estimate:*

$$\left\|\partial_x^l u(\cdot,t)\right\|_{L^2} \le CE_0(1+t)^{-\frac{1}{4}-\frac{l}{2}}, \quad t \ge 0,\ l = 0, 1. \tag{3}$$

Furthermore, if $xu_0 \in L^1(\mathbb{R})$, then the solution satisfies

$$\lim_{t\to\infty} t^{\frac{1}{2}\left(1-\frac{1}{q}\right)+\frac{1}{2}} \left\| u(\cdot,t) - MG_0(\cdot,t) + \left(m + \frac{\mathcal{M}}{p+1}\right)\partial_x G_0(\cdot,t) + \frac{2BM}{b^3} t\partial_x^3 G_0(\cdot,t) \right\|_{L^q} = 0, \tag{4}$$

for any $2 \le q \le \infty$, where $G_0(x,t)$, M, m and $\mathcal{M}$ are defined by

$$G_0(x,t) := \frac{1}{\sqrt{4\pi\mu t}} \exp\left(-\frac{\left(x - \frac{2B}{b}t\right)^2}{4\mu t} \right), \quad x \in \mathbb{R},\ t > 0, \tag{5}$$

$$M := \int_{\mathbb{R}} u_0(x)dx, \quad m := \int_{\mathbb{R}} xu_0(x)dx, \quad \mathcal{M} := \int_0^\infty \int_{\mathbb{R}} u^{p+1}(y,\tau)dyd\tau. \tag{6}$$

Remark 2. From the above result, we can see that the first and the second asymptotic profiles of the solution to (1) are given by $MG_0(x,t)$ and $-\left(m + \frac{\mathcal{M}}{p+1}\right)\partial_x G_0(x,t) - \frac{2BM}{b^3} t\partial_x^3 G_0(x,t)$, respectively. Thus, it can be said that the dispersion effect is not so strong on the first asymptotic profile and its affects as a convection effect. Moreover, we find that the effects of the dispersion and the nonlinear term essentially appear from the second term of asymptotics.

3. Keys of the Proof of Theorem 1

To analyze (1), we transform the dispersion term in (1) via the Fourier transform as follows:

$$\begin{aligned}&\int_{\mathbb{R}} Be^{-b|x-y|}u_y(y,t)dy = \mathcal{F}^{-1}\left[\frac{i2Bb\xi}{b^2+\xi^2}\hat{u}(\xi)\right](x)\\&= 2Bb(b^2-\partial_x^2)^{-1}\partial_x u = \frac{2B}{b}\partial_x u + \frac{2B}{b^3}\partial_x^3 u + \frac{2B}{b^3}(b^2-\partial_x^2)^{-1}\partial_x^5 u.\end{aligned}$$

Then, applying the Duhamel principle, we can rewrite (1) to the following integral equation:

$$u(t) = T(t) * u_0 - \frac{1}{p+1}\int_0^t \partial_x T(t-\tau) * \left(u^{p+1}(\tau)\right)d\tau, \tag{7}$$

where the integral kernel $T(x,t)$ is defined by

$$T(x,t) := \frac{1}{\sqrt{2\pi}}\mathcal{F}^{-1}\left[\exp\left(-\mu t\xi^2 - \frac{i2Bt\xi}{b} + \frac{i2Bt\xi^3}{b^3} - \frac{i2Bt\xi^5}{b^3(b^2+\xi^2)}\right)\right](x). \tag{8}$$

The global existence and the decay estimate (3) of the solutions to (1) can be shown by the standard argument, by using the contraction mapping principle to (7) in appropriate Banach space. Since that proof is almost the same as Theorem 2.2 in [3], we omit it.

In order to prove the asymptotic formula (4), we need to find the asymptotic profile of both the linear part and the Duhamel part of (7). First, we shall explain about the asymptotic analysis for the linear part. Applying the Fourier transform to $T(x,t)$, then from (8) and Taylor's theorem, there exist $\theta_0, \theta_1 \in (0,1)$ such that the following relation holds:

$$\begin{aligned}\hat{T}(\xi,t) &= \frac{1}{\sqrt{2\pi}}\exp\left(-\mu t\xi^2 - \frac{i2Bt\xi}{b}\right)\left\{1 + \frac{i2Bt\xi^3}{b^3} + \frac{1}{2}\left(\frac{i2Bt\xi^3}{b^3}\right)^2\exp\left(\frac{i\theta_0 2Bt\xi^3}{b^3}\right)\right\}\\&\quad - \frac{i2Bt\xi^5}{\sqrt{2\pi}b^3(b^2+\xi^2)}\exp\left(-\mu t\xi^2 - \frac{i2Bt\xi}{b} + \frac{i2Bt\xi^3}{b^3} - \frac{i\theta_1 2Bt\xi^5}{b^3(b^2+\xi^2)}\right)\\&=: \frac{1}{\sqrt{2\pi}}\exp\left(-\mu t\xi^2 - \frac{i2Bt\xi}{b}\right) + \frac{i2Bt\xi^3}{b^3}\frac{1}{\sqrt{2\pi}}\exp\left(-\mu t\xi^2 - \frac{i2Bt\xi}{b}\right) + R(\xi,t)\\&= \hat{G}_0(\xi,t) - \frac{2B}{b^3}t(i\xi)^3\hat{G}_0(\xi,t) + R(\xi,t),\ \ \xi\in\mathbb{R},\ t>0.\end{aligned}$$

Therefore, using the Plancherel theorem, we can show the following proposition which is a key to derive the leading term of (7). For some related results to this formula, see e.g. [3, 7].

Proposition 3. *Let l be a non-negative integer and $2 \le q \le \infty$. Then, we have*

$$\left\|\partial_x^l\left(T(\cdot,t) - G_0(\cdot,t) + \frac{2B}{b^3}t\partial_x^3 G_0(\cdot,t)\right)\right\|_{L^q} \le Ct^{-\frac{1}{2}\left(1-\frac{1}{q}\right)-1-\frac{l}{2}}\left(1+t^{-\frac{1}{2}}\right),\ \ t>0, \tag{9}$$

where $T(x,t)$ and $G_0(x,t)$ are defined by (8) *and* (5)*, respectively.*

Finally, we would like to introduce a key proposition to derive the leading term of the Duhamel term in (7). By virtue of the above discussion (i.e. Proposition 3, see also Lemma 4.1 in [3]), we can see that the integral kernel $T(x,t)$ is well approximated by the Gaussian function $G_0(x,t)$. Combining this fact and the method used in the proof of Lemma 6.2 in [3], we are able to show the following proposition:

Proposition 4. *Under the same assumptions in Theorem 1, the solution to* (1) *satisfies*

$$\lim_{t\to\infty} t^{\frac{1}{2}\left(1-\frac{1}{q}\right)+\frac{1}{2}} \left\| \int_0^t \partial_x T(t-\tau) * \left(u^{p+1}(\tau)\right) d\tau - \mathcal{M}\partial_x G_0(\cdot,t) \right\|_{L^q} = 0, \tag{10}$$

for any $2 \le q \le \infty$*, where* $T(x,t)$*,* $G_0(x,t)$ *and* $\mathcal{M}$ *are defined by* (8)*,* (5) *and* (6)*, respectively.*

Combining Propositions 3, 4 and the asymptotic formula for the heat equation, we are able to prove the asymptotic formula (4), and then the proof of Theorem 1 can be completed.

Acknowledgment

This study is supported by Grant-in-Aid for Young Scientists Research No.22K13939, Japan Society for the Promotion of Science.

References

[1] A. Constantin, J. Escher: Wave breaking for nonlinear nonlocal shallow water equations, *Acta Mathematica*, **181** (1998), 229–243.

[2] B. Fornberg, G. Whitham: A numerical and theoretical study of certain nonlinear wave phenomena, *Philosophical Transactions of the Royal Society of London A: Mathematical, Physical and Engineering Sciences*, **289** (1978), 373–404.

[3] I. Fukuda, K. Itasaka: Higher-order asymptotic profiles of the solutions to the viscous Fornberg–Whitham equation, *Nonlinear Anal.*, **204C** (2021), 112200, 31 pp.

[4] S.V. Haziot: Wave breaking for the Fomberg–Whitham equation, *J. Differential Equations*, **263** (2017), 8178–8185.

[5] G. Hörmann, H. Okamoto: Weak periodic solutions and numerical case studies of the Fornberg–Whitham equation, *Discrete Contin. Dyn. Syst.*, **39** (2019), 4455–4469.

[6] K. Itasaka: Wave-breaking phenomena and global existence for the generalized Fornberg–Whitham equation, *J. Math. Anal. Appl.*, **502** (2021), 125247, 26 pp.

[7] G. Karch: Large-time behavior of solutions to non-linear wave equations: higher-order asymptotics, *Math. Meth. Appl. Sci.*, **22** (1999), 1671–1697.

[8] F. Ma, Y. Liu, C. Qu: Wave-breaking phenomena for the nonlocal Whitham-type equations, *J. Differential Equations*, **261** (2016), 6029–6054.

[9] M. Tanaka: On the wave breaking phenomenon in a model equation related to water wave, *RIMS Kôkyûroku*, **1847** (2013), 64–72 (in Japanese).

[10] G. Whitham: Variational methods and applications to water waves, *Proceedings of the Royal Society of London A: Mathematical, Physical and Engineering Sciences*, **299** (1967), 6–25.

The Characterization of the Gyrator Transform by way of the Fractional Fourier Transform

Toshinao Kagawa[1] and Toshio Suzuki[2,*]

[1]School of General and Management Studies, Suwa University of Science
[2]Department of Applied Mathematics, Tokyo University of Science

*tosuzuki@rs.tus.ac.jp

Abstract. The gyrator transform is an integral transform, which is used in image processing, filtering, optics and so on. In this study, we will explain the relationship between the fractional Fourier transform and the gyrator transform. Especially, we will show the properties of the gyrator transform, which is getting the eigenfunction and eigenvalue of gyrator transform, recursion formula, the relation between the Wigner distribution and the gyrator transform, the differential equation satisfied with the gyrator transform, and the representation of gyrator transform as the self-adjoint operator.

Keywords: Gyrator transform, Fractional Fourier transform, Unitary transform

1. Introduction

The gyrator transform is an integral transform introduced in 2000 in [4]. The gyrator transform is defined for $f \in L^2(\mathbf{R}^2)$ as follows:

$$R^\alpha f(\xi_1, \xi_2) = \int_{\mathbf{R}^2} f(x_1, x_2) G_\alpha(x_1, x_2; \xi_1, \xi_2)\, dx_1 dx_2 \tag{1}$$

where the integral kernel is

$$G_\alpha(x_1, x_2; \xi_1, \xi_2) = \frac{1}{2\pi|\sin\alpha|} \exp\left(i \frac{(x_1 x_2 + \xi_1 \xi_2)\cos\alpha - (x_2 \xi_1 + x_1 \xi_2)}{\sin\alpha} \right).$$

Although there are some studies about the gyrator transform (e.g. [1]), the properties of this transform is little known. The gyrator transform is a similar form with the fractional Fourier transform. Therefore, in this study, we explain the relationship between the fractional Fourier transform and the properties of the gyrator transform.

2. Properties of the Fractional Fourier Transform

The fractional Fourier transform is a linear integral transform which is the generalization of the Fourier transform [2]. To simplify the discussion, we consider the one dimensional

fractional Fourier transform. For $f \in L^2(\mathbf{R}), \alpha \in \mathbf{R}$, the 1-dimensional fractional Fourier transform is defined as the follows:

$$\mathcal{F}_\alpha f(\xi) = \int_{\mathbf{R}} f(x) K_\alpha(x, \xi)\, dx,$$

where the integral kernel is

$$K_\alpha(x, \xi) = \frac{1}{\sqrt{\pi(1 - e^{-2i\alpha})}} \exp\left(i \frac{(x^2 + \xi^2)\cos\alpha - 2x\xi}{2\sin\alpha}\right).$$

We can easily check that $\mathcal{F}_{\pi/2}$ coincide with the traditional Fourier transform and $\mathcal{F}_{-\pi/2}$ coincide with the inverse Fourier transform. Moreover, in the sense of distribution, the integral kernel $K_\alpha(x, \xi)$ of fractional Fourier satisfies that for $n \in \mathbf{Z}$,

$$\lim_{\alpha \to 2n\pi} K_\alpha(x, \xi) = \delta(x - \xi) \quad \text{and} \quad \lim_{\alpha \to (2n+1)\pi} K_\alpha(x, \xi) = \delta(x + \xi)$$

where δ represents the Dirac's delta function. The fractional Fourier transform is unitary operator from $L^2(\mathbf{R})$ to $L^2(\mathbf{R})$ and satisfies the property that $\mathcal{F}_\alpha \mathcal{F}_\beta = \mathcal{F}_\beta \mathcal{F}_\alpha = \mathcal{F}_{\alpha+\beta}$. The fractional Fourier transform has several properties. Especially, in [3], there are six definitions of the fractional Fourier transform. The first definition is the integral transform as the equation (1). The second definition is the summation of the Hermite functions. The Hermite function in $L^2(\mathbf{R})$ is defined by

$$h_n(x) = (2^n n!)^{-\frac{1}{2}} \pi^{-\frac{1}{4}} (-1)^n e^{x^2/2} \left(\frac{d}{dx}\right)^n e^{-x^2},$$

and $\{h_n\}$ consists the basis of $L^2(\mathbf{R})$. Using the Mehler's formula, the integral kernel can be represented as

$$\sum_{n=0}^{\infty} (e^{-\alpha i})^n h_n(x) h_n(\xi) = \frac{1}{\sqrt{\pi(1 - e^{-2i\alpha})}} \exp\left(i \frac{(x^2 + \xi^2)\cos\alpha - 2x\xi}{2\sin\alpha}\right).$$

Moreover, we put $K_\alpha(x, \xi) = \sum_{n=0}^{\infty} (e^{-\alpha i})^n h_n(x) h_n(\xi)$, then we can get the fractional Fourier transform. The third definition is the representation as the rotation in the time-frequency plane. The Wigner distribution of $f \in L^2(\mathbf{R})$ is defined by

$$W_f(x, \xi) = \int_{\mathbf{R}} f\left(x + \frac{u}{2}\right) \overline{f\left(x - \frac{u}{2}\right)} e^{iu\xi} du.$$

Then the fractional Fourier transform can be defined as the function $f \in L^2(\mathbf{R})$ satisfying

$$W_{\mathcal{F}_\alpha f}(x, \xi) = W_f(x\sin\alpha + \xi\cos\alpha, x\cos\alpha - \xi\sin\alpha).$$

The forth definition is a transform of coordinate multiplication and differential operators. We define the fractional Fourier transform of a $f \in \mathcal{S}$ such that it satisfies the properties

$$\mathcal{F}_\alpha(x^m f)(\xi) = \left((\cos\alpha)\xi + i(\sin\alpha)\frac{\partial}{\partial\xi}\right)^m \mathcal{F}_\alpha f(\xi) \quad \text{and}$$
$$\mathcal{F}_\alpha\left(\frac{\partial^m}{\partial x^m} f\right)(\xi) = \left((\cos\alpha)\frac{\partial}{\partial\xi} + i(\sin\alpha)\xi\right)^m \mathcal{F}_\alpha f(\xi).$$

The fifth definition uses the differential equation. Consider the partial differential equation

$$i\frac{\partial}{\partial\alpha}\mathcal{F}_\alpha f(\xi) = \frac{1}{2}\left(-\frac{\partial^2}{\partial\xi^2} + \xi^2 - 1\right)\mathcal{F}_\alpha f(\xi)$$

with the initial condition $\mathcal{F}_0(f) = f \in L^2(\mathbf{R})$. Then, the solution $\mathcal{F}_\alpha f$ is the fractional Fourier transform of f.
The sixth definition uses the hyperdifferential operator. Let the operators $\mathcal{D}_x f(x) = (i\partial/\partial x)f(x)$ and $\mathcal{U}_x f(x) = xf(x)$. The fractional Fourier transform for $L^2(\mathbf{R})$ can be represented as the self-adjoint unitary operator as

$$\mathcal{F}_\alpha = \exp(-i\alpha\mathcal{H}/2), \quad \text{where} \quad \mathcal{H} = \mathcal{D}_x^2 + \mathcal{U}_x^2 - 1.$$

3. The Gyrator Transform

For $f \in L^2(\mathbf{R}^2)$ and $(\alpha_1, \alpha_2) \in \mathbf{R}^2$, the 2-dimensional fractional Fourier transform is defined as the follows:

$$\mathcal{F}_{\alpha_1,\alpha_2} f(\xi_1, \xi_2) = \int_{\mathbf{R}} f(x_1, x_2) K_{\alpha_1,\alpha_2}(x_1, x_2; \xi_1, \xi_2)\, dx$$

where the integral kernel is $K_{\alpha_1,\alpha_2}(x_1, x_2; \xi_1, \xi_2) = K_{\alpha_1}(x_1, \xi_1)K_{\alpha_2}(x_2, \xi_2)$. Even the 2-dimensional fractional Fourier transform, the almost same definitions as above hold.

To see the properties of gyrator transform, we define the unitary operator. Putting the unitary matrix

$$A = \begin{bmatrix} \dfrac{1}{\sqrt{2}} & -\dfrac{1}{\sqrt{2}} \\ \dfrac{1}{\sqrt{2}} & \dfrac{1}{\sqrt{2}} \end{bmatrix}$$

and we define the unitary operator S_A from $L^2(\mathbf{R}^2)$ to itself as $S_A f(x) = f(Ax)$ for $x = (x_1, x_2)$. Then, we can obtain the relationship of the transforms.

Theorem 1. *Suppose $\alpha \neq n\pi$ with $n \in \mathbf{Z}$ and $f \in L^2(\mathbf{R}^2)$, then*

$$R^\alpha f = S_{A^{-1}} \mathcal{F}_{\alpha,-\alpha} S_A f.$$

This theorem gives us that the gyrator transform is the unitary operator from $L^2(\mathbf{R}^2)$ to itself and satisfies the properties $R^\alpha R^\beta = R^\beta R^\alpha = R^{\alpha+\beta}$. Moreover, we get the equivalent definition of the gyrator transform like the case of the fractional Fourier transform.

Theorem 2. *Putting that $\Phi_n(x_1, x_2) = h_{n_1}(x_1) \cdot h_{n_2}(x_2)$ $(n = (n_1, n_2))$ and*

$$\Psi_n(x_1, x_2) = \Phi_n\left(\frac{x_1 + x_2}{\sqrt{2}}, \frac{-x_1 + x_2}{\sqrt{2}}\right),$$

Then Ψ_n is the eigenfunction of the gyrator transform. That is,

$$R^\alpha \Psi_n(\xi_1, \xi_2) = (e^{-i\alpha})^{n_1 - n_2} \Psi_n(\xi_1, \xi_2).$$

Theorem 3. *For $m \in \mathbf{N}$, the gyrator transform of the function $f = f(x_1, x_2) \in \mathcal{S}(\mathbf{R}^2)$ satisfies that*

$$R^\alpha\left[\left\{(x_1+x_2)+\left(\frac{\partial}{\partial x_1}+\frac{\partial}{\partial x_2}\right)\right\}^m f\right](\xi_1,\xi_2) = e^{im\alpha}\left\{(\xi_1+\xi_2)+\left(\frac{\partial}{\partial \xi_1}+\frac{\partial}{\partial \xi_2}\right)\right\}^m R^\alpha f(\xi_1,\xi_2),$$

$$R^\alpha\left[\left\{(x_1+x_2)-\left(\frac{\partial}{\partial x_1}+\frac{\partial}{\partial x_2}\right)\right\}^m f\right](\xi_1,\xi_2) = e^{-im\alpha}\left\{(\xi_1+\xi_2)-\left(\frac{\partial}{\partial \xi_1}+\frac{\partial}{\partial \xi_2}\right)\right\}^m R^\alpha f(\xi_1,\xi_2),$$

$$R^\alpha\left[\left\{(x_1-x_2)+\left(\frac{\partial}{\partial x_1}-\frac{\partial}{\partial x_2}\right)\right\}^m f\right](\xi_1,\xi_2) = e^{-im\alpha}\left\{(\xi_1-\xi_2)+\left(\frac{\partial}{\partial \xi_1}-\frac{\partial}{\partial \xi_2}\right)\right\}^m R^\alpha f(\xi_1,\xi_2)$$

and

$$R^\alpha\left[\left\{(x_1-x_2)-\left(\frac{\partial}{\partial x_1}-\frac{\partial}{\partial x_2}\right)\right\}^m f\right](\xi_1,\xi_2) = e^{im\alpha}\left\{(\xi_1-\xi_2)-\left(\frac{\partial}{\partial \xi_1}-\frac{\partial}{\partial \xi_2}\right)\right\}^m R^\alpha f(\xi_1,\xi_2)$$

For $f \in L^2(\mathbf{R}^2)$, the 2-dimensional Wigner distribution W_f is defined as

$$W_f(x_1,x_2;\xi_1,\xi_2) = \iint_{\mathbf{R}^2} f\left(x_1+\frac{u_1}{2}, x_2+\frac{u_2}{2}\right)\overline{f\left(x_1-\frac{u_1}{2}, x_2-\frac{u_2}{2}\right)}\exp\left(i(u_1\xi_1+u_2\xi_2)\right)du_1du_2.$$

Theorem 4. *The gyrator transform $R^\alpha f$ of some $f \in L^2(\mathbf{R}^2)$ satisfies that*

$$W_{R^\alpha f}(x_1,x_2;\xi_1,\xi_2) = W_f(x_1\cos\alpha-\xi_2\sin\alpha, x_2\cos\alpha-\xi_1\sin\alpha; x_1\sin\alpha+\xi_2\cos\alpha, -x_2\sin\alpha-\xi_1\cos\alpha).$$

Theorem 5. *Suppose that $R^\alpha(f)$ is the gyrator transform of some $f \in L^2(\mathbf{R}^2)$. Then $R^\alpha(f)$ is the solution of the differential equation*

$$i\frac{\partial}{\partial\alpha}R^\alpha f(\xi_1,\xi_2) = \left(-\frac{\partial}{\partial\xi_1}\frac{\partial}{\partial\xi_2}+\xi_1\xi_2\right)R^\alpha f(\xi_1,\xi_2).$$

with the initial condition $R^0 f = f$.

Theorem 6. *The gyrator transform from the $L^2(\mathbf{R}^2)$ to itself can be represented as*

$$\mathcal{R}^\alpha = \exp(-i\alpha\mathcal{H}), \quad \textit{where} \quad \mathcal{H} = -\frac{\partial}{\partial\xi_1}\frac{\partial}{\partial\xi_2}+\xi_1\xi_2.$$

References

[1] J. A. Rodrigo, T. Alieva and M. L. Calvo : *Gyrator transform: properties and applications*, Optics Express, Vol. 15. Issue 5, pp. 2190-2203 (2007).

[2] V. Namias :*The fractional order Fourier transform and its application to quantum mechanics*, J. Inst. Math. Its Appl., 25 (1980), pp. 241-265

[3] H. M. Ozaktas, Z. Zalevsky and M. A. Kutay : *The Fractional Fourier Transform with Applications in optics and Signal Processing*, Wiley 2001.

[4] R. Simon and K. B. Wolf : *Structure of the set of paraxial optical systems*, J. Opt. Soc. Am. A 17, pp. 342-355 (2000).

JSST 2022

Rigorous simulation of reaction-diffusion models with neural networks

Kazuaki Tanaka[1,*], Kohey Yatabe[2], Taisei Asai[1], Sora Sawai[1]

[1]Waseda University
[2]Tokyo University of Agriculture and Technology

[*]tanaka@ims.sci.waseda.ac.jp

Abstract. We realize a rigorous numerical simulation for reaction-diffusion models with neural networks. We enclose a solution of a target equation using a sub- and super-solutions argument. Sub- and super solutions are constructed by neural networks, and the solution existence is proved between them. We apply the proposed method to the Allen-Cahn equation and show some numerical simulation results.

Keywords: Allen-Cahn equation, Computer-assisted proof, Neural networks, Reaction-diffusion model, Rigorous computation, Sub- and super-solutions

1. Introduction

Neural networks and deep learning methods have been applied to various problems, including the initial value and boundary value problems of differential equations. Rigorous verification of such computation results is an important issue because numerical computation by machine learning returns probabilistically incorrect solutions due to convergence to a local solution and other causes. However, no work has been conducted to obtain mathematically rigorous results from such computations.

We first introduce our method for the initial value problem of ODEs:

$$\begin{cases} \dfrac{du}{dt}(t) = f(t, u(t)), \quad t \in (0, T), \\ u(0) = a. \end{cases} \tag{IVP}$$

Here, $T > 0$, $a \in \mathbb{R}$, and $f : (0, T) \times \mathbb{R} \to \mathbb{R}$ is continuous. The classical argument of sub- and super-solutions method is the following.

Theorem 1 ([1])**.** *Suppose that there exists a pair of functions $\underline{u}, \overline{u} \in C^1((0, T)) \cap C([0, T])$ that satisfies*

$$\begin{cases} \dfrac{d\underline{u}}{dt}(t) \le f(t, \underline{u}(t)), \ t \in (0, T) \\ \underline{u}(0) \le a \end{cases} \qquad \begin{cases} \dfrac{d\overline{u}}{dt}(t) \ge f(t, \overline{u}(t)), \ t \in (0, T) \\ \overline{u}(0) \ge a \end{cases}$$

If $\underline{u}(t) \leq \overline{u}(t),\ t \in [0,T]$ *and* f *is continuous over* $\{(t,u)\ :\ \underline{u}(t) \leq \overline{u}(t),\ t \in [0,T]\}$*, then a solution* $u \in C([0,T])$ *of* (IVP) *exists and satisfies* $\underline{u}(t) \leq u(t) \leq \overline{u}(t)$ *for all* $t \in [0,T]$.

On the basis of this argument, we confirm the local existence of a target equation between sub- and super-solutions constructed by neural networks. We use fully connected neural networks with a periodic activation function (sin-function) [2]. The sub- and super-solutions are learned with the following cost function $L : C([0,T]) \times C([0,T]) \to \mathbb{R}$:

$$L(v,w) = \sum_{t \in \mathcal{S}} \left\{ h\left(f(t,v(t)) - \frac{dv}{dt}(t) \right) + h\left(\frac{dw}{dt}(t) - f(t,w(t)) \right) + h\left(w - v\right) \right\}$$

Here, $\mathcal{S}$ is the set of sample points chosen from $[0,T]$. The auxiliary function $h : \mathbb{R} \ni t \mapsto h(t) \in \mathbb{R}$ is a convex function for $t \geq 0$ and locally minimized at $t = \varepsilon$ for a small $\varepsilon > 0$ (the allowable error) so that the parameters inside $v,\ w$ are chosen to induce t to the positive direction.

We will apply extended arguments for sub- and super-solutions to elliptic and parabolic equations and realize a rigorous numerical simulation for the reaction-diffusion model of Allen-Cahn equation.

References

[1] G. S. Ladde, V. Lakshmikantham, and A. S. Vatsala, *Monotone iterative techniques for nonlinear differential equations*, vol. 27. Pitman Publishing, 1985.

[2] V. Sitzmann, J. Martel, A. Bergman, D. Lindell, and G. Wetzstein, "Implicit neural representations with periodic activation functions," Advances in Neural Information Processing Systems, vol. 33, 2020.

JSST 2022

Test floating-point matrices with specified solutions for numerical linear algebra

Katsuhisa Ozaki[1,*], Takeshi Terao[2], Yuki Uchino[3]

[1]Department of Mathematical Sciences, Shibaura Institute of Technology
[2]RIKEN Center for Computational Science
[3]Graduate School of Engineering and Science, Shibaura Institute of Technology

[*]ozaki@sic.shibaura-it.ac.jp

Abstract. In numerical computations, checking the accuracy of computed results is crucial because finite-precision arithmetic leads to rounding errors. This study proposes methods for generating test floating-point matrices whose exact solutions are given in advance, which allows the exact relative errors to be monitored. We focus on linear systems, standard eigenvalue problems, singular value decomposition, and least-squares problems. The proposed methods quickly generate test matrices with specified solutions using Householder matrices.

Keywords: Test matrix, Floating-point arithmetic, Numerical linear algebra

1. Introduction

Numerical computations use finite-precision floating-point arithmetic, which leads to rounding errors. Therefore, we propose methods for generating test floating-point matrices with exact solutions. These matrices allow the exact relative errors to be monitored. Ozaki and Ogita proposed generation methods for linear systems [1] and standard eigenvalue problems [2].

In this study, we extend the methods in [1, 2] to linear systems, eigenvalue decomposition, singular value decomposition, and least-squares problems, which are common in scientific computing. The condition number of the matrix can be approximately controlled. We apply Householder matrices to develop methods that quickly generate test matrices with exact solutions.

2. Previous studies

We briefly review previous studies on test matrices [1, 2]. Let $\mathbb{F}$ be a set of binary floating-point numbers. The notation $\mathtt{fl}(\cdot)$ indicates a computed result; each operation in parentheses is performed using floating-point arithmetic with rounding to nearest mode with ties to even (roundTiesToEven in IEEE 754 [3]). Let u be the roundoff unit, for example, $u = 2^{-24}$

for binary32 and $u = 2^{-53}$ for binary64 in IEEE 754. Assume that neither overflow nor underflow occurs in $\mathtt{fl}(\cdot)$. The notation $\mathtt{npt}(a)$ for $0 \neq a \in \mathbb{R}$ indicates

$$\mathtt{npt}(a) := 2^{\lceil \log_2 |a| \rceil}.$$

This represents the smallest power of two that is greater than or equal to $|a|$.

We use the following notation for linear systems:

$$Ax = b, \quad A \in \mathbb{R}^{n \times n}, \quad b \in \mathbb{R}^n. \tag{1}$$

From a given matrix $A \in \mathbb{F}^{n \times n}$ and a vector $x \in \mathbb{F}^n$, the method in [1] produces $A'(\approx A) \in \mathbb{F}^{n \times n}$ such that $\mathtt{fl}(A'x) = A'x =: b \in \mathbb{F}^n$. Therefore, the exact solution of the linear system is known in advance. We can generate A' to satisfy $a_{ij} = a_{k\ell} \Longrightarrow a'_{ij} = a'_{k\ell}$.

We use the following notation for the standard eigenvalue problem for $A = A^T \in \mathbb{R}^{n \times n}$:

$$A = XDX^T, \tag{2}$$

where the ith column vector in X is an eigenvector that corresponds to the eigenvalue d_{ii}. Assume that we can know the exact eigenvalue from D, for example, D is a diagonal, upper-triangular, or 2-by-2 block diagonal matrix. Here, X is an orthogonal matrix. The method in [2] produces D' such that

$$\mathtt{fl}\left(X\left(D'X^T\right)\right) = XD'X^T.$$

Therefore, the exact eigenvalue d'_{ii} is known in advance. For symmetric eigenvalue problems, a scaled Hadamard matrix is used as the candidate of X.

3. Proposed methods

In this study, we use the Householder matrix for matrix X. A Householder matrix is a symmetric and orthogonal matrix. This is useful for quick generation of the test matrices introduced in [4]. Let $H(v) \in \mathbb{R}^{n \times n}$ for a non-zero vector $v \in \mathbb{R}^n$ be

$$H(v) := I - \frac{2vv^T}{v^T v},$$

where I is the n-by-n identity matrix. We define $H'(v)$ as

$$H'(v) := v^T vI - 2vv^T.$$

Note that $H'(v) = v^T vH(v)$. If $v \in \mathbb{Z}^n$ and $v^T v \leq u^{-1}$, then $H'(v) \in \mathbb{F}^{n \times n}$. To avoid the generation of trivial test sets, we assume that $v_i \neq 0$ for all i.

3.1. Eigenvalue decomposition

We set a Householder matrix as X in (2). Here, let D be a diagonal matrix with expected eigenvalues. Then, a symmetric eigenvalue problem is

$$XDX^T = H(v)DH(v) = H'(v)\left(D/\left(v^T v\right)^2\right)H'(v).$$

Let the constant $\sigma \in \mathbb{F}$ be

$$\sigma := 0.75 \cdot \mathtt{npt}\left(v^T v\right)^2 \cdot \mathtt{npt}(n) \cdot \mathtt{npt}\left(\max_{i,j} t_{ij}\right), \quad T := \mathtt{fl}\left(D/\left(v^T v\right)^2\right) \tag{3}$$

and compute

$$d'_{ij} := \begin{cases} \mathtt{fl}\left((\sigma + t_{ii}) - \sigma\right), & i = j \\ 0, & i \neq j \end{cases}. \tag{4}$$

Then,

$$H'(v)D'H'(v) = \mathtt{fl}\left(\left(H'(v)D'\right)H'(v)\right) = \mathtt{fl}\left(H'(v)\left(D'H'(v)\right)\right) =: A. \tag{5}$$

Therefore, $(v^T v)^2 d'_{ii}$ and $H(v)$ are the exact eigenvalue and eigenvector matrix of the matrix A, respectively. Note that $(v^T v)^2 d'_{ii} \in \mathbb{F}$ may not be satisfied. This is not a serious problem because the computational cost is low and we can apply accurate computations with sufficient precision or rational arithmetic. The product of a matrix B and $H'(v)$ never requires full matrix multiplication, namely

$$BH'(v) = v^T vB - 2(Bv)v^T. \tag{6}$$

Therefore, the cost of generating A in (5) is very low. However, it is difficult to set

$$\frac{\max_i d_{ii}}{\min_i d_{ii}} \geq u^{-1}.$$

3.2. Singular value decomposition

We use the following notation for singular value decomposition:

$$A = UDV^T, \tag{7}$$

where $D \in \mathbb{R}^{m \times n}$ is a rectangular diagonal matrix with singular values ($m \geq n$), and $U \in \mathbb{R}^{m \times m}$ and $V \in \mathbb{R}^{n \times n}$ are orthogonal matrices. It is simple to extend the discussion to reduced (economy-size) singular value decomposition.

We set the Householder matrices as $U := H(v)$ for $v \in \mathbb{R}^m$ and $V := H(w)$ for $w \in \mathbb{R}^n$ in (7) and a rectangular diagonal matrix D with expected singular values. Then,

$$UDV^T = H(v)DH(w) = H'(v)\left(D/\left(v^T v\right)/\left(w^T w\right)\right)H'(w).$$

Let σ be

$$\sigma := 0.75 \cdot \mathtt{npt}\left(v^T v\right) \cdot \mathtt{npt}\left(w^T w\right) \cdot \mathtt{npt}(n) \cdot \mathtt{npt}\left(\max_{i,j} t_{ij}\right), \quad T := \mathtt{fl}\left(D/\left(v^T v\right)/\left(w^T w\right)\right) \tag{8}$$

and compute (4). Then,

$$H'(v)D'H'(w) = \mathtt{fl}\left(\left(H'(v)D'\right)H'(w)\right) =: A$$

Therefore, $(v^T v)(w^T w)d'_{ii}$ is the exact singular value of matrix A. For a reason similar to that for (6), matrix A can quickly be generated.

3.3. Linear systems and least-squares problems

We define the least-squares problem using the normal equation for $A \in \mathbb{R}^{m\times n}$ and $b \in \mathbb{R}^m$ as

$$A^T Ax = A^T b, \tag{9}$$

where $m \geq n$ and A has full column rank. We apply singular value decomposition to A as in (7). From the discussion in Subsection 3.2, it is possible to set

$$A = H'(v)D'H'(w) = \mathtt{fl}(H'(v)(D'H'(w))) \in \mathbb{F}^{m\times n}.$$

Then, we have

$$x = A^{-1}b = \frac{H'(w)(D')^{-1}H'(v)b}{v^T v \cdot w^T w}, \quad b \in \mathbb{F}^n \tag{10}$$

for (1), and

$$x = \frac{H'(w)\left((D')^T D'\right)^{-1} H'(w)A^T b}{(w^T w)^2}, \quad b \in \mathbb{F}^m \tag{11}$$

for (9). Note that some elements in x in (10) and (11) are not represented as a floating-point number in many cases. Equations (10) and (11) contain only matrix-vector multiplications, and the computational cost is low even if we apply rational arithmetic or high precision arithmetic with sufficient precision. Alternatively, if the reliability of x is guaranteed, for example, by interval arithmetic, it is sufficient to use the result as a test matrix.

Setting small σ in (3) and (8) is important to fill gaps in d_{ii} and $(v^T v)^2 d'_{ii}$ for the eigenvalue and d_{ii} and $(v^T v)(w^T w)d'_{ii}$ for the singular value. We apply iterative refinements with a trial and error approach. The efficiency of this strategy will be demonstrated in the presentation at the conference.

References

[1] K. Ozaki, T. Ogita: Generation of Linear Systems with Specified Solutions for Numerical Experiments, *Reliable Computing*, 25 (2017), 148–167.

[2] K. Ozaki, T. Ogita: Generation of Test Matrices with Specified Eigenvalues using Floating-point Arithmetic, *Numerical Algorithms*, 90 (2022), 241–262.

[3] IEEE Computer Society, IEEE Standard for Floating-Point Arithmetic (IEEE Std 754-2008), IEEE, 2008.

[4] M. Fasi, N. J. Higham: Generating Extreme-Scale Matrices With Specified Singular Values or Condition Number, *SIAM Journal on Scientific Computing*, 43 (2021), A663–A684.

Inclusion Methods for Multiplication of Three Point Matrices

Yuki Uchino[1,*], Katsuhisa Ozaki[2], Takeshi Terao[3]

[1]Graduate School of Engineering and Science, Shibaura Institute of Technology
[2]Department of Mathematical Sciences, Shibaura Institute of Technology
[3]RIKEN Center for Computational Science

[*]nb22105@shibaura-it.ac.jp

The full paper of this paper has been published in Journal of Advanced Simulation in Science and Engineering (JASSE).

DOI: https://doi.org/10.15748/jasse.10.83

JSST 2022

Weight Parameter Estimation from compressed data on Boltzmann machines via L_2-norm minimisation

Chako Takahashi[1,2*]

[1]AI Design Education and Research Promotion Center, Yamagata University
[2]Graduate School of Science and Engineering, Yamagata University

*chako@yz.yamagata-u.ac.jp

Abstract. In this study, we consider estimation of the weight parameters of Ising Hamiltonian (equivalent to the Boltzmann machine, which has binary random variables), from a smaller number of data than the number of parameters. We investigate the conditions under which adequate estimation is possible by L_2-norm minimisation, via the replica method.

Keywords: Boltzmann machine, Ising spin glass, parameter estimation, L_2-norm minimisation, compressed sensing

1. Introduction

Boltzmann machines are fundamental models in machine learning. The Ising model in statistical mechanics is known to be equivalent to the Boltzmann machine, and the theoretical aspects of machine learning and deep learning have been enhanced by applying the analytical methods used for the Ising model to investigate Boltzmann machine's performance. When we aim to use a machine learning system based on Boltzmann machines to make predictions or regressions, the parameters of the Boltzmann machine must first be determined from supervised data in a general supervised learning scheme. However, it may be difficult to prepare a sufficient number of supervised data due to the difficulty of the observations or the cost of annotation. If the number of unknown parameters is larger than the number of data, this parameter estimation problem is called an underdetermined system, for which the solution is not uniquely determined and estimation of the parameters is usually not able to be done adequately. In this case, assuming that the unknown parameters are sparse, it has been shown that this problem can be solved rigorously in some cases. In Ising spin glass, the performance of interaction parameter estimation by L_1-norm minimization is being evaluated [1, 2]. Besides L_1-norm minimisation, for which there are many practical algorithms, theoretical performance evaluation in L_0 or L_2 minimisation may contribute to the application of sparse modeling techniques in machine learning.

In this study, we evaluate the performance of the parameter estimation of the Boltzmann machine using L_2-norm minimisation in a theoretical way. Using the replica method [3, 4], which has been used in statistical mechanics to analyse the Ising model, we theoretically

assess whether there are conditions under which the parameter estimation of the Boltzmann machine by L_2-norm minimisation can be solved exactly.

2. Problem Setting

Let us consider a full-connect Boltzmann machines with N nodes. The Ising variables $\sigma_i \in \{-1, +1\}$ are assigned at each of the nodes $i \in V$, where V is a set of nodes. The weight parameters are assigned at each of the edges, and defined as J_{ij} for nodes i and j in V. We assume that the interaction between spins are symmetric and that no self-interaction occurs. The energy function is expressed as

$$H(\boldsymbol{\sigma}) := -\frac{1}{N}\sum_{i<j} J_{ij}\sigma_i\sigma_j. \tag{1}$$

In physics, its observed value is usually referred to as energy. We then obtain a set of M ($< N(N-1)/2$) values of the energy $\boldsymbol{E} := (E^{(1)}, E^{(2)}, \cdots, E^{(M)})^{\mathrm{T}}$ and an observation matrix of the variables' configurations S, which is an $M \times N(N-1)/2$ matrix expressed as

$$S := \begin{pmatrix} \sigma_1^{(1)}\sigma_2^{(1)} & \cdots & \sigma_1^{(1)}\sigma_N^{(1)} & \sigma_2^{(1)}\sigma_3^{(1)} & \cdots & \sigma_{N-1}^{(1)}\sigma_N^{(1)} \\ \sigma_1^{(2)}\sigma_2^{(2)} & \cdots & \sigma_1^{(2)}\sigma_N^{(2)} & \sigma_2^{(2)}\sigma_3^{(2)} & \cdots & \sigma_{N-1}^{(2)}\sigma_N^{(2)} \\ \vdots & \cdots & \vdots & \vdots & \cdots & \vdots \\ \sigma_1^{(M)}\sigma_2^{(M)} & \cdots & \sigma_1^{(M)}\sigma_N^{(M)} & \sigma_2^{(M)}\sigma_3^{(M)} & \cdots & \sigma_{N-1}^{(M)}\sigma_N^{(M)} \end{pmatrix}.$$

We assume that a set of $N(N-1)/2$ original weight parameters is expressed as $\boldsymbol{J}^0 := (J^0_{12}, \cdots, J^0_{1N}, J^0_{23}, \cdots, J^0_{N-1,N})^{\mathrm{T}}$, and a set of energies $\boldsymbol{E}$ is expressed as

$$\boldsymbol{E} := -\frac{1}{N} S\,\boldsymbol{J}^0. \tag{2}$$

In general, the case that the number of unknown variables $\boldsymbol{J}^0$ is larger than the number of linear equations, as in Eq. (2), is called an underdetermined system. When we simply solve Eq. (2), we cannot obtain a unique solution. Hence, a method that can adequately estimate the unknown $\boldsymbol{J}$ only from the given M pairs of energies and configurations of the variables is desired.

For this objective, we utilize the concept of compressed sensing. We impose an assumption of sparsity on $\boldsymbol{J}^0$. In particular, we assume that the probability distribution of J^0_{ij} is $P(J^0_{ij}) := (1-\rho)\delta(J^0_{ij}) + \rho\mathcal{N}(0,1)$, where $\delta(x)$ denotes the Dirac delta function, $\rho = 2K/N(N-1)$ ($0 \le \rho \le 1$) denotes the density of the nonzero components in the vector $\boldsymbol{J}^0$, and $\mathcal{N}(0,1)$ denotes the Gaussian distribution with a zero mean and unit variance. Note that we do not know which component in $\boldsymbol{J}^0$ is nonzero or zero.

We then formulate the estimate of $\boldsymbol{J}^0$ as the L_2-norm minimisation with respect to $\boldsymbol{J} := (J_{12}, \cdots, J_{1N}, J_{23}, \cdots, J_{N-1,N})^{\mathrm{T}}$. The L_2-norm minimisation in the present setting is formulated as

$$\min_{\boldsymbol{J}} \|\boldsymbol{J}\|_2 \ \text{ subject to } \ \boldsymbol{E} = -\frac{1}{N} S\,\boldsymbol{J}. \tag{3}$$

where $\|\boldsymbol{J}\|_2 := (\sum_{i<j} J_{ij})^{1/2}$ denotes the L_2 norm with respect to $\boldsymbol{J}$.

3. Strategy of Theoretical Analysis

In this study, we are interested in how the estimation performance obtained from Eq. (3) depends on ρ and $\alpha = 2M/N(N-1)$. We investigate the typical behavior of parameter estimation proposed in the former section, employing the replica method [3, 4], which is one of the analytical methods used in statistical mechanics. The replica method is frequently employed to analyse free energy, which is defined through a partition function as the normalization constant of the distribution (this is difficult to calculate analytically in most cases). The replica method gives an analytical representation of the configurational average of a partition function instead of the partition function itself based on the self-averaging property.

The typical behavior of the estimation of the parameters described in Eq. (3) can be investigated by analyzing the partition function of the distribution

$$P(\boldsymbol{J} \mid \boldsymbol{E}) = \frac{1}{Z_\beta(\boldsymbol{E})} P(\boldsymbol{E} \mid \boldsymbol{J}) P(\boldsymbol{J}), \tag{4}$$

via the replica method, where $Z_\beta(\boldsymbol{E})$ is the partition function of the distribution. The logarithm of $Z_\beta(\boldsymbol{E})$ is an important quantity, namely, the free energy, and is defined as

$$\begin{aligned} f &= -\lim_{\beta\to\infty}\lim_{N\to\infty}\frac{1}{\beta N^2}[\ln Z_\beta(\boldsymbol{E})]_{S,\boldsymbol{J}^0} \\ &= -\lim_{\beta\to\infty}\lim_{n\to 0}\frac{\partial}{\partial n}\lim_{N\to\infty}\frac{1}{\beta N^2}\ln[Z_\beta^n(\boldsymbol{E})]_{S,\boldsymbol{J}^0}, \end{aligned} \tag{5}$$

where $[\cdots]_{S,\boldsymbol{J}^0}$ denotes the configurational average with respect to S and $\boldsymbol{J}^0$. According to the procedure of general replica analysis [5], we evaluate $[Z_\beta^n(\boldsymbol{E})]_{S,\boldsymbol{J}^0}$ in Eq. (5) for $n \in \mathbb{N}$. Furthermore, $[Z_\beta^n(\boldsymbol{E})]_{S,\boldsymbol{J}^0}$ is performed with an analytical continuation for $n \in \mathbb{R}$ after completing the computation of the partition function as a closed form and obtaining a function form of n.

Unlike this problem setting, the analysis for the case where the elements of the observation matrix are given by continuous values is already given in [5, 6]. Note that in the problem setting considered in this study, each element of the observation matrix is the product of two Ising variables, given by 1 or -1.

4. Related Works

In the problem setting of the previous section, theoretical reconstruction limits of the coupling constants (namely, weight parameters of Boltzmann machines) when we use L_1-norm minimisation have been derived [1, 2]. It has been found that this reconstruction limit agrees with the L_1 reconstruction limit of the [5, 6] with different problem settings, namely, when components of observation matrix S are $\sigma_i\sigma_j \in \mathbb{R}$. It has also been confirmed that the numerical results of Hamiltonian estimation using ADMM approximately reproduce the theoretical reconstruction limits, as shown in Fig. 1.

In [5], the case where the elements of the observation matrix consist of continuous values, the results show that reconstruction is impossible by L_2-norm minimisation on any ρ

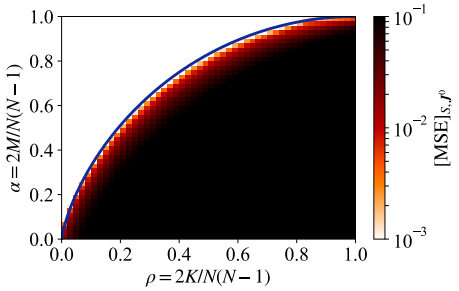

Figure 1: Typical reconstruction limit of the L_1-norm minimisation obtained from the replica analysis [1]. The blue curve is the theoretical boundary between successful and failed estimation. The region colored white to red to black shows the values of the MSE between $\boldsymbol{J}$ and $\boldsymbol{J}^0$, which indicate whether or not the estimation is successful. The white and black blocks represent regions of successful and failed estimations, with respect to MSE, respectively.

and α. A detailed analysis of the conditions under which reconstruction by L_2-norm minimisation is possible in our problem setting, where each element of the observation matrix is represented by the product of two Ising variables, will be presented at the presentation.

Acknowledgments

This work is supported by JSPS KAKENHI (Grant Numbers JP20K23342, JP21K17804).

References

[1] C. Takahashi, M. Ohzeki, S. Okada, M. Terabe, S. Taguchi, and K. Tanaka, "Statistical-mechanical analysis of compressed sensing for Hamiltonian estimation of Ising spin glass," *Journal of the Physical Society of Japan*, vol. 87, no. 7, p. 074001, 2018.

[2] M. Ohzeki, C. Takahashi, S. Okada, M. Terabe, S. Taguchi, and K. Tanaka, "Quantum annealing: next-generation computation and how to implement it when information is missing," *Nonlinear Theory and Its Applications, IEICE*, vol. 9, no. 4, pp. 392–405, 2018.

[3] H. Nishimori, *Statistical Physics of Spin Glasses and Information Processing*. Oxford University Press, 2001.

[4] V. Dotsenko, *Introduction to the Replica Theory of Disordered Statistical Systems*. Cambridge University Press, 2000.

[5] Y. Kabashima, T. Wadayama, and T. Tanaka, "A typical reconstruction limit for compressed sensing based on L_p-norm minimization," *Journal of Statistical Mechanics: Theory and Experiment*, vol. 2009, p. L09003, Sep 2009.

[6] S. Ganguli and H. Sompolinsky, "Statistical mechanics of compressed sensing," *Phys. Rev. Lett.*, vol. 104, p. 188701, May 2010.

Image processing for analyzing the number of DNA breaks using deep learning

Seiki Saito[1,*], Ayumi Kobashi[1], Hiroaki Nakamura[2, 3], Takahiro Kenmotsu[4], Yasuhisa Oya[5], Yuji Hatano[6]

[1]Department of Informatics and Electronics, Faculty of Engineering, Yamagata University
[2]Fundamenal Physics Simulation Research Division, Department of Helical Plasma Research, National Institute for Fusion Science
[3]Department of Electrical Engineering, Graduate School of Engineering, Nagoya University
[4]Faculty of Life and Medical Sciences, Doshisha University
[5]Center for Radioscience Education and Research, Faculty of Science, Shizuoka University
[6]Hydrogen Isotope Research Center, Organization for Promotion of Research, University of Toyama

[*]saitos@yz.yzmagata-u.ac.jp

The full paper of this paper has been published in Journal of Advanced Simulation in Science and Engineering (JASSE).

DOI: https://doi.org/10.15748/jasse.10.172

Evaluation of Tritium substitution probabilities For investigation of tritium resistance of DNA

Yohei Tsuchida[1], Seiki Saito[1]*, Hiroaki Nakamura[2] , Yoshiteru Yonetani[3]

[1] Yamagata University
[2] National Institute for Fusion Science
[3] National Institutes for Quantum and Science and Technology

* saitos@yz.yamagata-u.ac.jp

Abstract. Tritium water is generated as a result of the decommissioning of the Fukushima Daiichi Nuclear Power Plant. In addition, tritium is planned to be used as a fuel for nuclear fusion power generation, which is expected to be a future power generation technology. Therefore, it is important to understand in detail how tritium affects biomolecules. Using molecular dynamics (MD) methods, we aim to elucidate the mechanism of DNA damage caused by the decay effect that occurs when tritium replaces light hydrogen in human DNA. In this study, in order to clarify the correlation between the solvent accessible surface area (SASA) and the tritium substitution probability, we aim to evaluate the relationship between the SASA and the tritium substitution probability by calculating the SASA and the substitution probability in the same DNA model. In this preliminary report, we will present the results of the stabilization of the ion distribution in the simulation model, which was done as a preliminary step, using MD calculations. We also explain the introductory equation that we are considering using to obtain the substitution probability.

Keywords: DNA, solvent-accessible surface area, tritium, radioactive decay effect

1. Research Background

Currently, there is much debate over how to dispose of treated water with residual tritium generated by the accident at Fukushima Daiichi Nuclear Power Plant. In addition, fusion power generation is a method of power generation using a nuclear fusion reaction between deuterium and tritium, and is expected to be a new energy source. In these circumstances, there is a need to elucidate the effects of tritium on biomolecules in detail. Now, it is known that there is a correlation between the reaction rate of OH radicals in hydrogen in DNA surrounded by water molecules and the SASA in hydrogen in solvent [1]. In a previous research, the SASA in human DNA was calculated using the positional coordinates of atoms obtained from MD calculations for backbone hydrogen in human DNA, based on the idea that the SASA in human DNA is correlated with the ease of tritium substitution[2, 3]. In order to clarify the correlation between the SASA and the tritium substitution probability, we will calculate the substitution probability

in the DNA model used in our previous research[2] and establish a method to evaluate the probability of substitution of light hydrogen in DNA for tritium. In this preprint, we present the results of the stabilization of the ion distribution in the simulation model using MD calculations as a preliminary step to the stochastic calculations.

2. Simulation Model

The telomere structure of human DNA is placed in a 100 Å cubic computational domain filled with molecules in which one of the light hydrogen of the water molecule is replaced by tritium (HOT). The sequence of the telomere structure is TCTAGGGTTAGGGGTTAG. To neutralize the DNA charge, Na^+ and Cl^- are added to neutralize the system containing the unneutral DNA The ion concentration is set to 0.15 mol (in vivo concentration). The simulation model is shown in Figure 1.

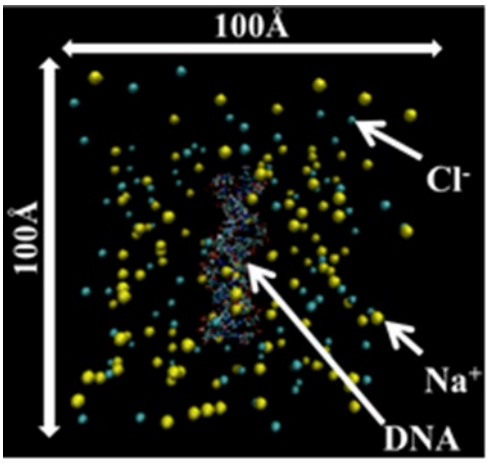

Figure 1. Simulation Model

The surrounding HOTs are hidden in Figure 1. LAMMPS is used for the MD simulation and CHARMM is used for the force field. Periodic boundary conditions are applied in the *x, y, z* directions. The simulation model is initially configured in CHARMM. However, the energy stabili-zation of initial configuration is insufficient. Therefore, we perform the structural relaxa-tion calculations int the first. Then, motion of all atoms in the system are solved under the condition of constant number of particles *N*, pressure *P*, and temperature *T* (*NPT* ensemble). The Nosé-Hoover method used for pressure baths and heat baths. The referential value of pressure and temperature are set to 1.0 atm and 310 K, respectively, to make it close to the temperature and pressure in the human body. The time is set to 1 fs, and the motion is calculated for 10 ns. Before performing the *NPT* ensemble calculations, structural relaxation calculations are performed to stabilize the simulation model. The temperature of the simulation model is then increased from 0 K to 310 K for 37.5 ns with a time step of 0.75 fs.

3. Calculation Result

The results of the structural relaxation calculations for the simulation model are shown in Figure 2. The horizontal axis shows the calculation time and the vertical axis shows the potential

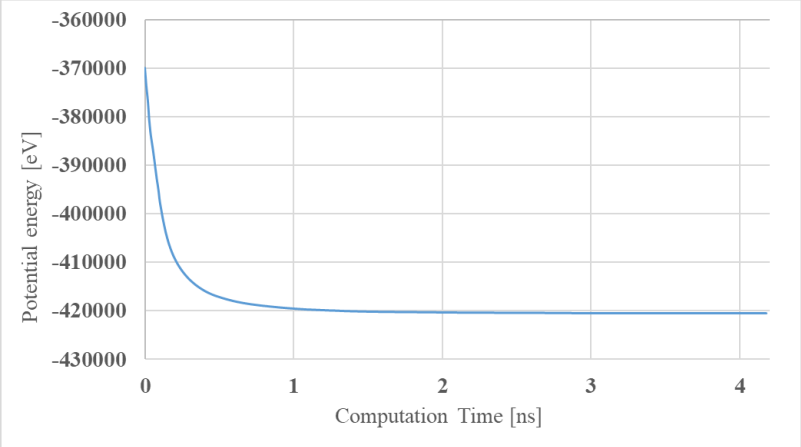

Figure 2. Calculation results of structural relaxation calculation

energy of the entire system. From the graph, it was confirmed that the stabilization was sufficient.

4. How to analyze the probability of substitution

The formula for determining the probability of substitution is calculate $P_i(r,t)drdt$ that the i-th light hydrogen is substituted by the tritium which is initially located at a distance of $r \sim r + dr$ during $t \sim t + dt$. We believe that this can be derived for $P_i(r,t)drdt$ by calculating Δt: the time step of the MD calculation, ΔT: the arbitrarily defined time step width, and Δr: the distance from the light hydrogen to tritium. P_i is then used to calculate $\Pi_i(\tau)$, the fraction of time during τ s that the i-th light hydrogen is replaced by tritium in the surrounding molecules.

$$\Pi_i(\tau) = \frac{1}{\tau}\int_0^{\tau}\int_0^{\infty}\frac{P_i(r,t)}{N_i(r)}\tilde{N}(r)drdt$$

By considering this $\Pi_i(\tau)$ as the substitution probability, we believe that it is possible to calculate the substitution probability with HOT in the backbone hydrogen in human DNA.

In this preliminary paper, as a preliminary step in the calculation of tritium substitution probabilities, the ion distribution of DNA in the simulation model is stabilized using MD calculations. The simulation results are discussed, especially the structural relaxation calculations. The formulas required to calculate the substitution probability are also discussed. In the presentation, We will discuss the correlation between the SASA and the tritium substitution probability by calculating the substitution probability between the SASA and the substitution probability of HOT in the backbone hydrogen in human DNA and evaluating the results.

Acknowledgement

The research was partially supported by Grant-in-Aid for Scientific Research, No.22K03572 from the Japan Society for the Promotion of Science, and by the NIFS Collaborative Research Program NIFS20KUTR158, NIFS22KISS021 and NIFS22KIGS002. The computations were performed using the JFRS-1 supercomputer system at Computational Simulation Centre of International Fusion Energy Research Centre (IFERC-CSC) in Rokkasho Fusion Institute of QST (Aomori, Japan), Research Center for Computational Science (Okazaki, Aichi, Japan) and Plasma Simulator of NIFS (Toki, Gifu, Japan) .

References

[1] Y. Yonetani, H. Nakagawa: Understanding water-mediated DNA damage production by molecular dynamics calculation of solvent accessibility, *Chem. Phys. Lett.*, 749 (2020), 137441.

[2] 土田陽平, 齋藤誠紀, 中村浩章, 米谷佳晃, 藤原進: 分子動力学法を用いたDNAテロメア構造中バックボーン水素の溶媒接触表面積の評価, 日本シミュレーション学会論文誌, 13, (2021), 32-26.

[3] H. Nakamura, H. Miyanishi, T. Yasunaga, S. Fujiwara, T. Mizuguchi, A. Nakata, T. Miyazaki, T. Otsuka, T. Kenmotsu, Y. Hatano and S. Saito: Molecular dynamics study on DNA damage by tritium disintegration, *Jpn. J. Appl. Phys.*, 59 (2020), SAAE01.

JSST 2022

Incidence Angle Dependence of Excitation Modes in Corrugated Waveguides

Yoshihisa Fujita[1,*], Hiroaki Nakamura[2], Hideki Kawaguchi[3], Shin Kubo[4], Yuki Goto[2], Soichiro Ikuno[5]

[1]College of Information Science and Engineering, Ritsumeikan University
[2]National Institute for Fusion Science, National Institute of Natural Science
[3]Division of Information and Electronic Engineering, Muroran Institute of Technology
[4]Engineering Science Laboratory, Chubu University
[5]School of Computer Science, Tokyo University of Technology

[*]yfujita@fc.ritsumei.ac.jp

Abstract. Although optical vortices are expected to be utilized in various fields, no definitive method of excitation has yet been proposed. As the first step for optical vortex generation, a Gaussian beam is irradiated into the aperture of the cylindrical waveguide to investigate the excitation modes. In addition, the relationship between the angle of incidence and the excitation mode will be clarified. Since the theoretical calculation of axisymmetry breaking is difficult, it is treated numerically using the FDTD method.

Keywords: Corrugated waveguide, FDTD method, Gaussian beam

1. Introduction

The three-dimensional phase structure of the optical vortex is expected to improve the efficiency of electron cyclotron resonance heating (ECRH)[1]. To realize ECRH using optical vortices, three issues must be solved: generation, transmission, and control.

The existing transmission lines used in fusion devices are cylindrical corrugated waveguides. Optical vortices in free space are written in terms of Laguerre functions, whereas the eigenmodes of a cylindrical waveguide are written in terms of Bessel functions. Therefore, it is known that they cannot be transmitted as they are in principle. However, even corrugated waveguides have been shown to have a three-dimensional phase structure by superposition of existing modes, called vortex beam (VB) modes[2]. The transition process at the waveguide aperture can be obtained theoretically from the equation relating the VB mode to the optical vortex. In other words, if a method to efficiently excite VB modes is clarified, it will be possible to propagate optical vortices using existing transmission lines.

Currently, the focus is only on exciting one fundamental mode by injecting a Gaussian beam generated from the gyrotron horizontally with respect to the waveguide. It is

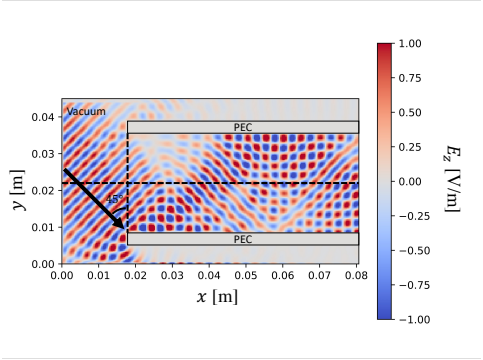

Figure 1: Propagation of Gaussian beam at oblique incidence

known that higher-order modes will be generated by oblique incidence angles. However, it is thought that multiple modes can be excited simultaneously if the incident angle is set at an appropriate angle. At present, the relationship between the angle of incidence and higher-order modes is not clear because it is difficult to treat theoretically.

In this study, Gaussian beams are injected at various angles and the excitation modes in the waveguide are numerically investigated. We aim to clarify the relationship between the angle of incidence and the excitation modes by following the trend.

2. Numerical Method and Result

A high-frequency electromagnetic wave is injected into a corrugated waveguide with grooves in wavelength scales according to the actual parameters. Therefore, both the temporal and spatial resolution must be sufficiently smaller than the expected wave. In addition, the adaptive mesh structure does not provide much benefit because the proportion of higher-order modes also be studied in detail. For these reasons, the finite-difference time-domain (FDTD) method is used to simulate the propagation phenomenon because it is a simple algorithm. Reflections at the waveguide wall are accurately observed by calculating the scattering field as well. The perfect matched layer (PML) is adopted as the absorbing boundary condition for the entire circumference. The result of the calculation under the above conditions is shown in Fig.1. Detailed results, including the extension to three dimensions and the ratio of excitation modes, will be presented at JSST2022.

References

[1] T. Tsujimura, and S. Kubo: Propagation properties of electron cyclotron waves with helical wavefronts in magnetized plasma, *Phys. Plasmas*, 28:012502 (2021).

[2] M. Bernas, K. Zolnacz, M. Napiorkowski, G. Statkiewicz-Barabach, and W. Urbanczyk Conversion of LP_{11} modes to vortex modes in a gradually twisted highly birefringent optical fiber, Opt. Lett., 46:18 (2021), 4446–4449.

Boundary Element Analysis of Surface Roughness Wake Field in an Accelerator Beam Pipe

Kazuhiro Fujita[1,*]

[1]Department of Information Systems, Faculty of Engineering, Saitama Institute of Technology

[*]kfujita@sit.ac.jp

Abstract. The interaction of a relativistic charged particle beam with a vacuum chamber beam pipe with surface roughness is of great interest in accelerator physics. In this work, we apply the recently proposed boundary element method (BEM) to surface roughness wake field analysis. A beam coupling impedance due to surface roughness in a round beam pipe is demonstrated. The BEM simulation is cross-checked with an analytical calculation.

Keywords: Boundary element method, electromagnetic field, surface roughness, wake field

1. Introduction

Modern X-ray free electron lasers (FELs) use very short bunches with a high peak current. When such a bunch passes through an undulator vacuum chamber beam pipe, it generates strong electromagnetic fields known as wake fields, which act back on the bunch itself, due to its radius smallness. The longitudinal wake field generated in the undulator induces an energy variation along the bunch, which can limit the FEL performance [1, 2]. One major source for the wake field generation is surface roughness, as discussed in [3]. Round and flat geometries are usually assumed in the theoretical wake field analysis, as in [4]. The effects of finite-length pipe including small periodic corrugations were discussed through numerical calculations with a londitudinally dispersionless finite-difference time-domain (FDTD) scheme in [5]. On the other hand, to estimate the integrated effect of the field on the beam in the frequency domain, so-called beam coupling impedance [6] is often used in the design stages of accelerators. Note that, as a simplified model, a straight beam trajectory is assumed in calculating beam coupling impedances due to the surface roughness, even for the undulators (see e.g. [1, 3, 4]). This assumption is used in the present study.

Recently, the author has proposed a two-diemsnional boundary element method (BEM) [7] for analyzing beam coupling impedances of infinitely long accelerator vacuum chambers of general cross section. In this study, the proposed 2-D BEM is applied to surface roughness wake field analysis. This will be realized by introducing the roughness surface impedance of Ref. [3] into the BEM [7]. It should be mentioned that it is difficult to deal with this

surface impedance [3] in the time domain and to incorporate it into the FDTD [5] due to its complicated frequency dependency. Therefore, we limit our dicussion to the BEM.

2. Boundary Element Method

We assume that the accelerator vacuum chamber is infinitely long and longitudinally uniform, and the beam has the total charge Q and moves with constant velocity $\mathbf{v} = v\mathbf{e}_z = \beta c\mathbf{e}_z$, where $\beta = v/c$, c is the speed of light in vacuum, and $\mathbf{e}_z$ is the unit vector in the direction of the beam motion. Because of the longitudinal uniformity, we also assume that the beam charge and current densities and all field components are proportional to $\exp j(\omega t - kz)$, where $k = \omega/v$ is the wavenumber, ω is the angular frequency. We omit this factor from the expressions described below.

The total electromagnetic fields $(\mathbf{E}, \mathbf{H})$ in the vacuum region surrounded by chamber cross section C in the transverse plane (xy plane) can be described by Kirchhoff's boundary integral representation in the frequency domain [7] as follows:

$$\begin{aligned}\mathbf{E}(\mathbf{r}) = \mathbf{E}_b(\mathbf{r}) \quad &+ \quad \frac{k_\gamma}{2\pi\varepsilon_0}\int_C K_1\left(k_\gamma R\right)\frac{\mathbf{R}}{R}\sigma(\mathbf{r}')\,d\mathbf{r}' - \frac{j\omega\mu_0}{2\pi}\int_C K_0\left(k_\gamma R\right)\mathbf{K}(\mathbf{r}')\,d\mathbf{r}' \\ &- \quad \frac{k_\gamma}{2\pi}\int_C K_1\left(k_\gamma R\right)\mathbf{M}(\mathbf{r}')\times\frac{\mathbf{R}}{R}d\mathbf{r}', \qquad (1)\\ \mathbf{H}(\mathbf{r}) = \mathbf{H}_b(\mathbf{r}) \quad &+ \quad \frac{k_\gamma}{2\pi\mu_0}\int_C K_1\left(k_\gamma R\right)\frac{\mathbf{R}}{R}\eta(\mathbf{r}')\,d\mathbf{r}' - \frac{j\omega\varepsilon_0}{2\pi}\int_C K_0\left(k_\gamma R\right)\mathbf{M}(\mathbf{r}')\,d\mathbf{r}' \\ &+ \quad \frac{k_\gamma}{2\pi}\int_C K_1\left(k_\gamma R\right)\mathbf{K}(\mathbf{r}')\times\frac{\mathbf{R}}{R}d\mathbf{r}', \qquad (2)\end{aligned}$$

where $R = |\mathbf{R}|$, $\mathbf{R} = \mathbf{r} - \mathbf{r}'$, $\mathbf{r} = (x, y)$ is the observation point, $\mathbf{r}' = (x', y')$ is a point on the wall surface, $k_\gamma = k/\gamma$, $\gamma = (1 - \beta^2)^{-1/2}$ is the Lorentz factor, $(\mathbf{E}_b, \mathbf{H}_b)$ are the beam self-fields, $(\mathbf{K}, \sigma)$ are the electric surface current and charge densigies and $(\mathbf{M}, \eta)$ are the magnetic surface current and charge densities, K_1 is the modified Bessel function of the second kind of order one, $(\mathbf{E}_b, \mathbf{H}_b)$ are assumed to be known. The effect of surface roughness in the beam pipe are modeled as the surface impedance boundary condition (SIBC):

$$\mathbf{M} = Z_s\mathbf{K}\times\mathbf{n}, \qquad (3)$$

where Z_s is the surface impedance. For this, we use the roughness surface impedance described in [3].

According to the discretization procedure of BEM [7], we finally have the following system of linear equations:

$$[A]\,\mathbf{x} = \mathbf{b}, \qquad (4)$$

where $\mathbf{x}$ is a unknown vector which consists of surface current densities to be solved, $[A]$ denotes a complex coefficient matrix determined by the boundary integrals, $\mathbf{b}$ is a given vector calculated with the self-fields on the boundary elements. We use a direct method based on the LU decomposition to solve Eq. (4).

Once all the boundary values are calculated, the electromagnetic fields at any point in the bounded vacuum region can be obtained from Eqs. (1) and (2).

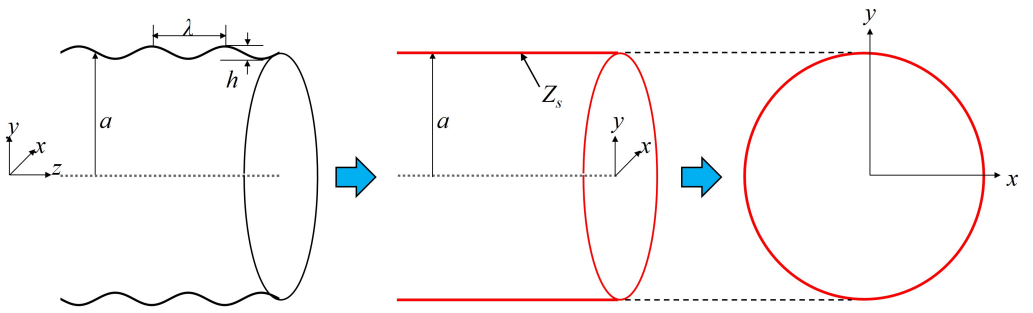

(a) Original model (b) Equivalent model (c) 2-D model (cross section)

Figure 1: Infinitely long round beam pipe with a sinusoidal corrugation of the wall

3. Numerical Result

In order to verify our approach (introducing the roughness surface impedance Z_s of Ref. [3] into the 2-D BEM [7]), we simulate in the frequency domain the surface roughness wake field excited by a charged particle beam moving with Q=1pC and γ = 10000 on the axis of an infinitely long round beam pipe (radius a=2.5mm) with a sinusoidally varing wall profile with height h=4.052μm and a wall oscillation wavelengh λ=300μm as shown in Fig. 1. In the same way as Ref. [3, 4], we evaluate its integrated effect by using the beam coupling impedance $Z_{\parallel} = -E_z/I$, where E_z is the electric field component along the z-axis (direction of beam motion), $I = Qv$ is the beam current. Note that (a) the original roughness model can be replaced by (b) an equivalent model with Z_s. See [3, 4] for more detailed discussions on Z_s. Finally, the original model is reduced to the 2-D model as shown in Fig. 1(c). The BEM simulation is performed for this 2-D model. Its numerical result is shown in Fig. 2. The BEM-computed beam coupling impedance is in good agreement with the analytical one obtained with

$$Z_{\parallel} = \frac{Z_s}{2\pi a}. \tag{5}$$

A frequency dependency of the beam coupling impedance due to the surface roughness is reproduced in this BEM simulation.

4. Conclusion

We have applied the recently proposed BEM to the surface roughness wake field analysis. This has been realized by introducing the roughness surface impedance into the BEM. The beam coupling impedance due to the surface roughness in the round beam pipe is computed with the BEM. Good agreement between the BEM and analytical results has been obtained.

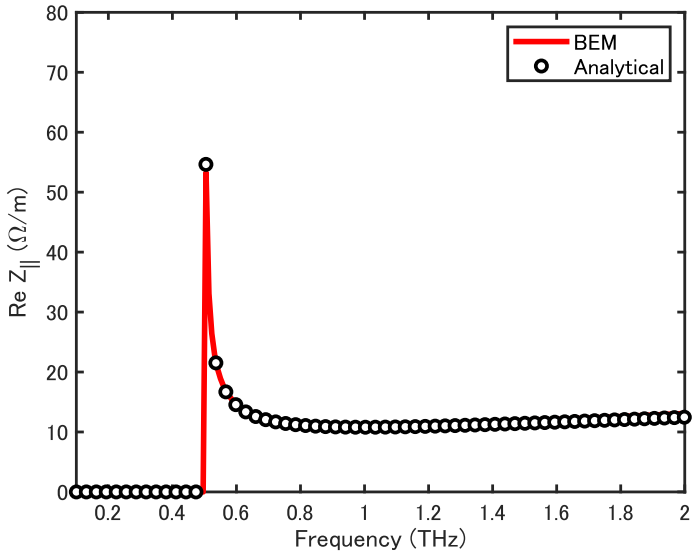

Figure 2: Comparison of the real parts of beam coupling impedance due to the surface roughness in the round beam pipe calculated with the BEM and analytical formula.

References

[1] G. Stupakov and R. E. Thomson and D. Walz and R. Carr: Effects of beam-tube roughness on x-ray free electron laser performance, *Phys. Rev. ST Accel. Beams.*, 2 (1999), 060701.

[2] K. Bane and G. Stupakov: Resistive wall wakefield in the LCLS undulator beam pipe, *SLAC-PUB-10707*, (2004).

[3] G. Stupakov and S. Reiche: Surface roughness wakefield in FEL undulator, *Proceedings of FEL2013*, MOPSO73 (2013), 127–131.

[4] K. Bane and G. Stupakov: Roughness Tolerance Studies for the Undulator Beam Pipe Chamber of LCLS-II, *SLAC-PUB-15951*, (2014).

[5] K. Fujita: Modeling of beam-wall interaction in a finite-length metallic pipe with multiple surface perturbations, *IEEE J. Multiscale Multiphys. Comput. Techn.*, 2 (2017), 237–242.

[6] B. W. Zotter and S. A. Kheifets: *Impedance and Wakes in High-Energy Accelerators*, Singapore, World Scientific (1998).

[7] K. Fujita: Impedance computation of cryogenic vacuum chambers using boundary element method, *Phys. Rev. Accel. Beams*, 25:6 (2022), 064601.

Time structure of the undulator radiation

Elham Salehi[1,*], Masahito Hosaka[2], Masahiro Katoh[1,3]

[1]UVSOR, Institute for Molecular Science, National Institutes of Natural Sciences
[2]National Synchrotron Radiation Laboratory, University of Science and Technology of China, China
[3]Hiroshima Synchrotron Radiation Center, Hiroshima University, Higashi-Hiroshima, Japan

[*]elham@ims.ac.jp

The full paper of this paper has been published in Journal of Advanced Simulation in Science and Engineering (JASSE).

DOI: https://doi.org/10.15748/jasse.10.164

Molecular dynamics simulation of water dynamics in zwitterionic polymer brush-water interface

Susumu Fujiwara[1*], Yuya Fujinaga[1], Tomoko Mizuguchi[1]

[1]Kyoto Institute of Technology

*fujiwara@kit.ac.jp

Abstract. All-atom molecular dynamics simulations of zwitterionic polymer brushes in water were performed to determine the effect of the tacticity of the polymer brush on the interfacial water dynamics. Our simulations show that syndiotactic and isotactic zwitterionic polymer brushes have different chain shapes and water dynamics. The hydrogen bond lifetimes of the syndiotactic model were found to be longer than those of the isotactic model. These results actually confirm that there are differences in the dynamics of interfacial water depending on the tacticity of the polymer brush.

Keywords: Polymer brush, Molecular dynamics simulation, Tacticity, Dynamics of water, Zwitterionic polymer brush, Antifouling

1. Introduction

The surface properties of materials can be modified by polymer brushes. One of the useful properties obtained by polymer brushes is their antifouling effect. The antifouling effect prevents the adsorption of proteins that trigger the biological defense system, making it a very effective material for in vivo use [1]. For this reason, the application of polymer brushes in the medical field has attracted much attention in recent years. In particular, zwitterionic polymer brushes such as 2-methacryloyloxyethyl phosphorylcholine (MPC) are expected to be promising antifouling materials due to their high hydrophilicity, long life, and environmental stability [2] (Fig. 1).

Recent studies have recognized the structure of hydrated polymer brushes and the dynamics of hydrated water as important factors for antifouling [3]. Numerous efforts have been made to achieve highly antifouling properties with polymer brushes. One of these is the control of tacticity and molecular weight distribution of polymer brushes. Experimental studies have been conducted to control them [4], but atomistic understanding of primary structures such as tacticity is not yet sufficient. In this study, molecular dynamics (MD) simulations of an all-atom model consisting of MPC polymer brush and water were performed to determine the effect of the polymer brush tacticity on the dynamics of interfacial water.

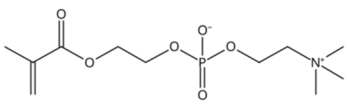

Figure 1 Molecular structure of MPC.

2. Simulation details

All simulations were carried out using Gromacs [5]. Sixteen polymer brushes (each brush consists of 19 MPC monomers) were grafted onto the *x*-*y* plane (8 nm×8 nm) of the MD box. TIP3P water molecules were placed on a layer of MPC brushes.

As the force field, we selected the general AMBER force field (GAFF) for MPC brushes. The Restrained Electrostatic Potential (RESP) charge calculated using Winmostar was adopted as the point charge for each atom [6]. After heating processes, 100 ns MD simulations were performed with NPT (constant number of atoms, constant pressure, constant temperature) ensemble, 2-dimensional periodic boundary conditions in the *x* and *y* directions, and an integration time step of 1 fs. Temperature and pressure were set to $T = 310$ K and $P = 1$ atm, assuming in vivo conditions. MD simulations of syndiotactic and isotactic models of MPC polymer brushes were performed to clarify the effect of tacticity.

3. Results and discussion

Figure 2 shows the radius of gyration, R_g, of the MPC polymer brush. The average values of R_g were 1.13 nm for syndiotactic polymer brushes and 1.22 nm for isotactic brushes. It can be seen from this figure that the dimensions of isotactic brushes are larger than those of syndiotactic brushes. The results show that isotactic brushes are more elongated than syndiotactic brushes.

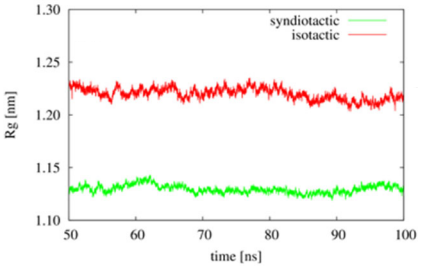

Figure 2 Radii of gyration for MPC polymer brushes.

The mean square displacement (MSD) of water between brushes in the z direction was calculated (Fig. 3). Figure 3 shows that water between isotactic brushes moves slightly more easily in the z direction than water between syndiotactic brushes. The results indicate that water is less likely to exit the brush in the syndiotactic model than in the isotactic model.

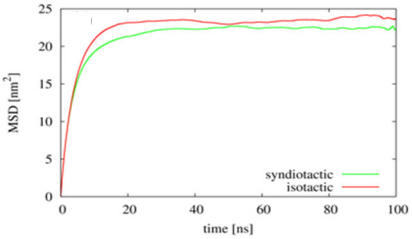

Figure 3 Mean square displacement (MSD) of water between brushes in the *z* direction.

4. Conclusion

Understanding the effect of the tacticity of polymer brushes on interfacial water dynamics will be useful in creating highly antifouling surfaces. To advance our understanding of this effect at the atomic level, we performed all-atom MD simulations of MPC polymer brushes in water. The chain shape of the polymer brush, the dynamics of interfacial water, and the lifetime of the hydrogen bonds are all affected by the tacticity of polymer brush.

References

[1] K. Ishihara: Highly lubricated polymer interfaces for advanced artificial hip joint through biomimetic design, *Polym. J.*, 47:9 (2015), 585-597.

[2] C. Liu, J. Lee, J. Ma, M. Elimelech: Antifouling Thin-Film Composite Membranes by Controlled Architecture of Zwitterionic Polymer Brush Layer, *Environ. Sci. Technol.*,

51:4 (2017), 2161-2169.

[3] Y. Higaki, M. Kobayashi, D. Murakami, A. Takahara: Anti-fouling behavior of polymer brush immobilized surfaces, *Polym. J.*, 48:4 (2016), 325-331.

[4] T. Hirai: Design and Fabrication of Polymer Interfaces and Evaluation of Their Molecular Aggregation Structure, *Kobunshi Ronbunshu* (in Japanese), 73:5 (2016), 428-441.

[5] https://www.gromacs.org/.

[6] https://winmostar.com/jp/.

[7] D. van der Spoel, P.J. van Maaren, P. Larsson, N. Timneanu: Thermodynamics of Hydrogen Bonding in Hydrophilic and Hydrophobic Media, *J. Phys. Chem. B*, 110:9 (2006), pp. 4393-4398.

JSST 2022

Shape Modeling of Metal Foam Based on Implicit Surfaces Generated from Deformed Polyhedra

Naoki Hamano[1,*], Taku Itoh[2,*], Kohei Tateyama[3],
Susumu Nakata[4], Keiko Watanabe[5]

[1]Graduate School of Industrial Technology, Nihon University, Japan
[2]College of Industrial Technology, Nihon University, Japan
[3]Graduate School of Engineering, Muroran Institute of Technology, Japan
[4]College of Information Science and Engineering, Ritsumeikan University, Japan
[5]College of Science and Engineering, Ritsumeikan University, Japan

[*]cina22005@g.nihon-u.ac.jp, itoh.taku@nihon-u.ac.jp

Abstract. The purpose of this study is to propose a simple modeling method of open- and closed-cell metal foams so that the models have complex-shaped edges and cells. To this end, we basically employ the idea of a sphere-function-based method. Note that, in the proposed method, we adopt deformed polyhedra-based implicit surfaces instead of sphere-function-based ones. The results show that open- and closed-cell models obtained by the proposed method have various shapes of edges and cells in comparison with those obtained by the sphere-function-based method.

Keywords: Open/closed-cell metal foams, Implicit surfaces, Polyhedra, Shape modeling

1. Introduction

A model of metal Foams has been generated as a scalar field based on implicit surfaces. In [1], the implicit surfaces are generated from Voronoi diagram based on Poisson-disk sampling (PDS), for modeling of closed-cell metal foams. In addition, in [2], they are generated from sphere functions for modeling of open-cell metal foams. Besides, in [3], the methods described in [1] and [2] are integrated so that these methods can represent both open- and closed-cell structures together with their intermediates.

Although the method in [1] can generate complex-shaped edges and cells, a little complicated procedures such as generating PDS nodes and the Voronoi diagram are contained in the modeling algorithm. On the other hand, the algorithm in [2] is simple. However, since sphere-function-based implicit surfaces are adopted, all edges and cells have almost the same simple structures.

The purpose of this study is to generate open- and closed-cell models that have complex-shaped edges and cells by a simple algorithm. To this end, a method based on [2] is pro-

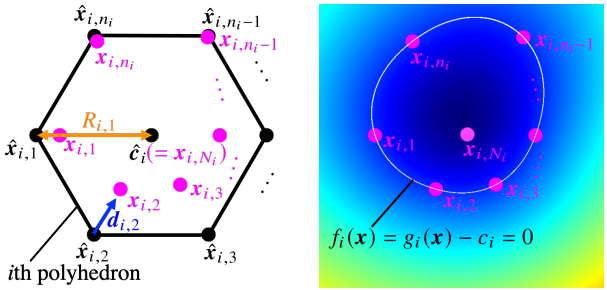

(a) (b)

Figure 1: Schematic view of (a) moved vertices $\boldsymbol{x}_{i,j} = \hat{\boldsymbol{x}}_{i,j} + \alpha_{i,j}\boldsymbol{d}_{i,j} (j = 1, 2, \ldots, n_i)$, and (b) ith implicit surface $f_i(\boldsymbol{x}) = g_i(\boldsymbol{x}) - c_i = 0$. In this figure, we assume that $h_{i,j} = c_i$.

posed. In the proposed method, we adopt deformed polyhedra-based implicit surfaces instead of sphere-function-based ones.

2. Shape Modeling of Metal Foam Based on Implicit Surfaces

In this study, we basically employ the idea of method in [2]. The proposed method generates a scalar field as an implicit function, and both open- and closed-cell models can be represented by the implicit function, similarly with the strategy described in [3].

Procedures of the proposed method are as follows:

1. To construct Plateau borders [2] in an open-cell model, polyhedra are put similarly with spheres shown in [2] (see Figs. 10 and 11 in [2]). Note that we usually employ regular polyhedra, and the centers of gravity for the polyhedra coincide those for the spheres in [2].

2. The ith polyhedron is deformed by moving the vertices $\hat{\mathcal{X}}_i = \{\hat{\boldsymbol{x}}_{i,1}, \hat{\boldsymbol{x}}_{i,2}, \ldots, \hat{\boldsymbol{x}}_{i,n_i}\}$ of polyhedron. Vertices of the deformed ith polyhedron are represented as $\boldsymbol{x}_{i,1}, \boldsymbol{x}_{i,2}, \ldots, \boldsymbol{x}_{i,n_i}$. In addition, we define $\mathcal{X}_i = \{\boldsymbol{x}_{i,1}, \boldsymbol{x}_{i,2}, \ldots, \boldsymbol{x}_{i,N_i}\}$, where $N_i = n_i + 1$ and $\boldsymbol{x}_{i,n_i+1} (= \boldsymbol{x}_{i,N_i})$ coincides the gravity of center $\hat{\boldsymbol{c}}_i$ of the ith polyhedron (see Fig. 1(a)).

3. In the ith polyhedron, a scalar field $g_i(\boldsymbol{x})$ is generated as an implicit function based on radial-basis-functions (RBFs)from $\mathcal{X}_i$. Here, an iso-surface $g_i(\boldsymbol{x}) = c_i$ is considered in each scalar field $g_i(\boldsymbol{x})$, where c_i is a constant value. Here, we define $f_i(\boldsymbol{x}) = g_i(\boldsymbol{x}) - c_i$. By the definition, any iso-surface of $g_i(\boldsymbol{x})$ can be represented as an implicit surface $f_i(\boldsymbol{x}) = 0$ (see Fig. 1(b)).

4. Functions $f_i(\boldsymbol{x})$ $(i = 1, 2, \ldots, M)$ are combined by a constructive solid geometry (CSG). Here, let the combined function be $F_M(\boldsymbol{x})$ (see Fig. 2).

5. A metal foam model is generated by extracting an implicit surface $F_M(\boldsymbol{x}) = 0$. Note that various models between open- and closed-cell structures can be generated by changing c_i.

In what follows, we describe the above procedures concretely.

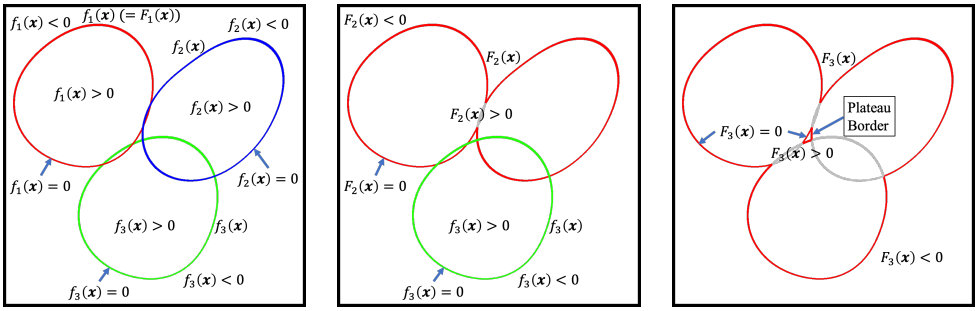

(a) (b) (c)

Figure 2: Schematic view of (a) initial arrangement of functions $f_1(\boldsymbol{x}), f_2(\boldsymbol{x})$ and $f_3(\boldsymbol{x})$, (b) $F_2(\boldsymbol{x}) = \min\{F_1(\boldsymbol{x}), f_2(\boldsymbol{x})\}$ and $f_3(\boldsymbol{x})$, and (c) $F_2(\boldsymbol{x}) = \min\{F_2(\boldsymbol{x}), f_3(\boldsymbol{x})\}$. A Plateau border is constructed by $F_2(\boldsymbol{x}) = 0$.

2.1. Polyhedra and their Deformation (Procedures 1 and 2)

In the procedure 1, although we can choose some kinds of polyhedra, one kind of polyhedra is chosen for simplicity. Concretely, we adopt truncated octahedra as polyhedra. A truncated octahedron has 24 vertices. They are $\hat{\mathcal{X}}_i$ and $n_i = 24$ in this case ($i = 1, 2, \ldots, M$).

In the procedure 2, $\boldsymbol{x}_{i,1}, \boldsymbol{x}_{i,2}, \ldots, \boldsymbol{x}_{i,24}$ for the ith deformed truncated octahedron can be generated by $\boldsymbol{x}_{i,j} = \hat{\boldsymbol{x}}_{i,j} + \alpha_{i,j}\boldsymbol{d}_{i,j}$ ($j = 1, 2, \ldots, 24$), where $\alpha_{i,j}$ is a parameter whose value is randomly determined in a range $\alpha_{i,j} \in [\alpha_i^{\min}, \alpha_i^{\max}]$. In addition, $\boldsymbol{d}_{i,j} = (\hat{\boldsymbol{c}}_i - \hat{\boldsymbol{x}}_{i,j})/|\hat{\boldsymbol{c}}_{i,j} - \hat{\boldsymbol{x}}_{i,j}|$. Note that $\boldsymbol{x}_{i,N_i} = \boldsymbol{x}_{i,25} = \hat{\boldsymbol{c}}_i$.

2.2. Implicit Surfaces Generated from Deformed Polyhedra (Procedure 3)

In the procedure 3, to generate a scalar field as an implicit function, we employ a radial-basis-function (RBF)-based method.To generate the scalar field, scalar height values $\mathcal{H}_i = \{h_{i,1}, h_{i,2}, \ldots, h_{i,N_i}\}$ must be set, and we can think of the surface as a scalar-valued function $g_i(\boldsymbol{x})$ such that $g_i(\boldsymbol{x}_{i,j}) = h_{i,j}$ ($j = 1, 2, \ldots, N_i$).

In the RBF-based method, we assume that the ith interpolating function $g_i(\boldsymbol{x})$ is expressed as follows:

$$g_i(\boldsymbol{x}) = \sum_{j=1}^{N_i} \lambda_{i,j}\phi(|\boldsymbol{x} - \boldsymbol{x}_{i,j}|) + p_i(\boldsymbol{x}), \tag{1}$$

where ϕ is an RBF, λ_j are weights, and $p_i(\boldsymbol{x})$ is a degree one polynomial: $p_i(\boldsymbol{x}) = \alpha_{i,0} + \alpha_{i,1}x + \alpha_{i,2}y + \alpha_{i,3}z$. The unknowns $\lambda_{i,j}$ and $\alpha_{i,j}$ are determined by solving the $(N_i + 4) \times (N_i + 4)$ linear systems.After $g_i(\boldsymbol{x})$ is generated, $f_i(\boldsymbol{x}) = g_i(\boldsymbol{x}) - c_i$ is defined.

2.3. Combined Function $F(\boldsymbol{x})$ (Procedures 4 and 5)

In the procedure 4, $f_1(\boldsymbol{x}), f_2(\boldsymbol{x}), \ldots, f_M(\boldsymbol{x})$ are combined by CSG. Figure 2(a) shows the process of combining $f_1(\boldsymbol{x}), f_2(\boldsymbol{x})$, and $f_3(\boldsymbol{x})$. Note that lines in Fig. 2(a) are the implicit surfaces, $f_i(\boldsymbol{x}) = 0$ ($i = 1, 2, 3$). Here, we define $F_1(\boldsymbol{x}) = f_1(\boldsymbol{x})$, and combined functions $F_2(\boldsymbol{x})$ and $F_3(\boldsymbol{x})$ are obtained by $F_2(\boldsymbol{x}) = \min\{F_1(\boldsymbol{x}), f_2(\boldsymbol{x})\}$, and $F_3(\boldsymbol{x}) = \min\{F_2(\boldsymbol{x}), f_3(\boldsymbol{x})\}$,

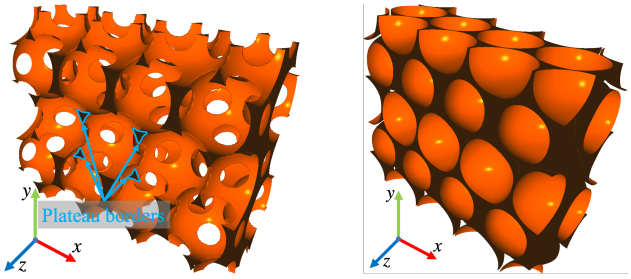

(a) (b)

Figure 3: Results of (a) open-cell model ($c_i = -2.0$), and (b) closed-cell model ($c_i = 0.0$).

respectively. In Figs. 2(b) and (c), $F_2(\boldsymbol{x}) = 0$ and $F_3(\boldsymbol{x}) = 0$ are represented as red lines, respectively. As shown in Fig. 2(c), a Plateau border, whose shape of cross-section is a concave triangle, can be constructed, for the case where an open-cell model is represented. Generally for M functions $f_1(\boldsymbol{x}), f_2(\boldsymbol{x}), \ldots, f_M(\boldsymbol{x})$, kth combined function $F_k(\boldsymbol{x})$ can be obtained by $F_k(\boldsymbol{x}) = \min\{F_{k-1}(\boldsymbol{x}), f_k(\boldsymbol{x})\}$ $(k = 2, 3, \ldots, M)$.

In the procedure 5, a metal foam model can be obtained by extracting $F_M(\boldsymbol{x}) = 0$. Note that $F_M(\boldsymbol{x}) = 0$ can be extracted by the marching-cubes method as polygonal surfaces.

3. Results

In this section, we show results of open- and closed-cell models obtained by the proposed method in Figs. 3(a) and (b), respectively. Note that, to visualize a mid-layer of the results, Figs. 3(a) and (b) are halved by z-direction. To generate these models, we employ 113 truncated octahedra, i.e., $M = 113$, and their arrangements are similarly set with spheres shown in Figs. 10 and 11 of [2]. In addition, we set $h_{i,1} = h_{i,2} = \cdots = h_{i,24} = -1.0$, $h_{i,25} = 5.0$, $\alpha_i^{\min} = -0.05R_{i,j}$, and $\alpha_i^{\max} = -0.3R_{i,j}$, where $R_{i,j} = |\hat{\boldsymbol{x}}_{i,j} - \hat{\boldsymbol{c}}_i|$ shown in Fig. 1(a) $(i = 1, 2, \ldots, M)$. Besides, to extract the surfaces shown in Figs. 3(a) and (b), we set $c_i = -2.0$ and 0.0 $(i = 1, 2, \ldots, M)$, respectively. As an RBF, we adopt $\phi(r) = r^3$.

By comparing with the results in Table 1 of [3], Figs. 3(a) and (b) have multiple shapes of edges and cells. Since real open- and closed-cell metal foams have various kinds of edges and cells, we consider that Figs. 3(a) and (b) may be more closed to real metal foams.

References

[1] Y. Hanaoka, M. Nojiri, T. Itoh, S. Nakata, K. Watanabe: Three-dimensional shape modelling of metal foam with rounded cells by implicit surfaces, *JASSE*, 6:1 (2019), 195–214.

[2] Y. Hanaoka, T. Itoh, S. Nakata, K. Watanabe: Sphere-function-based shape modelling of open cell metal foam with Plateau borders, *JASSE*, 7:1 (2020), 89–101.

[3] Y. Hanaoka, T. Itoh, K. Tateyama, S. Nakata, K. Watanabe: Shape modelling of metal foams of open/closed states and their intermediates by implicit function, *JASSE*, 8:1 (2021), 143–153.

JSST 2022

Improvement of wavelet-synchrosqueezing transform with time shifted angular frequency

Takashi Matsubara[1,*], Akira Kakutani[2], Keisuke Iwai[1], Takakazu Kurokawa[1]

[1]Department of Computer Science, National Defense Academy
[2]Kaiyo Densi Kogyo Co., Ltd.

[*]matubara@nda.ac.jp

The full paper of this paper has been published in Journal of Advanced Simulation in Science and Engineering (JASSE).

DOI: https://doi.org/10.15748/jasse.10.53

JSST 2022

Image denoising using directional wavelet-based approaches

Kensuke Fujinoki*

[1]Department of Electrical, Electronics and Information Engineering, Faculty of Engineering, Kanagawa University

*fujinoki@kanagawa-u.ac.jp

Abstract. For image analysis, efficient representations of geometrical edges are important. In our previous study, we proposed a directional lifting wavelet transform that can analyze multiscale edge structures of an image. The present paper focuses on the denoising properties of the directional lifting wavelet transform. We show that the unique directional property of our approach can also be used for image denoising.

Keywords: Directional wavelets, Redundant transform, Denoising

1. Introduction

Directional wavelets, which are multidimensional extensions of wavelets, have been studied as tools for geometric multiscale analysis. In particular, frame-type directional wavelet methods, including curvelets, contourlets and shearlets, are one of the most notable categories of wavelets and are used both for developing the theory and in applications.

In [2, 3], we have proposed a directional wavelet transform by incorporating directional selectivity into the lifting scheme [4]. While the standard discrete wavelet transform (DWT) has a directional selectivity of $N = 3$, our directional lifting wavelet transform (DLWT) extends it to $N = 12$, which enables analysis of signals approximately every 15 degrees. We have previously shown that this directional property plays an important role in the analysis of image edge components and provides better edge detection.

This paper focuses on the denoising properties of the DLWT that take advantage of its directional selectivity. Since the DLWT successfully can detect both global and local edge structures, the directional property of the DLWT could be useful in a simple image denoising algorithm.

2. Directional methods

Let $\{c_j[\boldsymbol{t}]\}_{\boldsymbol{t}\in\mathbb{Z}^2}$ be an image with a resolution level of $j \in \mathbb{N} \cup \{0\}$. The DWT decomposes an image $\{c_j[\boldsymbol{t}]\}_{\boldsymbol{t}\in\mathbb{Z}^2}$ into one coarse component $\{c_{j-1}[\boldsymbol{t}]\}_{\boldsymbol{t}\in\mathbb{Z}^2}$ and three detailed components

$\{d_{k,j-1}[\boldsymbol{t}]\}_{\boldsymbol{t}\in\mathbb{Z}^2,k=1,2,3}$, which consist of horizontal, vertical and diagonal directions. We say that the directional selectivity is $N = 3$. Also, note that each component has half the resolution of the original image. The decomposition can be iterated to reach an arbitrary decomposition level $J \geq 1$ by using the resulting coarse component as the new input signal. From the iteration process, the following sequences of coefficients are obtained by the DWT:

$$c_j[\boldsymbol{t}] \mapsto \left\{d_{k,j-1}[\boldsymbol{t}],\, d_{k,j-2}[\boldsymbol{t}],\, \ldots,\, d_{k,j-J}[\boldsymbol{t}],\, c_{j-J}[\boldsymbol{t}]\right\}_{\boldsymbol{t}\in\mathbb{Z}^2,\ k=1,2,3}.$$

The DLWT decomposes images similarly, but it has twelve directional components, and thus the directional selectivity is $N = 12$. Each approximated degree can be defined by $\theta \approx (180\,(d-1)\,/N)^\circ$, $d \in D = \{\ell \in \mathbb{Z} \mid 1 \leq \ell \leq N\}$. The J-th level decomposition with the DLWT can be written as

$$c_j[\boldsymbol{t}] \mapsto \left\{d_{k,j-1}[\boldsymbol{t}],\, d_{k,j-2}[\boldsymbol{t}],\, \ldots,\, d_{k,j-J}[\boldsymbol{t}],\, c_{j-J}[\boldsymbol{t}]\right\}_{\boldsymbol{t}\in\mathbb{Z}^2,k\in D}.$$

The DLWT is superior to the conventional method in directional selectivity as well as other aspects. Namely, although this is a redundant transform with a redundancy of $(N \times J + 1)/4$, an efficient computational algorithm owing to the lifting implementation is possible, as it achieves an efficient trade-off between computational cost and directional selectivity.

3. Numerical results

In this section, we show numerical experimental results for image denoising using either the DLWT or the conventional DWT. To make the comparison simple, we treat only the Haar wavelet case, which is the lowest order used in the DLWT. All the images used for the experiments have a size of 512×512. Gaussian noise is added so that the signal-to-noise ratio (SNR) of an image is 28.14 [dB]. A standard hard thresholding algorithm with universal thresholding is applied for denoising [5].

Figure 1 shows a comparison of the results of denoising using the test images "Lenna" and "Barbara". A zoomed-in version is shown in Figure 2. From subjective observation, the DLWT appears to provide a better visual quality for both images, especially in terms of the gradation of the skin and the background. However, evaluation of the peak signal-to-noise ratio (PSNR) indicates that "Lenna" has a PSNR value of 30.20 [dB] using the DWT and 30.68 [dB] using the DLWT, whereas "Barbara" has a PSNR value of 23.33 [dB] using the DWT and 23.27 [dB] using the DLWT. In other words, for the case of "Lenna", the DLWT is better, but for the case of "Barbara", the DWT is slightly better. This may be due to differences in the frequency components of the images. These results suggest that the directional property of the DLWT is effective for images with low frequency components, but not good for images with high frequency components.

To confirm this, we conducted further experiments using other test images similar to Lenna and Barbara. Table 1 lists the PSNR values for all test images. In order to ignore the effects of boundaries processing, we also evaluated the images with their pixels at the borders cropped, because the DLWT is calculated across multiple boundary pixels. We set these images to have a periodic boundary condition. The results summarized in Table 1

(a) (b) (c)

Figure 1: Results of denoising. (a) Original, (b) DWT and (c) DLWT.

show that the DLWT outperforms DWT for images that do not have many high frequency components, such as “Lenna”, “Peppers” and “Woman”. On the other hand, “Mandrill”, which contains a relatively large number of high-frequency components, shows a similar kind of result as the “Barbara” case.

4. Conclusion

In this paper, we investigated the image denoising properties of the DLWT. Through numerical experiments with a variety of images, we have confirmed that our method outperforms the conventional wavelet-based method in cases where the images do not have many high frequency components. We used here a simple denoising method with hard thresholding, but more complex methods and comparisons with state-of-the-art methods will be the subject of future work.

Acknowledgment

The present work was partially supported by JSPS KAKENHI (Grant Number 21K11945).

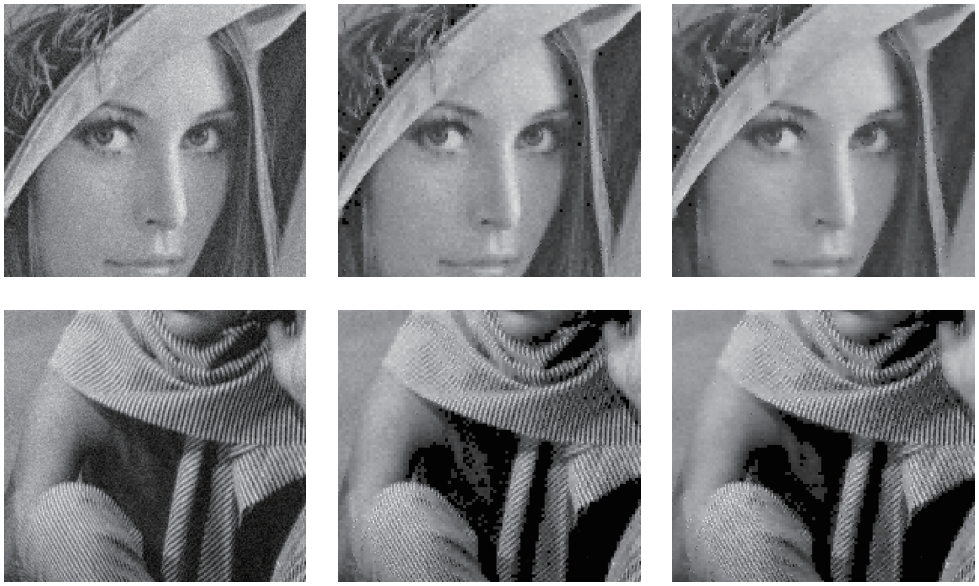

(a) (b) (c)

Figure 2: Zoomed-in results of denoising. (a) Original, (b) DWT and (c) DLWT.

Table 1: The PSNR [dB] for reconstructed images.

	Lenna	Peppers	Woman	Barbara	Mandrill
DWT	30.20	25.65	28.17	23.33	24.64
DWT (cropped)	30.39	25.83	28.65	23.47	24.79
DLWT	30.68	25.84	28.34	23.27	24.36
DLWT (cropped)	30.86	25.99	28.50	23.40	24.50

References

[1] K. Fujinoki and K. Ashizawa, Directional redundant polyphase transforms, in: Proc. of the 13th International Conference on Wavelet Analysis and Pattern Recognition (ICWAPR 2016), 258–263, Jeju Island, South Korea, July 2016.

[2] K. Fujinoki and K. Ashizawa, A lapped directional wavelet transform based on B-splines, in: Proc. of the 14th International Conference on Wavelet Analysis and Pattern Recognition (ICWAPR 2017), 43–47, Ningbo, China, July 2017.

[3] W. Sweldens, The lifting scheme: a custom-design construction of biorthogonal wavelets, J. Appl. Comput. Harmon. Anal., **3** (1996), 186–200.

[4] D.L. Donoho and I.M. Johnstone, Ideal spatial adaptation via wavelet shrinkage, Biometrika, **81** (1994), pp. 425–455.

JSST 2022

A mixed-precision algorithm of the CG method using the group-wise update strategy

Kensuke Aihara[1,*], Katsuhisa Ozaki[2], Daichi Mukunoki[3]

[1]Department of Computer Science, Tokyo City University
[2]Department of Mathematical Sciences, Shibaura Institute of Technology
[3]RIKEN Center for Computational Science

[*]aiharak@tcu.ac.jp

Abstract. The conjugate gradient (CG) method is the most basic iterative solver for large sparse linear systems. In this study, we propose a mixed-precision algorithm of CG with a group-wise update strategy to improve the accuracy of the approximate solutions.

Keywords: linear systems, CG method, group-wise update, mixed-precision arithmetic

1. Introduction

We consider solving $A\boldsymbol{x} = \boldsymbol{b}$, where $A \in \mathbb{R}^{n\times n}$ is a large sparse and symmetric positive definite matrix and $\boldsymbol{b} \in \mathbb{R}^n$. The CG method is an effective and widely used iterative solver. However, in finite precision arithmetic, the error norms of CG often stagnate, particularly for ill-conditioned matrices, owing to rounding errors. The group-wise update strategy [1] is useful for improving the attainable accuracy in terms of the (true) residual norm; however, the error norms cannot be reduced when there is a severe loss of information in updating approximations. To overcome this problem, we propose a simple mixed-precision CG algorithm using a group-wise update strategy. In particular, we perform the underlying CG iterations with standard double precision and compute the parts of the group-wise update using high-precision arithmetic. The numerical experiments conducted in this study demonstrate that the proposed method avoids the stagnation of error norms and efficiently generates accurate approximate solutions.

2. Mixed-precision CG with the group-wise update

Suppose that the approximations and residuals are updated in the forms $\boldsymbol{x}_{k+1} = \boldsymbol{x}_k + \alpha_k \boldsymbol{p}_k$ and $\boldsymbol{r}_{k+1} = \boldsymbol{r}_k - \alpha_k A\boldsymbol{p}_k$, respectively. Then, the group-wise update is performed by $\hat{\boldsymbol{x}}_{\pi(j+1)} = \hat{\boldsymbol{x}}_{\pi(j)} + \boldsymbol{y}_j$ and $\hat{\boldsymbol{r}}_{\pi(j+1)} = \hat{\boldsymbol{r}}_{\pi(j)} - A\boldsymbol{y}_j$, where $\boldsymbol{y}_j := \alpha_{\pi(j)}\boldsymbol{p}_{\pi(j)} + \alpha_{\pi(j)+1}\boldsymbol{p}_{\pi(j)+1} + \cdots + \alpha_{k-1}\boldsymbol{p}_{k-1}$ for $k = \pi(j+1)$, and $\pi(j) \in \mathbb{N}$ ($\pi(0) := 0$) is an increasing sequence. The cumulative

Algorithm 1 Mixed-precision CG with the group-wise update

1: Select an initial guess $\boldsymbol{x}$.
2: Compute $\boldsymbol{r} = \boldsymbol{b} - A\boldsymbol{x}$ and $\rho_{old} = (\boldsymbol{r}, \boldsymbol{r})$, and set $\boldsymbol{p} = \boldsymbol{r}$.
3: Set $\hat{\boldsymbol{x}} = \mathrm{mp}(\boldsymbol{x})$ and $\hat{\boldsymbol{r}} = \mathrm{mp}(\boldsymbol{r})$. *% Define high precision vectors*
4: **for** $k = 1, 2, \ldots,$ until convergence **do**
5: $\quad \boldsymbol{w} = A\boldsymbol{p}, \quad \sigma = (\boldsymbol{p}, \boldsymbol{w}), \quad \alpha = \rho_{old}/\sigma, \quad \boldsymbol{x} = \boldsymbol{x} + \alpha\boldsymbol{p}, \quad \boldsymbol{r} = \boldsymbol{r} - \alpha\boldsymbol{w}$
6: $\quad$ **if** $\mod(k, m) == 0$ **then**
7: $\quad\quad \hat{\boldsymbol{x}} = \hat{\boldsymbol{x}} + \boldsymbol{x}, \quad \hat{\boldsymbol{r}} = \hat{\boldsymbol{r}} - A \cdot \mathrm{mp}(\boldsymbol{x}), \quad \boldsymbol{x} = \boldsymbol{0}, \quad \boldsymbol{r} = \mathrm{double}(\hat{\boldsymbol{r}})$
8: $\quad$ **end if**
9: $\quad \rho_{new} = (\boldsymbol{r}, \boldsymbol{r}), \quad \beta = \rho_{new}/\rho_{old}, \quad \boldsymbol{p} = \boldsymbol{r} + \beta\boldsymbol{p}, \quad \rho_{old} = \rho_{new}$
10: **end for**
11: $\boldsymbol{x} = \mathrm{double}(\hat{\boldsymbol{x}} + \boldsymbol{x})$

vector $\boldsymbol{y}_j$ (=: $\boldsymbol{x}^{(k)}$) is computed recursively as $\boldsymbol{x}^{(i+1)} = \boldsymbol{x}^{(i)} + \alpha_i \boldsymbol{p}_i$ with $\boldsymbol{x}^{(i)} := \boldsymbol{0}$ for $i = \pi(j), \pi(j) + 1, \ldots, k - 1$. For more details, see [1].

Algorithm 1 displays a mixed-precision CG combined with the group-wise update strategy, where the vectors with a hat symbol '^' and its associated calculations are implemented in high-precision arithmetic; the remaining parts are computed naively in double precision. Note that mp(·) and double(·) denote the results of converting the vector in parentheses to high and double precision, respectively. Lines 6–8 correspond to the group-wise update, and, for simplicity, we set $\pi(j) = jm$ for a predetermined constant m (e.g., $m = 10$) that implies a number of cumulative vectors.

A closely related mixed-precision algorithm using group-wise update was studied in [2]. However, the purpose and approach of these studies were different. In particular, low-precision arithmetic was leveraged to speed up the underlying CG iterations in the study by Clark, whereas our study partially applies high-precision arithmetic to the group-wise update to avoid the stagnation of error norms. In Algorithm 1, $\hat{\boldsymbol{x}}$ and $\hat{\boldsymbol{r}}$ can be computed with high relative accuracy. Moreover, we expect that the attainable accuracy of the approximate solutions in terms of the error norms is improved. Furthermore, despite requiring an additional sparse matrix–vector multiplication (with high precision) for every m iterations, our approach incurs only a small overhead on the computation time using Dot2 [3].

The details of the proposed approach and numerical results will be presented at the JSST2022 conference.

References

[1] G. L. G. Sleijpen, H. A. van der Vorst: Reliable updated residuals in hybrid Bi-CG methods, *Computing*, 56:2 (1996), 141–163.

[2] M. A. Clark, R. Babich, K. Barros, R. C. Brower, C. Rebbi: Solving lattice QCD systems of equations using mixed precision solvers on GPUs, *Computer Physics Communications*, 181:9 (2010), 1517–1528.

[3] T. Ogita, S. M. Rump, S. Oishi: Accurate sum and dot product, *SIAM Journal on Scientific Computing*, 26:6 (2005), 1955–1988.

JSST 2022

Numerical experiments for verified numerical computations for linear systems

Tomoki Aoyama[1,*] and Katsuhisa Ozaki[1]

[1]Department of Mathematical Sciences, Shibaura Institute of Technology

[*]bv19021@shibaura-it.ac.jp

Abstract. Verified numerical computations produce an error bound for an approximate solution. In this study, we focus on linear systems. We report the numerical behavior of iterative refinement with mixed-precision and tightness of the error bound from the verified numerical computations using a method generating linear systems with a coefficient matrix, solution vector, and right-hand side vector represented in floating-point numbers.

Keywords: Verified numerical computations, Linear systems, Iterative refinement

1. Introduction

Numerical computations use floating-point arithmetic, which causes problems of rounding errors because of finite-precision. We focus on the following linear systems:

$$Ax = b, \quad A \in \mathbb{R}^{n\times n}, \quad b \in \mathbb{R}^n, \quad \det(A) \neq 0. \tag{1}$$

If the accuracy of the approximate solution is unsatisfactory, iterative refinement is an effective method to improve accuracy (for example, see Chapter 12 in [1] and [2, 3]). A technique known as verified numerical computations [4] produces an error bound using numerical computations. We monitor the accuracy of the computed result using the iterative refinement and the tightness of the error bound from the verified numerical computations using a linear system whose exact solution is known in advance,

2. Test problems

Let $\mathbb{F}$ be a set of binary floating-point numbers defined in IEEE 754 [5]. We focus on the following case:

$$\frac{\max|x_i|}{\min|x_i|} \geq u^{-1}, \quad \min|x_i| \neq 0, \tag{2}$$

where u is the unit roundoff. Assume $A \in \mathbb{F}^{n\times n}$ and $x, b \in \mathbb{F}^n$. Because precision of floating-point numbers is finite, setting the case (2) is not trivial . We use Miyajima-Ogita-Oishi's

method [6] to generate a test set of (1) with (2). Let $\widehat{x}$ be an approximation of the linear system's solution (1). If $\widehat{x}$ is obtained using LU decomposition and forward and backward substitutions, the accuracy of the small element in x is unsatisfactory in many cases.

Let I be the identity matrix. If there exists a matrix R such that $\|RA - I\| < 1$, then A is nonsingular and

$$|A^{-1}b - \widehat{x}| \leq |R(b - A\widehat{x})| + \frac{\|R(b - A\widehat{x})\|_\infty}{1 - \|G\|_\infty}|G|e \tag{3}$$

is satisfied [7], where $G := RA - I$ and $e = (1, 1, \ldots, 1)^T$. Note that the notation $|\cdot|$ for a matrix and a vector indicates that we take the absolute value componentwise.

Numerical examples,

- monitoring the relative error using the iterative refinement with/without mixed-precision,
- checking the overestimation of the error bound based on (3), and
- checking the proper digits in high precision arithmetic [8] for the computation of the residual,

will be presented at the conference.

References

[1] N. J. Higham: Accuracy and Stability of Numerical Algorithms, 2nd ed, *SIAM*, Philadelphia, 2002.

[2] R. D. Skeel: Iterative refinement implies numerical stability for Gaussian elimination, *Math. Comp.*, 35:817–832, 1980.

[3] E. Carson, N. J. Higham: Accelerating the Solution of Linear Systems by Iterative Refinement in Three Precisions, *SIAM J. Sci. Comput.*, 40:A817-A847, 2018.

[4] S. M. Rump: Verification methods: Rigorous results using floating-point arithmetic, *Acta Numerica*, 19:287–449, 2010.

[5] IEEE Computer Society, IEEE Standard for Floating-Point Arithmetic (IEEE Std 754-2008), IEEE, 2008.

[6] S. Miyajima, T. Ogita, S. Oishi. A method of generating linear systems with an arbitrarily ill-conditioned matrix and an arbitrary solution, Proc. 2005 International Symposium on Nonlinear Theory and its Applications (NOLTA 2005), pp. 741-744, 2005.

[7] T. Yamamoto: Error bounds for approximate solutions of systems of equations, *Japan J. Appl. Math.*, 1:157–171, 1984.

[8] Advanpix: Multiprecision Computing Toolbox for MATLAB. `https://www.advanpix.com/`

Molecular Dynamics Simulation on Hydrogen Trapping on Tungsten Vacancy

Hiroaki Nakamura[1,2,*], Kazuki Takasan[2,†], Miyuki Yajima[1], Seiki Saito[1,3]

[1]National Institute for Fusion Science
[2]Nagoya University
[3]Yamagata University

[*]hnakamura@nifs.ac.jp, [†]present address:Shiga University

The full paper of this paper has been published in Journal of Advanced Simulation in Science and Engineering (JASSE).

DOI: https://doi.org/10.15748/jasse.10.132

Investigation of hydrogen recycling on tungsten divertor by molecular dynamics simulation

Yuki Kojima [1], Seiki Saito [1*], Hiroaki Nakamura [2,3], Keiji Sawada [4], Kazuo Hoshino[5]
Masahiro Kobayashi [2,6] Masahiro Hasuo [7]

[1] Department of Information and Electronics
, Graduate School of Science and Engineering , Yamagata University
[2] Department of Helical Plasma Research, National Institude for Fusion Science
[3] Department of Electrical Engineering, Graduate School of Engineering, Nagoya University
[4] Department of Material System Engineering, Faculty of Engineering, Shinsyu University
[5] Department of Applied Physics and Physico-Informatics, Fuculty of Science and Technology, Keio University
[6] Department of Fusion Science, Physical Sciences Research Section, The Graduate University for Adcanced Studies
[7] Department of Mechanical Engineering and Science, Graduate School of Engineering, Kyoto University

[*]**saitos@yz.yamagata-u.ac.jp**

Abstract.

We developed a hydrogen recycling model on tungsten divertor by molecular dynamics simulation. In this model, numerical simulation of one hydrogen atom injection into a tungsten material is performed. NVE ensemble, in which the number of particles (N), volume (V), and energy (E) is adapted for calculation of motion of atoms in the tungsten target material. As a result, the hydrogen molecules in relatively high viblational and rotational states are observed.

Keywords: Molecular dynamics simulation, Recycling, Nuclear fusion.

1. Introduction

Plasma facing materials are bombarded by hydrogen plasma in magnetic confinement plasma devices such as ITER in France. In the case of ITER, the divertor which directly contacts to plasma is made of tungsten materials. Because heat flux density to the divertor is expected 10 MW/m^2, detached plasma (DP) is suggested to control heat load method. However, behavior of edge plasma is not well understood. To understand it, the neutral transport code which calculates the process of neutral particles process is solved. When the divertor plates are irradiated by plasmas and particles, some hydrogen molecules are emitted with high rotational and viblatonal states. In the neutral particle transport process, the value of rotational and vibrational states of hydrogen molecules is important information because it affects behavior of particles of edge plasma region. However, there is no neutral transport code dealing with both rotational and vibrational states. Therefore, we develop the calculation model of recycling hydrogen atoms

and molecules by molecular dynamics (MD) simulation [1-4] and calculate the distribution of rotational and viblational states of emitted hydrogen molecules.

2. Simulation method

To calculate the rotational and vibrational states, potential energy of hydrogen molecule is used. However, Figure 1 shows that EAM (Embedded Atoms Model) potential [5] is less accurate than the ideal potential of hydrogen molecule. Therefore, we switch the potential energy of hydrogen molecular from the EAM potential to ideal potential [6] at the intersection of two potentials. In addition, to calculate the distribution of rotational and viblational states of emitted hydrogen molecules, the result of MD simulation is needed to convert to the quantum value because MD simulation deals with the value of classical dynamics [7].

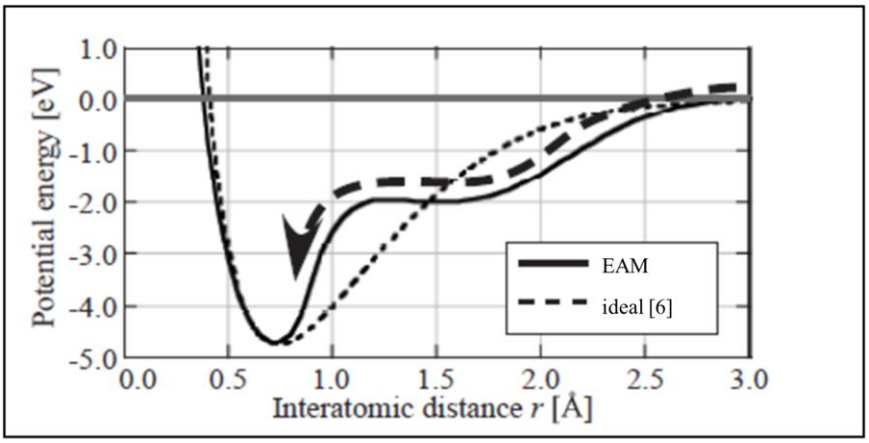

Fig. 1 : Graph of EAM potential (Classic) and ideal potential of hydrogen molecule. [4]

3. Simulation results

Figure 2 shows the distribution of rotational and vibrational states of hydrogen molecules. Vartical axis is the value of the number of emitted hydrogen molecules divided by the number of simulations. Horizontal axis is the value of rotational and vibrational states, respectively. Increasing the value of the number of hydrogen molcules are divided by the number of tungsten atoms (H/W) and the value of the incident energy, the number of emitted hydrogen molecules is increase and high rotational and vibrational states of emitted hydrogen is increase. Therefore, this result means that the value of rotational and vibrational states of hydrogen molecules cannot be ignored to calculate the neutral transport code because the value of rate coefficient of molecular assisted recombination process is increased as the value of rotational and vibrational states are increased [8].

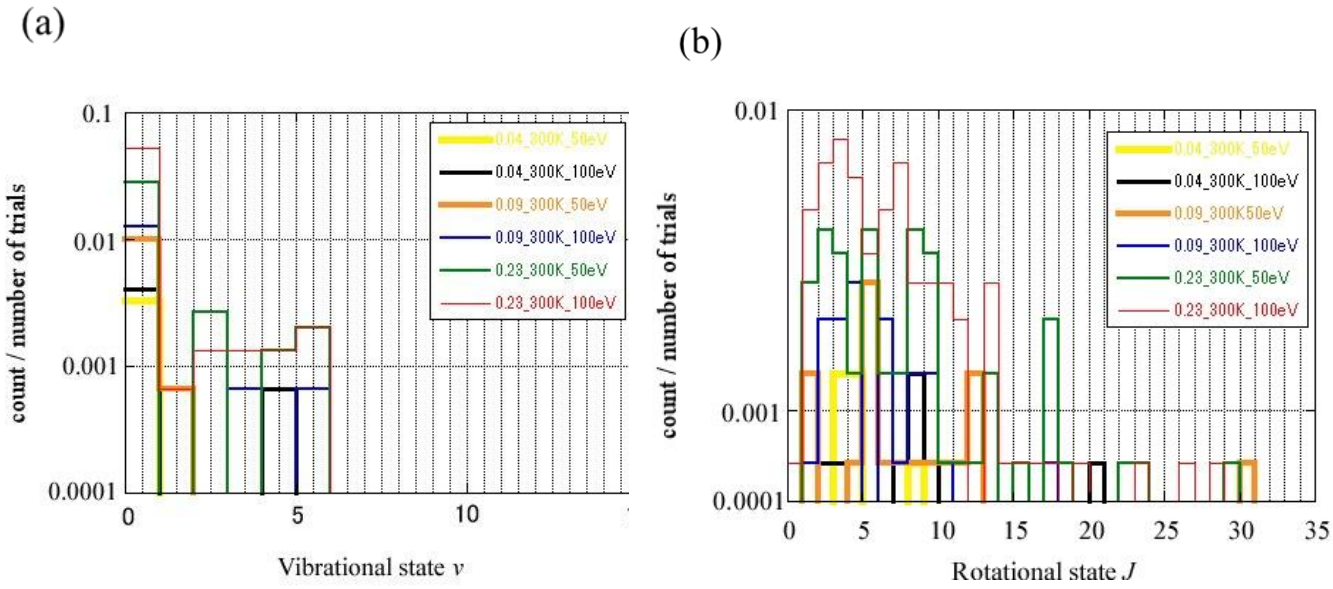

Fig. 2 : Distribution of rotational (a) and vibrational (b) states.

Acknowledgment

The research was partially supported by Grant-in-Aid for Scientific Research, No.22K03572 from the Japan Society for the Promotion of Science, and by the NIFS Collaborative Research Program NIFS20KUTR158, NIFS22KISS021 and NIFS22KIGS002. The computations were performed using the JFRS-1 supercomputer system at Computational Simulation Centre of International Fusion Energy Research Centre (IFERC-CSC) in Rokkasho Fusion Institute of QST (Aomori, Japan), Research Center for Computational Science (Okazaki, Aichi, Japan) and Plasma Simulator of NIFS (Toki, Gifu, Japan) .

References

[1] S. Saito, H. Nakamura, K. Sawada, G. Kawamura, M. Kobayashi, M. Hasuo. Molecular dynamics simulation model of hydrogen recycling on carbon divertor for neutral transport analysis in large helical device. Contributions to Plasma Physics. 2020; e201900152.

[2] K. Sawada, H. Nakamura, S. Saito, G. Kawamura, M. Kobayashi, K. Haga, T. Sawada, and M. Hasuo, Contrib. Plasma Phys. e201900153 (2020).

[3] S. Saito, H. Nakamura, K. Sawada, G. Kawamura, M. Kobayashi, and M. Hasuo, Plasma Fusion Res. **15**, 2403073 (2020).

[4] S. Saito, H. Nakamura, K. Sawada, M. Kobayashi, G. Kawamura, T. Sawada, and H. Masahiro: *Molecular dynamics simulation for hydrogen recycling on tungsten divertor for neutral*

transport analysis, Jpn. J. Appl. Phys. **60** SAAB08 (2021).

[5] L. F. Wang, X. Shu, G. H. Lu. and F. Gao: Embedded-atom method potential for modeling hydrogen and hydrogen-defect interaction in tungsten, J. Phys. Condens. Matter 29, 435401 (2017).

[6] L. Wolniewicz: Nonadiabatic energies of the ground state of the hydrogen molecule, J. Chem. Phys. 103 1792 (1995).

[7] S. Saito, H. Nakamura, K. Sawada, G. Kawamura, M. Kobayashi, M. Hasuo: Molecular dynamics simulation model of hydrogen recycling on carbon divertor for neutral transport analysis in large helical device, Contributions to Plasma Physics, e201900152 (2020).

[8] K. Sawada, M. Goto : Rovibrationally Resolved Time-Dependent Collisional-Radiative Model of Molecular Hydrogen and Its Application to a Fusion Detached Plasma, Atoms, doi:10.3390/atoms4040029 (2016, 4, 29).

Full-torus simulation of the tungsten transport in the closed helical divertor region in the Large Helical Device using the three-dimensional plasma-wall interaction simulation code ERO2.0

Mamoru Shoji[1,2*], Gakushi Kawamura[1,2], Juri Romazanov[3], Andreas Kirschner[3], Suguru Masuzaki[1,2], Gen Motojima[1,2], Masahiro Kobayashi[1,2], Masayuki. Tokitani[1,2], Sebastijan. Brezinsek[3]

[1]Department of Helical Plasma Research, National Institute for Fusion Science
[2]The Graduate University for Advanced Studies (SOKENDAI)
[3]Forschungszentrum Jülich GmbH, Institut für Energie- und Klimaforschung - Plasmaphysik, Partner of the Trilateral Euregio Cluster (TEC)

*shohji.mamoru@nifs.ac.jp

Abstract. The tungsten transport in magnetic plasma confinement devices has been investigated using the three-dimensional Monte-Carlo plasma-wall interaction simulation code ERO2.0. This code was applied to the analysis of the tungsten transport in the peripheral plasma in the closed helical divertor region in the Large Helical Device (LHD) in which tungsten coated divertor plates were installed in the inboard side of the torus in one helical section. The full-torus simulation of tungsten transport using the ERO2.0 code showed the localization of the emission of neutral tungsten atoms in front of the tungsten coated divertor plates in the closed helical divertor region only in high temperature plasma discharge operational conditions. This is because the physical sputtering yield of tungsten due to intrinsic incident carbon ions in the peripheral plasma for low temperature plasma discharge conditions is significantly low. The emission rate of neutral tungsten atoms was integrated along the lines of sight of spectrometers for monitoring the plasma-wall interactions on the tungsten divertor plates, which enabled to compare the observed line integrated intensity profile with the ERO2.0 simulation.

Keywords: Tungsten transport, Monte-Carlo simulation, plasma-wall interaction, ERO2.0, Large Helical Device

1. Introduction

The investigation of tungsten transport in the magnetic plasma confinement devices has been a critical issue for evaluating the lifetime of the plasma-facing components (PFCs) and the tritium retention on the surface, etc [1]. In the Large Helical Device (LHD) [2], tungsten coated

divertor plates were installed in the inboard side of the torus in one helical section in a previous experimental campaign for investigating the tungsten transport in the peripheral plasma. After the experimental campaign, the tungsten coated layers were eroded on the surface of about half of the tungsten divertor plates. For analyzing the physical mechanism of the observed erosion of the tungsten layers, the three-dimensional Monte-Carlo plasma-wall interaction and impurity transport simulation code ERO2.0 was applied in LHD [3]. A full-torus three-dimensional grid model including the vacuum vessel and the PFCs was constructed for the simulation, in which the tungsten coated divertor plates were installed in one helical section with carbon divertor plates in the other helical section. The ERO2.0 code successfully reproduced the tungsten erosion profile on the tungsten coated divertor plates by the effect of the physical sputtering of tungsten by intrinsic carbon ions in the peripheral plasma in high temperature plasma discharge operational conditions [4]. To evaluate the ERO2.0 code from the viewpoint of the tungsten transport in the peripheral plasma, simulations of the tungsten density profile should be compared to the observations. Thus, the three-dimensional density profile of tungsten atoms and ions in the peripheral plasma was calculated by the code. The three-dimensional distribution of the rate of line emission from tungsten atoms and ions is obtained from the plasma parameters and calculated tungsten density profiles in the plasma. The plasma-wall interactions on the tungsten coated divertor plates have been monitored with a multi-channel spectrometer, which provided the measurements of the intensity profile of the line emission in front of the tungsten coated divertor plates. In the next section, the setup for calculating the intensity profile of the line emission using the ERO2.0 code is described in detail. The comparison of the simulations of the intensity profile with the measurements will evaluate the ERO2.0 code on the

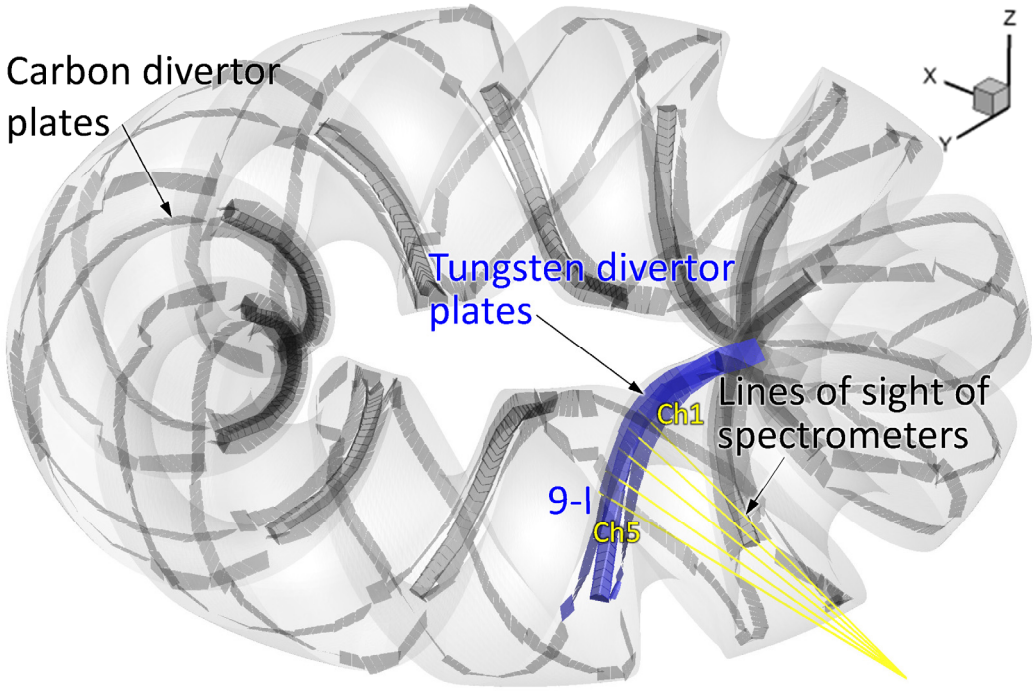

Figure 1: A full-torus three-dimensional grid model of the PFCs in the closed helical divertor region in the Large Helical Device for the ERO2.0 simulation. Yellow lines indicate the lines of sight of a multi-channel spectrometer viewing the tungsten coated divertor plates.

tungsten transport in the peripheral plasma.

2. Calculation of the intensity profile of the line emission from tungsten atoms in the closed helical divertor region

Figure 1 shows a full-torus three-dimensional grid model of the PFCs in the closed helical divertor region in LHD for the ERO2.0 simulation. In this model, tungsten divertor plates are set in one helical section in the inboard side of the torus as shown in transparent blue plates in this figure. Here, it was assumed that the other divertor plates and the surface of the vacuum vessel consisted of carbon. In the ERO2.0 simulation, the migration and transport of impurities such as tungsten and carbon are calculated by tracking the trajectories of test particles which are representative of the impurity atoms, ions, and molecules. The trajectories are calculated based on the database on the plasma-wall interactions by the SDTrimSP code [5] and atomic molecular processes by the Atomic Data and Analysis Structure (ADAS) [6]. Tungsten atoms are produced by the physical sputtering on the tungsten divertor plates caused by incident intrinsic carbon ions in the peripheral plasma, in which the carbon ions originate from the physical and chemical sputtering on the carbon divertor plates by the background deuterium plasma which profile is provided from the calculations by a three-dimensional edge plasma transport simulation code (EMC3-EIRENE) [7, 8]. For obtaining a steady-state solution of the density profile of tungsten atoms and ions in the peripheral plasma, a multiple iteration step calculation scheme implemented in ERO2.0 was adopted. In the 0th step, the test particles (carbons) are created by the background deuterium plasma on the carbon divertor plates. The trajectories of the test particles are tracked until it hits the surface of the vacuum vessel and the PFCs in the grid model, by which the total erosion profile is obtained by summing up the sputtering rate for all incident test particles on the surface. The additional sputtered particles in the previous step are included as new test particles in the next step. By repeating these steps, converged

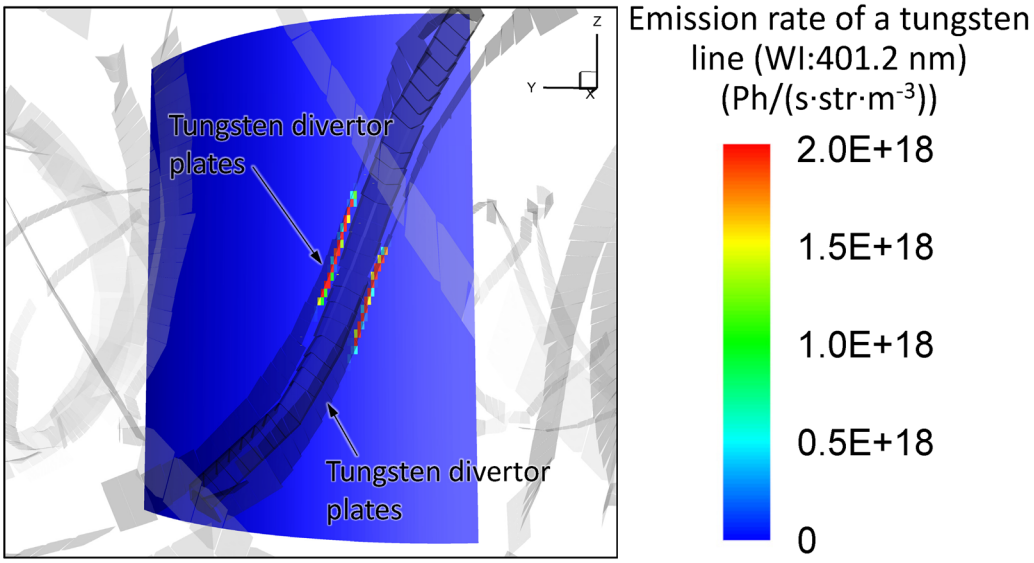

Figure 2: A perspective view of the simulation of the three-dimensional distribution of the line emission from tungsten atoms (WI) in the helical section where the tungsten coated divertor plates were installed in the inboard side of the torus.

carbon and tungsten erosion and deposition profiles are obtained, which consequently provides a steady-state solution of the three-dimensional density profile of tungsten atoms and ions in the peripheral plasma.

Figure 2 displays a perspective view of the simulation of the three-dimensional distribution of a line emission rate of tungsten atoms (WI) in the helical section where the tungsten coated divertor plates were installed for a typical high temperature plasma discharge (the plasma heating power P^{LCFS}=8 MW, and the plasma density $n_e^{LCFS}=1\times10^{19}$ m^{-3} at the Last Closed Flux Surface (LCFS)). The ERO2.0 simulation shows that the line emission is localized near the front of the surface of the tungsten divertor plates in the inboard side of the torus, which is because the first ionization electric potential of tungsten atoms (7.98 eV) is much lower than the typical electron temperature in the peripheral plasma (T_e~40 eV) near the divertor plates. The ERO2.0 simulation predicts that the line emission from neutral tungsten atoms will be observed only with the channel of the spectrometer which directly observes the front surface of the tungsten coated divertor plates.

Acknowledgment

This work was performed under the auspices of the NIFS Collaboration Research program (NIFS22KIST004). The author would like to thank Y. Feng for permission to use the EMC3-EIRENE. This work is also supported by JSPS KAKENHI Grant Numbers 21K18620, 19K03802, and 18H01203, and by the Numerical Simulation Reactor Research Project (NIFS11UNTT004).

References

[1] V. Philipps: Tungsten as material for plasma-facing components in fusion devices, *J. Nucl. Mater.*, 415 (2011), S2-S9.

[2] Y. Takeiri, T. Morisaki, M. Osakabe, et al.: Extension of the operational regime of the LHD towards a deuterium experiment, *Nucl. Fusion*, 57 (2017), 102023.

[3] J. Romazanov, S. Brezinsek, B. Borodin, et al.: Beryllium global erosion and deposition at JET-ILW simulated with ERO2.0, *Nucl. Mater. Energy*, 18 (2019), 331-338.

[4] M. Shoji, G. Kawamura, R. Smirnov, et al.: Full-torus impurity transport simulation for optimizing plasma discharge operation using a multi-species impurity powder dropper in the large helical device, *Contrib. Plasma Phys.*, 60 (2021), e201900101.

[5] W. Möller, W. Eckstein, J.P. Biersack, et al.: Tridyn-binary collision simulation of atomic collisions and dynamic composition changes in solids, *Comput. Phys. Commun.*, 51 (1988), 355-368.

[6] The ADAS User Manual (version 2.6) http://adas.phys.strath.ac.uk/ (2004).

[7] Y. Feng, F. Sardei, P. Grigull, et al.: Transport in island divertors: physics, 3D modelling and comparison to first experiments on W7-AS, *Plasma Phys. Control. Fusion*, 44 (2002), 611-625.

[8] G. Kawamura, Y. Feng, M. Kobayashi, et al.: First EMC3-EIRENE Simulations with Divertor Legs of LHD in Realistic Device Geometry, *Contrib. Plasma Phys.*, 54 (2014), 437-441.

High-Frequency Electromagnetic Field Analysis in Microwave Oven by Paralle Finite Element Method

Kento Ohnaka[1*], Amane Takei[2]

[1]Graduate School of Engineering, University of Miyazaki, Japan

[2]Faculty of Engineering, University of Miyazaki, Japan

[*]hl16004@student.miyazaki-u.ac.jp

Abstract. With a view to improving the performance of microwave ovens, we analyze the electromagnetic environment in a heating chamber using the ultra-large-scale high-frequency electromagnetic finite element analysis solver "ADVENTURE_FullWave". In this study, a simple model of a microwave oven is first used to analyze of electromagnetic field environment when the model is empty and when water is heated. The antenna is subjected to a large load during the heating process when that is empty, while the water absorbed the electromagnetic waves strongly during the water heating.

Keywords: High-frequency electromagnetic fields, Finite element analysis, Microwave oven

1. Introduction

Microwave ovens, which heat food by irradiating high-frequency electromagnetic waves at 2.45 GHz to resonate water molecules, are widely used as a familiar high-frequency electronic device because of their convenience. However, their high output makes direct measurement of the internal environment difficult. In response to this, we believe that the prediction of the electromagnetic field environment in the heating chamber by simulation using the high-frequency electromagnetic field finite element analysis solver “ADVENTURE_FullWave” will lead to more efficient heating and other developments toward higher-performance microwave ovens. In this study, a simple model of a microwave oven is used to obtain a guideline for the analysis.

2. Governing equations and algorithm for parallel computing

In ADVENTURE_Fullwave, the full-wave analysis based on an E method [1] is considered. $\mathbf{E}_{\mathrm{h}}$ and $\mathbf{J}_h$ are finite element approximations of electric field $\mathbf{E}$ [V/m] and current density $\mathbf{J}$ [A/m2], respectively. The permeability is given by $\mu = \mu_0\mu_r$ [H/m], μ_0 is the vacuum permeability [H/m], and μ_r is the relative permeability. The complex permittivity is given by $\varepsilon = \varepsilon_0\varepsilon_r - \sigma/j\omega$ [F/m], ε_0 is the vacuum permittivity [F/m], ε_r is the relative permittivity, and ω is the angular frequency [rad/s]. The following equation is the finite element equation to be solved:

$$\iiint_{\Omega} (1/\mu) rot\mathbf{E}_{\mathrm{h}} \cdot rot\mathbf{E}_{\mathrm{h}}{}^{*} dv - \omega^2 \iiint_{\Omega} \varepsilon \mathbf{E}_{\mathrm{h}} \cdot \mathbf{E}_{\mathrm{h}}{}^{*} dv = j\omega \iiint_{\Omega} \mathbf{J}_h \cdot \mathbf{E}_h{}^{*} dv. \quad (1)$$

The equation contains complex numbers and becomes a complex symmetric matrix. In the present study, the electric field $\mathbf{E}$, which is unknown, is obtained using the conjugate orthogonal conjugate gradient (COCG) method. The finite element approximation (1) is rewritten as $Ku = f$ by the coefficient matrix K, the unknown vector u, and the right-hand side vector f. Next, Ω is divided into N subdomains (Eq. (2)). Eq. (3) and (4) are obtained from Eq. (2).

$$\begin{bmatrix} K_{II}^{(1)} & 0 & 0 & K_{IB}^{(1)} R_B^{(1)\mathrm{T}} \\ 0 & \ddots & 0 & \vdots \\ & & K_{II}^{(N)} & K_{IB}^{(N)} R_B^{(N)\mathrm{T}} \\ 0 & 0 & & \\ R_B^{(1)} K_{IB}^{(1)\mathrm{T}} & \cdots & R_B^{(N)} K_{IB}^{(N)\mathrm{T}} & \sum_{i=1}^{\mathrm{N}} R_B^{(i)} K_{BB}^{(i)} R_B^{(i)\mathrm{T}} \end{bmatrix} \begin{bmatrix} u_I^{(1)} \\ \vdots \\ u_I^{(N)} \\ u_B \end{bmatrix} = \begin{bmatrix} f_I^{(1)} \\ \vdots \\ f_I^{(N)} \\ f_B \end{bmatrix} \quad (2)$$

$$K_{II}^{(i)} u_I^{(i)} = f_I^{(i)} - K_{IB}^{(i)} u_B^{(i)} \quad (i = 1, \ldots, N) \quad (3)$$

$$\left\{ \sum_{i=1}^{\mathrm{N}} R_B^{(i)} \left\{ K_{BB}^{(i)} - K_{IB}^{(i)\mathrm{T}} \left(K_{II}^{(i)} \right)^{-1} K_{IB}^{(i)} \right\} R_B^{(i)T} \right\} u_B = \sum_{i=1}^{\mathrm{N}} R_B^{(i)} \left\{ f_B^{(i)} - K_{IB}^{(i)T} \left(K_{II}^{(i)} \right)^{-1} f_I^{(i)} \right\} \quad (4)$$

where $f_B{}^{(i)}$ is the right-hand vector for u_B, and $\left(K_{II}^{(i)}\right)^{-1}$ is the inverse matrix of $K_{II}^{(i)}$. Equation (4) is referred to as an interface problem and is an equation for satisfying the continuity between domains in the domain decomposition method. For simplicity, rewrite equation (5) as follows:

$$Su_B = g, \qquad S = \sum_{i=1}^{N} R_B^{(i)} S^{(i)} R_B^{(i)T}, \quad S^{(i)} = K_{BB}^{(i)} - K_{IB}^{(i)T} \left(K_{II}^{(i)} \right)^{-1} K_{IB}^{(i)}. \quad (5)$$

3. Perform analysis using a simplified model

The analysis is performed using a typical household micro-wave oven model. The model consists of a 1 cm thick stainless steel housing, air, antenna, mug, and water. The computer used in this analysis is the PC cluster "Amaterus" owned by our laboratory. The computations are performed on 20-node (160-core) Intel Core i7-9700K 3.60GHz multi-core CPUs with 32 [GB] RAM per node. The compiler is gcc. MPI is used for the parallelization library. The simulation statistics are shown in Table 1. More details will be shown at the conference. And we will discuss numerical results.

Table 1 Simulation statistics

Frequency	2.45 [GHz]
Number of elements	2,144,346
Number of cores used	160
Elapsed time	109 [sec]
Number of iterations	4,000

References

[1] A.Takei, S.Sugimoto, M.Ogino, S.Yoshimura, H.Kanayama: Full wave analyses of electromagnetic fields with an iterative domain decomposition method, *IEEE Trans. on Magn.*, 46:8 (2010), 2860-2863.

3D magnetostatic FIT analysis of rotating magnetic field generator for orientation control of diamagnetic materials

Shuta Yanai[1], Yuka Takeuchi[1] , Atom Hamasaki[2], Hideki Kawaguchi[1*]

[1] Division of Information and Electronic Engineering, Muroran Institute of Technology.
[2] Shinshu University
*kawa@mmm.muroran-it.ac.jp

Abstract. The magnetic field orientation in diamagnetic materials is applied to reduce energy consumption in graphite preparation. Then it is known that magnetic field orientation can be done effectively to apply rotating magnetic field. For effectively control of the magnetic field orientation phenomenon, quadrupole rotating magnetic field generator has been developed. In this work, 3D finite integration technique(FIT) analysis of rotating magnetic field generator is presented to aim to improve the magnetic field generator to be better convenience.

Keywords: diamagnetic material, magnetic field orientation, 3D magnetostatic analysis, finite integration technique

1. Introduction

When a magnetic field is applied to diamagnetic materials with anisotropic magnetic susceptibility, the crystalline inside the materials are oriented in the direction of axis of easy magnetization. This phenomenon is called magnetic field orientation. When a rotating magnetic field is applied to the diamagnetic materials, both of the easiest and second easiest magnetization axes are aligned, and magnetic field orientation occurs efficiently. It is expected that the magnetic field orientation by a rotating magnetic field can improve the efficiency of the processing process in the production of graphite. In a typical conventional apparatus for generating the rotating magnetic field, a turntable is placed inside the Helmholtz coil. However, such the method involving mechanical moving parts have difficulties in flexible control of magnetic field distribution, and compatibility with heating systems having wiring. To solve such the difficulties, a method of electrically rotating the magnetic field using quadrupole magnets was proposed, and it was confirmed that the magnetic field appropriately rotates in the prototype device[3]. In this work, we present magnetic field analysis of triple poles rotating magnetic field generator to consider improvement of access of the diamagnetic material sample to the center of the rotating the magnetic field.

2. Quadru-pole and triple-pule rotating magnetic field generators

The quadrupole rotating magnetic field generator consists of four coil windings around magnetic poles[3]. The four poles face each other at the device center and are surrounded by an magnetic material outer frame to make closed magnetic circuit (Fig.1(a)). If currents are excited only on a pair of horizontal coils, magnetic field is generated horizontally at the center gap between the poles (Fig.1(b)). On the other hand, the currents are excited both on horizontal and vertical coils with ratios of $\sqrt{3}/2 : 1/2$ respectively, $30°$ oriented magnetic field is created at the center gap(Fig.1(c)). In addition, magnetic field oriented to any directions can be created by adjusting the coil currents. Then it is readily imagined that it is not easy to put diamagnetic material sample into the narrow center gap in Fig.1(a). To solve this difficulty in the access of the material sample, we here consider a triple-pole rotating magnetic field generator (Fig.2(a)). The magnetic field vectors distributions simulated by 3-D finite integration technique(FIT) for the triple-pole rotating magnetic field generator are indicated in Fig.2(b) and (c). Fig.2(b)shows horizontal magnetic field distribution and Fig.2(c) is for $30°$ orientation. It is confirmed that any directions of the magnetic field can be achieved to adjust the ratio of holizontal and vertical coil currents apporopriatly in the triple-pole magnetic field generator, but it is not easy to keep constant intensity of the magnetic field at the center. We need to do further investigation on detail current excitation method for creating uniform magnetic field constant and wide range for all field direction.

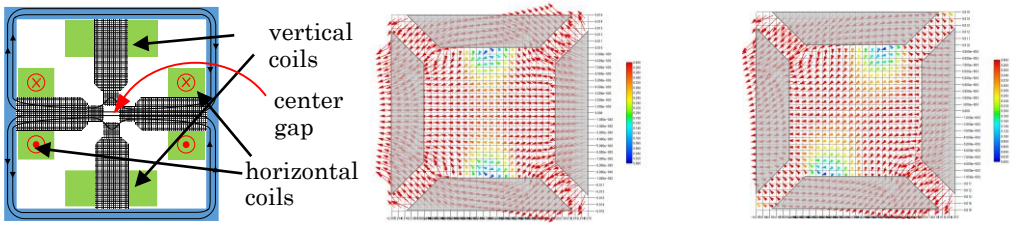

(a) quadrupole model (b) horizontal magnetic field (c)30° magnetic field

Fig.1 quadrupole rotating magnetic field generator

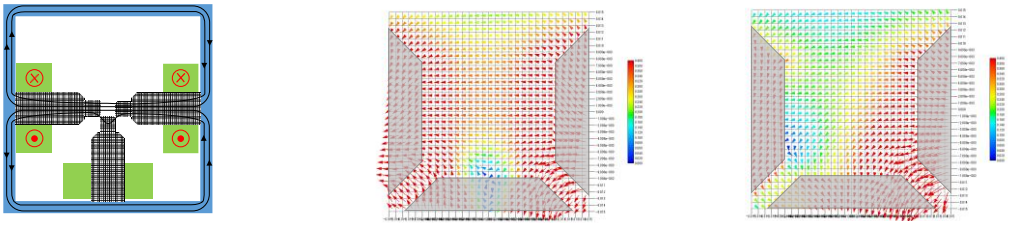

(a) triple-pole model (b) horizontal magnetic field (c)30° magnetic field

Fig.2 triple-pole rotating magnetic field generator

References

[1] A. Hamasaki, A. Furuse, Y. Sekinuma, K.Fujio, M.Iide, S.Ozeki: *Improving the Micropore Capacity of Activated Carbon by Preparation under a High Magnetic Field of 10 T*, Sci Rep.9,7489 (2019).

[2] F. Kimura, T. Kimura: *Magnetic alignment and patterning of cellulose fibers*, Sci Technol Adv Mater.9,024212 (2008).

[3] Y. Takeuchi, H. Kawaguchi, M. Matsuda, A. Hamasaki: : *Development of a quadrupole magnet for a mechanical-part-free rotational magnetic field*, Phys. Express 14,057002 (2008).

FE Analysis of Numerical Human Body Model with 100 Million DOFs in Electromagnetic Field – Heat Conduction Coupled Problem

Shin-ichiro Sugimoto[1*], Amane Takei[2], Masao Ogino[3]

[1]Department of Mechanical Engineering, Faculty of Engineering, Hachinohe Institute of Technology

[2]Department of Electrical and System Engineering, Faculty of Engineering, University of Miyazaki

[3]Department of Information Systems, Faculty of Informatics, Daido University

*sugimoto@hi-tech.ac.jp

Abstract. This paper deals with a high-frequency electromagnetic field - heat conduction coupled analysis of a numerical human body model in a parallel environment. The iterative substructuring method has been considered to be an efficient parallel computing method.

Keywords: High-Frequency Electromagnetic Field - Heat Conduction Coupled Analysis, Parallel Computing, Finite Element Method, Hierarchical Domain Decomposition Method, Numerical Human Body Model

1. Introduction

In order to evaluate an effect of cancer treatment by hyperthermia quantitatively, we have been studying its high-frequency electromagnetic field – heat conduction coupled analysis in a parallel environment. In our study, the NICT numerical human body model [1] is analyzed. This model uses a binary data format wherein types of organs are encoded using voxels with a size of 2 mm. However, the boundaries of its different materials are not smooth; thus, unwanted reflection and scattering of electric fields has been observed in numerical simulator results. To reduce this numerical noise, some mesh smoothing techniques with tetrahedral elements have been developed [2]. Furthermore, the diameters of cancers treated with hyperthermia are several millimeters. Therefore, elements must be refined to obtain sufficient accuracy. However, there are approximately 130 billion degrees of freedom (DOFs) provided that the element sizes are 0.25 mm. In addition, smoothing techniques increase the DOFs further.

The efficient parallel computing method for large-scale finite element analysis (FEA) that we have been studying is the iterative substructuring method in the form known as the domain decomposition method (DDM) based on the iterative method [3]. It is expected to obtain scalable parallel efficiency on distributed memory parallel computers with the implementation of a Hierarchical Domain Decomposition Method (HDDM) [4].

The HDDM has been applied to the large-scale FEA of structural mechanics [5], and heat transfer [6]. In structural analysis, the problem with 100 billion DOFs has been analyzed [7]. In addition, the HDDM has been applied to the large-scale FEA of electromagnetics [8]-[9], too. In recent years, it has been clarified that the conjugate orthogonal conjugate residual (COCR) method [10] is very effective for problems that involve symmetric systems with complex numbers and ill-conditioned systems [11]-[12]. Thus, in the electromagnetic field analysis, high-frequency electromagnetic field problems have been solved with 30 billion DOFs [11] and 130 billion DOFs [13]. These achievements have been implemented as a parallel electromagnetic field analysis module called ADVENTURE_Magnetic [14].

In order to analyze large-scale problems, the parallel analysis of the electromagnetic field problem has been mainly studied. As the next step, a parallel coupled analysis of the high-frequency electromagnetic field and the heat conduction problems is considered. In this paper, the numerical human body model involving 270 million DOFs is analyzed in the parallel environment.

2. High-Frequency Electromagnetic field – heat conduction coupled problem

Since the hyperthermia heats the human body from normal body temperature (36-37 degrees Celsius) to the temperature at which the cancer dies (42-43 degrees Celsius), the temperature change is only about 5 degrees; thus, changes in physical quantities related to the electromagnetic field analysis due to temperature are negligible. Therefore, in this paper, a one-way coupled analysis using the results of the electromagnetic field analysis for the heat conduction analysis is performed.

The numerical human body model is composed of voxels generated from tomographic images obtained by CT or MRI. Therefore, the boundaries of its different materials are not smooth; thus, unwanted reflection and scattering of electric fields has been observed in numerical simulator results. To reduce this numerical noise, some mesh smoothing techniques with tetrahedral elements will be used in the future; thus, the HDDM based on the finite element method is used for the numerical analysis, in this paper. Since the one-way coupled problem is considered, separate solvers are used for the electromagnetic field and heat conduction analyses. In this paper, ADVENTURE_Magnetic is used for the electromagnetic field analysis, and a parallel heat conduction analysis module called ADVENTURE_Thermal [14] is used for the heat conduction analysis.

3. Hierarchical Domain Decomposition Method (HDDM)

In the HDDM, an original domain Ω is divided without overlapping elements. Furthermore, the original domain is hierarchically divided into parts, which are further decomposed into smaller domains called subdomains.

$$\Omega = \bigcup_{i=0}^{N_p-1} \bigcup_{j=0}^{N_s-1} \Omega^{(i,j)}, \tag{1}$$

where $\Omega^{(i,j)}$ denotes the subdomain j in the part i, the superscript (i,j) corresponds to the subdomain $\Omega^{(i,j)}$. N_p and N_s are the number of parts and that of subdomains in each part, respectively. N_s is equal for all parts. In Fig. 1, the original domain is first divided into two parts, and then further decomposed into two subdomains within each part ($N_P = N_s = 2$). The

solid circles in the figure are the DOFs shared between parts and subdomains, which are called interface DOFs.

In the HDDM, the interface problem which is obtained by statically reducing DOFs to the interface DOFs is solved by the parallel iterative methods such as the Conjugate Gradient method and COCR method.

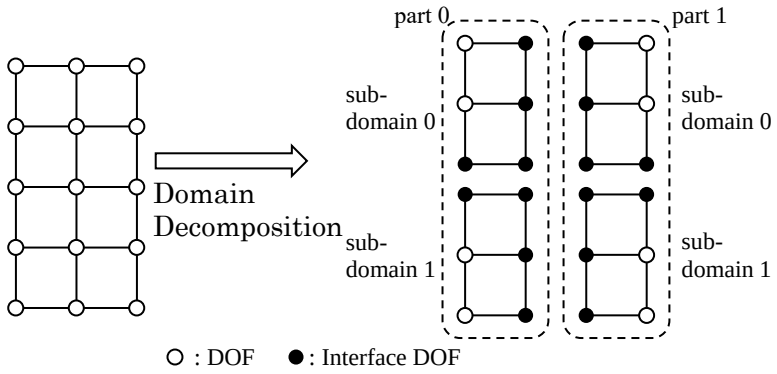

Fig. 1. Hierarchical domain decomposition.

4. Numerical example

The NICT numerical human body model involving 270 million DOFs provided that the element sizes are 2 mm (Fig. 2) is analyzed in parallel environment. Assumption of the treatment of the chest, the electromagnetic waves are emitted from the antenna in front of the chest. The physical quantities of each organ are quoted from [15] and [16]. Table 1 and Table 2 show physical quantities of typical organs.

Table 1. Physical quantities for the electromagnetic field analysis.

	Magnetic reluctivity [m/H]	Permittivity [F/m]	Conductor [S/m]
Heart	7.958e+05	5.627e-10	1.019e+00
Lung	7.958e+05	3.387e-10	4.520e-01
Liver	7.958e+05	4.441e-10	5.200e-01
Muscle	7.958e+05	5.041e-10	7.470e-01

Table 2. Physical quantities for the heat conduction analysis.

	Thermal conductivity [W/m℃]	Density [kg/m^3]	Specific heat [J/kg℃]
Heart	5.576e-01	1.081e+03	3.686e+03
Lung	3.874e-01	3.940e+02	3.886e+03
Liver	5.191e-01	1.079e+03	3.540e+03
Muscle	4.950e-01	1.090e+03	3.421e+03

Fig. 3 and Fig. 4 show the eddy current density and temperature distribution, respectively. It can be confirmed that the eddy current density around the heart near the antenna is strong, and temperature around the heart is rising.

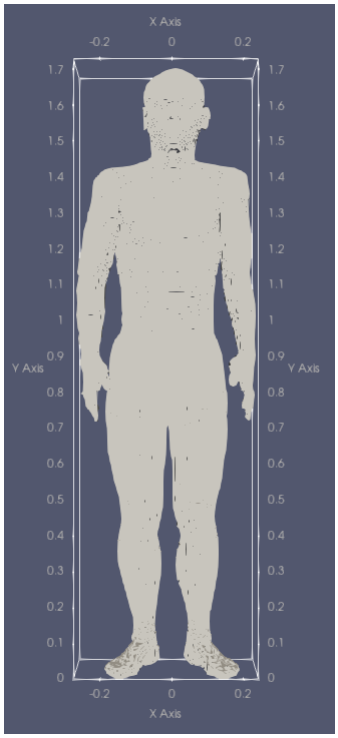

Fig. 2. Numerical human body model with 270 million DOFs.

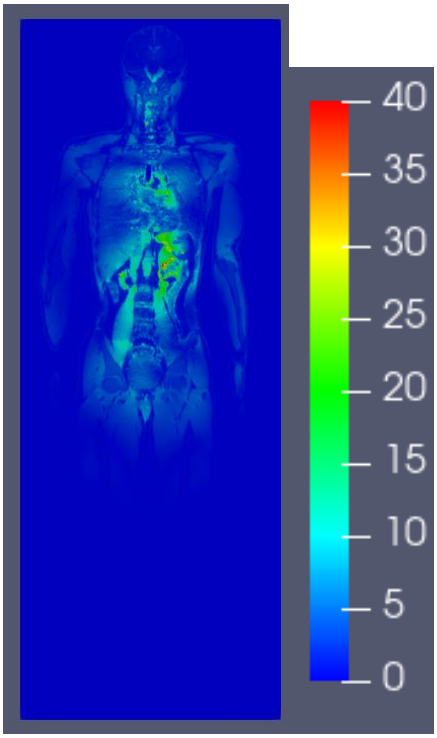

Fig. 3. Result of the electromagnetic field analysis. Eddy current density (real part) [A/m^2]

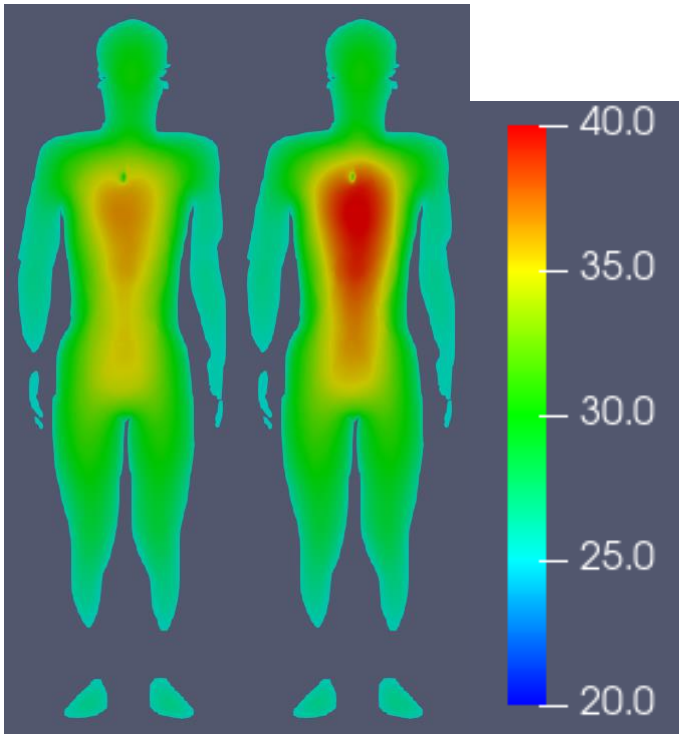

Fig. 4. Results of the heat conduction analysis (body temperature (degrees Celsius)). Left: without heating, Right with heating.

5. Conclusions

In this paper, the high-frequency electromagnetic field – heat conduction coupled analysis of the numerical human body model involving 270 million DOFs provided that the element sizes are 2 mm has been attempted in the parallel environment. In the future, the analysis of larger models and the analysis considering the influence of blood flow will be tried.

Acknowledgment

This work is partially supported by Takahashi Industrial and Economic Research Foundation, and JSPS KAKENHI Grant Number 17H02829 and 22H03605.

References

[1] Electromagnetic Compatibility Laboratory, Applied Electromagnetic Research Institute, National Institute of Information and Communications Technology HP: http://emc.nict.go.jp/index_e.html

[2] A. Takei, K. Murotani, S. Sugimoto, M. Ogino, H. Kawai: High-Accuracy Electromagnetic Field Simulation using Numerical Human Body Models, *IEEE Transaction on Magnetics*, Vol.52, Issue 3, 7402704 (2016), 4p.

[3] A. Quarteroni, A. Valli: Domain Decomposition Methods for Partial Differential Equations, *Clarendon Press, Oxford* (1999).

[4] R. Shioya, G. Yagawa: Iterative domain decomposition FEM with preconditioning technique for large scale problem, *ECM'99 Progress in Experimental and Computational Mechanics in Engineering and Material Behaviour* (1999), pp.255-260.

[5] S. Yoshimura, R. Shioya, H. Noguchi, T. Miyamura: Advanced general-purpose computational mechanics system for large-scale analysis and design, *Journal of Computational and Applied Mathematics*, Vol.149, Issue 1 (2002), pp.279-296.

[6] A.M.M. Mukaddes, M. Ogino, M, H. Kanayama, R. Shioya: A scalable balancing domain decomposition based preconditioner for large scale heat transfer problems, *JSME International Journal Series B Fluids and Thermal Engineering*, Vol,49, No.2 (2006), pp.533-540.

[7] M. Ogino, R. Shioya: Scalable non-overlapping domain decomposition method for finite element simulations with 100 billion degrees of freedom model, *Proceedings of the 1st International Conference on Computational Engineering and Science for Safety and Environmental problems* (2014), pp.96-99.

[8] H. Kanayama, S. Sugimoto: Effectiveness of A-ϕ method in a parallel computing with an iterative domain decomposition method, *IEEE Transactions on Magnetics*, Vol.42, Issue 4 (2006), pp.539-542.

[9] A. Takei, S. Yoshimura, H. Kanayama: Large-scale parallel finite element analyses of high frequency electromagnetic field in commuter trains, *Computer Modeling in Engineering & Sciences*, Vol.31, No.1 (2008), pp.13-24.

[10] T. Sogabe, S.L. Zhang: A COCR method for solving complex symmetric linear systems,

Journal of Computational and Applied Mechanics, Vol.199, No.2 (2007), pp.297-303.

[11] S. Sugimoto, A. Takei, M. Ogino: Finite Element Analysis with Tens of Billions of Degrees of Freedom in A High-Frequency Electromagnetic Field, *Mechanical Engineering Letters*, Vol.3, p.16-0067 (2017), 10p.

[12] M. Ogino, A. Takei, H. Notsu, S. Sugimoto, S. Yoshimura: Finite element analysis of high frequency electromagnetic fields using a domain decomposition method based on the COCR method, *Theoretical and Applied Mechanics Japan*, Vol.61 (2013), pp.173-181.

[13] S. Sugimoto, A. Takei, M. Ogino: High-Frequency Electromagnetic Field Analysis with 130 Billion of Degrees of Freedom, *The 38th JSST Annual Conference, International Conference on Simulation Technology*, (2019), pp.290-295.

[14] ADVENTURE Project HP: https://adventure.sys.t.u-tokyo.ac.jp/

[15] Human organs property Database for Computer simulation, RIKEN: http://cfd-duo.riken.go.jp/cbms-mp/index.htm

[16] Tissue Properties Database V4.0: https://itis.swiss/virtual-population/tissue-properties/downloads/database-v4-0/

JSST 2022

Optical Vortex Analysis Using Empirical Mode Decomposition

Ran Dong[1,*], Yoshihisa Fujita[2], Hiroaki Nakamura[3],
Hideki Kawaguchi[4], Soichiro Ikuno[1]

[1]School of Computer Science, Tokyo University of Technology
[2]College of Information Science and Engineering, Ritsumeikan University
[3]Department of Helical Plasma Research, National Institute for Fusion Science
[4]Department of Information and Electronic Engineering, Muroran Institute of Technology

[*]randong@stf.teu.ac.jp

Abstract. Many studies have been focused on optical vortex due to its critical priorities in the plasma and fusion fields. In this study, to investigate the optical priorities of a generated optical vortex, we simulated the optical vortex by inputting HE_{11} mode through a helical lens. Moreover, we also adopted the empirical mode decomposition to analyze simulation results in the spatial frequency domain to verify the simulated optical vortex. Our results revealed that decomposed frequency components correspond to the phase distribution, providing detail to estimate orbital angular momentum for evaluation.

Keywords: Optical vortex, Finite-difference time-domain, Empirical mode decomposition

1. Introduction

The optical vortex was discovered in 1992 [1], and much research focused on it, such as generating optical vortexes using a spiral phase plate as the filterer [2]. However, synthesizing optical vortex using filters may occur in reflection that is difficult to verify.

In this study, we apply a helical lens as a filter to generate an optical vortex from HE_{11} mode based on [2], as shown in Fig. 1 (a). To verify the generated optical vortex, we adopt the empirical mode decomposition (EMD) to decompose the simulation result obtained by the finite-difference time-domain (FDTD) method. Then, the generated optical vortex could be estimated by decomposing the electric field intensity in the spatial frequency domain.

2. Bidimensional empirical mode decomposition

EMD is proposed for analyzing the nonlinear properties of the time series data. After nonlinearly decomposing data into several monochromatic waves, so-called intrinsic mode functions (IMFs), and one residual, the nonlinear properties of each IMF and the residual can be investigated with their physical meanings.

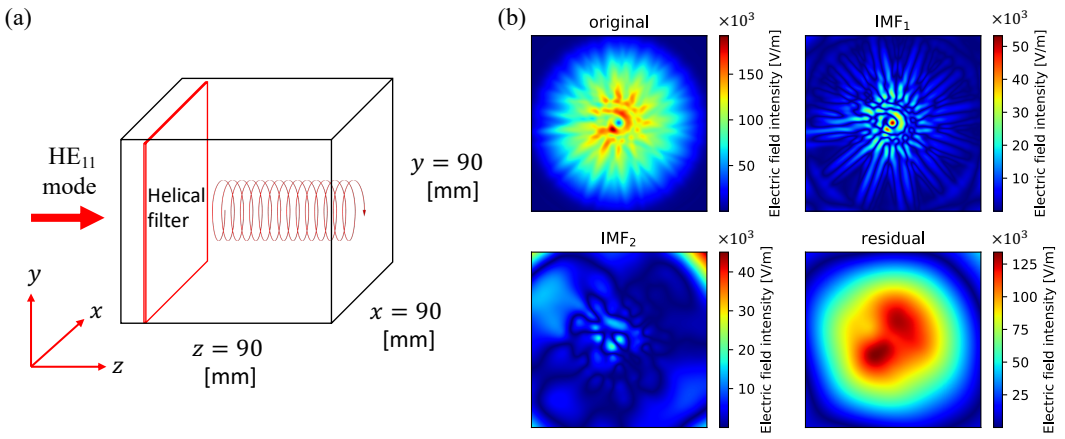

Figure 1: Optical vortex analysis of x - y plane in spacial frequency domain. (a) 3-D FDTD simulation model. (b) BEMD decomposition result where $t = 14.89$ [ns].

Unlike EMD analyzes data in the time-frequency domain, bidimensional empirical mode decomposition (BEMD) performs spatial frequency analysis [3]. In this study, we apply BEMD to the electric field intensity, investigating and verifying the generated optical vortex.

3. Optical vortex analysis

Figure 1 (a) shows simulation results by FDTD plotted from x-y plane labeled as original. Additionally, two decomposition IMFs and one residual also demonstrated in Fig. 1 (b).

The original was difficult to confirm if the optical vortex had been generated correctly due to the reflection. In contrast, IMF_1 and IMF_2 extracted these reflections and clearly remained the residual as the wave interference. Since the residual has no local extremum, the distribution of the phase of the generated optical vortex was correctly decomposed from the original. Thus, our results could be applied to estimate the orbital angular momentum l of the Laguerre-Gaussian beam. Other detailed results will be shown at the conference.

References

[1] L. Allen, M. W. Beijersbergen, R. J. C. Spreeuw, J. P. Woerdman: Orbital angular momentum of light and the transformation of Laguerre-Gaussian laser modes. *Physical review A*, 45:11 (1992), 8185-8189.

[2] A. E. Willner: Communication with a twist, *IEEE Spectrum*, 53:8 (2016), 34-39.

[3] J. C. Nunes, Y. Bouaoune, E. Delechelle, O. Niang, P. Bunel: Image analysis by bidimensional empirical mode decomposition. *Image and vision computing*, 21:12 (2003), 1019-1026.

A Design of Smart Glasses-based Gesture Recognition and Translation System for Sign Languages

Chu Zhang[1*], Bo Wu[1], Kiminori Sato[1]

[1]School of Computer Science, Tokyo University of Technology, Hachioji, Japan

*g2122019df@edu.teu.ac.jp

Abstract. Sign languages are not understood by most people with no hearing disabilities. Therefore, translation systems for sign languages to written or spoken languages are useful. However, existing software and hardware that can translate sign languages are very difficult to carry and use. Smart glasses are becoming increasingly widespread, and with the development of software and hardware, they have become capable of recognizing hand movements. Therefore, this study attempts to propose a real-time translation system based on smart glasses with an Android OS, to facilitate better communication with deaf people. When the user puts on the smart glasses, the sign language gestures can be translated in to written language, in real-time, in the smart glasses. This will make it smoother and easier for the people who are not versed in sign languages to communicate with the deaf people. The results will improve the functions of smart glasses and contribute to the development of the communication systems for the deaf people.

Keywords: Smart glasses, Gestures recognition system, Deaf people support, Sign language translation

1. Introduction

With the development of wearable technology, smart glasses have become more popular and commonplace. Because the vast majority of smart glasses comes with front facing cameras, image recognition technologies can be directly applied to smart glasses [1]. Many previous studies have focused on the use of image recognition technologies based on the front camera of smart glasses. For example. Gao et. al. has provided a smart glasses-based warning system that identifies and takes precautions against people who are not wearing face masks [2]. Smart glasses as a device that can be equipped with image recognition technologies, the relevant research is of great significance to the development of wearable devices.

The most common form of communication for deaf people is sign language. However, most people with no hearing disabilities do not have the opportunity to fully understand most of the implications of sign language. In the daily life of the general public, sign languages are only seen on television news, which means that it is difficult for the most people to communicate normally with deaf people. Therefore, it is very important and necessary to develop a device

that can directly translate the sign languages.

Some previous sign-language-related research has focused on the analysis and translation of sign language for the deaf. For example, Huang et. al. has provided a leap motion-based sign language dialogue system, which can connect to a healing dialogue robot for the related mental therapy and sign language interpretation [3]. M. Ahmed et. al. has provided a Kinect V2 based 3D animated sign language translation system, which can translate the sign language from deaf people [4]. However, there is a lack of more intuitive systems for recognizing and interpreting sign languages. In particular, devices such as smart phones, which are used for recognition and translation of sign languages, the portability and intuitiveness are not very strong. A system which can provide real-time translation of sign language to written language is needed.

Based on the use of the latest, highly configurable smart glasses, and related recognition & translation technologies, this study attempts to propose an Android-based system to facilitate the communication with deaf people more smoothly. The algorithm, named YOLO [5], is used for related gesture identification. Unlike the traditional recognition algorithms, YOLO's prediction is based on an entire image, which simultaneously outputs all the target information detected, including category and location. The results of this study will contribute to the construct of smart glasses-based system in the field of recognition and provide ideas for the development of the future translation applications.

2. Research Methodology

In this study, the EPSON smart glasses (BT-40s) were chosen as the system carrier. This is because the device has a transparent, high resolution, and high brightness display, which can provide clear and colorful information to user, with minimum disruption of the view. The BT-40s is also equipped with 2-core CPU, 2 GB of RAM, and 6 hours of battery life. Based on our system, we plan to use the transparent screen of BT-40s smart glasses to realize the real-time recognition & translation function of sign language. Since the operating system of BT-40s is Android OS, this study will use the Android APIs (Ver.5.1) with the program language for related development.

For the image recognition, YOLO algorithm will be used. YOLO is characterized by its speed, because it uses regression approach and does not use a complex framework [6]. Since YOLO can identify multiple targets at once, it can be used to identify all targets (hands used for of sign language) from the front facing camera of the smart glasses. In this research, smart glasses can be used to translate sign languages from multiple people simultaneously, which can be used to deal with situations where the wearer of the smart glasses is communicating with multiple sign language users. When a person uses sign language, the smart glasses with YOLO can automatically help the wearer to recognize the person’s hand movements and interpret the gestures into a set of easily understandable captions in real-time.

Our system will be secondarily developed on a similar recognition system via Android and YOLO method. As shown in Fig. 1, the system flow chart is as follows, including four important modules:

Image acquisition module. The image acquisition unit captures the image. After the preprocessing unit, the image is converted to computer-identifiable data. Finally, the data is transmitted to the image recognition unit through the data transmission unit.

Image processing module. The image recognition unit receives data from the image acquisition module and data from the data storage center module. The data is constructed in three

dimensions. The image of the data processing currency is constructed, and then the text is matched according to the data from the library. And finally, the text is displayed in the three-dimensional display unit.

Data storage center module. User can also process photos stored in smart glasses for image information processing.

Sound playback module. Information converted from the image is then broadcasted over the sound system in the form of sound. The study could also provide services for blind people.

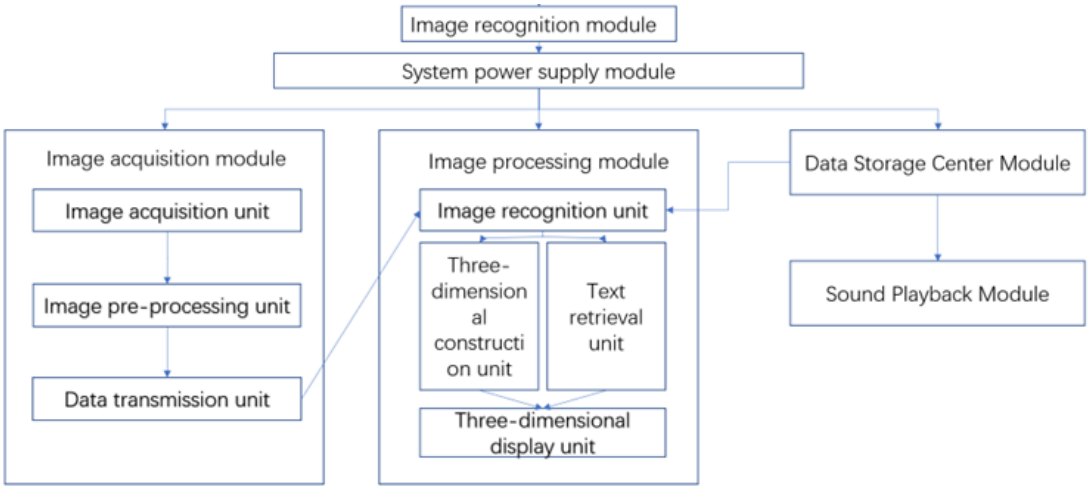

Fig. 1. The pre-braking behaviors in this study

Whole process of the system is described as follows: AR camera of the smart glasses captures the hand gesture image. The image is imported to the image processing module, which converts the image data into computer-recognizable form. Data is then passed to pre-trained YOLO, which matches the hand gesture with the corresponding translation. If the sign language is entered incorrectly, the word "Unrecognized" will be displayed in the smart glasses.

3. Result

With the completion of this system, targeted use of smart glasses will be easier and more practical. Bulky extra storage device for smart glasses can be removed. When the user is interacting with deaf people, not knowing sign languages will no longer be an issue. And pulling out a phone to look up what the sign language means will be unnecessary. This will increase the utilization of smart glasses in the lives of people surrounding deaf people.

The system can be optimized with a camera with higher resolution. This is because a good high-definition camera can more clearly identify the subtle differences in forms of the gestures, and therefore it will increase the number gesture the system can identify. Faster processors can also improve the whole process, because running the YOLO algorithm and the image processing in real-time requires a high processing power.

For the study, YOLO algorithm was trained with sign language hand gestures in advance. To improve gesture recognition accuracy, sample size of training data should be increased to include diverse variations of hand gestures. Since all person's hands are different, large number of hand samples are required in order to reduce errors and improve accuracy of the recognition capabilities of the system.

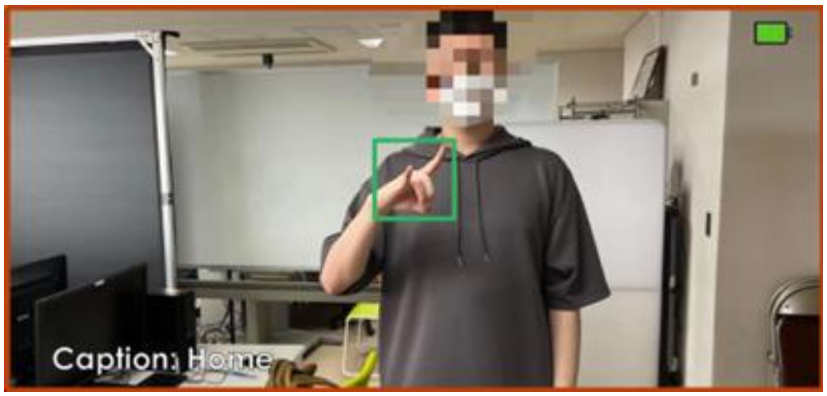

Fig. 2. The pre-braking behaviors in this study

4. Conclusion

In this hypothetical study, we designed a new sign-language interpretation system based on smart glasses and an Android OS. The system uses YOLO image recognition algorithm to recognize the image and translates the hand gestures into written language in real-time. The results of the study can provide guidance for the development of barrier-free communication and provide useful inspiration for the support of disabled people, and the people surrounding them. The system will be updated in future to provide additional services.

References

[1] N. M. Kumar, N. Kumar Singh and V. K. Peddiny, "Wearable Smart Glass: Features, Applications, Current Progress and Challenges," 2018 Second International Conference on Green Computing and Internet of Things (ICGCIoT), 2018, pp. 577-582

[2] J. Gao, B. Wu and K. Sato, "A Wearable Warning System Design for Mask Recognition via AR Smart Glasses," 2021 IEEE Intl Conf on Cyber Science and Technology Congress (DASC/PiCom/CBDCom/CyberSciTech), 2021, pp. 896-900

[3] X. Huang, B. Wu and H. Kameda, "Development of a Sign Language Dialogue System for a Healing Dialogue Robot," 2021 IEEE Intl Conf on Cyber Science and Technology Congress (DASC/PiCom/CBDCom/CyberSciTech), 2021, pp. 867-872

[4] X. Huang, B. Wu and H. Kameda, "Development of a Sign Language Dialogue System for a Healing Dialogue Robot," 2021 IEEE Intl Conf on Cyber Science and Technology Congress (DASC/PiCom/CBDCom/CyberSciTech), 2021, pp. 867-872

[5] Redmon, J., Divvala, S., Girshick, R., & Farhadi, A.. "You only look once: Unified, real-time object detection. " In Proceedings of the IEEE conference on computer vision and pattern recognition 2016, pp. 779-788

Numerical Approach to Enhanced-Performance of Superconducting Linear Accelerator Using Multiple-Electromagnets

Teruou Takayama[1,*], Ayumu Saitoh[1], Atsushi Kamitani[1]

[1]Graduate School of Science and Engineering, Yamagata University, Japan

[*]takayama@yz.yamagata-u.ac.jp

The full paper of this paper has been published in Journal of Advanced Simulation in Science and Engineering (JASSE).

DOI: https://doi.org/10.15748/jasse.10.21

Atomistic analysis of strand breaks of DNA in tritiated water using Geant4-DNA simulation

Tsukasa Aso[1*], Masahara Hara[2], Yoshiyuki Hirano[3],
Yoshiteru Yonetani[4], Susumu Fujiwara[5]

[1]Electronics and Computer Engineering, National Institute of Technology, Toyama College
[2]Faculty of Science, Academic Assembly, University of Toyama
[3]Graduate School of Medicine, Nagoya University
[4]Quantum Beam Science Research Directorate and Institute for Quantum Life Science, National Institutes for Quantum Science and Technology
[5]Faculty of Materials Science and Engineering, Kyoto Institute of Technology

*aso@nc-toyama.ac.jp

Abstract. The strand breaks in a double strand B-form DNA in tritiated water were studied using Geant4-DNA simulation. The purpose of this study is to establish an analysis scheme for evaluating strand breaks with atomistic structure of DNA. The simulations were performed in homogeneous water, and strand breaks were estimated by superimposing the interaction points on the atomistic structure of DNA. The results were evaluated in terms of the yield ratio of single strand breaks (SSBs) to double strand breaks (DSBs), the contribution of the direct and the indirect effects to SSB and DSB, and the reaction probability of hydroxyl radical by abstraction of hydrogen atom in DNA.

Keywords: Geant4-DNA, Monte Carlo simulation, DNA strand break

1. Introduction

Ionizing radiation induces DNA damages by direct interaction of DNA molecules with particle (direct effect) and indirect interaction of DNA with molecular species created during water radiolysis (indirect effect). The Geant4-DNA simulates the electromagnetic physics and water radiolysis in water in atomic scale including diffusions and chemical reactions of dissociated molecular products [1]. In order to evaluate DNA damages in simulations, however, interactions between these reactions and atoms in DNA molecules need to be considered.

In present study, the Geant4-DNA simulation was performed with an atomistic structure of DNA. The strand breaks in tritiated water were estimated by superimposing the interaction points on the atoms in DNA. Tritium emits a low energy beta-ray with the maximum energy of 18.6 keV, which will damage a living body through internal exposure. The results were evaluated in terms of the yield ratio of single strand breaks (SSBs) to double strand breaks (DSBs),

the contribution of the direct-type and the indirect-type effect in the yields of SSB and DSB, and the reaction probability of hydroxyl radical through abstraction of hydrogen atom in DNA.

2. Methods

The simulation has been developed on the Geant4-DNA. We used the Geant4 version of 10.07 patch 02 [2]. The Geant4-DNA simulates the electromagnetic physics and water radiolysis in atomic scale including diffusions and chemical reactions of dissociated molecular products. The physics-list in the Geant4 defines physics and chemistry processes. We activated the G4EmDNAPhysics_option2 for electromagnetic physics and G4EmDNAChemistry_option3 for dissociation, diffusion and reactions of chemical species in the physics-list. In order to achieve better computational efficiency, the independent reaction time technique in the Geant4-DNA was adopted for fast-diffusion control of the radiolysis species instead of the default step-by-step technique [3].

The simulation has an interface for importing atomistic structures of molecules in the protein data bank (PDB) format. In this study, a 12-bp double strand B-form DNA (B-DNA) was imported from the PDB after adding the omitted hydrogens. The simulations were performed in homogeneous water, and the spatial coordinates of interaction points were superimposed on the atomistic structure in the B-DNA to determine whether each reaction point forms a strand break (SB). Tritium was randomly placed inside the B-DNA bounding box and disintegrated using G4RadioactiveDecay process in Geant4. The size of bounding box was set to fit the B-DNA volume of $2.32\times2.42\times4.76$ nm^3. Figure 1 shows the B-DNA geometry in the simulation and the schematic view of atomistic structure of backbone sugar-phosphate group.

The SB was assumed to occur if there was a "hit" inside the Van der Waals radius of atom in the backbone sugar-phosphate group shown in Fig.1(b). In the direct effect of charged particles, the "hit" was defined as the energy deposition exceeding the energy threshold of E_{th}=10.78 eV, which corresponds to the ionization threshold of liquid water. In the indirect-type effect of chemical species, only hydroxyl radical was assumed to induce a "hit". Instead of simulating scavenging effects for each hydroxyl radical along the step-by-step diffusion, lifetime of hydroxyl radical for interactions was assumed to 2.5 ns referencing to a scavenging capacity in the cellular environment [4]. After 2.5 ns diffusion, the hydroxyl radical was considered to create a "hit" if the spatial coordinate was within the Van der Waals radius of atom in the DNA backbone. The double strand break (DSB) was defined as two opposite SBs within 10 bp, otherwise the SB was counted as a single strand break (SSB).

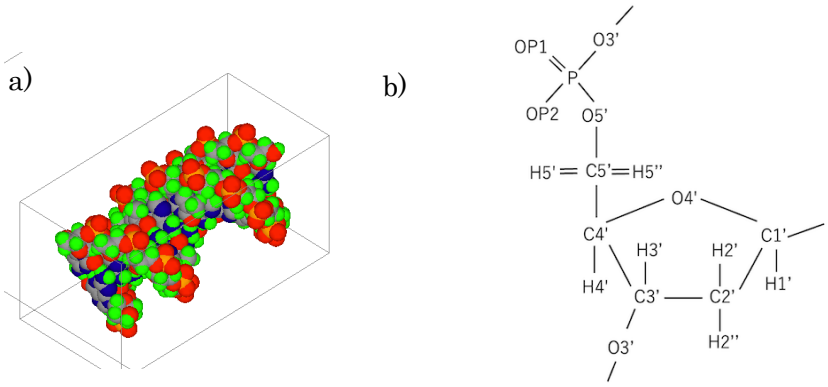

Figure 1: (a) B-DNA geometry in the simulation and (b) schematic view of atomistic structure of backbone sugar-phosphate group.

3. Results and discussion

The contributions of direct and indirect effects in the SBs were 72 % and 28 %. Since tritium was placed inside the bounding box of B-DNA, the direct effect becomes a main source of SBs. This is because the emitted beta-rays crossing the DNA strand. The detail contribution of direct and indirect effects to SSB and DSB are summarized in Table 1. Although a major part of SSBs was caused by direct effect, existence of chemical reactions converts the direct-type SSBs to DSBs by combining it with indirect SBs, so that the DSBs increases about 50% compared to that for only physics interactions. The yield ratio of SSB and DSB is consistent with the other simulation result in [4] as shown in Fig. 2, that uses a clustering algorithm and a simple cylindrical geometry for modeling hits and DNA, respectively.

Table 1: Contributions of direct and indirect effect in SSB and DSB.

SSB (%)		DSB (%)	
Direct	74.4±0.5	Direct-Direct	45.6±2.1
Indirect	27.6±0.3	Direct-Indirect	47.7±2.2
		Indirect-Indirect	6.8±0.8

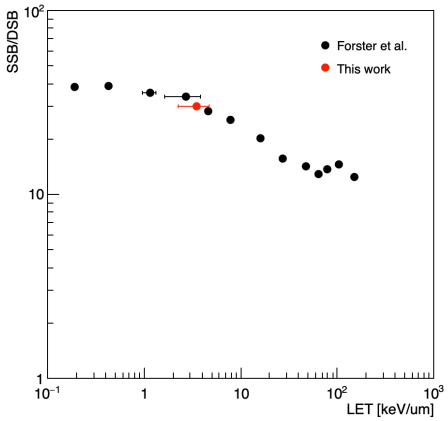

Figure 2: Yield ratio of SSB and DSB.

The SB of indirect effect is known as to occur mostly through chemical reactions of DNA molecule with hydroxyl radical, which is initiated by abstraction of a deoxyribose hydrogen atom and leading to a SB. Balasubramanian et al. measured reactivity of hydroxyl radical at different sites of DNA backbone hydrogen [5]. Since the present simulation did not consider the molecular reactions between hydroxyl radical and hydrogen of DNA, we assumed that the SBs were associating to abstraction of hydrogen in the backbone sugar-phosphate group in the B-DNA. The SBs were analyzed in

terms of the closest atom, and the closest atoms in backbone were categorized according to hydrogen sites as: 1' (H1', C1'), 2' (H2', H2", C2'). 3' (H3', O3', C3'), 4' (H4', O4', C4'), 5' (H5', H5", O5', C5', P, OP1, OP2) in Fig.1(b). The DNA-hydroxyl radical reactivity was calculated from the sum of SBs in each hydrogen site and normalized in the same way with [5]. The calculated reactivity is consistent with the measured result in [5] as shown in Fig.3.

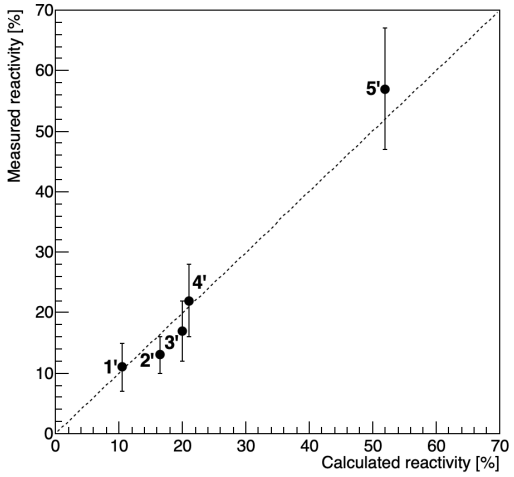

Figure 3: Correlation of DNA-hydroxyl radical reactivity between the simulation and the measurement in [5].

References

[1] S.Incerti et al.: Geant4-DNA example applications for track structure simulations in liquid water -a report from the Geant4-DNA project, *Med. Phys.*, 45 (2018), e722-e739.; M.A.Bernal et al.: Track structure modeling in liquid water -A review of the Geant4-DNA very low energy extension of the Geant4 Monte Carlo simulation toolkit, *Phys. Med.*, 31(2015), 861-874.; S.Incerti et al.: Comparison of Geant4 very low energy cross section models with experimental data in water, *Med. Phys.*, 37(2010) 4692-4708.; S.Incerti et al.: The Geant4-DNA project, I*nt. J. Model. Simul. Sci. Comput.*, 1(2010), 157-178.

[2] J.Allison et al.: Recent developments in GEANT4, *Nucl. Instrum. Meth. A*, 835(2016)186-225.; J. Allison et al.: Geant4 developments and applications, *IEEE T. Nucl. Sci.*, 53:1(2006)270-278.; S.Agostinelli et al.: GEANT4 -a simulation toolkit, *Nucl. Instrum. Meth. A*, 506:3(2003)250-303.

[3] J.Ramos-Méndez et al.: Independent reaction times method in Geant4-DNA – Implementation and performance, *Med. Phys.* 47:11(2020)5919-5930.

[4] J.C Forster et al.: Monte Carlo simulation of the oxygen effect in DNA damage induction by ionizing radiation, *Radiat. Res.*, 190:3(2018)248-261.

[5] B.Balasubramanian et al.: DNA strand breaking by the hydroxyl radial is governed by the accessible surface areas of the hydrogen atoms of the DNA backbone, *Proc. Natl. Acad. Sci. USA*, 95:17(1998) 9738-9743.

JSST 2022

Evaluation tolerance of DNA damaged by tritium beta decay using MD simulation

Kento Ishiguro[1,*], Hiroaki Nakamura[1,2], Shunsuke Usami[2], Susumu Fujiwara[3], Seiki Saito[4]

[1]Department of Electrical Engineering, Nagoya University,
[2]National Institute for Fusion Science,
[3]Kyoto Institute of Technology,
[4]Yamagata University

[*]naka-lab@nifs.ac.jp

Abstract. In order to quantitatively elucidate the effect of tritium β decay in MD simulations, the initial structure of DNA must be stabilized under human body conditions with ReaxFF, which can handle covalent bonds. The arrangement of counterions around DNA plays an important role in the stable structure of DNA. Therefore, focusing on the arrangement of sodium ions in the system, we performed simulations in which sodium ions move to a position where they can shield the charge of the DNA. As a result, we were able to create a stable DNA structure that could be used to simulate tritium decay effects.

Keywords: Molecular dynamics simulation, Double strand break, Telomeric DNA, Tritium, β-decay

1. Introduction

Tritium (^{3}H) is radioactive material used for fuel of fusion power generation. When one tritium decays, it splits into one helium-3 (^{3}He) and one electron (β-radiation). The energy of β-radiation is too small ($\leq$ 18.6 keV) to effect on the human body from external exposure [1]. On the other hand, internal exposure affects DNA. Double-strand breaks (DSBs) is a typical bad effect of internal exposure on DNA. DSBs is the cleavage that occurs on both strands of DNA, with the two cleaved positions in proximity. The DNA that has been subjected to DSBs can die intact. Even if the DSBs is repaired by enzymes, the DNA can easily mutate, leading to cancer and cell death [2]. The processes by which tritium damages DNA can be divided into three types: direct, indirect and decay effects. In the research by a single molecule observation (SMO), the influence of the decay effect has not been clarified. Therefore, we are attempting to understand the impact of tritium decay effects by means of MD simulations [3]. We are currently in the process of modelling stable DNA structures under human conditions for tritium decay simulations.

2. Molecular dynamics simulation

We prepared the initial structure as Fig.1 by CHARMM-GUI [4]. We use Telomeric DNA (d(TCTAGGGTTAGGGTTAG)$_2$) in 3SJM [5]. Because telomeres are important parts of cell division and their length is directly related to the number of cell divisions. The telomeric DNA structure is surrounded by 30,773 water molecules, 120 sodium ions and 88 chloride ions. The sodium ions neutralize the negative charge of the DNA.

The DNA is approximately 50 Å × 20 Å × 20 Å. The size of the simulation box is 100 Å cubic.

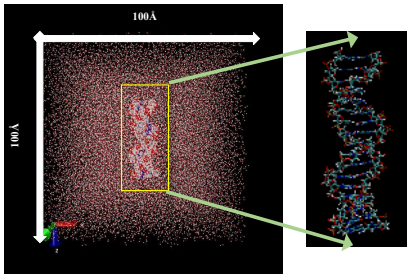

Figure 1: Snapshot of the initial structure.

We use Large-scale Atomic/Molecular Massively Parallel Simulator (LAMMPS) [6, 7, 8] as the MD code. We performed MD simulation of 11.21 ns with two force fields, CHARMM [9] and ReaxFF [10][11](Fig.2). First, the calculation was performed using CHARMM, a force field with low computational cost. We increase temperature of simulation box from 0 K to 310 K over 0.5 ns while the coordinates of the DNA are fixed. Thereafter, the temperature is kept at 310 K, and the pressure is kept at 1 bar. From 0.5ns to 1.5ns, the coordinates of the entire DNA are fixed. From 1.5ns to 3.5ns, the coordinates of the main strand of the DNA are fixed. From 3.5ns to 10.5ns, the coordinates are not fixed at all. From the results, we confirmed that the ions were in the proper configuration[12]. Next, calculations were performed using ReaxFF, which can handle covalent bond breaking. As changing the force field makes the system unstable, the calculations are again performed with the DNA coordinates fixed stepwise. From 10.5ns to 10.51ns, the coordinates of the entire DNA are fixed. From 10.51ns to 10.61ns, the coordinates of the main strand of the DNA are fixed. From 10.61ns to 11.21ns, the coordinates are not fixed at all.

Force field	CHARMM	ReaxFF	
Contents	1. Raise temperature (0->310[K]) 2. Move the sodium ions	1. Create a stable DNA under human body condition	
Calculation time	10.5 ns	0.71 ns	total 11.21 ns

Figure 2: Table of the performed simulation.

3. Results

The distribution of ions around the DNA helical axis after the sodium ions have moved to a charge-shielding position is shown in Fig. 3.

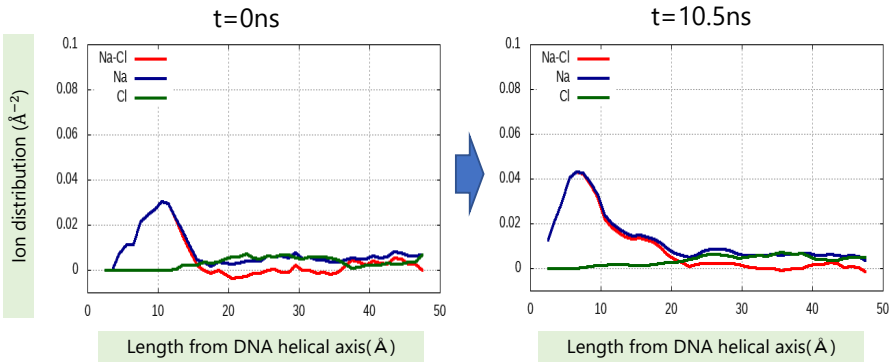

Figure 3: Time variation of the ion distribution around the DNA.

Two snapshots of the structure under steady state conditions in ReaxFF are shown in Fig.4. The left figure shows the structure of the entire DNA. The right figure shows the structure of the main strand of the DNA. The DNA maintains the bond and duplex structure of the main strand.

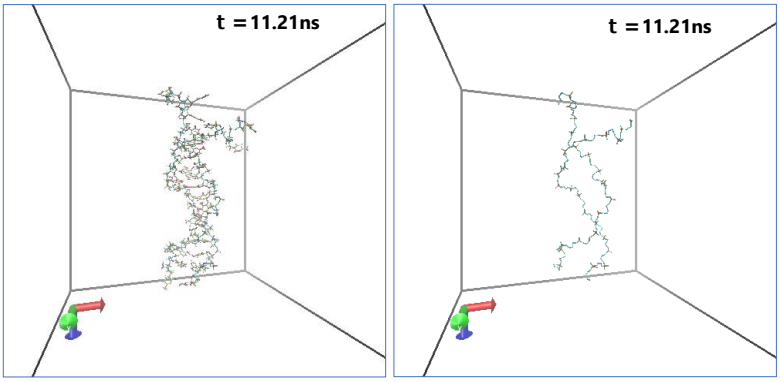

Figure 4: The DNA structure in steady condition in ReaxFF.

4. Conclusion

A stable DNA structure was obtained under human body conditions in ReaxFF required for simulating tritium decay effects. The structure will be used for tritium decay simulations in the future to confirm its effectiveness.

Acknowledgments

This work was supported in part by the NIFS Collaborative Research Programs NIFS22KIIP003 and NIFS22KISS021, Research Center for Computational Science, Okazaki, Japan (Project: 21-IMS-C117, 22-IMS-C117) and JSPS KAKENHI Grant Numbers Nos. 19K03800, 21K19845 and 22K03572, from the Japan Society for the Promotion of Science.

References

[1] H. Tauchi, T. Umata, and A. Tachibana: *J. Plasma Fusion Res.*, Vol. 88:No. 2(2012), p. 119.

[2] A. Kurosawa, N. Adachi: *Isotope News*, No.721(2014), pp. 8-14.

[3] Hiroaki Nakamura et al. 2020 *Jpn. J. Appl. Phys.* 59 SAAE01

[4] S. Jo, T. Kim, V.G. Iyer, and W. Im: CHARMM-GUI: A Web-based Graphical User Interface for CHARMM, *J. Comput. Chem.*, 29(2008), pp. 1859-1865.

[5] S.K. Nair, S.K. Sliverman, J.H. Chen, and Y. Xiao, Crystal structure analysis of TRF2-Dbd-DNA complex. 2012.

[6] Steve Plimpton, Fast parallel algorithms for short-range molecular dynamics, Journal of Computational Physics, Vol. 117:No. 1(1995), pp. 1–19.

[7] H. M. Aktulga, C. Knight, P. Coffman, K. A. OHearn, T. R. Shan, and W. Jiang, Optimizing the performance of reactive molecular dynamics simulations for multi-core architectures, *Int. J. High Perform Comput. Appl.*, toappear.

[8] Adri C. T. van Duin, Siddharth Dasgupta, Francois Lorant, and William A. Goddard. Reaxff: A reactive force field for hydrocarbons, *The Journal of Physical Chemistry A*, Vol. 105, No. 41, pp. 9396–9409, 2001.

[9] B. R. Brooks, C. L. Brooks III, A. D. Mackerell, L. Nilsson, R. J. Petrella, B. Roux et al. CHARMM: The Biomolecular simulation Program, *J. Comp. Chem.* 30, pp. 1545-1615, 2009.

[10] H. M. Aktulga, J. C. Fogarty, S. A. Pandit, and A. Y. Grama. Parallel reactive molecular dynamics: Numerical methods and algorithmic techniques, *Parallel Computing*, Vol. 38(2012), pp. 245–259.

[11] Susanna Monti, Alessandro Corozzi, Peter Fristrup, Kaushik L. Joshi, Yun Kyung Shin, Peter Oelschlaeger et al. : Exploring the conformational and reactive dynamics of biomolecules in solution using an extended version of the glycine reactive force field, *Phys. Chem. Chem. Phys.*, Vol. 15:No. 36(2013), pp. 15062–15077.

[12] Friis, I, Verkhovtsev, A, Solov'yov, IA, Solov'yov, AV. Modeling the effect of ion-induced shock waves and DNA breakage with the reactive CHARMM force field. *J Comput Chem.* 2020; 41: pp. 2429–2439.

Protective behavior of various types of tea catechins on DNA double strand breaks by radiations

Yasuhisa Oya[1*], Shiori Hirata[1], Takahiro Kenmotsu[2], Yuji Hatano[3], Takashi Ikka[1], Takanori Oyoshi[1], Toshinobu Tokumoto[1], Kazutaka Hirakawa[1], Seiki Saito[4]

[1]Shizuoka University, Japan
[2]Doshisha University, Japan
[3]University of Toyama, Japan
[4]Yamagata University, Japan

*oya.yasuhisa@shizuoka.ac.jp

Abstract. Protective behavior of various types of tea catechins on DNA double strand breaks (DSBs) of genome-sized DNA was studied by single molecule observation method using fluorescence microscope. It was found that the addition of epigallocatechin gallate (EGCg) was the most effective on the protection of DNA double strand breaks by the radition of β-ray by tritium (^{3}H) and calcium-45 (^{45}Ca). This behavior would be correlated with the antioxidation effect by tea chatechins.

Keywords: DNA double strand breaks, tea catechins, radiation

1. Introduction

The evaluation of radiation effects on human body is necessary to promote a public acceptance for the operation of nuclear power plant. One of the key processes for DNA double strand breaks (DSBs) are though to be enhanced by reactive oxygen species (ROS) such as OH radicals which damage DNA indirectly. It is well-known that more than 40 % of tea leaves in Japan are produced in Shizuoka Prefecture and tea is thought to be good for health due to the existence of tea catechin in green tea brewing, which will work as antioxidation. These facts indicates that DSBs by radiation will reduce by the existence of tea catechin. There are four type of catechins, namely (-)-epigallocatechin gallate (EGCg), (-)-epigallocatechin (EGC), (-)-epicatechin gallate (ECg) and (-)-epicatechin (EC). In this study, protective behavior of four types of tea catechins (EGCg, EGC, ECg and EC) on DNA double strand breaks were extensively studied using genome-sized DNA by single molecule observation method using fluorescence microscope [1].

2. Experimental

Bacteriophage T4 GT7 DNA (Nippon Gene Co., Japan), with the length of 166 k base pairs (kbp) corresponding to 57 μm, was soaked in a sterilized water (Otsuka Pharmaceutical Factory, Inc.) with 70 mM Tris-HCl buffer (pH 7.0). 10 μM of tea catechin (EGCg, EGC, ECg or EC) was added in the sample and irradiated by β-rays by ^{3}H (LET (Linear Energy Transfer): 4700 eV/μm) or ^{45}Ca (LET: 610 eV/μm). For β-rays irradiation, the DNA was suspended in tritiated water, which was diluted from biological grade one (Moravek Co., USA), or $^{45}CaCl_2$ solution (PerkinElmer, Inc., USA) for 7 days. After the irradiation, the sample was mixed with YOYO-1 Iodide (Thermo Fischer Scientific Co., USA), 3-Mercapto-1,2-propanediol (FUJIFILM Wako Pure Chemical Corporation, JAPAN) and Tris-HCl. YOYO-1 was intercalated with DNA and acts as an fluorescent. DNA was observed using fluorescence microscope (IX73, Olympus Co., Japan) with a sCMOS camera (Zyla 4.3, Andor Technology Co., UK) and the length of DNA was evaluated by computer analysis using Image-J software.

3. Results and discussion

Fig. 1 shows the number of DSBs by ^{3}H and ^{45}Ca as a function of tea catechins. The Y axis of "n" means the number of DSBs. The results showed that the number of DSBs by higher LET (^{3}H) was reached to be more than 2.5, but that by lower LET (^{45}Ca) was located at 1.2, which can be explained by the difference of LET. In our previous paper [2], the mechanism of DSBs were proposed as follows. DNA was broken by radicals which were produced by radiations namely single strand brakes (SSBs). After SSBs, DSBs would be occurred if another DNA strand was broken, which is near the first SSBs within the distance of 10 bp. By mixing tea catechins, the number of DSBs were largely reduced and reached almost the half for both cases (β-rays by ^{3}H and ^{45}Ca). In especially, EGCg has the most effective to reduce the number of DSBs for both cases. It is known that the reactivity of EGCg with OH radical was larger than that of DNA [3]. The order of antioxidation by tea catechins were EC < ECg < EGC < EGCg and the present results were consistent with this antioxidation effect.

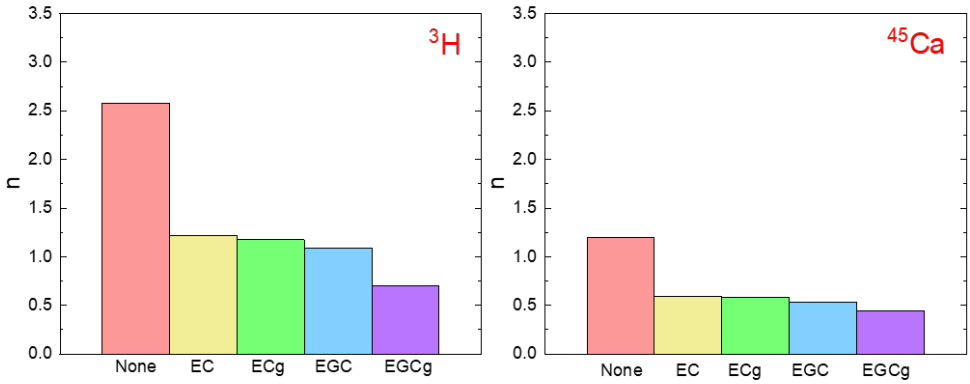

Fig. 1 The number of DSBs by ^{3}H or ^{45}Ca with various tea catechins.

4. Summary

The protective behavior of DSBs by radition was studied by mixing of various tea catechins.

Higher DSBs were achieved by the radiation with higher LET (^{3}H). By adding tea catechins, the numbers of DSBs were reduced almost the half, which can be explained that the tea catechins will work as radical scavengers. In especially, EGCg has the most effective to reduce the number of DSBs for both cases, ^{3}H and ^{45}Ca.

Acknowledgement

This work is performed with the support and under the auspices of University of Toyama Collaboration Research Program (HRC2021-01, HRC2022-08) and Promotion of interdisciplinary domain research at Shizuoka University.

References

[1] Y. Ma, N. Ogawa, Y. Yoshikawa, T. Mori, T. Imanaka, Y. Watanabe, K. Yoshikawa, Protective effect of ascorbic acid against double-strand breaks in giant DNA: marked differences among the damage induced by photo-irradiation, gamma-rays and ultrasound, Chem. Phys. Lett. 638 (2015) 205–209.

[2] T. Wada, A. Koike, S. Yamazaki, K. Ashizawa, F. Sun, Y. Hatano, H. Shimoyachi, T. Kenmotsu, T. Ikka and Y. Oya, Protective behavior of tea catechins against DNA double strand breaks produced by radiations with different linear energy transfer, Fusion Eng. Des. 172 (2021) 112700.

[3] Y. Yoshioka, H. Kurosaki, H. Yoshioka, Kinetics of reaction between hydroxyl radical formed by beta-rays in tritiated water and Tea Catechin: apprication of the solid state spin trapping method, J. Radioanal. Nucl. Chem. 239 (1999) 217–220.

Finite element analysis of multilayered flexible piezoelectric energy harvesting devices using strongly coupled structure-piezoelectric-circuit interaction

P.C. Ramegowda[1,*], D. Ishihara[1], R. Takata[1], N. Takayama[1], T. Niho[1], T. Horie[1]

[1]Department of Intelligent and Control Systems, Kyushu Institute of Technology, 680-4 Kawazu, Iizuka, Fukuoka, Japan,820-0067

[*]prakasha@solid.mse.kyutech.ac.jp

Abstract. Thin flexible piezoelectric energy harvesting devices (FPED) are a new future harvesting technology which are highly flexible and lightweight than the familiar cantilever piezoelectric energy harvesters. This mechanical vibration driven FPED is a strongly coupled multiphysics phenomena that involve interaction between the piezoelectric structure, the electric charge accumulated in the piezoelectric material, and a controlling electrical circuit attached to it. In this study, the finite element analysis results for the deflection and the generated voltage of FPED under base exciation at different electric load resisnatance are compared with the experimental solutions using a partitioned iterative algorithm developed using a hierarchical decomposition approach. The simulation results matched the experiment results very well.

Keywords: Energy harvesting, finite element method, partitioned iterative coupling.

1. Introduction

Most recently, piezoelectric devices are increasingly employed throughout the field of energy harvesting [1, 2], vibration control [3], and nano-aerial vehicles [4, 5, 6]. During vibration energy harvesting, piezoelectric materials convert mechanical strain into an electrical charge or voltage via the direc-piezoelectric effect. Erturk et al., [1] had extensively studied the electromechanical behavior of piezoelectric energy harvesters (PEHs) connected to external resistive load using analystical modeling based on single degree of freedom (SDOF) Euler-Bernoulli beam models which are commonly referred to as lumped parameter and distributed parameters approaches, respectively. On the numerical modeling front using finite element method, the electromechanical behavior of piezoelectric material has been extensively studied using a variety of numerical approaches [7, 8, 9, 10, 11, 12, 13, 14]. Authors in [13] were first to publish a partitioned iterative method for the structure-piezoelectric-circuit-interaction in the circuit-integrated piezoelectric oscillators. Here, the direct-piezoelectric and inverse-piezoelectric effects are formulated using the finite element method and the electrical circuit is formulated as SDOF equation of the general circuit. The structure-piezoelectric-circuit-interaction modeling is based on the hierarchical decomposition, the partitioned iterative method for two coupled fields [7, 8, 9], and loop union. In this

study, using the hierarchically decomposed partitioned iterative method for the structure-piezoelectric-circuit-interaction, a circuit-integrated FPED shown in Fig. 1 is analyzed. The simulation results are very close to that of experimental results [2].

2. Materials and methods

The spatially discretized equilibrium equations of linear piezoelectricity in the global coordinate system are derived using the variation principle with the standard procedure of the finite element method as

$$\mathbf{M_{uu}}\ddot{\mathbf{u}} + \mathbf{K_{uu}}\mathbf{u} + \mathbf{K_{u\phi}}\phi = \mathbf{F}, \quad (1) \qquad \mathbf{K_{\phi u}}\mathbf{u} + \mathbf{K_{\phi\phi}}\phi = \mathbf{q_{ext}} + \mathbf{q_c}, \quad (2)$$

where $\mathbf{M_{uu}}$ is the constant mass matrix, $\mathbf{K}_{\mathrm{uu}}$ is the mechanical stiffness matrix, $\mathbf{K}_{\mathrm{u}\phi}$ is the piezoelectric coupling matrix, $\mathbf{K}_{\phi\phi}$ is the dielectric stiffness matrix, $\mathbf{F}$ is the external force vector, $\mathbf{q_{ext}}$ is the external electric charge vector, and $\mathbf{q_c}$ is the vector of the surface charge supplied from the circuit. The inverse-piezoelectric effect (IPE) Eq.(1) and direct-piezoelectric effect (DPE) Eq.(2) are solved in two distint solvers using the partioned iterative approach wherein shell elements are used for IPE and solid elements are used for DPE [7, 8, 9, 16]. We consider the electrical resistance load (R) as the circuit attached to the electrodes covering the piezoelectric layers of FPED, as shown in Fig. 1. A SDOF governing equation describing the electric circuit can be derived using the Kirchhoff's law as

$$R\dot{Q} + V_p = V_c, \quad (3)$$

where R, V_p, and V_c are the electrical resistance, the electric potential difference given by the piezoelectric energy harvester, and the electric voltage given by the external electric power supply, respectively. The iterative procedures of the structure-piezoelectric and piezoelectric-circuit interaction are given in [13, 14, 15]. The coupled equations are reduced to the following single iterative procedure in the same time marching using loop union as

$$\hat{\mathbf{K}}_{\mathbf{uu}}\,{}^{t+\Delta t}\mathbf{u}^{(b)} = {}^{t+\Delta t}\hat{\mathbf{F}} - \mathbf{K}_{\mathbf{u}\phi}\,{}^{t+\Delta t}\phi^{(b-1)}, \quad (4)$$

$${}^{t+\Delta t}Q^{(b)} = {}^{t}Q + \Delta t\Big[(1-\alpha)^{t}\dot{Q} + \alpha\frac{{}^{t+\Delta t}V_c - {}^{t+\Delta t}V_p{}^{(b-1)}}{R}\Big], \quad (5)$$

$$\mathbf{K}_{\phi\phi}\,{}^{t+\Delta t}\phi^{(b)} = {}^{t+\Delta t}\mathbf{q_{ext}} + {}^{t+\Delta t}\mathbf{q_c}^{(b)} - \mathbf{K}_{\phi\mathbf{u}}\,{}^{t+\Delta t}\mathbf{u}^{(b)}, \quad (6)$$

where the right-hand superscript b in parentheses denotes the b-th iteration and $Q^{(b)}$ and $V_p^{(b)}$ are respectively given as

$$\mathbf{q_c}^{(b)} = \int_{S_+^c}\mathbf{N}_\phi\left(\mathrm{Q}^{(b)}/\mathrm{S}_+^c\right)dS - \int_{S_-^c}\mathbf{N}_\phi\left(\mathrm{Q}^{(b)}/\mathrm{S}_-^c\right)dS, \quad (7) \qquad V_p^{(b)} = \overset{*}{\phi}_+^{(b)} - \overset{*}{\phi}_-^{(b)}, \quad (8)$$

The frequency response functions (FRFs) for the FPEDs length 350 mm, 300mm, 250 mm,

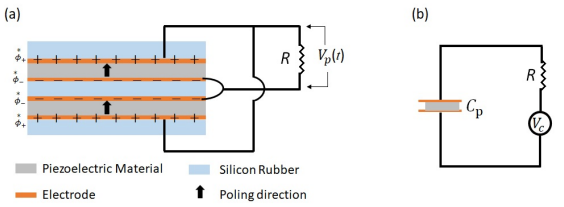

Figure 1: 2D illustration of FPED attached to an external circuit.

and 200 mm are shown in Fig. 2 for the amplitudes of the voltage at the quasi-steady state. Fig. 2 also include the analytical solutions [1] and the experimental solutions [2]. The finite element analysis results from the structure-piezoelectric-circuit interaction method are very close to those from the experiment and the analytical results. The FEM results show the accurate evaluation of the resonance for all the FPEDs dimensions.

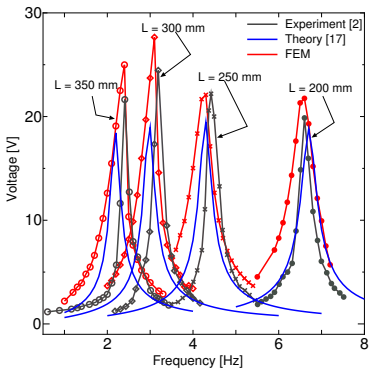

Figure 2: FEM, experiment, and theoretical voltage FRFs of the FPEDs for the lengths L =200 mm, 250 mm, 300 mm, and 350 mm with the resistive load $R = 1M\Omega$.

Acknowledgments

The present study was supported by JSPS KAKENHI Grant No. 19F19379. Authors thanks Prof. Y. Tanaka at Hiroshima university for helpful discussions.

References

[1] A. Erturk, D.J. Inman: On mechanical modeling of cantilevered piezoelectric vibration energy harvester, *Smart Materials and Structure* , 13 (2004), 1131–1144.

[2] Y. Tanaka, T. Oko. H. Mutsuda, A.A. Popov, R. Patel.: Forced vibration experiments on flexible piezoelectric devices operating in air and water environment, *International Journal of Applied Electromagnetics and Mechanics*, 45 (2014), 573–580.

[3] V. Shankar, P. C. Ramegowda, D. Ishihara: Computational control for strongly coupled structure, electric, and fluid systems, *International Journal for Computational Methods in Engineering Science and Mechanics* , 23 (2022), 1-16,

[4] D. Ishihara, N. Ohira, M. Takagi, T. Horie: Fluid-structure interaction design of insect-like micro flapping wing, *Proceeding of the VII International Conference on Computational Methods for Coupled Problems in Science and Engineering* , (2017), 870-875.

[5] R. Kant, D Ishihara, R Suetsugu, P. C Ramegowda: One-wing polymer micromachined transmission for insect-inspired flapping wing nano air vehicles, *Engineering Research Express* , 3 (2021), 045006.

[6] R. Kant, D Ishihara, R Suetsugu, S. Murakami, P. C Ramegowda: Improved Design of Polymer Micromachined Transmission for Flapping Wing Nano Air Vehicle, *2021 IEEE 16th International Conference on Nano/Micro Engineered and Molecular Systems (NEMS)*, (2021), 1320-1325.

[7] P. C. Ramegowda, D. Ishihara, T. Niho, T. Horie: Performance evaluation of numerical finite element coupled algorithms for structure–electric interaction analysis of MEMS piezoelectric actuator, *International Journal of Computational Methods*, 16 (2019), 1850106.

[8] P. C. Ramegowda, D. Ishihara, T. Niho, T. Horie: A novel coupling algorithm for the electric field–structure interaction using a transformation method between solid and shell elements in a thin piezoelectric bimorph plate analysis, *Finite Elements in Analysis and Design*, 159 (2019), 33–49.

[9] P .C. Ramegowda, D. Ishihara, R. Takata, T. Niho, T. Horie: Finite element analysis of thin piezoelectric bimorph with a metal shim using solid direct-piezoelectric and shell-inverse piezoelectric coupling with pseudo-piezoelectric evaluation, *Composite Structures*, 245 (2020), 112284.

[10] P. C. Ramegowda, D. Ishihara, R. Takata, T. Niho, T. Horie: Hierarchically decomposed finite element method for a triply coupled piezoelectric, structure, and fluid fields of a thin piezoelectric bimorph in fluid, *Computer Methods in Applied Mechanics and Engineering*, 365 (2020), 113006.

[11] R. Takata,D. .Ishihara, P. C. Ramegowda, T. Niho, T. Horie: Solid piezoelectric-shell inverse piezoelectric partitioned analysis method for thin piezoelectric bimorph with conductor layers, *Transactions of the Japan Society for Computational Engineering and Science*, 2019 (2019), 20190011.

[12] D. Ishihara, P. C Ramegowda, R. Takata, T. Niho, T. Horie: Coupled solid piezoelectric and shell inversepiezoelectric analysis using partitioned method for thin piezoelectric bimorph with metal layers, *Proceedings of VIII International Conference on Computational Methods for Coupled Problems in Science and Engineeringng*, (2019), 451-457.

[13] D. Ishihara, R. Takata, P. C. Ramegowda, N. Takayam: Strongly coupled partitioned iterative method for the structure-piezoelectric-circuit interaction using hierarchical decomposition, *Computers & Structures*, 253 (2021), 106572.

[14] D. Ishihara, R. Takata, P. C. Ramegowda: Partitioned iterative method for inverse piezoelectric-direct piezoelectric-electric circuit Interaction, *Transactions of the Japan Society for Computational Engineering and Science*, 2020 (2020), 20200015.

[15] P. C. Ramegowda, D. Ishihara, R. Takata, T. Horie: Hierarchical modeling and finite element analysis of piezoelectric energy harvester from structure-piezoelectric-circuit interaction, *Proceedings of 14th World Congress on Computational Mechanics (WCCM) ECCOMAS Congress*, (2020), 7 pages.

[16] P. C. Ramegowda, D. Ishihara, R. Takata, T. Niho, T. Horie: Fluid-structure and electric interaction analysis of piezoelectric flap in a channel using a strongly coupled fem scheme , *Proceedings of the 6th European Conference on Computational Methods (Solids, Structures and Coupled Problems) and the 7th European Conference on Computational Fluid Dynamics, Glasgow*, (2018), 382–393.

JSST 2022

Quantum algorithm for the Vlasov simulation of neutral gas

Kiichiro Toyoizumi[1,*] and Kazuo Hoshino[1]

[1]Graduate School of Science and Technology, Keio University

[*]toyoizumi@ppl.appi.keio.ac.jp

Abstract. Simulation of the Vlasov equation with a high resolution of a six-dimensional phase-space grid is still a challenging task. Quantum computing can be a solution to this issue. We propose a quantum algorithm for the equation for neutral gas. By discretizing the equation using the central differencing scheme with periodic boundary conditions, it can be represented as a form of the Schrödinger equation with a time-independent Hamiltonian. This means the time evolution of the equation can be calculated by a Hamiltonian simulation algorithm on a quantum computer. The quantum simulation is emulated on a classical computer, and the results show our algorithm can reproduce ballistic mode with the recurrence effect.

Keywords: the Vlasov equation, quantum computing, Hamiltonian simulation

1. Introduction

The numerical simulation of the Vlasov equation is one of the powerful methods in fusion plasma research. However, it requires extreme computational resources, and high resolution remains challenging even with powerful computers. Quantum computing can be a solution to this issue.

Quantum computers are computers using quantum-mechanical phenomena such as superposition and entanglement. They are expected to achieve speedups in some problems over the usual computer, i.e., classical computer. Quantum algorithms that obtain speedups are, for example, the search algorithm [1], the factorization algorithm [2], and the simulation algorithm [3].

Recently, some quantum algorithms for plasma simulation have been developed for the linearized Vlasov-Maxwell system [4] and radio-frequency wave system [5]. These systems can be represented as a form of the Schrödinger equation with a time-independent Hamiltonian. The time evolution of the equation is efficiently calculated on a quantum computer by a Hamiltonian simulation (HS) algorithm [6]. Using the algorithm suggested in the Ref. [4], recently, we have successfully simulated the linear Landau damping precisely and investigated the algorithm's performance as a plasma simulation. Quantum algorithms for other

plasma simulations are discussed in the Ref. [7]. However, these algorithms do not handle both position and velocity spaces.

Here, we discuss the algorithm for the Vlasov equation that deals with both spaces and periodic boundary conditions. For simplicity, we assume the Vlasov equation without electric and magnetic fields, i.e., $\boldsymbol{E}, \boldsymbol{B} = 0$. By discretizing the equation using the central differencing scheme, it can be represented as a form of the Schrödinger equation with a time-independent Hamiltonian. We use a state-of-art method called quantum singular value transformation (QSVT) [8, 9] to implement HS.

2. Theory and method

Assuming neutral gas with electric and magnetic fields $\boldsymbol{E}, \boldsymbol{B} = 0$, the Vlasov equation is represented as the following equation:

$$\frac{\partial f}{\partial t} + \boldsymbol{v} \cdot \nabla f = 0, \tag{1}$$

where $f = f(\boldsymbol{x}, \boldsymbol{v}, t)$ is a distribution function in phase space $(\boldsymbol{x}, \boldsymbol{v})$. Note that $\boldsymbol{x}$, $\boldsymbol{v}$, and t are normalized to characteristic length L, velocity v_0, and frequency ω in plasma such that $L\omega = v_0$. Equation (1) is rewritten as

$$\frac{\partial F}{\partial t} + \boldsymbol{v} \cdot \nabla F = 0, \tag{2}$$

where $F = \sqrt{f}$. We consider only one direction for simplicity, and the following discussion can easily be extended to the higher dimensional model.

The one-dimensional equation is discretized in phase space using the central differencing scheme for $l = 0, 1, \ldots, N_x - 1$ and $m = 0, 1, \ldots, N_v - 1$:

$$\frac{dF_{l,m}}{dt} + v_m \frac{F_{l+1,m} - F_{l-1,m}}{2\Delta x} = 0, \tag{3}$$

where $F_{l,m} \equiv F(x_l, v_m, t)$, N_x, and N_v are position and velocity space grid size, Δx and Δv are mesh size in position and velocity space. We assume the periodic boundary conditions in position space: $F_{l,m} = F_{l+N_x,m}$. Equation (3) can be rewritten in a form of a Schrödinger equation

$$\frac{d\,|\psi\rangle}{dt} = -iH\,|\psi\rangle\,, \tag{4}$$

where $|\psi\rangle$ is a quantum state of which the variables $F_{l,m}$ are encoded as the amplitudes, and H is a time-independent Hamiltonian. The solution of Eq. (4) is given by $U = \exp(-iHt)$ where t is a simulation time. An algorithm to implement U on quantum computers is called Hamiltonian simulation (HS) [6].

In recent years, some types of Hamiltonian simulation (HS) algorithms have been proposed [6, 10, 11]. One way to implement HS is to use quantum singular value transformation (QSVT) [8,9]. QSVT is a quantum algorithm for applying a polynomial transformation $P(A)$ to the singular values of a given matrix A. We must choose $A = H$ and apply QSVT to two different polynomials $\cos Ht$ and $\sin Ht$. We can construct $\exp(-iHt) = \cos Ht - i \sin Ht$ using these polynomials.

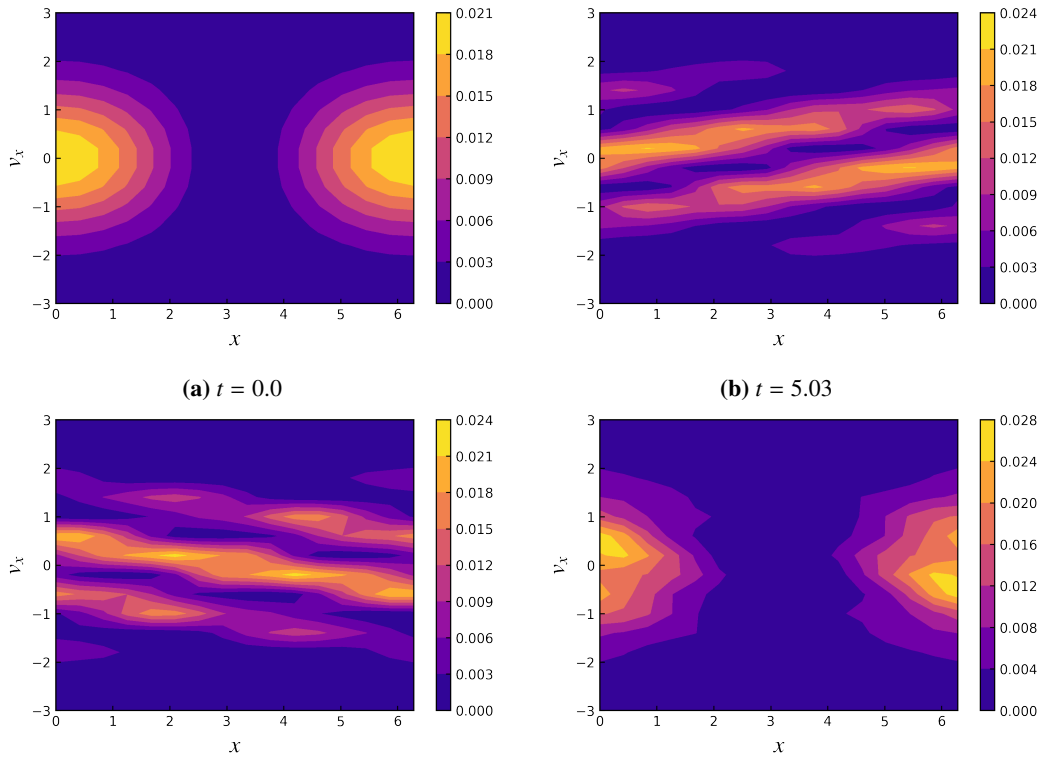

(a) $t = 0.0$ **(b)** $t = 5.03$

(c) $t = 11.3$ **(d)** $t = 34.4$

Figure 1: The time evolution of the distribution function $f(x, v_x, t)$.

3. Results

We implement our quantum algorithm on a classical emulator of a quantum computer using Qiskit [12], especially *statevector_simulator* as the backend, which gives us access to the whole output space at all moments. The numerical simulation is performed using the following parameters:

$$0 \leq x \leq 2\pi, \quad -3.0 \leq v \leq 3.0, \quad N_x = 16, \quad N_v = 16, \tag{5}$$

and the initial distribution function is given by

$$f(x, v, t = 0) = \frac{1}{2\pi} f_{\mathrm{M}}(v)(1 + \cos(x)), \tag{6}$$

where f_{M} is a Maxwellian distribution.

Figure 1 shows the time evolution of the distribution function $f(x, v, t)$. The initial distribution function is sheared, resulting in a high wavenumber in the v direction, i.e., ballistic mode occurs. The recurrence effect occurs at $t = 34.35$, which is comparable to the theoretical value $T_{\mathrm{R}} = 31.4$. This difference is due to the centralized difference in the Vlasov equation for neutral gas, which is equivalent to the free-streaming equation.

4. Summary

We propose the quantum algorithm for the Vlasov equation for neutral gas. The equation can be rewritten as a form of the Schrödinger equation with a time-independent Hamiltonian. Therefore, the time evolution $\exp(-iHt)$ can be calculated by Hamiltonian simulation (HS) algorithm using quantum singular value transformation (QSVT). The simulation is implemented on a classical computer. The result shows our algorithm reproduces ballistic mode with the recurrence effect. We leave the discussion about the algorithm for the Vlasov equation with electric and magnetic fields for future work.

References

[1] L. K. Grover, in *Proceedings of the Twenty-Eighth Annual ACM Symposium on Theory of Computing* (1996), 212–219.

[2] P. W. Shor, in *Proceedings 35th Annual Symposium on Foundations of Computer Science* (1994), 124–134.

[3] R. P. Feynman, *Int. J. Theor. Phys.*, **21** (1982), 467–488.

[4] A. Engel, *et al.*, *Phys. Rev. A*, **100** (2019), 062315.

[5] I. Novikau, *et al.*, *Phys. Rev. A*, **105** (2022), 062444.

[6] G. H. Low and I. L. Chuang, *Phys. Rev. Lett.*, **118.1** (2016), 010501.

[7] I. Y. Dodin and E. A. Startsev, *Phys. Plasmas*, **28** (2021), 092101.

[8] A. Gilyén *et al.*, in *Proceedings of the 51st Annual ACM SIGACT Symposium on Theory of Computing* (2019), 193–204.

[9] J. M. Martyn *et al.*, *PRX Quantum*, **2** (2021), 040203.

[10] D. Berry and L. Novo, *Quantum Info. Comput.*, **16** (2016), 1295.

[11] L. Novo and D. W. Berry, *Quantum Info. Comput.*, **17** (2017), 623.

[12] MD SAJID ANIS *et al.*, Qiskit: An open-source framework for quantum computing (2021).

JSST2022

A method to distinguish different material in Euler fluid dynamics for fuel pellet implosion analysis in inertial confinement fusion

Zhehao Lin[1*], Kazumasa Takahashi[2], Toru Sasaki[3], Takashi Kikuchi[4]

[1]Department of Energy and Environmental Science, Nagaoka University of Technology
[2]Department of Electrical, Electronics and Information Engineering, Nagaoka University of Technology
[3]Department of Science of Technology Innovation, Nagaoka University of Technology
[4]Department of Nuclear Technology, Nagaoka University of Technology
*s195084@stn.nagaokaut.ac.jp

Abstract. We have developed a numerical code for a model of 2D, two-temprature, Euler fluid and ideal gas equation-of-state for the study of implosion process in inertial confinement fusion (ICF). Since different kinds of materials were used in an ICF pellet, a way to distinguish different materials was necessary. In this code, we succeed it by adopting conservation equations of mole densities for each materials.

Keywords: Computational fluid dynamics, Multi-material flow, Inertial confinement fusion

1. Introduction

An inertial condinement fusion (ICF) system is a promising candidate for a thermonuclear fusion energy source [1]. Different kinds of materials are used in an ICF target, for which the way to distinguish different materials is a key issue for the simulation of implosion dynamics in ICF [2,3]. We have developed a computational fluid dynamics (CFD) code of a model of 2D, two-temperature, Euler fluid with ideal gas equation-of-state for the study of implosion process of ICF. In this CFD code, conservation equations of mole densities of each matertials are calculated to distinguish different materials.

2. Governing equations and numerial methods

The governing equations are showed as follows. Assume there are m kinds of different materials in this fluid system.

$$\frac{\partial n_l}{\partial t} + \boldsymbol{u} \cdot \nabla n_l = -n_l \nabla \cdot \boldsymbol{u} \ \ (l = 1,2, \dots m) \tag{1}$$

$$\rho = \sum_{l=1}^{m} n_l \times M_l \tag{2}$$

$$\frac{\partial \boldsymbol{u}}{\partial t} + \boldsymbol{u} \cdot \nabla \boldsymbol{u} = -\frac{1}{\rho} \nabla (P_\mathrm{i} + P_\mathrm{e} + Q_\mathrm{i} + Q_\mathrm{e}) \tag{3}$$

$$\frac{\partial T_{\mathrm{i}}}{\partial t}+\boldsymbol{u}\cdot\nabla T_i=-\frac{P_{\mathrm{i}}+Q_{\mathrm{i}}}{\rho C v_{\mathrm{i}}}\nabla\cdot\boldsymbol{u}-\omega_{\mathrm{ie}}(T_{\mathrm{i}}-T_{\mathrm{e}}) \tag{4}$$

$$\frac{\partial T_{\mathrm{e}}}{\partial t}+\boldsymbol{u}\cdot\nabla T_e=-\frac{P_{\mathrm{e}}+Q_{\mathrm{e}}}{\rho C v_{\mathrm{e}}}\nabla\cdot\boldsymbol{u}+\frac{\omega_{\mathrm{ie}}}{Z_{\mathrm{eff}}}(T_{\mathrm{i}}-T_{\mathrm{e}}) \tag{5}$$

$$P_{\mathrm{i}}=N_{\mathrm{i}}k_{\mathrm{B}}T_{\mathrm{i}} \tag{6}$$

$$P_{\mathrm{e}}=N_{\mathrm{e}}k_{\mathrm{B}}T_{\mathrm{e}} \tag{7}$$

Here, n_l is the mole density of l material; $\boldsymbol{u}$ is the fluid velocity; M_l is the mole mass of l material; ρ is the mass density; P_{i} and P_{e} are the ion and electron pressures, respectively; Q_{i} and Q_{e} are the ion and electron artificial viscousities, respectively; T_{i} and T_{e} are the ion and electron temperatures, respectively; Cv_{i} and Cv_{e} are the ion and electron isochoric specific heats, respectively; ω_{ie} is the ion-electron collision frequency; Z_{eff} is the average effective charge of the ions; N_{i} is the total number density of all kinds of ions; N_{e} is the number density of electrons; k_{B} is the Boltzmann constant.

Eq.(1-2) are the mass density conservation equations. The mass density conservation is calculated indirectly by the conservation of mole densities. For this reason, the materials can be distinguished. Eq.(3) is the momentum conservation equation. Eq.(4) and Eq.(5) are the ion and electron internal energy conservation equation, respectively. Eq.(6) and Eq.(7) are the equation of states of ions and electrons, respectively. The artificial viscousity presented by Kuropatenko [4] and modified by Ogata [5] is adopted, and the artificial viscousity is splited between ions and electrons by the method presented by Miller [6]. The ion and electron artificial viscousities are added in Eq.(3), Eq.(4) and Eq.(5) as ion and electron entropy increasements, respectively.

A uniform staggered mesh is adopted. The advection terms are calculated by the Constrained Interpolation Profile (CIP) method [4], and the advection velocity is determined by the Runge-Kutta method. The nonadvection terms are calculated by the finite difference method.

3. Calculation case

We present the calculation result of typical case for the ICF fuel pellet, which is a spherical structure in a 2D cylindrical coordinate systerm. At the initial condition, we distributed the materials as shown in Table I by using the method of adopting mole conservation of each kinds of materials. And the corresponding initial ion and electron temperatures are shown in Table I. Figure 1 shows the initial density and temperature conditions, respectively. Here, DT indicated the 50:50 mixture of deuterium and tritium. The calculation grid configuration is uniformly set as 200 × 200. The boundary conditions are symmetric boundaries at z = 0.0 mm and r = 0.0 mm, and free boundaries at z = 3.0 mm and r = 3.0 mm.

TABLE I. Material and temperature of target at initial condition.

Radius	Material	Density	Temperature
r < 2 mm	DT	0.0002 g/cm^3	300 K
2 mm < r < 2.2 mm	DT	0.256.4 g/cm^3	300 K
2.2 mm < r < 2.5 mm	Al	2.69 g/cm^3	30 eV
2.5 mm < r < 2.7 mm	Pb	11.3 g/cm^3	20 eV
others	DT	0.0001 g/cm^3	300 K

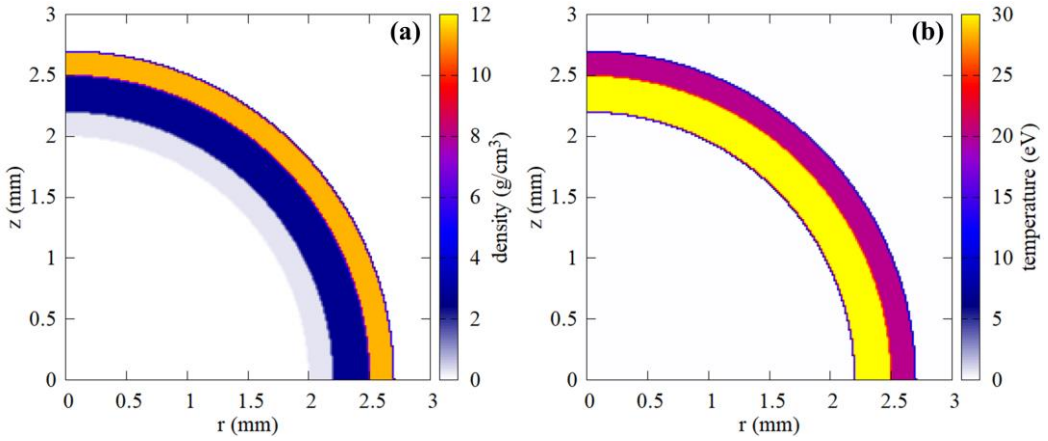

Fig.1 ICF pellet at Initial conditions. (a) Density distribution; (b) temperature distribution.

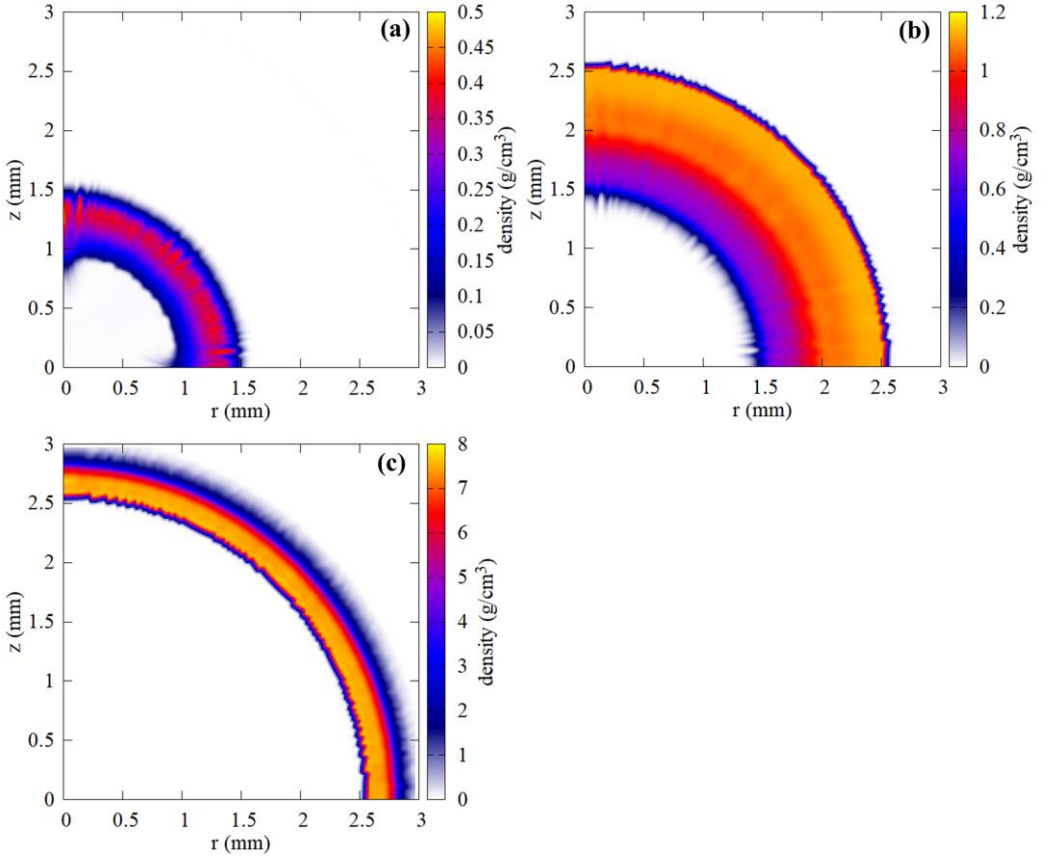

Fig.2 Density distribution in ICF pellet at 25.0 ns, (a) for DT, (b) for Al, and (c) for Pb.

Due to the initial condition, DT layer (2 mm < r < 2.2 mm) is compressed inward, Al layer (2 mm < r < 2.2 mm) expands outward and inward, Pb layer (2.5 mm < r < 2.7 mm) expands outward. Figure 2 shows the distributions of DT, Al, and Pb in the ICF fuel pellet at 25.0 ns. As shown in Fig.2, the distinguish method of different materials presented in this study works

well.

References

[1] K. Horioka, *Matter Radiat. Extremes* 3, 12 (2018)

[2] Z. Lin, et al, *Plasma Fusion Res.* 17, 2404064 (2022)

[3] N. Watanabe, et al., to be published in Plasma Fusion Res.

[4] V.F. Kuropatenko, *Amer. Math. Soc.*, Providence, 116 (1967)

[5] Y. Ogata, T. Yabe, *Comput. Phys. Commun*., 119, (1999), 179-193

[6] D.S. Miller, *Comput. Fluids.*, 210, (2020), 104672.

[7] T. Yabe, *J. Comput. Phys*. 169, (2001), 556–593

Characteristics of a limit-cycle oscillation observed in plasma fluid simulations of the GAMMA 10/PDX tandem mirror

Satoshi Togo[1,*], Kosuke Takanashi[1], Tomonori Takizuka[2], Naomichi Ezumi[1], Mizuki Sakamoto[1], Kenzo Ibano[2], Yuki Homma[3], Mafumi Hirata[1], Yousuke Nakashima[1], Keishi Honma[1]

[1]Plasma Research Center, University of Tsukuba
[2]Graduate School of Engineering, Osaka University
[3]National Institutes for Quantum Science and Technology

[*]togo@prc.tsukuba.ac.jp

Abstract. Self-excited oscillations observed in plasma fluid simulations of the GAMMA 10/PDX tandem mirror by a plasma fluid model based on the anisotropic ion pressure (AIP model) [S. Togo *et al.*, J. Adv. Simulat. Sci. Eng. **9** (2022) 185.] are studied. The spatiotemporal fluctuations of the fluid variables show that the oscillation is excited near the inner mirror throat and propagates both upstream and downstream. It is also found that the oscillation is classified as a limit-cycle oscillation (LCO) by the fact that the parameter trajectories approach asymptotically to a closed cycle regardless of their initial values.

Keywords: Plasma fluid model, Inhomogeneous magnetic field, Ion pressure anisotropy, Limit-cycle oscillation (LCO)

1. Introduction

Handling of the huge heat load onto the divertor plates is a crucial issue in future fusion devices. In a DEMO reactor such as JA DEMO, more than 70-80 % of heat flux entering the scrape-off layer (SOL) across the separatrix needs to be radiated before reaching the divertor plate [1, 2]. To design a divertor under such strict conditions, highly accurate simulation models for SOL-divertor plasmas are required. Conventional integrated codes for SOL-divertor plasmas such as SONIC [3, 4], SOLPS-ITER [5], UEDGE [6] and EMC3-EIRENE [7] utilize the Braginskii's plasma fluid model [8] for plasma modeling from the computational load point of view. It is thought that kinetic effects become important in simulations of DEMO SOL-divertor plasmas where the upstream plasma collisionality becomes marginal [9]. In addition, it is pointed out that, in such low collisionality, the ion temperature anisotropy becomes $T_{i\parallel}/T_{i\perp} = 0.2 \sim 0.3$ where $T_{i\parallel}$ and $T_{i\perp}$ denote the parallel and perpendicular ion temperature, respectively [10].

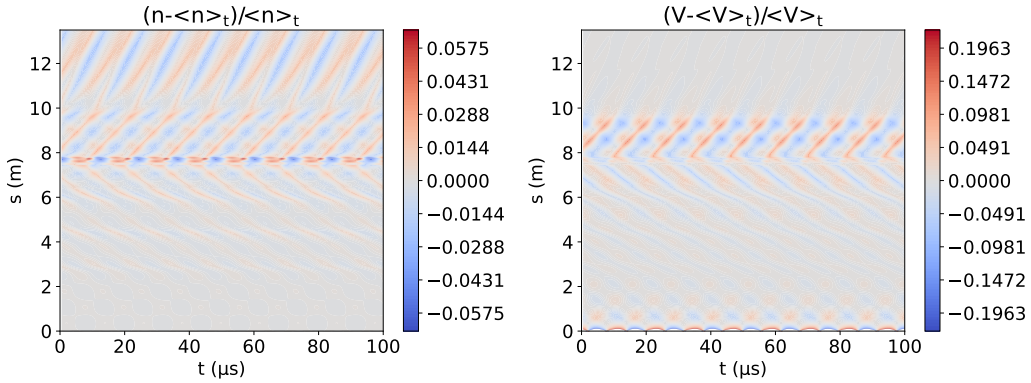

Figure 1: Spatiotemporal fluctuation profiles of (left) the plasma density $((n - \langle n \rangle_t)/\langle n \rangle_t)$ and (right) the ion parallel flow velocity $((V - \langle V \rangle_t)/\langle V \rangle_t)$ for the $Q_{i\perp}/Q_i = 0.1$ case in Ref. [14].

We have been developing a plasma fluid model based on the anisotropic ion pressure (AIP model) [11, 12, 13]. Recently, we have applied it to the GAMMA 10/PDX tandem mirror in order to understand the behavior and characteristics of the solutions of AIP model as well as to validate it [14]. There, we have found self-excited oscillations of profiles which look like a limit-cycle oscillation (LCO) when $T_{i\parallel}/T_{i\perp}$ at the midplane becomes close to unity. It is known, in circular plasmas, that an LCO appears in the parameter space associated with the H-mode transition [15]. Studying the characteristics of the limit-cycle is generally useful to understand the characterisitcs of its nonlinear, governing equations. In this study, therefore, the characteristics of the self-excited oscillations are studied focusing on the spatiotemporal fluctuation profiles and the parameter trajectories.

2. Fluctuation profiles and parameter trajectories

We focus on a simulated case in Ref. [14] with $Q_{i\perp}/Q_i = 0.1$ where $Q_{i\perp}/Q_i$ represents the fraction of the perpendicular ion heating to the total (i.e. parallel plus perpendicular) ion heating given in the central region. The time-averaged quasi-steady state profiles of this case are shown in Fig. 1 of Ref. [14].

The spatiotemporal fluctuation profiles of the plasma density n and the parallel ion flow velocity V are shown in Fig. 1. Here, s and t stand for the parallel-to-$\boldsymbol{B}$ coordinate and time, and the resolutions of them are 1 cm and 0.5 μs, respectively. The operator $\langle\cdot\rangle_t(s)$ means the time-average at s. It is clearly seen that the oscillation is excited near the inner mirror throat ($s \sim 7.5$ m) and propagates both upstream and downstream. The primary oscillation frequency there seems $\sim$ 80 kHz. The propagation velocity in the mirror-confined region ($|s| \leq 10$ m) is $\sim 10^5$ m/s which roughly corresponds to the ion sound speed c_s.

Figure 2 shows the parameter trajectories at $s = 7.7$ m. Here, we examine several initial profiles by starting from the quasi-steady state profiles of $Q_{i\perp}/Q_i = 0.05$, 1/3 and 1, which are shown in Fig. 1 of Ref. [14] (note that the total particle and power inputs are

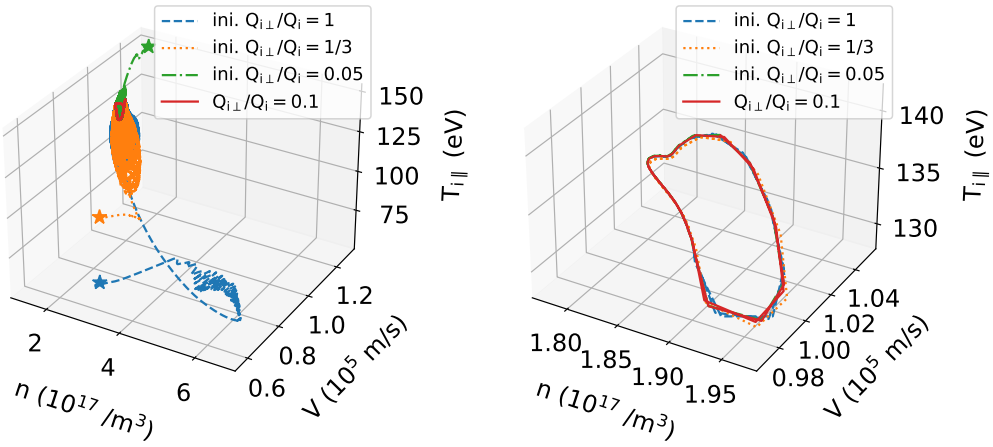

Figure 2: Parameter trajectories at $s = 7.7$ m when setting $Q_{i\perp}/Q_i = 0.1$; (left) full trajectories starting from different initial profiles indicated by the star symbols, and (right) an enlarged view of the trajectories for last 20 μs.

$\Gamma = 1.6 \times 10^{21}$ /s and $P_i = 100$ kW for all cases), and setting $Q_{i\perp}/Q_i = 0.1$. It shows that all trajectories approach asymptotically to a closed cycle regardless of their initial values. This fact indicates that the observed self-excited oscillation is classified as an LCO. Note that the range of this cycle is different depending on the chosen value of $Q_{i\perp}/Q_i$ (another cycle with a different range appears when $Q_{i\perp}/Q_i = 0.05$ is set as indicated in Figs. 1 and 2 in Ref. [14]). We will further focus on the phase differences between the parameters and investigate the mechanism of this cycle.

Acknowledgment

This work is performed with the support and under the auspices of the NIFS Collaboration Research Program (NIFS21KNST187 and NIFS22KIST031).

References

[1] N. Asakura, K. Hoshino, S. Suzuki *et al*: Studies of power exhaust and divertor design for a 1.5 GW-level fusion power DEMO, *Nuclear Fusion*, volume:57 (2017), 126050-1–12.

[2] N. Asakura, K. Hoshino, Y. Homma *et al*: Simulation studies of divertor detachment and critical power exhaust parameters for Japanese DEMO design, *Nuclear Materials and Energy*, volume:26 (2021), 100864-1–8.

[3] H. Kawashima, K. Shimizu, T. Takizuka *et al*: Development of Integrated SOL/Divertor Code and Simulation Study in JAEA, *Plasma and Fusion Research*, volume:1 (2006), 031-1–13.

[4] K. Shimizu, T. Takizuka, K. Ohya *et al*: Kinetic modelling of impurity transport in detached plasma for integrated divertor simulation with SONIC (SOLDOR/NEUT2D/IMPMC/EDDY), *Nuclear Fusion*, volume:49 (2009), 065028-1–9.

[5] S. Wiesen, D. Reiter, V. Kotov *et al*: The new SOLPS-ITER code package, *Journal of Nuclear Materials*, volume:463 (2015), 480–484.

[6] T.D. Rognlien, J.L. Milovich, M.E. Rensink *et al*: A fully implicit, time dependent 2-D fluid code for modeling tokamak edge plasmas, *Journal of Nuclear Materials*, volume:196-8 (1992), 347–351.

[7] Y. Feng, F. Sardei, J. Kisslinger: 3D fluid modelling of the edge plasma by means of a Monte Carlo technique, *Journal of Nuclear Materials*, volume:266-269 (1999), 812–818.

[8] S.I. Braginskii: Transport process in a plasma, *Reviews of Plasma Physics*, volume:1 (1965), 205.

[9] Y. Homma: Assessment of the impact of the kinetic effect of ion parallel heat conduction on DEMO-relevant SOL plasma using integrated SOL-divertor code SONIC, *Plasma Physics and Controlled Fusion*, volume:64 (2022), 045020-1–14.

[10] A. Froese, T. Takizuka, M. Yagi: Kinetic Particle Simulation Study of Parallel Heat Transport in Scrape-off Layer Plasmas over a Wide Range of Collisionalities, *Plasma and Fusion Research*, volume:5 (2010), 026-1–15.

[11] S. Togo, T. Takizuka, M. Nakamura *et al*: Self-consistent treatment of the sheath boundary conditions by introducing anisotropic ion temperatures and virtual divertor model, *Journal of Computational Physics*, volume:310 (2016), 109–126.

[12] S. Togo, D. Reiser, P. Börner *et al*: Benchmarking of B2 Code with a One-Dimensional Plasma Fluid Model Incorporating Anisotropic Ion Pressures on Simple Mirror Configurations, *Plasma and Fusion Research*, volume:13 (2018), 3403022-1–4.

[13] S. Togo, T. Takizuka, D. Reiser *et al*: Self-consistent simulation of supersonic plasma flows in advanced divertors, *Nuclear Fusion*, volume:59 (2019), 076041-1–11.

[14] S. Togo, N. Ezumi, M. Sakamoto *et al*: Fluid simulation of plasmas with anisotropic ion pressure in an inhomogeneous magnetic field of a tandem mirror device GAMMA 10/PDX, *Journal of Advanced Simulation in Science and Engineering*, volume:9 (2022), 185–197.

[15] T. Kobayashi, K. Itoh, T. Ido *et al*: Spatiotemporal Structures of Edge Limit-Cycle Oscillation before L-to-H Transition in the JFT-2M Tokamak, *Physical Review Letters*, volume:111 (2013), 035002-1–5.

JSST 2022

Numerical Method of Applying Shadow Theory to Scattering Fields by a Multiple Plane Grating

Hideaki Wakabayashi[1,*], Masamitsu Asai[2], Jiro Yamakita[1]

[1]Faculty of Computer Science and Systems Engineering, Okayama Prefectural University
[2]Faculty of Biology-Oriented Science and Technology, Kindai University

[*]waka@c.oka-pu.ac.jp

Abstract. This paper applies the shadow theory to scattering fields by a composite dielectric grating embedded with conducting strips. A new method is formulated to obtain scattering factors of the shadow theory from the electric current densities using the matrix eigenvalues method and the Galerkin method. Scattering properties by a multiple plane grating having conducting strips are numerically shown for all complex incident angles.

Keywords: shadow theory, matrix eigenvalues method, Galerkin method, multiple plane grating, Joule loss

1. Introduction

In Nakayama's shadow theory, a new description of electromagnetic fields using scattering factor enables to define the diffraction efficiencies for the low grazing limit and all complex incident angles. The theory originally treated only in the scattering problem of perfectly conducting gratings [1]. We have presented and developed the matrix eigenvalues method (MEM) to study scattering by dielectric gratings. Our method obtains numerical solutions by the matrix eigenvalues calculation. By applying the shadow theory to our method and formulating the field descriptions using the scattering factors, we resolved the cases where the eigenvalues degenerate by zero in all regions [2]. In practical numerical calculations, however, these are only few points, and are not worthwhile advantages of scattering factors.

Therefore, we have proposed two applications of scattering factors. As the first application, we discovered that the scattering factors are physical quantities directly linked to the spectral-domain Green's function. Using the Green's function of the scattering factors, we formulated scattering fields by periodic conducting strips [3]. However, the final solution was limited to obtain the conventional diffraction amplitudes.

We proposed that the second application of scattering factors is more strict accuracy criterion than the convergence of solutions in the analysis of multilayered dielectric gratings. We thought that even when the energy conservation law is not established, the reciprocity can be effective criterion for numerical check. We showed that the reciprocity appears in the scattering factor [4], and used the scattering factor to evaluate the calculation accuracy [5].

This paper applies the shadow theory to scattering fields by composite dielectric gratings embedded with conducting strips. We propose a new method to obtain scattering factors

being basic quantities and Joule losses from the electric current densities. Some numerical results are given for a multiple plane grating consisting of conducting strips. We newly show that in the case of a resistive plane grating, the diffraction efficiencies hold the reciprocity.

2. Analytical theory

We treat the scattering problem of a composite dielectric grating embedded with K layered conducting strips in Fig. 1. The grating periodicity is Λ. The conducting strips exist on the interfaces $x_{k'} = x_{(\bar{n}(k'))}$ between the regions $\bar{n}(k') - 1$ and $\bar{n}(k')$ with $\{\bar{n}(k')|k' = 1, \ldots, K\} \subseteq \{1, 2, \ldots, N\}$, and have the surface resistance $R_{k'}$ [Ω]. A plane wave of wavelength λ illuminates on the grating at an incident angle θ_a from region 0 or at θ_s from region N. $(\varepsilon_\mathrm{a}, \mu_\mathrm{a})$ and $(\varepsilon_\mathrm{s}, \mu_\mathrm{s})$ are the relative permittivity and permeability of regions 0 and N, respectively.

The primary fields are based on the assumption of the conducting strips removed completely. Considering the case where a plane wave is incident on the grating from the region 0 and normalizing the field by $2\xi_0^\mathrm{a}$, the y component $\overline{\Psi}_y^\mathrm{a} = \Psi_y^\mathrm{a}/(2\xi_0^\mathrm{a})$ is expressed by

$$\overline{\Psi}_y^\mathrm{a} = \sqrt{\zeta_\mathrm{a}}\left(\frac{e^{-j\xi_0^\mathrm{a}x} - e^{j\xi_0^\mathrm{a}x}}{2\xi_0^\mathrm{a}}e^{-js_0z} + \sum_m S_m^{\mathrm{a}-}e^{-j\xi_m^\mathrm{a}x}e^{-js_mz}\right) = \overline{\Psi}_y^{\mathrm{a[in]}} + \sqrt{\zeta_\mathrm{a}}\sum_m S_m^{(0)-}e^{-j\xi_m^\mathrm{a}x}e^{-js_mz}, \tag{1}$$

$$2\xi_0^\mathrm{a} S_m^{(0)-} = \delta_{m0} + g_m^{\mathrm{a}-}, \quad \xi_m^\mathrm{a} = \sqrt{\varepsilon_\mathrm{a}\mu_\mathrm{a} - s_m^2}, \quad s_m = s_0 + m\,n_\mathrm{K}, \quad s_0 = \sqrt{\varepsilon_\mathrm{a}\mu_\mathrm{a}}\sin\theta_\mathrm{a}, \quad n_\mathrm{K} = \lambda/\Lambda. \tag{2}$$

Here, $\zeta = \mu$ (TE) or ε (TM). $S_m^{(0)-}$ and $g_m^{(0)-}$ are the scattering factor and conventional diffraction amplitude for the mth-order reflection, respectively. δ_{m0} stands for Kronecker delta. Using Eq. (1) and its derivative, the z component $\overline{\Psi}_z^\mathrm{a}$ can be obtained. The responses to $\overline{\Psi}_{y(z)}^{\mathrm{a[in]}}$ are called the scattering factors $(S_m^\oplus, S_m^-)$ in each region.

Truncating at the order M, the $y\,(z)$ components of the fields can be approximated by $\Psi_{y(z)}(x,z) = \sum_m \psi_{y(z)m}(x)e^{-js_mz}$. Applying the shadow theory to the field description in the MEM, we obtain

$$\begin{bmatrix}\overline{\boldsymbol{\psi}}_y(x)\\ \overline{\boldsymbol{\psi}}_z(x)\end{bmatrix} = \left[\overline{\boldsymbol{T}}\right]\left[\overline{\boldsymbol{P}}(x)\right]\begin{bmatrix}\boldsymbol{S}^\oplus\\ \boldsymbol{S}^-\end{bmatrix} \tag{3}$$

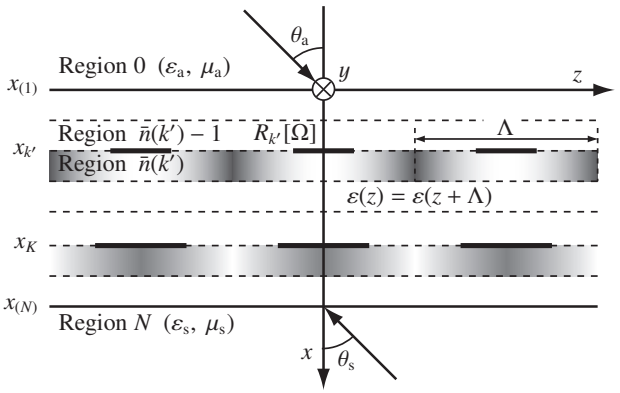

Figure 1: A composite dielectric grating.

where $\boldsymbol{\psi}_{y(z)} = \left[\psi_{y(z)-M} \cdots \psi_{y(z)0} \cdots \psi_{y(z)M}\right]^\mathrm{T}$ and $\boldsymbol{S} = [S_{-M} \cdots S_0 \cdots S_M]^\mathrm{T}$. $[\overline{\boldsymbol{T}}]$ and $[\overline{\boldsymbol{P}}]$ are the transformation and propagation matrices of the shadow theory, and are numerically given in the middle regions. The electric fields $\overline{\boldsymbol{\psi}}_y$ (TE), $\overline{\boldsymbol{\psi}}_z$ (TM) and the scattering factors $\boldsymbol{S}$ are quantities for the primary fields, we denote them by $\overline{\boldsymbol{e}^{1\mathrm{st}}} = \overline{\boldsymbol{e}}_y$ (TE) or $\overline{\boldsymbol{e}}_z$ (TM) and ${}^{1\mathrm{st}}\boldsymbol{S}$.

The spectral-domain Green's functions at the observation point x in region n are expressed using Eq. (3) by

$$\begin{bmatrix}\boldsymbol{G}_y(x|x_{k',m'})\\ \boldsymbol{G}_z(x|x_{k',m'})\end{bmatrix} = \left[\overline{\boldsymbol{T}}_n\right]\left[\overline{\boldsymbol{P}}_n(x)\right]\begin{bmatrix}\boldsymbol{S}_n^\oplus(x_{k',m'})\\ \boldsymbol{S}_n^-(x_{k',m'})\end{bmatrix}. \tag{4}$$

We need the Green's functions for electric fields, and write as $\boldsymbol{G} = \boldsymbol{G}_y$ (TE) and $\boldsymbol{G}_z$ (TM) being $(2M+1)$ dimensional. The sum of the secondary fields generated by $j_{m'}^{(k')}$ is expressed by using the mth-order component G_m of $\boldsymbol{G}$. The spectral-domain form $j_{m'}^{(k')}$ is expanded in terms of the known functions $\phi_{m\ell'}^{(k')}$. These are written as

$$e_m^{\mathrm{2nd}}(x) = \sum_{k'} e_m^{\mathrm{2nd}(k')} = \sum_{k'} \sum_{m'} G_m(x|x_{k',m'})\, j_{m'}^{(k')}, \qquad j_m^{(k')} = \sum_{\ell'=-L}^{L} \phi_{m\ell'}^{(k')}\, I_{\ell'}^{(k')}. \tag{5}$$

The resistive boundary condition on the kth plane grating having surface resistance R_k is satisfied at the interface $x = x_k$ as

$$\sqrt{Y_0} E_y^{\mathrm{total}}(x,z) = \sum_m \left[\overline{e_m^{\mathrm{1st}}}(x) + e_m^{\mathrm{2nd}}(x) \right] e^{-js_m z} = \frac{R_k}{Z_0} \sum_m j_m^{(k)} e^{-js_m z} \tag{6}$$

with wave admittance in vacuum $Y_0 = 1/Z_0$. Substituting Eqs. (3), (5) into Eq. (6), we get

$$\sum_m \sum_{k'} \sum_{m'} \left\{ G_m(x_k|x_{k',m'}) - \frac{R_k}{Z_0} \delta_{kk'} \delta_{mm'} \right\} \sum_{\ell'} \phi_{m'\ell'}^{(k')} I_{\ell'}^{(k')}\, e^{-js_m z} = -\sum_m \overline{e_m^{\mathrm{1st}}}(x_k)\, e^{-js_m z}. \tag{7}$$

Here, we employ the spectral-domain form $\phi_{m\ell'}^{(k')}$ of a Fourier expansion function $\Phi_\ell^{(k)}(z) = \exp\{-j\ell\,(\lambda/W_k)\,z\}$ to approximate the surface electric current density induced on the strips. We determine $I_{\ell'}^{(k')}$ in Eq. (7) using the Galerkin method, and obtain the current density $j_{m'}^{(k')}$. The scattering factors in regions 0 and N for the secondary fields are given by

$${}^{\mathrm{2nd}}S_m^{(0)-} = \sum_{k'} \sum_{m'} S_m^{(0)-}(x_{k',m'})\, j_{m'}^{(k')}, \qquad {}^{\mathrm{2nd}}S_m^{(N)+} = \sum_{k'} \sum_{m'} S_m^{(N)-}(x_{k',m'})\, j_{m'}^{(k')}. \tag{8}$$

We newly define the scattering factors for the total fields as

$$S_m^{\mathrm{a}-} = {}^{\mathrm{1st}}S_m^{(0)-} + {}^{\mathrm{2nd}}S_m^{(0)-}, \quad S_m^{\mathrm{s}+} = {}^{\mathrm{1st}}S_m^{(N)+} + {}^{\mathrm{2nd}}S_m^{(N)+}. \tag{9}$$

3. Numerical examples and discussions

The diffraction efficiency η_m^{a} (η_m^{s}) of the mth-order wave going into the air (substrate) is represented by using $S_m^{\mathrm{a}-}$ ($S_m^{\mathrm{s}+}$). In this paper, the energy conservation law is given by

$$\sum_m \eta_m^{\mathrm{a}} + \sum_m \eta_m^{\mathrm{s}} + \sum_k \mathrm{loss}_k = 1 \tag{10}$$

where loss_k is Joule loss on the kth conducting strips. We use Eq. (10) to check the accuracy of calculations.

We consider a multiple plane grating having periodicity Λ and consisting of conducting strips embedded in the middle uniform region, as shown in Fig. 2.

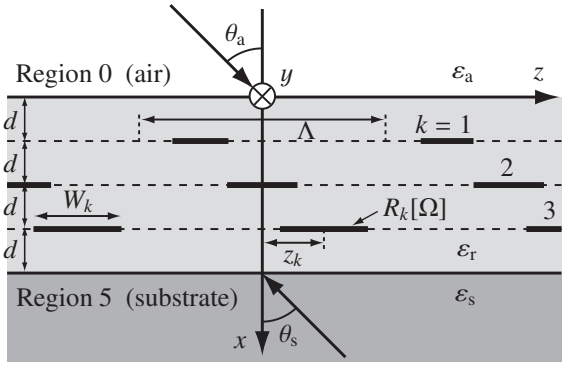

Figure 2: A multiple plane grating.

The relative permittivity of the middle region is denoted by ε_{r}. The thickness of each layer in the middle region is defined by d. The kth conducting strips have the width W_k and the surface resistance R_k with $k = 1, 2, 3$. The relative permeability is set to be 1.0 in all regions. Calculations are performed under $\varepsilon_{\mathrm{a}} = 1.0$, $\varepsilon_{\mathrm{r}} = 2.0$, $\varepsilon_{\mathrm{s}} = 2.25$, $\Lambda/\lambda = 1/n_{\mathrm{K}} = 1.2$ and $d/\Lambda = 0.2$. The kth conducting strips having $R_k/Z_0 = 0.05$ and $W_k/\Lambda = 0.2, 0.25, 0.3$ are arranged at the center of the strips $z_k/\Lambda = -0.2, 0, 0.2$.

Figure 3 plots the 0th and 1st transmitted diffraction efficiencies (TDEs) against s_0 in TE cases. The left and right superscripts of η represent incident and transmitted wave regions, respectively. "a" and "s" indicate the air and substrate, respectively. The TDEs have a reflected symmetry with the symmetrical axis $s_0 = -mn_{\mathrm{K}}/2$ and hold the reciprocity only for s_0 and m satisfying max $[-\sqrt{\varepsilon\mu}, -\sqrt{\varepsilon\mu} - mn_{\mathrm{K}}] \leq s_0 \leq$ min $[\sqrt{\varepsilon\mu}, \sqrt{\varepsilon\mu} - mn_{\mathrm{K}}]$ in a propagating incidence.

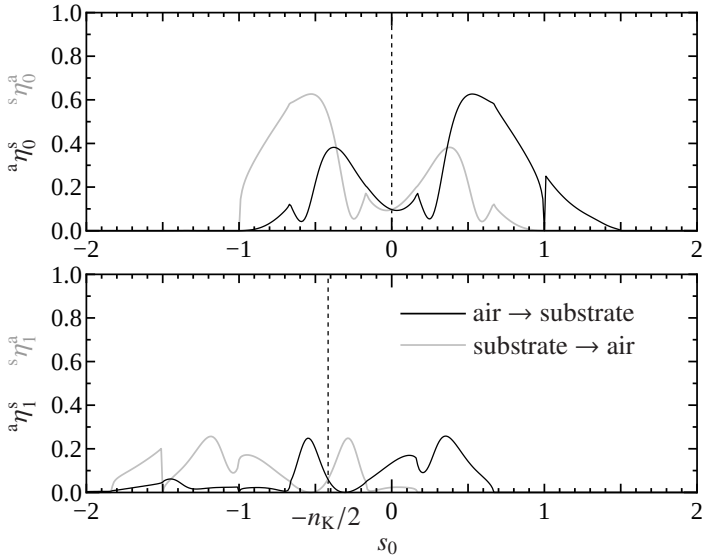

Figure 3: The TDEs against s_0 in TE cases.

References

[1] J. Nakayama, Shadow theory of diffraction grating, IEICE Trans. Electron., Vol. E92-C, No. 1, pp. 17–24, 2009.

[2] H. Wakabayashi, M. Asai, K. Matsumoto and J. Yamakita, Numerical method of applying shadow theory to all regions of multilayered dielectric gratings in conical mounting, J. Optical Society of Am. A, Vol. 33, No. 11, pp. 2188–2197, 2016.

[3] H. Wakabayashi, M. Asai, K. Matsumoto and J. Yamakita, Numerical methods for composite dielectric gratings embedded with conducting strips using scattering factors, IEICE Trans. Electron. Vol. E96-C, No 1, pp. 19–27, 2013.

[4] M. Asai, H. Wakabayashi and J. Yamakita, On the accuracy of the MoM analysis for the scattering factors of metallic strip gratings with dielectric slabs in terms of the reciprocity theorem, Proc. the 36th JSST Annual International Conf. Simulation Technology, pp. 263–265, 2017.

[5] H. Wakabayashi, M. Asai and J. Yamakita, Reciprocity theorem and accuracy evaluation on scattering fields by dielectric gratings, J. Optical Society of Am. A, Vol. 35, No. 11, pp. 1861–1870, 2018.

Topology Optimization of Motor Stator to Reduce Vibration

Hiroto Otsuki[1], Kota Watanabe[1,*], Takahiro Sato

[1]Graduate School of Engineering, Muroran Institute of Technology

[*]k-wata@muroran-it.ac.jp

The full paper of this paper has been published in Journal of Advanced Simulation in Science and Engineering (JASSE).

DOI: https://doi.org/10.15748/jasse.10.73

On the Rectangular Skew Layout of Helices for a Quasi-Isotropic Chiral Particle

Masamitsu Asai[1*], Hideaki Wakabayashi[2], Jiro Yamakita[2]

[1]Department of Computational Systems Biology, Kindai University
[2]Okayama Prefecture University

*asai@waka.kindai.ac.jp

Abstract. The rectangular skew layout of conducting helices is presented as the structure of a quasi-isotropic chiral particle. This research is done as part of the simplification of the particle structure under the trade-off with meintaining the quality of isotropic chirality. Effective con-stitutive parameters of the medium composed of the presented particles are analyzed by the quasi-static Lorentz theory combined with the method of moments to investigate the quality of isotropy and chirality. The extent of cancellation of electric quadrupole moments is also checked as a criterion for isotropic chirality.

Keywords: Artificial medium, chiral medium, electromagnetic theory, medium design.

1. Introduction

Artificial media (metamaterials) for electromagnetic waves have been of great interest in the fields of radio science, optics, and acoustics etc. They are composed of artificial particles or fine roughness in background matrices, and are designed to show required macroscopic electromagnetic characteristics. The size and spacing of each particle or roughness is to be much smaller than the wavelength. The Pasteur medium i.e. a reciprocal isotropic chiral medium was first developed for the magnified scale model of organic compounds by which K. F. Lindman investigated the optical activity in the microwave frequency in 1914 through 1922. Artificial bi-isotropic and bi-anisotropic media and artificial magnetic and dielectric media also have been studied [1]. The term ‘metamaterials’ has been given to those artificial media since the negative index of refraction in a left-hand material was realized by J. B. Pendry, D. R. Smith et al. in around 2000 [2]. Research on the artificial chiral medium has been intensively reported not only on the optical activity but on the biomimetic functions and the medical effects such as suppression of cancer proliferation etc. [3],[4]. Conventional isotropic chiral media are composed of random or homogeneous distributions of randomly-oriented chiral particles. In the practical design however, it is actually very hard to have the orientations and positions of particles perfectly random, then the isotropy with high accuracy is hard to realize. It is on the other hand more realistic and practical to design a three-dimensional periodic array of quasi-isotropic chiral particles. Each particle should be close to electromagnetically isotropic and should be downsized to around a tenth of wavelength that is known to be adequate granularity for chiral

media. Authors have presented the cubic layout of helices that has twelve helical or double-helical thin wires considering rotational symmetry and granularity. The resultant medium has shown high quality of isotropy and chirality [5]. Although it is still necessary to pursue optimal structure of particles, it is also important to simplify the structure for cost reduction and simplicity of fabrication under the trade-off with the quality of isotropy and chirality. Authors have investigated the case of regular tetrahedral layout of helices that is simpler than the cubic one, and demonstrated that they give isotropic chiral property at frequency region that is narrower than the cubic case [6].

In this work, the rectangular skew layout of thin-wire conducting helices is presented as the simplified structure of a quasi-isotropic chiral particle as part of the same study. Compared to the cubic layout, the number of helical or double-helical wires is reduced by half as with the regular tetrahedral case in our previous work [6]. This reduction is also likely to sacrifice the quality of isotropic chirality. To investigate the quality of isotropy and chirality of the medium composed of the presented particles, the effective constitutive parameters are numerically an-alyzed by the quasi-static Lorentz theory [8] combined with the method of moments for thin-wire approximation [5]-[7]. The electric and magnetic dipole moments and the electric quad-rupole moments are taken into account in the analyses [9],[10]. The extent of cancellation of the electric quadrupole moments is also checked as a criterion for the isotropic chirality.

2. Structure and Analysis

A Cartesian coordinate system (x,y,z) and three pairs of single or double helices that compose a single particle are assumed as shown in Fig. 1. The helical axes are on the sufaces of a cube of edge length L whose center of gravity is on the coordinate origin (Fig. 2). The axes of each pair of helices are parallel to either of the coordinate axes and make the skew positions with those of other pairs. The single helix (that also composes a double helix) is a right-handed

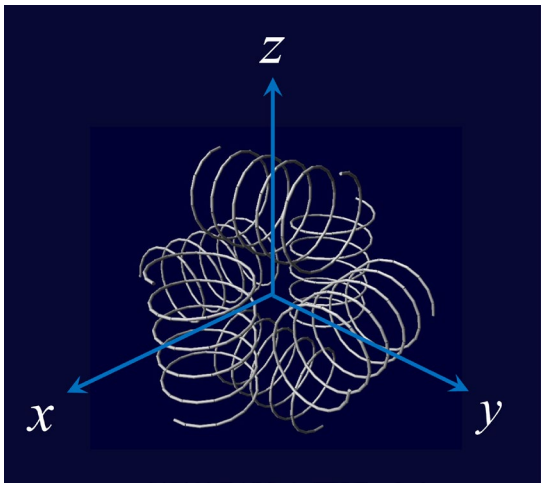

Fig. 1 particle structure

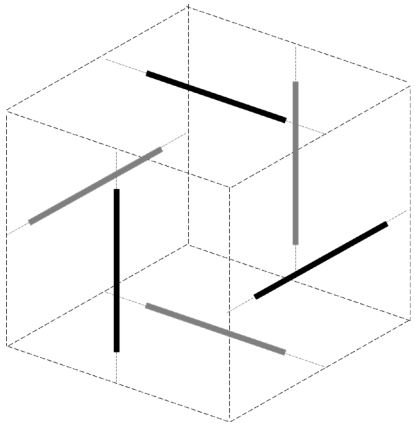

Fig. 2 layout of helical axes

five-turn perfectly-conducting helical thin wire with wire radius r, wire length l, helical radius a and axis length h. The edge length L of the cube is set as L=h+2r+2a. This structure has three axes of three-fold rotational symmetry as with the regular tetrahedral layout, and additionally has three axes of two-fold rotational symmetry. The medium is composed of three-dimensional periodic array of the particles along the coordinates in free space. The periodicity along each coordinate axis is identically d. Fig. 3 shows the normalized chirality constant at frequencies of 4.3 through 5.4 GHz where single helix is used for each element, and l=25.00 mm, r=0.03 mm, h/l=0.1, d=2L. The diagonal elements of the chirality tensor, averaged absolute values of non-diagonal elements, and the averaged absolute values of the electric quadrupole components of those elements are plotted. Three diagonal elements have almost the same values. It can be seen that at frequencies of lower than around 4.7GHz and those of higher than around 5.0 GHz, non-diagonal elements and the quadrupole components are very small compared to the diagonal elements, that shows almost perfect isotropic chirality. More detailed investigations will be presented in the conference.

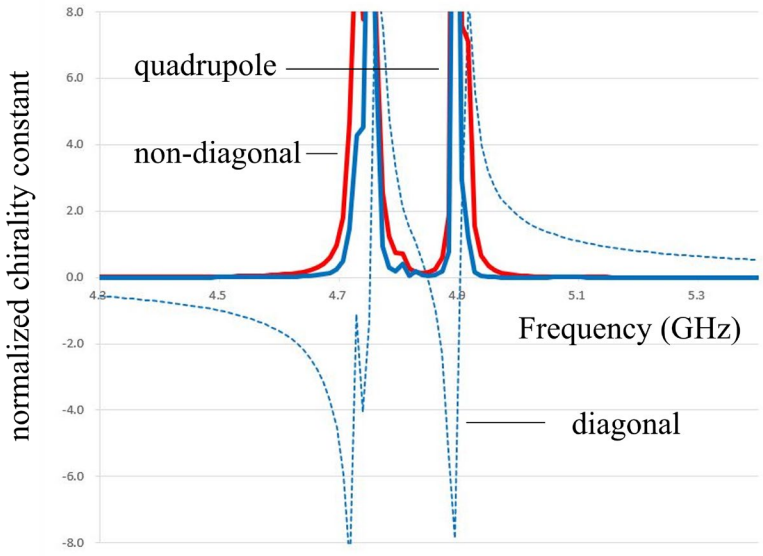

Fig. 3 Chirality constant for the case of double helix

3. Conclusion

In the presented layout of the particle, the number of helices was reduced by half compared to the cubic case as with the regular tetrahedral case in our previous work [6] . There are three axes of three-fold rotational symmetry as with the regular tetrahedral layout, and additionally are three axes of two-fold rotational symmetry. The present simplified particle turned out to be available as an almost isotropic chiral one for the limited region of frequency and magnitude of chiral constant. The simpler structures that can coexist with the high quality of isotropic chirality should be pursued in our future work.

References

[1] I. V. Lindell el al., Artech House, (1994), pp. 1-18, 193-243.

[2] D. R. Smith et al., *Physical Review Letters*, Vol. 84, No. 18 (2000), pp. 4184-4187.

[3] M. Asai et al., *Materials Integrations,* Vol. 25, No. 12 (2012), pp. 31-37.

[4] S. Motojima et al., *Applied Physics Letters*, Vol. 56, No. 4 (1995), pp.321

[5] M. Asai et al., *Proc. of JSST Int. Conf. Sim. Tech*, Vol. 1 (2019)

[6] M. Asai et al., *Proc. of JSST Int. Conf. Sim. Tech*, Vol. 1 (2021)

[7] M. Asai et al., *Proc. of ISAP*, Vol. 1, (2016), pp. 2C2-20584.

[8] A. Ishimaru et. al., *IEEE Trans. Antennas Propag*., Vol. 51, No. 10, (2003), pp. 2550-2557.

[9] A. D. Buckingham et al., *J. Chem. Soc.A*, (1971), pp. 1988-1991.

[10] I. P. Theron et al., *J. Electromag. Waves App*. Vol. 10, No. 4 (1996), pp. 539-561.

Feature Emphasis Visualization of 3D Measured Point Clouds by Proliferation using PCA

Takuto Sasano[1*], Kyoko Hasegawa[2*], Liang Li[2*], Satoshi Tanaka[2*]

[1]Graduate School of Information Science and Engineering, Ritsumeikan University
[2]College of Information Science and Engineering, Ritsumeikan University

*is0411ii@ed.ritsumei.ac.jp

Abstract. Recent advances in laser scanning technology have made it possible to measure and record a wide variety of objects. The data obtained by laser scanning are large 3D point clouds, many of which contain complex structures. In order to understand the structure accurately, it is necessary to visualize the internal and external structures simultaneously. Therefore, in this paper, we use "transparent visualization," which can visualize both internal and external structures at the same time. We also use "feature-enhanced visualization" to achieve clearer transparent visualization. In this study, "feature-enhanced visualization" is realized by up-sampling using principal component analysis. The effectiveness of the proposed method is verified by applying the method to actual 3D measured point clouds.

Keywords: Transparent visualization, Laser-scanned large-scale point cloud, Feature extraction

1. Introduction

The development of laser scanning technology has made it possible to measure various objects, including buildings and antiques of historical value, without directly touching them. This has led to the proliferation of the "digital archive" initiative. In this initiative, cultural properties are preserved as digital data, so they are not weathered by wind and rain. In addition, the data is useful as research material and for sharing information via the Internet. Laser scanning can be used to obtain three-dimensional (3D) point cloud data of the object. The measured point cloud data usually has a complex 3D structure. To fully grasp the 3D structure, transparent visualization is effective. In our previous studies, Stochastic Point-Based Rendering (SPBR)[1, 2] has been used as a transparent visualization method. However, transparent visualization can be cumbersome because the external and internal structures of a 3D object are visible at the same time, resulting in a reduction in visibility. Therefore, feature-enhanced visualization was used, which emphasizes the edges of the solid object [3]. This can improve the visibility in transparent visualization. However, the conventional feature-enhanced visualization does not change the point density and cannot sufficiently emphasize feature areas with sparse points. In

this paper, the point density is increased by multiplying feature points to emphasize feature areas with low point density. Principal component analysis (PCA) is then used to multiply points from feature points in the direction of the first principal component.

2. Determination of multiplication target points

In this study, we use PCA to determine the points to proliferate. The algorithm for determining the proliferation points is as follows.

1. PCA is performed on the coordinates of a group of 3D points in a sphere of arbitrary radius r centered at the point $P^{(i)}$. r is a parameter determined by the user.
2. Calculate the eigenvalues $(\lambda_1 \geq \lambda_2 \geq \lambda_3)$ from the covariance matrix obtained by PCA.
3. Calculate the feature values $F_c^{(i)}$ and $F_l^{(i)}$ by combining the eigenvalues.
4. Target points for multiplication are those satisfying $F_c^{(i)} > t_c$ and $F_l^{(i)} > t_l$. t_c and t_l are parameters to be determined by the user.

Feature value $F_c^{(i)}$ and $F_l^{(i)}$ is calculated as follows [4]:

$$F_c^{(i)} = \frac{\lambda_3}{\lambda_1 + \lambda_2 + \lambda_3} \qquad F_l^{(i)} = \frac{\lambda_1 - \lambda_2}{\lambda_1} \qquad (1-2)$$

3. Proliferation in the direction of the first principal component

We proliferate points in the direction of the first principal component from the subject point. However, when the target point is the endpoint, the multiplication rate is *d*, and the distance from the target point to the farthest multiplication point is L, the interval Δt of each point must satisfy $\Delta t = L/(d-1)$. In this method, feature extraction is the same as in the conventional method, but the method of highlighting is different. In the conventional method, feature points are duplicated at the same coordinates to increase opacity and emphasize them. Therefore, feature areas with low point density are insufficiently emphasized. On the other hand, in the proposed method, the proliferation points are placed at coordinates shifted from the feature point to the direction of the first principal component. This allows the point density of the feature region to be increased. Therefore, feature regions with low point density can be effectively emphasized and visibility can be improved.

4. Experimental results

In this section, we demonstrate the effectiveness of the proposed method through a case study using data from Kyoto Women's University. Fig. 1(a) shows the feature points in red without proliferation. On the other hand, Fig. 1(b) shows the feature points multiplied by the proposed method. From these figures, it can be seen that the points are appropriately multiplied in the feature area. Fig. 2(a) is the result in which feature points are emphasized by the conventional method. Fig. 2(b) shows the result in which feature points are multiplied by the proposed

method. In both cases, feature highlighting improves visibility, which has been a problem of transparent visualization. However, in Fig. 2(a), feature areas with relatively low point density are not emphasized very much. In contrast, Fig. 2(b) shows that feature areas with low point density can be emphasized, especially for linear feature areas.

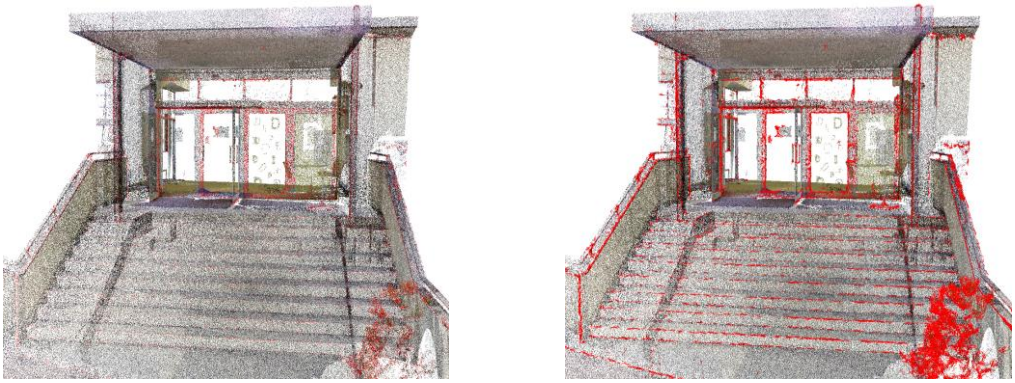

(a) Visualization result without proliferation (b) Visualization result of the proposal method

Figure 1: Visualization results with highlighting feature regions on the point cloud data of Kyoto Women's University.

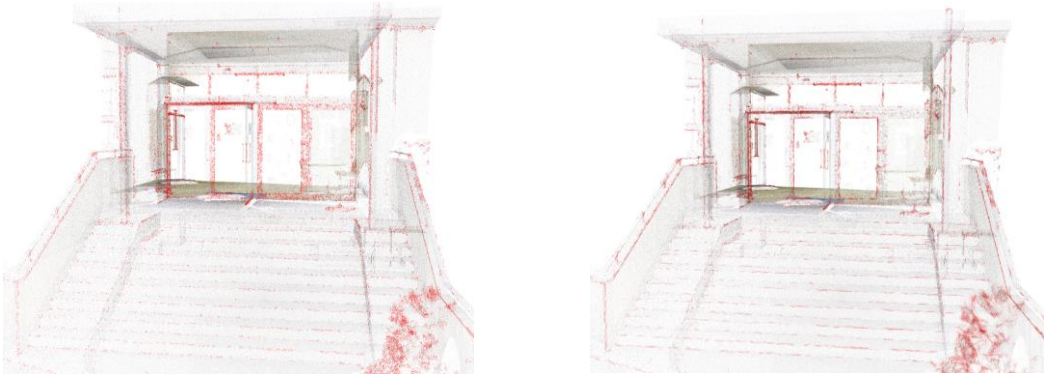

(a) Visualization result of the conventional method [3] (b) Visualization result of the proposal method

Figure 2: Transparent visualization results with highlighting feature regions on the point cloud data of Kyoto Women's University.

5. Conclusion

In this paper, we proposed a method for feature emphasis in transparente visualization using stochastic point-based rendering. The experimental results show that the proposed method effectively enhanced linear feature regions and improved the visibility of the 3D edges in the original point cloud.

References

[1] S. Tanaka, K. Hasegawa, N. Okamoto, R. Umegaki, S. Wang, M. Uemura, A. Okamoto, and K. Koyamada: See-Through Imaging of Laser-scanned 3D Cultural Heritage Objects based on Stochastic Rendering of Large-Scale Point Clouds, ISPRS Ann. Photogramm. Remote Sens. Spatial Inf. Sci., III-5, pp. 73-80, 2016.

[2] Tomomasa Uchida, Kyoko Hasegawa, Liang Li, Motoaki Adachi, Hiroshi Yamaguchi, Fadjar I. Thufail, Sugeng Riyanto, Atsushi Okamoto, Satoshi Tanaka: Noise-robust transparent visualization of large-scale point clouds acquired by laser scanning, ISPRS Journal of Photogrammetry and Remote Sensing, vol. 161, pp.124-134, March 2020.

[3] Naoya Okamoto, Kyoko Hasegawa, Liang Li, Atsushi Okamoto, Satoshi Tanaka,“ High-lighting Feature Regions Combined with See-Through Visualization of Laser-Scanned Cultural Herutage, ” Proc. 2017 International Conference on Culture and Computing, Sep.10, 2017.

[4] Martin Weinmann, Boris Jutzi, Cle´ment Mallet: Semantic 3D scene interpretation: A framework combining optimal neighborhood size selection with relevant features, IS-PRS Ann. Photogramm. Remote Sens. Spatial Inf. Sci., II-5/W2 (2013), 313–318.

Edge-Highlighting Visualization of 3D Scanned Point Cloud based on Adaptive Opacity Control

Takuto Nakayama[1*], Kyoko Hasegawa[2], Liang Li[2], Satoshi Tanaka[2],

[1]Graduate School of Information Science and Engineering, Ritsumeikan University
[2]College of Information Science and Engineering, Ritsumeikan University
[*]is0421@ed.ritsumei.ac.jp

Abstract. In recent years, "Digital archiving" has been conducted to preserve historical cultural properties. The development of laser measurement technology has made it possible to acquire large-scale 3D scanned point clouds. In order to analyze the internal structure of cultural properties, we have proposed a transparent visualization method, namely SPBR, to visualize 3D scanned point clouds. In addition, to facilitate the analysis, we have proposed an edge-highlighting visualization method. However, the conventional edge-highlighting visualization struggles to visualize edge areas of complex shapes with appropriate thickness. As a result, there is a problem that visibility is reduced in terms of the analysis of 3D structures. In this study, we propose a method for identifying the shape of feature areas and applied it to a 3D point cloud.

Keywords: 3D Scanned Point Data, Edge-Highlighting Visualization, opacity control

1. Introduction

"Digital archiving" is an effort to preserve cultural properties of historical value by converting them into digital data for the purpose of passing them on to future generations. In recent years, the development of laser measurement technology has made it possible to acquire large-scale 3D scanned point clouds. Since the obtained 3D point clouds also describe the external and internal geometry, it is possible to analyze the 3D structure using transparent visualization [1]. Furthermore, it is possible to facilitate the analysis by highlighting and visualizing the edges of the measurement target, i.e., the feature areas [2,3]. However, in the conventional edge-highlighting visualization, it is challenging to visualize sharp edges and soft edges optimally at the same time. As a result, inability to improve the visibility of objects with complex 3D structures. In this study, we propose a method for discriminating sharp edges from soft edges in feature areas using entropy [4]. Furthermore, the effectiveness of the proposed method is verified by adapting it to actual 3D scanned point clouds.

2. Transparent visualization

In this study, we propose a transparent visualization method called Stochastic Point-based Rendering (SPBR) [1]. SPBR does not require depth sorting, which allows for fast transparent visualization. The specific processing steps of SPBR are shown in STEP1-STEP3 below.

STEP1. Point generation: Based on the data to be visualized, it generates points on a plane or planar surface with uniform point density distribution and arbitrary opacity.

STEP2. Point projection: The generated point cloud is divided into multiple ensembles. Next, each ensemble of points is subjected to a pixel-by-pixel hidden point elimination process, and particle projection is performed to produce an intermediate image.

STEP3. Determination of luminance values by ensemble averaging: The average image is generated by averaging the luminance values of the generated intermediate image for each corresponding pixel.

3. Extraction of feature areas

In this study, we use 3D features based on eigenvalues to extract edge areas from a point cloud [2]. Structure features such as linearity, planarity, and change of curvature have been proposed. In this study, change of curvature is adopted because it works very stably.

$$\text{Change of curvature}: f_\lambda = \frac{\lambda_3}{\lambda_1+\lambda_2+\lambda_3} \qquad (1)$$

where $\lambda_1, \lambda_2, \lambda_3$ are the eigenvalues of the 3D covariance matrix, and $\lambda_1 \geq \lambda_2 \geq \lambda_3 \geq 0$. In this study, the 3D covariance matrix is computed for each spherical local region centered at each point, and features are assigned to each point.

4. Opacity function

In this study, we take advantage of the SPBR's degree of freedom in controlling opacity and use two opacity functions for visualization [3]. **Figure1** shows the two opacity functions.

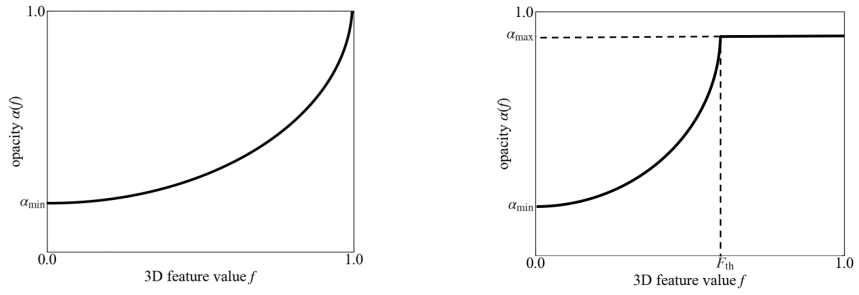

Figure1. Opacity functions : (a) Opacity function for sharp edges (b) Opacity function for soft edges

For the above function, we define an equation that relates the 3D feature f to the opacity α at each point.

$$\alpha(f) = \begin{cases} \dfrac{\alpha_{\max} - \alpha_{\min}}{{F_{\text{th}}}^d} f^d + \alpha_{\min} & (0 \leq f < F_{\text{th}}) \\ \alpha_{\max} & (F_{\text{th}} \leq f \leq 1) \end{cases} \qquad (2)$$

$\alpha_{\min}$ and $\alpha_{\max}$ are the minimum and maximum opacity, respectively. d is a parameter that controls the rate of increase of $\alpha(f)$. F_{th} is the threshold to the plateau region. Using these two opacity functions, sharp edges can be rendered thinner and soft edges can be enhanced.

5. Proposed method

In this study, we propose a method to discriminate sharp edges from soft edges using entropy. The definition of entropy in this study is as follows [4].

$$\text{Entropy}: E_\lambda = -(\lambda_3)\ln(\lambda_3) \quad (3)$$

The entropy defined above represents the magnitude of change in the high curvature section around the point of interest. An example shows the difference between sharp edges and soft edges from the point of interest is shown in **Figure2**.

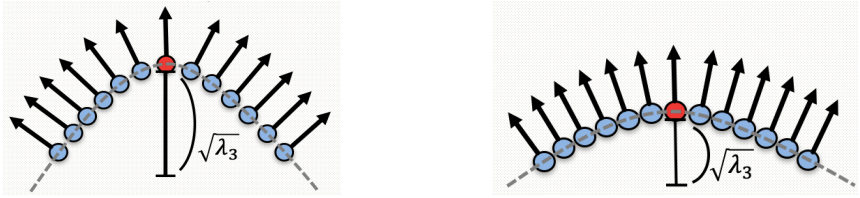

(a) **(b)**

Figure2. Measurement surfaces : (a) High curvature section (b) Low curvature section

Sharp edges have a larger change in curvature of the neighborhood than soft edges. In other words, sharp edges are considered to have larger entropy values than soft edges. In this study, we identify points with entropy values above a certain threshold as sharp edges and points with entropy values below the threshold as soft edges. Feature areas were extracted from the target point cloud data using conventional methods, and data from feature areas only were used to identify sharp and soft edges using entropy and to adapt an opacity function.

6. Experimental results

In this study, we conducted experiments using artificial point cloud data with both sharp and soft edge features. The experimental data is a cube with half sharp edges and half soft edges. **Figure3** shows the comparison results of the conventional and proposed methods.

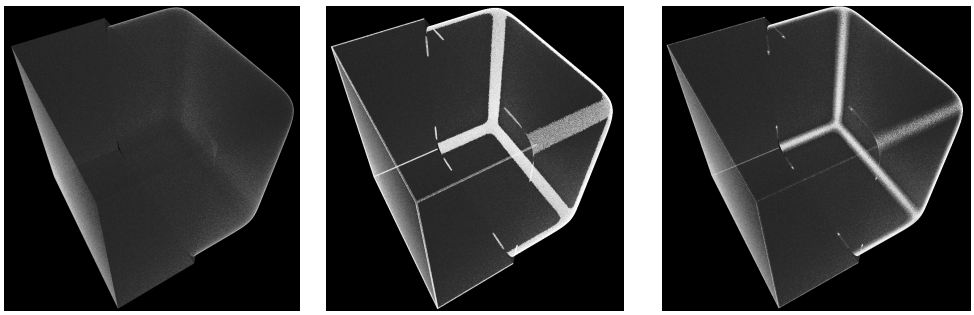

(a) **(b)** **(c)**

Figure3.Experimental results : (a) Input point cloud data (b) Conventional method (c) Proposed method

Figure3-(b) shows edge-highlighting visualization using the conventional method of binarization. **Figure 3-(c)** shows that the proposed method discriminates feature regions into sharp edges and soft edges, and adapts an appropriate edge-highlighting visualization method for each. First, we explain some common parameters. The feature threshold was set to 0.0005. The opacity of the feature areas was controlled by increasing the number of points, with the maximum value of $\alpha_{\max}$ being 20 and the minimum value of $\alpha_{\min}$ being 1. Next, we explain the parameters of the proposed method. The parameter d, which controls the rate of increase, was set to 2.0 for sharp edges and 4.0 for soft edges. The threshold F_{th} was set to 0.25. Comparing **(b)** and **(c)** in **Figure3**, we can see that the proposed method can visualize the features more clearly than the conventional method.

7. Conclusions

In this study, we proposed a method for edge highlight visualization of 3D scanning point clouds by adaptive opacity control. The experimental results showed that the proposed method can optimally perform edge-highlighting even for complex objects with both sharp and soft edges. Since the experiment was conducted using artificial point cloud data, we would like to adopt the proposed method to actual measured point cloud data and experiment with it in the future.

References

[1] S. Tanaka, K. Hasegawa, N. Okamoto, R. Umegaki, S. Wang, M. Uemura, A. Okamoto, and K. Koyamada: *See-Through Imaging of Laser-scanned 3D Cultural Heritage Objects based on Stochastic Rendering of Large-Scale Point Clouds*, ISPRS Ann. Photogramm. Remote Sens. Spatial Inf. Sci., III-5, pp. 73-80, 2016.

[2] J. Demantk´e, C. Mallet, N. David, B. Vallet: *Dimensioality based scale selection in 3D lidar point clouds*, The International Archives of the Photogrammetry, Remote Sensing and Spatial Information Sciences, Vol. XXXVIII, Part 5/W12(2011), 97-102.

[3] K. Kawakami, K. Hasegawa, L. Li, H. Nagata, , M. Adachi, H. Yamaguchi, F. I. Thufail, S. Riyanto, Brahmantara, S. Tanaka: *Opacity-based edge highlighting for transparent visualization of 3D scanned point clouds*, ISPRS Ann. Photogramm. Remote Sens. Spatial Inf. Sci. (Proc. XXIV ISPRS Congress), V-2-2020, pp.373–380, July 2020.

[4] Martin Weinmann, Boris Jutzi, Cle´ment Mallet: *Semantic 3D scene interpretation: A framework combining optimal neighborhood size selection with relevant features*, ISPRS Ann. Photogramm. Remote Sens. Spatial Inf. Sci., II-5/W2 (2013), 313-318.

High-Definition Contour Drawing for 3D Point-based Surfaces based on Adaptive Point Density Adjustment

Yukihiro Inada[1*], Hiroki Ito[1], Yousei Takeuchi[1], Kyoko Hasegawa[2], Liang Li[2], Satoshi Tanaka[2]

[1]Graduate School of Information Science and Engineering, Ritumeikan University
[2]College of Information Science and Engineering, Ritsumeikan University

*is0395is@ed.ritsumei.ac.jp

Abstract. In recent years, digital archiving of real objects by 3D laser scanning has been rapidly developing. In this study, we propose a method to draw contour lines in high resolution based on opacity adjustment of local regions. The contour lines extracted by the proposed method can be used as visual guides in the 3D point cloud data of digital archives.

Keywords: SPBR, 3D point-based surface, 3D point cloud data, Contour line

1. Introduction

Three-dimensional (3D) measurement technology has been rapidly developed in recent years as a method to record 3D shapes of land and cultural assets and convert them into digital data. In addition, by recording the shape of the land, various land use plans can be made. The measurement target is often a curved surface shape in the 3D measurement of cultural assets or land undulations. Stochastic point-based rendering (SPBR) has been developed as a method for transparent visualization of 3D scanned point clouds [1, 2, 3]. Based on this method, we have been conducting various studies on visualization using point clouds obtained by 3D measurement. In this study, we propose a method of superimposing high-definition contour lines on the visualization of 3D measurement point clouds as a visual guide for the 3D measurement data with curved surfaces. To draw contour lines on 3D point cloud data, it is sufficient to collect points at the height of the desired contour line and represent the curve as a set of points. In this study, we propose a method to make contour lines thinner by adjusting the local opacity of the point cloud based on point multiplication and thinning processes. This method allows us to draw sufficiently fine and precise contour lines using a sufficient number of points.

2. Proposed method

2.1. Visualization of sand undulations by luminance gradient using SPBR

At first, in SPBR, divide a point cloud randomly into multiple point subsets. The number of divided groups is called the repeat level L_{R}. The opacity α is calculated with the repeat level L_{R}, the number of generated points n, the local area of a point cloud on the planar image S, and the cross-sectional area of a point s. In SPBR, because the opacity α is set by the user, the number of generated points n needs to be determined by the opacity α. Furthermore, on a plane inclined by an angle θ to the horizontal plane, the apparent area seen by the camera is $s\cos\theta$, so the equation when the viewing direction is inclined can be defined as (2).

$$\boldsymbol{\alpha = 1 - \left(1 - \frac{s}{S}\right)^{\frac{n}{L_{\mathrm{R}}}}} \tag{1}$$

$$\boldsymbol{\alpha(\theta) = 1 - \left(1 - \frac{s}{S\cos\theta}\right)^{\frac{n}{L_{\mathrm{R}}}}} \tag{2}$$

2.2. The method of creating contour lines

In this research, we propose a method to draw contour lines from nearby points. When drawing contour lines, point clouds are extracted from within the range of width d around the contour lines. If the extracted point group is used without modification, the line becomes too thick. Therefore, the above issue is solved by adjusting the opacity of the point cloud that exists within the extraction area to emphasize the original height.

2.3. Opacity adjustment function

In this study, we adopt three opacity adjustment functions [4] (Figure 1): Type A (Figure1 (a)), Type B (Figure1 (b)), and their combination Type C (Figure1 (c)).

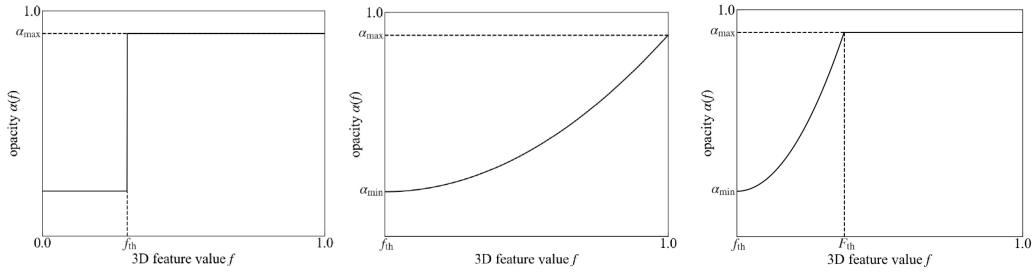

(a) Type A (b) Type B (c) Type C

Figure 1. Opacity adjustment functions

3. Experimental results

In this study, we use a test data of cosine wave to verify the proposed method (Figure 2). The visualization result of the contour lines drawn using the Type A function is shown in Figure 3. Because the Type A function is a step function thick contour lines can be drawn. Next, the visualization result of contour lines drawn using the Type B function is shown in Figure 4. Since the Type B function is a peak function, thin contour lines with gradients can be drawn. Finally, Figure 5 shows the visualization results of contour lines drawn using the Type C function, which is the combination of the Type A and Type B functions, so that moderately thick contour lines with gradations can be drawn.

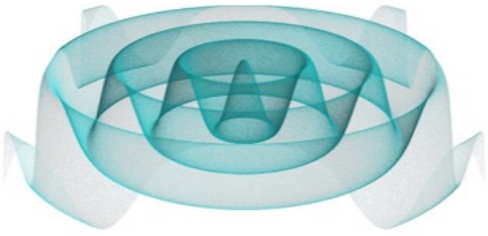

Figure 2. Test data (cosine wave)

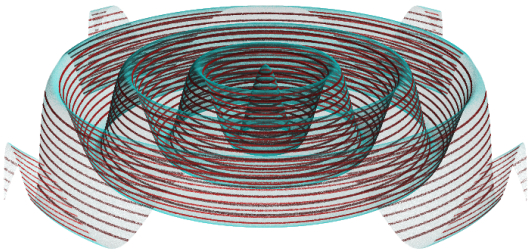

Figure 3. The visualization result of the contour lines drawn using the Type A function

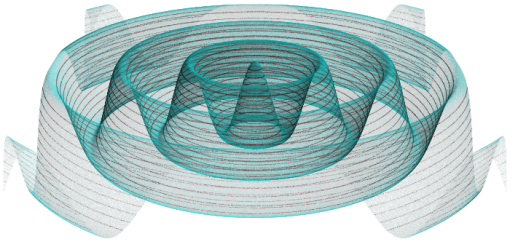

Figure 4. The visualization result of the contour lines drawn using the Type B function

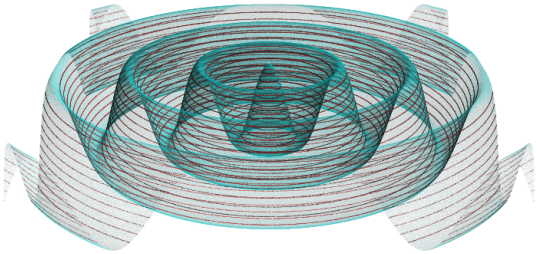

Figure 5. The visualization result of the contour lines drawn using the Type C function

4. Conclusion

In this study, we implemented a novel visualization method for contour lines drawn on 3D point cloud data. By adjusting the opacity of the point cloud, we could highlight the contour lines in desired positions and make them thinner. Future prospects include the

adaptive use of the three functions. Future work includes the adaptive use of the three functions.

5. References

[1] S. Tanaka, K. Hasegawa, N. Okamoto, R. Umegaki,S. Wang M. Uemura, A.Okamoto, and K. Koyamada: See-through imaging of laser-scanned 3D cultural heritage objects based on stochastic rendering of large-scale point clouds, ISPRS Ann. Photogramm. Remote Sens. Spatial Inf. Sci, III-5, (2016) pp.73-80.

[2] S. Tanaka, K. Hasegawa, Y. Shimokubo, T. Kaneko, T. Kawamura, S. Nakata, S. Ojima, S. Hiromi T. Tanaka, and K. Koyamada: Particle-based transparent rendering of implicit surfaces and its application to fused visualization, in Proc. of EuroVis 2012, (2012) pp.25–29.

[3] K. Hachimura, H. Tanaka, S. Tanaka: *New Developments in Digital Archives*, Nakanishiya Publishing (2012).

[4] K. Kawakami, K. Hasegawa, L. Li, H. Nagata, M. Adachi, H. Yamaguchi, Thufail, F.I., S. Riyanto, Brahmantara, and S. Tanaka: Opacity-based edge highlighting for transparent visualization of 3D scanned point clouds, ISPRS Ann. Photogramm. Remote Sens. Spatial Inf. Sci., V-2-2020, (2020) pp.373-380.

Computational performance evaluation of a new omnidirectional radiation imaging system using a fractal-shaped radiation detector

Miyuki Sasaki [1*], Yukihisa Sanada [1], Tatsuo Torii [2], Masao Yoshino [3], Akira Yoshikawa [3]

[1] Sector of Fukushima Research and Development, Japan Atomic Energy Agency
[2] Institute of Environmental Radioactivity, Fukushima University
[3] Institute of Materials Research, Tohoku University
[*]**sasaki.miyuki@jaea.go.jp**

Abstract. This study aims to develop an inexpensive and simple omnidirectional radiation imaging system using a fractal-shaped detector. This detector achieves sensitivity in all directions by arranging 1–2 cm tetrahedral detectors in a fractal shape and can identify the direction of radiation on the basis of the difference in sensitivity. Previous studies have shown that inverse problem analysis can better reproduce the distribution of radiation sources using radiation count rates. For the design of this system, we propose a new analysis method that uses the directional characteristics of radiation in addition to the count rates. This computational evaluation method was applied to an actual prototype detector system, and the sensitivity to actual radiation was compared with the calculated results to clarify the validity of the method.

Keywords: Radiation measurement, Radiation detector, Inverse problem analysis, Radiation direction vector

1. Introduction

In fields contaminated with radioactive materials, locating the radiation source is important. Specifically, three-dimensional (3D) measurements are required to locate radioactive materials in buildings. In this regard, this study aims to develop an inexpensive and simple omnidirectional radiation imaging system using a fractal-shaped detector. This detector can identify the direction of radiation based on the difference in sensitivity by arranging a tetrahedral detector with a side measuring 1.2 cm in a fractal shape. The idea of a fractal-shaped radiation detector was proposed by Torii et al., 2022[1]. Then, we designed an inverse problem analysis method that uses measurement data from multiple detectors. The inverse problem analysis algorithm in this study is based on maximum a posteriori–expectation maximization (Map-EM)[2]. Previous studies have shown that the maximum likelihood expectation maxi-

mization (ML-EM) of the inverse problem analysis can better reproduce the distribution of radiation sources using airborne radiation monitoring data[3]. Thus, we constructed an algorithm for estimating ground surface radioactivity that uses radiation direction vector information in the prior probabilities of the Map-EM algorithm. In this study, we propose the direction vector expectation maximization (DV-EM) method that can be used in a multicrystal radiation measurement system and show the evaluation results of the conversion characteristics when the DV-EM method is used for radioactivity estimation.

2. Method

Figure 1 shows the radiation detector model used in this study. The radiation measurement system has tetrahedral crystals measuring 12 mm on a side, and 16 crystals are arranged. This system has a tungsten shield between the crystals. The iterative formula for DV-EM used in this study is expressed as follows:

$$\lambda_j^{(k+1)} = \frac{\lambda_j^{(k)}}{\sum_{i=1}^{D}\sum_{d=1}^{16} C_{dij} + \beta \dfrac{\partial\left(\left|\overrightarrow{DV_y} - \overrightarrow{DV_\lambda}\right|\right)}{\partial \lambda_j}} \sum_{i=1}^{D}\sum_{d=1}^{16} \frac{y_{di} C_{dij}}{\sum_{j=1}^{B} C_{dij}\lambda_j^{(k)}}. \tag{1}$$

where y_{di} is the radiation count rate (cps) in a crystal d. i is the measurement position and has 3D coordinate information, and the total number of i is N. λ_j is the radioactivity (Bq) of the source at a position j, and the total number of j is B. C_{dij} is the radiation attenuation factor in the process from j to i (of a certain d). C_{dij} was obtained from the simulation results using the Particle and Heavy Ion Transport code System (PHITS: Version 3.110)[4]. $\overrightarrow{DV_y}$ is the direction vector of radiation detection. $\overrightarrow{DV_y}$ is the sum of the vectors obtained by multiplying the unit normal vector ($\overrightarrow{V^1}, \overrightarrow{V^2}, \overrightarrow{V^3}, \overrightarrow{V^4}$) by the total count rate of the crystals on each surface. k is the number of iterations. In DV-EM, the probability distribution of photons incident from j to i is calculated to follow the Poisson distribution, and the probability distribution of DV is calculated to follow the Gibbs distribution. β in Eq. (1) is a coefficient of Gibbs distribution. In this analysis of DV-EM, $\beta = 0.5$.

In this study, y_{di} was obtained using the values calculated from the simulation results of PHITS. In the measurement space for the simulation, two point radiation sources ((*X*, *Y*) = (2,0), (3,0)) are installed on a 5 m × 5 m flat plate (*Z* = 0 m). The radioactivity of the two sources was set to 10 MBq, and the separation distance was set to 1 m. The results of DV-EM and ML-EM calculated using y_{di} of the randomly determined measurement points in that space (*X* and *Y* are random, *Z* = 1 m) were compared. The height of all detectors' positions is

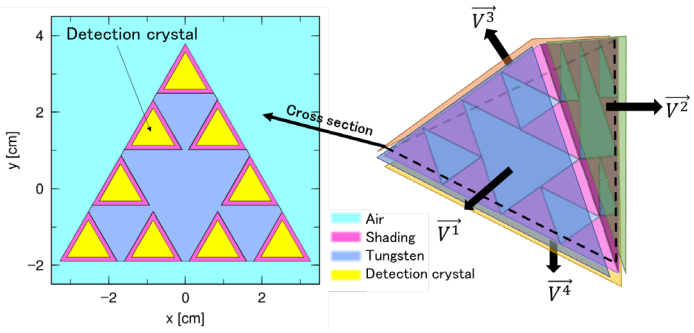

Fig. 1. The fractal-shaped radiation detector.

Z = 1 m, and the flat plate with the radiation source is Z = 0 m. The formula for ML-EM is β = 0 in Eq.(1). Assuming that D = 100 can be obtained in one measurement set, measurement sets of 1000 sets were made with different coordinates. The radioactivity distribution on the ground surface (Z = 0) was estimated using the created measurement sets and conversion algorithms (ML-EM and DV-EM). The evaluation methods for each conversion are as follows:

- **Peak detection rate** (%): We searched for peaks of the converted distribution and evaluated whether two peaks are detected. Peak detection was performed as follows: 1) Processing by maximum filter (filter size = 50 cm), 2) only the coordinate data with the same value as the original data was retained and the others were processed to 0, and 3) data with a value of 1500 Bq or less was processed to 0.
- **Position error** (cm): This refers to the average of the distances of the source position and detected peak position in the distribution created by each conversion.
- **Radioactivity error** E_R (Bq): This is the difference between source radioactivity (G) and total radioactivity (R) of a 30 cm square mesh centered on the peak detected in the conversion result. E_R is expressed as follows:

$$E_R = \sqrt{\frac{\sum_{p=1}^{2}(R_p - G_p)^2}{2}}. \tag{2}$$

3. Results and Discussion

Figure 2 shows the estimation results for the radioactivity distribution by ML-EM and DV-EM using a measurement set. The peak detection rate for each conversion was ML-EM = 32% and DV-EM = 98%. As shown in Fig. 2, even if ML-EM could not detect the existence of two radiation sources, DV-EM could detect them, indicating that DV-EM can better detect spot radiation sources.

Figure 3 shows histograms of the position error and radioactivity error of each conversion. The histograms are made up of only data with two peaks detected. The medians of position error were ML-EM = 20 cm and DV-EM = 5 cm. A position error close to 0 indicates high accuracy. The median of the position error of DV-EM was smaller than that of ML-EM, and the histogram in Fig. 3a shows that the position of DV-EM were closer to the radiation source position. The medians of radioactivity error were ML-EM = 84 kBq and DV-EM = 76 kBq. A radioactivity error close to 0 indicates high accuracy. The median of the radioactivity error of DV-EM was smaller than that of ML-EM, and the histogram in Fig. 3b shows that the radioactivity values of DV-EM were closer to the radiation source value.

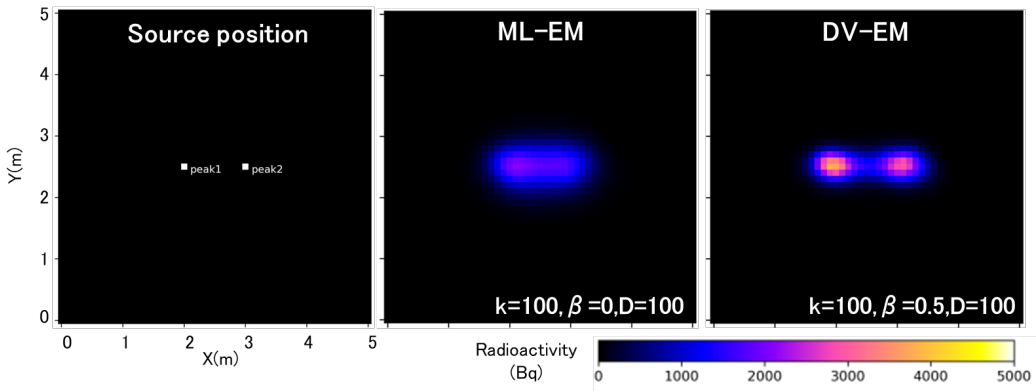

Fig. 2. Estimation results of the radiation source distribution by ML-EM and DV-EM.

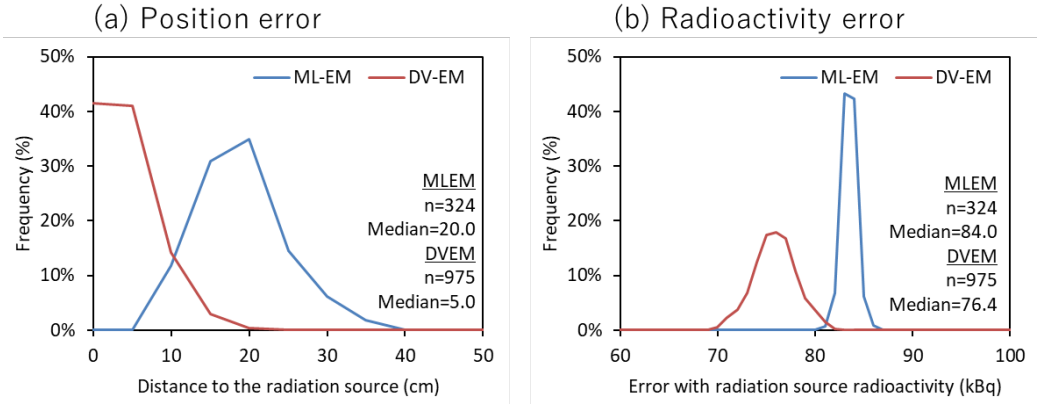

Fig. 3. Position error and radioactivity error of each conversion method.

These results show that the DV-EM has an excellent detection rate and radioactivity value accuracy of spot radiation sources. Thus, DV-EM is considered more accurate than ML-EM because it takes into account radiation contribution direction information.

4. Conclusions

This study proposed a new method for visualizing radioactivity distribution using DV-EM. DV-EM can detect spot radiation sources with high accuracy. Moreover, it can be applied to other radiation measurement systems to detect radiation on multiple detection surfaces. In this study, we evaluated the spot radiation source measurement of DV-EM. In the future, highly accurate detection of radioactive substances is expected by optimizing this algorithm and evaluating its conversion accuracy even for surface-based radioactive source distributions.

References

[1] T. Torii, T. Sugita, K. Ishizawa, M. Sasaki, Y. Sanada., Development of an omni-directional radiation detector - Invention of beta- and gamma-ray imager with fractal structure -., Proceedings of Annual / Fall Meetings of Atomic Energy Society of Japan, (2022)

[2] E. Levitan, G. T. Herman: A Maximum a Posteriori Probability Expectation Maximization Algorithm for Image Reconstruction in Emission Tomography, *IEEE Transactions on Medical Imaging*, 6:3 (1987), 185-192.

[3] M. Sasaki, A. Ishizaki, Y. Sanada: Development of analysis method for airborne radiation monitoring using the inverse problem solutions, *Prog. Nucl. Sci. Tech.*, 6 (2019), 63–67.

[4] T. Sato et al. Features of Particle and Heavy Ion Transport code System (PHITS) version 3.02, *Journal of Nuclear Science and Technology*, 55:6 (2018), 684-690.

Location estimation of radiation source using NaI spectrometer

Katsuhiko Yamaguchi[1*], Sota Suga[1], Yuka Kumada[1], Yuto Kondo[1], Kenji Suzuki[1], Masaharu Matsumoto[2]

[1]Faculty of Symbiotic Systems Science, Fukushima University
[2] Information Technology Center, Fukushima University
*yama@sss.fukushima-u.ac.jp

Abstract. Energy spectra of γ-rays generated from multiple nuclei were measured by NaI spectrometers located at various locations around the area. For comparison, simulation data by particle transport Monte Carlo code was generated by imitating this experimental system. This energy spectrum data was input to a trained neural network as training data using γ-ray source distributions arranged in various patterns on a two-dimensional surface so far, and the estimation accuracy was confirmed. These results are useful for estimating the radiation source distribution using an actual machine.

Keywords: machine learning, decommission

1. Introduction

It is difficult to estimate the spatial distribution of the nuclei by measuring the radiation emitted from the nuclei because it is a reverse problem. We have shown that this difficulty can be solved to some extent by machine learning using simulation data [1]. However, for actual use, it is necessary to make an estimation using experimental data. In this study, we will verify the estimation accuracy by obtaining experimental data using a NaI spectrometer that can actually measure the γ-ray energy spectrum and comparing it with the simulation data.

2. Method

In the experimental system, four NaI spectrometers (CANBERRA Ospray) are arranged as shown in the photograph on the left of Fig. 1 so that the measurement time can be shortened. Stable measurement can be performed by placing the γ-ray source on the plate at the bottom of the spectrometer and sliding the plate with the mesh in 4x4. As an example, as shown on the right side of Fig. 1, one ^{60}Co and two ^{137}Cs were arranged and measured.

The trained neural network consists of a three-layer structure consisting of an input layer (1024 nodes), an intermediate layer (1024 nodes), and an output layer (32 nodes). The γ-ray energy spectrum (0 to 1600 keV) used as input data on one mesh is divided every 25 keV, that is, divided into 64. Therefore, the input layer is 1024 nodes in order to input the γ-ray energy spectrum measured on the 4 × 4 = 16 mesh on the two-dimensional plane. The output layer has 32 nodes because the arrangement of ^{137}Cs and ^{60}Co is expressed on different 16 meshes. There are 1680 patterns in which two ^{137}Cs and one ^{60}Co are arranged on 16 mesh. The arrangement of 1500 patterns excluding the verification data pattern including the pattern as shown in Fig. 1 was used as the learning data pattern, and the γ-ray energy spectrum on 16 meshes corresponding to each pattern was calculated by the particle transport Monte Carlo code (PHITS). The neural network was trained based on the simulation results of this 1500 pattern. As shown by the error function in Fig. 2, after 10000 epochs, the error function decreased to the order of 10^{-7}. Using this trained neural network, verification data patterns were estimated.

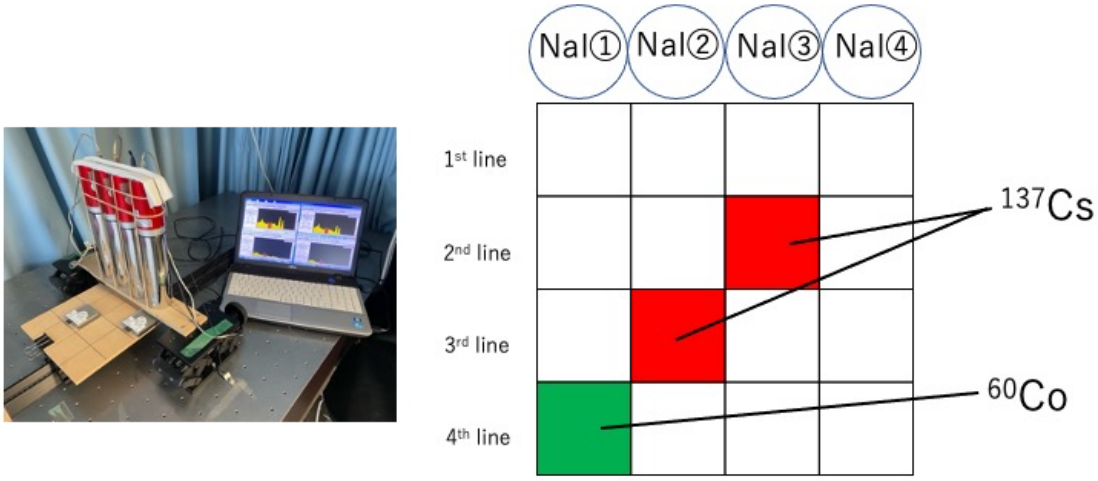

Fig. 1 (Left) A γ-ray energy spectrum measuring device that can measure simultaneously with four NaI spectrometers. (Right) Arrangement diagram of set ^{137}Cs and ^{60}Co.

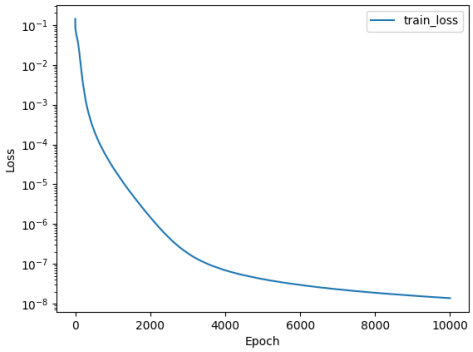

Fig. 2 Transition of loss function, which is the square of the difference between the estimated data and the answer data

3. Results and Discussion

The left column of Fig. 3 shows the results of measuring the γ-ray energy spectrum on each mesh with the NaI spectrometer for the verification pattern of Fig. 1. In addition, the results of the γ-ray energy spectrum obtained by simulating this pattern with PHITS are shown in the right column. All are processed into data separated by 25 keV intervals.

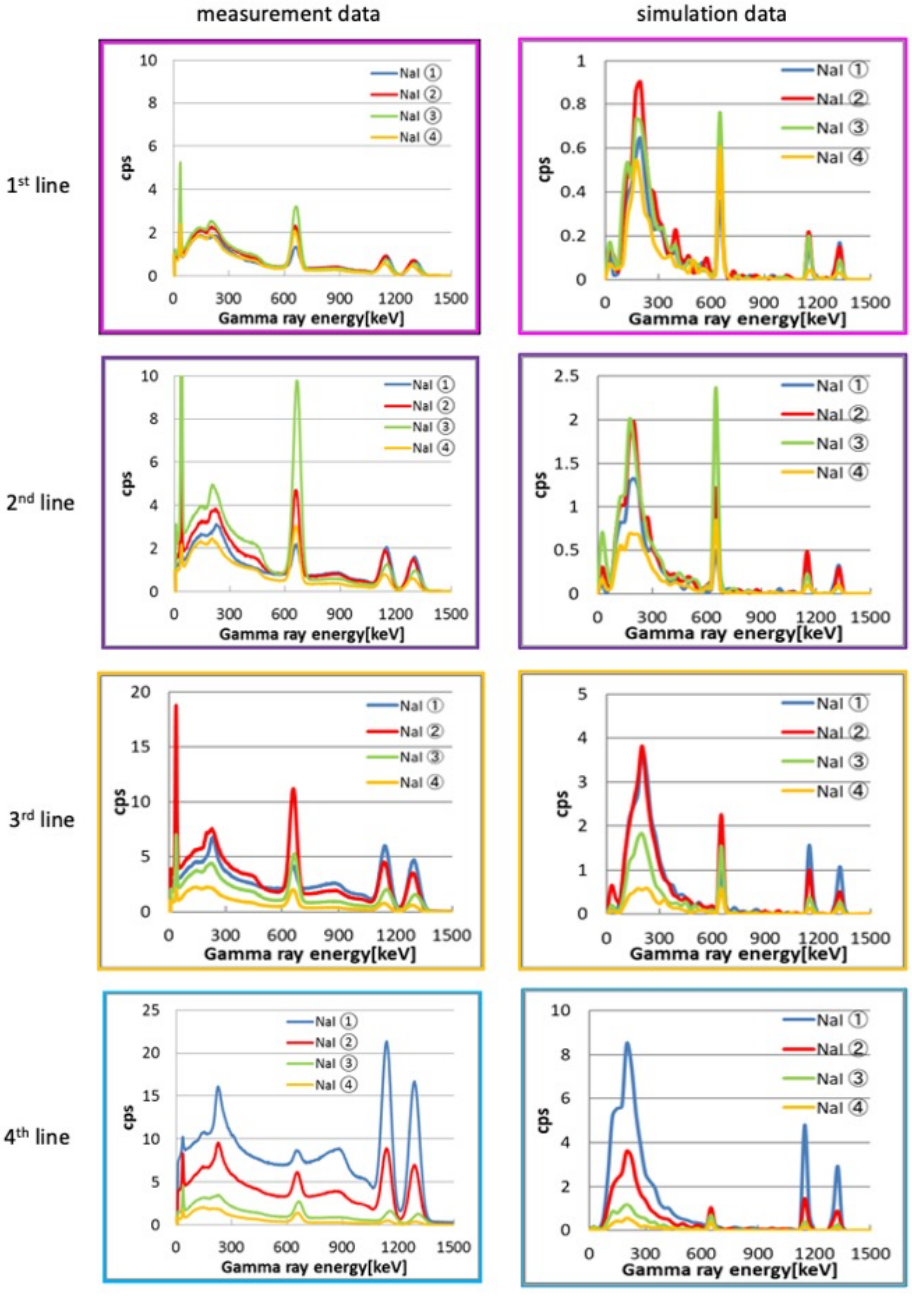

Fig. 3 γ-ray energy spectrum at each mesh position. (Left) Measurement data and (Right) Simulation data

First, the γ-ray energy spectrum obtained by the simulation was input to the neural network to calculate the estimation pattern. The result is that the answer data Fig.4(a) is sufficiently reproduced as shown in (b). The error function is 6.54×10^{-7}, which is the same level as the value at the time of training based on the training data. Next, the γ-ray energy spectrum obtained by the measurement was input to the neural network to calculate the estimation pattern. As a result, it was found that the position estimation of Co and Cs was sufficiently performed. However, in the position estimation of Cs, it is estimated that Cs is superimpose on the Co site. The γ-ray energy spectrum on this mesh corresponds to NaI ① in the 4th column in Fig. 2. In the measured data, it is considered that the main peak of Cs was emphasized because the Compton edge of Co raised the overall intensity, and as a result, the estimation was adversely affected. As can be seen from Fig. 2, the calculated data and the measured data correspond to the magnitude relationship of the main peak between the meshes, but there are many points where the shape of the peak and the detailed profile do not match. Since neural networks are trained based on calculated data, it is expected that estimation from measurement data will be difficult. Nevertheless, it can be said that the result of Fig. 4 (c) can estimate the outline of (a). This is amazing. It can be said that the neural network is able to extract the features of the calculated and measured γ-ray energy spectra well. From this result, it is expected that the nuclide distribution can be sufficiently estimated using the actual experimental data by devising a way to bring the profiles of the calculated data and the measured data a little closer.

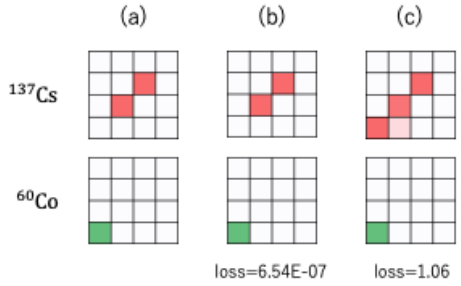

Fig. 4 Radioactive source position estimation results for ^{137}Cs (upper) and ^{60}Co (lower) using γ-ray energy spectrum data. (a) Answer data, (b) Estimated result using γ-ray energy spectrum data obtained by simulation, (c) Estimated result using γ-ray energy spectrum data obtained by measurement

References

[1] T. Uemura, K Yamaguchi: Estimation of radiation source distribution using machine learning with γ ray energy spectra, *Journal of Advanced Simulation in Science and Engineering,* 7/1, pp71-81. (DOI) 10.15748/jasse.7.71

JSST 2022

Coupled simulation of fluid and visco-hyperelastic solid with Eulerian unified formulation

Shusuke Takeuchi[1,*], Koji Nishiguchi[1], Tokimasa Shimada[2,3], Ryohei Katsumata[1], Hiroya Hoshiba[1], Junji Kato[1]

[1]Department of Civil Engineering, Graduate School of Engineering, Nagoya University
[2]Department of Computational Science, Graduate School of System Informatics, Kobe University
[3]RIKEN Center for Computational Science, RIKEN

[*]takeuchi.shusuke.c5@s.mail.nagoya-u.ac.jp

Abstract. Unified Eulerian structure-fluid formulation is suitable for massively parallel simulation of complex-shaped material. However, analyzing the viscoelastic material which has a large number of internal variables has not been applied in the existing research. Therefore, in this study, we proposed a unified Eulerian structure-fluid formulation that enables viscoelastic material analysis using Simo's visco-hyperelastic model. And through massively parallel simulation using a supercomputer, verify validity and effectiveness.

Keywords: Eulerian method, Finite volume method, Viscoelasticity, Fluid-structure interaction

1. Introduction

Solid analysis based on Eulerian description [1] is a method in which a solid deforms and moves in a cartesian mesh, and is one of the most effective methods for solid analysis involving large deformation and rupture. It is also easy to couple with fluids, and Nishiguchi et al. proposed a full Eulerian strongly coupled fluid-structure interaction analysis method [2] using the Building Cube Method (BCM) [3], which is a kind of hierarchical orthogonal mesh method. The Eulerian analysis method based on BCM has the advantages of high parallelization efficiency in a massively parallel computing environment and of easily analyzing the geometrically complex structures.

Furthermore, the authors introduced Lagrange particles to represent the solid region and proposed a unified Eulerian fluid-structure interaction analysis method [4], in which the solid volume fraction and physical quantities related to the solid are calculated using the information of Lagrange particles. The method using Lagrange particles avoids the numerical diffusion of solid interfaces and solid internal variables due to advection calculations, which has been a problem in conventional Eulerian solid analysis, and enables highly accurate calculations of solid material models with many internal variables, such as viscoelastic

and elastoplastic materials. However, these methods [4] are only applicable to hyperelastic and linearly elastic materials.

Against this background, the purpose of this study is to develop and validate a unified Eulerian fluid-structure interaction analysis scheme that can take into account viscoelastic materials and verify the effectiveness of this method by massively parallel simulations of shock-absorbing structures made of viscoelastic material(TPE).

2. Numerical method

In this study, the governing equations are the continuity equation and the equation of motion, which are the basic equations in continuum mechanics, volume-averaged in the control volume [5]. We assume an Simo's visco-hyperelastic model [6] as the constitutive equation for a solid and an incompressible Newtonian fluid as the constitutive equation for a fluid [2].

For the formulation of visco-hyperelasticity, we introduce Simo's visco-hyperelastic model. The Cauchy stress tensor can be split into isochoric and volumetric parts. Under the incompressibility assumption, the volumetric term, or pressure, is determined from the incompressibility constraint. On the other hand, the isochoric term is formulated by the generalized Maxwell model.

Define the velocity vector at the cell center and discretize it using the finite volume method. In this case, the stress is divided into pressure and deviation stress, and the velocity and pressure fields are computed separately using the fractional step method [2]. To avoid numerical diffusion due to advection of the interface and internal variables of the solid, Lagrangian marker particles are used, which not only represent the solid domain explicitly but also serve to compute the physical quantities of the solid.

3. Numerical examples

First, to verify the validity of the method, we analyze a uniaxial tensile problem shown in Figure 1. The deformant is given a constant velocity in the z-axis direction and pulled until the strain is 1. The physical properties of the solid and fluid are given in 1. The material properties of the visco-hyperelastic material are the Prony series identified from the dynamic viscoelasticity test results of the viscoelastic material (TPE), which is the material of the shock-absorbing structure that will be analyzed next. The prony series of 45 terms has been identified and is omitted here.

Figure 2 compares the stress-strain curves obtained by the analysis at three different tensile speeds with the exact solution. It is confirmed that the stress-strain curves are in good agreement with the exact solutions, indicating the validity of the present method.

The next is to analyze the deformation of the shock-absorbing structures shown in Figure 3. Push the upper rigid body into the deformed body without slipping. The solid is assumed to be a rubber-resin mixture and the fluid is assumed to be air at 20°C. The physical properties give the same values as in the uniaxial tensile problem. A hierarchical Cartesian mesh with a minimum cell size of about 0.35 mm and a total cell number of 11,190,272 is used, and the analysis time is up to 2.1 ms.

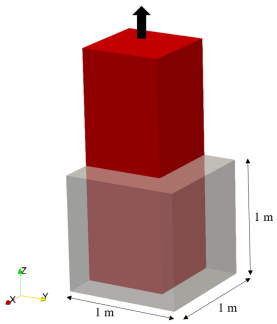

Figure 1: Uniaxial tensile problem.

Table 1: Physical properties .

Solid: incompressible viscoHyperelastic solid	
Mass density ρ_s [kg/m^3]	1.0×10^3
Young's modulus E [Pa]	4.0×10^7
Instantaneous shear modulus G_0 [Pa]	1.18×10^3
Fluid: incompressible Newtonian fluid	
Mass density ρ_f [kg/m^3]	1.2
Viscosity μ_f [Pa · s]	1.8×10^{-5}

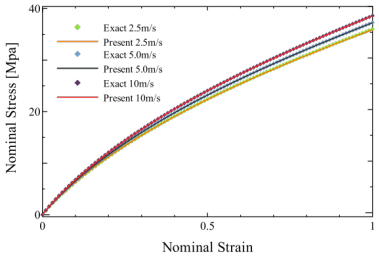

Figure 2: stress-strain curve.

Figure 4 shows the distribution of Mises stress in the structural area and the Qcriterio in the air area. It can be seen that air flows out of the gap while buckling occurs inside the structure. Figure 5 is the distribution of the velocity field. It can be confirmed that air with a velocity about 10 times faster than the pushing velocity of the rigid body is flowing out from the gap of the deformed body. Figure 6 is the distribution of the pressure field. It can be confirmed that there are areas where high pressure of more than 7 MPa is generated. Considering the thickness of the structure (about 2-3 mm) and Young ' s modulus (40 MPa), these effects cannot be neglected, suggesting that the interaction between the structure and the air is a strong phenomenon. The need for a coupled analysis for viscoelastic solid and air is confirmed.

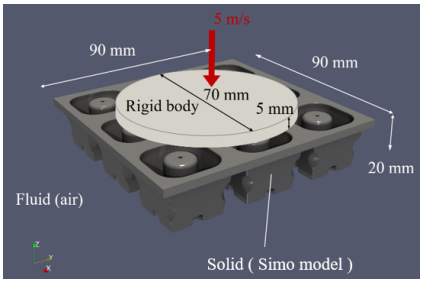

Figure 3: shock-absorbing structures.

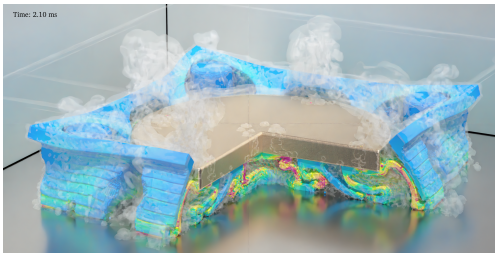

Figure 4: Mises stress and Qcritrion distribution.

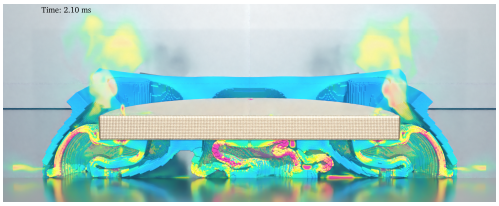

Figure 5: Mises stress and velocity field distribution.

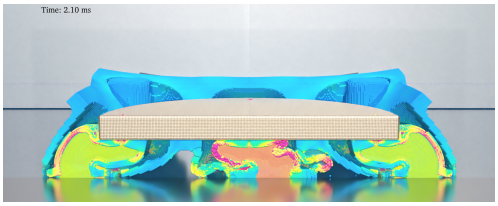

Figure 6: Mises stress and pressure field distribution.

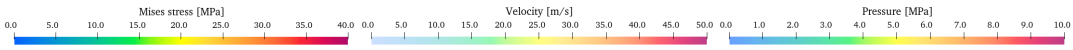

4. Conclusion

In this study, we proposed a unified Eulerian fluid-structure interaction analysis method that takes into account viscoelastic materials by introducing Simo visco-hyperelastic model. Then, the validity of this method was verified through a uniaxial tensile problem, and the effectiveness of this method was verified through the analysis of shock-absorbing structures. Future work includes quantitative comparison of the load-displacement curves with experiments and Applying to coupled structure-fluid problems with high Reynolds numbers, such as aerodynamic instability and vibration experiments simulating skyscrapers.

References

[1] Benson DJ. COMPUTATIONAL METHODS IN LAGRANGIAN AND EULERIAN HYDROCODES. *Computer Methods in Applied Mechanics and Engineering*. **99**(2-3), pp.235–394, 1992.

[2] Nishiguchi K, Bale R, Okazawa S, Tsubokura M. Full Eulerian deformable solid-fluid interaction scheme based on building-cube method for large-scale parallel computing. *International Journal for Numerical Methods in Engineering*, **117**(2), pp.221–248, 2019.

[3] Nakahashi K. Building-cube method for flow problems with broadband characteristic length. *Computational fluid dynamics 2002*. Springer, Berlin, Heidelberg, pp.77–81, 2003.

[4] Shimada, T., Nishiguchi, K., Bale, R., Okazawa, S., Tsubokura, M. Eulerian finite volume formulation using Lagrangian marker particles for incompressible fluid–structure interaction problems. *International Journal for Numerical Methods in Engineering*, **123**(5), pp.1294–1328, 2022.

[5] Nishiguchi K, Okazawa S, Tsubokura M. Multimaterial Eulerian finite element formulation for pressure-sensitive adhesives. *International Journal for Numerical Methods in Engineering*, **114**(13), pp.1368–1388, 2018.

[6] Simo, J.C. (1987) : ON A FULLY THREE-DIMENSIONAL FINITE-STRAIN VISCOELASTIC DAMAGE MODEL: FORMULATION AND COMPUTATIONAL ASPECTS, COMPUTER METHODS IN APPLIED MECHANICS AND ENGINEERING Vol.60,pp.153-173

Effect of wing's mass distribution on the aerodynamic performance in insect flapping wings

Minato Onishi[1*], Daisuke Ishihara[2]

[1]Department of Computer Science and Systems Engineering, Kyushu Institute of Technology
[2] Department of Intelligent and Control Systems, Kyushu Institute of Technology

*oonishi-m@solid.mse.kyutech.ac.jp

Abstract. In this study, the effect of the mass distribution on the passive motions and the aerdodynamic performance is evaluated. For this purpose, the pixel model wing which can simulate passive motions such as feathering and cambering is analyzed by the fluid-structure interaction (FSI). Several models of mass distribution are analyzed and evaluated these passive deformations and aerodynamic performance. The mass distribution which models that of acutual insects is demonstrated better aerodynamic performance.

Keywords: Fluid-structure interaction, Insect flapping wing, Mass distribution, Feathering, Cambering, Aerodynamic performance, Pixel model wing

1. Introduction

The mass distribution of insect flapping wing varies radially from the wing base and becomes smaller toward the wing tip [1]. The characteristic passive motions such as feathering and cambering by the Fluid-structure interaction (FSI) are observed many species of insect because wings have no interior muscle [2]. These motions are mainly caused by the wing's inertial and aerodynamic force. The effect of wing's inertial force apperers during the flapping reversal on dipteran wings [3]. Therefore, it is important to understand the effect of the mass distribution on the passive motions and the aerdodynamic performance. In this study, the effect of the mass distribution on the passive motions and the aerdodynamic performance is evaluated using FSI analysis for the pixel model wing, which can simulate passive feathering and cambering [4].

2. Fluid-structure interaction framework for the pixel model wing

Figure 1 shows the employed pixel model wing. The fundamental concept of this model is based on the Ref. [5]. The wing span length is R_w, and the wing chord length is c_w. The wing base is the point at $z = 0$ along the y-axis. The complicated support structure is simplified by the leading-edge support, the central support, and the traling edge support using the structured shell element. The different mechanical role of the wing membrane and their support is represented using the different set of the pseudo-elastic material properties. Figure 2 is the schematic of the fluid domain. The wing base O coincides with the origin of the local coordinate xyz. The

wing flaps in the horizontal stroke plane with the stroke angle Φ as shown in Fig.3. The middle of half stroke is defined when the leading edge coincides with z-axis (the angular flapping displacement $\varphi = 0°$). The flapping during back to front is defined down stroke and the flapping during front to back is defined up stroke, respectively. The feathering can be described using the feathering angular displacement θ, which is positive in the counter-clockwise direction about the torsional axis. The time history of angular flapping displacement φ as shown in Fig.4 is imposed on the leading edge as the boundary condition. f_φ is the flapping frequqency.
The finite element discretized equation of the incompressible viscous fluid and the equilibrium equation of the elastic body are combined using the interface conditions, and the monolithic equation systems of FSI is derived as follows:

$$ {}_{\mathrm{L}}\mathbf{M}\,\mathbf{a} + \mathbf{C}\,\mathbf{v} + \mathbf{N} + \mathbf{q}(\mathbf{u}) - \mathbf{G}\,\mathbf{p} = \mathbf{g}\,, \quad {}_{\tau}\mathbf{G}\mathbf{v} = \mathbf{0}\,, \tag{1a, b} $$

where the matrices **M**, **C**, and **G** are the mass, diffusive, and divergence operator, respectively, the vectors **a**, **v**, **N**, **q**, **u**, **p**, and **g** are the acceleration, velocity, convective term, elastic inertial force, displacement, pressure, and external force, respectively. The subscripts L and τ indicate lumping and transpose, respectively. Equation (1) is solved using a projection method [6].

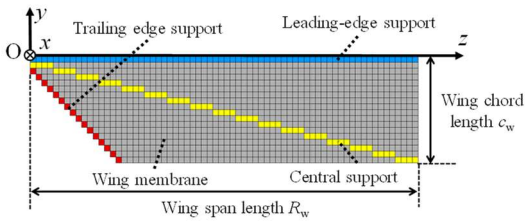

Figure 1 : Pixel model wing.

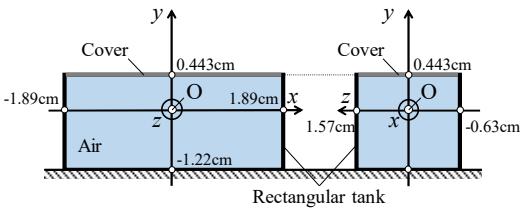

Figure 2 : Schematic of fluid domain.

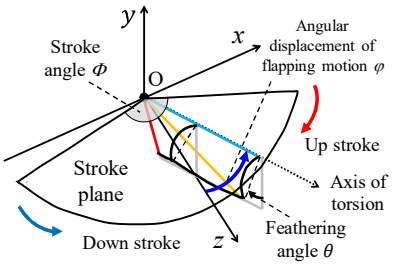

Figure 3 : Schematic of flapping motion.

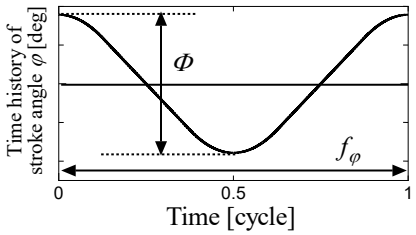

Figure 4 : Time history of the angular displacement of the stroke angle.

3. Analysis setup

The parameters used in this study are given based on actual insect's data [2, 7-10] as follows: The wing span length $R_w = 0.0113$ m, the wing chord length $c_w = 0.00311$ m, the wing's thickness $t = 2.0$ μm, Poisson's ratio $\nu = 0.49$, Young's modulus of wing membrane $E_m = 9.0 \sim 13.0$ GPa, $\Phi = 71°$, the flapping frequency $f_\varphi = 148$ Hz, the fluid mass density $\rho^f = 1.205$ kg/m^3, the fluid viscosity $\mu^f = 1.822\times10^{-5}$ Pa s, the time increment $\Delta t = (1/f_\varphi)/120{,}000$. The wing mass $m_w = 0.499\times10^{-6}$ kg. For the purpose of evaluating the effect of the mass distribution on the passive motions and the aerdodynamic performance, the mass distribution is varied as follows:
Type I : The mass density ρ is varied along the only spnawise direction as shown in Fig.5(a). ρ

decreases with the tip of spanwise direction.

Type II : ρ is varied along the spnawise and chordwise direction as shown in Fig.5(b). ρ decreases with the tip of spanwise and chordwise direction. This distribution models that of acutual insects.

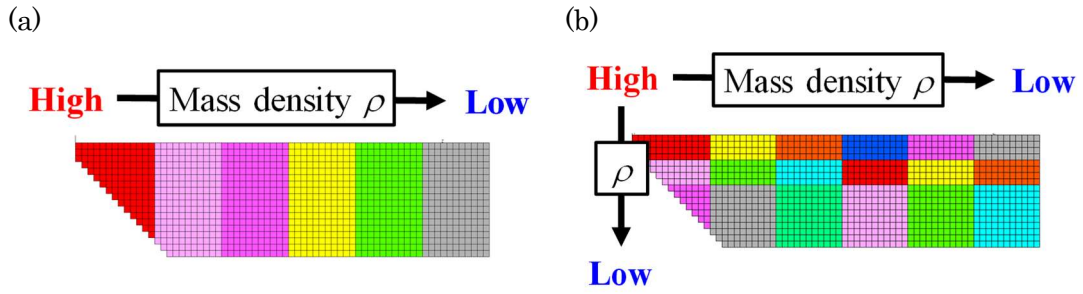

Figure 5 : Mass distribution of the pixel model wing.

4. Numerical results and discussion

Lift-power ratio $\bar{C}_L/\bar{C}_P$ is introduced to evaluated aerodynamic performance, where $\bar{C}_L$ is the mean lift coefficient; and $\bar{C}_P = \bar{P}_{aero}/0.5\rho^f V^3 R_w c_w$ is the mean power coefficient; and $V = 2r_2 \Phi R_w f_\varphi$ is mean flapping velocity, r_2 is the second moment of wing area; and $P_{aero} = \int_{wing} (\mathbf{F}_{aero} \cdot \mathbf{v})$ where $\mathbf{F}_{aero}$ and $\mathbf{v}$ are the nodal aerodynamic force and nodal velocity, respectively. A high $\bar{C}_L/\bar{C}_P$ indicates that less energy is required to generate lift force. Figure 6 shows the relationship between Young's modulus of wing membrane E_m and $\bar{C}_L/\bar{C}_P$. The circles shows the result of Type I, and the squares shows the result of Type II. Figure 7 shows the comparison of the feathering angle θ at the tip of wing. $\bar{C}_L/\bar{C}_P$ increases as E_m decreases from each result of the distribution as shown in Fig.6. A small E_m means that passive motions increase. Therefore, passive motions contributes to efficiency aerodynamic performance. $\bar{C}_L/\bar{C}_P$ of Type II is better than that of Type I from the comparison of both. This is because Type I obtains a larger $\bar{C}_P$ due to the increase of passive deformations as shown in Fig.7. Therefore, the mass distribution of actual insects such as Type II produces efficiency aerodynamic performance.

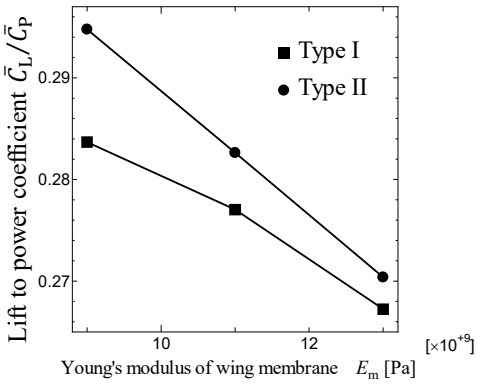

Figure 6 : Comparison of the lift to power coefficient.

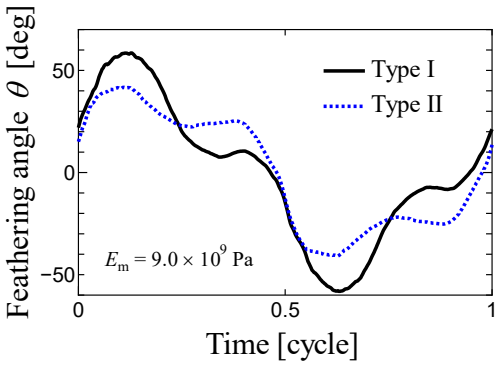

Figure 7 : Time history of the feathering angle at the tip of wing.

5. Concluding remarks

The effect of the mass distribution on the passive motions and the aerdodynamic performance is evaluated using the FSI frame work of the pixel model wing which can simulate passive feathering and cambering. The mass distribution which models that of acutual insects is demonstrated better lift to power coefficient. Therefore, the mass distribution of actual insects such produces efficiency aerodynamic performance. In our future work, the pixel model wing is introduced to the partiotion method for the maneuverability and evaluated effect on their maneuverability.

Acknowledgments

This work was supported by JSPS KAKENHI Grant number 20H04199 and 21J11321.

References

[1] A. R. Ennos, The inertial cause of wing rotation in Diptera, *The Journal of Experimental Biology*, Vol. 140, pp. 161-169, 1988.

[2] C. P. Ellington, The aerodynamics of hovering insect flight. III. Kinematics, *Philosophical Transactions of the Royal Society of London B*, Vol. 305, No. 1122, pp. 41-78, 1984.

[3] J. P. Whitney, R, J. Wood, Aeromechanics of passive rotation in flapping flight, *Journal of Fluid Mechanics*, Vol. 660, pp. 197-220, 2010.

[4] M. Onishi, D. Ishihara, Computational fluid-structure interaction framework for simulating characteristic deformations in insect flapping wings, *9th edition of the International Conference on Computational Methods for Coupled Problems in Science and Engineering*, DOI: 10.23967/coupled.2021.012, 2021.

[5] M. Onishi, D. Ishihara, Modeling the cambering of the flapping wings of an insect using rectangular shell finite elements, *Journal of Advance Simulation in Science and Engineering*, Vol. 7, No. 1, pp. 181-188, 2020.

[6] D. Ishihara, T. Horie, A projection method for the monolithic interaction system of an incompressible fluid and a structure using a new algebraic splitting, *Computer Modeling in Engineering and Sciences*, Vol. 101, pp. 421-440, 2014.

[7] H. Tanaka, R. J. Wood: Fabrication of corrugated artificial insect wings using laser micromachined molds, *Journal of Micromechanics and Microengineering*, 20, 075008, 2010.

[8] J. F. V. Vincent and U. G. K. Wegst: “Design and mechanical properties of insect cuticle”, *Arthropod Structure & Development*, 33, pp. 187-199, 2004.

[9] S. A. Wainwright, W. D. Biggs, J. D. Currey, J. M. Gosline: *Mechanical Design in Organism*, Princeton University Press, 1982.

[10] A. R. Ennos: The kinematics and aerodynamics of the free flight of some Diptera. *The Journal of Experimental Biology*, 142, pp. 49-85, 1989.

Partitioned-Monolithic Hybrid Strongly Coupled Method for Structure-Piezoelectric-Circuit Interaction in Piezoelectric Energy Harvesting

Shunnosuke NOZAKI[1], Daisuke ISHIHARA[2*], Tomoya NIHO[2]

[1]Department of Interdisciplinary Informatics, Kyushu Institute of Technology

[2]Department of Intelligent and Control Systems, Kyushu Institute of Technology

[*]**ishihara.daisuke399@mail.kyutech.jp**

Abstract. Various coupled algorithms are possible for the structure-piezoelectric-circuit interaction in piezoelectric bimorph energy harvesters. We propose a partitioned-monolithic hybrid strongly coupled method, which has both the advantages of the partitioned and monolithic methods for the structure-piezoelectric-circuit coupled phenomenon in the piezoelectric energy harvesting. Following the hierarchical decomposition for this coupling phenomenon, the structural analysis and the monolithic analysis of the piezoelectric-circuit coupling are strongly coupled using the block Gauss-Seidel algorithm. In a typical benchmark problem, we compare the results from the proposed method with those from the conventional strongly coupled partitioned iterative method, and the accuracy, the stability, and the computational cost are discussed.

Keywords: Multiphysics Coupling, Piezoelectric Energy Harvesting, Structure-Piezoelectric-Circuit Interaction, Partitioned Method, Monolithic Method, Block Gauss-Seidel Method

1. Introduction

Piezoelectric bimorph energy harvesters shown in Fig. 1 have been widely studied because of its high power generation efficiency[1]. They are thin composites of piezoelectric and metallic materials that produce a three-dimensional (3-D) potential distribution inside, and their vibration characteristics are affected by the coupling among the inverse-piezoelectric and direct-piezoelectric effects of the harvester and the circuitry. Hence, the design process for these devices requires the accurate prediction of this 3-D coupled problem [2]-[4]. This coupled phenomenon is multiphysics and hierarchical, allowing a variety of coupled algorithms. The conventional algorithms are roughly classified to either monolithic or partitioned ones. In this study, we propose a hybrid method that has the advantages of both the monolithic and partitioned methods. In the numerical examples of the typical piezoelectric bimorph energy harvester, we evaluate the performance of the proposed method in terms of accuracy, numerical stability, and computational cost by comparing with the fully partitioned iterative method[5].

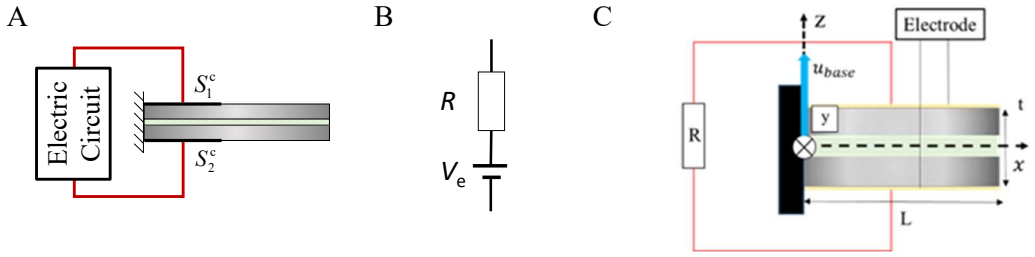

Fig.1 Piezoelectric bimorph energy harvester (A), the circuit (B), and the problem setup (C).

2. Materials and Methods

The spatially discretized equations of motion of linear piezoelectricity in the global coordinate system are derived using the variation principle with the standard procedure of the finite element method as

$$\mathbf{M}\ddot{\mathbf{u}} + \mathbf{C}\dot{\mathbf{u}} + \mathbf{K}_{uu}\mathbf{u} + \mathbf{K}_{u\phi}\boldsymbol{\phi} = \mathbf{F}, \qquad \mathbf{K}_{u\phi}^{T}\mathbf{u} + \mathbf{K}_{\phi\phi}\boldsymbol{\phi} = \mathbf{q}_e + \mathbf{q}_c, \tag{1a, b}$$

where $\mathbf{M}$ is the global mass matrix of the structure, $\mathbf{K}_{uu}$ is the global mechanical stiffness matrix of the structure, $\mathbf{K}_{u\varphi}$ is the global piezoelectric stiffness matrix of the piezoelectric continuum, $\mathbf{K}_{\varphi\varphi}$ is the global dielectric stiffness matrix of the piezoelectric continuum, $\mathbf{u}$ is the nodal global vector of the mechanical displacement, $\boldsymbol{\varphi}$ is the nodal global vector of the electric potential, $\mathbf{F}$ is the global equivalent vector of the mechanical external force, $\mathbf{q}_{ext}$ is the global equivalent vector of the external surface charge, $\mathbf{q}_c$ is the global equivalent vector of the surface charge supplied from the integrated electric circuit, and the right-hand superscript T denotes the transpose of the matrix. We consider the electrical resistance load as the circuit (Fig. 1B). A single-degree-of-freedom (SDOF) equation of this circuit can be derived using Kirchhoff's law as

$$R\dot{Q} + V_P = V_e, \tag{2}$$

where R, Q, V_p, and V_e are the electrical resistance, the electric charge, the electric potential difference given by the piezoelectric oscillator, and the electric voltage given by the external electric power supply. The continuities of the electric potential and the electric charge are satisfied at the interface between the piezoelectric continuum and the electric circuit. The electric circuit is connected to the piezoelectric oscillator via electrodes. Then, the continuity conditions imposed on the interface can be formulated as

$$V_P = \phi_1^* - \phi_2^*, \quad \mathbf{q}_c = \int_{S_1^c} \mathbf{N}_\phi (Q/S_1^c) dS - \int_{S_2^c} \mathbf{N}_\phi (Q/S_2^c) dS, \tag{3a, b}$$

where S_1^c and S_2^c denote the areas of the electrodes where the electric circuit is connected, and the subscripts 1 and 2 correspond to the positive and negative poles, respectively, which are defined in the general circuit expression. φ_x^* (x is 1 or 2) denotes the electric potential at a point in S_x^c and $\mathbf{N}_\varphi$ is the global assemblage of the interpolation functions used for the electric potential. Note that the formulation of Eq. (3a) assumes that the charge from the electric circuit is distributed uniformly and instantaneously throughout each electrode. The coupled conditions (3a) and (3b) can be rewrritten using the transformation matrices of the DOFs between the

piezoelectric material and the electric circuit on their interface as

$$V_P = \mathbf{T}_\mathrm{p}\boldsymbol{\phi}, \qquad \mathbf{q}_\mathrm{c} = \mathbf{T}_\mathrm{c} Q, \tag{4a,b}$$

where $\mathbf{T}_\mathrm{p}$ and $\mathbf{T}_\mathrm{c}$ are the transformation matrices for the electric potential and charge, respectively. $\mathbf{T}_\mathrm{p}$ and $\mathbf{T}_\mathrm{c}$ can be given using the finite element descritization as

$$\mathbf{T}_\mathrm{p} = \int_{S_1^c} \mathbf{N}_\phi^\mathrm{T}/S_1^c \, ds - \int_{S_2^c} \mathbf{N}_\phi^\mathrm{T}/S_2^c \, ds \,, \mathbf{T}_\mathrm{c} = \int_{S_1^c} \mathbf{N}_\phi/S_1^c \, ds - \int_{S_2^c} \mathbf{N}_\phi/S_2^c \, ds, \tag{5a,b}$$

where these matrices satisfy $\mathbf{T}_\mathrm{P} = \mathbf{T}_\mathrm{c}{}^\mathrm{T}$.

Temporally discretizing Eqs. (1b) and (2), and combining them using Eq. (4), the monolithic equation system for the direct-piezoelectric and circuit coupling can be obtained, after suitable rearrangement, as

$$\mathbf{K}_{\mathbf{u}\boldsymbol{\phi}}^\mathbf{T}{}^{t+\Delta t}\mathbf{u} + \widehat{\mathbf{K}}_{\boldsymbol{\phi}\boldsymbol{\phi}}{}^{t+\Delta t}\boldsymbol{\phi} = {}^{t+\Delta t}\mathbf{q}_\mathbf{e} + {}^{t+\Delta t}\widehat{\mathbf{q}}_\mathbf{c}, \tag{6}$$

where as

$$\widehat{\mathbf{K}}_{\boldsymbol{\phi}\boldsymbol{\phi}} = \mathbf{K}_{\boldsymbol{\phi}\boldsymbol{\phi}} + (\gamma \Delta t/R)\, \mathbf{T}_\mathrm{c}\mathbf{T}_\mathrm{p}, \tag{7}$$

$${}^{t+\Delta t}\widehat{\mathbf{q}}_\mathbf{c} = \mathbf{T}_\mathrm{c}\big[\, {}^{t}Q + \Delta t\big\{(1-\gamma)\, {}^{t}\dot{Q} + \gamma\, ({}^{t+\Delta t}V_e \;/R)\big\}\big]. \tag{8}$$

Eqs. (1a) and (6) are solved using . the structural analysis using Eq. (1a) and the monolithic analysis of the piezoelectric-circuit coupling using Eq. (6) are strongly coupled using the block Gauss-Seidel (BGS) method. In the fully partitioned iterative method[5], a convergence condition for the iteration is imposed on the time increment Δt as $\Delta t\gamma/RC_\mathrm{p} \leq 1$ (C_p is the electrical capacitance of the bimorph) because of partitioning the piezoelectric-circuit coupling. Note that this condition will increase the computational cost in the case of the piezoelectric energy harvester woking in the low frequency regime.

3. Results and Discussion

The present problem setup shown in Fig. 1C gives the critical time increment $\Delta t_\mathrm{c} = 7.11\times10^{-6}$ sec from the convergence condition. In the case of $\Delta t = 1.0 \times 10^{-6}$ sec $< \Delta t_\mathrm{c}$, the time histories of the tip displacement of the bimorph given by the fully partitioned and proposed hybirid methods are indistinguishable from each other as shown in Fig. 3. On the contrary, in the case of $\Delta t = 1.0 \times 10^{-5}$ sec $> \Delta t_\mathrm{c}$, the charge given by the fully partitioned method diverged in the BGS iteration at the first time step as shown in Fig.4, while the time history given by the hybrid method is indistinguishable from those in Fig. 3. Fig. 5 shows the frequency response functions (FRFs) of the charge for the various Δt given by the hybrid methoed. As shown in this figure,

the FRFs for Δt smaller than 10^{-4} sec are very close to each other. The solution given by the fully partitioned method was accurate sufficiently in the case of $\Delta t = 1.0\times10^{-6}$ sec [5]. This solution gives the resonace frequency and the maximum tip displacement as 510.6Hz and 8.213×10^{-5} m, respectively. Errors of these properties given by the hybrid method from these reference values were less than 1% for $\Delta t <= 7.0 \times 10^{-5}$ sec. Hence, the hybrid method is more efficient than the fully partitioned method in terms of the solution accuracy and the computational cost for solving the problems of the piezoelectric bimorph energy harvesting.

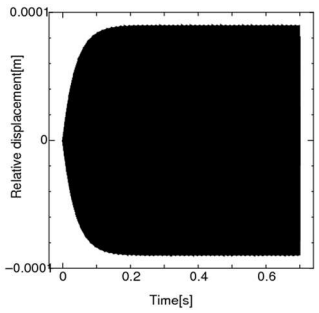

Fig.3 Time history of the relative tip displacement for f = 510.6Hz given by the fully partitioned and proposed methods in the case of Δt = 1.0×10^{-6} sec.

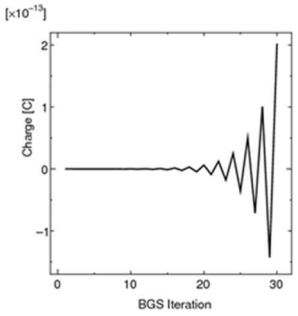

Fig.4. Charge transition for Δt = 1.0×10^{-5} sec given by the fully partitioned method.

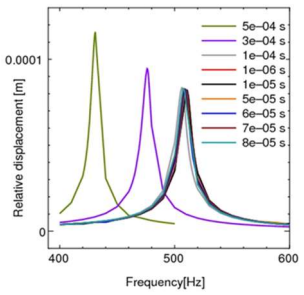

Fig.5 Frequency response functions for the various time increments given by the proposed method.

Acknowledgments

This work was supported by JSPS KAKENHI Grant number 20H04199.

References

[1] A. Ertuek and D. J. Inman, *Piezoelectric Energy Harvesting*, John Wiley & Sons, Ltd, 2011.

[2] P. C. Ramegowda, D. Ishihara, T. Niho and T. Horie, *Finite Elements in Analysis and Design*, Vol. 159, 2019, pp. 33-49.

[3] P. C. Ramegowda, D. Ishihara, R. Takata, T. Niho and T. Horie, *Computer methods in applied mechanics and engineering*, 2020, 113006

[4] P. C. Ramegowda, D. Ishihara, R. Takata, T. Niho and T. Horie, *Composite Structures*, Vol. 245, 2020, 112284.

[5] D. Ishihara, R. Takata, P. C. Ramegowda, N. Takayama, *Computers, and Structures*, Vol. 253, 2021, 106572.

JSST 2022

A study on information floating in a one-dimensional street considering effects of shadowing and side trips of pedestrians

Naoyuki Karasawa[1], Kazuyuki Miyakita[2], Takuma Kobayashi[3], Hiroshi Tamura[4], Keisuke Nakano[3]

[1]Kaishi Professional University
[2]Niigata University of International and Information Studies
[3]Niigata University
[4]Chuo University

*karasawa.naoyuki@kaishi-pu.ac.jp, miyakita@nuis.ac.jp, tamura@elect.chuo-u.ac.jp, nakano@ie.niigata-u.ac.jp

Abstract. Information floating permits mobile nodes to transmit information only in a transmittable area. By doing this, information floating can deliver information to mobile nodes passing around the transmittable area preventing the meaningless spread of information. In this paper, we consider information floating by pedestrians walking toward opposite directions along a one-dimensional street considering effects of shadowing. In such model, we assume that pedestrians sometimes take a side trip to a spot (e.g. store) from a street and stay in the spot. After staying at the spot for a short time, they enter the street and begin moving again. In such network, we evaluate performance of information floating and consider effects of such mobile nodes on information floating.

Keywords: information floating, pedestrians, shadowing, side trip

1. Introduction

In epidemic communication, mobile nodes such as vehicles and pedestrians spatially distribute and deliver information by direct wireless communication between them and their movements with information. Epidemic communication has a problem that information is disorderly spread. To overcome this problem, information floating (IF) that permits mobile nodes to transmit information only in transmittable areas (TAs) is proposed and discussed[1, 2, 3, 4, 5, 6, 7, 8]. In this paper, we consider IF by pedestrians walking toward opposite directions along a one-dimensional street where the node densities of opposite directions are uneven. In such IF, information exchanges between two mobile nodes moving in same direction are necessary for continuing IF. In such situation, shadowing caused by the pedestrians' body occurs because pedestrians often hold or carry user equipment in close

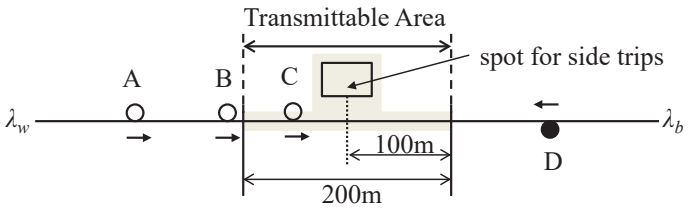

Figure 1: Network model.

proximity to the own body[8, 9, 10]. To consider this effect, in [8], we assumed that the communication range is different according to directions of two mobile nodes that communicate with each other, and theoretically analyzed the performance of IF considering such effects of shadowing. In this paper, in addition to considering the effects of shadowing, we assume that pedestrians sometimes take a side trip to a spot (e.g. store) from a street and stay in the spot. After staying at the spot for a short time, they enter the street and begin moving again. In such network, we evaluate performance of IF and discuss effects of such mobile nodes on IF.

2. Assumptions and models

In this paper, we consider a network model in Fig. 1. The nodes entering from left side of TA and the nodes entering from right side of TA are distributed based on a Poisson process with intensities λ_w and λ_b, respectively. Each node moves on a street at constant velocity v. The spot where nodes may stop by is located in the center of the TA. Assume that the spot is also a part of TA. This means that a node can transmit information to nodes in the spot while the node stays at the spot. We also assume that a node in the spot cannot communicate with a node walking on the street.

We consider the following two models. In Model 1, nodes do not take a side trip. In Model 2, nodes sometimes take a side trip from a street and stay in the spot. The probability that nodes take a side trip to a spot is denoted by P_s. The staying time in the spot obeys an exponential distribution with mean T_s. In Model 1 and Model 2, the communication range of a node is r. A node having information in TA can transmit information to other node if the distance between these nodes is not longer than r. In this paper, we consider shadowing as mentioned. When two nodes face each other, we assume that $r = r_a$. We also assume that $r = r_b$ when the direction of two nodes is the same. In general, we have $r_a \geq r_b$.

3. Simulation results and discussions

In this paper, we evaluate the mean lifetime of IF, denoted by $E(T_f)$, and reception rate of information, denoted by P_{rec}, by computer simulations. In the computer simulations, $\lambda_w = 0.03\text{m}^{-1}$, the length of TA is 200m, v = 1m/sec. P_s =0.05, 0.1, T_s = 300, 600sec, r_a = 100m, and r_b =50m.

The simulation results of Model 1 and Model 2 are shown in Fig. 2. From Fig. 2(a), we can confirm that $E(T_f)$ in Model 2 is larger than in Model 1 due to the effect of side trips of pedestrians. In particular, as P_s and T_s increase, $E(T_f)$ also increases. However, from Fig. 2(b), P_{rec} for Model 2 is sometimes smaller than that for Model 1. This is because information sometimes exists only in the spot, and nodes walking on the street cannot receive information, especially for large T_s.

In conclusion, we have to carefully decide the parameters for IF (e.g., the position and the length of TA) considering the effects of shadowing and side trips to satisfy the required values of $E(T_f)$ and P_{rec}.

References

[1] K. Nakano, "Epidemic Communication, Information Floating and Safety/Security," *IEICE Fundamentals Review,* vol. 10, no. 4, pp.282–292, April 2017. (in Japanese)

[2] A. V. Castro, et al., "Hovering Information - Self-Organising Information that Finds its Own Storage," *BBKCS-07-07, Technical Report, School of Computer Science and Information Systems,* Birkbeck College, London, UK, Nov. 2007.

[3] B. Liu, et al., "Analysis of the information storage capability of VANET for highway and city traffic," *Transportation Research Part C: Emerging Technologies,* vol.23, pp.68–84, 2012.

[4] J. Virtamo, et al., "Criticality condition for information floating with random walk of nodes," *Performance Evaluation,* Volume 70, Issue 2, pp.114–123, Feb. 2013.

[5] K. Nakano, K. Miyakita, "Information floating on a road with different traffic volumes between opposite lanes," *Journal of Advanced Simulation in Science and Engineering,* vol.3, no.1, pp.97–113, Aug. 2016.

[6] K. Nakano, K. Miyakita, "Analysis of information floating with a fixed source of information considering behavior changes of mobile nodes," *IEICE Trans. Fundamentals,* vol.E99-A, no.8, pp.1529–1538, Aug. 2016.

[7] K. Miyakita, N. Karasawa, Y. Inagawa, K. Nakano, "A consideration on traffic guidance by information floating," *IEICE Trans. Comm. (Japanese Edition),* vol.J101-B, no.8, pp.603–618, April 2018. (in Japanese)

[8] N. Karasawa, K. Miyakita, H. Tamura, K. Nakano, "Theoretical Analysis of Information Floating Considering Situations Where Pedestrians Themselves Become Obstacles," *Transaction of the Japan Society for Simulation Technology,* vol.14, no.1, pp.9–19, Jan. 2022. (in Japanese)

[9] D. Kotz, et al., "Experimental evaluation of wireless simulation assumptions," *Proc. of the 7th ACM Int. Symp. on Modeling, analysis and simulation of wireless and mobile systems (MSWiM),* pp.78-82, Oct. 2004.

[10] C. Bettstetter, C. Hartmann, "Connectivity of Wireless Multihop Networks in a Shadow Fading Environment," *Wireless Networks 11,* pp.571–579, Sept. 2005.

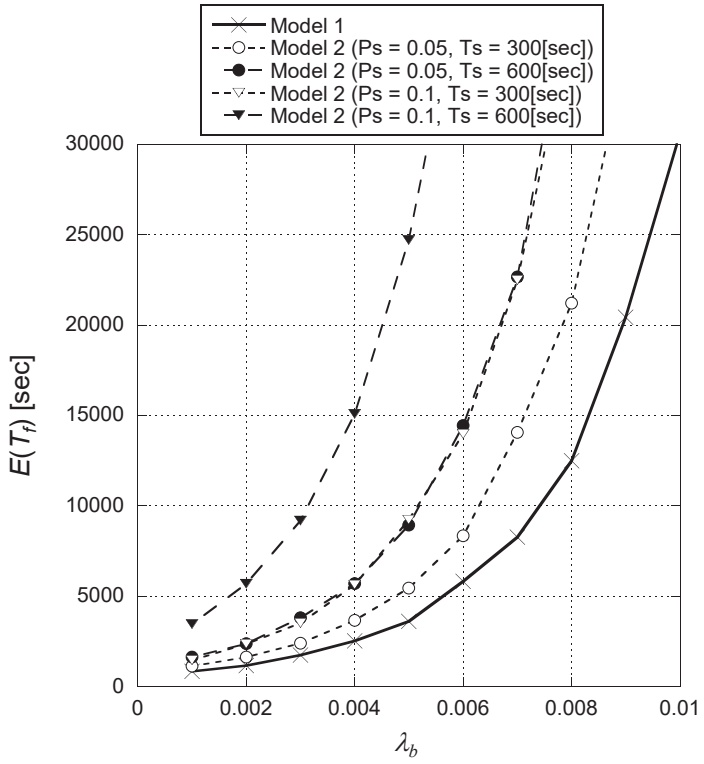

(a) Mean lifetime of IF.

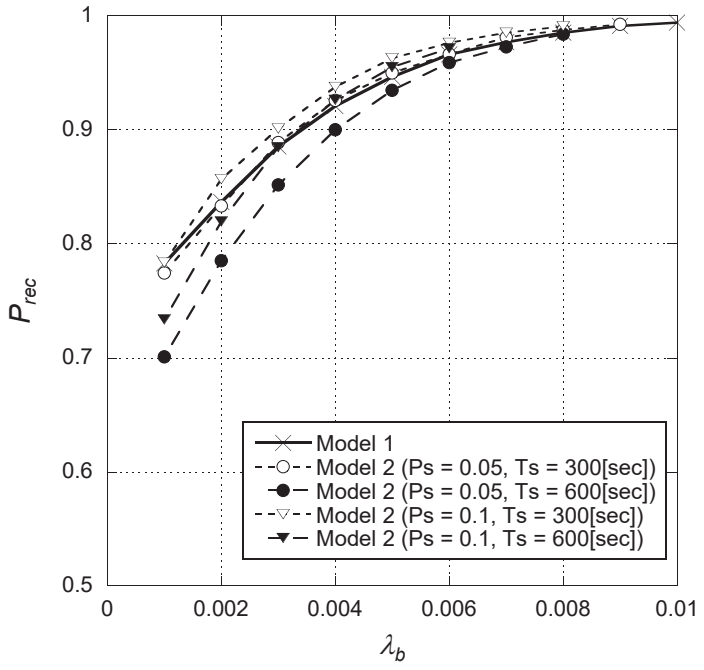

(b) Reception rate.

Figure 2: Simulation results.

A Consideration on Mobility Models for Evaluation of Delay Tolerant Networks in Road Networks

Kazuyuki Miyakita[1*], Hiroshi Tamura[2], Keisuke Nakano[3]

[1]Niigata University of International and Information Studies
[2]Chuo University
[3]Niigata University
[*] miyakita@nuis.ac.jp, tamura@elect.chuo-u.ac.jp,
nakano@ie.niigata-u.ac.jp

Abstract. In computer simulations of mobile networks including delay tolerant networks (DTNs), various mobility models have been used. In this paper, we focus on mobility models in road networks and evaluate two simple mobility models that can be used for evaluation of DTNs in road networks. In Model 1, each node chooses one from three directions (straight, left, right) with given probabilities at each intersection. In Model 1, each node sometimes makes a detour, and the length of trajectory of a node is not always the minimum. In Model 2, each node also decides its direction with given probabilities at each intersection; however, Model 2 can avoid a detour by classifying mobile nodes into four groups. From computer simulation results, we show that these mobility models have some similar characteristics from the viewpoint of the number of nodes in the service area; however, they differently affect performances of DTNs because of different properties of trajectories.

Keywords: Mobility models, Delay tolerant networks, Road networks

1. Introduction

There exist many types of mobile communication networks, and these networks are often evaluated by computer simulation. In computer simulations of mobile networks, various mobility models have been used[1]. The mobility model used in [2, 3, 4] is one of the oldest models and is based on actual measurements of mobility of vehicles. The model consists of the distribution of the length of time during which a vehicle moves straight, that of the velocity of a vehicle moving straight, and that of the angle between the direction before changing direction and the new direction. This model is used to evaluate the traffic characteristics of cellular networks.

A mobile ad-hoc network (MANET) is a type of mobile network, and uses direct wireless communication between nodes and multi-hop relays by mobile nodes. In the researches of MANETs, a mobility model called the random waypoint mobility model (RWP) has been often used[5]. In RWP, a node moves toward a waypoint randomly selected in a service area. Right after arriving at this waypoint, the node changes its direction toward a new waypoint. Such procedures are repeated. While this model was used in computer simulations for performance

evaluation of a MANET, some properties of the model were studied theoretically[5]. In RWP, each node chooses a new waypoint uniformly from the whole service area; however, the distribution of nodes in the service area is not uniform and mobile nodes tend to gather at the center of the service area. Using RWP, therefore, we have to take this tendency into account in performance evaluation.

Other than cellular networks and MANETs, delay tolerant networks (DTNs) have been widely studied. In DTNs, mobile nodes deliver data to the destination by spatially spreading the data. This spatial spreading is realized in an epidemic manner, in which the data are sent to adjacent mobile nodes by wireless direct communication and are carried by mobile nodes themselves. Due to the nature of DTNs, mobile nodes moving along road networks are suitable for DTNs because the mobile nodes on the same road segment pass by each other and can communicate with each other.

In this paper, we consider mobility models to evaluate DTNs in road networks. We evaluate two simple mobility models that can be used for evaluation of DTNs in road networks. In one mobility model (Model 1), each node chooses one from three directions (straight, left, right) with given probabilities at each intersection[6]. In another mobility model (Model 2), mobile nodes are classified into four groups[7]. At each intersection, mobile nodes in Group 1 move toward one of two directions (up or right). In the same manner, for Groups 2, 3 and 4, one direction is randomly selected from two directions (down and right), (up and left) and (down and left), respectively. We show that these mobility models have some similar characteristics from the viewpoint of the number of nodes in the service area; however, they differently affect performances of DTNs because of different properties of trajectories. These results help us to select an appropriate mobility model to evaluate DTNs in each of target situations.

2. Mobility models

As mentioned, we consider two mobility models (Models 1 and 2) to evaluate DTNs in road networks. Model 1 is an intuitive model, where each mobile node randomly chooses its direction every time it arrives at an intersection. In Model 1, each node sometimes makes a detour, and the length of trajectory of a node is not always the minimum. Instead, the mobility model provides a random movement and is easy to implement. Also, control parameters are only the three probabilities to select one from the three directions.

In Model 2, a node of Group 1 actually starts from the bottom side or the left side of the service area, and moves toward the top side or the right side of the service area. The node never makes a detour, namely, it moves along the shortest route. Due to this nature, this model is considered to be a more suitable model for mobile nodes moving without detours. The control parameters are two probabilities used to select one from the two directions. However, we have to carefully decide these probabilities to control the traffic volumes of each road segment.

As can be seen from these explanations, although Models 1 and 2 are both random mobility models, they are obviously different and are expected to differently affect performances of DTNs. However, these models have not been compared in detail. Hence, we try to show how these models are different, in particular, as the mobility models for evaluation of DTNs.

3. Results and discussions

Figure 1 shows the service area used in this paper. In the service area, there exist roads with 12×12 lattice structure. The length of each road segment is 500 m. Mobile nodes move along

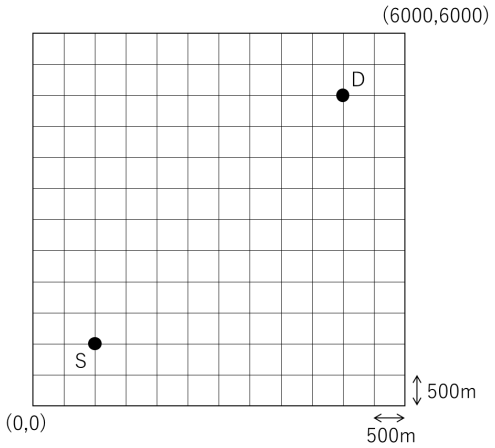

Figure 1: Road network.

Table 1: Mean staying time in the service area.

Model	p_{turn}	Mean staying time [s]
Model 1	0.1	597.935
	0.5	596.013
	0.9	599.969
Model 2	0.1	600.102
	0.5	600.036
	0.9	599.896

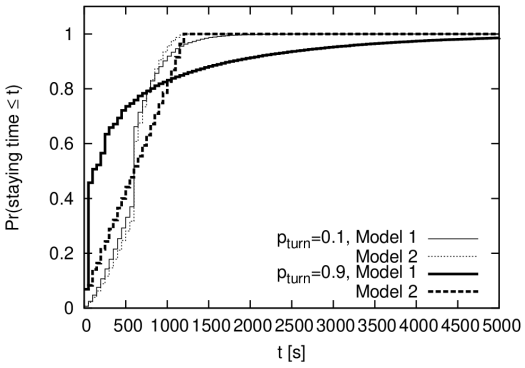

Figure 2: CDF of staying time.

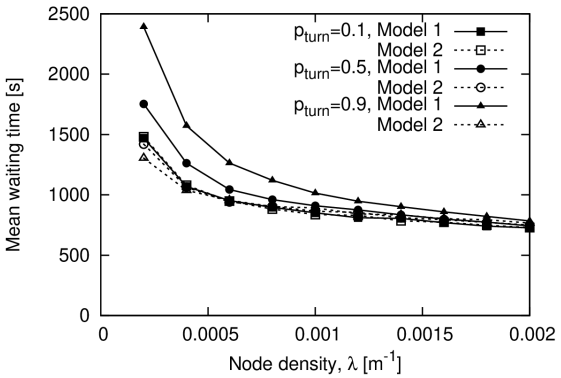

Figure 3: Mean waiting time from S to D.

the roads with constant velocity 36 km/h. For both Models 1 and 2, we use a parameter p_{turn} as the probability that a node arriving at an intersection turns left or right. Namely, in Model 1, a node goes straight, turns left, and turns right with probabilities $1 - p_{turn}$, $p_{turn}/2$, and $p_{turn}/2$, respectively. In Model 2, a node in Group 1 changes its direction (i.e., toward up or right) with probability p_{turn}, and does not change its direction with probability $1 - p_{turn}$. Nodes in Groups 2, 3, and 4 decide their directions at an intersection in the same manner.

Table 1 shows the mean length of staying time of a node in the service area. Figure 2 shows the cumulative distribution of the length of staying time of a node in the service area. From these results, we can see that in both models, the length of staying time is the same in average. Therefore, the densities of nodes are expected to be the same. Also, if p_{turn} is small, the distributions are also the similar for both models. Then, for the small value of p_{turn}, Models 1 and 2 are very similar. On the other hand, if p_{turn} is large, in Model 1, there exist more nodes with shorter staying time than Model 2. This means that in Model 1, more nodes go out of the service area shortly after entering the service area, and more nodes make detours than Model 2. In particular, for Model 1 with $p_{turn} = 0.9$, more than half of the nodes leave the service area within 100 seconds. This is because, due to the characteristics of Model 1, a node that enters the service area may immediately turn back and leave the service area.

Figure 3 shows performance of DTNs for Models 1 and 2. As a performance metric, we

use the mean waiting time from when a fixed source node S starts to send information to when a fixed destination node D receives the information. In the simulation, S and D are located at (1000, 1000) and (5000, 5000), respectively, as shown in Fig. 1. Other parameters are as follows: communication range is 100 m, and the node density for each direction for each road segment is λ (λ is used as the horizontal axis of Fig. 3).

The results of Fig. 3 show that in Model 2, data are delivered to the destination with less delay than Model 1 although the densities of nodes are expected to be the same. Hence, this performance is affected by the distribution of the length of staying time caused by the existence of detours.

As shown in this paper, Models 1 and 2 are similar, and Model 1 can be easily used; however, the effects of a difference between these models on the performance of DTNs can not be negligible. Therefore, we have to carefully select a mobility model for evaluation of DTNs in street networks.

References

[1] G. Solmaz, D. Turgut: A survey of human mobility models, *IEEE Access*, vol. 7, pp. 125711–125731, Dec. 2019.

[2] M. Sengoku et al.: Measurement of vehicle movements for traffic analysis of car telephone systems (I), *Proc. of Conference of IEICE Shin-etsu Section*, 59, Oct. 1984. (in Japanese)

[3] M. Sengoku et al.: Measurement of vehicle movements for traffic analysis of car telephone systems (II), *Proc. of Conference of IEICE Shin-etsu Section*, 79, Oct. 1985. (in Japanese)

[4] S. Nagatsuka, M. Sengoku, Y. Yamaguchi, T. Abe: An evaluation of telephone traffic characteristics of various channel assignment in a mobile radio communication system, *IEICE Transactions on Communications (Japanese Edition)*, vol. J71-B, no. 10, pp. 1167-1170, Oct. 1988. (in Japanese)

[5] C. Bettstetter, H. Hartenstein, X. Perez-Costa: Stochastic properties of the random waypoint mobility model, *Wireless Networks*, vol. 10, no. 5, pp. 555-567, Sept. 2004.

[6] A. Hanggoro, R. F. Sari: Performance evaluation of the manhattan mobility model in vehicular ad-hoc networks for high mobility vehicle, *Proc. of 2013 IEEE International Conference on Communication, Networks and Satellite (COMNETSAT)*, pp. 31-36, Dec. 2013.

[7] A. Otsuka, K. Nakano, K. Miyakita: Theoretical analysis of mean waiting time for message delivery in lattice ad hoc networks, *Journal of Circuits, Systems and Computers*, vol. 19, no. 8, pp. 1711-1741, Dec. 2010.

Distance Coloring and Grundy Number of Graphs

Hiroshi Tamura[1*], Keisuke Nakano[2]

[1]Faculty of Science and Engineering, Chuo University, Japan
[2]Graduate School of Science and Technology, Niigata University, Japan
[*]**tamura@elect.chuo-u.ac.jp**

Abstract. Relationship between graph coloring and channel assignment in wireless communication is well known. However, almost studies are about the minimum number of colors despite the difficulty of optimum coloring. In the previous study, we paid attention to graph coloring assigned maximum number of colors called Grundy coloring. Moreover, on the application to channel assignment, it may be necessary to assign a same color to vertices/edges at a distance. Therefore, in this paper, we pick up distance coloring and consider the upper bounds of the number of colors.

Keywords: Wireless communication, Channel assignment, Graph coloring, Distance coloring, Grundy number

1. Introduction

Relationship between graph coloring and channel assignment in wireless communication is well known. However, almost studies are about the minimum number of colors. This number is called the chromatic number of the graph and the problem of finding the chromatic number is NP hard. In the previous study [1], we paid attention to graph coloring assigned maximum number of colors called Grundy coloring. Because it is important to find the required number of channels. In [1], we showed some graphs expected to be assigned many colors theoretically. On the application to channel assignment, the cochannel interference may be too strong with the conventional coloring. Therefore, in this paper, we pick up distance coloring. Then we consider the upper bounds of the number of colors.

2. Assumptions and definitions

First of all, we define conventional graph coloring. Vertex/edge coloring means assigning differential colors to adjacent vertices/edges. Next, we define greedy coloring[2]. A ***greedy coloring*** is a coloring of the elements (vertices or edges) of a graph formed by a greedy algorithm that considers the elements of the graph in sequence and assigns each element its first available color. The number of colors produced by the greedy coloring for the worst ordering of a given graph G is called its ***Grundy number***[3] and its coloring is called ***Grundy coloring***. The vertex

Grundy coloring is common. The conventional edge coloring version called ***edge Grundy number*** and ***edge Grundy coloring*** is discussed in [4].

We explain edge Grundy coloring. We consider a path graph(Fig.1(a)). In Fig.1(a), the number with parenthesis represents edge ordering. The edge greedy coloring of Fig.1(a) is Fig.1(b).

(a) (b)

Fig.1 An edge ordering and coloring.

(a) (b)

Fig.2 An edge ordering different from Fig.1(a) and coloring.

Another case is in Fig.2. The number of colors is 2 in Fig.1(b) and 3 in Fig.2(b). Since the edge Grundy number is the maximum number of colors, the edge Grundy number of the path graph is 3.

In [1], we showed the graphs assigned many colors theoretically and vertex/edge ordering of coloring.

[Theorem 1][1]

Let G be a graph. For a greedy coloring, the number of colors is not greater than

max {deg(u) +1 | u is a vertex of G}, in case of vertex coloring,

max{deg(u)+deg(v) -1| (u,v) is an edge of G}, in case of edge colorings,

where deg(u) is the degree of vertex v.

Theorem 1 shows the upper bounds of colors for Grundy number/ edge Grundy number. Here we define the distance of vertices/edges and distance colorings of graphs. ***The distance of vertices/edges*** means the number of edges on the shortest path between the vertices/edges. ***The k- distance vertex/edge coloring*** means we cannot assign a same color to vertices/edges if the distance of the vertices/edges is not greater than k. Clearly, the conventional vertex coloring is 1- distance vertex coloring and the conventional edge coloring is 0- distance edge coloring. For example, Fig. 3(a) is a 2-distance vertex coloring, because, the distance of vertices u,v assigning color 1 is 3. Fig.3(b) is a 1-distance edge coloring, because, for edge e,e' assigning color 1, the distance of a vertex on e and a vertex on e' is equal or rather than 2.

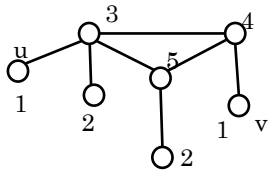

Fig.3(a) 2-distance vertex coloring

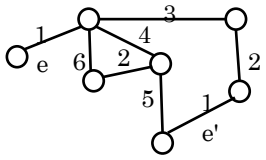

Fig.3(b) 1-distance edge coloring

3. Results

We obtain the following results about the Grundy number on distance coloring.

[Theorem 2]

Let G be a graph and Δ be the maximum degree, where the degree of vertex v is the number of edges being incident with v. The upper bounds of colors with greedy vertex colorings are as follows.

$$\begin{cases} 2k+1 & \text{if } \Delta=2 \\ \dfrac{\Delta((\Delta-1)^k-1)}{\Delta-2}+1 & \text{if } \Delta\neq 2 \end{cases}$$

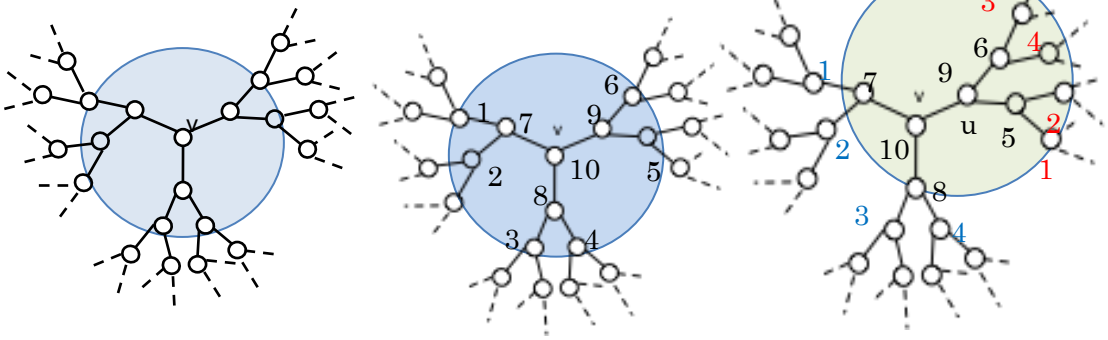

Fig.4(a)A tree with Δ=3. Fig.4(b) A coloring around v. Fig.4(c) A coloring around u.

Fig.4 is a tree that is an example of Δ=3. In case of k=2, all vertices in the circle centered on vertex v are assigned to different colors. The number of colors is 10(Fig.4(b)). This value is the value calculated to the above equation in case of Δ=3 and k=2.

In case of the circle centered on the vertex u in Fig.4(c), all vertices in the circle are also assigned to different color. In Fig.4(c), we assign colors 1,2,3,4(red number) to newly entered vertices in the circle. By repeating this operation, it is possible to color the maximum number of colors if it is an infinite graph.

In case of the conventional vertex coloring(k=1), the value is $\Delta+1$. So, Theorem 2 is an expansion of Theorem 1.

[Theorem 3]

Let G be a graph and Δ be the maximum degree, where the degree of vertex v is the number of edges being incident with v. The upper bounds of colors with greedy edge colorings is as follows.

$$\begin{cases} 2k+3 & \text{if } \Delta=2 \\ \dfrac{2((\Delta-1)^{k+2}-1)}{\Delta-2}-1 & \text{if } \Delta\neq 2 \end{cases}$$

In case of the conventional edge coloring(k=0), the value is $2\Delta-1$. So, Theorem 2 is an expansion of Theorem 1. Because, in Theorem 1, if deg(u)=deg(v)=Δ, the value is $2\Delta-1$.

Compared to general graphs, trees have the maximum number of vertices/edges that are less than or equal to the distance k from a vertex/edge. Therefore, Theorem 2.3 are also the upper

bounds of the number of colors in general graphs.

4. Conclusions

In this paper, we show the upper bounds of colors about distance coloring. However, we do not know how many channels will be required for real wireless communication systems. Therefore, verification with computer simulation is necessary.

References

[1] H. Tamura, S. Matsumoto, K. Nanano, M. Sengoku, On Graph Coloring with Relation to Channel Assignment in Wireless Networks, IEICE Trans. Fundamentals, Vol.J102-A,No.7,pp.214-223,Jul. 2019.

[2] Tommy R. Jensen, Bjarne Toft: Graph Coloring Problem, John Wiley & Sons,1994.

[3] P. M. Grundy:"Mathematics and games", Eureka, 2: 6–8, 1939.

[4] Leizhen Cai and Xuding Zhu: "Game Chromatic Index of k-Degenerate Graphs, J. Graph Theory, Vol.36, 3, pp.144-155, 2001.

Equivalent Circuit for Wireless Power Transfer Considering Eddy and Displacement Currents

Qiao Liu[1], Hajime Igarashi[1]

[1] Graduate School of Information Science and Technology, Hokkaido University

*liuqiao@em.ist.hokudai.ac.jp

Abstract. This paper presents an equivalent circuit of a wireless power transfer device simultaneously considering the eddy current and displacement currents. To consider the eddy currents in the spiral coils, complex inductance is introduced where the magnetic flux and eddy current loss are evaluated using finite element method (FEM). The capacitance between the coils is extracted using FEM. It is shown that the active power computed from the present equivalent circuit agrees well with that computed by FEM when the displacement currents are negligible. Moreover, the active power is shown to be greatly affected by the displacement currents between the spiral coils.

Keywords: Wireless power transfer, Printed spiral coil, Equivalent circuit, Self-resonant

1. Introduction

Magnetically coupled resonance wireless power transfer (WPT) systems have been developed in recent years. This type of WPT has several benefits, including no physical contact, applicability for moving objects and availability in wet and harsh environment. It has been accepted globally, and is used in several fields, such as consumer electronics[1] and electric vehicles[2].

The planar spiral coils printed on a substrate board, called printed spiral coil (PSC), has been studied for possible uses for small or medium electric devices [3]. A fast numerical model of PSC used in coupled magnetic resonance system has been required for its design [1,4]. For such a model, eddy currents in the coils and displacement currents flowing between the coils have to be adequately considered. However, FEM analysis needs large computing cost to consider both effects.

In this paper, we propose an equivalent circuit to consider both eddy current and displacement current. The complex inductance and capacitance extracted from the WPT device using FEM are included in the equivalent circuit. We also consider the dielectric loss precisely at same time. We analyze a magnetic coupled WPT system using PSC using the equivalent circuit.

2. PSC model and construction of equivalent circuit

a) PSC model

In this paper, we consider a PSC model used in coupled magnetic resonance WPT. The PSC composes of rectangular coils on one side, whose feasibility is demonstrated by [3]. The operating frequency of the WPT system of our interest is 6.78MHz (one of the ISM band) which is suitable

for consumer electronics applications. A 6 turns PSC model is shown as Figure. 1. The parameter is shown in Table 1.

Table 1. Parameters of PSC

Side length of outer turn	Number of turns	Wire width	Wire thickness	Clearance between turns	Substrate thickness
70mm	6	3mm	0.105mm	2mm	0.33mm

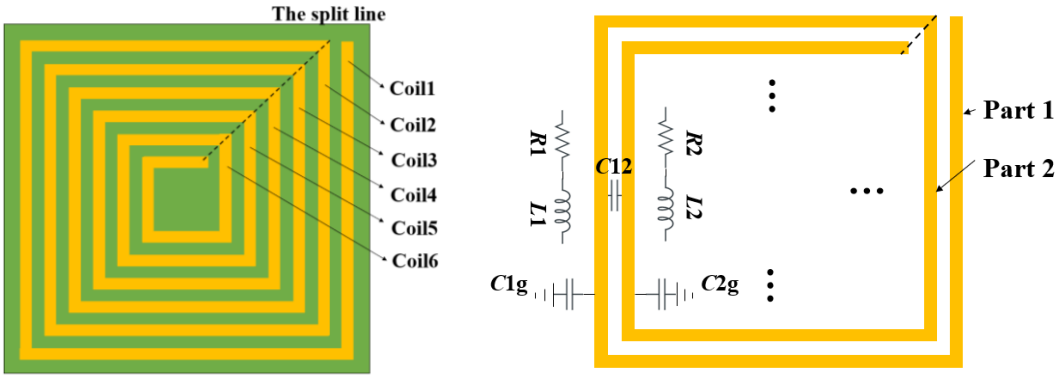

(a) Simplified structure of PSC (b) Schematic diagram of partition for part 1,2

Figure. 1. Simplified 6 turns PSC

To build the equivalent circuit, the PSC model is divided into six split rings. Each part has its own resistance, self-inductance and mutual inductance between among coils. Parasitic capacitance exists between every two split rings and substrate board.

b) Equivalent circuit

RLC equivalent circuit has been applied in [4] to analyze the PSC. In this work, we introduce the complex inductance in the equivalent circuit to emulate the coil more precisely. The power relevant to the inductance is expressed as follows:

$$P_{prox} = jw\frac{1}{2}\dot{L}_{11}I_1^2 + jw\frac{1}{2}\dot{L}_{22}I_2^2 + \cdots + jw\dot{M}_{12}I_1I_2 + jw\dot{M}_{13}I_1I_3 + \cdots \quad (1)$$

where the imaginary part in (1) represents the stored power whereas the real part represents the eddy current loss. The imaginary part of $\dot{M}$ included in (1) which is calculated by FEM only one time represents the eddy current loss and diamagnetic effect due to other coils, namely, proximity effect. $\dot{L}$ in (1) is also computed by FEM considering the skin effect.

The equivalent circuit of PSC is shown in Figure 2. Parasitic capacitance C_{ij} between the i-th and j-th split rings are computed by FEM. Resistors R_{kg} that represents the dielectric loss of the substrate board are evaluated from

$$R_{kg} = \frac{tan\,\delta}{\omega C_{kg}} \quad k = 1,2\cdots 6 \quad (2)$$

They are connected with capacitance C_{kg} between the split ring and ground plane in series.

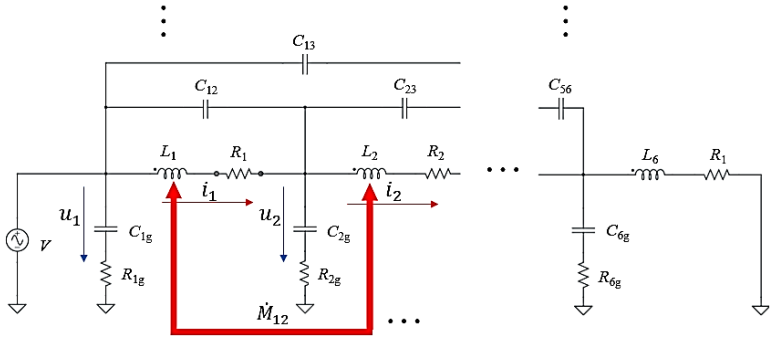

Figure 2. Equivalent circuit of PSC

We solve the circuit shown given by

$$\left\{jw\begin{bmatrix}[\dot{L}] & 0\\ 0 & [C]\end{bmatrix}+\begin{bmatrix}[R] & [K]\\ [K]^t & 0\end{bmatrix}\right\}\begin{bmatrix}\{I\}\\ \{U\}\end{bmatrix}=\begin{bmatrix}\{\alpha\}\\ \{\beta\}\end{bmatrix} \tag{3}$$

where R denotes resistance, C capacitance, $\dot{L}$ complex inductance, K matrix composed of constants, I, U current and voltage, α and β are source terms.

3. Numerical result

The resistance and inductance computed by the equivalent circuit and quasi-static FEM neglecting the parasitic capacitance are plotted in Figure 3.

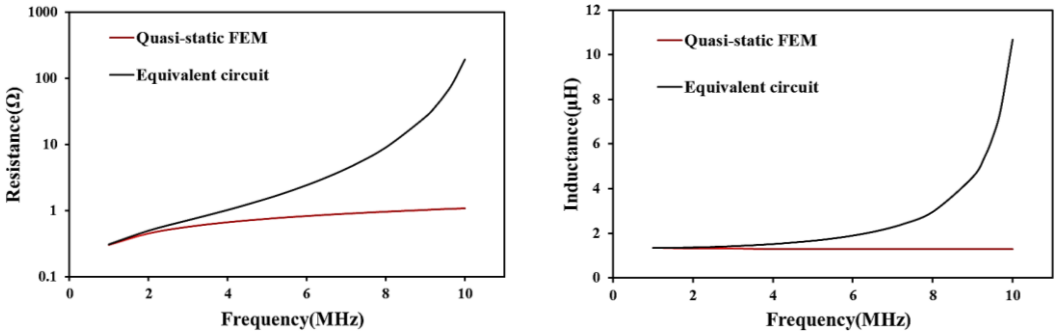

(a) Frequency response of resistance (b) Frequency response of inductance

Figure 3. Resistance and inductance characteristics of PSC

At low frequencies, results computed from proposed equivalent circuit are consistent with that computed by FEM under quasi-static approximation. As frequency increases, because of the self-resonance due to the parasitic capacitance, discrepancies between them grow.

For verification at low frequency limit, we compute the active power from the proposed equivalent circuit without parasitic capacitance on both side of WPT system and the conventional lumped circuit, shown in Fig.4, whose circuit parameters are computed from quasi-static FEM. The mutual inductance values between the split rings are considered in the former while the lumped mutual inductance is assumed in the latter. The coupling coefficient is set to 0.3 and the input voltage is 1V. The resonant frequency is set to 6.78MHz. Both results are in good agreement as shown in Fig.5.

We evaluate the active power considering the parasitic capacitance. The results are plotted in Fig.6 where the active power computed from the lumped circuit without parasitic capacitance is also plotted for comparison. It is concluded from these results that the parasitic capacitance greatly influences on the frequency characteristic of the active power.

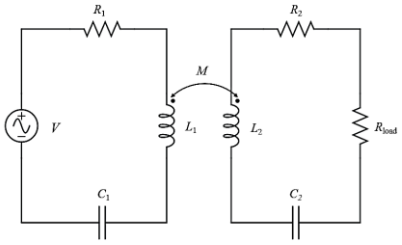

Figure 4. Conventional equivalent circuit using lumped parameter

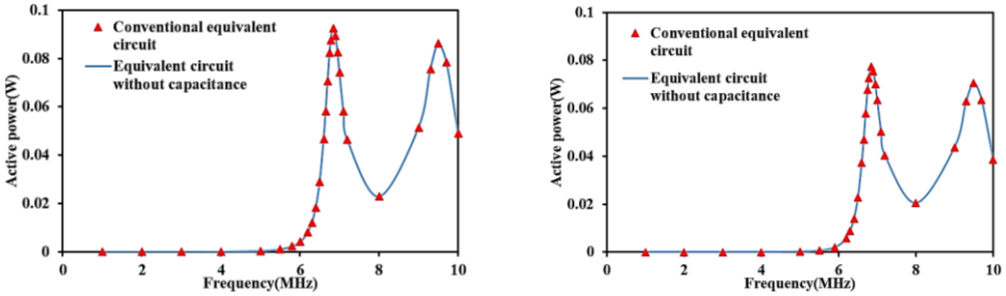

(a) Active power of transmitting side (b) Active power of load

Figure 5. Validation of proposed equivalent circuit

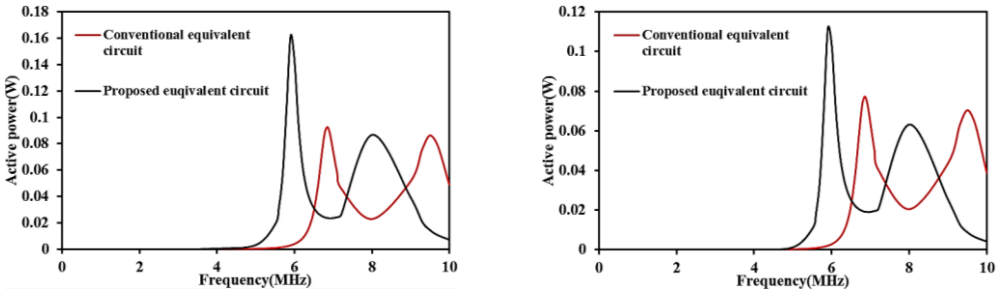

(a)Active power of transmitting side (b) Active power of load

Figure 6. Analysis results of WPT using different equivalent circuit

4. Conclusion

In this paper, we have proposed an equivalent circuit model of a WPT device. In this model, the skin and proximity effects are considered by introducing the complex inductance that is evaluated by FEM. The parasitic capacitance evaluated by FEM is also included in the equivalent circuit. It has been shown that the parasitic capacitance has a great influence on the frequency characteristic of the active power of the WPT device. In future, we plan to make verification of the computed results.

References

[1] N. Van T. "Magnetic resonance wireless power transfer using three-coil system with single planar receiver for laptop applications" in IEEE Transactions on Consumer Electronics,vol.61, no.2, pp.160-166, May 2015

[2] X. Mou, O. Groling and H. Sun, "Energy-Efficient and Adaptive Design for Wireless Power Transfer in Electric Vehicles," in IEEE Transactions on Industrial Electronics, vol. 64, no. 9, pp. 7250-7260, Sept. 2017

[3] W. -S. Lee, W. -I. Son, K. -S. Oh and J. -W. Yu, "Contactless Energy Transfer Systems Using Antiparallel Resonant Loops," in IEEE Transactions on Industrial Electronics, vol. 60, no. 1, pp. 350-359, Jan. 2013

[4] K. Chen and Z. Zhao, "Analysis of the Double-Layer Printed Spiral Coil for Wireless Power Transfer," in IEEE Journal of Emerging and Selected Topics in Power Electronics, vol. 1, no. 2, pp. 114-121, June 2013,

Conceptual design of dataflow machine for 2-D eddy current fields simulations

Chenxu Wang, Hideki Kawaguchi

Division of Information and Electronic Engineering, Graduate School of Engineering,
Muroran Institute of Technology, Japan
*kawa@mmm.muroran-it.ac.jp

Abstract. To aim to achieve a portable, low power consumption, low cost and green high-performance computing (HPC) technology for electromagnetic fields simulation, authors have been working on the development of a dedicated computer based on dataflow architecture for 2-D magneto-static field, 3-D electrostatic field and 3-D microwave simulations. In this paper, we consider to propose a conceptual design of dataflow architecture machine for 2-D eddy current field simulations.

Keywords: high-performance computing (HPC), dedicated computer, eddy current field

1. Introduction

For developments of portable, low power consumption, low cost and high-performance computing (HPC) technologies to be effectively used in industry applications, authors have been investigating a method of dedicated computers for electromagnetic fields simulations. In previous works, the authors proposed dataflow architecture machines of 3-D finite-difference time-domain (FDTD) method for microwave simulations[1] and finite integration technique (FIT) based on BiCG-Stab solver for 2-D magneto-static fields[2] and 3-D electrostatic simulations[3]. In this paper, we discuss a conceptual design of the FIT dataflow machine for 2-D eddy current fields simulations.

2. FIT formulation of 2-D eddy current simulation based on simple iteration method

The 2-D eddy-current field is governed by the following vector Poisson's equation:

$$\nabla\times\left(\frac{1}{\mu}\nabla\times\mathbf{A}\right)_z=-\sigma\frac{\partial A_z}{\partial t}+J_{0z} \tag{1}$$

where μ and σ are permeability and conductivity of a conductor, respectively. J is current density. The FIT discretization of the (1) can be expressed as follows:

$$\begin{aligned}&\left(\frac{\sigma}{\Delta t}+\frac{C^1+C^2+C^3+C^4}{2}\right)A_{zi,j}^{n+1}-\frac{C^1}{2}A_{zi,j-1}^{n+1}-\frac{C^2}{2}A_{zi+1,j}^{n+1}-\frac{C^3}{2}A_{zi,j+1}^{n+1}-\frac{C^4}{2}A_{zi-1,j}^{n+1}\\&=\left(\frac{\sigma}{\Delta t}-\frac{C^1+C^2+C^3+C^4}{2}\right)A_{zi,j}^{n}-\frac{C^1}{2}A_{zi,j-1}^{n}-\frac{C^2}{2}A_{zi+1,j}^{n}-\frac{C^3}{2}A_{zi,j+1}^{n}-\frac{C^4}{2}A_{zi-1,j}^{n}+\mathbf{J}\end{aligned} \tag{2}$$

$$C^1=\frac{1}{2\mu_{i-1,j-1}}+\frac{1}{2\mu_{i,j-1}},C^2=\frac{1}{2\mu_{i,j-1}}+\frac{1}{2\mu_{i,j}},C^3=\frac{1}{2\mu_{i,j}}+\frac{1}{2\mu_{i-1,j}},C^4=\frac{1}{2\mu_{i-1,j}}+\frac{1}{2\mu_{i-1,j-1}} \quad (3)$$

where $A_{zi,j}^n$ and $\mu_{i,j}$ are *n-th* time step value of *z*-component of the vector potential and permeability at *i-th, j-th* grid for *x* and *y* directions, respectively. And (2) is rewritten as,

$$A_{zi,j}^{n+1}=\frac{C^1}{2C^{01}}A_{zi,j-1}^{n+1}+\frac{C^2}{2C^{01}}A_{zi+1,j}^{n+1}+\frac{C^3}{2C^{01}}A_{zi,j+1}^{n+1}+\frac{C^4}{2C^{01}}A_{zi-1,j}^{n+1}+\frac{C^{00}}{C^{01}}A_{zi,j}^{n}+\frac{C^1}{2C^{01}}A_{zi,j-1}^{n}+\frac{C^2}{2C^{01}}A_{zi+1,j}^{n}+\frac{C^3}{2C^{01}}A_{zi,j+1}^{n}+\frac{C^4}{2C^{01}}A_{zi-1,j}^{n}+\frac{\mathbf{J}}{C^{01}} \quad (4)$$

$$C^{01}=\left(\frac{\sigma}{\Delta t}+\frac{C^1+C^2+C^3+C^4}{2}\right),C^{00}=\left(\frac{\sigma}{\Delta t}-\frac{C^1+C^2+C^3+C^4}{2}\right) \quad (5)$$

Accordingly we can calculate (n+1)-th time step value of A_z^{n+1} at *i-j* grid based on a simple iteration method by using previous time step *n*-th values A_z^n at peripheral grids.

3. Conceptual design of hardware circuit for eddy current fields

The overview of FIT dataflow machine for 2-D eddy-current fields simulation is depicted in Fig.1. The (n+1)-th and the previous time step values of the vector potentials $A_{zi,j}^{n+1}$, $A_{zi,j}^n$, current density $J_{i,j}^n$ and coefficients $\frac{C^1}{2C^{01}}$, $\frac{C^2}{2C^{01}}$, $\frac{C^3}{2C^{01}}$, $\frac{C^4}{2C^{01}}$, $\frac{C^{00}}{C^{01}}$ are stored in registers and allocated in 2-D grids space (Fig.1(a)). These registers are connected each other via arithmetic circuits which carry out the calculation of (4) in single clock cycle automatically. This arithmetic calculations at the unit grid are executed in parallel all over 2-D grids space. To iterate this operation until the calculated value of $A_{zi,j}^{n+1}$ are converged, we can obtain (n+1)-th time step values of $A_{zi,j}^{n+1}$. Therefore, we can do time-domain simulation of the 2-D eddy-current fields to repeat the above operation for pre-defined time steps. We are now designing the logic circuit by hardware description language VHDL, and the VHDL simulation results will be given in near future.

References

[1] H. Kawaguchi et.al, IEEE Trans. Magn, Vol.51, Issue 3, 7202404, 2015

[2] Wang.C et.al, 2021 International Conference on Electromagnetics in Advanced Applications(ICEAA). IEEE, 2021:223.

[3] Wang Chenxu et.al, Papers of Technical Meeting on Electromagnetic Theory, EMT-22-023, 2022-1.

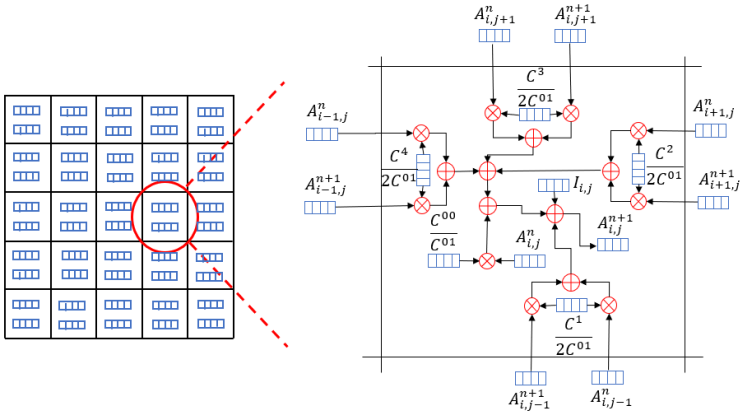

(a) Register allocation in 2-D grids space (b) unit grid circuit

Fig.1 The overview of arithmetic circuits based on simple iteration method

JSST 2022

Implementation of a hierarchical parallel solver for saddle point problems on a GPU cluster

Hiroto Tadano[1,*]

[1]Center for Computational Sciences, University of Tsukuba

[*]tadano@cs.tsukuba.ac.jp

The full paper of this paper has been published in Journal of Advanced Simulation in Science and Engineering (JASSE).

DOI: https://doi.org/10.15748/jasse.10.116

JSST 2022

Improved Variable-Reduction Method for Asymmetric Saddle-Point Problem

Atsushi Kamitani[1,*] and Teruou Takayama[1]

[1]Department of Informatics and Electronics, Graduate School of Science and Engineering, Yamagata University

[*]kamitani@yz.yamagata-u.ac.jp

Abstract. The improved Variable Reduction Method (iVRM) is extended so as to be applicable to asymmetric EFG-type Saddle-Point (EFG-SP) problems. A numerical code has been developed for solving an asymmetric EFG-SP problem with the extended iVRM and, by using the code, the performance of the extended method is investigated numerically. The results of computations show that, as a solver for a large-sized asymmetric EFG-SP problem, the iVRM is even superior to the preconditioned Krylov subspace method.

Keywords: Krylov subspace method, Meshless approach, Saddle-point problem

1. Introduction

The Element-Free Galerkin (EFG) method [1] and the eXtended Element-Free Galerkin (X-EFG) method [2] were developed as meshless approaches for solving a boundary-value problem. As is well known, the application of the EFG to a boundary-value problem yields a symmetric EFG-type Saddle-Point (EFG-SP) problem. In order to efficiently solving the problem, the authors developed the improved Variable Reduction Method (iVRM) and investigated its performance numerically [3]. As a result, it is found that, from the standpoint of both convergence property and computational cost, the iVRM can be a powerful tool for solving a symmetric EFG-SP problem.

On the other hand, if a boundary-value problem is discretized with the X-EFG, we obtain the following linear system that is slightly different from a symmetric EFG-SP problem:

$$\begin{bmatrix} B & C \\ D^T & O \end{bmatrix} \begin{bmatrix} \boldsymbol{u} \\ \boldsymbol{\lambda} \end{bmatrix} = \begin{bmatrix} \boldsymbol{c} \\ \boldsymbol{d} \end{bmatrix}. \tag{1}$$

Here, the submatrix $B \in \mathbb{R}^{N\times N}$ is asymmetric and singular, whereas $C, D \in \mathbb{R}^{N\times K}$ are full-column rank. Moreover, $\boldsymbol{u} \in \mathbb{R}^N$ and $\boldsymbol{\lambda} \in \mathbb{R}^K$ are both unknown vectors. In the present study, (1) is called an asymmetric EFG-SP problem. Apparently, (1) is unsolvable with the iVRM.

The purpose of the present study is to extend the iVRM so as to be applicable to an asymmetric EFG-SP problem. In addition, we numerically investigate the performance of the extended method.

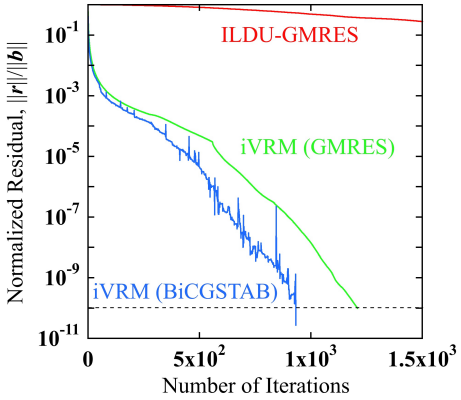

Figure 1: Residual histories of ILDU-GMRES and iVRMs for N = 1,050,625.

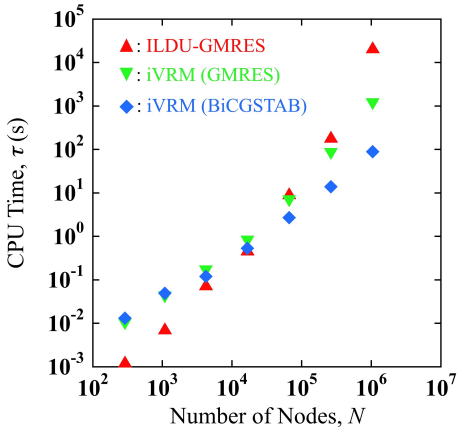

Figure 2: Dependence of the CPU time τ on the number N of nodes.

2. Extension of Improved Variable-Reduction Method

In the extended iVRM, two projection matrices, F and U, are first determined. Here, F and U are a projection matrix onto $\mathrm{Im}\, C$ along $(\mathrm{Im}\, D)^{\perp}$ and that onto $(\mathrm{Im}\, D)^{\perp}$ along $\mathrm{Im}\, C$, respectively. Note that neither F nor U is an orthogonal projection matrix. Next, a vector $\boldsymbol{\lambda}$ is eliminated from (1) by using the two projection matrices. Consequently, we get the following linear system:

$$B^{\dagger}\,\boldsymbol{u} = \boldsymbol{c}^{\dagger}, \tag{2}$$

where $B^{\dagger} \equiv U\,B\,U + F$ and $\boldsymbol{c}^{\dagger} \equiv U[\boldsymbol{c} - B\,\boldsymbol{d}^{\dagger}] + \boldsymbol{d}^{\dagger}$. Moreover, the vector $\boldsymbol{d}^{\dagger}$ is given by $\boldsymbol{d}^{\dagger} = C(D^{T}C)^{-1}\,\boldsymbol{d}$.

In the actual calculation, (2) is solved with the Krylov subspace method such as BiCGSTAB and GMRES to determine $\boldsymbol{u}$ numerically. Incidentally, for the purpose of calculating the vector $(D^{T}C)^{-1}\boldsymbol{v}$, BiCGSTAB is also employed. Throughout the present study, the method for solving (2) with BiCGSTAB and that with GMRES are called iVRM (BiCGSTAB) and iVRM (GMRES), respectively.

An asymmetric EFG-SP problem originating from a 2D Poisson problem is solved with ILDU-GMRES/iVRM (GMRES)/iVRM (BiCGSTAB). The residual histories and the dependence of the CPU time on the number N of nodes are depicted in Figures 1 and 2, respectively.

References

[1] T. Belytchko *et al.*: *Int. J. Numer. Mech. Eng.*, Vol. 37 (1994) 229-256.

[2] A. Kamitani *et al.*: *Plasma Fusion Res.*, Vol. 6 (2011) Art. No. 2401074.

[3] A. Kamitani *et al.*: *Plasma Fusion Res.*, Vol. 17 (2022) Art. No. 2403014.

Medical – Engineering collaboration for big data analysis and numerical modeling

Yoshihide Shibata[1,*]

[1]Department of Electrical and Computer Engineering,
National Institute of Technology, Gifu College

[*]shibata.yoshihide@gifu-nct.ac.jp

The full paper of this paper has been published in Journal of Advanced Simulation in Science and Engineering (JASSE).

DOI: https://doi.org/10.15748/jasse.10.206

The incidence reduction of Kawasaki disease before and after the COVID-19 pandemic onset by using data analysis technics in engineering

Yumika Makimura[1], Yoshihide Shibata[2*], Shinsuke Hoshino[3], Ryusuke Ae[4]

[1]Advanced Course for Interdisciplinary Technology Development,
National Institute of Technology, Gifu College
[2]Department of Electrical and Computer Engineering,
National Institute of Technology, Gifu College
[3] Department of Pediatrics, Shiga University of Medical Science
[4]Division of Public Health, Center for Community Medicine, Jichi Medical University

*shibata.yoshihide@gifu-nct.ac.jp

Abstract. In this study, using data of regional survey of Kawasaki Disease in Shiga prefecture, Japan, which includes many patients who developed Kawasaki Disease during the COVID-19 pandemic period, we aimed to assess the epidemiologic association between Kawasaki disease and the decrease in human – human contact to investigate the cause of Kawasaki Disease. As the first step, we made huge database for data analysis of Kawasaki Disease. This database consists of the following data: Kawasaki disease survey data in shiga prefecture as Kawasaki Disease patient data, the transient population data of major station in each administrative districts in Shiga pref. as data of movement restriction, Japanese surveillance of infectious diseases, and weather data linked to Kawasaki Disease patient data. As second step, we compared the number of patients who developed Kawasaki disease after April in 2020 with the mean number of patients who developed Kawasaki disease in the corresponding period during 2015-2019 to evaluate the epidemiologic association between Kawasaki disease and the decrease in human – human contact. After April, during national school closure, the monthly number of patients who developed Kawasaki disease in 2020 showed a decreasing trend and was lower than the minimum monthly patient numbers in previous years.

Keywords: Kawasaki disease, data analysis technics in engineering

1. Introduction

Kawasaki Disease (KD) is an acute, pediatric vasculitis affecting the coronary arteries. This disease has been reported in many countries as well as in children of all races and ethnicities. Japan has been well known as the highest incidence of KD[1]. However, the mechanism of onset in KD has not been clarified yet, and researches for understanding the mechanism of onset are still continued in the world.

The first patient of COVID-19 was reported at China in December 2019[2], and this virus

was rapidly spread whole the world. To prevent spreading COVID-19 virus, infection mitigation measures such as social distancing, mask wearing, and school closures were conducted from 2020. Therefore, the number of patients in pediatrics infections disease was drastically reduced in Japan[3]. Some studies in Japan were reported that the number of KD patients was decreased during the COVID-19 pandemic period[4,5]. These studies were suggested that potentially transmissible agents may trigger KD. However, more additional studies in Japan are necessary since locations of past studies were limited. In this study, we conducted a complete survey of KD patients in Shiga prefecture before and after the onset of the pandemic. We also assessed the association between reduced numbers of patients with KD and human to human contact restrictions.

2. Experimental Setup

A retrospective ecological study was conducted by using patients data hospitalized for KD in Shiga prefecture. The study period was from January 1 2015 to December 31 2020. Information of KD patients was obtained from 14 local based hospitals in Shiga prefecture by using a questionnaire. The collected data included sex, age(months), date of KD onset, date of hospitalication, diagnostics information(complete KD or incomplete KD), and zip codes of resident. The Ethics Committee of Shiga University of Medical Science approved the study and waived the requirement for informed consent from individual participants(R2020-139).

Japanese surveillance of infectious diseases[6] was used to investigate the reduction of pediatrics infectious diseases (respiratory syncytial virus infection, pharyngoconjunctival fever, group A streptococcal pharyngitis, infectious gastroenteritis, varicella, hand–foot–mouth disease, erythema infectiosum, exanthema subitum, herpangina, mumps). To assess movement restrictions in Shiga prefecture, the transient population data of major station in each regions of Shiga prefecture was used. NTT DOCOMO, which is famous mobile phone company, is sold the transient population data in all locations of Japan[7]. A transient population data is made from location information of user with NTT docomo, and the number of population is estimated within 500 meter square mesh as a transient population data. Shiga prefecture has 6 administrative districts. We obtained a transient population data in major stations of each administrative districts with every hours during study period(January 1 2015 - December 31 2020).

3. Results and Discussions

Table 1 shows the result of statistical analysis for KD patients in Shiga prefecture during study period. The number of patients with KD during 2015 – 2019 was 1144, and the number during 2020 was 172. In seasonally analysis, it was found that reduction of KD patients during April - June was larger than values of other periods, compared with the corresponding period in previous years. During season from April to June 2020, the large movement restricts was conducted due to the state of emergency for COVID-19 pandemic in Japan. This result may suggested that a large movement restricts for human may be affected the onset of KD. In ages analysis, the ratio of the number of patients aged < 1 year was increased during the period after the COVID-19 pandemic onset. In Japan, a mask wearing of children aged < 2 years is not recommended. This result may indicated that mask wearing is affected to trigger the onset of KD.

Figure 1 shows monthly trends of the number of KD patients in Shiga prefecture. Blue points

in figure 1 are the number of KD patients each month in 2020, black points are average values of KD patients during 2015 – 2019, respectively. Error bars of black points in figure 1 shows the range between minimum and maximum patients number. It was found from figure 1 that the number of KD patients during April -July in 2020 was clearly reduced, compared with the corresponding period in previous years. This result indicates that the COVID-19 pandemic has clearly contributed to a decrease in the number of KD cases in Shiga Prefecture.

In conclusion, we assessed the incidence of KD before and after COVID-19 pandemic onset in Shiga prefecture, Japan. The incidence of KD patients was significantly decreased after the pandemic onset of COVID-19. The COVID-19 pandemic has clearly contributed to a decrease in the number of KD cases in Shiga Prefecture.

References

[1] R. Ae, N. Makino, K. Kosami, M. Kuwabara, Y. Matsubara, Y. Nakamura: Epidemiology, treatments, and cardiac complications in patients with Kawasaki disease: The nationwide survey in Japan, 2017-2018, *Journal of Pediatrics*, **225**(2020), 23-9.e2.

[2] N. Zhu, D. Zhang, W. Wang, X. Li, B. Yang, J. Song, *et. al.*: A Novel Coronavirus from Patients with Pneumonia in China, 2019, *New Engl J Med.* **382**(2020) 727-733.

[3] R. Ae, Y. Shibata, T. Furuno, T. Sasahara, Y. Nakamura, H. Hamada: Human Mobility and Droplet-Transmissible Pediatric Infectious Diseases during the COVID-19 Pandemic, *Int J Environ Res Public Health*, **19**(2022), 6941.

[4] R. Ae, Y. Shibata, K. Kosami, Y. Nakamura, H. Hamada: Kawasaki disease and pediatric infectious diseases during the coronavirus disease 2019 pandemic. *Journal of Pediatrics*, **239**(2021), 50-8.e2.

[5] K. Iio, K. Matsubara, C. Miyakoshi, K. Ota, R. Yamaoka, J. Eguchi, *et. al.*: Incidence of Kawasaki disease before and during the COVID-19 pandemic: a retrospective cohort study in Japan, *BMJ Paediatr Open*. **5**(2021), e001034.

[6] National Institute of Infectious Disease, Japan [Website of IDWR Surveillance Data]. Available online: https://www.niid.go.jp/niid/en/data.html (accessed on 14 June 2022).

[7] Mobile spatial statics, NTT DOCOMO [Website of mobile spatial statics in NTT DOCOMO] (in Japanese). Available online: https://mobaku.jp (accessed on 14 June 2022).

Table1. Comparison of patients with Kawasaki Disease in Shiga prefecture before and after the onset of the COVID-19 pandemic.

Characteristics	Survey year				
	2015–2019 (n=1144)		2020 (n=172)		
	n	(%)	n	(%)	p value†
The number of Months					
January - March	326	(28.5)	65	(37.8)	
April – June	295	(25.8)	32	(18.6)	
July – September	224	(19.6)	34	(19.8)	
October – December	299	(26.1)	41	(23.8)	
Sex					
Male	652	(57.0)	105	(61.0)	
Female	492	(43.0)	67	(39.0)	0.39
Age of onset, years					
Median (IQR)	1.9 (2.4)		2.3 (2.5)		
<1	180	(15.7)	34	(19.7)	<0.01
1–5	874	(76.3)	125	(72.6)	0.28
6–10	77	(6.7)	12	(6.9)	0.63
≥11	12	(1.0)	1	(0.6)	0.53

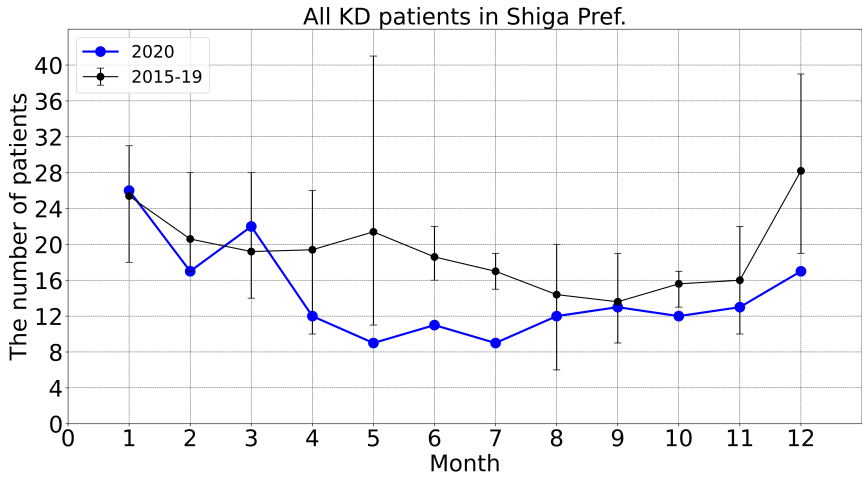

Figure 1. Monthly trends of the number of KD patients in Shiga prefecture. Blue points in figure 1 are the number of KD patients each month in 2020, black points are average values of KD patients during 2015 – 2019, respectively.

Wavelet analysis of COVID-19 pandemic

Kazumi Omata[1,*], Ayumi Shimazaki[1], Hiroaki Mitsuya[2,3,4]

[1]Mathematical Epidemiology Section, National Center for Global Health and Medicine, Japan
[2]Department of Refractory Viral Infections, National Center for Global Health and Medicine Research Institute, Japan
[3]Department of Clinical Sciences, Kumamoto University School of Medicine, Japan
[4]Experimental Retrovirology Section, Center for Cancer Research, National Cancer Institute, National Institutes of Health, USA

[*]komata@hosp.ncgm.go.jp

The full paper of this paper has been published in Journal of Advanced Simulation in Science and Engineering (JASSE).

DOI: https://doi.org/10.15748/jasse.10.214

How to make your own mesh generator using ADVENTURE AutoMESH ?

Hiroshi Kawai[1*]

[1]Faculty of Information Systems and Arts, Toyo University

*kawai063@toyo.jp

Abstract. ADVENTURE AutoMESH (pronounced as 'O-ta-me-shi') is mesh generation library and toolkit, dedicated for simulation-based research and development. It is designed for the simulation users to develop their own mesh generators and pre-processing tools. Currently, the library / toolkit is used among many researchers and simulation users, mainly in universities and national research centers. Its functionalities and supported platforms are explained. AutoMESH applications of various kinds of simulation methods are demonstrated also.

Keywords: Numerical Simulation, Pre- and post-processing, Mesh Generation, Simulation Data Management

1. Introduction

A variety of numerical simulation methods, including FDM, FVM, FEM, BEM, mesh-less and particle-based method, as well as MD (Molecular Dynamics), cellar automaton, multi-agent and so on, have been proposed and used among researchers and engineers. Each of them uses its own data structure and requires some special data manipulation. And they have to be visualized, created and modified in a flexible way.

ADVENTURE AutoMESH is a simple and handy library / toolkit fo mesh generation and pre-processing in general. Using this library, a researcher or a developer using numerical simulation methods can develop his or her own mesh generator or pre-processing tools, to generate and modify simulation model data. Currently, the library / toolkit is used among many researchers and simulation users, mainly in universities and national research centers. Its functionalities and supported platforms are explained. AutoMESH applications of various kinds of simulation methods are demonstrated also.

Currently, through on-going mini-project, a more robust and efficient version of the automatic tetrahedral mesh generator is being implemented and tested for ADVENTURE AutoMESH. It is designed from scratch, mainly dedicated for multi-core, parallel environment. The prototype implementation of the mesh generator is demonstrated, and its performance evaluation is shown.

References

[1] ADVENTURE project HP: http://adventure.sys.t.u-tokyo.ac.jp/

[2] Hiroshi Kawai: ADVENTURE AutoGL: A Handy Graphics and GUI Library for Researchers and Developers of Numerical Simulations, CMES, Vol. 11, No. 3, pp.111-120, 2006.

JSST 2022

Development of Paralle Microwave analysis software: ADVENTURE_Fullwave

Amane Takei[1]

[1]Faculty of Engineering, University of Miyazaki, Japan

*takei@cc.miyazaki-u.ac.jp

Abstract. In this presentation, a parallel microwave analysis code based on an iterative domain decomposition method is explained that is named ADVENTURE_Fullwave. A stationary vector wave equation for the high-frequency electromagnetic field analyses is solved taking an electric field as an unknown function. Then, to solve subdomain problems by the direct method, the direct method based on the LDL^T decomposition method is introduced in subdomains. The simplified Berenger's PML is introduced which these eight corners are given the average value of all PML's layers.

Keywords: Microwave analysis, E method, Parallelized finite element method, Domain decomposition method, ADVENTURE_Fullwave.

1. Introduction

Electromagnetic field analysis based on a numerical analysis method, such as the finite element method, has become widespread [1] due to recent improvements in computer performance and numerical calculation technology. In the case of accurately reproducing an analysis model of complicated shape, it is necessary to use many small the elements. In the case of analyzing the state of electromagnetic waves propagation in a wide range, a wide analysis domain is examined. Furthermore, to perform a high-accuracy analysis, it is necessary to model the analysis domain with a sufficiently small element for the wavelength, and, in this case, the number of elements also increases. Increasing the number of elements increases the scale of the problem. Therefore, a method that can calculate large-scale problems has come to be demanded. Moreover, large-scale problems must be solved with high accuracy. In the presentation, a large-scale analysis code: ADVENTURE_Fullwave is introduced, and detail of the parallel algorism is shown.

2. Governing equations and algorithm for parallel computing

In ADVENTURE_Fullwave, the full-wave analysis based on an E method [1] is considered. $\mathbf{E}_\mathrm{h}$ and $\mathbf{J}_h$ are finite element approximations of electric field $\mathbf{E}$ [V/m] and current density $\mathbf{J}$ [A/m^2], respectively. The permeability is given by $\mu = \mu_0\mu_r$ [H/m], μ_0 is the vacuum permeability [H/m], and μ_r is the relative permeability. The complex permittivity is given by $\varepsilon = \varepsilon_0\varepsilon_r - \sigma/j\omega$ [F/m], ε_0 is the vacuum permittivity [F/m], ε_r is the relative permittivity, and ω is the angular frequency [rad/s]. The following equation is the finite element equation to be solved:

$$\iiint_\Omega (1/\mu)\mathrm{rot}\mathbf{E}_\mathrm{h} \cdot rot\mathbf{E}_\mathrm{h}{}^* dv - \omega^2 \iiint_\Omega \varepsilon\mathbf{E}_\mathrm{h} \cdot \mathbf{E}_\mathrm{h}{}^* dv = j\omega \iiint_\Omega \mathbf{J}_h \cdot \mathbf{E}_h{}^* dv. \quad (1)$$

The equation contains complex numbers and becomes a complex symmetric matrix. In the present study, the electric field **E**, which is unknown, is obtained using the conjugate orthogonal conjugate gradient (COCG) method. The finite element approximation (1) is rewritten as $Ku = f$ by the coefficient matrix K, the unknown vector u, and the right-hand side vector f. Next, Ω is divided into N subdomains (Eq. (2)). Eq. (3) and (4) are obtained from Eq. (2).

$$\begin{bmatrix} K_{II}^{(1)} & 0 & 0 & K_{IB}^{(1)}R_B^{(1)\mathrm{T}} \\ 0 & \ddots & 0 & \vdots \\ & & K_{II}^{(N)} & K_{IB}^{(N)}R_B^{(N)\mathrm{T}} \\ 0 & 0 & & \\ R_B^{(1)}K_{IB}^{(1)\mathrm{T}} & \cdots & R_B^{(N)}K_{IB}^{(N)\mathrm{T}} & \sum_{i=1}^{\mathrm{N}} R_B^{(i)}K_{BB}^{(i)}R_B^{(i)\mathrm{T}} \end{bmatrix} \begin{bmatrix} u_I^{(1)} \\ \vdots \\ u_I^{(N)} \\ u_B \end{bmatrix} = \begin{bmatrix} f_I^{(1)} \\ \vdots \\ f_I^{(N)} \\ f_B \end{bmatrix} \tag{2}$$

$$K_{II}^{(i)}u_I^{(i)} = f_I^{(i)} - K_{IB}^{(i)}u_B^{(i)} \quad (i = 1, \dots, N) \tag{3}$$

$$\left\{\sum_{i=1}^{\mathrm{N}} R_B^{(i)}\left\{K_{BB}^{(i)} - K_{IB}^{(i)\mathrm{T}}\left(K_{II}^{(i)}\right)^{-1}K_{IB}^{(i)}\right\}R_B^{(i)T}\right\}u_B = \sum_{i=1}^{\mathrm{N}} R_B^{(i)}\left\{f_B^{(i)} - K_{IB}^{(i)T}\left(K_{II}^{(i)}\right)^{-1}f_I^{(i)}\right\} \tag{4}$$

where ${f_B}^{(i)}$ is the right-hand vector for u_B, and $\left(K_{II}^{(i)}\right)^{-1}$ is the inverse matrix of $K_{II}^{(i)}$. Equation (4) is referred to as an interface problem and is an equation for satisfying the continuity between domains in the domain decomposition method. For simplicity, rewrite equation (5) as follows:

$$Su_B = g, \qquad S = \sum_{i=1}^{N} R_B^{(i)}S^{(i)}R_B^{(i)T}, \quad S^{(i)} = K_{BB}^{(i)} - K_{IB}^{(i)T}\left(K_{II}^{(i)}\right)^{-1}K_{IB}^{(i)}. \tag{5}$$

3. Numerical example

For examining ADVENTURE_Fullwave on a real-world problem, we model the environment of a commuter train, including 48 human bodies placed inside it. In such a commuter train, dielectrics, such as reflecting barriers, walls, handrails, etc. and human bodies exist. The electromagnetic field distribution may change with the differences of geometric arrangement between these materials. Therefore, when developing the numerical environmental model use for calculation, it is necessary to perform the modeling in such a way that the real environment may be reproduced correctly. The train plan is referred for the modeling of the train. The computations are performed on a 20-node (160-core) PC cluster (Intel(R) Core(TM) i7-9700K, 3.60 GHz) with 36 GB RAM per node. The simulation statistics are shown in Table 1.
More detail thins will be shown at the conference.

Table 1 Simulation Statistic

Analysis Frequency	1.0 GHz
No. of Elements	15,712,684
No. of DOF	15,599,463
Platform	20-node PC cluster with Intel Core i7-9700K 3.60 GHz
No. of cores	160
Main memory per node	32 GB
Elapsed Time [s]	1,998

References

[1] A. Takei, S. Sugimoto, M. Ogino, S. Yoshimura, H. Kanayama: Full wave analyses of electromagnetic fields with an iterative domain decomposition method, *IEEE Trans. on Magn.*, 46:8 (2010), 2860-2863.

Scheme Design for High-Throughput Terahertz feeder link in Non-Terrestrial-Networks

Kazuhiko Tamesue[1*], San Hlaing Myint[1], Kunihisa Jitsuno[1], Toshio Sato[1], Takuro Sato[1], Tetsuya Kawanishi[1]

[1]Faculty of Science and Engineering, Waseda University

*ktamesue@aoni.waseda.jp

Abstract. The Non-Terrestrial Network (NTN) being considered for Beyond 5G (B5G) will utilize the High-Altitude Platform System (HAPS) and etc. as communication platforms. In this paper, we propose a transmission scheme using the THz band as a new feeder link from the viewpoint of ensuring link performance in bad weather conditions and achieving high speed and high capacity. The results of the evaluation of weather conditions, propagation attenuation, link budgets, and modulation schemes required for feeder links is discussed.

Keywords: non-terrestrial-networks, terahertz, feeder link, 5G system and beyond.

1. Introduction

Beyond 5G (B5G) envisions a scenario where terrestrial and space are seamlessly integrated and the Internet is accessed in the global domain, including satellites [1-2]. One of the core technologies is the Non-Terrestrial Network (NTN). Components include the High-Altitude Platform System (HAPS) as a so-called flying base station, mobile IoT, and low earth orbit (LEO) satellites. To realize such use cases, a high-speed, high-capacity feeder link connecting the backhaul on the ground to the sky is important. The 10 Gbps-class FSO (Free Space Optical) feeder link, which is currently under research and development, faces the challenge of being susceptible to clouds and rainfall.

The authors have studied THz feeder link using the THz band (100 GHz band), where atmospheric attenuation is relatively low and antennas can be miniaturized [3-4]. In this paper, we describe the results and discussion of the technical requirements for a 10 Gbps-class feeder link in the stratosphere at an altitude of 20 km with a ground station that ensures link performance even in relatively bad weather conditions.

2. System Design

2.1 System Model

The system model for the terahertz band feeder link assumes Frequency Division Duplex (FDD) radio communications from a gateway on the ground to a HAPS located 20 km vertically. Attenuation due to rainfall and cloud cover must also be taken into account, as well as cloudy

and rainy conditions. Radio propagation models are discussed in the following section 2.2.

2.2 Propagation Model

Fig.1 shows the atmospheric attenuation versus frequency characteristics for the mid-latitude region. The ITU-R model [5] was used as the propagation model. Atmospheric attenuation is strongly related to water vapor density. In Fig.1, the water vapor density in a typical mid-latitude region in summer when humidity is high and the vertical temperature distribution of [6] are used. There are few studies on vertical water vapor density. We referred to valuable measurements [7]. We plan to use the frequency band of 100 GHz (92 GHz-104 GHz), which is favorable for long-distance propagation in the THz band and avoids radio astronomy.

Fig.2 shows the vs. frequency characteristics of attenuation due to rainfall and vs. frequency characteristics due to clouds. For attenuation due to rainfall, [8] is referred, and rainfall amounts of 1.25 mm/h light rain and 10 mm/h severe rain were assumed. The attenuation due to rainfall was defined as the distance from the top of cloud height to 0 km. For cloud attenuation, nimbostratus clouds of different water vapor density and thickness were used for severe and light rain. And cumulus cloud was used for cloudy condition [9-10].

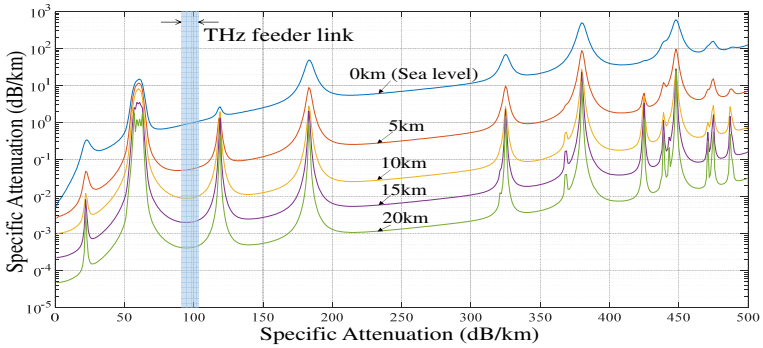

Fig. 1 Attenuation of radio propagation by atmospheric gases (Medium latitude area and Summer season)

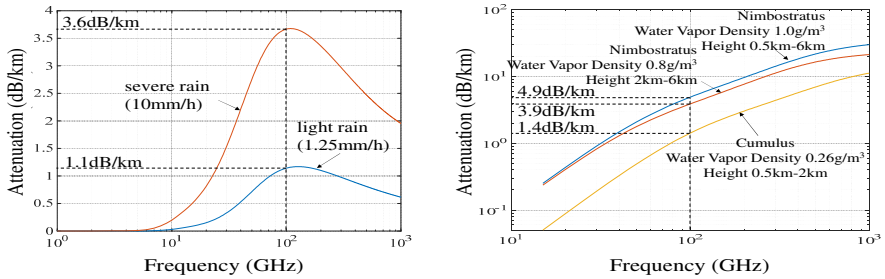

Fig. 2 Attenuation of radio propagation by (left) rain / (right) cloud

2.3 Link Budget Analysis

Table 1 shows an example of a link budget in the system model. The propagation model assumes atmospheric attenuation as shown in Section 2.2 and rainfall attenuation by a weather model consisting of clouds and rain. Since the THz feeder link is basically operated at a high elevation angle, multipath fading due to reflections from the earth is negligible. The range of attenuation of receiver C/No due to rainfall is -2.1 dB for cloudy weather, -22.2 dB for light rain, and -48.6 dB for severe rain compared to sunny weather for communications at a vertical altitude of 20 km between the gateway station and the HAPS station above in the weather model described in Section 2.2.

Table 1 Link Budget for NTN feeder link (Distance 20km)

		Sunny	Clouds	Light Rain	Severe Rain
Transmitter (HAPS)	Transmitter Output Power [dBm]	30	30	30	30
	Backoff and Loss [dB]	-20	-20	-20	-20
	Transmitter Antenna Gain [dBi]	40	40	40	40
	EIRP [dBm]	50	50	50	50
Propagation	Free Space Propagation Loss [dB]	-158.5	-158.5	-158.5	-158.5
	Atmospheric Absorption Loss [dB]	-2.3	-2.3	-2.3	-2.3
	Propagation Loss by Cloud [dB]	0	-2.1	-15.6	-26.9
	Propagation Loss by Rainfall [dB]	0	0	-6.6	-21.6
Receiver (Gateway)	Receiver Antenna Gain [dBi]	75	75	75	75
	Receiver Level [dBm]	-35.8	-37.9	-58.0	-84.4
	Antenna Noise Temperature [K]	217.2	217.2	217.2	217.2
	Receiver C/No [dBHz]	**153.2**	**151.1**	**131.0**	**104.6**

3. Performance evaluation

3.1 Simulation Results

Table 2 shows the simulation parameters. The occupied bandwidth of the baseband is 2GHz or less based on system requirements. LDPC (Low-Density Parity Check) error-correcting codes are used [11]. We considered the single-carrier and OFDM modulation schemes.

Fig.3 shows the BER characteristics of LDPC (1440, 1344) with and without error correction coding. From Fig.3, a coding gain of BER=10^{-6} for each modulation scheme was obtained.

Table 2 Simulation Condition and Results for baseband

Modulation	16-APSK	QPSK-OFDM	64-QAM-OFDM	256-QAM-OFDM
Symbol rate [Gsymbol/s]	0.7	2.0	2.0	2.0
Occupied Bandwidth [GHz]	2.0	2.0	2.0	2.0
[dBHz]	93.0	93.0	93.0	93.0
Desired Eb/No [dB]	16.7	10.5	18.7	23.8
SNR [dB]	22.7	13.5	26.5	32.8
Coding Gain [dB]	5.6	5.0	5.3	5.9
Desired C/No [dBHz]	**104.1 dBHz**	**98.5 dBHz**	**106.4 dBHz**	**110.9 dBHz**

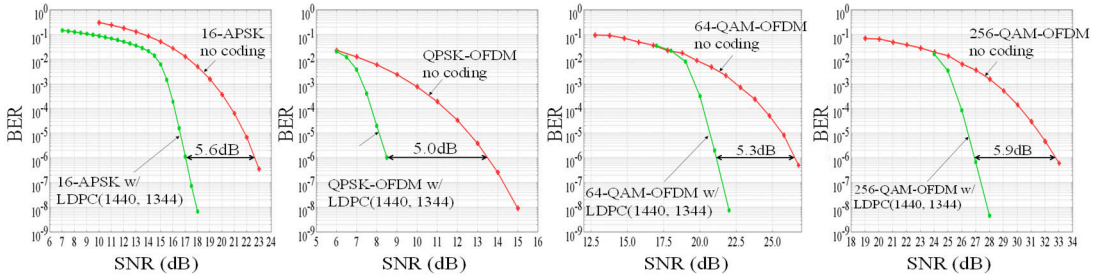

Fig. 3 BER v.s SNR 16-APSK / QPSK-OFDM / 64-QAM / 256-QAM

3.2 Discussion

From the link budget in Table 1 and the desired C/No in Table 2, 256-QAM-OFDM is applicable with a reception margin of 42.3 dB in sunny weather. In light rain, 64-QAM-OFDM and 16-APSK are applicable with a reception margin of 24.6 dB and 26.9 dB, respectively. In severe rain, QPSK-OFDM has a low receive margin of 6.1 dB. In such cases, the design should stabilize the link quality by lowering the coding rate or modulation index to lower the desired C/No.

An example of an estimate of the throughput in sunny conditions for 256-QAM-OFDM modulation and the OFDM symbol specifications described below is shown next. The OFDM

symbols are 4.5μs in OFDM symbol length, 0.4μs in Guard Interbal, 8,192 FFTs, 7,000 user-usable data carriers, and 244.41kHz subcarrier spacing (=2.0GHz/8,192), resulting in 12.76Gbps. Furthermore, with two-frequency carrier aggregation, 25.5 Gbps can be achieved. Similarly, 64-QAM-OFDM and 16-APSK provide 19.1 Gbps and 12.76 Gbps, respectively. The excessive reception margin in sunny conditions suggests the possibility of reducing the power consumption of HAPS stations by controlling the transmit power accordingly.

4. Conclusions

We proposed a system model for a THz-band feeder link using the 100 GHz band. In the proposed model, the throughput of 25.5 Gbps in sunny weather and 19.1 Gbps in light rain were estimated by evaluating the link budget and bit rate of the communication scheme based on the propagation conditions between the gateway on the ground and the stratosphere at 20 km. In the future, we plan to develop transmission equipment and verify the link budget of the THz feeder link with an experimental approach.

Acknowledgment

This paper contains the results of a research project commissioned by the National Institute of Information and Communications Technology (NICT), "Beyond 5G Research and Development Promotion Project", which is a research and development of wireless communication technology for realizing Beyond 5G ultra-high-speed and large-capacity communication using the terahertz band (task number 003).

References

[1] F. Rinaldi et al., “Non-Terrestrial Networks in 5G & Beyond: A Survey,” vol. 8, pp. 165178–165200, 2020.

[2] A. Vanelli-Coralli, A. Guidotti, T. Foggi et al., “5G and Beyond 5G Non-Terrestrial Networks: trends and research challenges,” Sep. 2020, pp. 163–169.

[3] Tetsuya Kawanishi, Kazuhiko Tamesue, Kunihisa Jitsuno et al., “THz communications for non-terrestrial-networks,” IEICE 2022 General Conference, March 2022.

[4] San Hlaing Myint, Kazuhiko Tamesue, Kunihisa Jitsuno et al., “100GHz 16-APSK Modulator and Compensation for triple multiplier RF Power Amplifier,” IEICE 2022 General Conference, March 2022.

[5] ITU-R, “Recommendation ITU-R P.676-12 : Attenuation by atmospheric gases and related effects. P Series Radiowave propagation,” 2019.

[6] “U.S. Standard Atmosphere, 1976”, Oct. 1976, https://ntrs.nasa.gov/api/citations/19770009539/downloads/19770009539.pdf

[7] http://www.meteoffice.info/1analysis_folder/pages_neturikigaku_folder/303_folder/315.htm

[8] ITU-R, “Recommendation ITU-R P.838-3 : Specific attenuation model for rain for use in prediction methods,” 2005.

[9] ITU-R, “Recommendation ITU-R P.840-8: Attenuation due to clouds and fog,” 2019.

[10] http://www-das.uwyo.edu/~geerts/cwx/notes/chap08/moist_cloud.html

[11] IEEE Std 802.15.3c-2009, “Part 15.3: Wireless Medium Access Control (MAC) and Physical Layer (PHY) Specifications for High Rate Wireless Personal Area Networks (WPANs) Amendment 2,” October 2009.

JSST 2022

Decoupling and Bandwidth Maintenance for Two Planar Inverted-F Antennas using Bridge Line

Quang Quan Phung[1,*], Naobumi Michishita[1], Hiroshi Sato[2], Yoshio Koyanagi[2], Hisashi Morishita[1]

[1]Graduate School of Science and Engineering, National Defense Academy
[2]Panasonic System Networks R&D Lab.

[*]em59045@nda.ac.jp

The full paper of this paper has been published in Journal of Advanced Simulation in Science and Engineering (JASSE).

DOI: https://doi.org/10.15748/jasse.10.40

Improvement of the efficient electrostatic plasma particle simulation code for the investigation of boundary layer plasmas

Hiroki Hasegawa[1,2*] and Seiji Ishiguro[1]

[1]National Institute for Fusion Science, National Institutes of Natural Sciences
[2]Department of Fusion Science, The Graduate University for Advanced Studies, SOKENDAI
*hasegawa.hiroki@nifs.ac.jp

Abstract. A three-dimensional (3D) electrostatic particle-in-cell (PIC) simulation code called "up3bd" has been developed in order to investigate transport phenomena in fusion boundary layer plasmas or other plasmas in nature. In this study, the up3bd code has been improved in order to make the code more efficient and more flexible. Not only one-dimensional but also two-dimensional domain decompositions have become able to be applied by improvement. In the two-dimensional domain decomposition in the up3bd code, the transfer of the data of particles which move out to the next processes is separated into two procedures, that is, the transfers in vertical and horizontal directions. This implementation has attained both high-speed capability and availability. The code has also been optimized in the FUJITSU FX1000 and the NEC SX-Aurora TSUBASA.

Keywords: particle-in-cell, domain decomposition, fusion boundary layer plasma

1. Introduction

Simulations with high performance computing are powerful methods to study complex plasma phenomena in fusion magnetic confinement devices, plasma processing devices, and nature. Although many numerical methods to investigate various plasma dynamics were presented, a particle-in-cell (PIC) simulation [1] was applied in order to analyze the kinetic, i.e., microscopic, dynamics in complex plasma phenomena. So far, we have developed three-dimensional (3D) electrostatic PIC simulation codes called "p3bd" [2] and "up3bd" [3] in order to investigate the kinetic dynamics on transport phenomena in fusion boundary layer plasmas or other plasmas in nature. Using these codes, we have made significant discoveries regarding non-diffusive radial plasma transport in fusion boundary layers, e.g., Ref. [4]. For further progress, we require larger scale simulations than those in our previous studies.

For large-scale simulations, one-dimensional (1D) domain decomposition has been already applied to the up3bd code [3]. However, two-dimensional (2D) domain decomposition is necessary for higher scalability and higher flexibility. Thus, in this study, we have improved the up3bd code by implementing the 2D domain decomposition in the code. We have also optimized the code in the FUJITSU FX1000 (FX) and the NEC SX-Aurora TSUBASA (SX).

2. 2D domain decomposition

In the 2D domain decomposition, the data of particles which move out to the next processes should be transferred in vertical, horizontal, or diagonal directions; that is, one process should communicate with eight others, if the data transfer is finished by a single time calling the transfer subroutines. However, in the up3bd code, the data transfer is separated into two procedures, i.e., in vertical and horizontal directions, as shown in Fig. 1.

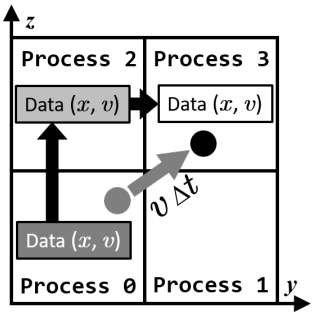

Figure 1: Schematic diagram of the particle data transfer in the up3bd code. The transfer is separated into two steps.

In the original up3bd code, in which only the 1D domain decomposition in the *z* direction is applied, the subroutine "pact" stores the numbers of particles which are out of the domain assigned to a process, that is, have been absorbed or moved out to the next domains. According to the stored numbers, the subroutine "adjust"' deletes the data of non-active particles in a process and stuffs the empty arrays caused by the deletion of non-active particle data with the active particle data. Furthermore, the data of particles moved to the next domains is transferred to these by message passing interface (MPI) communications in the subroutine "adjust" [3].

On the other hand, in the improved up3bd code, the same subroutines for the data transfer in the *y* direction are prepared. Those prepared subroutines are called "pacty" and "adjusty". After the update of particle positions, the subroutines "pact" and "adjust" are called. Next, the subroutines "pacty" and "adjusty" are performed. The transfer is completed with this procedure.

(a)
```
a0(1) = b0(1)
a1(1) = b1(1)
do i=2,N
   a0(i) = a0(i-1) + b0(i)
   a1(i) = a1(i-1) + b1(i)
end do
do i=1,N
   a0(i) = a0(i)*b0(i)
   a1(i) = a1(i)*b1(i)
end do
```

(b)
```
s0 = 0
s1 = 0
do i=1,N
   s0    = s0 + b0(i)
   s1    = s1 + b1(i)
   a0(i) = s0
   a1(i) = s1
end do
do i=1,N
   a0(i) = a0(i)*b0(i)
   a1(i) = a1(i)*b1(i)
end do
```

(c)
```
s0 = 0
s1 = 0
!ocl loop_nofusion
do i=1,N
   s0    = s0 + b0(i)
   a0(i) = s0
end do
!ocl loop_nofusion
do i=1,N
   s1    = s1 + b1(i)
   a1(i) = s1
end do
!ocl loop_nofusion
do i=1,N
   a0(i) = a0(i)*b0(i)
end do
!ocl loop_nofusion
do i=1,N
   a1(i) = a1(i)*b1(i)
end do
```

Figure 2: General frame of the do-loops including recurrence formula type calculations in subroutines "pact" and "pacty". The panels (a), (b), and (c) represent the original code, the code optimized by Opt. 0, and the code optimized by Opt. 2, respectively.

3. Optimization

In a code without optimization, the subroutine “pact” takes the longest computation time on the FX. Therefore, the subroutines “pact” and “pacty” have been optimized in this study. In the optimization in the FX, we have adopted four measures as follows.

Opt. 0. Modification of recurrence formula type calculations: In the subroutines “pact” and “pacty”, the do-loops including recurrence formula type calculations are performed. The structure of these do-loops can be briefly written as shown in Fig. 2 (a). In this optimization measure, recurrence formula type calculations are changed into the form shown in Fig. 2 (b). On the other hand, because the do-loop including recurrence formula type calculations can be vectorized, the original do-loops have not been modified in the code optimized in the SX. The directive for loop unrolling has been only inserted.

Opt. 1. Deletion of verbose calculation: In the subroutine “pact” without the optimization, the velocity of particles absorbed at the wall was given as zero. However, this computation is not necessary in the calculation flow. Thus, this substitution calculation has been removed.

Opt. 2. Division of do-loops: The do-loops including recurrence formula type calculations as mentioned above are separated, as shown in Fig. 2 (c).

Opt. 3. Size of particle data array: In the up3bd code, the particle data is saved in a four-dimensional array. In order from the inner dimension, each dimension of the particle data array corresponds to the component in a phase space, the particle number, the thread on OpenMP parallelization, and the species of particle, respectively. In this optimization, we have increased the size of the dimension corresponding to the thread from 12, which is the same as the total number of threads, to 36.

4. Performance analysis

The improved up3bd code has been performed on the FX of “Flow” at the Information Technology Center, Nagoya University. First, we evaluated the effect of the optimization measures described above. Table 1 shows the elapsed times and effective performances for the original and optimized codes for a 100 time steps calculation. Here, in the simulations, the system size is 64×64×256, the average number of particles per cell is 144, and four nodes are used in which 16 MPI processes are launched. Only the 1D domain decomposition is applied. This table indicates that the total performance of the optimized code is 1.7 times as high as that of the original code.

Next, we assessed the particle data transfer procedure for the 2D domain decomposition which is adopted in the improved code. If the data transfer is finished by a single time calling the transfer subroutines, the elapsed time and the effective performance are 18.569 s and 1.6661 %. On the other hand, those are 15.621 s and 1.9806 % when the procedure adopted in the improved code is used. Here, the optimized code is used. The numbers of MPI processes in the y and z directions are two and eight, respectively. The other simulation conditions are the same as those for Table 1. These results indicate that the particle data transfer procedure in the improved up3bd code has attained high-speed capability. Furthermore, the 2D domain decomposition (18.6 s for single time calling / 15.6 s for two steps) is slower than the 1D domain decomposition (13.8 s) because the “pact” procedure should be performed in vertical and horizontal directions (and also diagonally for single time calling) for the 2D domain decomposition. In other words, the performance on the FX becomes lower while increasing the number of times of performing the “pact” procedure.

Table 1: Evaluation of the effect of the optimization measures. The elapsed times and effective performances for the 100 time steps calculation on the FX are shown. Here, in the simulations, the system size is 64×64×256, the average number of particles per cell is 144, and four nodes are used in which 16 MPI processes are launched. Only the 1D domain decomposition is applied.

	Total Elapsed Time [sec]	Averaged Elapsed Time for Main Part in Subroutine "pact" [sec]	Effective Performance [%]
Original	23.628	7.643	1.3133
Opt. 0	20.866	4.869	1.4870
Opts. 0 and 1	17.725	3.026	1.7313
Opts. 0, 1, and 2	17.149	2.779	1.7897
Opts. 0, 1, 2, and 3	13.808	1.114	2.2242

Finally, the up3bd code is performed on the SX of the Plasma Simulator at NIFS under the same simulation conditions as those of the calculations for Table 1 with four vector engines in which 32 MPI processes are launched. As a result, the elapsed time and the effective performance are 15.773 s and 3.4 %. The computation speed on the FX is 1.1 times as fast as that on the SX, while the peak performance of the FX (3.3792 TFLOPS per node) is 1.4 times higher than that of the SX (2.433 TFLOPS per vector engine).

Acknowledgments

The simulations were carried out on the supercomputer "Flow" at the Information Technology Center, Nagoya University with the "Joint Usage/Research Center for Interdisciplinary Large-scale Information Infrastructures" and the "High Performance Computing Infrastructure" scheme in Japan (Project ID: jh210005-NAH and jh220004). Also, this work was performed on the "Plasma Simulator (PS)" (NEC SX-Aurora TSUBASA) of NIFS with the support and under the auspices of the NIFS Collaboration Research programs (NIFS21KNSS155 and NIFS22KISS004) and supported by JSPS KAKENHI Grant Number JP19K03787.

References

[1] C.K. Birdsall, A.B. Langdon: *Plasma Physics via Computer Simulation*, McGraw-Hill, New York (1985).

[2] Hiroki Hasegawa, Seiji Ishiguro: Development and Verification of the Three-dimensional Electrostatic Particle Simulation Code for the Study of Blob and Hole Propagation Dynamics, *Plasma and Fusion Research*, volume:12 (2017), 1401044-1-1401044-9.

[3] Hiroki Hasegawa, Seiji Ishiguro: Development of the efficient electrostatic plasma particle simulation code for the study of fusion boundary layer plasmas, *Proceedings of the 40th JSST Annual International Conference on Simulation Technology* (2021), 152-155.

[4] Hiroki Hasegawa, Seiji Ishiguro: Three-dimensional effect of particle motion on plasma filament dynamics, *Physics of Plasmas*, volume:26 (2019), 062104-1-062104-5.

Pseudo-Maxwellian and Ring Velocity Distributions in a Magnetized Plasma

Shunsuke Usami[1,2*], Ritoku Horiuchi[1]

[1]National Institute for Fusion Science, National Institutes of Natural Sciences

[2]The University of Tokyo

*usami.shunsuke@nifs.ac.jp

Abstract. By means of theory and particle simulations, we investigate properties of a ring velocity distributions with a finite width. We theoretically derive a function which exactly expresses a ring with a width. The function indicates that the width of a ring is larger than a criterion, the distribution shape changes from a ring into a mountain. We call it a pseudo-Maxwellian velocity distribution, because it is almost indistinguishable in shape from a genuine Maxwellian distribution. Plasma particle simulations show that pseudo-Maxwellian ion velocity distributions are formed during magnetic reconnection.

Keywords: Particle simulation, Pseudo-Maxwellian distribution, Ring distribution

1. Introduction

A ring velocity distribution in a plasma has been investigated by many researchers, because it generates various instabilities. So far they, however, employed model functions, assuming specific shapes of ring distributions with a width. In this work, we clarify the formation process of a ring velocity distribution with a width and show that the ring shape is transformed into a mountain shape, i.e., a pseudo-Maxwellian distribution.

2. Theory

Ring velocity distributions are created on the basis of the gyromotion of seed charged particles. Let us consider that seed particles are continuously supplied to a region in which an electric field $\boldsymbol{E}$ and magnetic field $\boldsymbol{B}$ causing the $E \times B$ drift with a velocity $\boldsymbol{v}_{\boldsymbol{E}\times\boldsymbol{B}}$ are imposed. First, we assume that the seed particles have the same initial velocity [1,2]. In a velocity space, the orbit of the seed particles is a circle whose center is $\boldsymbol{v}_{\boldsymbol{E}\times\boldsymbol{B}}$ so that a ring velocity distribution with no width is formed. Next, we consider that the seed particles initially have velocity variations [3]. Let us employ a plausible case in which the seed particles satisfy a shifted Maxwellian velocity distribution $(1/2\pi v_{T0}^2)\exp[-(\boldsymbol{v}-\boldsymbol{v}_0)^2/2v_{T0}^2]$, ignoring the velocity component parallel to $\boldsymbol{B}$. In a velocity space, the orbits of the seed particles are concentric circles whose center is $\boldsymbol{v}_{\boldsymbol{E}\times\boldsymbol{B}}$, and hence a ring velocity distribution with a width is created.

We derive a function G which expresses a ring distribution with a width as follows [3]:

$$G(\boldsymbol{v}) = \frac{1}{2\pi v_{T0}^2} \exp\left[-\frac{V^2 + v_R^2}{2v_{T0}^2}\right] I_0\left(\frac{V v_R}{v_{T0}^2}\right), \qquad (1)$$

where $v_R = |\boldsymbol{v}_0 - \boldsymbol{v}_{\boldsymbol{E}\times\boldsymbol{B}}|$, $V = |\boldsymbol{v} - \boldsymbol{v}_{\boldsymbol{E}\times\boldsymbol{B}}|$, and I_n is the modified Bessel function of the first kind. The shape expressed by G significantly depends on v_R and v_{T0}. Equation (1) demonstrates that if $v_{T0} > v_R/\sqrt{2}$, a hole in the ring center is transformed into the peak of a mountain. As a result, a pseudo-Maxwellian distribution is formed.

3. Simulation Results

As a phenomenon producing ring velocity distributions in a plasma, by means of particle simulations, we investigate magnetic reconnection [3]. Figure 1 shows the magnetic field lines and the ion temperature perpendicular to the magnetic field (the color contours). Magnetic reconnection takes place in the center of the simulation domain and the ion temperature is increased mainly in the downstream. Figure 2 (a) and (b) display ion velocity distributions at the boxed areas (A) and (B) designated in Fig. 1 in the reconnection downstream, respectively. This situation corresponds to a case of $\boldsymbol{v}_0 \simeq \boldsymbol{0}$ and $\boldsymbol{v}_{\boldsymbol{E}\times\boldsymbol{B}} \simeq (u_{\mathrm{out}}, 0)$ in Eq. (1), and $v_{T0} > v_R/\sqrt{2}$ holds, where u_{out} is the reconnection outflow speed. We can see that mountain-shaped velocity distributions are formed. They are too similar to a Maxwellian distribution to be distinguishable in shape, and thus we almost conclude that they are pseudo-Maxwellian distributions.

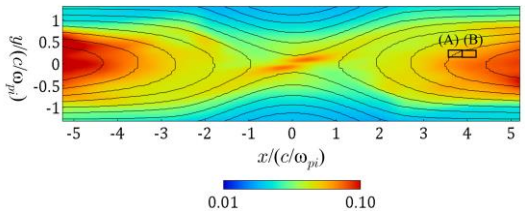

Figure 1: Particle simulation result of magnetic reconnection. Magnetic field lines and the profile of the ion temperature are shown.

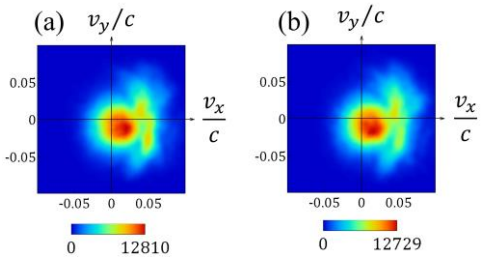

Figure 2: Ion velocity distributions at the areas (A) and (B) designated in Fig.1

In order to completely prove that they are not genuine-Maxwellian distributions, but pseudo-Maxwellian distributions, we have two types of evidence. One is to investigate the dependence of velocity distributions on the out-of-plane component of $\boldsymbol{B}$ (the guide field) and the other is to perform test particle simulations under hypothetical situations. For detail, see Ref. [3].

References

[1] S. Usami R. Horiuchi, H. Ohtani: Effective heating of nonadiabatic protons in magnetic reconnection with a guide field, *Phys. Plasmas*, 24 (2017) 092101.

[2] S. Usami et al.: Dependence of the pickup-like ion effective heating on the poloidal and toroidal magnetic fields during magnetic reconnection, *Phys. Plasmas*, 26 (2019) 102103.

[3] S. Usami and R. Horiuchi: Pseudo-Maxwellian velocity distribution formed by the pickup-like process in magnetic reconnection, *Front. Astron. Space Sci.*, 9 (2022) 846395.

Simulation study of Pixel Super-Resolution X-ray phase Imaging with Triangular Phase Grating

Ryosuke Ueda[1,*] and Atsushi Momose[1]

[1]Institute of Multidisciplinary Research for Advanced Materials, Tohoku University

[*]ryosuke.ueda.a7@tohoku.ac.jp

The full paper of this paper has been published in Journal of Advanced Simulation in Science and Engineering (JASSE).

DOI: https://doi.org/10.15748/jasse.10.64

VisAssets: Development of a visualization framework for the game engine

Shintaro Kawahara[1*], Hideo Miyachi[2], Hiroaki Ohtani[3, 4]

[1]Japan Agency for Marine-Earth Science and Technology
[2]Information Systems, Informatics, Tokyo City University
[3]National Institute for Fusion Science
[4]Department of Fusion Science, The Graduate University for Advanced Studies, SOKENDAI
*kawahara@jamstec.go.jp

Abstract. The development status of VisAssets which is a visualization framework for the game engine is reported. A module to load irregular grid dataset computed by a three-dimensional MHD equilibrium code and a user interface for the head-mounted displays is newly implemented. The implementation of the user interface is possible to change visualization parameters in virtual space when wearing a head-mounted display. This progress has been also possible to easily develop visualization applications that work with stand-alone head-mounted displays.

Keywords: Visualization, Game engine, Virtual reality

1. Introduction

We are developing a visualization framework for the game engine Unity named VisAssets[1] to represent visualization results on the head-mounted displays (HMDs) becoming increasingly powerful and inexpensive in recent years. In this framework, elements that construct a visualization flow are modularized as Prefabs of Unity. By connecting them appropriately in a visual editor of Unity, it enables us to develop visualization applications for multi-platform that includes HMDs without programming. Currently, the target dataset of this framework is a three-dimensional structure grid, and it supports uniform grids, rectangular grids, and irregular grids. Modules for filtering and mapping (rendering) can be used in common by loading these datasets into the internal data class. Figure 1 shows a screen capture of a visualization application constructed with VisAssets. In this figure, the application is running on the Unity editor. Executable files for various platforms can be generated by specifying the build target. The icons shown at the bottom of this figure are the visualization modules of VisAssets. Users can construct original visualization applications by connecting these modules in the hierarchy window of the Unity editor by drag-and-drop. VisAssets has three types of visualization modules: data loading, filtering, and mapping. Three template classes corresponding to each module type are provided in C# scripts, and users can add their original modules by creating subclasses that inherit from one of the template classes.
This paper reports on the development status of VisAssets, including examples of support for

an irregular grid dataset and a newly added user interface for HMDs.

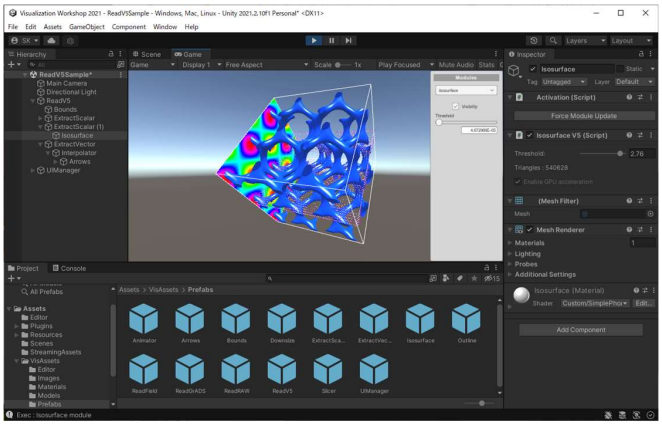

Fig. 1 An visualization application using VisAssets executed on Unity editor.

2. Development of a Module for Loading VLHD Data

In order to input user-specific data into VisAssets, it is necessary to develop a new data loading module. In this work, we developed a module for loading VirtualLHD[2] (VLHD) data into VisAssets. VLHD is visualization software for CAVE[3]-type virtual reality systems. It implements visualization algorithms to represent magnetic field lines and particle trajectories based on data calculated by HINT[4] which is a three-dimensional MHD equilibrium code. The dataset generated by HINT is constructed from several binary files. These are the coordinate data, the physical quantity data, and the header file. The header file contains information about the dataset such as the grid size. These are loaded into VLHD via a text format configuration file. In order to load this dataset into VisAssets, we created a subclass inheriting from the template class for developing the data loading module and implemented necessary routines on it. In this dataset, the pressure field is stored in the XYZ coordinate system and the velocity field is stored in the helical coordinate system. Currently, this module only supports loading pressure field data in the dataset. Fig. 2 shows an example of the visualization results.

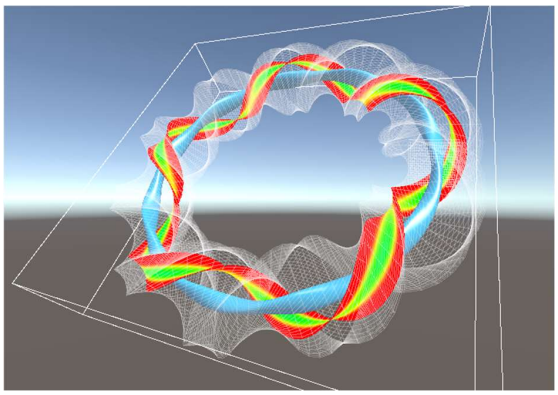

Fig. 2 Visualization result of VLHD data.

3. User Interface for HMDs

VisAssets has a graphical user interface for changing visualization parameters during application execution. However, a user interface for virtual reality devices (VRUI) to perform such operations while running on HMDs was not implemented. With the addition of VRUI, it is now possible to manipulate visualization parameters using a 6-DoF hand-held controller even while running on HMDs. For this functionality, we confirmed that VRUI is available not only for PC-connected HMDs but also for Meta Quest 2, a stand-alone HMD (Fig. 3).

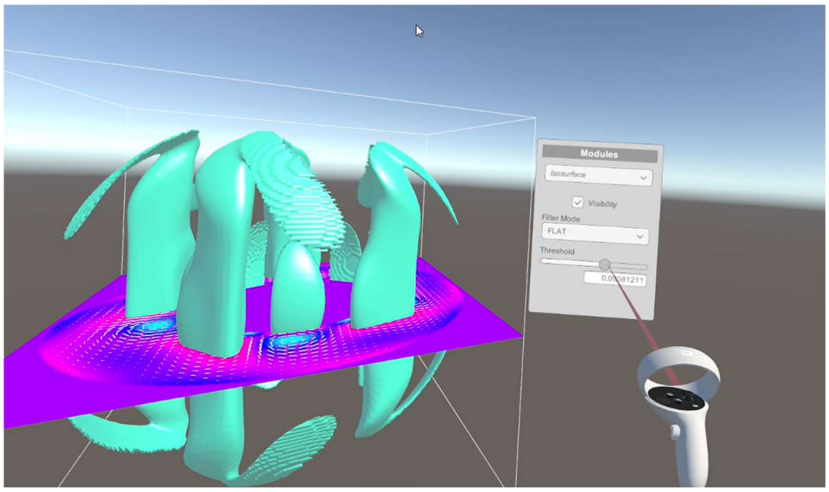

Fig. 3 Graphical user interface running on the stand-alone HMD.

4. Conclusion

In this paper, we introduced VisAssets which is a visualization framework for Unity. We also described the development of a module to load data for VLHD and the newly added VRUI. VisAssets can download from Github[5] and everybody can use it freely. Currently, we are planning to support not only structured grid data but also unstructured grid data.

References

[1] H. Miyachi, S. Kawahara: Development of VR visualization framework with game engine, *Transaction of the Japan Society for Simulation Technology*, 12:2 (2020), 59-67 (in Japanese).

[2] A. Kageyama, T. Hayashi, R. Horiuchi, K. Watanabe, T. Sato: Data visualization by a virtual reality system, *Proceedings of 16th International Conference on the Numerical Simulation of Plasmas* (1998), 138-142.

[3] C. Cruz-Neira, D.J. Sandin and T.A. DeFanti: Surround-Screen Projection-based Virtual Reality: the Design and Implementation of the CAVE, *Proceeding of SIGGRAPH'93* (1993), 135-142.

[4] K. Harafuji, H. Takaya, S. Tetsuya: Computational study of three-dimensional

magnetohydrodynamic equilibria in toroidal helical systems, *Journal of computational physics*, 81:1 (1989), 169-192.

[5] VisAssets: https://github.com/kawaharas/VisAssets (accessed June 16, 2022)

JSST 2022

VOIR: Interactive Visualization Software for Head-Mounted Display Devices

Nobuaki Ohno[1,*] and Akira Kageyama[2]

[1]Graduate School of Information Science, University of Hyogo, Japan
[2]Graduate School of System Informatics, Kobe University, Japan

[*]ohno@gsis.u-hyogo.ac.jp

Abstract. The high-quality, low-cost virtual reality environment provided by the modern head-mounted display (HMD) devices in tandem with the game engines has a potential impact on the renewed interest in the immersive visualization of simulation data by virtual reality. We have developed a new immersive visualization software for HMDs, VOIR, utilizing Unity and OpenXR. VOIR has fundamental visualization functions such as isosurfaces, streamlines, etc. VOIR is a rewritten software of VFIVE that we developed for CAVEs.

Keywords: scientific visualization, virtual reality, head-mounted display

1. Introduction

Head-mounted display (HMD) devices are now gaining unprecedented popularity. The HMD devices offer almost the same virtual reality (VR) functions as the CAVE, a room-sized immersive VR system [1]. The immersive, stereoscopic vision with high-precision position sensors with 6 degrees of freedom is now provided by a modern HMD device at a drastically lower cost. The quality VR environment provided by the HMD devices is now utilized in entertainment, industries, education, training, visual analytics, and data visualization [2, 3]. Among them, data visualization is the focus of this paper.

We developed an application program for data visualization for CAVEs [4] in late 1990s. This software, VFIVE, was designed to be used by simulation researchers for interactive visualization of scalar and vector fields such as velocity/vorticity in computational fluid dynamics and electric current/magnetic fields in electrodynamics. VFIVE has been used for visualization of various kinds of simulation data [5, 6]. A newly found current structure in geomagnetic simulation was intensively analyzed by VFIVE [7].

Applying the experiences gained in the development and utilization of VFIVE, we have newly developed an interactive visualization program VOIR for HMD systems by making use of Unity and OpenXR. A demonstration video of VOIR is available on YouTube.[1] VOIR

[1]https://www.youtube.com/watch?v=svsDBmuZBRw

provides almost the same visualization methods for scalar and vector fields as those implemented in VFIVE. A similar graphical user interface (GUI) is also implemented.

Unity is a popular game engine that is easy to learn and use [8]. In addition to the significant decrease in the cost and space, the environment for the VR program development has also been greatly improved because of the advanced game engines such as Unity. OpenXR is an open standard API for VR and Augmented Reality (AR) devices.

There have been various approaches to data visualization with HMDs, such as CAVELib emulator [9], Unity framework [10], on-the-fly data exploration using game engines [11], and gesture control by hand [12]. For a recent review of VR visualization including HMDs, refer to [13].

2. Implementation of VOIR

VOIR is developed using Unity game engine. Compared to CAVE applications, which required the use of basic APIs such as OpenGL, glut, and CAVELib, Unity makes it extremely easy to implement various 3D visualization algorithms in the VR space. VR-related controls are implemented using Unity's OpenXR plug-in. In this work, we used Oculus for the development of VOIR. Considering versatility to other devices, GUI is developed using only Thumbstick, Trigger, and Grip buttons on the controller. We have confirmed that VOIR runs also on HTC VIVE Pro.

For visualization of scalar fields, we have implemented the isosurface, ortho-slice, and local-slice methods. For vector fields, we have implemented the stream-line, "local arrows" (glyphs in a region specified by the controller), "flashlight" (tracer particles in a cone region specified by the controller), and "fireflies" (tracer particles) methods. GUI is equivalent to VFIVE.

It is also possible to display objects with lines or surfaces in the VR space. The surfaces are specified by the STL format, which is a new feature that did not exist in VFIVE. Switching the visualization methods can be done intuitively via a GUI menu. There is also a snapshot function that saves the image displayed on the display in the PNG format.

3. Application Examples

Shown in Fig. 1 are sample snapshots of the VOIR visualization. A fluid simulation (thermal convection in a rotating spherical shell) is interactively analyzed in the VR environment. Panels (a) to (f) are snapshots of the VR scene. The images are copies of the frame buffer, that are taken by selecting "Snap Shot" menu of VOIR's GUI. Panels (a) to (c) show visualization methods for a scalar field. In this case, ω_z, the vorticity component along the rotation axis, is visualized by (a) isosurface, (b) ortho-slice, and (c) local-slice methods, respectively. Panels (d) to (f) show visualization methods for a vector field. Convection velocity $\boldsymbol{v}$ is visualized by (d) tracer particles, (e) "local arrows", and (f) "flashlight", respectively.

In the isosurface visualization, the surface color can be specified or it can be determined by another scalar field. In the local-slice visualization, a small square plane appears in the VR space and the color contour on the plane visualizes the specified scalar field. The

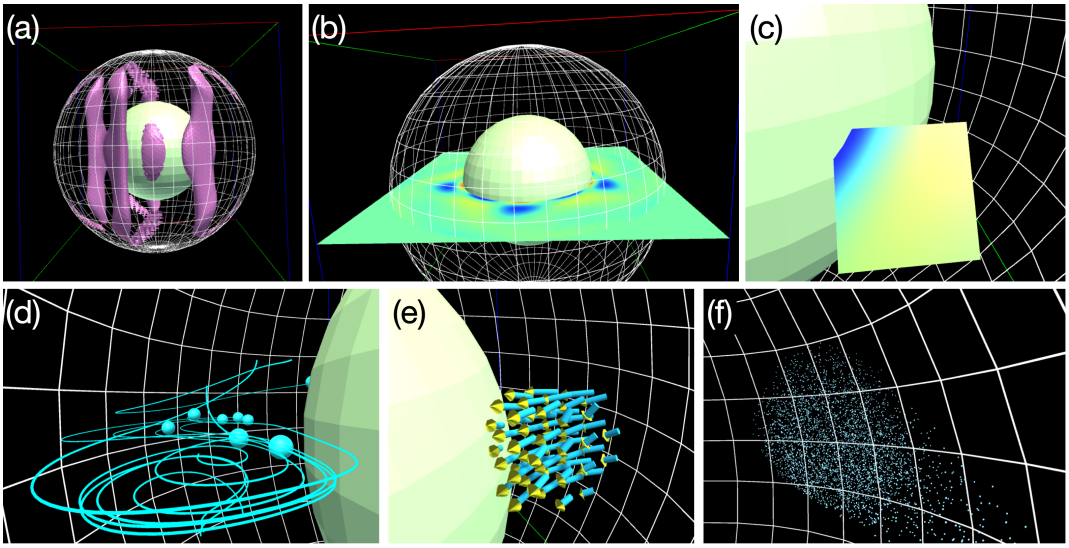

Figure 1: Sample snapshots of the VOIR visualization with HMD.

tracking of the controller is fully utilized in the vector field visualizations. The seed point of the tracer particle [panel (d)] is specified by the controller with the button pressing. The arrow glyphs in "local arrows" [panel (e)] appear around a point specified by the controller in real-time. One can intuitively grasp the velocity field distribution by moving the controller in the VR space and observing the dynamic changes in the glyphs' size and direction. In the flashlight visualization [panel (f)], a virtual flashlight is emitted from the controller, and hundreds of tracer particles are observed in the flashlight cone.

4. Summary

We have developed an application program VOIR with Unity for immersive visualizations in VR space provided by modern HMD devices. We have implemented in VOIR the same visualization features as VFIVE, which is a proven application for scientific visualization for CAVE devices, by rewriting the visualization methods and GUI in Unity. VOIR provides fully interactive immersive visualization experiences in a quality VR environment which is as high as that by CAVEs.

References

[1] Carolina Cruz-Neira, Daniel J Sandin, and Thomas A De Fanti. Surround-Screen Projection-Based virtual reality: The design and implementation of the CAVE. In *Proceedings of the 20th annual conference on Computer graphics and interactive techniques*, pages 135–142, 1993.

[2] Chongsan Kwon. Verification of the possibility and effectiveness of experiential learning using HMD-based immersive VR technologies. *Virtual Real.*, 23(1):101–118, March 2019.

[3] Penelope Atsikpasi and Emmanuel Fokides. A scoping review of the educational uses of 6DoF HMDs. *Virtual Real.*, 26(1):205–222, March 2022.

[4] Akira Kageyama, Yuichi Tamura, and Tetsuya Sato. Visualization of vector field by virtual reality. *Progr. Theoret. Phys.*, 138:665–673, April 2000.

[5] Akira Kageyama and Nobuaki Ohno. IMMERSIVE VR VISUALIZATIONS BY VFIVE PART 1: DEVELOPMENT. *Int. J. Model. Simul. Sci. Comput.*, 04(supp01):1340003, August 2013.

[6] Akira Kageyama, Nobuaki Ohno, Shintaro Kawahara, Kazuo Kashiyama, and Hiroaki Ohtani. IMMERSIVE VR VISUALIZATIONS BY VFIVE PART 2: APPLICATIONS. *Int. J. Model. Simul. Sci. Comput.*, 04(supp01):1340004, August 2013.

[7] Akira Kageyama, Takehiro Miyagoshi, and Tetsuya Sato. Formation of current coils in geodynamo simulations. *Nature*, 454(7208):1106–1109, August 2008.

[8] Nicolas Alejandro Borromeo. *Hands-On Unity 2021 Game Development: Create, customize, and optimize your own professional games from scratch with Unity 2021, 2nd Edition*. Packt Publishing, 2 edition, August 2021.

[9] Shintaro Kawahara and Akira Kageyama. Development of CAVELib compatible library for HMD-type VR devices. *J. Adv. Simul. Sci. Eng.*, 6(1):234–248, 2019.

[10] Hideo Miyachi and Shintaro Kawahara. Development of VR visualization framework with game engine. *Transaction of the Japan Society for Simulation Technology (in Japanese)*, 12:59–67, 2020.

[11] Brandon K Horton, Rajiv K Kalia, Erick Moen, Aiichiro Nakano, Ken-Ichi Nomura, Michael Qian, Priya Vashishta, and Anders Hafreager. Game-Engine-Assisted research platform for scientific computing (GEARS) in virtual reality. *SoftwareX*, 9:112–116, January 2019.

[12] Yuichi Tamura, Hiroaki Nakamura, and Susumu Fujiwara. An intuitive interface for visualizing numerical data in a Head-Mounted display with gesture control. *Plasma and Fusion Research*, 11:2406060–2406060, 2016.

[13] Elif Hilal Korkut and Elif Surer. Visualization in virtual reality: a systematic review. *arXiv*, 2203.07616, March 2022.

JSST 2022

VR Extension of Particle-based Remote Visualization Application

Takuma Kawamura[1,*] and Naohisa Sakamoto[2]

[1]Japan Atomic Energy Agency
[2]Kobe University

[*]Kawamura.takuma@jaea.go.jp

The full paper of this paper has been published in Journal of Advanced Simulation in Science and Engineering (JASSE).

DOI: https://doi.org/10.15748/jasse.10.31

Molecular dynamics study of microscopic mechanism of OH radical-induced DNA damage

Ryuta Kawanami[1,2*], Susumu Fujiwara[1], Tomoko Mizuguchi[1], Yoshiteru Yonetani[2], Tsukasa Aso[3], Hiroaki Nakamura[4,5]

[1]Kyoto Institute of Technology
[2]National Institutes for Quantum and Radiological Science and Technology
[3]National Institute of Technology, Toyama College
[4]National Institute for Fusion Science
[5]Nagoya University

*d2871005@edu.kit.ac.jp

Abstract. The backbone of DNA has sugars joined by phosphodiester bonds. Highly reactive hydroxyl radicals are produced by ionizing radiation in a cell, which can abstract any hydrogen atoms from DNA. Carbon centerd sugar radicals produced by the hydrogen abstraction from sugar moiety triggers a common lesion, single-strand break which induces disease such as carcinogenesis. However, the abstraction mechanisms at the molecular level remain unsolved. Thus, we employed molecular dynamics simulations on hydroxyl radicals around DNA to evaluate their accessibility to hydrogen atoms on sugar moiety. In particular, we introduced restraining potentials on the hydroxyl radicals, which enabled us to sufficient sampling of the hydroxyl radicals to each hydrogen atom on DNA. Our simulation results were very different from those reported previously. This indicates that the conventional evaluations based on the solvent-accessible surface area or the water accessibility are needed to be modified.

Keywords: DNA damage, Hydrogen abstraction, Hydroxyl radical, Molecular dynamics simulation

1. Introduction

Hydroxyl (OH) radical which is produced by irradiation of water molecule in cells is one of the major DNA damaging agents which possess high and nonselective reactivity [1]. The main target sites for damage on DNA by OH radical are bases and sugar moieties. The latter ratio is about 10-15%, and the carbon centered radicals produced by hydrogen abstraction from carbon atoms are unstable and cause strand breaks and other damages that are difficult to be repaired [2]. Unrepaired damage induces various diseases such as neurodegeneration as well as cancer. There are seven hydrogen atoms present in sugar moiety, H1', H2', H2'', H3', H4', H5', and H5'' (Fig. 1), corresponding to the carbon atoms to which they bond, respectively. The issue of which hydrogen atom OH radical is most likely to abstract is important, since the variation of

the final product depends on the position of the carbon centered radical.

Previous study [3] has shown that strand break due to hydrogen abstraction is more likely to occur in the order C5' > C4' > C3' > C2' > C1', and that the ratio of the reaction frequency is proportional to the solvent-accessible surface area (SASA) of the hydrogen atoms [3]. Furthermore, molecular dynamics (MD) simulations have shown that the ratio is proportional to the accessibility, or number of times water molecules approache the sugar hydrogen atoms [4]. Thus, hydrogen abstraction have been evaluated by SASA which does not take into account the property of the molecule or accessibility of water molecules. In particular, because of the high sampling cost of OH radical in simulations, the accessibility of solvent water molecules has been calculated instead. However, water molecules and OH radical are different in their molecular behavior [5] and may have different accessibility to DNA. In this study, we re-evaluated the rate of hydrogen abstraction from MD simulations of OH radical. To increase the sampling efficiency, we here employed restraining potentials and calculated the accessibility of OH radical directly to sugar hydrogens.

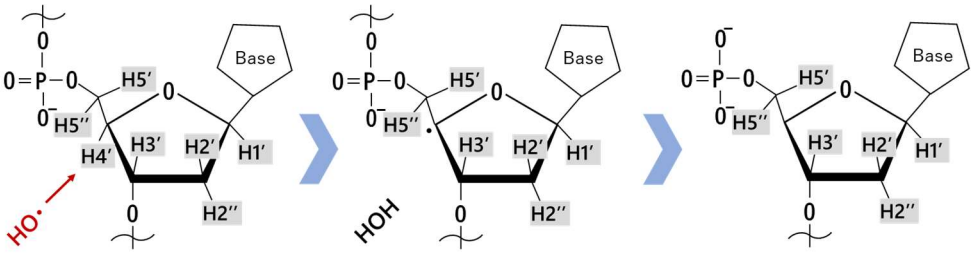

Figure 1. Scheme for hydrogen abstraction from sugar moiety. There are seven possible hydrogen atoms in the sugar moiety that can be abstracted.

2. Methods

We prepared the DNA system, 6 base pairs of B-form (3'-ATATAT-5') with 1783 water molecules, and 8 OH radicals, as shown in Fig. 2. The force fields of ParmBSC1 and TIP3P were used for DNA and water molecules, respectively. Three different models of Refs. 5-7 were used for OH radicals. The MD simulations were performed using sander module in AmberTools20. The initial molecular configuration was created using LEaP module in AmberTools20. The initial simulation box was a truncated octahedron of 45.3 Å with periodic boundary conditions. The cutoff distance for the Lennard-Jones interaction and the electrostatic interaction was set to 8 Å. The electrostatic interaction between particles more than 8 Å apart was calculated using the Particle-Mesh-Ewald (PME) method. For electric neutralization for the PME calculation, 10 Na^+ was added to the system. Initially, 20 ps of relaxation was performed under NVT conditions while DNA was restrained, followed by 100 ps of relaxation under NPT conditions. The production run was performed for 100 ns under NPT conditions. Time step was set to 2 fs. The temperature was set to 310 K using Langevin dynamics (γ = 1.0), and the pressure was set to 1 atm using Berendsen barostat with the relaxation time of 2 ps.

Accessibility of the OH radicals was calculated for each sugar hydrogen. As in Ref. 4, we counted the number of times OH radicals were within 3 Å of each sugar hydrogen. In this calculation, we employed 50,000 snapshots from the 100 ns MD simulation. For efficient sampling of the OH configurations, restraining potentials, with a flat bottom and parabolic sides out to 8 Å, were imposed between the OH radicals and oxygen atoms of the sugar moiety. The test calculation with water molecules confirmed that the restraing potential introduced here did

not make any effect on the result of the radical accessibility.

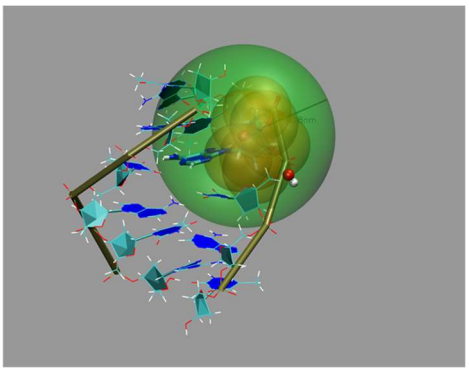

Figure 2. Simulation model of DNA and OH radical. The green sphere represents the range of restraint potential of one of the eight pairs. The orange spheres represent the access criterion for each hydrogen atom. For clarity, water molecules are omitted.

3. Results and Discussion

Fig. 3(left) shows the result of the radical accessibility. The accessibility of the OH radical did not show clear correlation with the experimental result[3]. This trend did not change with a different DNA sequence (3'-CGCGCG-5') and different molecular models of OH radicals [5-7].

Here, we consider the orientation of OH radical. Quantum chemical calculation studies suggest that the OH radical begins to abstract when it approaches the sugar hydrogen at a specific angle, i.e., when OH radical is oriented to form a water molecule[8, 9]. Based on this insight, in order to count the arrangements that would lead to a hydrogen abstraction reaction, we added the criterion of 104.5 ± 10˚ to the accessibility count. The reuslt in Fig. 3 (right) showed a better correlation. These results indicates that the conventional explanation of the hydrogen abstraction reaction rate by water molecule accessibility is apparently consistent with the ratio of the reaction frequency[3] and must be accurately evaluated from the accessibility of the OH radicals by taling orientation into account.

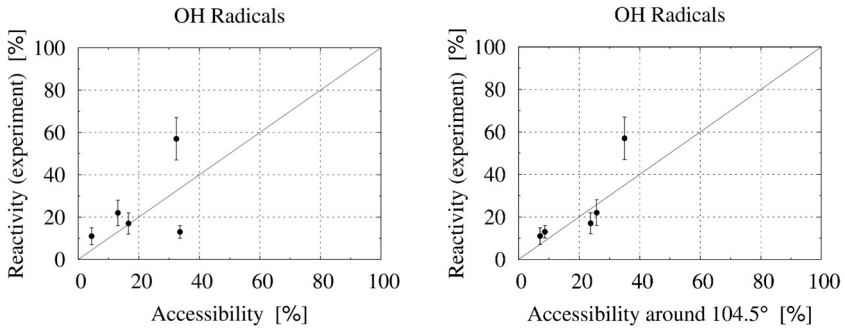

Figure 3. Comparison of accessibility and experimental [3] values. Left: criterion of within 3 Å, right: within 3 Å and 104.5 ± 10˚.

References

[1] W. K. Pogozelski, T. D. Tullius: Oxidative Strand Scission of Nucleic Acids: Routes Initiated by Hydrogen Abstraction from the Sugar Moiety, *Chemical Reviews*, 98:3 (1998), 1089-1108.

[2] L. P. Candeias, S. Steenken: Reaction of HO· with Guanine Derivatives in Aqueous Solution: Formation of Two Different Redox-Active OH-Adduct Radicals and Their Unimolecular Transformation Reactions. Properties of G(-H)·, *Chemistry Europe*, 6:3 (2000), 475-484.

[3] B. Balasubramanian, W. K. Pogozelski, T. D. Tullius: DNA strand breaking by the hydroxyl radical is governed by the accessible surface areas of the hydrogen atoms of the DNA backbone, *Proceedings of the National Academy of Sciences*, 95:17 (1998), 9738-9743.

[4] Y. Yonetani, H. Nakagawa: Understanding water-mediated DNA damage production by molecular dynamics calculation of solvent accessibility, *Chemical Physics Letters*, 749:16 (2020), 137441.

[5] M. G. Campo, J. R. Grigera: Classical molecular-dynamics simulation of the hydroxyl radical in water, *The Journal of Chemical Physics*, 123:8 (2005), 084507.

[6] B. Fiser, B. Jójárt, I. G. Csizmadia, B. Viskolcz: Glutathione – Hydroxyl Radical Interaction: A Theoretical Study on Radical Recognition Process, *PLOS ONE*, 8:9 (2013), e73652.

[7] E. Lindahl, B. Hess, D. van der Spoel: GROMACS 3.0: a package for molecular simulation and trajectory analysis, *Molecular Modeling Annual*, 7 (2001), 306-317.

[8] A. Hamza, H. Broch, D. Vasilescu: Quantum molecular simulation of the H abstraction at C4' of DNA sugar moiety by the free radical ·OH, *Journal of Molecular Structure: THEOCHEM*, 491:1-3 (1999) 237-247.

[9] R. M. Abolfath, R. K. Biswas, R. Rajnarayanam, T. Brabec, R. Kodym, L. Papiez: Multiscale QM/MM Molecular Dynamics Study on the First Steps of Guanine Damage by Free Hydroxyl Radicals in Solution, *The Journal of Physical Chemistry A*, 116:15 (2012) 3940-3945.

JSST 2022

Large-scale urban flood simulation with building-cube method

Masashi Morishita[1,*], Koji Nishiguchi[2], Tokimasa Shimada[3,4], Tetsuro Tamura[5]

[1]Environmental Engineering and Architecture, Graduate School of Environmental Studies, Nagoya University
[2]Department of Civil Engineering, Graduate School of Engineering, Nagoya University
[3]Department of Computational Science, Graduate School of System Informatics, Kobe University
[4]RIKEN Center for Computational Science, RIKEN
[5]Tokyo Institute of Technology School of Environment and Society

[*]morishita.masashi@s.mail.nagoya-u.ac.jp

Abstract. In recent years, climate change has increased the risk of flooding in urban areas. However, one- or two-dimensional models based on the general shallow-water equation cannot compute the complex three-dimensional flow of water and unsteady hydrodynamic forces acting on structures in urban areas where structures are densely built. Therefore, this study proposes a gas-liquid two-phase flow analysis method based on the finite volume method using the building cube method (BCM), which is suitable for large-scale parallel computations, and verifies the validity and effectiveness of the method.

Keywords: Eulerian method, Two-phase flow analysis, Building-cube method, Finite volume method

1. Introduction

In recent years, climate change has increased the risk of flooding in urban areas. However, one- or two-dimensional models based on the general shallow-water equation cannot compute the complex three-dimensional flow of water and unsteady hydrodynamic forces acting on structures in urban areas where structures are densely built. Therefore, this study proposes a finite volume gas-liquid two-phase flow analysis method based on the building cube method (BCM), which is suitable for large-scale parallel computations. The cell-centered finite volume method based on BCM has been conventionally applied to single-phase flows and coupled fluid-structure problems, but has not been applied to gas-liquid two-phase flows. In this study, a three-dimensional dam-break problem and building flooding analysis are conducted to verify the validity and effectiveness of the method.

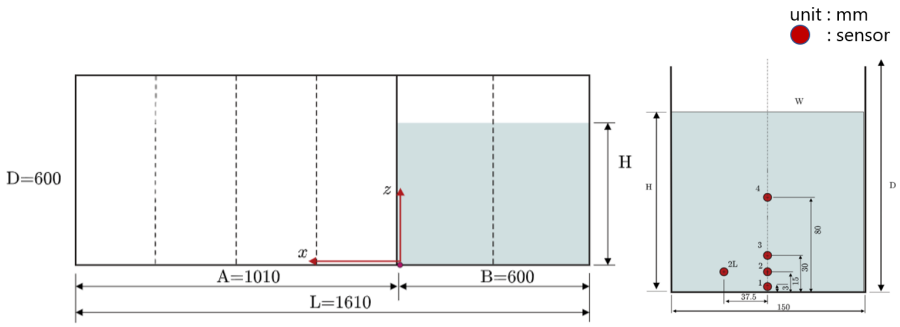

Fig. 1: Experimental setting of 3D dam-break problem and positions of pressure sensor

2. Numerical method

In this study, the governing equations are the continuity equation and the equation of motion, which are the basic equations in continuum mechanics, volume-averaged in the control volume. We assume an incompressible Newtonian fluid as the constitutive equation for a fluid. Define the velocity vector at the cell center and discretize it using the finite volume method. In this case, the stress is divided into pressure and deviation stress, and the velocity and pressure fields are computed separately using the fractional step method. In this study, the above space-averaged equations of motion are separated into velocity and pressure fields by the partial step method, and the cell-centered finite volume method is used for spatial discretization. The SOR method with Red-Black ordering is used to solve the pressure Poisson equation. The second-order Adams-Bashforth method is used to compute the intermediate velocity and the time evolution of the advection equation of the VOF function, and the fifth-order WENO scheme is applied to the advection term. The numerical examples in this paper were computed on the supercomputer "Fugaku" (processor: A46FX) in hybrid parallel using OpenMP and MPI.

3. Dam break analysis

In the numerical analysis, convection boundary conditions are assumed on the top surface of the tank and slip-wall boundary conditions are assumed on the other surfaces. The analysis domain is divided uniformly by cubes with only 16^3 cubic cells of side length 1.171875 mm, for a total cell count of 53,764,096. The mass density of air is $1.18\,\mathrm{kg\,m^{-3}}$ and the viscosity coefficient of air is 1.84×10^{-5} Pa s. The mass density of water is $997\,\mathrm{kg\,m^{-3}}$ and the viscosity of water is 8.87×10^{-4} Pa s as the viscosity coefficient of water. Fig. 1 shows the free interface, where t^* is the non-dimensional time. Fig. 2 shows that the numerical solution by the proposed method and the experimental results are in good agreement. Next, Fig. 3 shows a comparison of the non-dimensional pressure time histories for sensor 1. Fig. 3 shows that the peak pressure values were captured with high accuracy. Because of the large variability of measurements in dam-break experiments, 100 experiments were conducted under the same conditions, and Fig. 3 compares the pressure time histories at the 2.5th percentile, median, and 97.5th percentile values with the results of the numerical analysis.

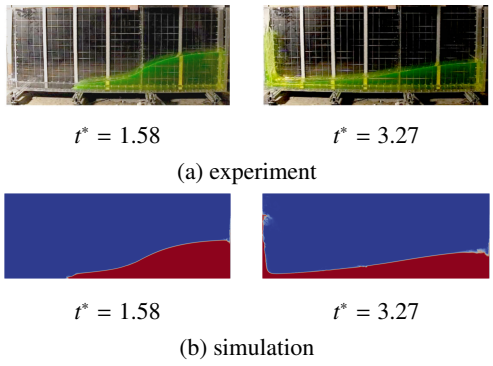

Fig. 2: Comparison of free surface between experiment and simulation

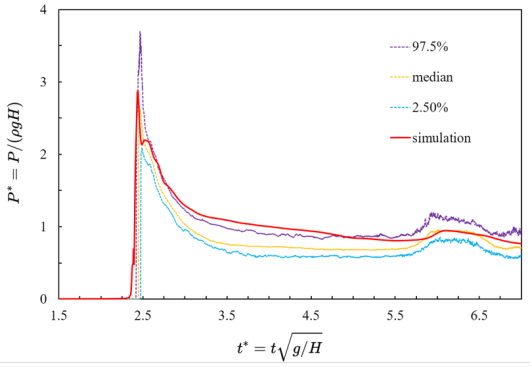

Fig. 3: Comparison of time history of pressure at sensor 1 between experiment and simulation

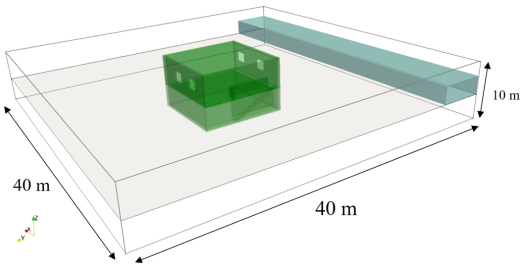

Fig. 4: Numerial model for estimating water immersion inside building during flooding

4. Building Flooding Analysis

Next, consider the analytical model in Fig. 4. A dam break flow with a height of 2 m is assumed to flow from the boundary of the analysis domain at a velocity of 3 m s^{-1} as shown in Fig. 4. The building is assumed to be a structure with a staircase and a basement space, and the inflow is assumed to be through a window. In this study, the building is modeled by the embedded boundary method. The fluid properties are the same as in the previous section. Inflow boundary conditions are applied to the upstream face of the analysis domain, slip-wall boundary conditions are applied to the bottom face, and convection boundary conditions are applied to the other end faces of the analysis domain. The analysis domain is divided hierarchically by an orthogonal mesh with a minimum cell size of 78.125 mm and a total cell count of 14,876,672. The analysis results are shown in Fig. 5. Fig. 5 shows that the dam break flow flows into and around the building. The complex water flow is reproduced by the collision of the water flow with the structure. In particular, the behavior of the water flow colliding with the walls of the building and bouncing up, and water entering the building through the windows can be confirmed. Fig. 6 shows the pressure distribution, which shows that the unsteady water flow causes the pressure values to rise and fall in a complex manner before and after the impact. The three-dimensional flow of water and the unsteady hydrodynamic forces on the building walls as described above are difficult to evaluate with one- or two-dimensional flood analysis models, and can be evaluated only with a three-dimensional analysis.

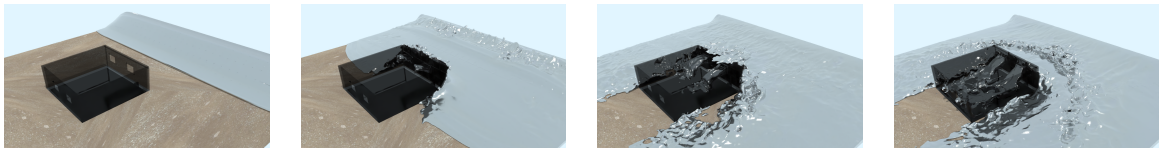

t = 0.75 s t = 1.75 s t = 2.50 s t = 4.00 s

Fig. 5: Numerical result of free surface of water immersion inside building during flooding

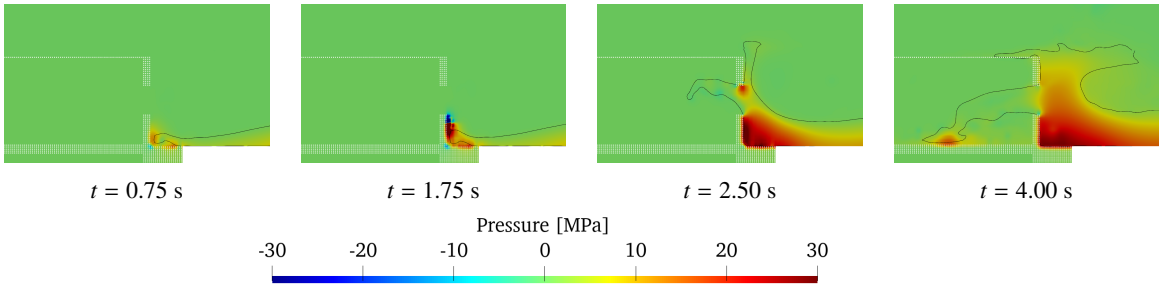

t = 0.75 s t = 1.75 s t = 2.50 s t = 4.00 s

Fig. 6: Pressure distribution at x = 18.85 m. Black line represents 0.5 contour line of VOF function.

5. Conclusion

In this study, we focused on a large-scale third-order two phase flow problem to evaluate unsteady hydrodynamic forces acting on the three-dimensional flow and structure of water around and inside buildings, which are difficult to compute with one-dimensional or two-dimensional flood analysis models. A gas-liquid two-phase flow analysis method using a cell-centered finite volume method based on the building cube method, which can achieve high scalability in a massively parallel computer environment, is proposed to evaluate the inundation of buildings during floods. The space-averaged equations of motion described in this paper are formulated to handle coupled structure-fluid problems by assuming elastic bodies and Newtonian fluids in the constitutive equations. Therefore, future research may include the evaluation of unsteady stress distribution inside the structure.

References

[1] 西口浩司，岡澤重信，坪倉誠: 大規模並列計算に適した階層型直交メッシュ法による完全オイラー型固体-流体連成解析， 土木学会論文集 A2（応用力学）, volume:73 (2017), 153–163.

[2] Lobovsky, L., et al.: Experimental investigation of dynamic pressure loads during dam break, *Journal of Fluids and Structures*, volume:48, (2014), 407–434.

[3] Shimada, T., Nishiguchi, et al.: Eulerian finite volumeformulation using Lagrangian marker particles for incompressible fluid-structure interaction problems, *Int JNumer Methods Eng*, volume:123, (2021) 1294–1328.

JSST2022

Gas-liquid-solid Three-phase Finite Element Analysis based on Multi-phase-field Model

Junichi Matsumoto[1*], Tomohiro Sawada[1]

[1]National Institute of Advanced Industrial Science and Technology (AIST)

*matsumoto-junichi@aist.go.jp

Abstract. The numerical solution of multi-phase-field model three-phase analysis in gas, liquid, and solid using a tetrahedron (unstructured grid) is investigated. The multi-phase-field model employed the Cahn-Hilliard equation of the conservative system. In this study, an implicit method in the time direction and a mixed finite element method using MINI elements in the space direction are proposed.

Keywords: Unstructured grid, Multi-phase-field model, Cahn-Hilliard equation, Implicit finite element method, Gas-liquid-solid three-phase analysis

1. Introduction

An implicit mixed finite element method based on a multi-phase-field model [1] for gas-liquid-solid three-phase flow is proposed for the finite element parallel analysis. A bubble function element stabilization method [2,3] is employed for incompressible Navier-Stokes equations. Allen-Cahn equation [4] and Cahn-Hilliard equation [5,6] are applied to estimate interface of gas, liquid and solid. MINI element, bubble function element /linear element, is used to solve Cahn-Hilliard equation. As for the temporal discretization, an implicit scheme is used. In the implicit scheme, N-R method is employed to solve non-linear equations. A three dimensional three-phase field fluid analysis is computed in this research.

2. Numerical example

As a solid-liquid three-phase flow simulation of the multi-phase-field model, a spherical structure with a diameter of 1.6 cm from a position of 7.5 cm in a liquid (water surface) with a depth of 5 cm shown in Fig.1 has an initial velocity of 2 m/s. The computation of falling with s was performed. The computational method of fluid analysis uses the implicit method. The division width was 0.1 cm, the time increment was 0.0001 s. The density and viscosity coefficient assuming water is used for the liquid and air is used for the gas. For the solid, a density of 7870 kg/m^3. Looking at the Fig. 1, it can be confirmed that the structure falls while the water surface expands in a cylindrical shape without mixing the liquid and the solid.

3. Conclusions

In this paper, the Cahn-Hilliard equation is used as a gas-liquid solid by the multi-phase-field three-phase model, and the fall computation of the structure is performed as a computational example to show the effectiveness of the proposed method.

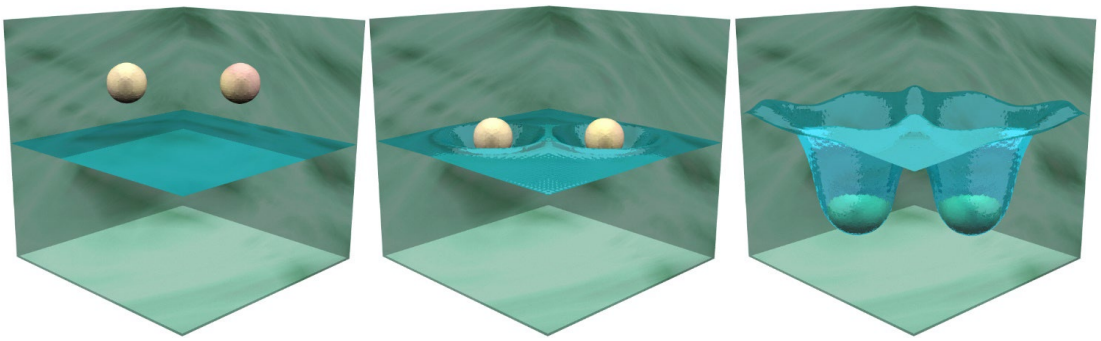

(a) Gas-liquid interface and solid interface, solid interface

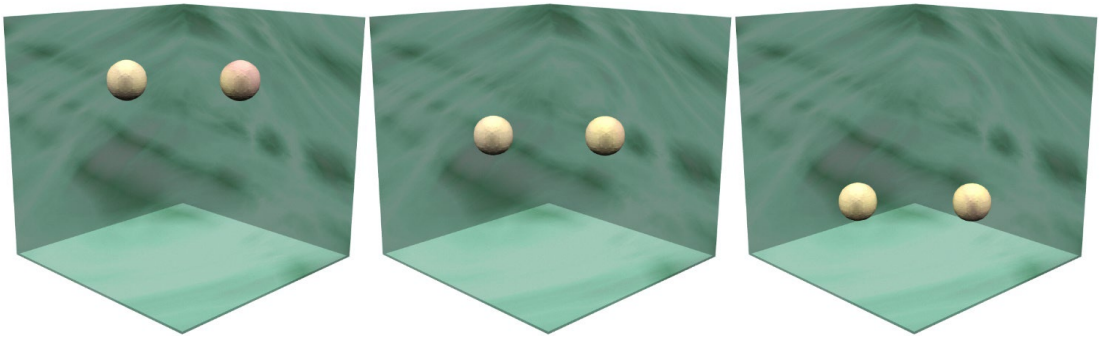

(b) Solid interface

Fig. 1 Computatinal result

References

[1] S. Dong: An efficient algorithm for incompressible N-phase flows, *J. Comput. Phys.*, 276 (2014), 691-728.

[2] J. Matsumoto: A Relationship between stabilized FEM and bubble function element stabilization method with orthogonal basis for incompressible flows, *J. Appl. Mech. JSCE*, 8 (2005), 233-242.

[3] J. Matsumoto: A fractional step method for incompressible viscous flow based on bubble function element stabilization method, *Int. J. Comput. Fluid Dyn.*, 20(3-4) (2006), 145-155.

[4] N. Takada, J. Matsumoto and S. Matsumoto: Phase-field model-based simulation of motions of a two-phase fluid on solid surface, *Journal of Computational Science and Technology*, 7 (2013), 322-337.

[5] T. Biben and C. Misbah: Tumbling of vesicles under shear flow within an advected-field approach, *Physical Review E*, 67 (2003), 031908(1-5).

[6] J. Beaucount, T. Biben, A. Leyrat and C. Verdier: Modeling breakup and relaxation of newtonian droplets using the advected phase-field approach, *Physical Review E*, 75 (2007), 021405(1-8).

JSST 2022

Large-Scale Computation of Transient Topology Optimization Using the Building-Cube Method

Ryohei Katsumata[1,*], Koji Nishiguchi[1], Tokimasa Shimada[2], Hiroya Hoshiba[1], Junji Kato[1]

[1]Department of Civil Engineering, Graduate School of Engineering, Nagoya University
[2]Department of Computational Science, Graduate School of System Informatics, Kobe University

[*]katsumata.ryohei.a3@s.mail.nagoya-u.ac.jp

Abstract. In recent years, topology optimization methods have been adopted not only for structural problems but also for fluid flow problems. Topology optimization for transient flows requires a fine mesh, especially for high Reynolds number flows, which is computationally expensive. Therefore, we propose a transient flow topology optimization method based on the building-cube method (BCM), which is suitable for massively parallel computing. The transient Navier-Stokes equations in the topology optimization procedure are solved by finite volume discretization, and the sensitivity of the objective function is obtained by continuous sensitivity analysis based on the adjoint method.

Keywords: Topology optimization, Unsteady flow, Finite volume method, Parallel computing

1. Introduction

In recent years, topology optimization methods have been adopted not only for structural problems but also for fluid flow problems. Most topology optimization methods for fluid flow problems assume steady-state flow, but Deng *et al.*[1][2] proposed a topology optimization method for unsteady flow. The solid domain is simulated using artificial friction force against the incompressible Navier-Stokes equations to optimize unsteady fluid flow. The topology optimization procedure is implemented using a continuous sensitivity analysis formulation based on the adjoint method and a discretization using the finite element method. However, topology optimization for unsteady flows requires a fine mesh, especially for high Reynolds number flows, and is computationally expensive.

On the other hand, recent exponential performance improvements in parallel computers have made possible massively parallel computations with high-resolution computational meshes. Jansson *et al.*[3], Nishiguchi *et al.*[4] and Shimada *et al.*[5] used the building-cube

method (BCM), a hierarchical Cartesian mesh method, and the cell-centered finite volume method for unsteady fluid analysis and unsteady fluid-structure interaction analysis. The BCM enables even computational load on each processor and localized/continuous memory access, and achieves high scalability on massively parallel computers.

Based on the above background, we propose an unsteady incompressible flow topology optimization method using BCM suitable for massively parallel computing. The unsteady Navier-Stokes equations in the topology optimization procedure are discretized by a cell-centered finite volume method based on the BCM. The sensitivity of the objective function is determined by a continuous sensitivity analysis based on the adjoint method.

2. Governing equations

In the computational domain Ω, the flow velocity, pressure, and body force at position $\boldsymbol{x} \in \Omega$ and time $t \in [0, T]$ are $\boldsymbol{u}$, p, and $\boldsymbol{f}$, respectively. The governing equations for unsteady incompressible flow, the equations of motion (Navier-Stokes equations) and the continuity equation can be expressed as follows

$$\rho \frac{\partial \boldsymbol{u}}{\partial t} + \rho (\boldsymbol{u} \cdot \nabla) \boldsymbol{u} = -\nabla p + \mu \nabla \cdot \left(\nabla \boldsymbol{u} + \nabla \boldsymbol{u}^{\top} \right) + \boldsymbol{f} \ , \quad \text{in } \Omega \times [0, T] \tag{1}$$

$$-\nabla \cdot \boldsymbol{u} = 0 \ , \quad \text{in } \Omega \times [0, T] \tag{2}$$

where ρ is the mass density and μ is the viscosity. The following initial conditions are given for the flow velocity.

$$\boldsymbol{u} (\boldsymbol{x}, 0) = \boldsymbol{u}_0 (\boldsymbol{x}) \ , \quad \text{in } \Omega \tag{3}$$

In addition, the following boundary conditions are given on the Dirichlet boundary Γ_D and the Neumann boundary Γ_D.

$$\boldsymbol{u} (\boldsymbol{x}, t) = \boldsymbol{u}_D (\boldsymbol{x}, t) \ , \quad \text{on } \Gamma_D \times [0, T] \tag{4}$$

$$\left[-p \boldsymbol{I} + \mu \left(\nabla \boldsymbol{u} + \nabla \boldsymbol{u}^{\top} \right) \right] \cdot \boldsymbol{n} = \boldsymbol{g} (\boldsymbol{x}, t) \ , \quad \text{on } \Gamma_N \times [0, T] \tag{5}$$

where $\boldsymbol{I}$ is the unit tensor and $\boldsymbol{n}$ is the outward unit normal vector at the boundary $\partial\Omega$.

In the solid domain, an artificial frictional force[1][2] is applied so that the flow velocity is $\boldsymbol{0}$.

$$\boldsymbol{f} = -\alpha \boldsymbol{u} \tag{6}$$

where α is a parameter that represents the impermeability assuming the solid is a porous medium, and is expressed by the following equation using the design variable $\gamma \in [0, 1]$.

$$\alpha (\gamma) = \alpha_{\min} + (\alpha_{\max} - \alpha_{\min}) \frac{q (1 - \gamma)}{q + \gamma} \tag{7}$$

where $\alpha_{\min}$ and $\alpha_{\max}$ are the minimum and maximum values of α, respectively. $q \in \mathbb{R}^{+}$ is a parameter to ensure convexity in the interpolation function of α expressed in the equation (7).

3. Topology optimization problem

Using the above governing equations, the topology optimization problem for unsteady incompressible Navier-Stokes flow[1][2] is formulated as follows

$$
\begin{aligned}
&\min J(\boldsymbol{u}, p; \gamma) \\
&\text{s.t.} \begin{cases}
\rho \dfrac{\partial \boldsymbol{u}}{\partial t} + \rho (\boldsymbol{u} \cdot \nabla) \boldsymbol{u} = -\nabla p + \mu \nabla \cdot \left(\nabla \boldsymbol{u} + \nabla \boldsymbol{u}^{\top} \right) + \boldsymbol{f}, \quad \text{in } \Omega \times [0, T] \\
-\nabla \cdot \boldsymbol{u} = 0, \quad \text{in } \Omega \times [0, T] \\
\boldsymbol{u}(\boldsymbol{x}, 0) = \boldsymbol{u}_0(\boldsymbol{x}), \quad \text{in } \Omega \\
\boldsymbol{u}(\boldsymbol{x}, t) = \boldsymbol{u}_D(\boldsymbol{x}, t), \quad \text{on } \Gamma_D \times [0, T] \\
\left[-p\boldsymbol{I} + \mu \left(\nabla \boldsymbol{u} + \nabla \boldsymbol{u}^{\top} \right) \right] \cdot \boldsymbol{n} = \boldsymbol{g}(\boldsymbol{x}, t), \quad \text{on } \Gamma_N \times [0, T] \\
\displaystyle\int_{\Omega} \gamma \, \mathrm{d}\Omega \leq \theta V_0 \\
0 \leq \gamma \leq 1
\end{cases}
\end{aligned}
\tag{8}
$$

where $V_0 = \int_{\Omega} \mathrm{d}\Omega$ is the volume of the whole computational domain Ω, $\theta \in (0, 1]$ is the upper bound of fluid volume fraction. Equation (8) represents the equality constraint due to the governing equations and the inequality constraint due to the volume constraint. The external force term $\boldsymbol{f}$ uses the artificial friction force shown in the equations (6)-(7) to treat the computational domain including the solid domain in a unified form. The generalized objective function J is defined using domain and boundary integrals of the physical quantity as follows

$$
J(\boldsymbol{u}, p; \gamma) = \int_0^T \int_{\Omega} \beta_1 A(\boldsymbol{u}, \nabla \boldsymbol{u}, p; \gamma) \, \mathrm{d}\Omega \mathrm{d}t + \int_0^T \int_{\partial\Omega} \beta_2 B(\boldsymbol{u}, p; \gamma) \, \mathrm{d}\Gamma \mathrm{d}t \tag{9}
$$

where A is a physical quantity inside the computational domain and B at the domain boundary. The β_1 and β_2 are parameters (constants) that weight the objective function.

4. Numerical methods

As mentioned before, topology optimization for unsteady flow requires a fine mesh, especially for high Reynolds number flows, and is computationally expensive. Therefore, in this research, the governing equations are discretized using a cell-centered finite volume method based on the BCM[3][4][5], which is suitable for massively parallel computing, and a massively parallel computer is used to perform the massively parallel computation. As shown in Figure 1, BCM divides the computational domain into cubic regions, called cubes. Each cube is divided into a Cartesian mesh with the same number of computation cells, and the same

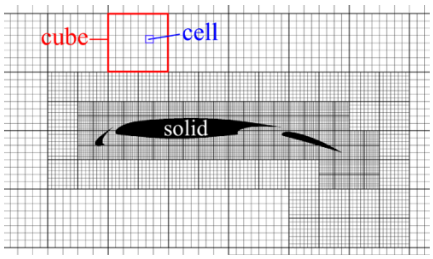

Figure 1: Mesh Division based on the BCM

number of cubes are distributed to each computation core, with spatial loop processing performed within each cube. This allows each computation core to share the same number of computation cells, thus equalizing the computation load and localizing and continuing memory accesses, which results in high parallelization efficiency. In previous research, discretization has been performed mainly using the finite element method, but in this research, discretization is performed using the cell-centered finite volume method.

Topology optimization uses the density method to optimize the design domain. The sensitivity of the objective function is obtained using the continuous sensitivity formulation[1][2] based on the adjoint method using the equations (1)-(5). The adjoint equations in the sensitivity analysis are also discretized using a cell-centered finite volume method based on the BCM. Using the obtained sensitivity, the design variables are updated based on the gradient method, and the optimal solution of the design variables is computed such that the objective function is minimized.

5. conclusion

In this research, we proposed a topology optimization method for unsteady flow using a cell-centered finite volume method based on the BCM, which is suitable for massively parallel computation. In the presentation, we will demonstrate several numerical examples to verify the proposed method.

References

[1] Y. Deng, Z. Liu, P. Zhang, Y. Liu., Y. Wu: Topology optimization of unsteady incompressible Navier-Stokes flows, *Journal of Computational Physics*, 230:17 (2011), 6688–6708.

[2] Y. Deng, Z. Liu, Y. Wu: Topology optimization of steady and unsteady incompressible Navier-Stokes flows driven by body forces, *Structural and Multidisciplinary Optimization*, 47 (2012), 555–570.

[3] N. Jansson, R. Bale, K. Onishi, M. Tsubokura: CUBE: A scalable framework for large-scale industrial simulations, *The International Journal of High Performance Computing Applications*, 33:4 (2019), 678–698.

[4] K. Nishiguchi, R. Bale, S. Okazawa, M. Tsubokura: Full Eulerian deformable solid-fluid interaction scheme based on building-cube method for large-scale parallel computing, *International Journal for Numerical Methods in Engineering*, 117:2 (2019), 221–248.

[5] T. Shimada, K. Nishiguchi, R. Bale, S. Okazawa, M. Tsubokura: Eulerian finite volume formulation using Lagrangian marker particles for incompressible fluid-structure interaction problems, *International Journal for Numerical Methods in Engineering*, 123:5 (2021), 1294–1328.

Systematization of the newly developed energy density topology optimization method for the interior noise problems

Aya Abe[1*], Dahai Mi[2], Masanori Hashiguchi[2], Ichiro Hagiwara[1]

[1]Meiji Institute for Advanced Study of Mathematical Sciences, Meiji University
[2]Keisoku Engineering System Co., Ltd.
*aya_abe@meiji.ac.jp

Abstract. As an optimization for vehicle interior noise reduction, it is to minimize the integral of sound pressure at the driver's ear position within the frequency band of interest. It has considered to be very effective for this optimization for the eigen frequencies to be moved out of the frequency band of interest. But the present topology optimization method is difficult to deal with this concept. Recently we have developed a high speed and high efficiency control method for plural eigen frequencies by changing topology based on strain energy and kinetic energy distributions of each interest eigen frequency. This new method named “Energy Density Topology Optimization Method” is based on the concept such that it is to raise the stiffness of spring parts and/or to reduce the mass part of the eigen mode for raising the eigenfrequency. Here this new method is shown to be effective for vehicle interior problem. However, systematization is necessary in order to use it interactively, which is a characteristic of this new method.

Keywords: Strain Energy Distribution, Kinetic Energy Distribution, Control for Plural Eigen Frequencies, Energy Density Topology, Optimization Method

1. Introduction

In order to bring an automobile vehicle to market, it is necessary to simultaneously satisfy many of the trade-offs. Advances in computational mechanics have contributed to the revolution of development styles from conventional ones of clay models, prototypes, and experiments to three-dimensional CAD, precise model generation, analysis simulations, and new development styles, thereby contributing to a significant reduction in development time [1]. Interior noise reduction is also addressed by the incorporation of computational mechanics, but there are still problems such as long calculation time and insufficient use of natural frequency information. Therefore, it is examined whether the "new high-speed, high-efficiency eigenvalue control method by phase change based on information on eigenmode distortion and kinetic energy" that is recently developed and systematized can solve the above problems.

2. A new high-speed, high-efficiency eigenvalue control method by phase change based on eigenmode strain and kinetic energy density distribution

In this paper, we will only continue to explain briefly enough to discuss here. The most promising aspect of eigenvalue control is probably the phase optimization method. One of the authors, Hagiwara, applied phase optimization analysis by homogenization method and density method to vibration problems,[2] and also applied it to automobile design.[3] From this experience, it is extremely difficult to bring it to the actual design. What can be obtained by optimization is one with a plate thickness distribution, and it is difficult to manufacture it. Therefore, a certain threshold value is set and a hole is made in the element below it, but at that point it deviates from the convergence value of the angle of the angle. Also, convergence is of course difficult depending on the problem setting. This method shows that it can interactively and efficiently control multiple major changes [4]. In addition, it is shown that a plate with one core by origami forming method is effective for sound insulation characteristics at the low frequency below 500Hz that cannot be compensated with sound absorbing materials depending on the balance between plate thickness and core height [5]. So it is expected to use this type of the plate for this analysis in the future.

3. Analytical Models and Simulations

In the truck cabin model, the sound pressure of the driver's ear position is shown in Fig.1 by applying the vibration in the center point of the floor to the direction perpendicular to the floor. The result obtained by the conventional method of minimizing the integral value of 50-60 Hz is also drawn in the same figure, the integration value has been reduced to 4.16%. where the integral value is calculated by the trapezoidal law based on the value in 0.2 Hz increments. Since the outline is set to be immutable, the design variable is the thickness of all elements except the boundary element, the front, back, top, left and right sides of the truck cabin are the design target, and the total number of design variables is 4. The upper limit of the thickness is 2 mm, the lower limit is 0.3 mm, and the optimum plate thickness values are all about 1 mm, which are reasonable values.

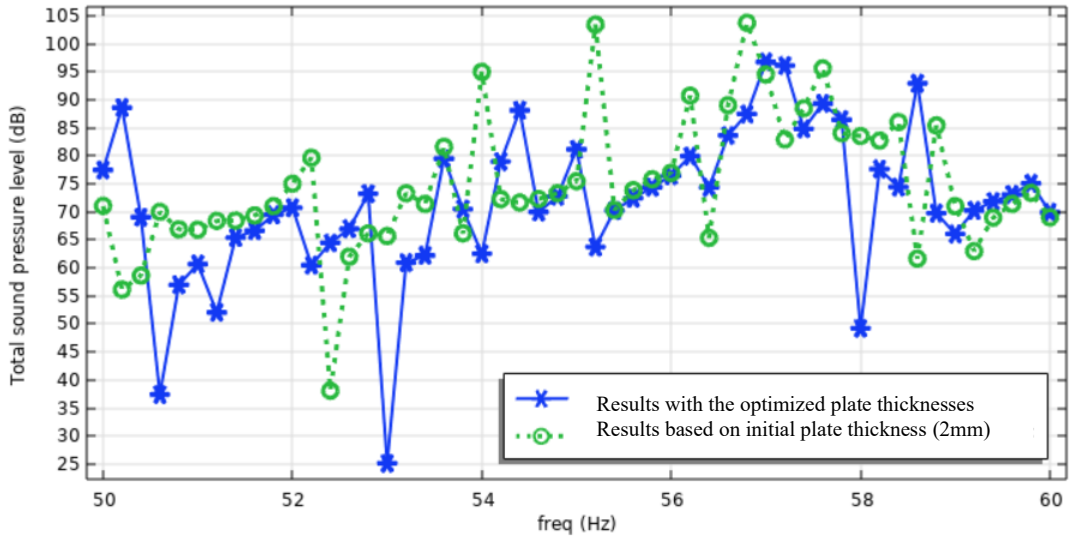

Fig.1 Ear positional sound pressure levels and their optimal results

In contrast, a new method described above will be applied. Therefore, there are 39 natural frequencies between 50-60 Hz. Here, among them, 54 Hz, 55.2 Hz, 56.8 Hz which shows the remarkable sound pressure in Fig.1, The eigenmodes of 53.995 Hz, 55.198 Hz, and 56.853 Hz in the vicinity of them are noted. The strain and kinetic energy distributions of each are shown in Fig. 2. In order to lower the integral value between 50-60 Hz, in order to make the natural frequencies of 53.995 Hz, 55.198 Hz, and 56.853 Hz 60 Hz or more, respectively, a hole is provided in each square or reinforced in the spring part. From Fig.2, it can be seen that the kinetic energy is locally concentrated in the lower half of the front panel and the forward half of the floor panel. Therefore, As shown in Fig.3, the inner plate is set to be deleted. The outer plate keeps and so no holes exists in the model. This corresponds to reducing the plate thickness in the simulation. The sound pressure of the driver ear position at the time of the design specification of Fig.3 is shown in Fig.4. From them, it can be seen that the ear position sound pressure level of the 3 eigenmodes that we paid attention to at the time of design has all decreased. The integral value of 50-60 Hz has been reduced to 5.99% from the initial state. However, in order to use this new method interactively, which is a feature of this new method, the following systematization is necessary, and it will be implemented in the future. 1) Simultaneous visualization of the energy density distribution of the panels surrounding the room, 2) Recalculate just by hovering the mouse over the deleted part of the inner plate, 3) Output of the moving frequency of the natural frequency group in the band, output of the sound pressure level integration value in the band.

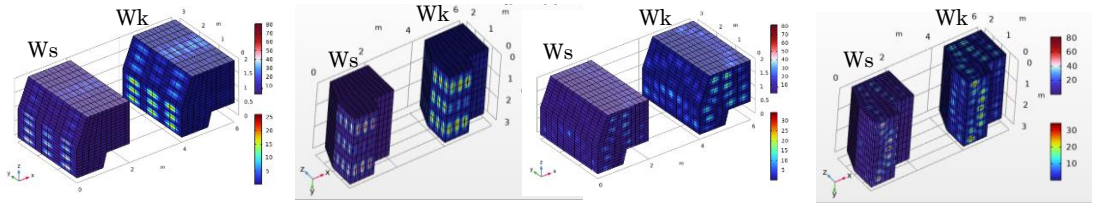

(a) Strain / kinetic energy distribution at 53.995Hz (b) Strain / kinetic energy distribution at 55.198Hz

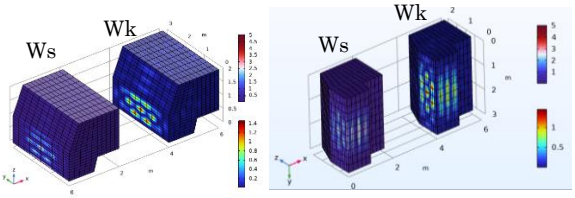

(c) Strain / kinetic energy distribution at 56.853H

Fig.2 Strain and kinetic energy distribution at the time of the target eigenmode, Ws: Strain energy, Wk: Kinetic energy

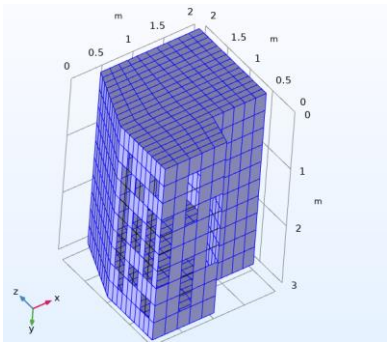

Fig.3 Design changes due to energy distribution

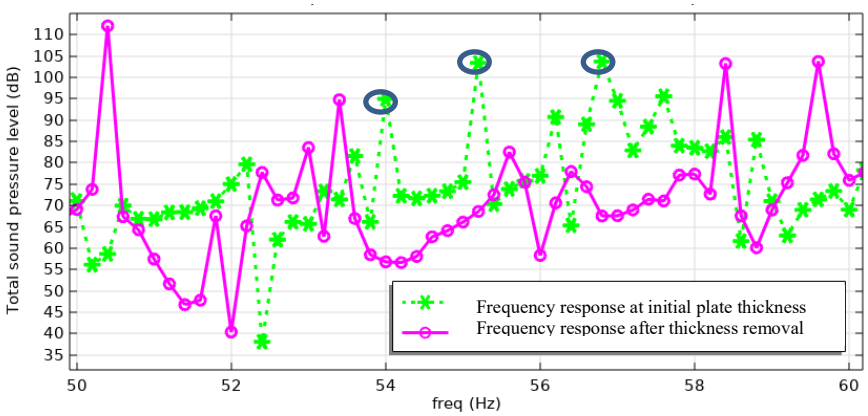

Fig.4 Ear position sound pressure level after design change

4. Conclusion

As an optimization of interior noise reduction, it is possible to minimize the integral value of the sound pressure at the occupant ear position in the frequency band of interest. It is considered effective to drive the resonant frequency that gives a large maximum value out of the band for this minimization. Using the developed method, the effectiveness of a method of ,moving outstanding natural frequencies out of band is found.
Results that show the potential of this technique is obtained. However, systematization is necessary to realize the interactive solution that is a feature of this method, and the contents were described.

References

[1] I. Hagiwara, Dreams and Roadmaps in Computational Science, *Academic Trends*, 619(10),3,2014-10, pp.12-17.

[2] L. H. Tenek and I. Hagiwara, Static and Vibrational Shape and Topology Optimization Using Homogenization and Mathematical Programming, *Comput. Methods in Appl. Mech. Engrg.* ,Vol.109 (1993-10), pp.143-154.

[3] T. Torigaki, I. Hagiwara, Y. Kitagawa, M. Ueda, Z.D. Ma and N. Kikuchi, Development and Application of a Shape-Topology Optimization System Using a Homogenization Method, *SAE International Congress and Exposition*(1994-3).

[4] T. Sasaki, I. Hagiwara, Development of New Phase Optimization Methods and their Application to Origami Boxes, The Japan Society of Mechanical Engineers, Dynamics and Design Conference 2021, *Proceedings of the Lectures Electronic Edition* No.524.

[5] A. Abe, I. Hagiwara, Development of New Sound Insulation Simulation Technology Using Finite Element Method for Efficiency of High Aspect Ratio Core in Low Frequency Range, *International Journal of Mechanical Engineering and Applications*, Vol. 10, Issue 1, February 2022, pp.7-16, DOI: 10.11648/j.ijmea.20221001.12

JSST 2022

Simulation analysis of undressing methods in snakes and arthropods

Taiju Yoneda[1,*] and Kazuya Saito[1]

[1]Faculty of Design, Kyushu University

[*]yoneda.taiju.508@m.kyushu-u.ac.jp

Abstract. The act of undressing is not limited to human clothing, but also in the act of peeling off wrapping paper and in the molting of living creatures. However, there are several modes in the process. The first is undressing that forms a jagged pattern, as seen in the molting of arthropods. For example, ”Loose socks” match this mode, and the diamond pattern in origami is well known. The second mode of undressing is to reverse the front and back of the thin membrane, as in the molting snakes. This mode is similar to socks that has been roughly removed, and is expected to require membrane stretching and low-friction. Numerical analysis was performed to investigate the boundary conditions under which these modes emerge.

Keywords: Thin structure, Membrane, Undressing, Molting

1. Introduction

Thin structures, such as origami, have the structural advantage of being lightweight with a low material cost, and yet can provide high strength due to the folds and other structures. Foldable thin structures, ubiquitous in engineering, arts, and architecture, are currently exploited in a range of applications including solar sails, soft robotics, mechanical metamaterials, and biomechanics[1]. These are functions that manifest themselves not due to material properties by any means, but due to the geometry of thinness, which allows for several properties that volumetric materials cannot. In particular, the rigid origami is a structure of non-deformable panels connected by hinges, and there are significant research results[1, 2]. Rigid origami structure provides a stable development with a geometrically unique driving direction.

Many examples of the use of thin structures have been reported for the bodies of living things, and often has a characteristic that is very different from rigid origami, which has been studied in engineering. Such a thin structure can use not only hinges but also the deformation of bending and streching due to the elasticity of the membrane, allowing for a variety of unfolding behaviors. Finite thickness thin structures are expected to acquire useful development method not found in rigid origami, such as multi-stability with buckling or self-driving by elasticity. To understand geometrical and mechanical properties of

those functional solid systems, the study of deployable thin structures has become an active research field in physics in the last two decades. This paper focuses on the molting process of animal and describes the deformation of thin cylindrical structures that is elastically undressed.

2. Method

Snakes and catapillars with cylindrical bodies have acquired an identical function in that they use the elastic flexibility of their skins to molt. The process of molting is the way many arthropods grow, and generally the old skin is rigid and cannot be molted without a complex process, like undressing a space suit. On the other hand, snakes and catapillars can molt in a shoter time with a simple one axis movement, similar to undressing socks. However, the shape of the molt is quite different. Simply, both can be modeled as a cylinder and a skin which civers it, as shown in Figure 1 (a). Snakes reverse their skin from head with undressing socks roughly, as shown in Figure 1 (c), while catapillars molt by folding their skins like ”Slouch socks”, as shown in Figure 1 (b). The difference between the tow is expected to be due to the streching and bending stiffness of the outer skin. We discuss the work efficiency of molting in each geometric parameter and the mechanical properties are explained by simulation.

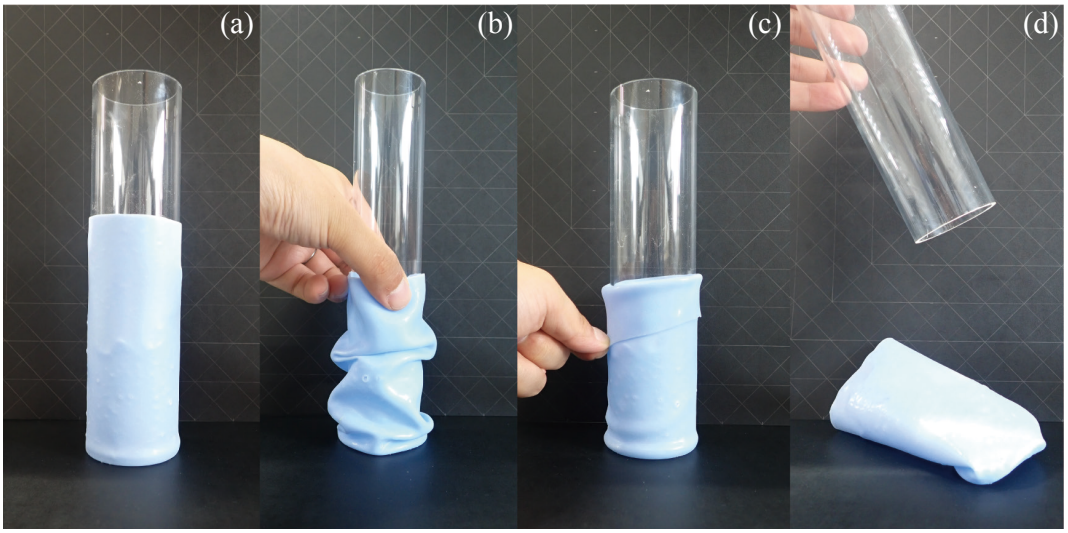

Figure 1: There are many ways to undress the outer skin like (a). (b) How to shed the caterpillar’s skin, such as loose socks. (c) The method of reversing the front and back, like snakes. (d) Molting the outer skin without losing the shape of it, as in arthropods.

3. Result & Discussion

Limited to the results of our experiments, we found that each mode of molting is realized under the influence of the radial gap between the body and the outer skin, the stiffness of the body and the skin, and the friction.

References

[1] P. Jackson: Designing freeform origami tessellations by generalizing resch ' s patterns, *Journal of mechanical design*, 135: 11 (2013).

[2] K. Bertoldi, V. Vitelli, J. Christensen, M. V. Hecke: Flexible mechanical metamaterials, *Nature Reviews Materials*, 2: 11 (2017), 1–11.

Designing of earwig inspired 3D deployable structures based on the algorithmic design tool

Chisaki Kitajima[1*], Kazuya Saito[2]

[1] Graduate School of Human-Environment Studies, Kyushu University
[2] Faculty of Design, Kyushu University
* kitajima.chisaki.218@s.kyushu-u.ac.jp

Abstract. Earwigs fan is the most compactly foldable of all insects, therefore they have great potential for engineering applications. The previous study has already revealed how to design the crease pattern of this earwig fan. Here we showed a new method to create new three-dimensional forms of the earwig fan from a simulation of their folding process with an algorithmic design tool. Furthermore, the method enables to control the position of hinge in order not to interfere each other with an algorithmic design parameter. As a result, we propose the design compact deployable dome-shape structures based on earwig fan folding.

Keywords: Algorithmic design, Biomimetics, Folding Simulation, Origami

1. Introduction

Folding large structures into compact shapes is required in various situations like umbrellas and folding fans to solar battery panels on satellites. In nature, there is the same problem for multiple organisms as represented by insect wing folding. These naturally evolved structures are interesting objects of research from the viewpoint of biomimetics. In particular, the wings of earwigs have the most sophisticated crease patterns enabling the most compact wing folding in insects. As regards the special folding, its process can reduce surface area more than 1/15 depending on the species [1]. Authors revealed the simple geometric rules internalized in the complex folding pattern of these earwig fans [2]. Additionally, the proposed design software can customize the fan shape into various shapes [3]. However, in order to realize the earwig fan to the deployable structures, it is necessary to properly design the shape and arrangement of the hinge and frame besides the crease pattern. Moreover, the proposed design software could only output 2D crease patterns and expanding to 3D structures such as domes and parabolic surfaces remains challenge.
Here we show the design strategy about 3D deployable structures based on earwig fan dome by using the algorithmic design tool. The proposed software can simulate the 3D shape during folding process. In addition, it enables not only to design the shape and position where the frame and hinge do not interfere each other, but also to customize the pattern in accordance with the dome shape.

2. Folding Simulation of Earwig Fan

We developed the folding simulation design tool of earwig fan with Rhino 7 (Robert McNeel & Associates) and Grasshopper [3]. These programs simulates the folding process from the input crease pattern. By adjusting the position of hinges on the simulated fold lines, it enables to confirm whether the hinges are colliding or not during the folding process (Fig. 1).

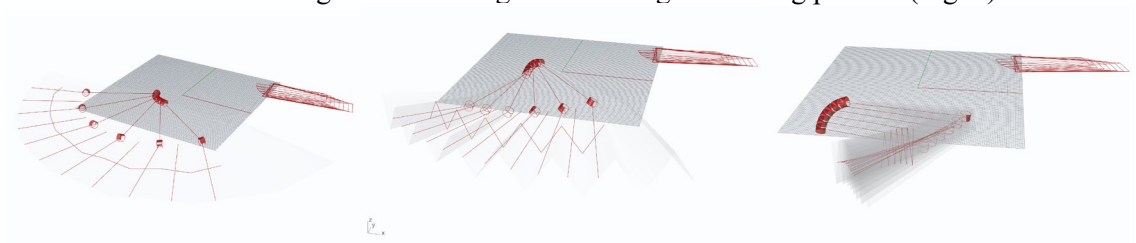

Fig. 1 Folding simulation of the earwig fan.

3. Dome-shape frames of earwig fan

In the proposed simulation technique, the frames and the hinges are arranged on the 2D crease pattern to achieve the same folding mechanism as the origami model. To prevent interference in hinge parts, shafts of hinges are shift to thickness direction according to the diameter of the frames (Fig. 2). Accordingly, this tool assists in designing and simulating a deployable dome-shape structure regardless of types of frames (Fig. 3). Figure 4 shows the prototype of the proposed model made by a 3D printer.

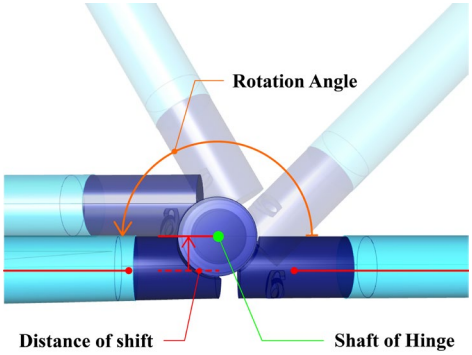

Fig. 2 Shift the shaft of hinge.

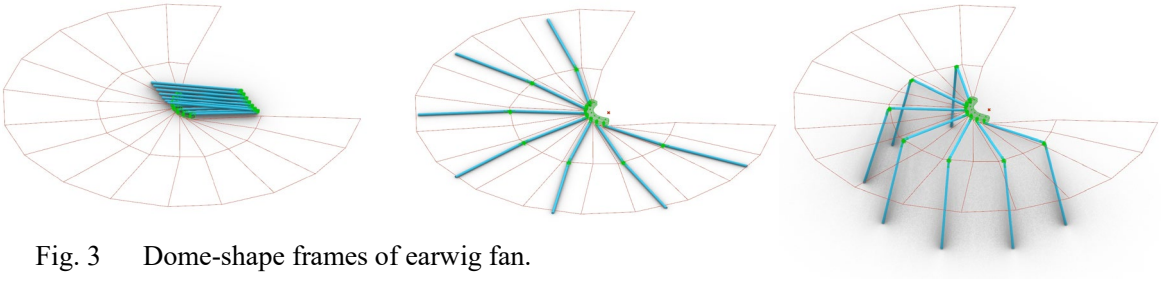

Fig. 3 Dome-shape frames of earwig fan.

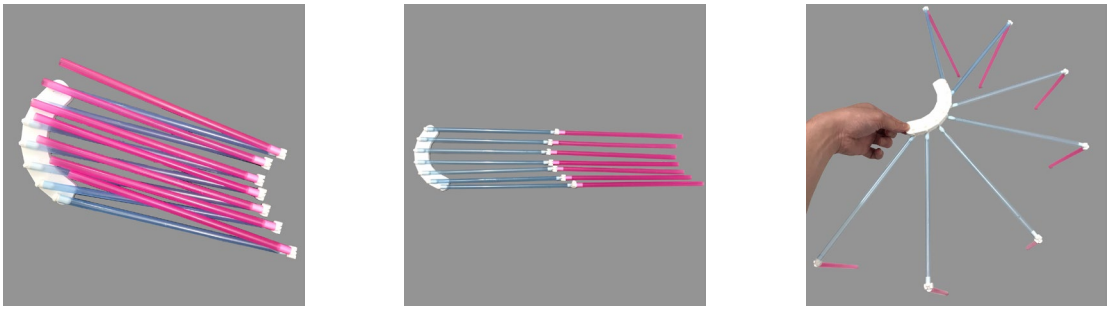

Fig. 4 3D deployable model with 3D printer.

4. Conclusion

We proposed a simulation technique using the algorithmic design tool enabling to expand the 2D crease pattern of earwig fan into the 3D deployable structures. Unlike previous research, this code adjusts the position of the hinges three-dimensionally in consideration of the frame thickness. Thereby, it is possible to design a frame for a deployable dome-shape structure. In addition, the developed software assists in making a model using a 3D printer to confirm the deployment and folding function.

Acknowledgements

This work has been partially supported by JST FOREST (Grant Number JPMJFR203E4).

References

[1] K. Saito, et al.: Earwig fan designing: Biomimetic and evolutionary biology applications, *Proceedings of the National Academy of Sciences,* 117(2020), 17622-17626.

[2] K. Saito et al.: Earwig fan designing: biomimetic and evolutionary biology applications, *Open Science Framework*. https://osf.io/j9ufg/. Accessed 25 June 2020.dd

[3] R. McNeel, Grasshopper (2014). https://www.grasshopper3d.com/. Accessed 18 May 2020.

Computation of laminar-turbulent flow transitions in a circular pipe with a bellmouth inlet

Riku Sato[1], Hiroki Kijima[1], Tomotaka Kobayashi[1], Ken Naitoh[1*]

[1]Factuly of Science and Engineering, Waseda University, Japan

*k-naito@waseda.jp

Abstract. We proposed the numerical method called “stochastic determinism” based on the stochastic Navier-Storks equation to compute the transition point from laminar flow to turbulent flow in internal flows, which revealed the transition point in a circular pipe while varying inlet disturbance. An important point of our method is that the level of indeterminacy is determined by the intensity of inlet disturbance. And also, it’s included the finite difference method based on the multi-level formulation which accurately computes the spatial derivatives of physical and integrated quantities. In this research, we clarify the transition point of an incompressible flow in a circular pipe with a bellmouth inlet to compare the experiments by Kanda. We computed for various cases of Reynolds number.

Keywords: Numerical method, Internal flow, Stochastic determinism, Turbulence, Transition

1. Introduction

Predicting the transition point to turbulence is crucial for research on laminar airfoils, next-generation engines, blood flow, and so on. In recent, Large Eddy Simulation (LSE) and Direct Numerical Simulation (DNS) are used for calculations based on the deterministic Navier-Srokes equation. However, due to the cyclic boundary condition between the inlet and outlet, the spatial transition point where the laminar flow changes into turbulence couldn’t be captured[1,2].

Therefore, we proposed the new method called “stochastic determinism”, where widow-scale for averaging smaller than Kolmogorov scale is employed [3,4,5]. This smaller window-scale theoretically leads to the fact that we added the random fluctuation of density or velocity to the deterministic Navier-Stokes equation in order to capture the transition point by resolving the exceedingly thin early boundary layer.

Equation (1) is the stochastic incompressible Navier-Stokes equation in the non-conservative form derived by “stochastic determinism”[3,4,5] as the governing equation, which is transformed by multil-level formulation [7, 8].

$$\begin{bmatrix} \dfrac{\partial \bar{u}_i}{\partial t} + \sum_j \bar{u}_j \dfrac{\partial \bar{u}_i}{\partial x_j} + \dfrac{\partial \bar{p}}{\partial x_i} - \dfrac{1}{Re} \sum_j \dfrac{\partial^2 \bar{u}_i}{\partial {x_j}^2} \\ \sum_i \dfrac{\partial \bar{u}_i}{\partial x_i} \\ \sum_i \dfrac{\partial^2 \bar{p}}{\partial {x_i}^2} + \dfrac{\partial}{\partial t}\left(\sum_i \dfrac{\partial \bar{u}_i}{\partial x_i} \right) + \Phi \\ \int_V \sum_i \dfrac{\partial \bar{u}_i}{\partial x_i} dV \end{bmatrix} = \begin{bmatrix} \varepsilon_1 \\ \varepsilon_2 \\ \varepsilon_3 \\ \varepsilon_4 \end{bmatrix} \quad (1)$$

where, $\bar{u}_i, \bar{p}, \varepsilon_i$, Re, Φ, t and V denote the dimensionless quantities of velocity components in derection i, pressure, random fluctuations, Reynolds number, the spatial derivative of the convection term, and control volume respectively. Each equtation describes the law of conservation of momentum, the law of conservation of mass, the Poisson equation of pressure, and the overall mass conservation.

An important part when we use this equation is how to determine ε_2, which is the level of indeterminacy of the law of the conservation of mass. In our recent research, we proposed that ε_2 is proportional to the intensity of practical inlet disturbance δ, which is calculated from the divergence of flow velocities. As both of inlet disturbace and internal random fluctuation are indeterminat, we hypothesize that these two levels are identical.

$$|\varepsilon_2| = Ce|\delta| \quad (2)$$

Constant Ce in the proportional expression is the arbitary one [3,4,5]. In this research, we set constant Ce to 1. For regular grid system, the value of ε_2 can be controlled by the number of iterations of SOR-method[5], while we will given the values for ε_2. by using random number generator after reducing strongly the divergence of velocity.

The computational domain that we use is shown in Figure.1. In the present study, we computed vairous cases of Reynolds number for comparing with the boundary conditions of non-slip condition at the wall, the Neumann boundary condition for flow velosity at the outlet and pressure at all of boundaries, and a fix constant velocity at the inlet. The potential flow is given as the initial condition. We used a staggered grid for avoiding a large numerical error that happens when we use a regular grid. Figure.2 shows an example of our computational result of vorticity at 50 seconds.

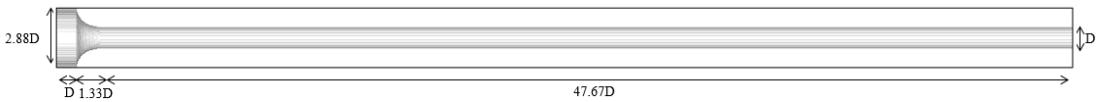

Fig.1 The computational domain

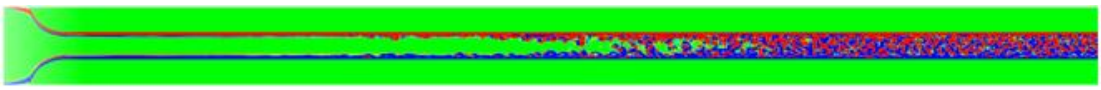

Fig.2 An example of computational result of vorticity(Re=20265)

The total domain consists of 51,840,000 grid points (2500×144×144), of which 4,844,447 grid points configure the shape between bellmouth and pipe, which is quite similar to the shape of Kanda's experiments[6].

2. Computational Result

For five Reynolds numbers, the computational results of transition lengths and inlet disturbances are shown in Table.1. The acceleration factor for the SORmethod is given to be 1, following the previous study[5]. We will also show the comparison of Kanda's experiments and our calculations with a picture of vorticity at 50 seconds in Fig 3.

Table.1 Computational results of transition point and inlet distubance

Reynolds number	Inlet disturbance δ	Transition length
Re=13510	0.676 %	29D
Re=13581	0.669 %	28D
Re=16405	0.768 %	24.1D
Re=18142	0.802 %	23.9D
Re=20265	0.838 %	23.1D

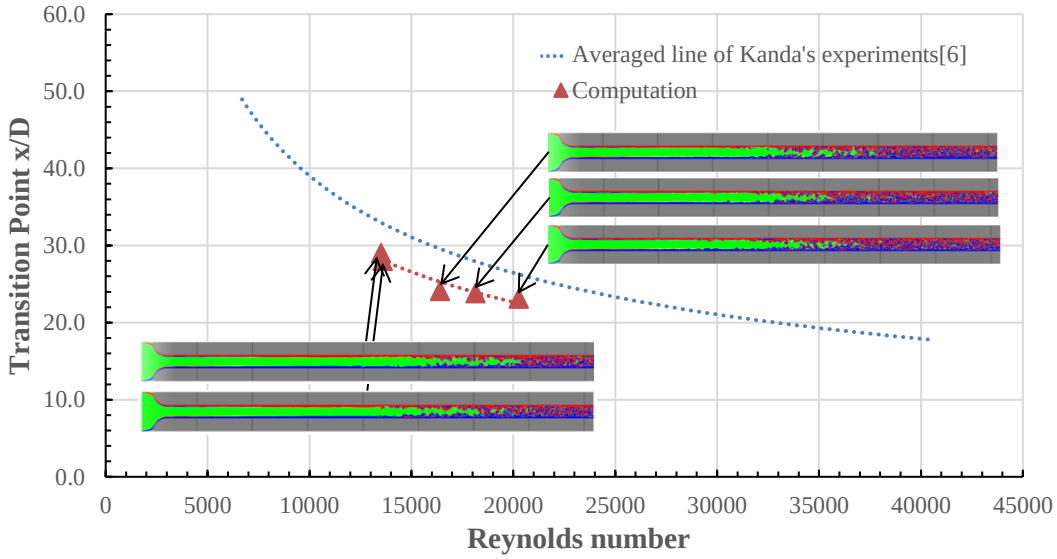

Fig.1 Comparison of computations and experimental results by Kanda

Reynolds number and the inlet disturbance affected the transition point from laminar flow to turbulence. The inlet disturbaces in the present computations are almost at an identical level, i.e., a constant inlet disturbance. Thus, computational results on transition lengths become monotonously shorter according to increasing Reynolds numbers, which are close to the averaged values of the experimental results of Kanda's experiments [6]. The averaged line added in Fig.3 is obtained by using a power approximation of the thirty experimental results for Reynolds numbers rasing from 6690 to 40530 done by Kanda [6]. All computational results of us are a little smaller than the averaged values of experiments. However, the whole computational results of us lie in the dispersion width of experimetns of Kanda [6], about the range having width of ±10 for x/D.

3. Conclusion

We computed the transition processes from laminar flow to turbulence, while revealing the spatial laminar-turbulent transition point in a circular pipe with a bellmouth inlet for varying Reynolds numbers, by using the approach based on stochastic determinism. In the very near future, we will also examine influence of inlet disturbance level on the transition point.

References

[1] P. Moin, J. Kim: *Numerical investigation of turbulent channel flow*, J. Fluid Mech,118 (1982), pp. 341-377.

[2] T. Kawamura, K. Kuwahara: *Direct simulation of a turbulent inner flow by finite-difference method,* AIAA paper 85-0376 (1985).

[3] K. Naitoh, Y. Nakagawa, H. Shimiya: *Stochastic determinism approach for simulating the transition points in internal flows with various inlet disturbances*, Proceedings of 5th International Conference on Computational Fluid Dynamics, (ICCFD5) (also in Computational Fluid Dynamics 2008, Springer, 2008), pp.671-676.

[4] K. Naitoh, H. Shimiya: S*tochastic determinism for capturing the transition point from laminar flow to turbulence*, Japan J. of Industrial and Applied Mathematics (2011), pp.3-14.

[5] H.Kijima, K.Naitoh, T.Kobayashi, Y.Yamashita: *Spatial transition point from laminar flow to turbulence in a circular pipe with bellmouth inlet by solving a weakly-stochastic Navier-Stokes equation*, AIAA 2021-0631(2021), pp.1-12.

[6] H.Kanda: *Numerical Study pf the Entrance Flow and its Transition in a Circular Pipe*, The Institute of Space and Astronautical Science Report, No:626 (1988)

[7] K. Naitoh and K. Kuwahara: *Large eddy simulation and direct simulation of compressible turbulence and combusting flows in engines based on the BI-SCALES method*, J. of Fluid Dynamics Research (1992), pp. 299-325.

[8] K. Naitoh, K. Kuwahara et al.: *Cycle-resolved computation of compressible turbulence and premixedflame in an engie*, Computers and Fluids (1993), pp. 623-648.

JSST 2022

On a simple dynamical map with a flooring function

Toru Ohira[1,*]

[1]Nagoya University, Japan

[*]ohira@math.nagoya-u.ac.jp

Abstract. We report here a computational study of a recently proposed simple dynamical map. In spite of its simplicity, it offers wide variety of dynamical paths depending on the initial value. Some analytical properties and future directions are also discussed.

Keywords: Dynamical map, Recursion relation, Nonlinear dynamics

1. Introduction

Investigations of dynamical maps have gained much attention in mathematical sciences. Representative example is a logistic map[1, 2] that has been investigated extensively. Many researchers are intrigued by the chaotic dynamics produced by this very simple map.

Against this background, we numerically study here a recently proposed dynamical map, which we call the "N-map". In spite of its simplicity, this map gives rise to a variety of dynamical patterns; monotonic approach to a single fixed point, divergence, oscillations. Interestingly, the map does not contain any tuning (bifurcation) parameter and all these can be achieved solely by the change of the initial value. Some analytical properties are also discussed as well as future extension of the study of the N-map.

2. N-map

The N-map is given by the following first order recursion relation.

$$X_{n+1} = 3F[X_n + \frac{1}{2}] - 2X_n, \quad X_0 = a, \quad (0 < a < 1, \quad n = 0, 1, 2, \dots). \tag{1}$$

where $F[x]$ is a flooring function which returns largest integer N with $N \leq x$.

We can analytically prove some properties of this map, such as

- If $X_n - F[X_n] \geq \frac{1}{2}$, then $X_n < X_{n+1}$,
- If $a = \frac{1}{3}$, then $X_\infty \to -\infty$,
- If $a = \frac{2}{3}$, then $X_\infty \to \infty$,

- If $X_n > X_{n+1}$, then $F[X_{n+1}] = F[X_n] - 1$.

However, details of dynamical path has not been investigated analytically.

We performed numerical simulation for this map with varying the initial value a. The representative results are shown in Fig. 1. These representative path show variety of dynamical patterns out of this simple map just by change of initial value a: monotonic convergence, non-monotonic convergence, oscillations, complex oscillatory path, divergence. We confirm the divergences for $a = 1/3$ and $a = 1/3$ as stated above. In Figure 2, we also see a curious relation between the dynamics of a and $1 - a$. They are connected by phase and base shifts.

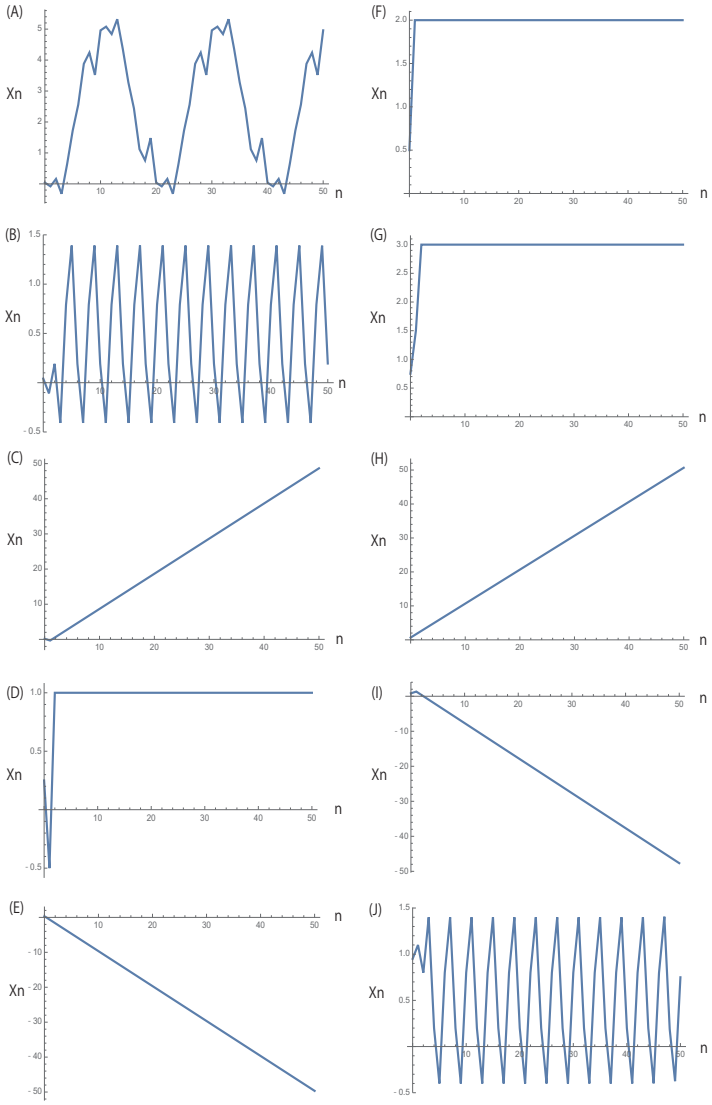

Figure 1: Sample of Dynamical Paths from the N-map. The values of a are (A) 0.04, (B) 0.05, (C) 1/6, (D) 1/4, (E) 1/3, (F) 1/2, (G) 3/4, (H) 2/3, (I) 5/6, (J) 0.95

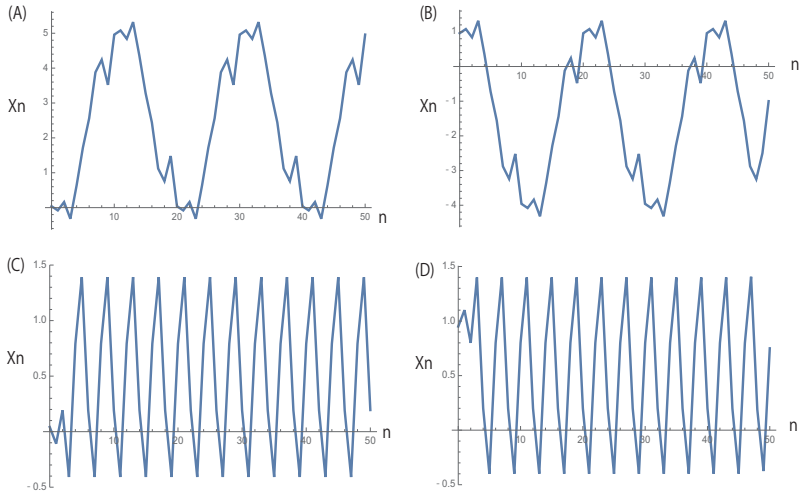

Figure 2: Sample of Dynamical Paths from the N-map for a and $1-a$. The values of a are (A) 0.04, (B) 0.96, (C) 0.05, (D) 0.95

3. Discussion

We have presented rather preliminary numerical study of a simple map with a flooring function. More thorough investigations are needed to reveal the nature of this N-map. The natural extension of the N-map is given as

$$X_{n+1} = \alpha F[X_n + \frac{1}{2}] - \beta X_n, \quad X_0 = a, \quad (0 < a < 1, \quad n = 0, 1, 2, \dots), \tag{2}$$

With the real parameters α and β. We expect to see more intricate dynamics for some ranges of these parameters.

Acknowledgements

The author would like to thank Prof. Hiroyuki Nakaoka of Nagoya University for his enlightening comments. This work was supported by funding from Ohagi Hospital, Hashimoto, Wakayama, Japan, and by Grant-in-Aid for Scientific Research from Japan Society for the Promotion of Science No.19H01201.

References

[1] R. M. May: Simple mathematical models with very complicated dynamics, *Nature*, 261 (1976), 59—467.

[2] R. L. Devaney: *An Introduction to Chaotic Dynamical Systems Second Edition*, Perseus Books Publishing, (1989).

[3] This map first appeared in the entrance examination of Nagoya University (Japan) on February 26, 2021.

Automatic generation of training data for AI for posture estimation of demolition heavy machinery in CG

Hideo Miyachi[1*] and Koshiro Murakami[2]

[1]Department of Simulation, School of Technology, Tokyo City University
[2]Graduate School of Environmental and Information Studies, Tokyo City University
*miyachi@tcu.ac.jp, g2293014@tcu.ac.jp

Abstract. The practical application of image processing using machine learning is progressing. However, the cost of creating training data has become a bottleneck in some fields, and practical application has not progressed. We have developed a system to support the creation of process charts for heavy demolition equipment using AI-based posture estimation to improve the process of home appliance recycling, but the problem is that it is necessary to create corresponding training data for various types of heavy demolition equipment. To solve this bottleneck, we have developed a computer graphics-based system for automatically generating training data for machine posture estimation. By using the training data generated with this system, the posture of heavy machinery in CG was estimated almost accurately.

Keywords: AI, Posture estimation, Computer Graphics,Data Augmentation

1. Introduction

We analyzed work processes in the A-STEP project sponsored by JST (Japan Science and Technology Agency) using machine learning posture estimation (Openpose) to examine differences in work behavior between skilled and unskilled workers.[1,2] At this time, two types of analysis were conducted: demolition work by human hands and demolition work using heavy machinery. Many training data have been published for human posture estimation. However, training data for heavy demolition equipment, whose size and moving parts differ from job to job, had to be created individually, and a lot of time was required to create the training data. 2000 images were marked while a human visually checked the joints of the heavy equipment. This was a very time-consuming process, and ordering this work from a company would have resulted in high costs. It also became clear that there was no way to check the accuracy of the training data because the work was manual.

Many researchers have pointed out that acquiring large amounts of training data is a challenge for machine learning [3,4]. To solve this problem, many methods of data augmentation and automatic generation of training data have been proposed [5]. Most of the methods are based on generating a large number of images from a small number of photographs, while leaving the necessary information for classification. On the other hand, the effectiveness of methods that generate training images using images rendered from 3D models has also been

suggested [6]. Here, the effect of rendering parameters on estimation performance was investigated, and realism was shown to be important. They also point out that adding a few real-images improves the accuracy. In this study, we tried to use this 3D rendering-based training data generation method to estimate the attitude of a dismantling heavy machine. As a first step, we created a very simple model of a heavy demolition machine and developed a system to automatically generate training data using 3D rendering. As a test of the system's performance, we verified its accuracy by performing posture estimation on rendered images of the same model of a heavy demolition machine.

2. Process analysis by posture estimation of demolition heavy machinery

Figure 1 shows an image of a heavy demolition machine dismantling a household appliance (outdoor unit of a cooler) with posture estimation and skeletal information overlaid. The machine is shaped like a crane. The tip of the arm has a scissors-like structure, which is used to dismantle the home appliance. The dismantled parts are sorted into several baskets placed around the heavy machine according to their materials.

Fig.1 Posture estimation results for the heavy demolition machinery in A-STEP project

Figure 2 is a graph showing the left and right positions of the "wrist" of this machine within the photograph. The horizontal axis represents time, and the vertical axis represents the left-right position of the "wrist. The coordinates are normalized to ±1, with the arm in front of the machine as 0, the left side as minus, and the right side as plus in the photograph. Operations with a vertical axis near zero indicate the operation of dismantling the appliance, while waveforms with upward peaks indicate the operation of placing the dismantled parts into the basket. A large waveform greater than 0.9 indicates when the parts are placed in the rightmost basket, which signifies the end of one cycle of disassembly operations. This interpretation of the graph reveals that five appliances were dismantled in the video shown in Figure 2.

This posture estimation is based on the VGG-19 model[8] used in Openpose[9] for human posture estimation.The training data consisted of approximately 2,000 images extracted from the video of the demolition heavy equipment shown in Figure 1. Using the annotation creation tool: cco-Anotater, five workers visually judged 12 joint positions and clicked on them with the mouse to create the correct image. The system estimates posture with sufficient accuracy to enable automatic calculation of the number of units to be demolished and processed from the video. However, after the development of this system was completed, the heavy demolition machinery was updated to a slightly smaller machine with the same capabilities The system analyzed the working videos of the new machine, but could hardly estimate the posture of the

machine. It is assumed that the system would work correctly if training data of 2000 images were manually generated again, but it is difficult to generate training data every time a machine is updated.. Therefore, we started a project to develop a system to automatically generate training data for posture estimation of such heavy demolition machinery by rendering 3D CAD data with computer graphics.

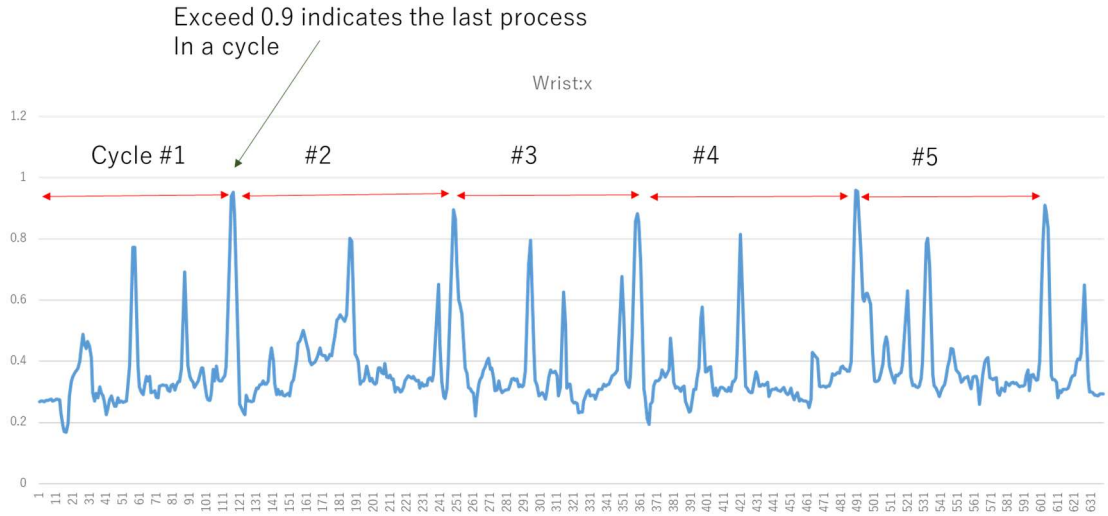

Fig.2 Waveforms of attitude estimation output by the system developed in the A-STEP project

3. Overview of the proposed system

Our proposed system for automatic generation of training data consists of four programs, as shown in Fig. 3.

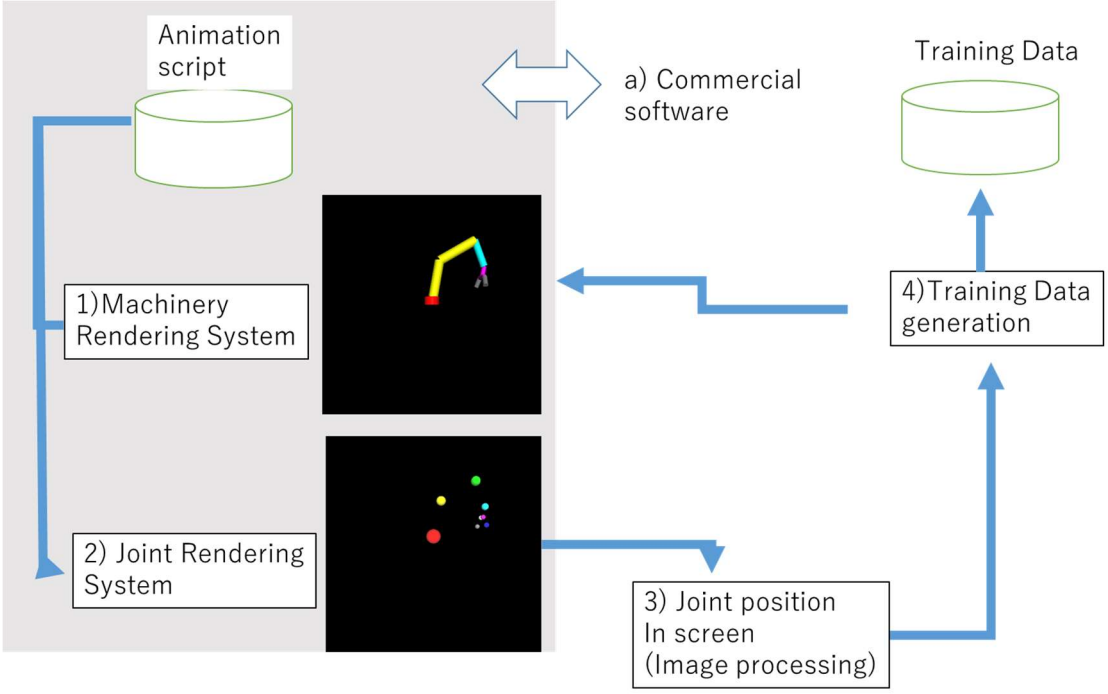

Fig.3 Overview of proposed auto-training data generation system

The 1st program renders the machine. Currently, a model of a heavy demolition machine is coded in the program. The model consists of eight cylinders as shown in Figure 4 and listed in Table.1. Cylinder 1 constitutes the body, 2 and 3 the upper arms, 4 the lower arms, 5 the wrists, 6 the palms, and 7 and 8 the right and left fingers, respectively. The 2nd program renders the spheres placed at the joints of the machine. The joints are the five locations from A0 to A4 in Figure 4 and listed in Table.2. The 1st and 2nd programs operate according to the description of the animation script file defined in this system. Thus, when the two programs are run using the same animation script, the two programs display the machine in the same posture. The center position of the sphere rendered by the 2nd program will be the same pixel position on the screen as the joint position of the machine displayed by the 1st program. The 3rd program is an image processing program that extracts the center position of the sphere in the rendered image generated by the 2nd program. Finally, the 4th program generates the training data necessary for posture estimation, including the information on the joint positions extracted by the 3rd program and the path information to the rendered image generated by the 1st program. The part of Fig. 4 a) containing programs 1 and 2 will be replaced in the future by commercial software with animation capabilities, e.g., blender.

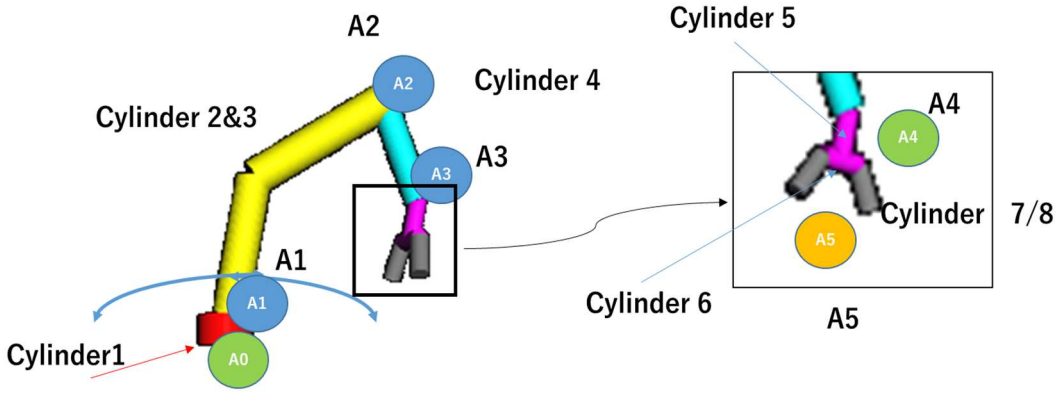

Fig.4 Machinemodel and joint locations

Table.1 Parts list

Cylinder No.	Name
1	BODY
2	UPPER ARM
3	
4	LOWER ARM
5	WRIST
6	PALM
7	L-FINGER
8	R-FINGER

Table.2 Joint list

JOINT Name	Angle making cylinder	Notice
A0	BODY	Horizontal rotation
A1	BODY-UPPER ARM	Up/Down
A2	UPPER ARM-LOWER ARM	Up/Dwown (ELBOW)
A3	LOWER-ARM WRIST	Up/Down
A4	WRITE-PALM	Horizontal rotation relative to wrist
A5	PALM-L/R FINGER	OPEN/CLOSE

4. Experiment

The proposed system was used to create 695 rendered images and training data. The computation time for the creation of the data is a few seconds since it is generated automatically by the

program. Currently, the time is required because it includes manual work such as copying files. It then took 28 minutes to train these. Four rendered images of the posture that were not used for training were allowed to estimate the posture. Figure 5 shows the skeletal information overlaid on the rendered images and the average of the five joint certainty scores. The scores ranged from 86.7% to 98.9%. In addition, all of the posture estimates were accurate based on visual judgments.

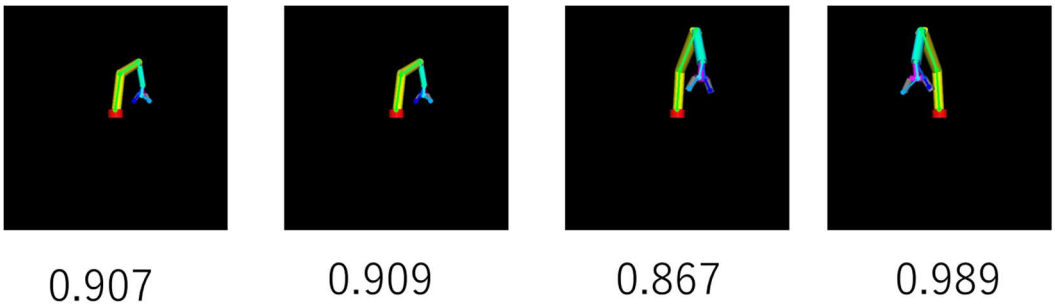

Fig.5 Experimental results. The figure shows the skeletal information resulting from the posture estimation superimposed on the rendered image.The number is the average of the five joint scores (certainty).

5. Conclusion

Machine learning is used to estimate the posture of heavy equipment for demolition for use in improving recycling operations. However, the problem is that new training data for posture estimation must be created each time new heavy equipment is introduced. To solve this problem, we are aiming to develop a system that automatically generates training data for posture estimation using computer graphics from 3D CAD model data. As a first step toward this goal, we have developed a prototype system that automatically generates the training data. Using this system, training data was automatically generated from 695 3D rendered images. The training results showed that the system was able to correctly estimate postures with more than 86% certainty, even for postures that were not used in the training. In the future, we plan to apply the system to more complex models and to investigate the relationship between rendering parameters and estimation accuracy.

References

[1] Minagi Miyokawa,Mami Kimura,Takumi Yamane,Koshiro Murakami,Hideo Miyachi：A Study on Motion Analysis of Disassembly Work of Home Appliances Using Arm Posture Information Obtained by Openpose、Proceedings of 7th International Symposium on BioComplexity、2022.1

[2] Takumi Yamane,Mami Kimura,Minagi Miyokawa,Koshiro Murakami,Hideo Miyachi：Process Visualization and Verification of Improvement Methods and Effects、Proceedings

of 7th International Symposium on BioComplexity、2022.1

[3] Akiko Kato, Miki Hori, Tadasuke Hori, Makoto Jincho, Hironao Sekine and Tatsushi Kawai:Generating Training Data Using Python Scripts for Automatic Extraction of Landmarks from Tooth Models, Journal of Hard Tissue Biology 31[2] (2022) 95-100 2022 The Hard Tissue Biology Network Association Printed in Japan, All rights reserved. CODEN-JHTBFF, ISSN 1341-7649

[4] Tsukasa Kudo:Application Method of Deep Learning Model Trained with CG Images to Real Images.,January 2021 Procedia Computer Science 192(1):1484-1493 DOI:10.1016/j.procs.2021.08.152

[5] Shorten, C., Khoshgoftaar, T.M. A survey on Image Data Augmentation for Deep Learning. J Big Data 6, 60 (2019). https://doi.org/10.1186/s40537-019-0197-0

[6] Movshovitz-Attias, Yair & Kanade, Takeo & Sheikh, Yaser. (2016). How useful is photo-realistic rendering for visual learning?. https://www.researchgate.net/publication/301837317_How_useful_is_photo-realistic_rendering_for_visual_learning

[7] K. Simonyan and A. Zisserman, "Very deep convolutional networks for large-scale image recognition," in ICLR, 2015.

[8] Zhe Cao, Gines Hidalgo, Tomas Simon, Shih-En Wei, Yaser Sheikh: OpenPose: Realtime Multi-Person 2D Pose Estimation using Part Affinity Fields, Computer Vision and Pattern Recognition, arXiv:1812.08008v2, *18 Dec 2018 (v1), last revised 30 May 2019 (this version, v2)*

JSST 2022

Relationship between size perception and vergence in virtual space

Hiroyuki Makino[1*], Nobuaki Ohno[1*], Yuichi Tamura[2]

[1] Graduate School of Information Science, University of Hyogo

[2]Faculty of Intelligence and Informatics, Konan University

*ohno@gsis.u-hyogo.ac.jp

Abstract. Differences in the perceived size of objects in virtual reality (VR) and real space have been researched. In particular, these studies have shown that objects are perceived as smaller than their original size in VR environments. However, no studies have focused on eye movements and investigated the relationship between eye movement and size perception. Our purpose of this study is to quantitatively clarify the relationship between eye movements and size perception by measuring eye movements during VR image experiences.

Keywords: Virtual Reality, vergence, Head mount display, Vergence angle

1. Introduction

Virtual reality (VR) devices enable users to experience reality that cannot be experienced in real space. The range of VR applications is wide and includes entertainment and various training systems. In recent years, many consumer-oriented VR devices, especially head-mounted displays (HMDs), have been released, making the VR experience more accessible. However, there is a problem that objects displayed in a VR space are perceived as smaller than their original size when experiencing a VR space using an HMD. This not only reduces the sense of immersion in the VR environment, but also becomes an obstacle when conducting rigorous experiments.

Itaguchi [1] has studied "reaching": the behavior of reaching out and grasping an object in a VR environment and showed that objects in a VR environment are perceived to be about 5% smaller than they actually are, whether they are virtual hands or objects used daily. Hamamoto et al.[2] assumed that objects appear to be far away based on the results of reaching, and have studied how to correct the images by adjusting the distance between the screens presented to both eyes of the HMD. In a study comparing the size perception of objects in real space and in a mirror, participants were asked to indicate the distance between an imaginary image in a mirror of an object behind them and the experimental participants, and it was shown that they

perceived objects smaller in the mirror than in real space [3].

We already conducted an experiment regarding convergence in VR environment. The experiment is as follows. In order to investigate eye movements in a VR environment, we used eye tracking function of an HMD (fig. 1: HTC VIVE Pro Eye, [4]) to measure the convergence distance, which is the distance between the eye and the object being viewed. In the experiment in which we measured the convergence distance while changing the distance by moving the object, we found that the participants looked farther from the object in the VR environment than they did in the actual environment. When we displayed a gazing object in a VR environment and measured the convergence distance of the participants, we found that the distance from the viewpoint to the object in the VR environment was almost the same as the convergence distance. On the other hand, in the experiment in which the convergence distance was measured dynamically by moving the gazing object and changing the distance between the viewpoint and the gazing object, the distance between the viewpoint and the gazing object in the VR environment was longer than that in the VR environment, which means that the participants gazed farther. When VR images are presented using an HMD, the distance between the image presentation surface (LCD display surface) and the eyeball is constant, so the convergence distance is considered to be a constant distance rather than the distance to the target, but we obtained different results from this.

Previous studies have not investigated eye movements during size perception in VR environments in detail, and the relationship between size perception has not been clarified. Therefore, the purpose of this study is to investigate the relationship between the convergence distance and the participant's subjective perception of the object in a VR environment.

2. Experimental method

2.1 System configuration

The VIVE Pro Eye HMD is used as a VR device (Fig. 1). Since the VIVE Pro Eye is equipped with an eye tracking function that can measure visual line, this device can measure the detail of participant’s eye movements while wearing the HMD.

Figure 1. Head Mounted Display (VIVE Pro Eye)

The Unity, a game engine, is used to create the VR experimental environment. A pupillary distance (PD) meter (NIDEK, PM-700) is used to measure the distance between the participant’s eyes.

2.2 Experimental procedure

We will conduct an experiment similar to the experimental procedure of Itaguchi [1]. The PD of the participants in the experiment is measured using a PD meter. Using this distance,

optically accurate images are presented on the LCDs for both eyes of the HMD.

Participants confirm the shape of a 350 ml soft drink can in real space beforehand, and then wear individually adjusted HMDs to observe a 3D model of the can (Figure 2), which is the same size as that observed in real space in the VR environment. Next, 36 patterns of can models were prepared, ranging from 0.6 to 1.3 times the original size in 0.02-fold step increments, and these models are randomly presented to the participants.

Figure 2. A 3D can object presented in a VR environment

The participants answer how they felt the model of the can in the VR space was "bigger", "smaller", or "actual size" compared to the size of the actual can they had observed beforehand. In order to investigate the influence of the image of the size of the can in the real space, the participant puts off his/her HMD and reconfirm the size of the can in real space every time they see a few patterns of the can in the VR experimental environment. The frequency of this reconfirmation is every time the size of the cans in the VR environment is changed (Figure 3(a)) and once in every six patterns (Figure 3(b)).

The eye movements of participants is measured with changing the size of the can in VR space.

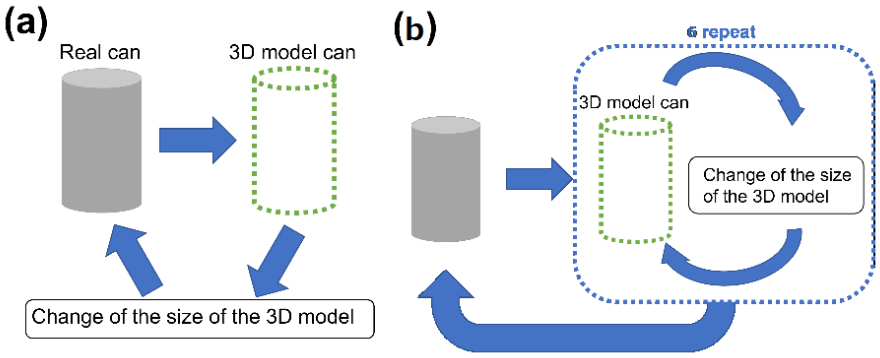

Figure 3 Participant reconfirm the real size of the can. (a) every time, (b) once in every six times.

2.3 Preliminary experiment

We carried out a preliminary experiment with three male participants in their 20's, 40's and 50's to measure the point of subjective equalities (PSE). The measured PSEs are 1.100 (for every time reconfirmation of the real can) and 1.098 (for once in six times). Therefore, the cans

in the VR space are perceived to be about 10% smaller than they actually are in our preliminary experience, which shows that they are perceived smaller than the previous study. We will increase the number of participants and investigate it in more detail.

Acknowledgement

This work was supported by Grant-in-Aid for Scientific Research (KAKENHI) 18K11416.

References

[1] Itaguchi, Y., Front. Virtual Real. 2:712378. (2021) , doi: 10.3389/frvir.2021.712378

[2] Hamamoto, K, IEICE technical report, 116 (104), pp.35-38 (2016) (in Japanese)

[3] Higashiyama, A, Journal of the Virtual Reality Society of Japan,Vol. 22, No. 4, pp. 15-21 (2017) (in Japanese)

[4] https://www.vive.com/us/

Continuous quantity visualization of time history response analysis results using individual building attributes

TSUTSUI Kanta [1*], HONDA Rina [2], NAGANO YASUYUKI [3]

[1] Graduate School of Information Science. University of Hyogo.
[2] former Graduate School of Simulation Studies. University of Hyogo.
[3] Graduate School of Disaster Resilience and Governance. University of Hyogo.

* ad21u008@gsis.u-hyogo.ac.jp

Abstract. Japan is one of the most earthquake-prone countries in the world. With the recent development of computers, methods for modeling individual buildings in a city and conducting seismic response analysis for the entire city have begun to be used. The purpose of this study is to visualize the results of the maximum interlaminar deformation angle from an urban-scale seismic response analysis as a continuous quantity using color bars without a threshold value.

Keywords: Disaster Prevention, visualization, Response Analysis, Disaster Prevention Planning

1. Introduction

Japan is one of the most earthquake-prone countries in the world and has experienced several major earthquakes in the past. Based on the experience of earthquake damage, countermeasures against future earthquakes are becoming increasingly important, and earthquake damage prediction is indispensable for urban disaster prevention planning. Conventional methods for predicting damage to buildings on an urban scale are based on damage rate curves. This method can predict damage to an entire city in a simple manner, but it is impossible to predict damage to individual buildings. On the other hand, recent advances in computer performance have made large-scale calculations possible, and the RIKEN Center for Computational Science (R-CCS) Research Team for Integrated Earthquake Simulator (hereinafter referred to as "IES") is conducting research and development [1]. IES is a platform for storing seismic analysis models of ground and buildings. By storing vibration models appropriate for individual buildings in a city and applying them appropriately to the platform, it is possible to predict damage to city-scale buildings with high accuracy. Honda et al. classified the results of seismic response analysis of the Fukura district in Minami-Awaji City, Hyogo Prefecture, as an example, into three damage categories by setting a threshold value for the maximum inter-story displacement, and conducted urban damage prediction [2]. While the

damage prediction with threshold values has the advantage of clarifying the damage categories, it also has the disadvantage of classifying different damage categories even if the difference in the maximum interlaminar deformation angle is negligible. The objective of this study is to visualize the results of the maximum interlaminar deformation angle from an urban-scale earthquake response analysis as a continuous quantity without a threshold value.

2. Setting up an urban scale time history response analysis

The Fukura area of Minami-Awaji City, Hyogo Prefecture (hereinafter referred to as "the subject area") is the closest to the epicenter of a hypothetical Nankai earthquake in the prefecture, and is predicted to have a large potential for extensive damage from an earthquake and tsunami. In this report, the earthquake motion is input for the case where the epicenter of the assumed Nankai earthquake is close to land (hereinafter referred to as the "land-side case"), and the results of city-scale seismic response analysis are visualized as a continuous quantity to predict and understand the damage to buildings caused by the earthquake on a city scale. The input acceleration is the ground surface acceleration adjusted for amplitude based on ground analysis (SAA analysis) from the substrate acceleration in consideration of ground characteristics. The total number of wooden and non-wooden buildings in the target area is 2,746. By structure type, there are 2,064 wooden structures and 682 non-wooden structures. The distribution of buildings is based on the Zenrin Electronic Residential Map Digitown Minami-Awaji City. Figure 1 shows the distribution of buildings by structure type. Figure 2 shows the seismic intensity distribution based on SAA analysis.

Fig.1 Buildings existing in the subject area

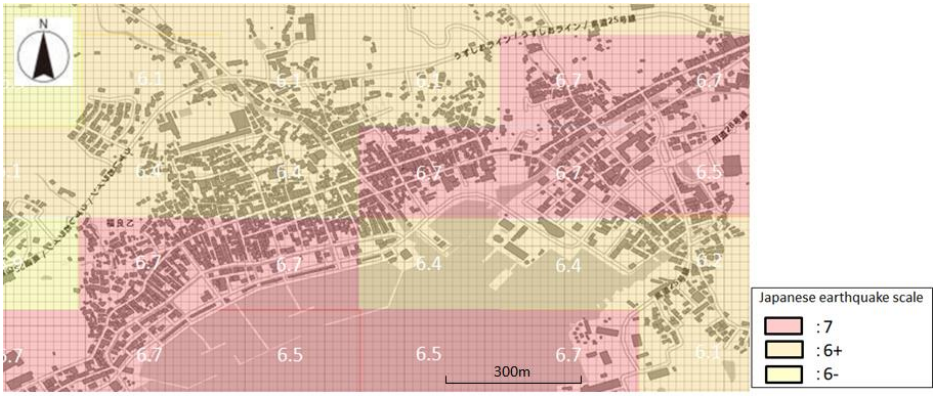

Fig.2 Seismic intensity distribution

3. Visualization of the continuous amount of maximum interlaminar deformation angle by time history response analysis

The results of the seismic response analysis in the target area are used to visualize the con-tinuous amount of the maximum interlaminar deformation angle. The seismic response analysis was performed using the mass vibration model in the Integrated Earthquake Simulator IES, and the analysis environment was a supercomputer owned by the Graduate School of the University of Hyogo. The maximum inter-story deformation angles of buildings in the target area were visualized using a desktop GIS application (ArcGSI Pro ver. 2.9.0). Each building is a polygon element. The base map was a monochrome map included in ArcGSI Pro. For the range of visualization, the minimum value was set to 0, the maximum value to 10/100 for wooden structures and 4/100 for non-wooden structures. The color bar was set to be green (safe color) closer to the minimum value and red (dangerous color) closer to the maximum value[3]. The results of the maximum interlaminar deformation angle in the subject area are shown in Figure 3.

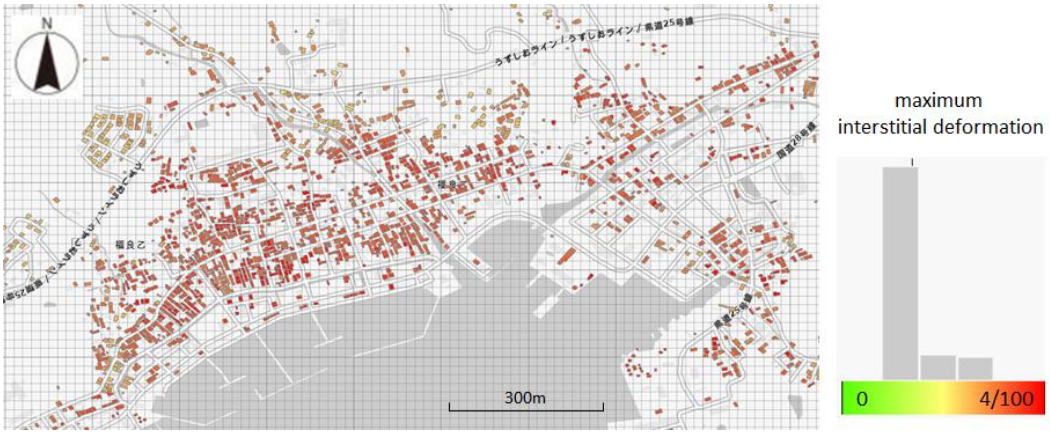

(a) Wooden buildings

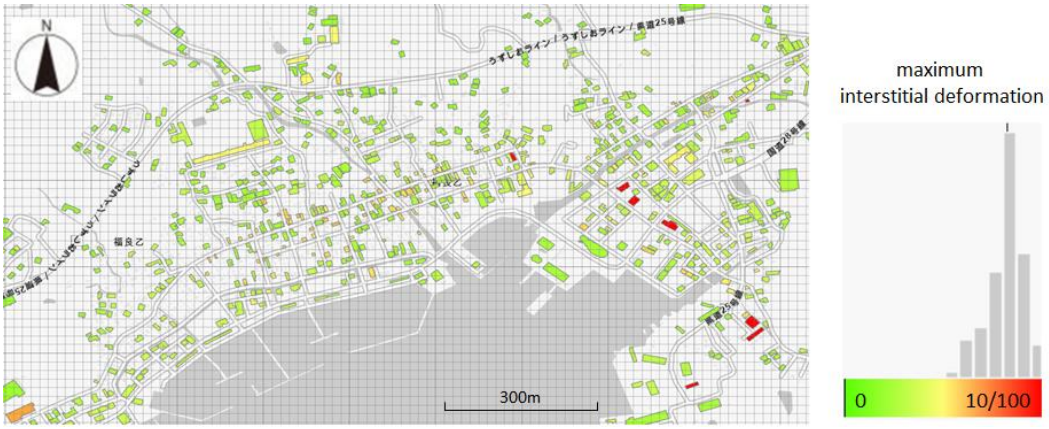

(b) Non-wood buildings

Fig.3 Maximum interlaminar deformation angle response

The analysis results for the wooden building confirmed that the seismic intensity 7 ground surface acceleration occurs in the coastal area and that a large maximum interlaminar deformation angle occurs within the target area. It was also confirmed that the maximum interlaminar displacement response tends to be smaller as one moves away from the coastal area. The analysis results for non-wooden buildings showed that the buildings in the eastern part of the port had a large maximum interlaminar displacement response. Some of the buildings with large maximum interlaminar displacement angles in the non-timber buildings were located within the seismic intensity 7 range, while others were located in the seismic intensity 6+ range. Based on these results, it is predicted that in the event of a hypothetical Nankai earthquake (landward case) used in this analysis, the damage in the northern part of the port may be larger than in other areas. We also believe that we can more easily identify the areas where more damage is likely to occur than the results presented in a previous study [2].

4. Conclusion

While the damage prediction with a threshold value has the advantage of clarifying the damage classification, it has the disadvantage of classifying the damage into different damage categories even if the difference in the maximum interlaminar deformation angle is negligible. In this study, the maximum interlaminar deformation angle results from the urban-scale earthquake response analysis were visualized as continuous quantities without a threshold value. From the results of the continuous quantity visualization, we pointed out the possibility that the damage in the northern part of Fukura Port may be larger than that in other areas if the assumed Nankai earthquake (landward case) used in this analysis were to occur. In addition, we could easily identify areas where more damage is likely to occur than the results presented in a previous study [2].

References

[1] Kouhei FUJITA, Tsuyoshi ICHIMURA, Seizo TANAKA, Munero HORI, Lalith MADDEGEDARA: Time history earthquake response analysis using a set of steel structural building models assuming urban scale, Journal of JSCE A1 (Structural and Earthquake Engineering), Vol. 71, No. 4 (Journal of Earthquake Engineering, Volume 34), pp. 680-688, 2015

[2] Rina HONDA, Hideyuki OHTANI, Yasuyuki NAGANO: "Integrated Evaluation of Building Damage Prediction by Time History Response Analysis Method Using Individual Building Attributes and Empirical Method," 2022 Kinki Branch Research Meeting of Architectural Institute of Japan, pp.185-188, 2022.06

[3] Meaning of safety color and contrasting color, as well as their locations and examples of use, Japanese Standards Association (JSA), Safety colours General specification, Z 9103:2018, pp.15-16

JSST 2022

Discussing surface reconstruction of plasma shape boundary in a fusion reactor

Kunqi Hu[1] and Koji Koyamada[1,*]

[1]Kyoto University, Kyoto, Japan

[*]koyamada.koji.3w@kyoto-u.ac.jp

Abstract. Observing plasma shape is an important part in designing a fusion reactor. Generally, magnetic field lines are used to describe the plasma shape, but they are not able to provide a continuous, clear boundary. Besides, rendering thousands of lines put heavy burden on computing resource. It's suitable to represent the plasma shape with surface. In this paper, we mainly discuss two methods, the 3d alpha shape and the marching cubes method towards surface reconstruction of plasma shape. Their merit and demerit are introduced, respectively.

Keywords: Surface reconstruction, Plasma shape, Alpha shape, Marching cubes

1. Introduction

A magnetic confinement fusion reactor generates helical magnetic field to limit plasma in a certain region. To achieve continuous nuclear reaction, it is important to prevent plasma from having a collision with the inner components. Therefore, the shape of this region, plasma shape, is relative to inner components design of a fusion reactor. To represent shape of this region, thousands of magnetic field lines are traced in the helical magnetic field. it brings some problems. First, rendering all the lines costs a lot of time. Besides, to check for interferences, it is unnecessary to consider those magnetic field lines buried under other lines. Second, separated lines can't provide a continuous surface as a clear boundary. Finally, Larmor radius is hard to be represented with lines. Therefore, it is suitable to represent plasma shape boundary with surface.

We take magnetic field lines as point cloud data and apply the 3d alpha shape[1] and the marching cubes method[2] to surface reconstruction. The 3d alpha shape can be used for surface reconstruction from an unorganized set of data points in 3d space. An alpha value is set in advance to decide precision of line segments on boundary. The marching cubes method works on volume data. It generates different triangular elements in cubes arranged continuously according to scalar value of the volume data. The distance between each cube decides resolution of final result. We discuss the performance of these two methods and have a conclusion on surface reconstruction of plasma shape boundary.

2. Method and result

There have 7200 magnetic field lines been traced within a static magnetic vector field. Data size ups to 16.3GB. To compress the data volume, magnetic field lines with circles less than half circle and more than 4 circles are moved. Because the first ones are considered as magnetic field lines between coils which have no influence on plasma shape, the last ones present almost the same movement feature. In this way, it remains 2420 magnetic field lines. Larmor radius is presented as surrounding points at each point which constitutes a magnetic field line.

For the 3d alpha shape, we tested alpha value from 1 to 0.01 in steps of 0.1 time and alpha value in 0, which has the same performance as convex hull algorithm, on data set. For the marching cubes method, voxelization is conducted based on the distance between two cubes. We tested distance from 1 to 0.001 in steps of 0.1 time. The scalar value is either set as 1 if a voxel had a point inside or 0. The threshold is set as 0.5.

Figure 1 shows results of two approaches. Both results indicate that when the value becomes too small, it appears wave-like surface. This is because points distribution at some place is not dense enough. Helical magnetic field lines are hard to adjust their location to get an even distribution. As to the marching cubes method, voxelization further reduces data size while the marching cubes method can reach similar result as the 3d alpha shape do. It took 24 minutes in running the 3d alpha shape comparing with 1.5 minutes in running the marching cubes method. On the other hand, voxelization may slightly move a point from its original position. It introduces error.

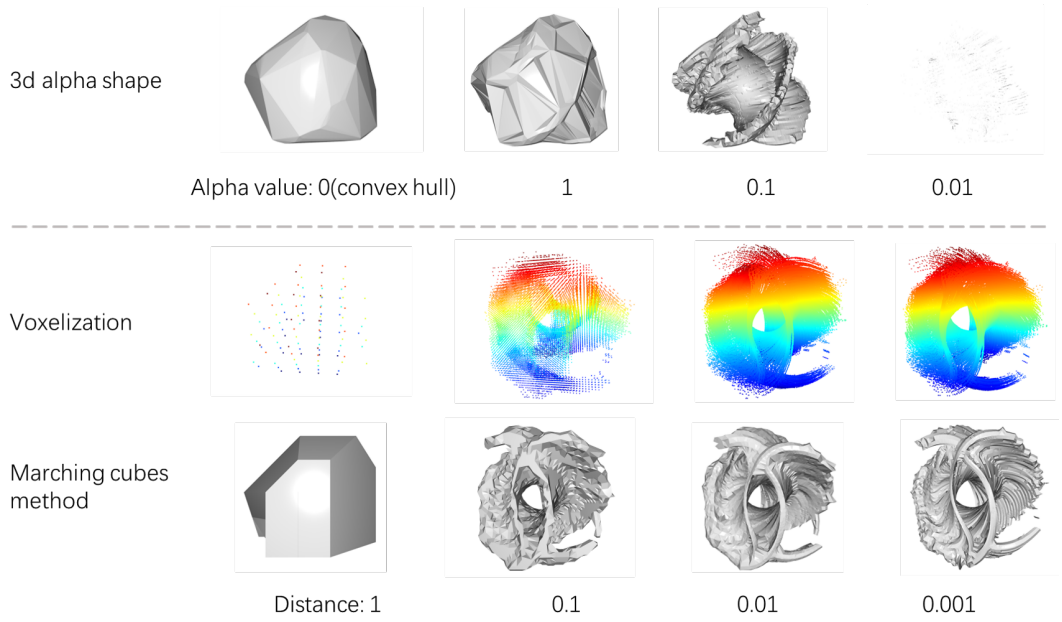

Figure 1: Surface reconstruction by using the 3d alpha shape(up) and the marching cubes method(down).

3. Conclusion

By choosing a suitable value, both surface reconstruction methods can find plasma shape boundary. While generated surface is greatly effected by magnetic field lines distribution. At the same time, large data size will distinctly increase computing time. In this task, we recommend reducing data size before conducting surface reconstruction. Further, adaptive solutions should be considered.

References

[1] Edelsbrunner, Herbert, Ernst P. Mücke: Three-dimensional alpha shapes, *ACM Transactions on Graphics (TOG)*, 13.1 (1994), 43-72.

[2] Lorensen, William E.,and Harvey E: Marching cubes: A high resolution 3D surface construction algorithm, *ACM siggraph computer graphics*, 21.4 (1987), 163-169.

Order-N first-principles DFT molecular dynamics calculations for large-scale biomolecular systems: Early stage behavior of temperature-controlled molecular dynamics calculations

Takao Otsuka[1*]

[1]Department of Biomedical Data Intelligence, Graduate School of Medicine, Kyoto University

*otsuka.takao.8k@kyoto-u.ac.jp

Abstract. We have performed an order-N first-principles density functional theory (DFT) molecular dynamics (FPMD) calculations of a large-scale DNA + H2O system, as an example of large-scale biomolecular systems, by using the order-N first-principles DFT code CONQUEST. The order-N DFT methodology on CONQUEST is based on the combination of McWeeny's purification transformation scheme and the density matrix minimization scheme in the framework of DFT. In MD part, the extended Lagrangian Born-Oppenheimer molecular dynamics (XL-BOMD) scheme is used. We have shown the stable FPMD calculations of large-scale biomolecular system and the good energy conservation in NVE ensemble by CONQUEST. In this study, we show the temperature controlled FPMD simulation such as velocity scaling, stochastic velocity scaling, and Nosé-Hoover chain methods. Our protocols using temperature control method are very effective for the early stage of the order-N FPMD calculations. Our order-N FPMD simulation would be able to realize the large-scale biomolecular simulations.

Keywords: Order-N first-principles density functional theory (DFT), linear scaling method, first-principles molecular dynamics, DNA + H_2O system,

1. Introduction

Molecular simulation technology is now commonly used to explore biological functions of biomolecular systems. Especially, it is expected to help us understand the mechanism or phenomena on biomolecular systems with dynamical molecular motions, for examples, such as enzyme reaction, photoexcitation, or molecular interaction and so on. In this biological mechanism and/or phenomena, electron often plays an important role. Recently, as one of the kinds of the computational approaches, quantum mechanics and its combined method with molecular

mechanics (QM/MM) hybrid methods are also used well in this field. The QM/MM method has done well to elucidate the biological functions and mechanism [1]. However, there are some open questions in the QM/MM hybrid method; for example, the artificial boundary problem, which is usually constrained with the artificial boundary between QM and MM regions, and the limitation of the size of QM region, which is also restricted due to the computational costs of QM calculation. Therefore, there are increasing demands for all-atom QM simulations on complex bio-molecular systems.

In recent progress for the QM calculations, an order-N (or a linear-scaling) methodology for the first-principles density functional theory (DFT) have been developed [2]. We have also developed an order-N DFT code, CONQUEST, which realize high parallel efficiency and enable us to perform DFT studies on very large-scale systems [2]. Recently, CONQUEST have been introduced very stable and efficient order-N first-principles MD (FPMD) method combined with the extended Lagrangian Borm-Oppenheimer MD scheme proposed by Niklasson [3,4] and have shown the reliable and efficient FPMD on large-scale systems [5,6].

In practical application of large-scale FPMD to large-scale biomolecular systems, in many cases, the initial structure is still prepared by using classical MD simulations. The equilibrium structure obtained by classical MD simulation is set as ones of large-scale FPMD simulation. In such case, especially huge-scale biomolecular systems, it is very important to achieve the setting temperature rapidly, without taking too much real computational time in large-scale FPMD simulations. In this study, we report further progress and preliminary results for the temperature controlled FPMD simulations on the order-N FPMD code in biomolecular system. As the temperature-controlled method, we used velocity scaling method, stochastic velocity rescaling method [7] and Nosé-Hoover chain method [8-10] in NVT ensemble. Especially, in this study, we focused on the early stage of large-scale FPMD calculations in order to investigate the initial behavior of temperature in order-N FPMD simulations. We demonstrate that the FPMD simulations on hydrated DNA system are robust and accurate even in NVT ensemble.

2. Method

In the MD simulation using CONQUEST, the XL-BOMD scheme proposed by Niklasson [3,4] is introduced into CONQUEST code [5]. The XL-BOMD scheme can maintain the time-reversal symmetry while keeping the efficiency of density matrix reuse. The Born-Oppenheimer Lagrangian in the XL-BOMD scheme is expressed by

$$L^{XBO}\left(\boldsymbol{X},\dot{\boldsymbol{X}},\boldsymbol{R},\dot{\boldsymbol{R}}\right) = L^{BO}\left(\boldsymbol{R},\dot{\boldsymbol{R}}\right) + \frac{\mu}{2}\mathrm{Tr}\left[\dot{\boldsymbol{X}}^{\boldsymbol{2}}\right] - \frac{\mu\omega^2}{2}\mathrm{Tr}[(\boldsymbol{LS}-\boldsymbol{X})^{\boldsymbol{2}}],$$

$$L^{BO}\left(\boldsymbol{R},\dot{\boldsymbol{R}}\right) = \frac{1}{2}\sum_{I=1}^{N} M_I\dot{\boldsymbol{R}}_I^2 + E_{tot}(\boldsymbol{R}_I),$$

where the potential energy E_{tot} is defined by the self-consistent ground state density matrix at nuclear positions $\boldsymbol{R_I}$ with masses M_I. The matrix $\boldsymbol{X}$ is a sparse matrix with the range of the matrix $\boldsymbol{LS}$, "μ" is the fictitious electronic mass, and "ω" is the curvature of the electronic harmonic potential. As shown in previous study [5], we use the $\boldsymbol{LS}$ matrix as an auxiliary degree of freedom in the BO Lagrangian and the time-reversible Verlet scheme to obtain the

matrix $\boldsymbol{X}$. The matrix $\boldsymbol{X}$ is time-reversible and evolves in a harmonic potential centered on the ground-state $\boldsymbol{LS}$. In the practical numerical propagation of the matrix $\boldsymbol{X}$, the equation of motion with a dissipative force is used to maintain the numerical stability of the matrix $\boldsymbol{X}$.

3. Application

We have performed the order-N DFT calculations of a large-scale DNA + H_2O system with 3,439 atoms (Figure 1). The DNA system is relatively rigid system compared with a protein system due to the hydrogen bonding of Adenine-Thymine and Guanine-Cytosine base pairs.

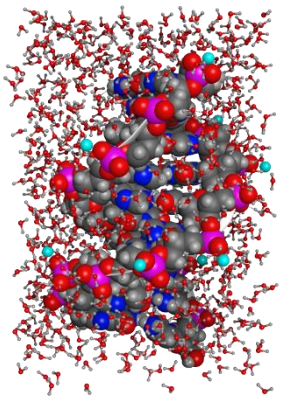

Figure 1. Structure of DNA + H_2O system (PDB ID: 1WQZ).

Here we investigate one of the results of the temperature controlled FPMD simulations by using the velocity scaling and and Nosé-Hoover chain method. In this study, we focused on the temperature behavior in early stage of order-N FPMD simulation. Figure 2 shows the energy profile obtained by the order-N FPMD simulation with the velocity scaling method. We set the controlled temperature as 300 K (Fig. 2(a)) and 600 K (Fig. 2(b)), respectively. In the velocity scaling calculations, we performed the velocity correction for each step. As seen in Figure 2, although the fluctuation of the kinetic energy is large in the early MD steps (that is, 0-50 MD steps), then the kinetic energy converges to around the setting temperature. We can expect that this rapid convergence in the early steps of FPMD simulation would be very useful.

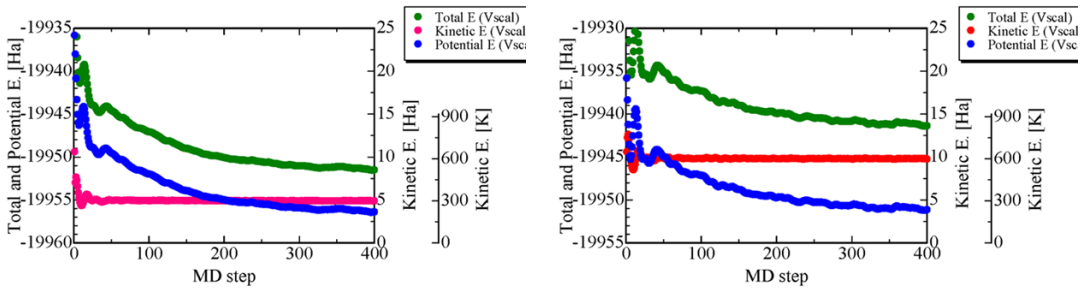

Figure 2. Energy profile calculated by order-N FPMD simulation with velocity scaling method as (a) 300 K and (b) 600 K; total energy (green), potential energy (blue), and kinetic energy of 300 K (pink) and of 600K (red).

Figure 3 shows the energy profile obtained by Nosé-Hoover chain method. From Fig. 3 we can see that the temperature control by the Nosé-Hoover chain method in the early MD steps of FPMD simulations is relatively slow convergence in present conditions, unlike that of the velocity scaling method. This slow convergence of velocity by Nosé-Hoover chain method takes many MD steps in FPMD simulations. In order to find the clear reason for this slow

convergence of the temperature, it is neccesarry to do the assessment study for the appropriate calculation conditions such as the number of thermostats, the fictitious thermostat masses and the size of biomolecular system. In this study, we just applied the general parameter reported in previous study [8], hence we cannot describe the further discussion.

In my talk, detailed analysis including the comparison for another thermostat will be reported.

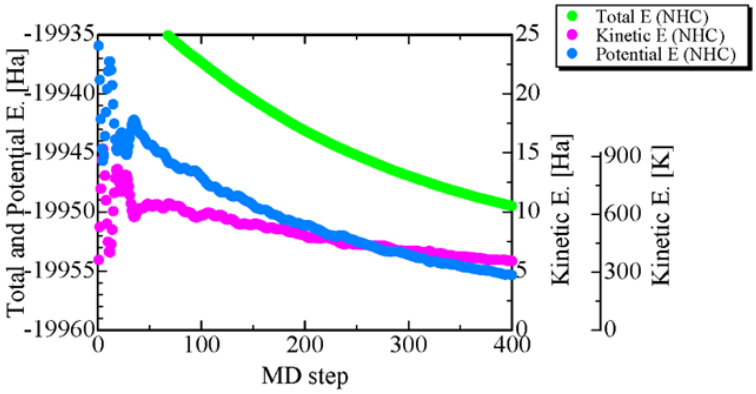

Figure 5. Energy profile calculated by order-N FPMD simulation with Nosé-Hoover chain method as 300 K for 0-400 MD steps (total energy (yellow green), potential energy (aqua blue), and kinetic energy of 300 K (bright pink)).

References

[1] For example, Novel prize of chemistry 2013, Martin Karplus, Michael Levitt, Arieh Warshel, “for the development of multiscale models for complex chemical systems”.

[2] D. R. Bowler and T. Miyazaki, *Rep. Prog. Phys.*, 75 (2012), 036503 and see the web page; http://www.order-n.org/

[3] A. M. N. Niklasson, C. J. Tymczak, M. Challacombe, *Phys. Rev. Lett.*, 97 (2006), 123001.

[4] A. M. N. Niklasson, *Phys. Rev. Lett.*, 100 (2008), 123004.

[5] M. Arita, D. R. Bowler, T. Miyazaki, *J. Chem. Theory Comput.*, 10 (2014), 5419.

[6] T. Otsuka, M. Taiji, D. R. Bowler, T. Miyazaki, *Jpn. J. Appl. Phys.*, 55 (2016), 1102B1.

[7] G. Bussi, D. Donadio, and M. Parrinello, J. Chem. Phys. 126 (2007), 014101.

[8] S. Nosé, J. Chem. Phys. 81 (1985), 511.

[9] W. G. Hoover, Phys. Rev. A 31 (1985), 1695.

[10] G. J. Martyna, M. E. Tuckerman, D. J. Tobias, and M. L. Klein, Mol. Phys. 87 (1996), 1117.

Reactive molecular dynamics study on intermolecular structural changes of hydrogen-abstracted polyethylene chains

Haolun Li[1*], Susumu Fujiwara[1], Hiroaki Nakamura[2,3], Tomoko Mizuguchi[1],

Shinji Saito[4], Wataru Sakai[1]

[1]Kyoto Institute of Technology
[2]National Institute for Fusion Science
[3]Nagoya University
[4]Institute for Molecular Science

*d0871005@edu.kit.ac.jp

Abstract. One of the effects that radiation causes on polymeric materials is the hydrogen abstraction reaction, which induces radicalization and the subsequent structural changes such as disorder of structure, cross-link and chain scission. However, at a nanoscale, the changes of the entire chain and the reaction paths on local segments are difficult to be independently and completely caught by experiment. In our former reactive molecular simulations, we observed structural disruption, formation of C=C double bond, cyclic structure and conjugated bond, and chain scission. In this research, we investigate the structural changes of hydrogen-removed polyethylene by means of reactive molecular dynamics simulations using one of ReaxFF force field parameter sets, called CHO-2006.

Keywords: Molecular dynamics simulation, Polyethylene, Structural change, Reactive force field

1. Introduction

Hydrogen abstraction occurs on polymeric materials after exposure to radiation within a high energy or for a long time, leading to structural changes and chemical bond rearrangements including structural disruption, formations of C=C double bonds, chain scissions, cross-link, etc. For the reason that hydrogen-abstraction reaction occurs with other radiation effects, it is difficult to independently study the structural change of polymers induced by hydrogen-abstraction at a nanoscale through experiment. In our former research [1], by using reactive molecular dynamics (MD) simulations, intramolecular chemical reactions were observed, including chain scissions and the formation of C=C double bonds and cyclic structures, etc. However, cross-link, which is confirmed occurring during radiation exposure, was not observed during our former simulations. The reason is suggested that cross-link occurs most in the amorphous regions of polymers where has an extreme environment because of the high energy emitted by radiation. Thus, in this research, we remove hydrogen atoms from the amorphous regions of

polyethylene models and predict the intermolecular structural change of the models in an extreme environment by MD simulations, using a reactive force field called ReaxFF.

2. Simulation models and methods

Hydrogen-removed polyethylene models were made by the following steps. In step (*i*), an all-atom polyethylene chain ($C_{300}H_{602}$) was cooled in 100 K for 0.3 ns and it formed a chain-folding structure. In step (*ii*), we made a copy of the chain and aligned the two chains in the direction of the orientational order, along the *y* axis as in Fig. 1. In step (*iii*), we randomly removed hydrogen atoms from the adjacent amorphous regions of two chains. In step (*iv*), Lennard-Jones (LJ) walls were put around the two chains in six directions, left and right (x-low and x-high), rear and front (z-low and z-high) and bottom and top (y-low and y-high) as in Fig. 2. The LJ wall on the top (the y-high wall) was set moving down during the simulation and the positions of the other five walls were fixed. In step (*v*), to compare the structural changes of the chains at different temperatures, the models were kept at 100 K, 150 K, 200 K, 250 K, 300 K, 350 K, 400 K separately for 0.3 ns (3,000,000 time steps, 1 fs per time step) with the y-wall moving down in a constant speed. The models are treated in a vacuum simulation box by ReaxFF MD simulations using CHO-2006 parameter set [2]. In all simulations, NVT ensemble is employed and the size of the vacuum simulation box is set to 400 Å × 400 Å × 400 Å. The Nosé–Hoover method is applied to control the temperature. The simulation software used is LAMMPS.

3. Results and discussions

The short-time simulation of two original polyethylene chains in the same conditions is also done. From the simulation results, after the equlibration, the average distance of two nearest carbon atoms from different chains (about 3.55 Å) is shorter than the distance between successice planes (about 3.75 Å). During the simulation of two hydrogen-abstracted polyethylene chains where the y-high wall is fixed, the intramolecular chemical reactions are not observed. It suggests that the models only for intermolecular chemical reactions are suitable for this research.

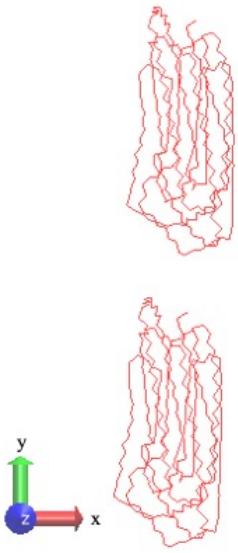

Fig. 1 Initial configuration of two hydrogen-abstracted polyethylene chains. Hydrogen atoms are not shown.

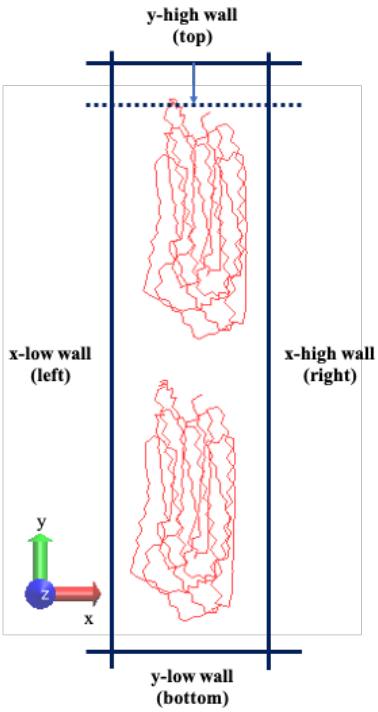

Fig. 2 Image of LJ walls in different directions. The y-high wall moves down in a constant speed during the simulation. Hydrogen atoms and z-low and z-high walls are not shown.

4. Conclusions

In our research, at the present stage, from the simulation results of two original polyethylene chains, it is possible enough that cross-link occurs in the amorphous regions of two hydrogen-abstracted polyethylene chains rather than the crystalline regions. More detials of simulations at different temperatures will be given on the presentation. For further research, the effects of the different speeds of the y-high LJ wall moving down will be investigated.

References

[1] H. Li, S. Fujiwara, H. Nakamura, T. Mizuguchi, A. Nakata, T. Miyazaki and S. Saito: Structural change of damaged polyethylene by beta-decay of substituted tritium using reactive force field, *Jpn. J. Appl. Phys.*, 60 (2021), SAAB06-01 - SAAB06-07.

[2] K. Chenoweth, A. van Duin, W. A. Goddard: ReaxFF Reactive Force Field for Molecular Dynamics Simulations of Hydrocarbon Oxidation, *J. Phys. Chem. A*, 112 (2008), 1040-1153.

Determination of Resonant Mechanism of Polymer Micromachined Insect Inspired Flapping Device Using Finite Element Modal Analysis

Kazuya Ishiba[1], Minato Onishi[2], Daisuke Ishihara[3*]

[1] Department of Interdisciplinary Informatics, Kyushu Institute of Technology

[2] Department of Computer Science and Systems Engineering, Kyushu Institute of Technology

[3] Department of Intelligent and Control Systems, Kyushu Institute of Technology

*ishihara.daisuke399@mail.kyutech.jp

Abstract. We have proposed the polymer micromachined insect-inspired flapping device with a 2.5-D structure. Actual insects use the resonant flapping mechanism. Hence, in this study, we determine the resonant mechanism of our device using a finite element (FE) modal analysis for the whole FE model of the flexible transmission, the supporting frame, and the thin piezoelectric bimorph as the monolithic solid structure, since they are strongly coupled and behave like a single oscillator. As the result, we found the first and second modes are available for the resonant flapping, since their frequencies are close to those in actual insects. The comparison with the experiment demonstrates the feasibility of the proposed resonant mechanism.

Keywords: Insect inspiration, resonance, modal analysis, flapping, polymer micromachining

1. Introduction

Evolution of insects has achieved their efficient flight using the resonant mechanism of a flapping system that consists of the thorax exoskeleton, flight muscles, and wings [1], which behave like a single oscillater. We have developed a polymer micromachined flapping device with a 2.5-D structure [2, 3], which is insect-inspired as shown in Fig. 1, where the correspondence to the insect's flapping system is schematically presented. Our insect-inspired flapping device consists of the transmission using a pair of parallel elastic hinges, the supporting frame, a thin piezoelectric bimorph, and a micro wing, which are strongly coupled to each other and vibrate as a single elastic oscillator. Hence, from the similariy to the insect's flapping system, we can use the resonant mechanism for the flapping efficiency. In this study, we determine the resonant mechanism of our flapping device using the finite element (FE) modal analysis. We developed a full FE model of our flapping device as the monolithic solid structure. This model is investigated using the FE modal analysis. As the result, we found the first and second modes are available for the resonant flapping, since their frequencies are close to those for actual insects. The comparison with the experiment demonstrates the feasibility of the proposed resonant

mechanism.

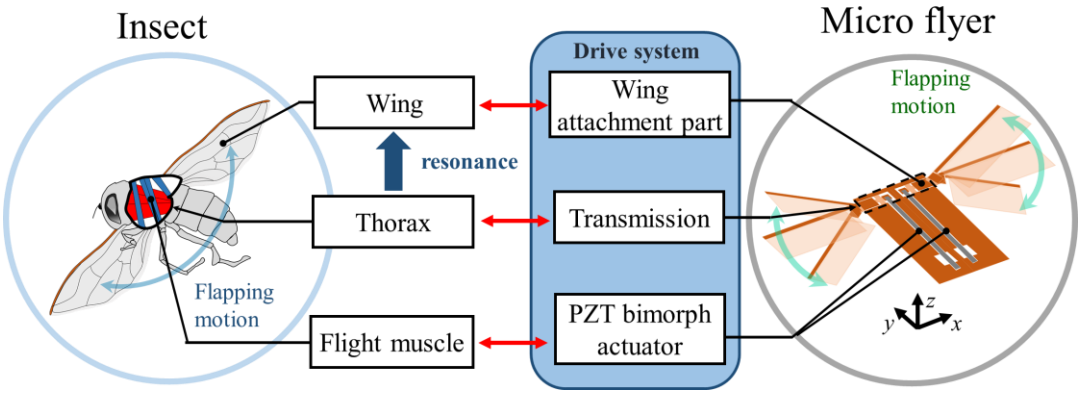

Figure 1: Conceptual view of the proposed resonant flapping.

2. Finite Element Modeling of Insect-Inspired Flapping Device

An insect-inspired flapping device is shown in Fig. 2. The thin bimorph actuator is glued to the flexible transmission and the support frame using a epoxy resin adhesive. They are strongly coupled and behave as a single elastic oscillator. Hence, a finite element model for the whole device is constructed as shown in the Fig. 3. Here, we consider the uncertainity of the epoxy resin adhesive volume using the occupation ratio for the possible maximum volume r_o.

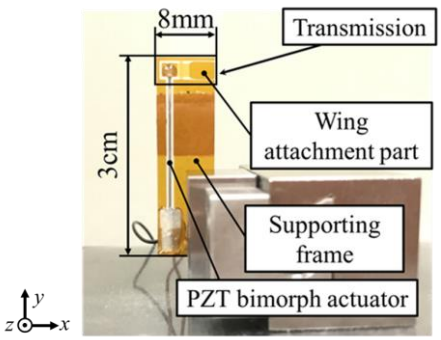

Figure 2: Polymer micromachined insect-inspired flapping device.

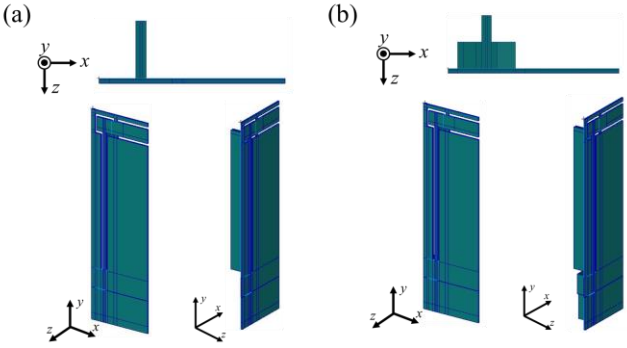

Figure 3: Finite element models of the insect-inspired flapping device with (a) r_o = 0 %, and (b) r_o = 100 %.

Fig. 4 shows the model of the adhesive volume, where the height h and width w are given, respectively, following the prescribed in-plane design of the actuator attachment of the supporting frame, while the maximum thickness t is estimated as a half of the overhang length of the bimorph actuator in the out-of-plane direction, which is based on the actual observation in Fig. 5. t is changed from 0% to 100%, which corresponds to r_o = 0% and 100% in Fig. 3, respectively. Furthermore, we also consider the uncertainty of the epoxy resin material properties (mass density and Young's modulus) using three sets of possible material properties, which are the polyimide material properties, and the lower and upper limits of the typical epoxy resin material properties.

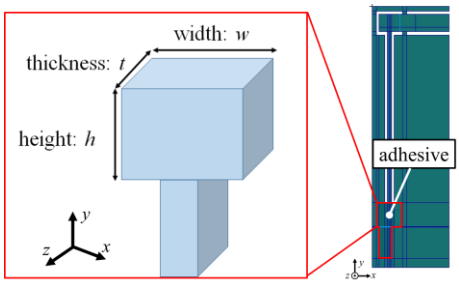

Figure 4: Possible adhesive volume.

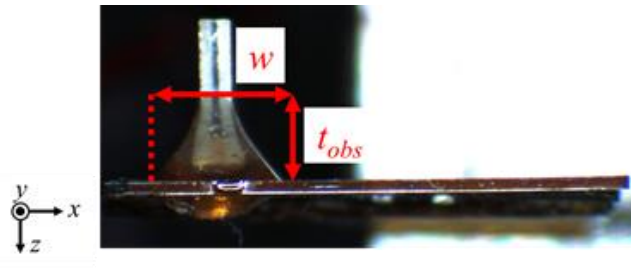

Figure 5: Fabricated insect-inspired flapping device.

3. Results and Disscusion

Figs. 6 and 7 show the results of the modal analysis with r_o = 0% and 100%, respectively, using the upper limit of the typical epoxy resin material properties. The first mode natural frequencies f for r_o = 0% and 100% are 71 Hz and 103 Hz, respectively, which are given by the FE modal analysis, while the resonant frequency f_φ in the corresponding experiment is 83.33 Hz. Fig. 8 shows the relationship between the first mode natural frequency and the occupation ratio r_o for each material peoperties. As shown in this figure, f_φ obtained from the corresponding experiment lies in the range of all possible frequencies of the first mode predicted using the FE modal analysis. It follows from these results that the resonance observed in the experiment is due to the first mode vibration of the flapping device. We can use the resonant mechanism since the determined frequency is close to the flapping frequency observed in the actual insects. Furthermore, we found that the second mode deformation clearly shows the flapping motion. The second mode natural frequency is also close to the flapping frequency in the actual insects. Hence, the resonant mechanism determined here will be feasible for the polymer micromachined insect-inspired flapping device.

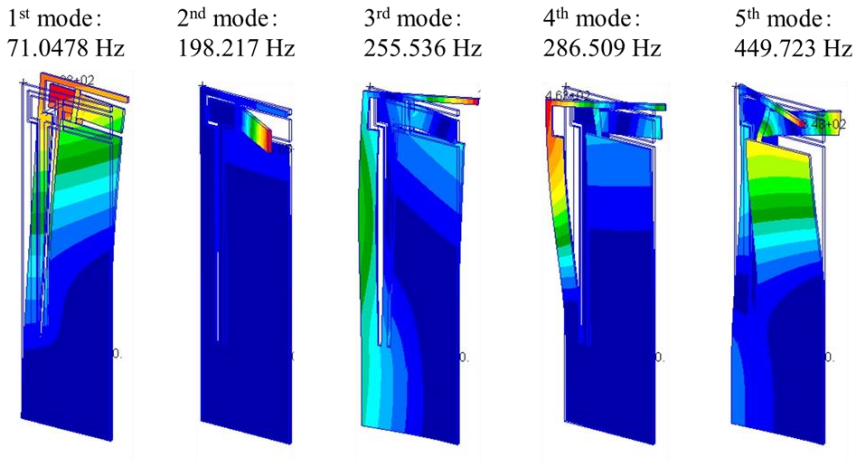

Figure 6: Result of the modal analysis for the FE model with r_o = 0% using the upper limit of the typical epoxy resin material properies in a bird's-eye-view.

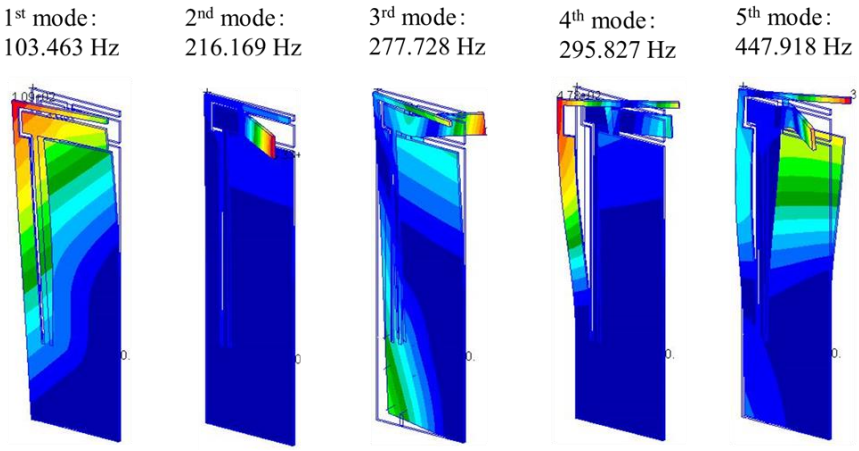

Figure 7: Result of the modal analysis for the FE model with r_o = 100% using the upper limit of the typical epoxy resin material properies in a bird's-eye-view.

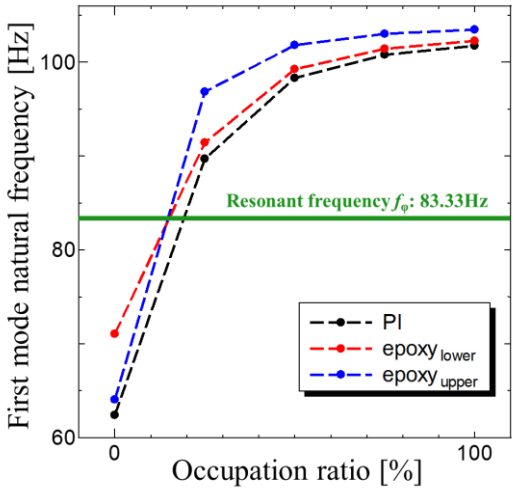

Figure 8: Relationship between the occupation ratio and the first mode natural frequency.

References

[1] Jankauski, M.A., Measuring the frequency response of the honeybee thorax, *Bioinspiration & Bimomimetics*, 15 046002(2020).

[2] Ishihara, D., et al, Polymer micromachined transmission for insect-inspired flapping wing nano air vehicles, *Proceedings of 15th IEEE International Conference on Nano/Micro Engineered and Molecular System*, 9265594(2020), 176-179.

[3] Rashmikant, et al., One-wing polymer micromachined transmission for insect-inspired flapping wing nano air vehicles, *Engineering Research Express*, 3 045006 (2021).

Sound field evaluation of experimental environment with ADVENTURE_Sound

Akihiro Kudo[1*], Amane Takei[2]

[1] Department of Engineering for Innovation, Tomakomai Collage, Japan
[2] Faculty of Engineering, University of Miyazaki, Japan

*kudo@tomakomai-ct.ac.jp

Abstract. We have presented a performance evaluation of a wave-sound analysis code in previous presentation at JSST2021. There, we covered the sphere model and the loudspeaker-snowman model. The loudspeaker-snowman model modeled a situation in which a listener is listening to sound waves emitted from a loudspeaker. In this presentation, we will attempt to evaluate the sound field in a more realistic experimental environment by adding some objects to the acoustic space containing the loudspeaker-snowman model.

Keywords: Wave-sound analysis, Parallelized finite element method, Domain decomposition method, ADVENTURE_Sound, Experimental environment

1. Introduction

A wave-sound analysis based on a numerical analysis method, such as the finite element method, has become widespread due to recent improvements in computer performance and numerical calculation technology. In the case of accurately reproducing an analysis model of complicated shape, it is necessary to use many small the elements. In the case of analyzing the state of wave-sound propagation in a wide range, a wide analysis domain is examined. Furthermore, to perform a high-accuracy analysis, it is necessary to model the analysis domain with a sufficiently small element for the wavelength, and, in this case, the number of elements also increases. Increasing the number of elements increases the scale of the problem. Therefore, a method that can calculate large-scale problems has come to be demanded. Moreover, large-scale problems must be solved with high accuracy.

We have presented a performance evaluation of a wave-sound analysis code in previ-ous presentation at JSST2021. There, we covered the sphere model and the loudspeak-er-snowman model. The loudspeaker-snowman model modeled a situation in which a listener is listening to sound waves emitted from a loudspeaker. In this presentation, we will attempt to evaluate the sound field in a more realistic experimental environment by adding some objects to the acoustic space containing the loudspeaker-snowman model.

2. Basic target model

Figure 1 shows the target model used for a simulation. This model is practical because the model includes a loudspeaker and listener. These enable us to reproduce a situation at the psychoacoustical experiments.
The listener is a snowman that consists of two spheres. The diameters of the listener head and torso are 0.177[m] and 0.3[m], respectively. The distance from the loudspeaker to the listener is set to 1.5[m]. This distance assumes that ordinary psychoacoustical experiment.

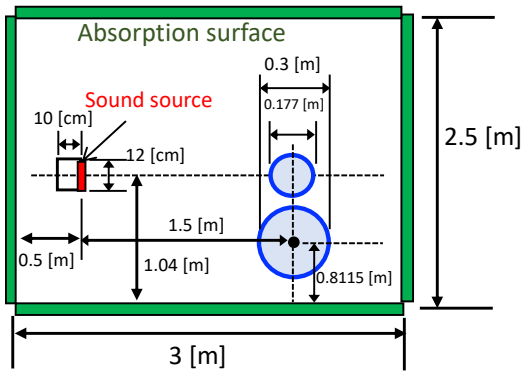

Fig.1 Dimensions of the side view in the loudspeaker-snowman model

We will develop this model to more complex model with obstacles that disturbs the sound field. A few cases will be picked up including a chair to hold listener and multiple loudspeakers as a loudspeaker array. Although these are necessary to conduct the experiment, the sound fields changes differently from original. These sound fields will be evaluated on these models.

3. Numerical example

For examining ADVENTURE_Sound on a real-world problem, we model the environment of acoustic experiments. The computations are performed on a 10-node (160-core) PC cluster (Intel® Xeon E5-2650L,1.8GHz with 16 cores L2 20480[KB]) with 32 GB RAM per node. The simulation statistics are shown in Table 1. More detail thins will be shown at the conference.

Table 1 Simulation Statistic

Frequency	2000 [Hz]
No. of Elements	1.0×10^8
No. of DOF	1.0×10^8
Platform	10-node workstation cluster with Intel Xeon, 1.8 GHz
No. of cores	16
Main memory per node	32 [GB/node]

References

[1] A. Takei, A. Kudo: Over 100 million degrees of freedom scale wave sound analysis based on parallel finite element method, JSST, 12:2 (2020), 76-84.
[2] A. Takei, S. Sugimoto, M. Ogino, S. Yoshimura, H. Kanayama: Full wave analyses of electromagnetic fields with an iterative domain decomposition method, *IEEE Trans. on Magn.*, 46:8 (2010), 2860-2863.
[3] A. Kudo, A. Takei: Performance evaluation of wave-sound analysis code: ADVENTURE_Sound, JSST, 17:1 (2021).

JSST 2022

Numerical study on compressive behaviour of truncated origami structures

Wei Qiang[1], Yvonne Durandet[1], Guoxing Lu[1,*]

[1]School of Engineering, Swinburne University of Technology, Hawthorn, VIC 3122, Australia

[*]glu@swin.edu.au

The full paper of this paper has been published in Journal of Advanced Simulation in Science and Engineering (JASSE).

DOI: https://doi.org/10.15748/jasse.10.182

The research on damper for cylindrical origami structure using reversed spiral model

Jingchao GUAN[1]*, Jingshun ZUO[1], Xilu ZHAO[1]

[1]Graduate School of Engineering, Department of Mechanical Engineering, Saitama Institute of Technology

* Guanjingchao123@gmail.com

Abstract. It is a common method to use dampers to dampen structures. In this research, we will use origami to propose a new damper structure that can use its own deformation to squeeze the internal hydraulic oil to generate new damping system. We will conduct an actual measurement experiment, and the effectiveness of the damper for cylindrical origami structure using reversed spiral model will be examined using the obtained measurement results.

Keywords: Origami engineering, Origami damper, Vibration control technology

1. Introduction

Vibration isolating structures of buildings and impact measures of precision machinery are very important projects. Japan is prone to earthquakes and lots of companies use precision instruments, so it is important to develop vibration control technology in the future.This study we proposes the damper for cylindrical origami structure using reversed spiral model. It is use of structures related origami engineering and we output the seismic waves of vibration effect at any time, use acceleration and displacement sensor to confirm the response effect of this damper device.

2. Methods and Materials

Figure 1 a and b shows the experimental apparatus of the vibration model made of four linear bearings with 110mm long springs and load platform carrying mass weighing up to 1.43kg.figure 1 c shows the actual manufacturing. Insert the origami cylinder into a polyethylene tube, fold it from a pattern of crease that appears on the surface of the cylinder. For the surface of the origami cylinder does not swell locally during compression, we attached the hard plastic sheet. Finally aluminum joints are placed at both ends and the completed inverted spiral origami damper is shown in figure 1 d.

Figure 2 is schematic of origami structure damper. m is the concentrated mass of the main structure at the top of the damper and equivalent elastic modulus k,which is a combination of four springs, c is Damping effect against vibration from oil inside origami damper.

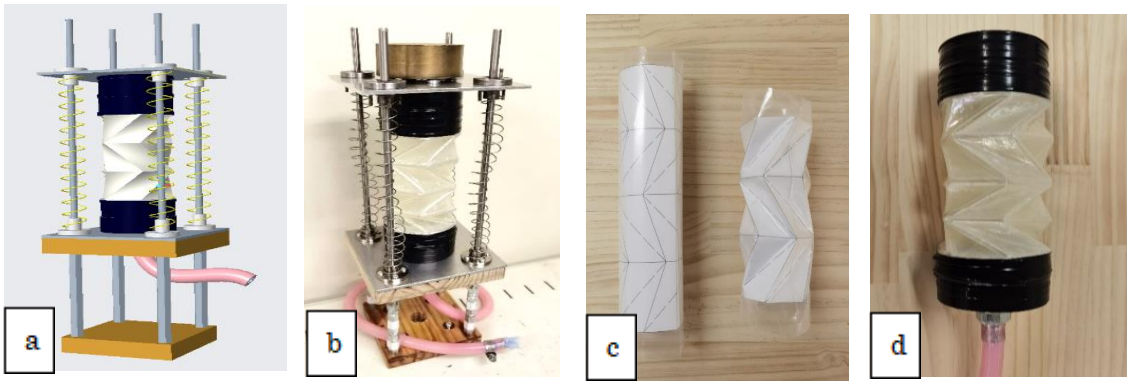

Fig.1 Experiment mode

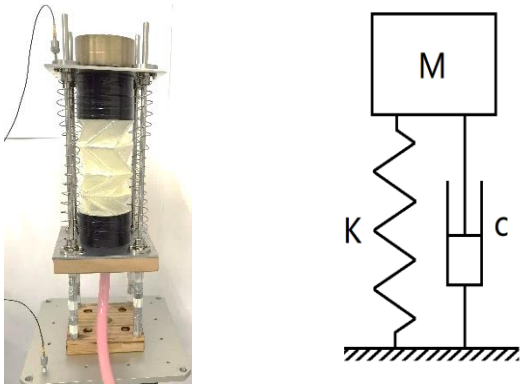

Fig.2 Schematic of origami structure damper

3. Vibration Experiment

This time we use seismic wave for vibration experiment which the maximum acceleration is 341cm/s2, and the acceleration waveform is shown in figure 3.

In this study the vibration characteristic measurement system includes experimental device, FFT analyzer (DS-3000), accelerometer, laser displacement meter, shaking table, amplifier, earthquake signal generator, and PC for measurement. The laser displacement meter and accelerometer were placed parallel to the experimental device. The measurement flow chart is shown in figure 4.

Figure 5 shows the time-displacement response waveform of the damper when sinusoidal waves are inset.The dotted lines show the measured waveform, and the solid lines show the numerical analysis results. In this way, it can be seen that the analysis results obtained separately and the experimental results are in good agreement.

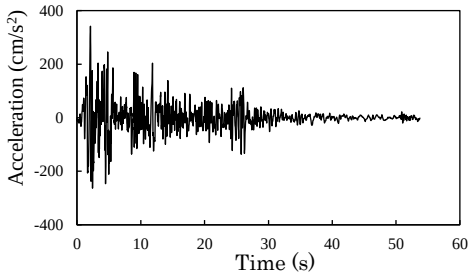

Fig.3 Acceleration singnal of the EI-Centro

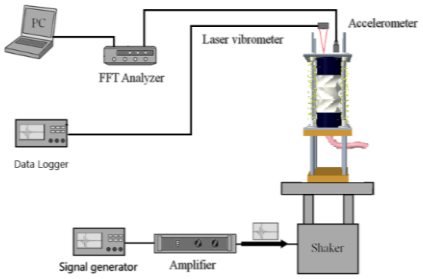

Fig.4 Diagram of testing system

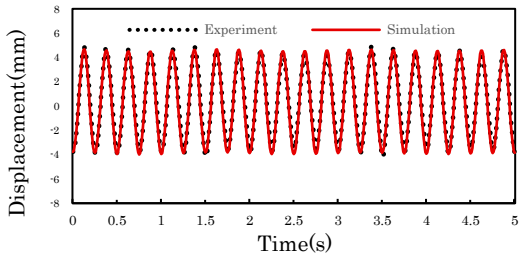

Fig.5 Displacements of origami damper model under sinusoidal excitation

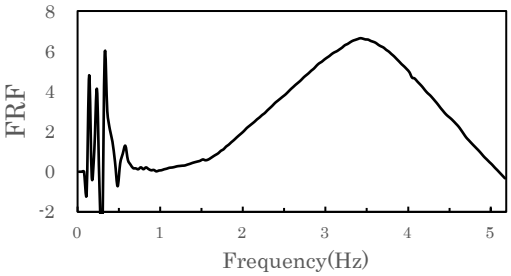

Fig.6 Frequency response analysis of the origami damper

Figure 6 shows the results of sweep excitation with sinusoidal excitation frequency from 0 to 6Hz, and the change of the frequency response function which represents the relationship between input and output.It can be seen that the corresponds to the peak value of the frequency response function was 3.49Hz,which is natural frequency of origami damper system.

In addition, to examine the response characteristics of an origami damper device when it receives a seismic vibration. Displacement and acceleration response is shown in figure 7, and time domain results displacement response frequency domain,a Fourier transform of the results is shown in figure 8.The largest part tends to be concentrated around the natural frequency of 3.49Hz of the origami damper.

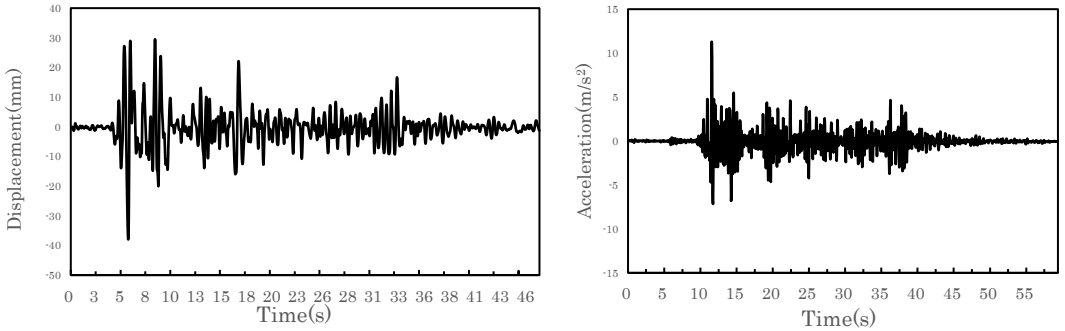

Fig.7 Displacement and acceleration responses under the EI-Centro

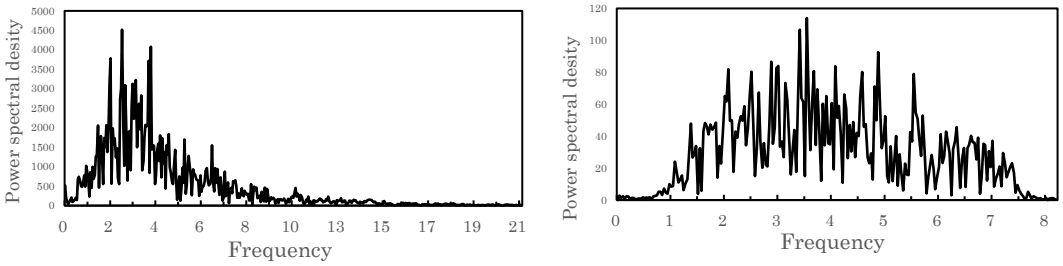

Fig.8 Frequency responses under the EI-Centro seismic waves from displacement and acceleration

4. Results

Figure 9 shows the displacement and acceleration of the experimental model with and without fluid respectively. The displacement and acceleration of the main mass block are then Fourier transformed, and the results are shown in figure 10.

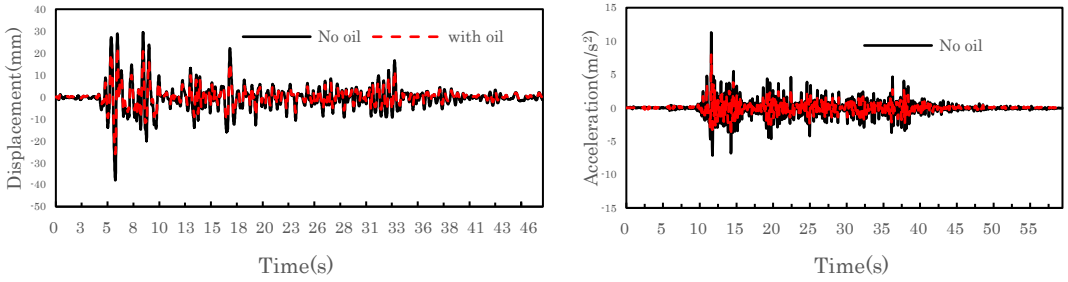

Fig.9 Displacement and acceleration responses under the EI-Centro seismic waves

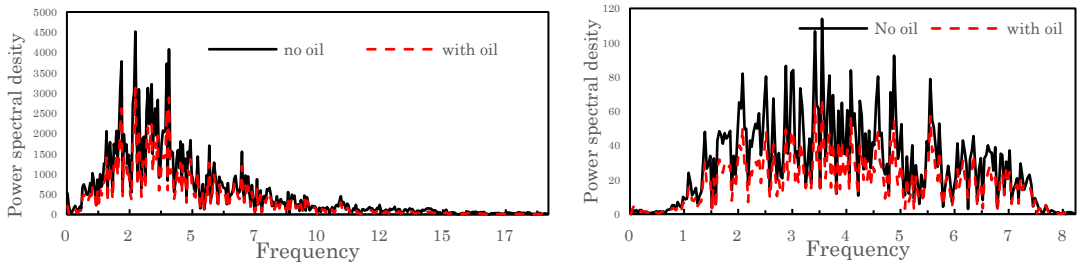

Fig.10 Power spectral density of the displacement and acceleration under the El-Centro seismic wave

5. Conclusions

In this study, seismic response analysis proved that the experimental model has a damping effect on origami damper. It can be seen that the maximum displacement and maximum acceleration of the experimental model are reduced by 29.98% and 38.00% by using oil fluid.

References

[1] Q. Wu, X.L. Zhao, R.C. Zheng, and K. Minagawa, “High response performance of a tuned-mass damper for vibration suppression of offshore platform under earthquake loads,” Shock and Vibration, no.7383679, pp. 1-11, 2016. DOI: 10.1155/2016/7383679.

JSST 2022

Kirigami Fabrication of Shaped, Flat-foldable Metamaterials based on Reverse Spiral Origami (RSO) Polyhedrons for Life Jacket

Luis Diago[1,2,*], Junichi Shinoda[2], Ichiro Hagiwara[1]

[1]Meiji University
[2]Interlocus Inc.

[*]luis_diago@meiji.ac.jp

Abstract. In this paper we propose to extend the manufacturing method based on the kirigami honeycomb (HC) technology to obtain new metamaterials that can absorb impact energy in directions perpendicular to the complex surfaces of the human body using origami polyhedra. The work shows preliminary results on the design of a new type of jacket.

Keywords: Kirigami fabrication, Reverse spiral origami, Inverse projection

1. Introduction

In many applications, such as sports, police work and industry, it is often important to use a protective shield to prevent injury to certain parts of the human body. The head can be protected with a rigid, padded helmet[1], but some areas of the body, for example the rib cage[2], must be protected with a flexible material. For example, a soccer player cannot wear a rigid rib cage protector because it would restrict movement and because the rigid protector itself could cause injury if it were to receive an impact from below and dig into, for example, the player's armpit. In this work we propose a solution for fitting honeycomb-like structures to flexible parts of the human body.

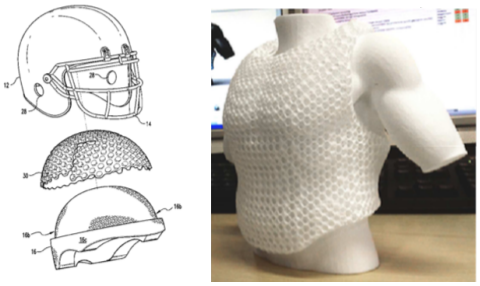

Figure 1: Body Protectors: a) Football Helmet[1] b) Chest Protector concept from [2]

2. Fitting a honeycomb structure to the human body

Several methods have been identified to fit a structure to the shape, i.e., to generate a conformal structure: 1) ”trimming method”[3], 2) ”sweep method”[4], and 3) ”mesh-based methods”[5]. The ”trimming method” trims a regular tessellation to fit a given conformal shape. The structure retains its orientation and only the cells at the boundaries of the structure are affected by the trimming method. Mullen et al[3] use trimming to generate lattice structures for medical applications. The ”sweep method” deforms a structure to follow a surface of the conformal shape and, as such, is only suitable for use in sheet-like shapes, as used by Chu et al [4]. Mesh-based methods are a two-step process in which a finite element meshing algorithm is used to generate a volumetric mesh. Gervasi et al.l[5] used this mesh as a skeleton to map the struts of the lattice structure.

Figure 2 shows an application of the trimming method for diaper design. In the developed application we start by photographing the body of the person to be reproduced (a Manikin is shown in figure 2a) and the 3D surface of figure 2b) is obtained. This triangular mesh is simplified as shown in 2c) and the 2D pattern shown in figure 2d) is obtained by the method proposed in [8] that allows to reconstruct the surface shown in 2e) from the union of the parts in 2d).The main disadvantage of the trimming method is that the boundary regions of the structure are weakened where the cells have been cut. Hence, the structure (or a part of it) must be reinforced with a sheet of solid material, often referred to as a ”skin” in 2e). The figure also shows the patterns of honeycombs obtained by the methods in [6] and [7]. In [6], panels with different inclinations can be obtained as long as the obtained cells are not non-convex. In [7], the Miura pattern is introduced to include an energy absorption in the direction of the cell. To work with more complex geometries we combine the trimming method with a mesh-based method.

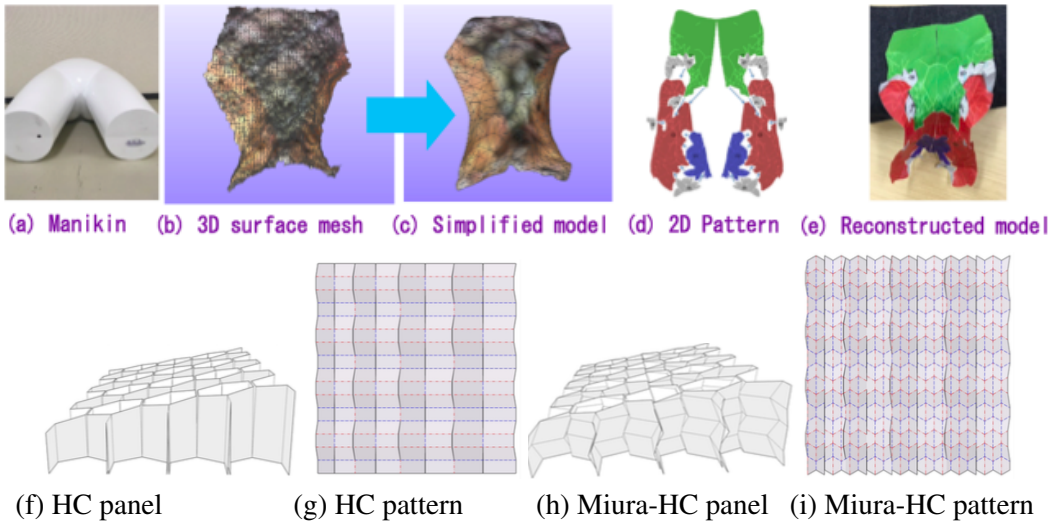

Figure 2: Diapers design application using honeycomb panels

3. Handling geometric complexity with Reverse Spiral Origami (RSO) Polyhedrons

Figure 3 shows an application of the proposed method for the design of a new type of jacket. For the 3D model in 3a) we use a method similar to the one proposed in [8][1]to obtain the parts in 3b) and 3c). The proposed combination consists of projecting each of the pieces on a 3D panel as shown in 3d) and obtaining the 2D pattern of the piece from the inverse projection of the intercepting points in 3D to the patterns in 2g) or 2h). For Tachi-Miura Polyhedron (TMP) in 3e), applying forces as in 3f) in the perpendicular direction of the panel allows flat foldability as shown in the two directions in 3g) and 3h). The RSO-type polyhedron in figure 3i) also is flat foldable (figure 3j) but there are shocks in the intermediate layers that must be considered in the design (see figure 3k). Although TMP has been widely explored in cellular structures to absorb energy, its design parameters must be well explored to avoid self-intercepting vertices. On the other hand, RSO-polyhedron has not been widely explored in cellular structures but it allows controlling deformation modes, has a low initial peak force and has better absorption properties than TMP. Using the dual model of 3a) to generate a hexagonal mesh directly and avoid the problems mentioned above is under consideration. Figure 3l) shows the dual model to the model in 3a).

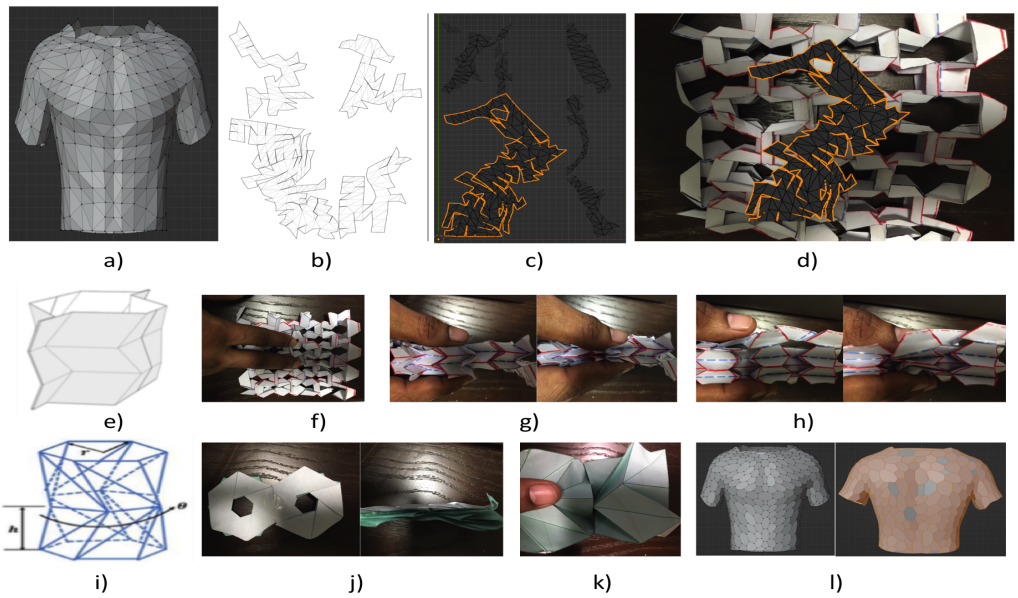

Figure 3: Honeycomb suit using Miura and RSO polyhedrons: a) Triangular mesh b-c) 2D pattern d) Inverse projection e) Miura polyhedron f) Perpendicular forces to Miura-polyhedron panel g-h) Lateral views in two directions i) RSO polyhedron j) Top ad lateral view of two folded polyhedrons k) Crashes in RSO panels l) Dual mesh from a)

[1]Available at http://blender.org

4. Conclusions and future work

In addition to being flexible, it is desirable for a protective shield to be lightweight, preventilated so that the areas beneath it can be ventilated, and not damaged by water or perspiration. In the past, these protective shields have been largely made of elastomeric foam. Increasing the shock absorbing qualities of a foam body shield necessarily requires making the entire shield thicker, less flexible, bulkier and more difficult to ventilate. The proposed kirigami-based manufacturing technology is a viable option to solve the above problems.

References

[1] SaferSports, LLC: FOOTBALL HELMET HAVING IMPROVED IMPACT ABSORPTION, *US Patent US10,201,743B1*, Feb 12, (2019).

[2] J Brennan-Craddock, D Brackett, R Wildman and R Hague: The design of impact absorbing structures for additive manufacture, *Journal of Physics: Conference Series* , 382 (2012).

[3] L. Mullen, R. C. Stamp, W. K. Brooks, E. Jones, and C. J. Sutcliffe: Selective Laser Melting: a regular unit cell approach for the manufacture of porous, titanium, bone in-growth constructs, suitable for orthopedic applications, *Journal of biomedical materials research. Part B, Applied biomaterials* , vol. 89, no. 2, pp. 325-34, May. (2009).

[4] C. Chu, G. Graf, and D. W. Rosen: Design for Additive Manufacturing of Cellular Structures, *Computer-Aided Design and Applications* ,vol. 5, no. 5, pp. 686-696, (2008) .

[5] V. R. Gervasi and D. C. Stahl: Design and fabrication of components with optimized lattice microstructures, *Proceedings of the Solid Freeform Fabrication Symposium*, (2004).

[6] Saito, K., Pellegrino, S., and Nojima, T.: Manufacture of Arbitrary Cross-Section Composite Honeycomb Cores Based on Origami Techniques. *ASME. J. Mech. Des.* 136(5): 051011. May (2014)

[7] Calisch, SE, and Gershenfeld, NA. Towards Continuous Production of Shaped Honeycombs. *Proceedings of the ASME 2018 13th International Manufacturing Science and Engineering Conference*. Volume 3: Manufacturing Equipment and Systems, V003T02A007. June 18-22, (2018).

[8] Bo Yu and Maria Savchenko and Junichi Shinoda and Luis Diago and Ichiro Hagiwara and V. Savchenko. TProducing Physical Copies of the Digital Models via Generating 2D Patterns for "Origami 3D Printer" system. *Journal of Advanced Simulation in Science and Engineering*. vol. 3, no. 1, pp. 58-77, (2016) .

JSST 2022

Effectiveness of Turn Alternation Strategy

Atsushi Tanaka[1,*] and Tetsu Takahashi[2]

[1]Graduate School of Science and Engineering, Yamagata University
[2]Faculty of Engineering, Yamagata University

[*]tanaka@yamagata-u.ac.jp

The full paper of this paper has been published in Journal of Advanced Simulation in Science and Engineering (JASSE).

DOI: https://doi.org/10.15748/jasse.10.198

JSST2022

An image analysis for automatic detection of social interaction between drosophila: biased courtship behavior

Tasuku Arai[1], Ki-Hyeon Seong[2], Siu Kang[1*]

[1]Department of Mechanical Systems Engineering, Graduate School of Science and Engineering, Yamagata University

[2]Department of Liberal Arts and Science, Kanagawa University of Human Service

*siu@yamagata-u.ac.jp

Abstract. Drosophila has been frequently used in genetic research field. In many drosophila research, it is important to detect each stage of life-events of individual insect. Furthermore, social interaction such as mating is also crucial for keeping of species. Here, we developed an algorithm for detection of social interaction of drosophila by some image processings. Especially, we focused on the courtship behavior from female to male, which is less known because the ones from male to female is dominant in natural condition. We extracted approaching behavior of freely-moving females toward immobilized-male and female from sequential images obtained by long-time monitoring. Also we quantified a differences of the behavior as biased courtship behavior. As a result, it was demonstrated that some female drosophila showed much approaching during the recording. This result implies that female drosophila has also gender-preference in their behavior even it is weaker than the ones of male. It is expected that present result contributes to genetic research such as seeking of mating-events-related genes of drosophila.

Keywords: Image processing, Social interaction, Biological data, Behavioral analysis

1. Introduction

Drosophila is model animal in genetic research field. The animal has been used in screening through several gene manipulation such as gene knock-in/out, and so on. Drosophila is also holometabola insect and it has distinct life-stage accompanying drastic morphological changes. In many genetic research, the genetic effect onto the timing and duration of life-events has been well examined. We previously developed the Drosophila Individual Activity Monitoring and Detection System (DIAMonDS) toward high-throughput screening in genetic research field [1]. The system provides automatic and high-accurate detection of drosophila life-events such as pupariation, eclosion, and death with single animal resolution. However, social interaction among multiple insect is not covered. Present study focused on courtship behavior which occurs before the mating as one of indicator of it. In this study, we tried to capture the feature of

female drosophila's courtship behavior through the image processing to the sequential images obtained by continuous monitoring of drosophila.

2. Method

2.1. Analyzed data

We analyzed the movie data which were recorded at RIKEN Tsukuba Institute. Each movie includes six wells (2rows x 3columns) and three flies were placed in a well (Fig1).
Adult of freely-moving female is located in the center of a well, and adult drosophila of female and male immobilized by surgical treatment were placed in both side of the freely-moving female (Fig2). Sequential images were extracted from movie data and the images were performed additional processings described in next section.

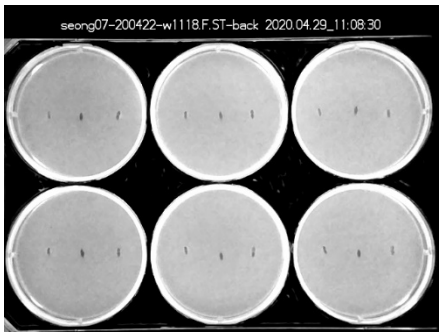

Fig1 An image example of six wells

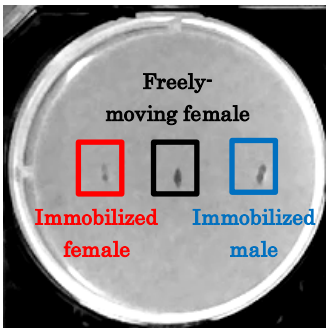

Fig2 Configuration of individual drosophila in a well

2.2. Preprocessing for behavioral analysis

Image processing for behavior analysis is as follows:
First, each well was trimmed and separated from an entire image (Fig3(a)). Second, target individuals (freely-moving female) were extracted by background subtraction using Mixture Gaussian after the noise reduction (Fig3(b)). Third, extracted target image was binarized and performed morphological filter for filling to target region and reduction of noise (Fig3(c)). Fourth, center of mass of target animal was calculated from the binary images for tracking of trajectory of behavior.

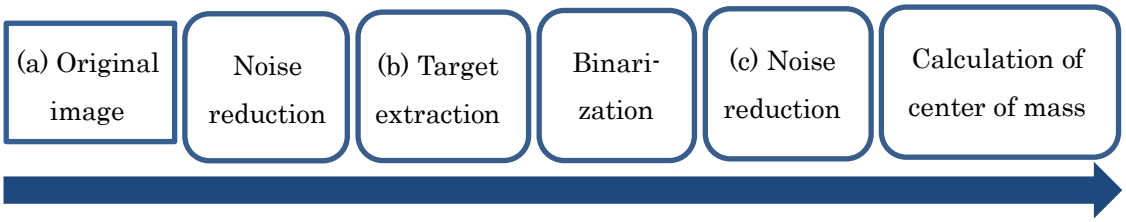

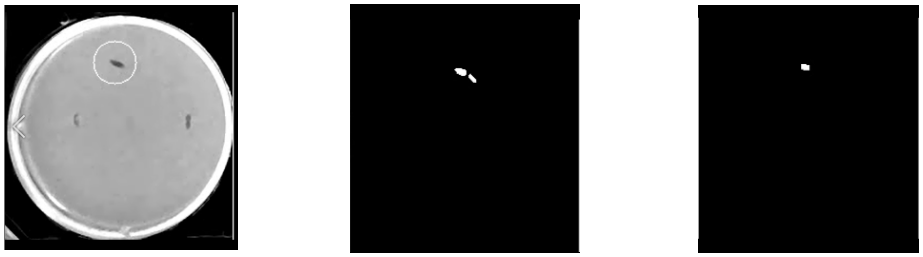

(a) Original image (b) Extracted target (freely-moving drosophila) (c) Image after Noise reduction

Fig3 Preprocessing flow chart

2.3. Evaluation of approaching behavior

From the time series of gravity center, we quantified and evaluated courtship behavior of freely-moving female drosophila. We calculated distance from a target to a immobilized male located at right side and immobilized female placed at left side as *dR*, *dL*. In order to quantify courtship behavior, we introduced *bias index* (*BI*) with the *dR*, *dL* as follows:

$$Bias\ index\ (BI) = \frac{dR - dL}{dR + dL}$$

Approaching behavior of freely-moving female and its bias was quantified by using the *bias index*. In addition, time-dependent characteristics of the biased courtship behavior was also evaluated.

3. Results

Figure 4 indicates heatmap of stay-time distribution of freely-moving female in well 1. Some females showed bias in its stay-time such that it spent longer time at nearby male. It was also shown that target individuals often move along an edge of well.

Figure 5 corresponds the time series of cumulative *bias index* for six wells. In four of six female, cumulative bias showed positive values at the end of frame. In other words, frequency of approaching behavior to male was higher than the ones to female in these four females.

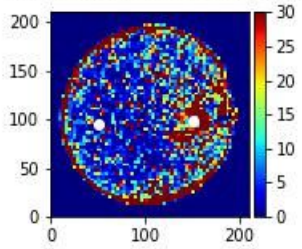

Fig4 An example of stay-time distribution (well 1)

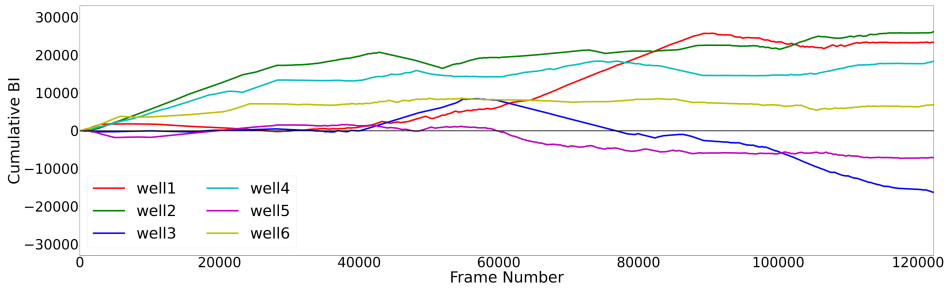

Fig5 Time course of cumulative BI

4. Conclusions

In the present study, we tried to capture the feature of female drosophila's courtship behavior by image analysis of sequential images obtained from continuous recording. As a result, it was demonstrated that some female drosophila more frequently approached to male than female. This result indicates the existence of biased courtship behavior of female drosophila. The biased courtship behavior, which is usually varied into more dominant male's active behavior in natural condition, was captured in specific condition in which targets of courtship behavior were immobilized.

Because it was reported that mating between drosophila pair much occur in early morning [2], cumulative *bias index* in limited time range is effective to reveal the time-dependent structure of the biased courtship behavior. The biased courtship behavior in present study was incompatible with normal mating, however, it was suggested that mating was interaction between both gender. It is expected that present study might contribute genetic research related with social interaction between drosophila.

Reference

[1] Seong K.H., Matsumura T., Shimada-Niwa Y., Niwa R., Kang S. (2020) "The Drosophila Individual Activity Monitoring and Detection System (DIAMonDS)", *eLife*, DOI: 10.7554/eLife.58630

[2] Sakai T. and Ishida N. (2001) "Circadian rhythms of female mating activity governed by clock genes in Drosophila", *Proc Nat Acad Sci*, Vol.98, No.16, pp.9221-9225

Activation Functions for Chaotic and Random Neural Networks

Hitoaki YOSHIDA[1*], Takeshi MURAKAMI[2]

[1]Faculty of Education, Iwate University, Japan

[2]Technical Division, Iwate University, Japan

*hitoaki@iwate-u.ac.jp

Abstract. A new activation function has been proposed for the computation of Chaotic and Random Neural Network (CRNN) on GPU instead of Asymmetric Piecewise-Linear-Function (APLF). CRNN with the proposed function generates statistically appropriate pseudo-random number (PRN) series, but the periods of PRN series were too long to compute. The periods have been estimated by the exponential-approximation function at 5×10^{18} - 3×10^{20}.

Keywords: Controller Area Network, Neural Network, Pseudo-Random Number

1. Introduction

The information security of the Controller Area Network (CAN) has attracted considerable attention in these years. We have reported the fast and secure PRN generator (PRNG) by using GPU [1-3] and the application to the secure CAN [4]. The PRNG consists of the Chaotic and Random Neural Network (CRNN) with the fix-point arithmetic (Q5.26) and the asymmetric piecewise-linear-function (APLF) [1-3].

This study aims to implement a high-performance PRNG by using a new activation function for the GPU architecture.

2. Asymmetric Piecewise-Linear-Functions (APLFs)

APLFs that have been used in our studies are shown in Figures 1-2, and the typical examples of the coordinate values of APLFs are shown in Table 1. The APLF has no symmetric operation except an identity operation. The first APLF is designed for floating-point arithmetic to improve computation performance as the approximate function of the logistic sigmoid function (Figure 1). The value range is limited [0, 1] by APLF, itself.

APLF1 is designed for the fix-point arithmetic (Q5.26) and to avoid periodic windows on the chaotic time series, the value range is limited [-32, $32-2^{-26}$] by the fix-point arithmetic (Figure 2a). The graph of $f(u) = u$ is superimposed on the graph of APLF with a dashed line. An intersection of two graphs is a fixed point of the activation function. Actually APLF1 has 3 fixed points; 2 attractive fixed points near (20.999784, 20.999784) and (-20.999900, -20.999900), and the repelling fixed point near (-0.292066, -0.292066). Therefore, the distribution of CRNN outputs (the attractor of outputs) was not uniform.

APLF3 is designed to reduce the effect of the fixed point of the activation function and to change the distribution of CRNN outputs close to a uniform distribution.

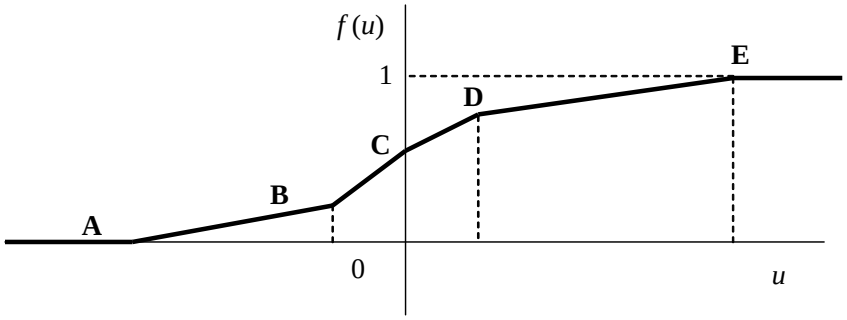

Figure 1: APLF for Floating-Point Arithmetic.

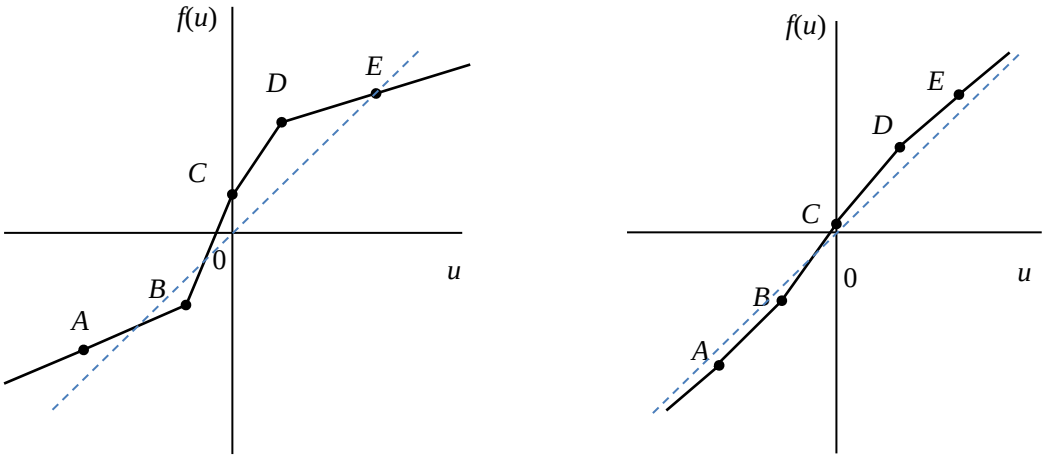

(a) APLF1 (b) APLF3

Figure 2: APLFs for Fix-Point Arithmetic (Q5.26).
The graph of $f(u) = u$ is superimposed on the graph of APLF with a dashed line.

Table 1: Typical Examples of Parameters of APLFs. [a)]

		A	B	C	D	E
APLF [1]	u	-51.00010	-1.980101	0.000000	1.980101	64.000100
	$f(u)$	0.000000	0.098990	0.499012	0.889100	1.000000
APLF1 [2]	u	-21.000100	-4.980101	0.000000	4.980101	21.000200
	$f(u)$	-21.000000	-12.989900	0.499012	12.689100	21.000000
APLF3 [3]	u	-31.000100	-7.981100	0.000100	7.981101	31.000200
	$f(u)$	-31.001000	-8.299990	0.500012	8.690100	31.009990

a) The values of a decimal place can be randomly determined.

3. New Type Activation Functions

One of the bottleneck processes of the CRNN program in GPU is APLF since it involves conditional branches. The revised method in this work is expected to replace APLF without

conditional branches as follows. As for APLF3, the slopes are almost 1, *e.g.*, d*f*/d*u* = 0.9862 in (*A*, *B*), 1.1026 in (*B*, *C*), 1.0262 in (*C*, *D*), 0.9696 in (*D*, *E*), it may be regarded as random number addition as shown in Figure 3. The possible modification is shown in Equation 1, where *pr* is an additional PRN, $x_i(t)$ is an output from the *i*th neuron at time *t*, *w* is a synaptic weight, and *I* is an external input. Ideal examples of outputs $x_j(t+1)$ are shown with cross marks in Figure 3.

$$x_j(t+1) = \sum_{i=1}^{n} w_{ij} x_i(t) + I + pr \qquad (1).$$

The question is how to generate a pseudo-random number (*pr*) in Equation 1. The time series generated from CRNN can separate into 2 independent subseries [1,2], therefore, a possible choice of *pr* is a PRN extracted from another subseries.

$$pr = g_m(x_k(t)) \qquad (2),$$

where $k = (j + 2)\ \%\ 4$ or $k = j$ (j = 0, 1, 2, 3). Let us call the former Method 1 and the latter Method 2. $g_m(x)$ is a function of PRN extraction from a time series *x*, *m* is the number of upper bits of the time series that is truncated from $x_k(t)$.

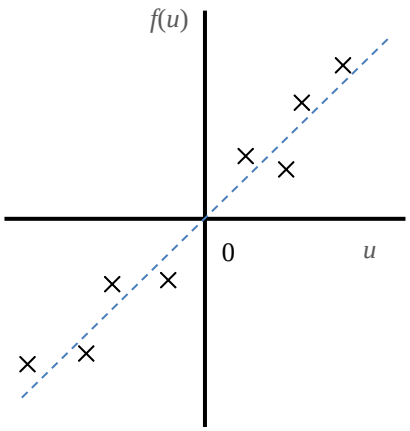

Figure 3: Concept of New Type Activation Function for GPU.

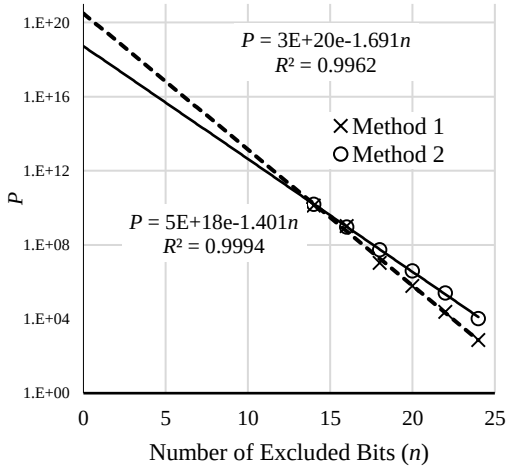

Figure 4: Empirically Obtained Period (*P*) by using Methods 1 and 2.

For the purpose of extracting secure PRN, a possible value of *m* has been estimated at 2 by using the NIST SP800-22 test suite [5] and by the other requirements for security. Only the results of Method 2 are shown in Table 2 because Method 1 didn't afford appropriate results.

Table 2: Result of Proportion of Sequences Passing a Test in NIST SP800-22 test suite. [a)]

Method	*m*	**FR**	**FB**	**CS**	**RU**	**LR**	**RK**	**OT**
2	0	1.1	12.9	1.0	0.9	0.3	0.4	0.4
2	1	0.2	0.0	0.1	0.0	0.3	0.0	0.8
2	2	0.4	0.0	0.1	0.2	0.2	0.1	0.8

a) The tests are repeated by 1000 times and obtained fail rates (%) are listed in the Table.

Next, we tried to compute the period of the PRN series (P), but it was too long to directly compute. The PRN series excluded n-lower-bit are used to estimate the period of the PRN series. The result is shown in Figure 4, where the dashed line is the approximate curve for Method 1 and the solid line is that for Method 2. The extrapolated value to 0 is 3×10^{20} for Method 1, and 5×10^{18} for Method 2.

4. Results and Discussion

A new type of activation function $g_m(x)$ without the bottleneck process of the computation on GPU has been proposed in this work. An empirical study by the NIST SP800-22 test suite suggests $m = 2$, which is the number of the truncated-upper-bit of the time series. The additional PRN has been extracted from outputs of the kth neuron, where $k = (j + 2)$ % 4 or $k = j$. The proposed activation function generates statistically appropriate PRN series, but the periods of PRN series were too long to compute. The periods of the PRN series have been estimated by the exponential-approximation curve at 3×10^{20} as for Method 1, and at 5×10^{18} as for Method 2. The periods are considerably large compared with the period of the normal series ($\approx10^{10}$).

5. Future Work

Accurate periods of the PRN series should be determined for reasons of information security, therefore a method of preparing PRN will be modified instead of Equation 2.

To evaluate the performance of the new activation function the rate of PRN generation will be studied by using a PC equipped with the latest GPU board.

Acknowledgments

Part of the experimental results in this research was obtained using supercomputing resources at Cyberscience Center, Tohoku University.

References

[1] H. Yoshida, Y. Kon, and T. Murakami: Chaos Neural Network for Ultra-Long Period Pseudo-Random Number Generator, *Proceedings of Papers, ITISE 2017,*1 (2017), pp.102-113.

[2] H. Yoshida, Y. Akatsuka and T. Murakami: Implementation of High-Performance Pseudo-Random Number Generator by Chaos Neural Networks using Fix-Point Arithmetic with Perturbation, *Proceedings of Papers, NOLTA 2018,* (2018), pp46-49.

[3] H. Yoshida, H. Fukuchi and T. Murakami: Implementation of High-Speed Pseudo-Random-Number Generator with Chaotic and Random Neural Networks, *Proceedings of Papers, HICSS53 2020*, (2020), pp.6418-6425.

[4] Z. Liu, T. Murakami, S. Kawamura, and H. Yoshida: Fast Stream Cipher based Chaos Neural Network for Data Security in CAN Bus, *Advances in Science, Technology and Engineering Systems Journal*, 5:5(2020), pp.63-68.

[5] A. Rukhin, J. Soto, J. Nechvatal, M. Smid, E. Barker, S. Leigh, M. Levenson, M. Vangel, D. Banks, A. Heckert, and J. Vo. S. Dray, *A Statistical Test Suite for Random and Pseudorandom Number Generators for Cryptographic Applications, NIST SP800-22 rev.1a, Revised: July 2015 (sts-2.1.1)*, Lawrence E. Bassham III, (2015).

JSST 2022

In-situ Visualization of 3-D Cellular Automata

Ren Sakai*[1], Wang Yan[1], Akira Kageyama[1]

[1]Graduate School of System Informatics, Kobe University, Japan

*225x209x@stu.kobe-u.ac.jp

Abstract. In situ visualization in computer simulations requires predetermination of the viewpoint and view direction. However, knowing the appropriate camera settings in advance for highly complex phenomena with unpredictable dynamics is challenging. We have made a visualization camera an autonomous entity. The camera agent automatically tracks a focal point in the simulation by following the equation of motion under a virtual force field emitted from the focal point. We have applied the in situ visualization with the camera agent method to a three-dimensional cellular automaton with complex time development.

Keywords: In-situ visualization, Cellular automaton, High performance computing

1. Introduction

In situ visualization is indispensable in large-scale computer simulations today [1]. One can retrieve quality visualization images with high resolution both in space and time by using the in situ visualization. A challenge with the in situ visualization approach is the parameter setting for the visualization camera. One must specify the viewing position and viewing direction for the in situ visualization in advance. For highly complex phenomena, however, it is difficult to predict the location of focus or volume of interest (VOI) to which in situ visualization is applied.

We proposed a new approach to the in situ visualization in which the viewing positions and viewing directions are automatically controlled in accordance with the running simulation [2]. In this method, we make the visualization camera an autonomous entity or an agent. The camera agent for in situ visualization is assigned to track the unpredictable behavior of VOI. A key point of this agent camera is the design of rules that realize the automatic detection of VOI in the simulation region and automatic tracing of its motion in the simulation's time development.

This study aims to propose a rule for the camera agent for 3-dimensional (3D) cellular automaton (CA) calculation. 3D CA is a prototype for computer simulation of highly complex phenomena with unpredictable VOI.

The automatic setting of the camera path has been intensively investigated in computer graphics [3, 4, 5]. Here, a relatively simple algorithm for the camera motion is adopted because the camera agent should respond to ever-changing simulation data.

2. 3D CA and the Rule of Camera Agent Motion

In this paper, we consider the following 3D CA in the Cartesian alignment of cube cells. Each cell may have n different states. The state is designated by an integer from 0 to $n-1$. Cells with a 0-state are called *non-alive*. Cells with i-state ($0 < i < n$) are called *alive*. A non-alive cell turns into 1-state in the next time step if the number of alive cells in its Moore neighbor is in a set B. It remains non-alive otherwise. Note that the number of Moore neighbors for each cell is 26. For example, when $B = \{2, 3, 5, 7\}$, a non-alive cell turns into state 1 ("born") in the next time step if its Moore neighbor has 2, 3, 5, or 7 alive cells. An alive cell keeps being alive in the next time step ("survive") if the number of 1-state cells in its Moore neighbors is in a set S. It turns into non-alive otherwise. For example, when $S = \{8\}$, an alive can remain alive only when it has 8 Moore neighbors. The state integer in every alive cell increases its value for one, at every time step. When the state integer reaches its maximum value ($n-1$), it turns into non-alive (0) in the next time step. A 3D CA is specified by $[B, S, n]$.

The rule of the camera motion proposed in this paper is basically described by the equation of motion under a potential field generated by the VOI. (The definition of VOI will be described below.) The potential ψ is defined as a function of the radius r to the VOI as $\psi(r) = c(r - r_0)^2$, where c and r_0 are constant. The agent follows Newton's equation of motion with the force from the potential ψ accompanied by a friction force that is proportional to the velocity. The friction is introduced to smooth the motion when the VOI accompanies rapid changes.

A VOI in this paper is simply defined as the center of gravity of alive cells. By this definition, the camera agent can trace the motion of an isolated pattern in 3D space. For example, when we calculate a 3D CA of rule $[B, S, n] = [\{5\}, \{4, 5\}, 2]$, several alive cells can form a sliding pattern with constant velocity. This is a 3D analog of "glider" in the well-known 2D CA, Game of Life. When there is only one glider in this 3D CA, the camera agent follows its motion by the attraction force toward the center of gravity of the glider.

In practice, more than one VOI can exist in 3D CA as well as in computer simulations in general. To pick up a VOI among multiple candidates, here we adopt the following algorithm. We first divide the entire simulation region into multiple D subdomains. Next, we count the number of 1-state cells in each subdomain before we select one subdomain that has the maximum number. Finally, we calculate the center of gravity of alive cells in the subdomain and define it as VOI.

In the present paper, the automatic control of the viewing direction of the camera agent is straightforward; it is always toward the focal point (center of gravity) in the VOI.

3. In-situ Visualization Results of 3D CA

We performed a 3D CA computation with rule $[B, S, n] = [\{4\}, \{4\}, 5]$. The total cell size is $N_x \times N_y \times N_z = 10^2 \times 10^2 \times 10^2$. We assume the periodic boundary conditions in all (x, y, and z) directions. In the initial condition, the cells in the central region were randomized to state-1 and state-0 with probabilities of 0.25 and 0.75, respectively.

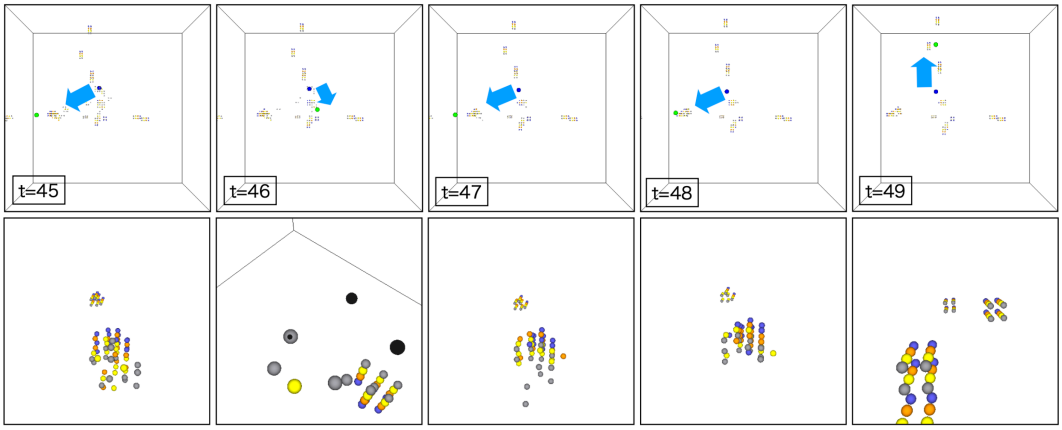

Figure 1: In situ visualization by an agent camera.

3D CA computation was performed on π-computer system of Kobe University, comprising 16 nodes of AMD EPYC CPU (512 cores in total). We applied the in-situ visualization with a camera agent in the framework of KVS [6]. The output images are stored as a sequence of image files in the hard disk drive of the computer system. These images are then combined into a video file that is played on PCs.

After a short interval of self-organization, this CA exhibits intriguing structures and dynamics, such as glider-like flying objects, their collisions followed by an explosive increase in alive cells, and the formation of bar-like straight objects.

Fig. 1 shows the time sequence of the snapshots. The above row shows the entire cells observed from outside the simulation region. The lower row shows the in situ visualization images taken by the agent camera at corresponding times. The green and blue balls in the above row indicate the positions of the focal point in the VOI and the camera agent, respectively. The blue arrows stand for the viewing direction of the camera agent. Colored small spheres show the cell states of alive cells. Non-alive cells are invisible. This figure indicates that the agent camera successfully tracked a VOI.

4. Summary

We have developed a method to apply automatic control of the viewing position and viewing direction for the in situ visualizations. The key idea is to regard the visualization camera as an autonomous entity. The method is applied to a 3D CA computation that exhibits complex and unpredictable state changes. The agent camera successfully tracks a VOI and produces a sequence of visualization images captured near the VOI from an appropriate distance.

Acknowledgements

We thank Dr. Naohisa Sakamoto for valuable technical advice and fruitful discussions.

References

[1] Hank Childs, Janine C Bennett, and Christoph Garth, editors. *In Situ Visualization for Computational Science*. Springer International Publishing, 2022.

[2] Wang Yan and Akira Kageyama. Toward agent-based in situ visualization. In *Proc. AsiaSim 2021*.

[3] Steven M Drucker and David Zeltzer. Intelligent camera control in a virtual environment. In *Graph. Interface '94.*, pages 190–199.

[4] Alaa Tharwat, Mohamed Elhoseny, Aboul Ella Hassanien, Thomas Gabel, and Arun Kumar. Intelligent bézier curve-based path planning model using chaotic particle swarm optimization algorithm. *Cluster Comput.*, 22(s2):4745–4766.

[5] Zeqiu Chen, Jianghui Zhou, Ruizhi Sun, and Li Kang. A new evolving mechanism of genetic algorithm for multi-constraint intelligent camera path planning.

[6] Naohisa Sakamoto and Koji Koyamada. KVS: A simple and effective framework for scientific visualization. *J. adv. simul. sci. eng.*, 2(1):76–95, 2015.

Virtual-reality visualization of number density of intersection points of energetic tritons and plasma-facing wall

Hiroaki Ohtani[1,2*], Kunihiro Ogawa[1,2], Suguru Masuzaki[1,2], Seiji Ishiguro[1,2]

[1]National Institute for Fusion Science
[2]Department of Fusion Science, The Graduate University for Advanced Studies (SOKENDAI)
*ohtani.hiroaki@nifs.ac.jp

Abstract. We develop virtual-reality (VR) visualization software to display the number density of intersection points of tritons and a plasma-facing wall by a heat map method. The divertor plate and vacuum vessel wall are displayed by triangles colored according to the number density. The triangles of the divertor plates and vacuum vessel wall are superimposed onto the rendered CAD data of the vacuum vessel wall by Unity and displayed in one VR space in real time. It is possible to check where the tritons attack on the wall and to investigate the number density.

Keywords: virtual-reality visualization, number density, intersection point

1. Introduction

Since fusion basically solves energy and environment problems, it is a key energy source to realize carbon neutrality. Realization of a fusion energy power plant has many issues. One of them is a tritium inventory. Tritium circulates in the fuel system of the fusion reactor. However, the tritium stays in an unnecessary space and does not circulate in areas such as the divertor plates and the vacuum vessel wall. When the amount of tritium inventory increases, circulation is stagnant, and its operation faces difficulty. The divertor plates and vacuum vessel wall are directly approached by the tritium and the plasma-facing wall and affects the increase of the inventory at the wall. Since the first deutrerium operation in the Large Helical Device (LHD) of the National Institute for Fusion Science (NIFS) [1], the accumulated tritium in the plasma-facing wall has been experimentally investigated [2-4]. Material probes were placed on the wall to measure the energetic triton accumulation on the vacuum wall. In the previous paper [5], we visualized the intersection points of energetic tritons with the wall as spheres through the virtual-reality (VR) system “CompleXcope” of NIFS with the CAD data of divertor plates and the vacuum vessel wall to determine the appropriate positions of the material probes. In this paper, we report the other VR visualization of the collision points by a heat map method for a quantitative analysis.

2. Trajectory and intersection points of triton[6]

The triton generation distribution is given from a neutron generation distribution in the deuterium operations of the LHD by the FIT3D-DD code [7]. The initial positions of tritons are determined by using uniform random numbers to reproduce the generation distribution. Under conditions in which the velocity distributions are isotropic along the parallel and perpendicular to the magnetic field, respectively, the initial velocities of tritons are given by uniform random numbers. The LORBIT code [8] calculates the triton trajectory by solving the Newtonian equation of motion without any collision effects under conditions in which the magnetic field is in a vacuum, the effect of the plasma is not included, and the electric field is negligibly small. The intersection points of the tritons and the plasma facing wall are detected. The divertor plate is expressed by triangles based on the design data and the vessel wall is constituted of triangles by the row of coordinate points of the vessel wall on each poloidal angle. A winding number algorithm calculates whether a triton orbit exists inside or outside the polygons, and the intersection points are detected. We count the number of intersection points on each triangle and store the number of the points and the three-dimensional coordinates of the vertex of the triangle in the Cartesian coordinate system.

3. VR visualization

We develop VR visualization software for a CAVE-type VR system based on the Virtual LHD [9] for displaying the number density of the collision points by a heat map method. The developed software reads the three-dimensional coordinate data of the triangle vertex and the number of intersection points and calculates the number density of the intersection points on the triangle. The triangle is colored according to the value of the number density and presented as a triangle, configured by the three vertex coordinates, by OpenGL. The normal vector pointing to the inside of the vessel is used for describing the triangle surface. Unity [10] renders the internal wall and the divertor plates of the LHD, based on the CAD design data, which was used for construction of the real LHD. The version of Unity is 5.3.4 because of the following software: FusionSDK [11]. FusionSDK captures the OpenGL image data rendered by different software, superimposes them in one VR space and displays them in real time [12,13]. By this Fusion SDK, the triangle rendered by OpenGL and the inner components of the LHD are visualized integrally in the VR space.

4. Visualization results

The number of triangles is 466,316. The left figure in Fig. 1 shows the distribution $f(n)$ and the cumulative distribution $F(n)$ of the triangle numbers as a function of the number density n. The distribution $f(n)$ indicates the number of triangles at the density n, and the cumulative distribution $F(n)$ is defined as $F(n) = \sum_{m=n}^{N} f(m)$, where N is the maximum of the number density. The average, maximum and minimum values of the triangle area are 4.17×10^4 mm^2, 7.15×10^{-1}mm^2, and 4.28×10^3mm^2, respectively. Since the number density of almost all the triangles is zero, as shown in Fig.1 (left), we display the triangles whose number density is larger than zero with the vacuum vessel CAD data in the VR space. The right panel of Fig.1 shows the triangles in the vacuum vessel in the VR space. The divertor plates are in the center region of the figure and the plates are expressed by the OpenGL triangles, colored according to the number density. The gray wall in the left region of the figure is the vacuum vessel wall, and several OpenGL triangles are distributed on the wall. The color of the triangles is dark blue. Since the maximum number density is about 50.6 (1/mm^2), the dark blue

indicates the value from 1 (1/mm^2) to 5 (1/mm^2). Almost all triangles are colored dark blue and those with other colors are rare, since the number of triangles of 10 (1/mm^2) or greater is approximately 30 in the left figure of Fig.1. The right figure in Fig.1 shows that energetic tritons attack not only the divertor plates but also the vacuum vessel wall. This tendency was shown in the previous work [2]. By using this type of visualization, it is also possible to detect the position where the tritons attack. However, since almost all the triangles are the same color, it is needed to perform a fine-tuning of the color function in such a way that the color sensitively depends on the number density around 1 to 10 (1/mm^2). Moreover, the CAD data of the divertor plates is not shown integrally, because the triangles of the divertor plates are superimposed on the same position as the CAD data. However, since the triangles with a number density of 0 (1/mm^2) are not shown, it is impossible to see the divertor structure. Research into effective visualization for this situation is a future work.

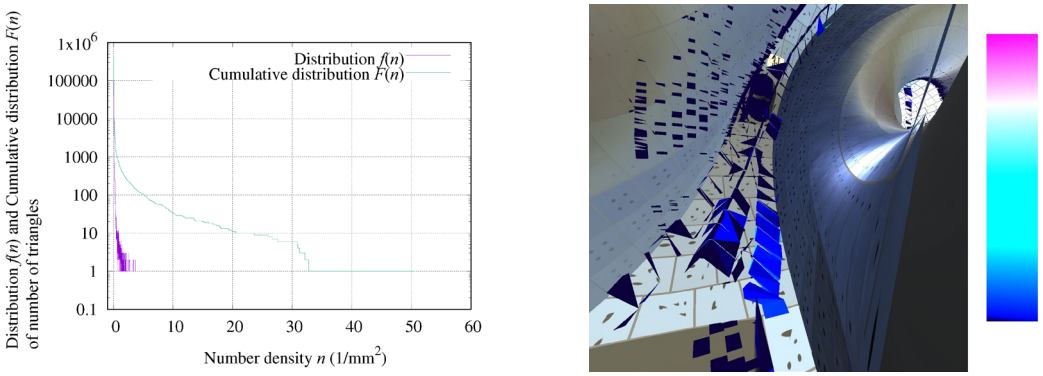

Fig.1: (left) Distribution $f(n)$ and cumulative function $F(n)$ of triangle numbers as function of number density n, and (right) polygons displayed in vacuum vessel in VR space with color map.

5. Conclusion

We visualized the number density of the intersection points of energetic tritons and the plasma-facing wall by using the triangle in the VR space with the CAD data of the vacuum vessel wall. To reduce the number of visualized polygons, we displayed the polygons with a number density greater than 0 (1/mm^2). This visualization made it possible to check the attacked region and the number density. Effective visualization for investigating quantitatively the number density is a future work.

Acknowledgements

This work is performed with the support and under the auspices of the NIFS Collaboration Research program (NIFS22KIIS001, NIFS22KIGS001) and by the LHD project budget (NIFS20ULHH003, NIFS20ULHH034).

References

[1] M. Osakabe et al: *Fusion Science Technology*, Vol.72 (2017), 199.

[2] S. Masuzaki et al: *Physica Scripta*, Vol. T170 (2020), 014068.

[3] S. Masuzaki et al: *Nuclear Material Energy*, Vol. 26 (2020), 100884.

[4] M. Yajima et al: *Nuclear Science Technology*, Vol. 27 (2021), 100906.

[5] H. Ohtani et al: *Journal of Visualization*, Vol. 25 (2022), 281-292.

[6] K. Ogawa et al: *Plasma Science Technology*, Vol. 21 (2019), 025102.

[7] R. Seki et al: *Plasma and Fusion Research*, Vol.14 (2019), 3402126.

[8] M. Isobe et al: *Journal of Plasma and Fusion Research*, Vol. 8 (2009), 330.

[9] A. Kageyama et al: Proc. 1*6th international conference on the numerical simulation of plasmas (ICNSP)*. (1998), 138.

[10] Unity: https://unity.com/

[11] FusionSDK: https://www.fiatlux.co.jp/product/virtual/easyvr/

[12] H. Miyachi et al: *IEEE Comp Soc* (2005), 530.

[13] H. Miyachi et al: *IEEE Comp Soc* (2007), 536.

Evaluation of Electrostatic Potential of Molecules by Electron Diffraction Technology

Takuo Yasuanga[1*], Yasuhisa Honda[1]

[1]Department of Physics and Information Technology, School of Computer Science and Systems Engineering, Kyushu Institute of Technology

*yasunaga@phys.kyutech.ac.jp

Abstract. In electron microscopy, the interference by the phase shifts of electron waves, which occur when electrons interact electrostatically with a sample, gives us the contrast of images. Thus, electron microscopy elucidates the ionic nature and polarization due to the electron clouds. Previous research has visualized the charge of each atom. Moreover, the Mirco-ED (electron diffraction) techniques can produce structural information with a resolution of over 1 Å. Thus, one can also obtain the polarization of electron clouds. Here, combining quantum chemical calculations with experimental results by micro ED, we report how to refine the molecular structure and determine the positions of hydrogens of a hydroxy group, a methyl group etc., which have less than one electron.

Keywords: Electron microscopy, Electrostatic potential, Quantum chemical calculation

1. Introduction

The phases of electron waves shift when electrons interact electrostatically with atoms and produce image contrast of electron microscopy. In other words, the image contrast or diffraction patterns reflect the electrostatic potentials. The potentials are due to the positive charge of the atomic nucleus by shielding surrounding electrons. Thus electron microscopy can elucidate the ionic nature and polarization of the electron clouds. Previous research has reported that it is possible to visualize the partial charge of each atom.

Furthermore, the recent mircoED (electron diffraction) method gives structural information with a resolution of over 1 Å. However, researchers have often used the analysis programs for the X-ray diffraction method to analyze microED data. Thus these may generate some artefacts since current versions of tools do not fully utilize the ED data. Here, we compared the molecular electrostatic potentials calculated by quantum chemical calculations with experimental data obtained by micro ED and here show detection of the polarization of the electron cloud of each atom.

2. Matarials and Methods

We obtained microED data of acetaminophen with a transmission microscope (JEM2100,

JEOL) and a detector(HyPix-3000, RIGAKU) and then determined the initial atomic model by CrysAlis (RIGAKU). We automatically set the initial atomic coordinates of hydrogen atoms by Chimera and Eos. Then we obtained the electrostatic potential maps calculated quantum-chemically by GAMESS [1] and Gaussian [2], calculated the intensities of diffraction spots, Fc, from the maps, and compared the calculated ones and experimental ones as R-factor. The R-factors show the validity of electrostatic maps due to calculated atomic coordinates and the electron density map.

3. Results and Discussion

We obtained diffraction patterns of acetaminophen by micro-ED and solved its three-dimensional structure except for hydrogen atoms at the atomic levels. Then we added hydrogen atoms and optimized their coordinates of the hydroxy groups and the methyl groups by using their R-factors from each of the electron density maps and electrostatic potential maps. The R-factors from electron density maps were worse than those from the potential maps (Fig 1). The optimal positions were different. This situation shows that the polarization of electron distributions could be detectable and important for refinement of atomic coordinates.

Furthermore, we adapted the temperature factors of the whole molecule or each atom, and then the R-factors decreased. This decrease shows the possibility of fluctuations of each atom. At present, the calculation time of quantum chemical calculation is too long, and it is not easy to precisely refine the coordinates and electron distributions in each electron orbital. We will challenge new tools to determine them.

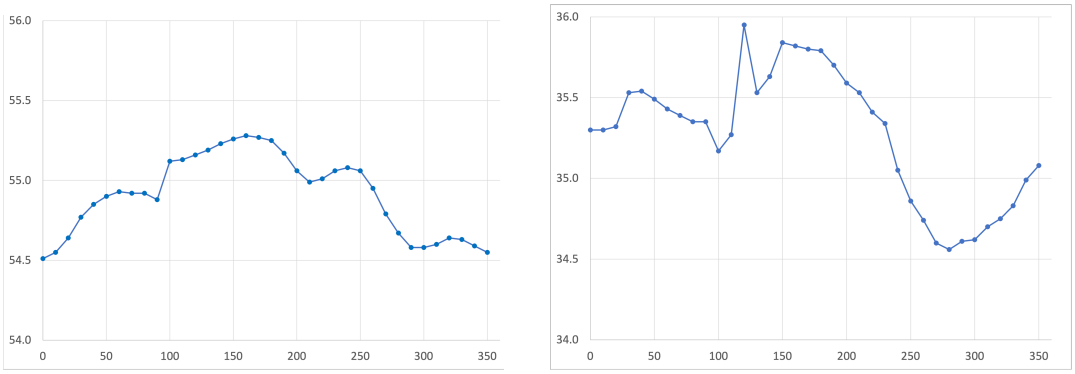

Fig. 1. The R-factors from electron density maps (left) and electrostatic potential maps. The horizontal axis shows the rotaton angles of the hydrogen of the hydroxy group and the vertical axis shows the R-factors.

References

[1] Schmit MW. et al.: General atomic and molecular electronic structure system, *J. Computational Chem.*, **14**:11 (1993), 1347-1363

[2] 安永 卓生, 田中 康太郎, 岩嵜 彩夏, 塚本 崇文, 本多 康久: 巨大システムとしてのクライオ電子顕微鏡法の自動化から自働化への展開, *顕微鏡* 56:1 (2021), 43-47 https://doi.org/10.11410/kenbikyo.56.1_43

Generation of Cell-Sized Water/Water Droplets through Phase-Separation under Confinement

Takahiro Kenmotsu[1*], Mayu Shono[2], Hiroki Sakuta[1], Kenichi Yoshikawa[1]

[1]1Faculty of Life and Medical Sciences, Doshisha University, Kyoto 610-0321, Japan
[2] Faculty of Science and Engineering, Doshisha University, Kyoto 610-0321, Japan
*tkenmotsu@mail.doshisha.ac.jp

Abstract. We have studied the stabirity of cell-sized micro-driplets entarping DNA and living cells in an aqueous two-phase system with a binary polymer, adapting and solving the Cahn–Hilliard Equation to interpret the essence of the observed phenomena of water/water phase separation. Based on the calculation results, we found that the tubule confinement of the glass capillary takes an essential role for the formation of uniform micro-droplets in size.

Keywords: self-organaization, water/water phase separation, cell-sized micro-driplet,

1. Introduction

We have developed a novel methodology to generate cell-sized droplets of polymer in a self-organized manner, adapting water/water (w/w) phase separation in an aqueous solution with binary polymers and performed experiments in the presence of both polyethylene glycol (PEG) and dextran (DEX) [1-3]. The micro-droplets of DEX is formed in PEG-rich phase in the concentraction of 5 wt % DEX and 5 wt % PEG. The micro-droplets distribute widely in size up to several hundreds micrometer. Recently, we have succeeded in arranging size of the droplets, inserting the droplets into a glass capillary with an inner diameter of 140 μm and aligning them in a row inside the capillary in a stable manner. We have constructed experiments, appling linearly arranged micro-droplets of DEX with the coexistence of DNA molecules of salmon sperm or living cells of red blood cells (RBC) and epithelial cells (NMuMG). The experimental results indicated that these biopolymers and cells are entapped inside the micro-droplets. In the present work, we show the culculation results on the stabirity in size of the formation of cell-sized doloplets through water/water phase separation, compaeing with experimental results.

2. Results and Discussion

In order to clarify and interpret the contribution of geometry of boundary condition on glass capillary for the formation of the micro-droplets through water/water phase separation, we have performed numerical calculations by adopting and solving the Cahn–Hilliard equation [3, 4] with two different boundary conditions; glass capillary and between planar glass plates, which hereafter are called ‘tubule’ and ‘planar-gap’, respectively. Figure 1 (a) and (b) shows the calculated results of formation of w/w droplets inside the tubule and planar-gap in a self-organized

manner under phase-separation in the presence of a binary polymer. The results indicated that uniform cell-sized droplets are generated with the boundary condition of tubule in a self-organized manner. Mwanwhile, w/w droplets tend to merge into larger droplets over time in the condition of the planer-gap. Shown in Fig.1 (c) is the snopshot of obaserverd linearly-arranged w/w microdroplets of DEX, indicating that uniform cell-sized droplets are generated in a self-organized manner [3].

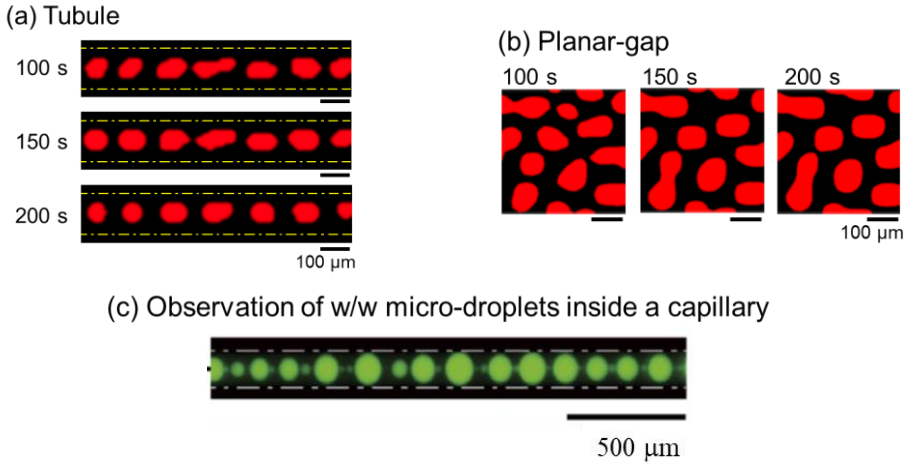

Fig. 1 Formation of w/w droplets under phase-separation with a bainary polymer over time. (a) Bounday condition of Tubule, (b) Boundary condition of Planar-gap. (c) Snapshot of observrd w/w/micro-droplets inside a capillary [3].

Summary

The calculation results indicated that the tubule confinement of the glass capillary take an essential role for the formation of micro-droplets with uniform size. Based on the experimental and numerical results, we expect that the cell-sized droplets launched in the present work are adopted to study on the self-construction of protocells and micro organoids [5].

References

[1] N. Nakatani, H. Sakuta, M. Hayashi, S. Tanaka, K. Takiguchi, K. Tsumoto, K. Yoshikawa, *ChemBioChem*, 19 (2018) 1370–1374.

[2] H. Sakuta, F. Fujita, T. Hamada, M. Hayashi, K. Takiguchi, K. Tsumoto, K. Yoshiakwa, *ChemBioChem,* 21(2020) 3323-2228.

[3] M. Shono, R. Ito, F. Fujita, H. Sakuta, K. Yoshikawa1, *Scientific Reports*, 11 (2021) 23570:1-9.

[4] J. W. Cahn, J. E. Hilliard, *J. Chem. Phys*. 28 (1958) 258–267.

[5] T. Yamazaki, T. Kishimoto, P. Leszczynski, K. Sadakane, T. Kenmotsu, H. Watanabe, T. Kazama, T. Matsumoto, K.i Yoshikawa, H. Taniguchi, *Materials*, 12 (2019) 1759:1-9.

Flight performance evaluation of polymer micromachined flapping-wing nano air vehicle using fluid-structure interaction analysis

Rashmikant, Daisuke Ishihara*, Minato Onishi

Department of Computer Science and Systems Engineering, Kyushu Institute of Technology, 680-4 Kawazu, Iizuka, Fukuoka 820-8502, Japan

*ishihara.daisuke399@mail.kyutech.jp

Abstract. In this study, the flight performance of insect-inspired and polymer micromachined flapping-wing nano air vehicle (FWNAV) has been evaluated using fluid-structure interaction (FSI) analysis. Polymer micromachined FWNAV is a complete 2.5-dimensional structure and it consists of a micro transmission, a pair of the micro wing, a bimorph actuator, and a support frame. The results indicate that the flight performance of FWNAV is approaching comparative to the weight of FWNAV. This study will lead to the development of flyable FWNAVs which can be further miniaturized since all of the components of our FWNAVs except the bimorph actuator are developed using polymer micromachining.

Keywords: FWNAV, 2.5-dimensional structure, polymer micromachining, insect-inspired design, computational biomimetics, FSI analysis

1. Introduction

Nowadays, with the fast development in science and technology, FWNAVs become the hottest research area. Researchers all over the world try their best to reduce the size and weight of FWNAVs similar to an insect. Consequently, some of the FWNAVs with a wingspan of 30-40 mm have been developed which generated sufficient lift and drag forces to hover but these FWNAVs are based on complex mechanical transmission mechanisms so their further miniaturization will be difficult [1,2]. One of the main challenges given to developing FWNAV equivalent to insect size is sufficient lift and drag force to hover.

There are two approaches to predicting the flight performance of the FWNAVs; experimental and computational approaches. A computational approach would be better for the prediction of flight performance of the designed FWNAV because of coupled physics between air and FWNAV structure simply known as fluid-structure interaction analysis (FSI). FSI design of a flexible micro wing can also accurately predict the flight performance [3] and at the same time, the micro wing actively uses the FSI to create passive wing deformation [4].

The conceptual design of polymer micromachined FWNAVs is shown in Fig. 1. This FWNAV

consists of a pair of micro wings and micro transmission with the 2.5-D structure, and a micro actuator of the piezoelectric bimorph [5]. These components can be easily fabricated using the polymer micromachining technique because of their 2.5-D structure.

In our previous study, FWNAV has been designed which produces a stroke angle of about 100° transmitted from the small amplitude of the piezoelectric bimorph actuator using the large deformation of the elastic hinges while flapping at a frequency similar to small insects [6].

The objective of this study is to estimate the flight performance of the previously designed FWNAV using nonlinear structural dynamics and FSI analyses. This study will lead to the development of flyable FWNAV which can be easily miniaturized because of the 2.5-D structure.

2. Fluid-structure interaction analysis

In FSI, the interaction between the elastic body and surrounding air is simulated by solving the incompressible fluid Navier-Stokes equation, the equation of motion for an elastic body, and the fluid-structure interface conditions using the arbitrary Lagrangian-Eulerian method [3,4].

A monolithic equation system for FSI has been formulated by applying finite element discretization to the above nonlinear equilibrium equation of motions and interface conditions to obtain these equations in matrix form. Thus, a monolithic equation system can be written as

$$ {}_{\mathrm{L}}\mathbf{Ma} + \mathbf{Cv} + \mathbf{N} + \mathbf{q(u)} - \mathbf{Gp} = \mathbf{g} \qquad (1) $$

$$ {}_{\tau}\mathbf{Gv} = \mathbf{0} \qquad (2) $$

where **M**, **C**, and **G** denote the mass, diffusive, and divergence operator matrices, respectively, and **N**, **q**, **g**, **a**, **v**, **u**, and **p** represents the convective term, elastic internal force, external force, acceleration, velocity, displacement, and pressure vectors, respectively, and finally the subscripts L and τ indicate the lumping of the matrix and the transpose of the matrix, respectively. These equations are solved by the projection method using algebraic splitting in the parallel computation environment.

3. Flight performance evaluation of flapping wing nano air vehicle

In a previous study, I designed the FWNAVs using an iterative design window search methodology [6]. In the following sub-section, the flight performance of this FWNAV has been evaluated using nonlinear structural dynamic analysis of FWNAV and FSI analysis of a micro wing.

3.1. Nonlinear structural dynamic analysis of FWNAV

Fig. 2 shows the problem setup for dynamic analysis of the FWNAV along with the material property distribution for the development of FWNAV using polymer micromachining. The material properties of two polyimides PI and PN-2000 are as follows: Mass density of 1420 kg/m^3, Poisson's ratio are 0.289 and 0.3, respectively and elastic modulus are 2.5 and 3.5 GPa respectively. In the problem setup, the sinusoidal forced vibration $u_x = U_x \times \sin 2\pi ft$ is applied to the transmission's area, where the free end of the bimorph is attached. The evaluation of forced vibration amplitude U_x = 81 μm has been discussed in the previous study [5]. The flapping frequency f = 100 Hz is chosen to avoid the sticking between elastic hinges during flapping motion [6]. The lower part of the supporting frame is fixed where the bimorph actuator is attached. In this setup, the finite element mesh with 17,582 elements and 78,451 nodes is

employed. The time increment is $\Delta t = T/4000$, and T is the flapping period and is equal to the inverse of f.

Fig. 3 shows the time history of flapping angular displacement at the position of wing attachment tip and the stoke angle from this time history is 39.25° which will be used for FSI analysis.

3.2. Fluid-structure interaction analysis of FWNAV

Fig. 4 shows the problem setup for FSI analysis. In this problem setup, the stroke axis is considered at a position similar to the wing attachment tip, see Fig. 2, and the MITC shell element is used for the micro wing (number of nodes: 143, number of elements: 120). In the problem setup, sinusoidal angular displacement $\Phi = \Phi_0 \times \sin 2\pi ft$ has been applied where angular amplitude $\Phi_0 = 39.25°$ is the stroke angle and $f = 100$ Hz is the flapping frequency, these parameters are given by the nonlinear structural dynamic analysis of FWNAV. The time increment is $\Delta t = T/5000$, and T is the flapping period which is equal to the inverse of f.

Fig. 5 shows the fluid mesh in 3-dimension and stabilized linear equal-order-interpolation velocity-pressure elements are used for the fluid mesh with the number of nodes 50460 and the number of elements 271922. Fluid (air) properties are as follows; mass density $\rho_a = 1205$ kg/m^3 and viscosity μ_a = 1,837e-05 kg/m-sec. FSI analysis has been carried out using the in-house code which is already validated [4].

Fig. 6 shows the time history of produced lift force which is evaluated at the position of r_2 nondimensional second-moment area and its mean value is 0.05mN which is approaching the comparative weight of FWNAV 54mN. The lift force can be further increased by optimization.

4. Conclusion

Flight performance of polymer micromachined FWNAV has been evaluated using FSI analysis. The mean lift force produced by FWNAV is 0.05mN approaching compared to the weight of FWNAV. Thus the development of flyable FWNAV is feasible and this can be further miniaturized because FWNAV is a complete 2.5-dimensional structure that can be easily fabricated using polymer micromachining.

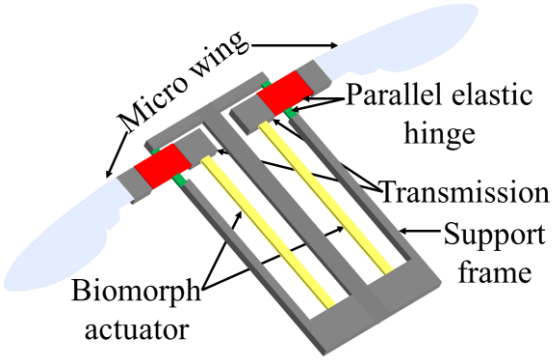

Figure 1: Conceptual view of polymer micromachined flapping-wing nano air vehicle

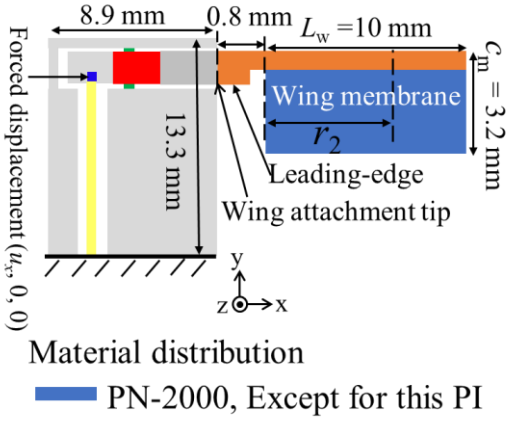

Figure 2: Problem setup for nonlinear structural dynamic analysis of FWNAV

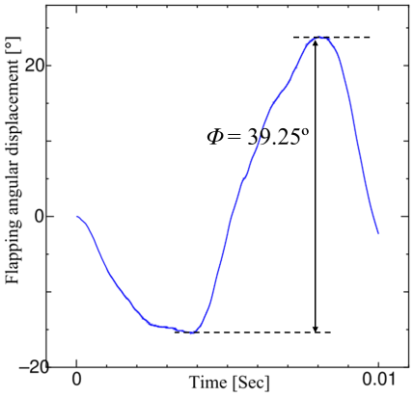

Figure 3: Time history of flapping angular displacement

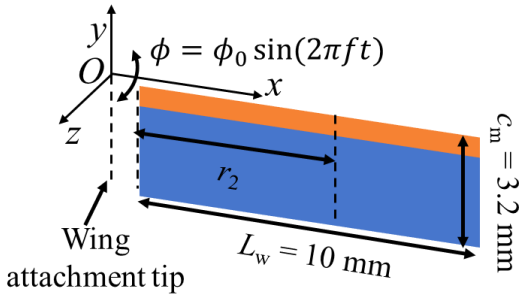

Figure 4: Problem setup for FSI analysis

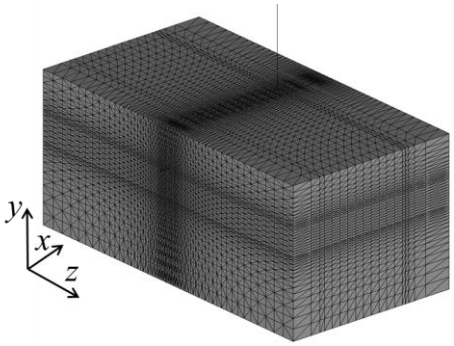

Figure 5: Fluid mesh in 3-dimension

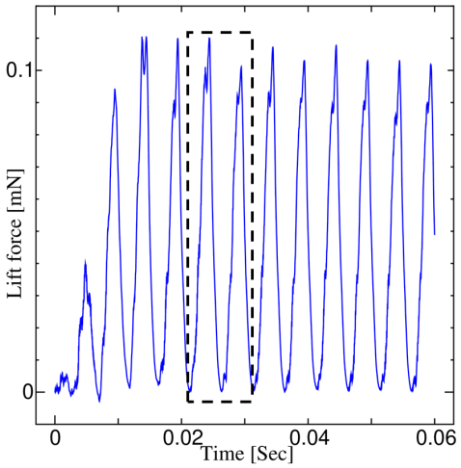

Figure 6: Lift force time history and mean value is obtained for a cycle enclosed by dash line

5. Acknowledgment

This work was supported by JSPS KAKENHI Grant Number 20H04199. We appreciate the support from Toray Industries, Inc.

References

[1] R. J. Wood: *IEEE Transactions on Robotics*, 24 (2008), 341–347.

[2] A. Bontemps et al.: *Smart Material and Structures*, 22 (2013), 014008–20.

[3] D. Ishihara: *Fluids*, 7 (2022), 7010026–20.

[4] D. Ishihara et al.: *Bioinspiration and Biomimetics*, 9 (2014), 046009–23.

[5] Rashmikant et al.: *Engineering Research express*, 3 (2021) 045006–25.

[6] Rashmikant et al.: *Computers and Structures*, (appear in September 2022), 20 pages.

JSST 2022

Fluid-structure interaction design of the polymer micromachined insect-inspired flapping wings

Vinay Shankar[1,], Minato Onishi[2,], Daisuke Ishihara[3,*]

[1, 2, 3*]Department of Intelligent and control systems, Kyushu Institute of Technology,

*ishihara.daisuke399@mail.kyutech.jp

Abstract. An insect-inspired flapping-wing nano air vehicle (FWNAVs) can use the fluid-structure interaction (FSI) to create the characteristic motion of the flapping wing. Computational approaches for FSI will be needed to analyze the aerodynamic performance because the insect-inspired micro wing concept is a complex system, so FSI is necessary to treat these complex interaction systems. In this research, FSI design approach for a micro wing where all the material used will be polymer is presented as a case study based on the previous study where a micro wing consists of leading-edge made up of single crystal silicon, wing membrane, and plate spring is made up of polymer. This FSI design approach consists of direct numerical modeling of the strongly coupled FSI, the dynamic similarity framework, and the design window (DW) search. It leads to an insect-inspired micro flapping wing with the 2.5-dimensional structure designed using the FSI design approach that gives frequency response function for stroke angle and lift force. The result demonstrates that the FSI design approach will be suitable for designing the micro wings of FWNAVs.

Keywords: fluid-structure interaction design, flapping wing micro air vehicle (FWNAV), 2.5-D structure, design window

1. Introduction

Insects' flight is popularly well known for the capabilities of robust maneuvering [1]. These flight capabilities have become increasingly sophisticated over a period of time [2]. Considering these capabilities and replicating these nature's solutions in engineering leads to flapping wing nano air vehicles (FWNAVs). In the recent past, the insect-inspired mimetic wing with robust aerial maneuvers has attracted the interest of many researchers in the field of FWNAVs. This bio-mimetic insect wing is a multidisciplinary approach concept. Hence, FSI design approach for this insect-inspired wing is necessary which leads to computational bio-mimetics as well it reduces the mechanical complexity of the FSI.

In this research, a case study using the FSI design approach for the insect-inspired micro flapping wing with the 2.5-dimensional (2.5-D) structure is presented. A projection method using the algebraic splitting [3][4] is used to solve this problem directly. The dynamic similarity law for the FSI [5] is used as the framework for the systematic treatment

of FSI complexities. The simulation based on the direct numerical modeling for the strong coupling of the lumped flexibility model [5], and the underlying mechanism is effectively investigated, which is the basis of the FSI design. DWs are defined as the existing areas of satisfactory solutions in a design parameter space. They can adapt to changes in the design problem because because of the novelty of the bio-mimetic concept, and the formulation as a single design problem is difficult in each design process. Hence, the DW search is effective for the above-mentioned issues in the design of FWNAVs. The DW is determined such that each solution in the DW can create the sufficient lift and stroke angle to support the weight of small insects.

2. Methodology

There are two types of approaches to model these structures [6]. One is the reduced-order modeling [5], and the other is the realistic modeling. In Reference [5], the lumped flexibility model is used, where the spring encapsulates the detailed structures as the macroscopic constitutive relationship that describes their elastic mechanism. The reduced-order modeling can be incorporated in the computational FSI analysis using the current computer resources [5]. Hence, in this study, the lumped flexibility model is used.

The key of the FSI design is the accurate prediction for the 3-D strong coupling of the thin flexible flapping wing and the surrounding air flow. Here, a projection method using the algebraic splitting [3][4] solves this problem directly. The monolithic equilibrium equations and the incompressibility constraint for the fluid can be written as follows:

$$_{\mathbf{L}}\mathbf{Ma} + \mathbf{Cv} + \mathbf{N} + \mathbf{q}(\mathbf{u}) - \mathbf{Gp} = \mathbf{g}, \tag{1}$$

$$_{\mathbf{T}}\mathbf{Gv} = 0, \tag{2}$$

where **M** is the mass matrix, **C** is the diffusion of matrix, **N** is the convective term vector, **G** is the divergence operator matrix, **g** is the external force vector, **q** is the internal force vector, **a**, **v**, **u** and **p** are acceleration vector, velocity vector, displacement vector, and pressure vector, respectively. Subscript T and L denote lumping of matrix and transpose of matrix.

3. Results and discussion

3.1. Problem setup

In this problem setup Figure 1, leading-edge, wing membrane, plate spring, and spring length l_s are made up of polymer material. The surrounding fluid is considered as air. The material properties of polymer and other parameter can be referred from [7].

3.2. Analysis results

The purpose of this analysis is to demonstrate the FSI design approach for a micro wing where leading-edge, wing membrane and plate spring are made up of polymer which can be

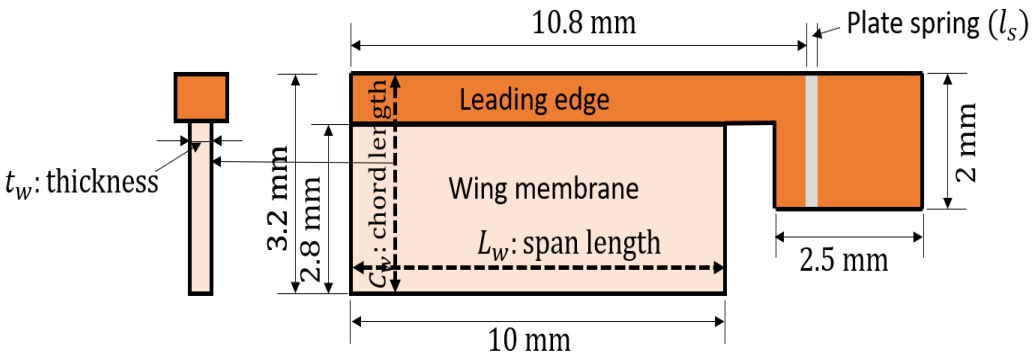

Figure 1: Problem setup of 2.5-dimensional wing

further used in future to investigate micro wing with veins [8]. Lift force is defined as the total fluid force acting on the wing in the direction perpendicular to the stroke plane.

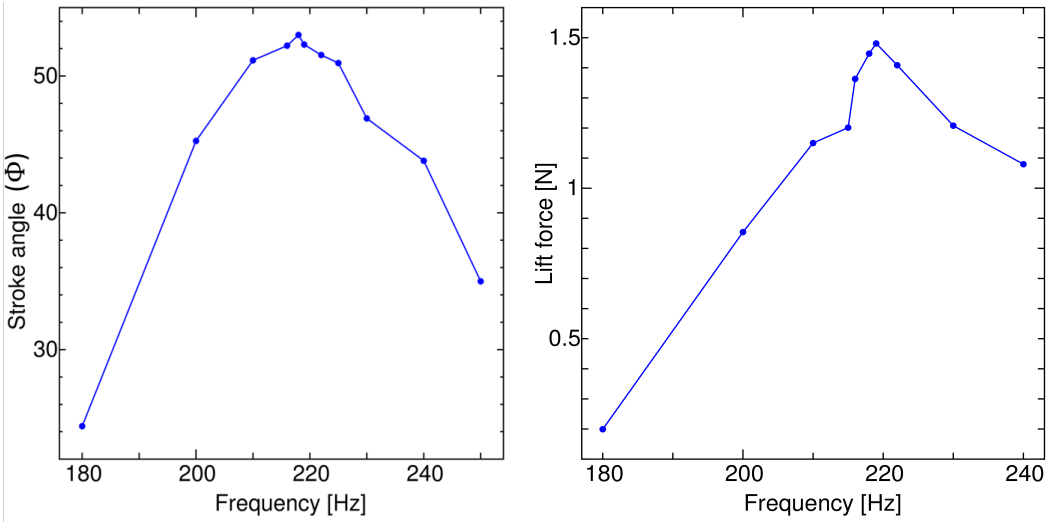

(a) Frequency response of stroke angle

(b) Frequency response of lift force

Figure 2: Frequency response functions of stroke angle and lift force

The DW search was done based on the frequency response functions (FRFs). Figure 2a shows the FRF for the stroke angle. As shown in this Figure 2a, the stroke angle is larger than 50°approximately in the DW, which is comparable to the stroke angle in actual insects. Using the FRF for the mean lift, which is shown in Figure 2b, the DW is given as the flapping frequency area ranging from 200Hz to 240Hz approximately. This means that the the proposed wing using any frequency in this DW generates the sufficient lift to support the weight of the small fly. From the above results, it clearly demonstrates that this micro wing is suitable for the possibility to achieve a micro flapping wing for FWNAVs where all

materials used will be polymer.

4. Conclusions

In this research, a computational approach for 2.5-D FSI design of insect-inspired micro flapping wings were investigated. This approach consists of the simulation based on the direct numerical modeling of the strongly coupled FSI. Here, a projection method using the algebraic splitting was used to solve this problem directly. The results shows that the proposed wing using any frequency in this DW generates the sufficient stroke angle and lift to support the weight of the small fly. Hence, FSI design approach will be suitable for designing the micro wings of FWNAVs.

In future work, wing membrane with veins will be designed and investigated, further this wing will be fabricated using the polymer micromachining technique. Hence, this proposed research will give insight and help to achieve polymerised micro wing which will support the weight of small fly.

5. Acknowledgement

This research was supported by the Japan Society for the Promotion of Science under KAKENHI Grant No. 20H04199.

References

[1] C. P. Ellington: *Phil. Trans. R. Soc. Lond. B*, 305 (1984), 41–78.

[2] A. K. Brodsky: *Oxford Science Publication*, (1994)

[3] D. Ishihara et al.: *Int. J. Numer. Methods Eng.*, 64 (2005), 167–203.

[4] D. Ishihara et al.: *Comput. Modeling Eng. Sci.*, 101 (2014), 421–440.

[5] D. Ishihara et al.: *J. Exp. Biol.*, 212 (2009), 1–10.

[6] R. J. Wootton et al.: *Philos. Trans. R. Soc. Lond.*, B358 (2003), 1577–1587.

[7] D. Ishihara: *Fluids*, 7, 26 (2022).

[8] V. Shankar et al.: *The 17th IEEE NEMS*, (2022).

High-Speed and High-Precision Eigen frequencies Control Technology Using Energy Density

Toshie Sasaki[1], Ichiro Hagiwara[1*]

[1]Meiji Institute for Advanced Study of Mathematical Sciences,Meiji University

*ihagi@meiji.ac.jp

Abstract. The problem of damage or death of fruits,vegitables,cells,and blood during transportation has not yet been solved. Presumably the biggest factor in these situations is a mortal vibration frequency band. In this study, we will examine the basic issues in moving the resonance frequencies to solve the above-mentioned problems. Therefore, in this paper, we propose a new method named "Energy Density Topology Optimization Method" which has been discovered by returning to the origin of vibration where the eigen frequency is determined by equivalent stiffness and equivalent mass.

Keywords: Space Filling, Control of Plural Eigenfrequencies, Origami safe carrier box, Index of generalized eigenfrequency, Energy Density Topology Optimization Method

1. Introduction

Fruits, vegetables, blood, induced pluripotent stem(iPS) cells, bottles of liquor, and wine have frequency bands that are susceptible to damage when they are being transported. By designing a box that does not have an eigenfrequency within these frequency bands,the items can be safely transported. In addition, when a car is running, if the vibration between 5 Hz and 10 Hz is large, passengers are likely to get car sickness. Therefore, automobile companies design seats such that the resonant frequency of the floor structure system does not lie in this frequency band. In this way, it is necessary for product development and manufacturing to control the eigen frequency.

Eigen frequency optimization had been mainstream in topology optimization [1]-[5]. However, in this method (1) Changing multiple eigen frequencies simultaneously, (2) Controling significantly, (3) Controlling a part of eigen frequencies lower and controlling other eigen frequencies high; these three controling were very difficult. In the eigenvalue problem involving stiffness and mass, if the plate thickness of an arbitrary part is increased, the frequency may be in the case of increase and in the case of decrease, and it was difficult to

blindly apply the topology optimization method.

Therefore, trying to control the frequency by returning to the origin of the vibration that the eigenfrequency is determined by the equivalent stiffness and equivalent mass, and the frequencies lower by making a hole in the spring part, or the frequencies raise by making a hole in the mass part, the ideal structure can be obtained [6]-[8]. This is the “Energy Density Topology Change Method” that we proposed in 2021.

2. Transfer of eigen frequencies on a flat plate

Here, we present the algorithm of moving eigen frequencies using the “Energy Density Topology Change Method” through a flat plate as a material of origami transport box. The size of the flat plate is 420 mm × 300 mm and its thickness 1 mm. The material of the plate is cardboard, which has a density of 256.9 kg/m^3, Young’s modulus of 0.664 Gpa, and Poisson’s ratio of 0.34. Our goal is to avoid eigen frequencies ranging from 7 Hz to 17 Hz. To ensure that there is no adverse effect on other modes while examining, we make holes at the position of spring area on the seventh and eighth order, and at the position of mass area on the ninth and tenth order. Figure1 depicts an example of using the algorithm to control the eigen frequency.

The flat plate was analyzed by unrestraint condition. The first - sixth order is the rigid body mode. We calculated the eigen frequency of the seventh - tenth order. The initial eigen frequencies were 8.24 Hz, 9.38 Hz, 19.14 Hz, and 19.34 Hz. Fig. 1 displays the results of eigen value analysis and the energy density of each mode: the kinetic energy density distribution (mass part Yellow) is the upper part and the strain energy density distribution (spring part Green) is the bottom part. The energy density is indicated by the color bar on the right, with the lowest in navy blue and the highest in red. For each eigen frequency of the seventh - tenth order, we examined the position of the hole or the reinforcing from the energy density distribution. Next, to lower the seventh and eighth orders, holes were made in the spring part of the central that overlapping of the seventh and eighth orders. In the ninth and tenth order, it is necessary to make a hole in the mass part, however, the mass part becomes the end of the flat plate, the shape may change if a hole is provided here. In addition, even if the shape does not change, the strength is weak and it is not practical; therefore, holes were not made in the mass part.

The shape is as shown in Step 1 of Fig.1, and the next, it is performed modal value analysis. The eigen frequencies were 5.49 Hz,7.17 Hz,16.26 Hz and 18.01 Hz. As expected, the seventh- and eighth-order eigen frequencies decreased although the ninth and tenth order decreased too. Therefore,the eigen frequencies of the ninth and tenth orders increased by making a hole on

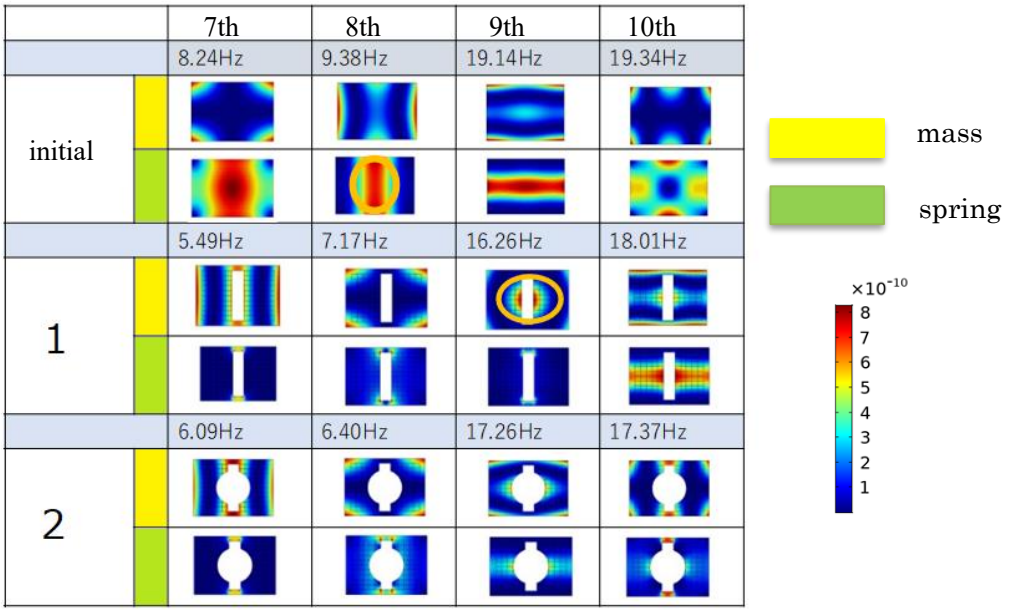

Fig.1 An example of using "Energy Density Topology Change Method" to control the eigen frequency.

the ninth order mass, and the final shape is shown in Step 2 of Fig. 1. The eigen frequencies were 6.09 Hz, 6.40 Hz, 17.26 Hz,and 17.37 Hz. This indicates that the goal was achived.

3. Conclusion

In the structural-design field, there is a desire to change multiple eigen frequencies simultaneously and sometimes significantly. The most useful method for realizing this is topology optimization, which has been significantly studied. However, applying this method to the actual design is difficult. Therefore we have developed a new algorithm called the “Energy Density Topology Change Method” that demonstrates excellent performance in addressing the problem of eigen frequency optimization and indicates that a practical solution can be obtained.

In order for these new technologies to gain understanding in research areas and development sites, preparing an environment where the system can be realized is necessary. By systematizing the verification of the algorithm, efficiently identifying the positions of the hole and reinforcement was possible;therefore, engineers and researchers in the field can perform plural eigen frequencies control in a short time. It will be important for more people to understand the energy density topology optimization method using the developed system. In the future, it is important to move eigen frequencies by combining the proposed method with the “Response Surface Method”.

References

[1] M. P. Bendsoe, N. Kikuchi, : Generating optimal topologies in structural design using a homogenization method, Comput. Meths Appl. Mech. Engrg., **71**, (1988), pp. 197 -224.

[2] N. Kikuchi, Optimum theory based on homogenization method, JSIAM 3(1), 2 -26, 1993 (in Japanese).

[3] Z. D. Ma, N. Kikuchi, H. C. Cheng, I.Hagiwara, Development of Structural Optimization Method for Vibration Reduction (1st Report, Structural Optimization Theory Using the Homogenization Method), Series C, Vol.59, No.562(1993-6), pp. 1730 -1736(in Japanese)

[4] L. H. Tenek, I. Hagiwara , Static and Vibrational Shapeand Topology Optimization Using Homogenization and Mathematical Programming, Comput. Methodsin Appl. Mech. Engrg. , Vol.109 (1993-10), pp. 143 -154.

[5] L.H. Tenek, I. Hagiwara, Optimal Plate and Shell Topologies Using Thickness Distribution or Homogenization,
Comput. Methods in Appl.Mech.Engrg. Vol.115(1994-7) Nos.1 -2, pp. 111 -124.

[6] T. Sasaki and I. Hagiwara ," The development of the new optimization method and application to the Carrier Box", JSME, CMD2021 Proceedings (2021-9).

[7] T. Sasaki and I. Hagiwara ,"Development of a New Topology Optimization and Its Application to Origami Carrier Box (Optimization Method for Eigenfrequency)", JSME, Dynamics and Design Conference 2021 Proceedings (2021-9).

[8] T. Sasaki and I. Hagiwara, "Vibration control of origami structure focusing on energy density", JSIAM Proceedings (2021-9).

Out-of-plane stiffness and strength of bio-inspired honeycomb cores with extra hollows

Sachiko Ishida[1*], Mudong Li[1], Kazuya Saito[2]

[1] Department of Mechanical Engineering, Meiji University

[2] Faculty of Design, Kyushu University

*sishida@meiji.ac.jp

Abstract. In this study, we numerically investigated the out-of-plane stiffness and strength of the new honeycomb cores with extra hollows inspired by a microstructure observed in beetle elytron plates. We summarized the relationship between the configuration and out-of-plane properties of the bio-inspired honeycomb cores including theoretical estimation. The contribution of the extra hollows to the properties are finally discussed.

Keywords: Honeycomb cores, Structural material, Composite material, Finite element analysis, Biomimetics

1. Introduction

Honeycomb cores are widely used as core material of sandwich structures in industrial applications owing to the light weight, high strength and high energy absorbing capability. Chen et al. [1] studied bio-inspired honeycomb cores, on which small extra hollows were embedded on the corners of hexagonal cores in order to improve compressive properties of the cores. However, general manufacturing methods were not applicable to their honeycomb cores due to geometrical constraints of the extra hollows so that they were only 3D-printed. To overcome the above shortcoming, we designed new bio-inspired honeycomb cores on which the general corrugation method is applicable, and numerically investigated that the out-of-plane properties were improved compared to the conventional honeycomb cores [2, 3]. In this study, we summarize the relationship between the configuration and out-of-plane properties of the bio-inspired honeycomb cores including theoretical estimation.

2. Configuration

Figure 1 shows the configuration of the bio-inspired honeycomb cores of this study [3]. We arranged square hollows in the middle of adhesive surfaces. The size of the square hollows x is fixed so as to be equal to the width of the adhesive surfaces such that

$$x = \frac{1}{\sqrt{3}\left(2+\sqrt{2}\right)}a \tag{1}$$

where a is the size of primary core. The thickness of adhesive surfaces is expressed as $2t$, where t is the thickness of the single surface.

3. Results and Discussion

Aluminum alloy with bilinear plasticity was applied on the bio-inspired honeycomb cores. We performed numerical computation on ANSYS by inputting compressive displacements on the top of the bio-inspired honeycomb cores with sufficiently low constant speed and obtained reaction forces on the bottom of the cores which were simply supported. Figure 3 shows the force-displacement diagram of the both bio-inspired and conventional honeycomb cores with equivalent core size; $a = 12.7$ mm, $t = 0.0762$ mm and $h = 20.0$ mm. The peak loads were observed at the beginning of the compression on the both cores, and the load of the bio-inspired cores was 1.9 times higher with 8% increase of the mass. This relationship was also described as the ultimate strength-core density diagram in Fig. 4. The ultimate strengths of the conventional honeycomb cores reasonably agreed with theoretical estimation by Kunimoto [4]. The ultimate strengths of the bio-inspired honeycomb cores were 1.5–2.0 times higher on four configurations calculated in this study. The large improvement of the ultimate strengths could provide a considerable effect to cancel a negative effect by increase of the core density. As for the out-of-plane stiffness of the cores in linear deformation region, the increase on the bio-inspired cores was 8%, which was simply equivalent with the increase of the mass or core density.

The size of the square hollows x was fixed by Eq. (1), but tuning of the size could find the optimum shape for further improvement of the ultimate strength. The range $x_{\min} \leq x \leq x_{\max}$ should be determined by constraints on the fabrication, because the configuration with a small x needs a fine fabrication method and a large x leads to adhesion failure due to reduction of the adhesive surfaces.

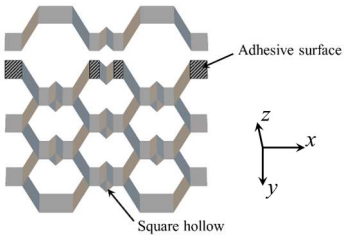

Fig. 1 Honeycomb cores with extra hollows [3]

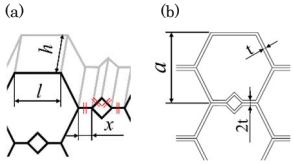

Fig. 2 Design details [3]

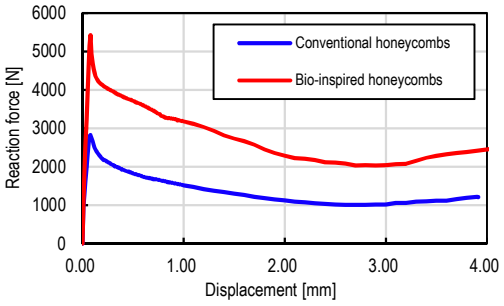

Fig. 3 Reaction force-displacement diagram ($a = 12.7$ mm, $t = 0.0762$ mm)

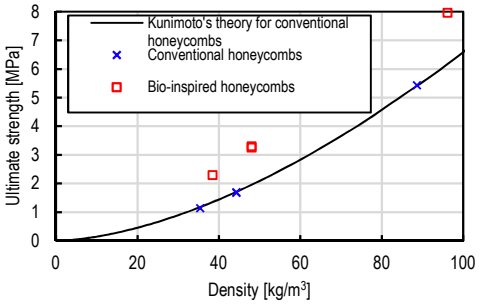

Fig. 4 Relationship between ultimate strength and core density of the honeycomb cores

4. Conclusions

In this study, we obtained the relationships between the core configuration and out-of-plane properties of the bio-inspired and conventional honeycomb cores. The increase of the stiffness of the bio-inspired cores was equivalent to that of the mass, while the strength was 1.5 to 2 times improved on the configurations studied here. Since the reaction force of the bio-inspired honeycomb cores were higher at any displacements in the compression process, the bio-inspired cores are promissing as energy absorbers.

Acknowledgement

This study is financially supported by JSPS KAKENHI Grant No. 21K03755.

References

[1] J. Chen, X. Zhang, Y. Okabe, K. Saito, Z. Guo, L. Pan: The deformation mode and strengthening mechanism of compression in the beetle elytron plate, *Material and Design*, 131 (2017), 481–486.

[2] K. Saito, S. Ishida, M. Li: Method for producing honeycomb structure and honeycomb structure (in Japanese), Published patent No. JP2022-075629.

[3] M. Li, S. Ishida, K. Saito: Numerical evaluation on the out-of-plane properties of bio-inspired honeycomb cores with extra hollows, *Proceedings of the 40th JSST Annual International Conference on Simulation Technology* (2021), 35–38.

[4] T. Kunimoto, H. Yamada: Study on buffer characteristic of the honeycomb sandwich construction under dynamic loading (in Japanese), *Journal of Japan Institute of Light Metals*, 37:5 (1987), 327–331.